

MAY 2019

**AJNR**

VOLUME 40 • PP 757-926

# AJNR

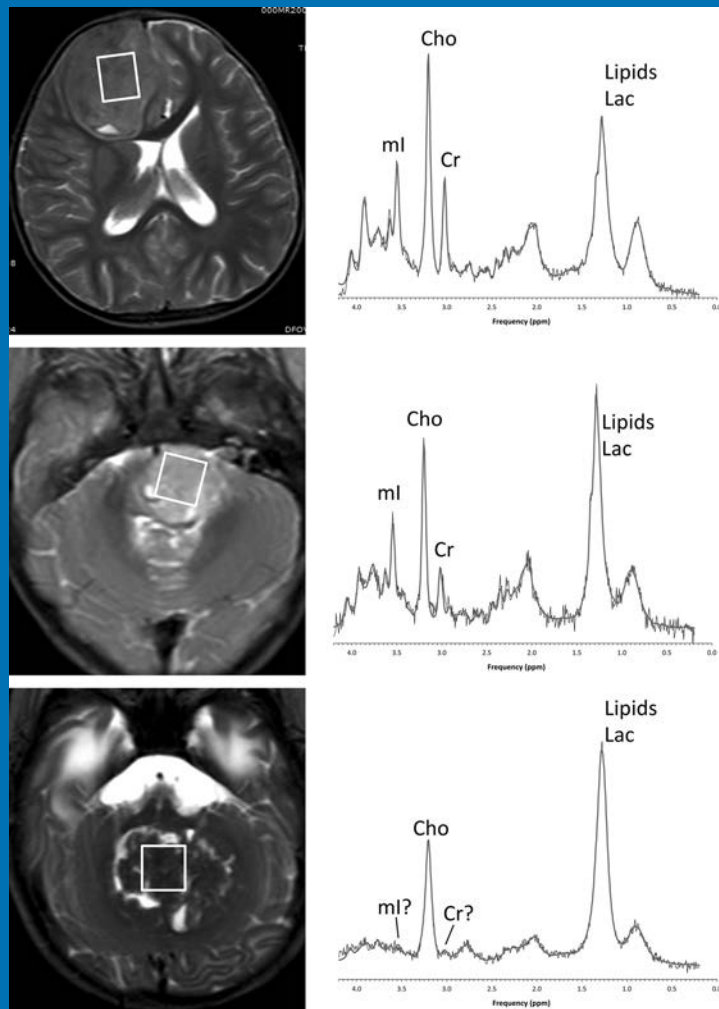
## AMERICAN JOURNAL OF NEURORADIOLOGY

MAY 2019  
VOLUME 40  
NUMBER 5  
WWW.AJNR.ORG

THE JOURNAL OF DIAGNOSTIC AND  
INTERVENTIONAL NEURORADIOLOGY

Predicting motor outcome in acute intracerebral hemorrhage  
Intravoxel incoherent motion MR imaging of pediatric  
intracranial tumors  
Lumbar stenosis severity and response to epidural  
corticosteroid versus lidocaine injections

Official Journal ASNR • ASFNR • ASHNR • ASPNR • ASSR





# ONE AND DONE

## INDICATIONS FOR USE:

The WEB Aneurysm Embolization System is indicated for use at the middle cerebral artery (MCA) bifurcation, internal carotid artery (ICA) terminus, anterior communicating artery (AComm) complex, or basilar artery apex for the endovascular treatment of adult patients with saccular, wide neck bifurcation intracranial aneurysms with dome diameter from 3 mm to 10 mm and either neck size 4 mm or greater or the dome-to-neck ratio is greater than 1 and less than 2.

The WEB Aneurysm Embolization System is contraindicated for patients with known bacterial infection that may interfere with or negatively affect the implantation procedure and patients with known hypersensitivity to nickel. For complete indications, contraindications, potential complications, warnings, precautions, and instructions, see instructions for use (IFU provided with the device).

The VIA® Catheter is intended for the introduction of non-liquid interventional devices (such as stents/\_ow diverters) and infusion of diagnostic (such as contrast media) or non-liquid therapeutic agents into the neuro, peripheral, and coronary vasculature. The VIA Catheter is contraindicated for use with liquid embolic materials, such as n-butyl 2-cyanoacrylate or ethylene vinyl alcohol & DMSO (dimethyl sulfoxide). The VIA Catheter is contraindicated for use in the pediatric population (<22 yrs of age).

Caution: Federal law restricts these devices to sale by or on the order of a physician.

# WEB<sup>®</sup>

## Aneurysm Embolization System

MicroVention<sup>®</sup> delivers the first intrasaccular solution for wide neck bifurcation aneurysms.

The **world leader**  
and **first**  
**PMA - approved**  
**device** in an  
important new  
category of  
intrasaccular  
flow disruptors.

The WEB<sup>®</sup> System is a safe  
and effective single-device  
solution for treating wide  
neck bifurcation aneurysms.



SL Device



SLS Device

Contact a MicroVention sales associate to learn more  
about integrating the WEB<sup>®</sup> device into your practice.



MicroVention Worldwide  
Innovation Center

35 Enterprise  
Aliso Viejo, CA 92656 USA

MicroVention UK Limited

MicroVention Europe, S.A.R.L.

MicroVention Deutschland GmbH

[microvention.com](http://microvention.com)

PH +1.714.247.8000

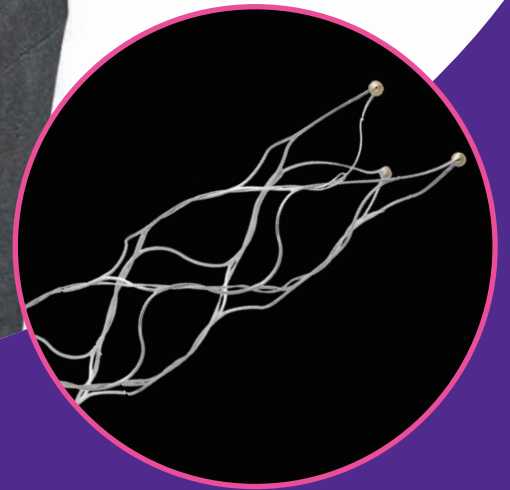
PH +44 (0) 191 258 6777

PH +33 (1) 39 21 77 46

PH +49 211 210 798-0

**stryker**

Now you have **24 hours** to make a lifetime of difference in stroke patients like Nora



The Trevo Retriever is the only device cleared to **reduce disability in stroke patients up to 24 hours** from time last seen well.

For more information, visit [strykerneurovascular.com/trevo24hours](http://strykerneurovascular.com/trevo24hours)

**Trevo<sup>®</sup> XP**  
PROVUE RETRIEVER

Copyright © 2018 Stryker  
AP002078 v1.0

## Neuroform Atlas® Stent System

See package insert for complete indications, contraindications, warnings and instructions for use.

**Humanitarian Device.** Authorized by Federal law for use with neurovascular embolic coils in patients who are ≥ 18 years of age for the treatment of wide neck, intracranial, saccular aneurysms arising from a parent vessel with a diameter of ≥ 2 mm and ≤ 4.5 mm that are not amenable to treatment with surgical clipping. Wide neck aneurysms are defined as having a neck ≥ 4 mm or a dome-to-neck ratio < 2. The effectiveness of this device for this use has not been demonstrated.

### INDICATIONS FOR USE

The Neuroform Atlas® Stent System is indicated for use with neurovascular embolic coils in patients who are ≥ 18 years of age for the treatment of wide neck, intracranial, saccular aneurysms arising from a parent vessel with a diameter of ≥ 2 mm and ≤ 4.5 mm that are not amenable to treatment with surgical clipping. Wide neck aneurysms are defined as having a neck ≥ 4 mm or a dome-to-neck ratio of < 2.

### CONTRAINDICATIONS

Patients in whom antiplatelet and/or anticoagulation therapy is contraindicated.

### POTENTIAL ADVERSE EVENTS

The potential adverse events listed below, as well as others, may be associated with the use of the Neuroform Atlas® Stent System or with the procedure. Allergic reaction to nitinol metal and medications. Aneurysm perforation or rupture. Coil herniation through stent into parent vessel. Death. Embolus. Headache. Hemorrhage. In-stent stenosis, infection, ischemia, Neurological deficit/intracranial sequelae. Pseudoaneurysm, Stent fracture, Stent migration/embolization, Stent misplacement, Stent thrombosis, Stroke, Transient ischemic attack, Vasospasm, Vessel occlusion or closure, Vessel perforation/rupture, Vessel dissection, Vessel trauma or damage, Vessel thrombosis, Visual impairment, and other procedural complications including but not limited to anesthetic and contrast media risks, hypotension, hypertension, access site complications.

### WARNINGS

- Contents supplied STERILE using an ethylene oxide (EO) process. Do not use if sterile barrier is damaged. If damage is found, call your Stryker Neurovascular representative.
- For single use only. Do not reuse, reprocess or resterilize. Reuse, reprocessing or resterilization may compromise the structural integrity of the device and/or lead to device failure which, in turn, may result in patient injury, illness or death. Reuse, reprocessing or resterilization may also create a risk of contamination of the device and/or cause patient infection or cross-infection, including, but not limited to, the transmission of infectious disease(s) from one patient to another. Contamination of the device may lead to injury, illness or death of the patient.
- After use, dispose of product and packaging in accordance with hospital, administrative and/or local government policy.
- This device should only be used by physicians who have received appropriate training in interventional neuroradiology or interventional radiology and preclinical training on the use of this device as established by Stryker Neurovascular.
- Select a stent size (length) to maintain a minimum of 4 mm on each side of the aneurysm neck along the parent vessel. An incorrectly sized stent may result in damage to the vessel or stent migration. Therefore, the stent is not designed to treat an aneurysm with a neck greater than 22 mm in length.
- If excessive resistance is encountered during the use of the Neuroform Atlas® Stent System or any of its components at any time during the procedure, discontinue use of the stent system. Continuing to move the stent system against resistance may result in damage to the vessel or a system component.
- Persons allergic to nickel titanium (Nitinol) may suffer an allergic response to this stent implant.
- Purge the system carefully to avoid the accidental introduction of air into the stent system.
- Confirm there are no air bubbles trapped anywhere in the stent system.

### CAUTIONS / PRECAUTIONS

- Federal Law (USA) restricts this device to sale by or on the order of a physician.
- Use the Neuroform Atlas Stent System prior to the "Use By" date printed on the package
- Carefully inspect the sterile package and Neuroform Atlas Stent System prior to use to verify that neither has been damaged during shipment. Do not use kinked or damaged components; contact your Stryker Neurovascular representative.
- The stent delivery microcatheter and the Neuroform Atlas Stent delivery wire should not be used to recapture the stent.
- Exercise caution when crossing the deployed stent with adjunctive devices.
- After deployment, the stent may foreshorten from up to 6.3%.
- The max OD of the coiling microcatheter should not exceed the max OD of the stent delivery microcatheter.
- Standard interventional devices with distal tips > 1.8 F may not be able to pass through the interstices of the stent.
- Safety of the Neuroform Atlas Stent System in patients below the age of 18 has not been established.
- In cases where multiple aneurysms are to be treated, start at the most distal aneurysm first.

### MAGNETIC RESONANCE IMAGING (MRI)

#### Safety Information Magnetic Resonance Conditional

Non-clinical testing and analysis have demonstrated that the Neuroform Atlas Stent is MR Conditional alone, or when overlapped with a second stent, and adjacent to a Stryker Neurovascular coil mass. A patient with the Neuroform Atlas Stent can be safely scanned immediately after placement of this implant, under the following conditions:

- Static magnetic field of 1.5 and 3.0 Tesla
- Maximum spatial gradient field up to 2500 Gauss/cm (25 Tesla/m)
- Maximum MRI system reported whole body averaged specific absorption rate of 2 W/kg (Normal Operating Mode) and head averaged specific absorption rate of 3.2 W/kg

Under the scan conditions defined above, the Neuroform Atlas Stent is expected to produce a maximum temperature rise of 4°C after 15 minutes of continuous scanning. The Neuroform Atlas Stent should not migrate in this MRI environment.

In non-clinical testing, the image artifact caused by the device extends approximately 2 mm from the Neuroform Atlas Stent when imaged with a spin echo pulse sequence and 3 Tesla MRI System. The artifact may obscure the device lumen. It may be necessary to optimize MRI imaging parameters for the presence of this implant.

## Excelsior® XT-17™ Microcatheter

See package insert for complete indications, contraindications, warnings and instructions for use.

### INTENDED USE / INDICATIONS FOR USE

Stryker Neurovascular's Excelsior XT-17 Microcatheters are intended to assist in the delivery of diagnostic agents, such as contrast media, and therapeutic agents, such as occlusion coils, into the peripheral, coronary and neurovasculature.

### CONTRAINDICATIONS

None known.

### POTENTIAL ADVERSE EVENTS

Potential adverse events associated with the use of microcatheters or with the endovascular procedures include, but are not limited to: access site complications, allergic reaction, aneurysm perforation, aneurysm rupture, death, embolism (air, foreign body, plaque, thrombus), hematoma, hemorrhage, infection, ischemia, neurological deficits, pseudoaneurysm, stroke, transient ischemic attack, vasospasm, vessel dissection, vessel occlusion, vessel perforation, vessel rupture, vessel thrombosis

### WARNINGS

- The accessories are not intended for use inside the human body.
- Limited testing has been performed with solutions such as contrast media, saline and suspended embolic particles. The use of these microcatheters for delivery of solutions other than the types that have been tested for compatibility is not recommended. Do not use with glue or glue mixtures.
- Carefully inspect all devices prior to use. Verify shape, size and condition are suitable for the specific procedure.
- Exchange microcatheters frequently during lengthy procedures that require extensive guidewire manipulation or multiple guidewire exchanges.
- Never advance or withdraw an intravascular device against resistance until the cause of the resistance is determined by fluoroscopy. Movement of the microcatheter or guidewire against resistance could dislodge a clot, perforate a vessel wall, or damage microcatheter and guidewire. In severe cases, tip separation of the microcatheter or guidewire may occur.
- Contents supplied STERILE using an ethylene oxide (EO) process. Do not use if sterile barrier is damaged. If damage is found, call your Stryker Neurovascular representative.
- For single use only. Do not reuse, reprocess or resterilize. Reuse, reprocessing or resterilization may compromise the structural integrity of the device and/or lead to device failure which, in turn, may result in patient injury, illness or death. Reuse, reprocessing or resterilization may also create a risk of contamination of the device and/or cause patient infection or cross-infection, including, but not limited to, the transmission of infectious disease(s) from one patient to another. Contamination of the device may lead to injury, illness or death of the patient.
- After use, dispose of product and packaging in accordance with hospital, administrative and/or local government policy.
- These devices are intended for use only by physicians trained in performing endovascular procedures.
- Inspect product before use for any bends, kinks or damage. Do not use a microcatheter that has been damaged. Damaged microcatheters may rupture causing vessel trauma or tip detachment during steering maneuvers.
- The shipping mandrel is not intended for use inside the human body.
- Discontinue use of microcatheter for infusion if increased resistance is noted. Resistance indicates possible blockage. Remove and replace blocked microcatheter immediately. DO NOT attempt to clear blockage by over-pressure. Doing so may cause the microcatheter to rupture, resulting in vascular damage or patient injury.
- Do not exceed 2.0/0 kPa (300 psi) infusion pressure. Excessive pressure could dislodge a clot, causing thromboemboli, or could result in a ruptured microcatheter or severed tip, causing vessel injury.

### CAUTIONS / PRECAUTIONS

- To reduce the probability of coating damage in tortuous vasculature, use a guide catheter with a minimum internal diameter as specified in Table 1 above, and is recommended for use with Stryker Neurovascular hydrophilically coated microcatheters.
- To control the proper introduction, movement, positioning and removal of the microcatheter within the vascular system, users should employ standard clinical angiographic and fluoroscopic practices and techniques throughout the interventional procedure.
- Exercise care in handling of the microcatheter during a procedure to reduce the possibility of accidental breakage, bending or kinking.
- Use the product prior to the "Use By" date printed on the label.
- Limited testing indicates that Excelsior XT-17 Microcatheter is compatible with Dimethyl Sulfoxide (DMSO). The compatibility of Excelsior XT-17 Microcatheter with individual agents suspended in DMSO has not been established.
- Federal Law (USA) restricts this device to sale by or on the order of a physician.
- Wet dispenser coil or packaging tray and hydrophilically coated outer shaft of microcatheters prior to removal from packaging tray. Once the microcatheter has been wetted, do not allow to dry.
- The packaging mandrel is not intended for use. The packaging mandrel is not intended for use inside the human body.
- Check that all fittings are secure so that air is not introduced into guide catheter or microcatheter during continuous flush.
- In order to achieve optimal performance of Stryker Neurovascular Microcatheters and to maintain the lubricity of the Hydroline® Coating surface, it is critical that a continuous flow of appropriate flush solution be maintained between the Stryker Neurovascular Microcatheter and guide catheter, and the microcatheter and any intraluminal device. In addition, flushing aids in preventing contrast crystal formation and/or clotting on both the intraluminal device and inside the guide catheter and/or the microcatheter lumen.
- Do not position microcatheter closer than 2.54 cm (1 in) from the steam source. Damage to the microcatheter may result.
- Excessive tightening of a hemostatic valve onto the microcatheter shaft may result in damage to the microcatheter. Removing the peel away introducer without a guidewire inserted in the microcatheter lumen might result in damage to the microcatheter shaft.
- To facilitate microcatheter handling, the proximal portion of the microcatheter does not have the hydrophilic surface. Greater resistance may be encountered when this section of the microcatheter is advanced into the RHV.

## Excelsior® SL-10™ Microcatheter

See package insert for complete indications, contraindications, warnings and instructions for use.

### INTENDED USE / INDICATIONS FOR USE

Stryker Neurovascular Excelsior SL-10 Microcatheter is intended to assist in the delivery of diagnostic agents, such as contrast media, and therapeutic agents, such as occlusion coils, into the peripheral, coronary and neurovasculature.

### CONTRAINDICATIONS

None known.

### POTENTIAL ADVERSE EVENTS

- Potential adverse events associated with the use of microcatheters or with the endovascular procedures include, but are not limited to: access site complications, allergic reaction, aneurysm perforation, aneurysm rupture, death, embolism (air, foreign body, plaque, thrombus), hematoma, hemorrhage, infection, ischemia, neurological deficits, pseudoaneurysm, stroke, transient ischemic attack, vessel dissection, vessel occlusion, vessel perforation, vessel rupture, vessel thrombosis
- Contents supplied STERILE using an ethylene oxide (EO) process. Do not use if sterile barrier is damaged. If damage is found, call your Stryker Neurovascular representative.
- For single patient use only. Do not reuse, reprocess or resterilize. Reuse, reprocessing or resterilization may compromise the structural integrity of the device and/or lead to device failure which, in turn, may result in patient injury, illness or death. Reuse, reprocessing or resterilization may also create a risk of contamination of the device and/or cause patient infection or cross-infection, including, but not limited to, the transmission of infectious disease(s) from one patient to another. Contamination of the device may lead to injury, illness or death of the patient.
- After use, dispose of product and packaging in accordance with hospital, administrative and/or local government policy.
- **These devices are intended for use only by physicians trained in performing endovascular procedures.**
- Limited testing has been performed with solutions such as contrast media, saline and suspended embolic particles. The use of these catheters for delivery of solutions other than the types that have been tested for compatibility is not recommended. Do not use with glue or glue mixtures.
- The accessories are not intended for use inside the human body.
- Carefully inspect all devices prior to use. Verify shape, size and condition are suitable for the specific procedure.
- Exchange microcatheters frequently during lengthy procedures that require extensive guidewire manipulation or multiple guidewire exchanges.
- Never advance or withdraw an intravascular device against resistance until the cause of the resistance is determined by fluoroscopy. Movement of the microcatheter or guidewire against resistance could dislodge a clot, perforate a vessel wall, or damage microcatheter and guidewire. In severe cases, tip separation of the microcatheter or guidewire may occur.
- Inspect product before use for any bends, kinks or damage. Do not use a microcatheter that has been damaged. Damaged microcatheters may rupture causing vessel trauma or tip detachment during steering maneuvers.
- Shipping mandrel is not intended for use inside the human body.
- Discontinue use of microcatheter for infusion if increased resistance is noted. Resistance indicates possible blockage. Remove and replace blocked microcatheter immediately. DO NOT attempt to clear blockage by over-pressure. Doing so may cause the microcatheter to rupture, resulting in vascular damage or patient injury.
- Do not exceed 2.0/0 kPa (300 psi) infusion pressure. Excessive pressure could dislodge a clot, causing thromboemboli, or could result in a ruptured microcatheter or severed tip, causing vessel injury.

### CAUTIONS / PRECAUTIONS

- Federal Law (USA) restricts this device to sale by or on the order of a physician.
- To facilitate microcatheter handling, the proximal portion of the microcatheter does not have the hydrophilic surface. Greater resistance may be encountered when this section of the microcatheter is advanced into the RHV.
- Exercise care in handling of the microcatheter during a procedure to reduce the possibility of accidental breakage, bending or kinking.
- To reduce the probability of coating damage in tortuous vasculature, use a guide catheter with a minimum internal diameter that is ≥ 1.00 mm (0.038 in) and is recommended for use with Stryker Neurovascular hydrophilically coated microcatheters.
- To control the proper introduction, movement, positioning and removal of the microcatheter within the vascular system, users should employ standard clinical angiographic and fluoroscopic practices and techniques throughout the interventional procedure.
- Flush dispenser coil of hydrophilically coated microcatheters prior to removal from dispenser coil. Once the microcatheter has been wetted, do not allow to dry. Do not reinsert the microcatheter into dispenser coil.
- Do not position microcatheter closer than 2.54 cm (1 in) from the steam source. Damage to the microcatheter may result.
- Check that all fittings are secure so that air is not introduced into guide catheter or microcatheter during continuous flush.
- In order to achieve optimal performance of Stryker Neurovascular Microcatheters and to maintain the lubricity of the Hydroline® Coating surface, it is critical that a continuous flow of appropriate flush solution be maintained between the Stryker Neurovascular Microcatheter and guide catheter, and the microcatheter and any intraluminal device. In addition, flushing aids in preventing contrast crystal formation and/or clotting on both the intraluminal device and inside the guide catheter and/or the microcatheter lumen.
- Excessive tightening of a hemostatic valve onto the microcatheter shaft may result in damage to the microcatheter.

## Copyright © 2019 Stryker AP00243 v1.0 | Page 2 of 2

### Trevo® XP ProVue Retrievers

See package insert for complete indications, complications, warnings and instructions for use.

### INDICATIONS FOR USE

1. The Trevo Retriever is indicated for use to restore blood flow in the neurovasculature by removing thrombus for the treatment of acute ischemic stroke to reduce disability in patients with a persistent, proximal anterior circulation, large vessel occlusion, and smaller core infarcts who have first received intravenous tissue plasminogen activator (IV-tPA). Endovascular therapy with the device should start within 6 hours of symptom onset.
2. The Trevo Retriever is intended to restore blood flow in the neurovasculature by removing thrombus in patients experiencing ischemic stroke within 8 hours of symptom onset. Patients who are ineligible for intravenous tissue plasminogen activator (IV-tPA) or who fail IV-tPA therapy are candidates for treatment.
3. The Trevo Retriever is indicated for use to restore blood flow in the neurovasculature by removing thrombus for the treatment of acute ischemic stroke to reduce disability in patients with a persistent, proximal anterior circulation, large vessel occlusion of the internal carotid artery (ICA) or middle cerebral artery (MCA-M1) segments with smaller core infarcts (0-50cc for age < 80 years, 0-20cc for age ≥ 80 years). Endovascular therapy with the device should start within 8-24 hours of time last seen well in patients who are ineligible for intravenous tissue plasminogen activator (IV-tPA) or who fail IV-tPA therapy.

### COMPLICATIONS

Procedures requiring percutaneous catheter introduction should not be attempted by physicians unfamiliar with possible complications which may occur during or after the procedure. Possible complications include, but are not limited to, the following: air embolism; hematoma or hemorrhage at puncture site; infection; distal embolization; pain/headache; vessel spasm; thrombosis, dissection, or perforation; emboli; acute occlusion; ischemia; intracranial hemorrhage; false aneurysm formation; neurological deficits including stroke; and death.

### COMPATIBILITY

3x20mm retrievers are compatible with Trevo® Pro 14 Microcatheters (REF 90231) and Trevo® Pro 18 Microcatheters (REF 90238). 4x20mm retrievers are compatible with Trevo® Pro 18 Microcatheters (REF 90238). 4x30mm retrievers

are compatible with Excelsior® XT-27® Microcatheters (150cm x 6cm straight REF 275081) and Trevo® Pro 18 Microcatheters (REF 90238). 6x25mm Retrievers are compatible with Excelsior® XT-27® Microcatheters (150cm x 6cm straight REF 275081). Recommended minimum vessel ID for all Retriever sizes is ≥ 2.5mm. Compatibility of the Retriever with other microcatheters has not been established. Performance of the Retriever device may be impacted if a different microcatheter is used.

Balloon Guide Catheters (such as Merit® Balloon Guide Catheter and FlowGate® Balloon Guide Catheter) are recommended for use during thrombus removal procedures.

Retrievers are compatible with the Abbott Vascular DOC® Guide Wire Extension (REF 22258).

Retrievers are compatible with Boston Scientific Rotating Hemostatic Valve (Ref 412142).

### SPECIFIC WARNINGS FOR INDICATION 1

- The safety and effectiveness of the Trevo Retrievers in reducing disability has not been established in patients with large core infarcts (i.e. ASPECTS ≤ 7). There may be increased risks, such as intracerebral hemorrhage, in these patients.
- The safety and effectiveness of the Trevo Retrievers in reducing disability has not been established or evaluated in patients with occlusions in the posterior circulation (e.g., basilar or vertebral arteries) or for more distal occlusions in the anterior circulation.

### SPECIFIC WARNINGS FOR INDICATION 2

- To reduce risk of vessel damage, take care to appropriately size Retriever to vessel diameter at intended site of deployment.

### SPECIFIC WARNINGS FOR INDICATION 3

- The safety and effectiveness of the Trevo Retrievers in reducing disability has not been established in patients with large core infarcts (i.e., ASPECTS ≤ 7). There may be increased risks, such as intracerebral hemorrhage, in these patients.
- The safety and effectiveness of the Trevo Retrievers in reducing disability has not been established or evaluated in patients with occlusions in the posterior circulation (e.g., basilar or vertebral arteries) or for more distal occlusions in the anterior circulation.
- Users should validate their imaging software analysis techniques to ensure

robust and consistent results for assessing core infarct size.

### WARNINGS APPLIED TO ALL INDICATIONS

- Administration of IV-tPA should be within the FDA-approved window (within 3 hours of stroke symptom onset).
- To reduce risk of vessel damage, adhere to the following recommendations:
  - Do not perform more than six (6) retrieval attempts in same vessel using Retriever devices.
  - Maintain Retriever position in vessel when removing or exchanging Microcatheter.
- To reduce risk of kinking/fracture, adhere to the following recommendations:
  - Immediately after unsheathing Retriever, position Microcatheter tip marker just proximal to shaped section. Maintain Microcatheter tip marker just proximal to shaped section of Retriever during manipulation and withdrawal.
  - Do not rotate or torque Retriever.
  - Use caution when passing Retriever through stented arteries.
- The Retriever is a delicate instrument and should be handled carefully. Before use and when possible during procedure, inspect device carefully for damage. Do not use a device that shows signs of damage. Damage may prevent device from functioning and may cause complications.
- Do not advance or withdraw Retriever against resistance or significant vasospasm. Moving or torquing device against resistance or significant vasospasm may result in damage to vessel or device. Assess cause of resistance using fluoroscopy and if needed reshoot the device to withdraw.
- If Retriever is difficult to withdraw from the vessel, do not torque Retriever. Advance Microcatheter distally, gently pull Retriever back into Microcatheter, and remove Retriever and Microcatheter as a unit. If undue resistance is met when withdrawing the Retriever into the Microcatheter, consider extending the Retriever using the Abbott Vascular DOC guidewire extension (REF 22260) so that the Microcatheter can be exchanged for a larger diameter catheter such as a DAC® Catheter. Gently withdraw the Retriever into the larger diameter catheter.
- Administer anti-coagulation and anti-platelet medications per standard interventional guidelines.
- Users should take all necessary precautions to limit X-radiation doses to patients and themselves by using sufficient shielding, reducing

fluoroscopy times, and modifying X-ray technical factors where possible.

### PRECAUTIONS

- Prescription only – device restricted to use by or on order of a physician.
  - Store in cool, dry, dark place.
  - Do not use open or damaged packages.
  - Use by "Use By" date.
  - Exposure to temperatures above 54°C (130°F) may damage device and accessories. Do not autoclave.
  - Do not expose Retriever to solvents.
  - Use Retriever in conjunction with fluoroscopic visualization and proper anti-coagulation agents.
  - To prevent thrombus formation and contrast media crystal formation, maintain a constant infusion of appropriate flush solution between guide catheter and Microcatheter and between Microcatheter and Retriever or guidewire.
  - Do not attach a torque device to the shaped proximal end of DOC® Compatible Retriever. Damage may occur, preventing ability to attach DOC® Guide Wire Extension.
- DOC is a trademark of Abbott Laboratories.

**Stryker Neurovascular**  
47900 Bayside Parkway  
Fremont, CA 94538

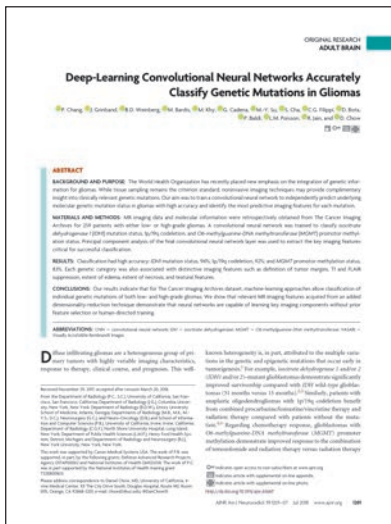
[strykerneurovascular.com](http://strykerneurovascular.com)

Date of Release: APR/2018

EX\_EN\_US

## 2018 LUCIEN LEVY BEST RESEARCH ARTICLE AWARD WINNER AND NOMINEES NAMED

This award is named for the late *AJNR* Senior Editor who championed its establishment and recognizes the best original research paper accepted in 2018. The winning paper was published electronically on May 10, 2018 and appeared in the July print issue. It was selected by a vote of the *Journal's* Editor-in-Chief and Senior Editors.



The Editors of *AJNR* are pleased to announce the annual Lucien Levy Best Research Article Award has been presented to

### “Deep-Learning Convolutional Neural Networks Accurately Classify Genetic Mutations in Gliomas”

by P. Chang, J. Grinband, B.D. Weinberg, M. Bardis, M. Khy, G. Cadena, M.-Y. Su, S. Cha, C.G. Filippi, D. Bota, P. Baldi, L.M. Poisson, R. Jain, and D. Chow

#### Other nominated papers were:

“Hybrid 3D/2D Convolutional Neural Network for Hemorrhage Evaluation on Head CT” by P.D. Chang, E. Kuoyo, J. Grinband, B.D. Weinberg, M. Thompson, R. Homo, J. Chen, H. Abcede, M. Shafie, L. Sugrue, C.G. Filippi, M.-Y. Su, W. Yu, C. Hess, and D. Chow

“Contrast-Enhanced 3D-FLAIR Imaging of the Optic Nerve and Optic Nerve Head: Novel Neuroimaging Findings of Idiopathic Intracranial Hypertension” by E. Golden, R. Krivochenitser, N. Mathews, C. Longhurst, Y. Chen, J.-P.J. Yu, and T.A. Kennedy

“Quantitative Susceptibility Mapping after Sports-Related Concussion” by K.M. Koch, T.B. Meier, R. Karr, A.S. Nencka, L.T. Muftuler, and M. McCrea

“Diagnosing Early Ischemic Changes with the Latest-Generation Flat Detector CT: A Comparative Study with Multidetector CT” by I.L. Maier, J.R. Leyhe, I. Tsogkas, D. Behme, K. Schregel, M. Knauth, M. Schnieder, J. Liman, and M.-N. Psychogios

“Predictors and Clinical Impact of Delayed Stent Thrombosis after Thrombectomy for Acute Stroke with Tandem Lesions” by R. Pop, I. Zinchenko, V. Quenardelle, D. Mihoc, M. Manisor, J.S. Richter, F. Severac, M. Simu, S. Chibbaro, O. Rouyer, V. Wolff, and R. Beaujeux

“Aberrant Structural Brain Connectivity in Adolescents with Attentional Problems Who Were Born Prematurely” by O. Tymofiyeva, D. Gano, R.J. Trevino Jr, H.C. Glass, T. Flynn, S.M. Lundy, P.S. McQuillen, D.M. Ferriero, A.J. Barkovich, and D. Xu

## IMPORTANT SAFETY INFORMATION<sup>1</sup>

### WARNING: NEPHROGENIC SYSTEMIC FIBROSIS (NSF)

**Gadolinium-based contrast agents (GBCAs) increase the risk for NSF among patients with impaired elimination of the drugs. Avoid use of GBCAs in these patients unless the diagnostic information is essential and not available with non-contrast MRI or other modalities. NSF may result in fatal or debilitating fibrosis affecting the skin, muscle and internal organs.**

- **The risk for NSF appears highest among patients with:**
  - Chronic, severe kidney disease (GFR < 30 mL/min/1.73m<sup>2</sup>), or
  - Acute kidney injury.
- **Screen patients for acute kidney injury and other conditions that may reduce renal function. For patients at risk for chronically reduced renal function (e.g. age > 60 years, hypertension, diabetes), estimate the glomerular filtration rate (GFR) through laboratory testing.**
- **For patients at highest risk for NSF, do not exceed the recommended DOTAREM dose and allow a sufficient period of time for elimination of the drug from the body prior to any re-administration.**

## INDICATIONS AND USAGE

DOTAREM<sup>®</sup> (gadoterate meglumine) injection is a prescription gadolinium-based contrast agent indicated for intravenous use with magnetic resonance imaging (MRI) in brain (intracranial), spine and associated tissues in adult and pediatric patients (including term neonates) to detect and visualize areas with disruption of the blood brain barrier (BBB) and/or abnormal vascularity.

## CONTRAINDICATIONS

History of clinically important hypersensitivity reactions to DOTAREM.

## WARNINGS AND PRECAUTIONS

- **Hypersensitivity Reactions:** Anaphylactic and anaphylactoid reactions have been reported with DOTAREM, involving cardiovascular, respiratory, and/or cutaneous manifestations. Some patients experienced circulatory collapse and died. In most cases, initial symptoms occurred within minutes of DOTAREM administration and resolved with prompt emergency treatment.
- **Before DOTAREM administration, assess all patients for any history of a reaction to contrast media, bronchial asthma and/or allergic disorders.** These patients may have an increased risk for a hypersensitivity reaction to DOTAREM.
- **Administer DOTAREM only in situations where trained personnel and therapies are promptly available for the treatment of hypersensitivity reactions, including personnel trained in resuscitation.**
- **Gadolinium Retention:** Gadolinium is retained for months or years in several organs. The highest concentrations have been identified in the bone, followed by brain, skin, kidney, liver and spleen. The duration of retention also varies by tissue, and is longest in bone. Linear GBCAs cause more retention than macrocyclic GBCAs.
- **Consequences of gadolinium retention in the brain have not been established.** Adverse events involving multiple organ systems have been reported in patients with normal renal function without an established causal link to gadolinium retention.
- **Acute Kidney Injury:** In patients with chronically reduced renal function, acute kidney injury requiring dialysis has occurred with the use of GBCAs. The risk of acute kidney injury may increase with increasing dose of the contrast agent; administer the lowest dose necessary for adequate imaging.
- **Extravasation and Injection Site Reactions:** Ensure catheter and venous patency before the injection of DOTAREM. Extravasation into tissues during DOTAREM administration may result in tissue irritation.

## ADVERSE REACTIONS

- The most common adverse reactions associated with DOTAREM in clinical trials were nausea, headache, injection site pain, injection site coldness and rash.
- Serious adverse reactions in the Postmarketing experience have been reported with DOTAREM. These serious adverse reactions include but are not limited to: arrhythmia, cardiac arrest, respiratory arrest, pharyngeal edema, laryngospasm, bronchospasm, coma and convulsion.

## USE IN SPECIFIC POPULATIONS

- **Pregnancy:** GBCAs cross the human placenta and result in fetal exposure and gadolinium retention. Use only if imaging is essential during pregnancy and cannot be delayed.
- **Lactation:** There are no data on the presence of gadoterate in human milk, the effects on the breastfed infant, or the effects on milk production. However, published lactation data on other GBCAs indicate that 0.01 to 0.04% of the maternal gadolinium dose is present in breast milk.
- **Pediatric Use:** The safety and efficacy of DOTAREM at a single dose of 0.1 mmol/kg has been established in pediatric patients from birth (term neonates ≥ 37 weeks gestational age) to 17 years of age based on clinical data. The safety of DOTAREM has not been established in preterm neonates. No cases of NSF associated with DOTAREM or any other GBCA have been identified in pediatric patients age 6 years and younger.

You are encouraged to report negative side effects of prescription drugs to the FDA. Visit [www.fda.gov/medwatch](http://www.fda.gov/medwatch) or call 1-800-FDA-1088.

**Please see the full Prescribing Information, including the patient Medication Guide, for additional important safety information.**

**References:** **1.** Dotarem [package insert]. Princeton, NJ: Guerbet LLC; Apr 2018. **2.** Maravilla K et al. Comparison of Gadoterate Meglumine and Gadobutrol in the Diagnosis of Primary Brain Tumors: A Double-Blind Randomized Controlled Intraindividual Crossover Study (the REMIND Study). 2017 June 29. doi: 10.3174/ajnr.A5316. [Epub ahead of print]. **3.** de Kerviler E et al. Adverse reactions to gadoterate meglumine: review of over 25 years of clinical use and more than 50 million doses. Invest Radiol 2016;51:544–51 CrossRef Medline. **4.** Endrikat J et al. Safety of gadobutrol: results from 42 clinical phase II to IV studies and postmarketing surveillance after 29 million applications. Invest Radiol 2016;51: 537–43 CrossRef Medline. **5.** Port M et al. Efficiency, thermodynamic and kinetic stability of marketed gadolinium chelates and their possible clinical consequences: a critical review. Biometals. 2008;21:469–90. **6.** Frenzel T et al. Stability of gadolinium-based magnetic resonance imaging contrast agents in human serum at 37°C. Invest Radiol. 2008;43:817–828.

DOTAREM<sup>®</sup> is a registered trademark of Guerbet LLC, and is available by prescription only.

Gadavist<sup>®</sup> is a registered trademark of the Bayer group of companies, and is available by prescription only.

# DOTAREM<sup>®</sup>

(gadoterate meglumine) Injection

MR

Comparison of Dotarem<sup>®</sup> to Gadavist<sup>®</sup> for Overall Visualization and Characterization in the MRI Diagnosis of Primary Brain Tumors



Despite the difference in relaxivity between these 2 GBCAs

**There Is No Measurable Difference in Clinical Benefit Observed Between Dotarem<sup>®</sup> and Gadavist<sup>®2</sup>**

as demonstrated by the **REMIND Study**, a multicenter, double-blind, randomized, controlled intraindividual crossover study.<sup>2</sup>

This study “demonstrates the non-inferiority of gadoterate meglumine [Dotarem<sup>®</sup>] versus gadobutrol [Gadavist<sup>®</sup>] for overall visualization and characterization of primary brain tumors”.<sup>2</sup> Additionally, there was no preference of the readers for either contrast agent, in most cases, regarding border delineation, internal morphology, and the qualitative degree of contrast enhancement, despite quantitative mean lesion percentage enhancement being higher with gadobutrol.<sup>2</sup>

- For all readers in the REMIND Study, more than 90% of patients presented with good or excellent overall lesion visualization and characterization with either Dotarem<sup>®</sup> or Gadavist<sup>®</sup>.<sup>2</sup>
- The REMIND Study also demonstrated a low incidence of immediate reported AEs with Dotarem<sup>®</sup> and with Gadavist<sup>®</sup>, as shown in multiple previous studies.<sup>2,3,4</sup>
- Dotarem<sup>®</sup> is the only imaging contrast with macrocyclic and ionic structure for high thermodynamic and kinetic stability.<sup>5,6</sup>
- Dotarem<sup>®</sup> is not only trusted for high molecular stability<sup>5,6</sup>; the REMIND Study demonstrates that it is as effective as Gadavist<sup>®</sup> for MRI diagnosis of primary brain tumors.<sup>2</sup>

Please see Important Safety information on opposite page. For more information on Dotarem<sup>®</sup>, please see Full Prescribing Information including Boxed Warning and Medication Guide.

Guerbet | 

**COMMITTED**

Learn more at  
[RemindStudy.com](https://RemindStudy.com)



# Bending expectations of conformability and stability.

## **Enhanced conformability**

The hybrid cell structure is designed to enhance stent opening and conformability in bifurcations and tight curves.

## **Ease of use**

All sizes of the Neuroform Atlas Stent are deliverable through Excelsior® SL-10® and Excelsior XT-17™ Microcatheters.

## **Higher deployment accuracy**

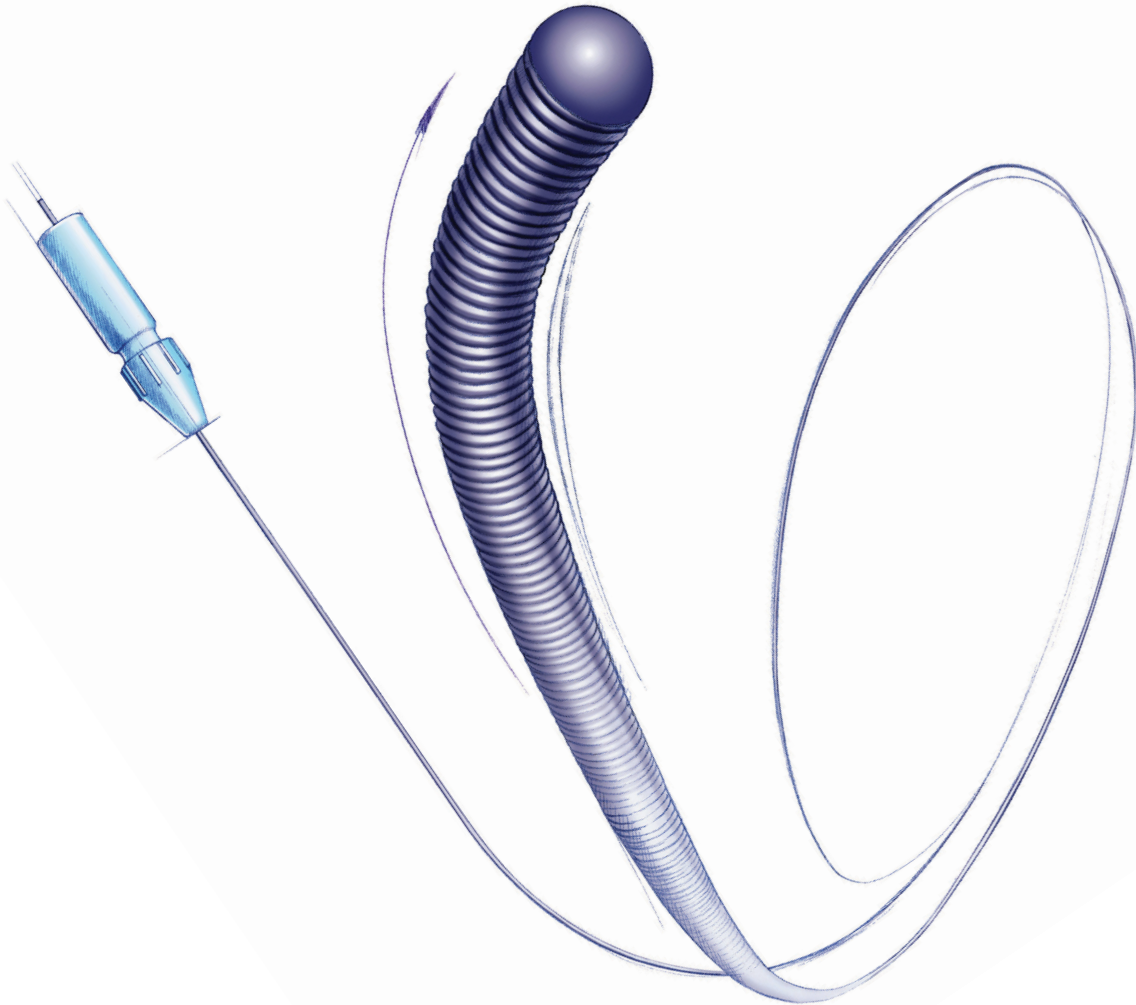
The Neuroform Atlas Stent is designed to have very low foreshortening, which enables very high deployment accuracy.



## **Neuroform Atlas®** STENT SYSTEM

# Hybrid

GUIDEWIRES



**UNIQUE OPTIONS FOR COMPLEX ANATOMIES**

Available in **.007"**, **.008"** and **.012"/.014"**

Visit Our Products Page at [www.balt-USA.com](http://www.balt-USA.com) to Learn More.

**Balt USA**

29 Parker, Irvine, CA 92618  
tel 949.788.1443 fax 949.788.1444

[balt-usa.com](http://balt-usa.com)

©2019 BALD USA MKTG-132 Rev. A



# AJNR

## AMERICAN JOURNAL OF NEURORADIOLOGY

MAY 2019  
VOLUME 40  
NUMBER 5  
WWW.AJNR.ORG

Publication Preview at [www.ajnr.org](http://www.ajnr.org) features articles released in advance of print. Visit [www.ajnrblog.org](http://www.ajnrblog.org) to comment on AJNR content and chat with colleagues and AJNR's News Digest at <http://ajnrndigest.org> to read the stories behind the latest research in neuroimaging.

757 **PERSPECTIVES** *M.T. Krüger, et al.*

### REVIEW ARTICLE

 758 **Non-Contrast-Enhancing Tumor: A New Frontier in Glioblastoma Research** *A. Lasocki, et al.*

**ADULT BRAIN**

### PRACTICE VIGNETTE

766 **Chimeric Antigen Receptor T-Cell Therapy: What the Neuroradiologist Needs to Know** *H.A. Valand, et al.*

### GENERAL CONTENTS

   769 **Predicting Motor Outcome in Acute Intracerebral Hemorrhage** *J. Puig, et al.*

**ADULT BRAIN  
FUNCTIONAL**

776 **The Central Vein Sign in Radiologically Isolated Syndrome** *S. Suthiphosuwat, et al.*

**ADULT BRAIN**

784 **Increased Water Content in Periventricular Caps in Patients without Acute Hydrocephalus** *T. Sichteremann, et al.*

**ADULT BRAIN**

 788 **GJA1 Variants Cause Spastic Paraplegia Associated with Cerebral Hypomyelination** *L. Saint-Val, et al.*

**ADULT BRAIN  
PEDIATRICS**

792 **Susceptibility-Weighted Angiography for the Follow-Up of Brain Arteriovenous Malformations Treated with Stereotactic Radiosurgery** *S. Finitzis, et al.*

**ADULT BRAIN**

798 **Image Processing to Improve Detection of Mesial Temporal Sclerosis in Adults** *F. Dahi, et al.*

**ADULT BRAIN**

  802 **Visualization of Aneurysmal Neck and Dome after Coiling with 3D Multifusion Imaging of Silent MRA and FSE-MR Cisternography** *T. Satoh, et al.*

**INTERVENTIONAL**

 808 **Usefulness of Silent MR Angiography for Intracranial Aneurysms Treated with a Flow-Diverter Device** *H. Oishi, et al.*

**INTERVENTIONAL**

815 **Pointwise Encoding Time Reduction with Radial Acquisition with Subtraction-Based MRA during the Follow-Up of Stent-Assisted Coil Embolization of Anterior Circulation Aneurysms** *Y.J. Heo, et al.*

**INTERVENTIONAL**

-  820 **Treatment of Wide-Neck Intracranial Aneurysms with the Woven EndoBridge Device Associated with Stenting: A Single-Center Experience** *F. Cagnazzo, et al.* **INTERVENTIONAL**
- 827 **Image Quality of Low-Dose Cerebral Angiography and Effectiveness of Clinical Implementation on Diagnostic and Neurointerventional Procedures for Intracranial Aneurysms** *J. Choi, et al.* **INTERVENTIONAL**
-    834 **Differences in Cerebral Aneurysm Rupture Rate According to Arterial Anatomies Depend on the Hemodynamic Environment** *S. Fukuda, et al.* **INTERVENTIONAL**
- 840 **Impact of Balloon-Guiding Catheter Location on Recanalization in Patients with Acute Stroke Treated by Mechanical Thrombectomy** *D.E. Jeong, et al.* **INTERVENTIONAL**
-  845 **Angiographic and Clinical Features of Noninvoluting Congenital Hemangiomas** *A. Patel, et al.* **INTERVENTIONAL PEDIATRICS**
-  849 **Reduced Jet Velocity in Venous Flow after CSF Drainage: Assessing Hemodynamic Causes of Pulsatile Tinnitus** *H. Haraldsson, et al.* **HEAD & NECK**
-  855 **The Black Turbinate Sign, A Potential Diagnostic Pitfall: Evaluation of the Normal Enhancement Patterns of the Nasal Turbinates** *Q. Han, et al.* **HEAD & NECK**
- 862 **Neuroimaging Findings in Moebius Sequence** *D.A. Herrera, et al.* **PEDIATRICS**
- 866 **Comparison of Iterative Model Reconstruction versus Filtered Back-Projection in Pediatric Emergency Head CT: Dose, Image Quality, and Image-Reconstruction Times** *R.N. Southard, et al.* **PEDIATRICS**
-  872 **Pediatric Atypical Teratoid/Rhabdoid Tumors of the Brain: Identification of Metabolic Subgroups Using In Vivo <sup>1</sup>H-MR Spectroscopy** *B. Tamrazi, et al.* **PEDIATRICS**
-    878 **Intravoxel Incoherent Motion MR Imaging of Pediatric Intracranial Tumors: Correlation with Histology and Diagnostic Utility** *K. Kikuchi, et al.* **PEDIATRICS**
-   885 **Brain and CSF Volumes in Fetuses and Neonates with Antenatal Diagnosis of Critical Congenital Heart Disease: A Longitudinal MRI Study** *N.H.P. Claessens, et al.* **PEDIATRICS**
-  892 **Focal Cortical Dysplasia and Refractory Epilepsy: Role of Multimodality Imaging and Outcome of Surgery** *S. Jayalakshmi, et al.* **PEDIATRICS**
- 899 **Persisting Embryonal Infundibular Recess in Morning Glory Syndrome: Clinical Report of a Novel Association** *A. D'Amico, et al.* **PEDIATRICS HEAD & NECK**
-   903 **Oculodentodigital Dysplasia: A Hypomyelinating Leukodystrophy with a Characteristic MRI Pattern of Brain Stem Involvement** *I. Harting, et al.* **PEDIATRICS**
-    908 **Lumbar Spinal Stenosis Severity by CT or MRI Does Not Predict Response to Epidural Corticosteroid versus Lidocaine Injections** *F.A. Perez, et al.* **SPINE**
- 916 **It Is Not Necessary to Discontinue Seizure Threshold-Lowering Medications Prior to Myelography** *M. Krupa, et al.* **SPINE INTERVENTIONAL**
- 920 **Assessing Vascularity of Osseous Spinal Metastases with Dual-Energy CT-DSA: A Pilot Study Compared with Catheter Angiography** *Y.-C. Huang, et al.* **SPINE**
- 926 **35 YEARS AGO IN AJNR**

## ONLINE FEATURES

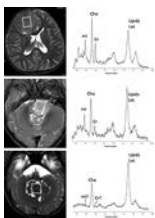
### LETTERS

- E20 Use of Balanced Steady-State Free Precession Sequences in Evaluation of Drop Metastases** *A. Vossough, et al.*
- E21 Reply** *K. Buch, et al.*
- E22 Across the Pons and to the Milky Way: Where Are the Neuroradiology Publications?** *V.T. Lehman*
- E24 Radiogenomics in Medulloblastoma: Can the Human Brain Compete with Artificial Intelligence and Machine Learning?** *A. Dasgupta, et al.*

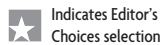
### BOOK REVIEWS

*R.M. Quencer, Section Editor*

Please visit [www.ajnrblog.org](http://www.ajnrblog.org) to read and comment on Book Reviews.



T2-weighted MRI and spectra of supratentorial AT/RT with ASCL1 expression (upper), a posterior fossa AT/RT with ASCL1 expression (middle), and posterior fossa AT/RT without ASCL1 expression (lower). Cr, Cho, and mIns are readily detectable in the spectra of supratentorial and posterior fossa ASCL1-expressing AT/RTs, whereas only Cho is clearly detectable in the ASCL1-nonexpressing posterior fossa AT/RT.



Indicates Editor's Choices selection



Indicates Fellows' Journal Club selection



Indicates open access to non-subscribers at [www.ajnr.org](http://www.ajnr.org)



Indicates article with supplemental on-line table



Indicates article with supplemental on-line photo



Indicates article with supplemental on-line video



Evidence-Based Medicine Level 1



Evidence-Based Medicine Level 2

### Official Journal:

American Society of Neuroradiology  
American Society of Functional Neuroradiology  
American Society of Head and Neck Radiology  
American Society of Pediatric Neuroradiology  
American Society of Spine Radiology

### EDITOR-IN-CHIEF

#### Jeffrey S. Ross, MD

Professor of Radiology, Department of Radiology,  
Mayo Clinic College of Medicine, Phoenix, AZ

### SENIOR EDITORS

#### Harry J. Cloft, MD, PhD

Professor of Radiology and Neurosurgery,  
Department of Radiology, Mayo Clinic College of  
Medicine, Rochester, MN

#### Thierry A.G.M. Huisman, MD

Radiologist-in-Chief, Texas Children's Hospital,  
Houston, TX

#### Yvonne W. Lui, MD

Associate Professor of Radiology,  
Chief of Neuroradiology,  
New York University School of Medicine,  
New York, NY

#### C.D. Phillips, MD, FACR

Professor of Radiology, Weill Cornell Medical  
College, Director of Head and Neck Imaging,  
New York-Presbyterian Hospital, New York, NY

#### Lubdhra M. Shah, MD

Associate Professor of Radiology and Director of  
Spine Imaging, University of Utah Department of  
Radiology and Imaging Sciences, Salt Lake City, UT

#### Charles M. Strother, MD

Professor of Radiology, Emeritus, University of  
Wisconsin, Madison, WI

### STATISTICAL SENIOR EDITOR

#### Bryan A. Comstock, MS

Senior Biostatistician,  
Department of Biostatistics,  
University of Washington, Seattle, WA

### ARTIFICIAL INTELLIGENCE DEPUTY EDITOR

#### Christopher G. Filippi, MD

Professor and Vice Chair of Biomedical and  
Translational Science,  
Donald and Barbara Zucker School of Medicine at  
Hofstra/Northwell,  
Lenox Hill Hospital and Greenwich Village  
Healthplex, New York, NY

### EDITORIAL BOARD

Ashley H. Aiken, *Atlanta, GA*  
Lea M. Alhilali, *Phoenix, AZ*  
Kubilay Aydin, *Istanbul, Turkey*  
John D. Barr, *Dallas, TX*  
Ari Blitz, *Baltimore, MD*  
Barton F. Branstetter IV, *Pittsburgh, PA*  
Jonathan L. Brisman, *Lake Success, NY*  
Keith Cauley, *Danville, PA*  
James Y. Chen, *San Diego, CA*  
Asim F. Choudhri, *Memphis, TN*  
Daniel Chow, *Irvine, CA*  
J. Matthew Debnam, *Houston, TX*  
Seena Dehkharghani, *New York, NY*  
Yonghong Ding, *Rochester, MN*  
Clifford J. Eskey, *Hanover, NH*  
Saeed Fakhraan, *Phoenix, AZ*  
Massimo Filippi, *Milan, Italy*  
Reza Forghani, *Montreal, Quebec, Canada*  
Nils D. Forkert, *Calgary, Alberta, Canada*  
Wende N. Gibbs, *Los Angeles, CA*  
Christine M. Glastonbury, *San Francisco, CA*  
John L. Go, *Los Angeles, CA*  
Philipp Göllitz, *Erlangen, Germany*  
Allison Grayev, *Madison, WI*  
Brent Griffith, *Detroit, MI*  
Ajay Gupta, *New York, NY*  
Rakesh Kumar Gupta, *Haryana, India*  
Lotfi Hacein-Bey, *Sacramento, CA*  
Christopher P. Hess, *San Francisco, CA*  
Andrei Holodny, *New York, NY*  
Benjamin Huang, *Chapel Hill, NC*  
Mahesh V. Jayaraman, *Providence, RI*  
Valerie Jewells, *Chapel Hill, NC*  
Christof Karmonik, *Houston, TX*  
Timothy J. Kaufmann, *Rochester, MN*  
Hillary R. Kelly, *Boston, MA*  
Toshibumi Kinoshita, *Akita, Japan*  
Kenneth F. Layton, *Dallas, TX*  
Alexander Lerner, *Los Angeles, CA*  
Michael Lev, *Boston, MA*  
Karl-Olof Lovblad, *Geneva, Switzerland*  
Franklin A. Marden, *Chicago, IL*  
Joseph C. McGowan, *Merion Station, PA*  
Stephan Meckel, *Freiburg, Germany*  
Christopher J. Moran, *St. Louis, MO*  
Takahisa Mori, *Kamakura City, Japan*  
Suresh Mukherji, *Ann Arbor, MI*  
Alexander J. Nemeth, *Chicago, IL*  
Renato Hoffmann Nunes, *Sao Paulo, Brazil*  
Sasan Partovi, *Cleveland, OH*  
Laurent Pierot, *Reims, France*  
Jay J. Pillai, *Baltimore, MD*  
Whitney B. Pope, *Los Angeles, CA*  
Joana Ramalho, *Lisbon, Portugal*  
Otto Rapalino, *Boston, MA*

Álex Rovira-Cañellas, *Barcelona, Spain*

Paul M. Ruggieri, *Cleveland, OH*  
Amit M. Saindane, *Atlanta, GA*  
Erin Simon Schwartz, *Philadelphia, PA*  
Lubdhra M. Shah, *Salt Lake City, UT*  
Maksim Shapiro, *New York, NY*  
Timothy Shepherd, *New York, NY*  
Mark S. Shiroishi, *Los Angeles, CA*  
Bruno P. Soares, *Baltimore, MD*  
Maria Vittoria Spampinato, *Charleston, SC*  
Khin Khin Tha, *Sapporo, Hokkaido, Japan*  
Krishnamoorthy Thamburaj, *Hershey, PA*  
Cheng Hong Toh, *Taipei, Taiwan*  
Aquila S. Turk, *Greenville, SC*  
Anja G. van der Kolk, *Utrecht, the Netherlands*  
Willem Jan van Rooij, *Tilburg, Netherlands*  
Arastoo Vossough, *Philadelphia, PA*  
Elysa Widjaja, *Toronto, Ontario, Canada*  
Max Wintermark, *Stanford, CA*  
Ronald L. Wolf, *Philadelphia, PA*  
Kei Yamada, *Kyoto, Japan*  
Carlos Zamora, *Chapel Hill, NC*  
Vahe M. Zohrabian, *New Haven, CT*

### EDITORIAL FELLOW

Alireza Radmanesh, *New York, NY*

### SPECIAL CONSULTANTS TO THE EDITOR

#### AJNR Blog Editor

Neil Lall, *Denver, CO*

#### Case of the Month Editor

Nicholas Stence, *Aurora, CO*

#### Case of the Week Editors

Juan Pablo Cruz, *Santiago, Chile*  
Sapna Rawal, *Toronto, Ontario, Canada*

#### Classic Case Editor

Sandy Cheng-Yu Chen, *Taipei, Taiwan*

#### Health Care and Socioeconomics Editor

Pina C. Sanelli, *New York, NY*

#### Physics Editor

Greg Zaharchuk, *Stanford, CA*

#### Podcast Editor

Wende N. Gibbs, *Los Angeles, CA*

#### Twitter Editor

Jennifer McCarty, *Houston, TX*

Founding Editor  
Juan M. Taveras

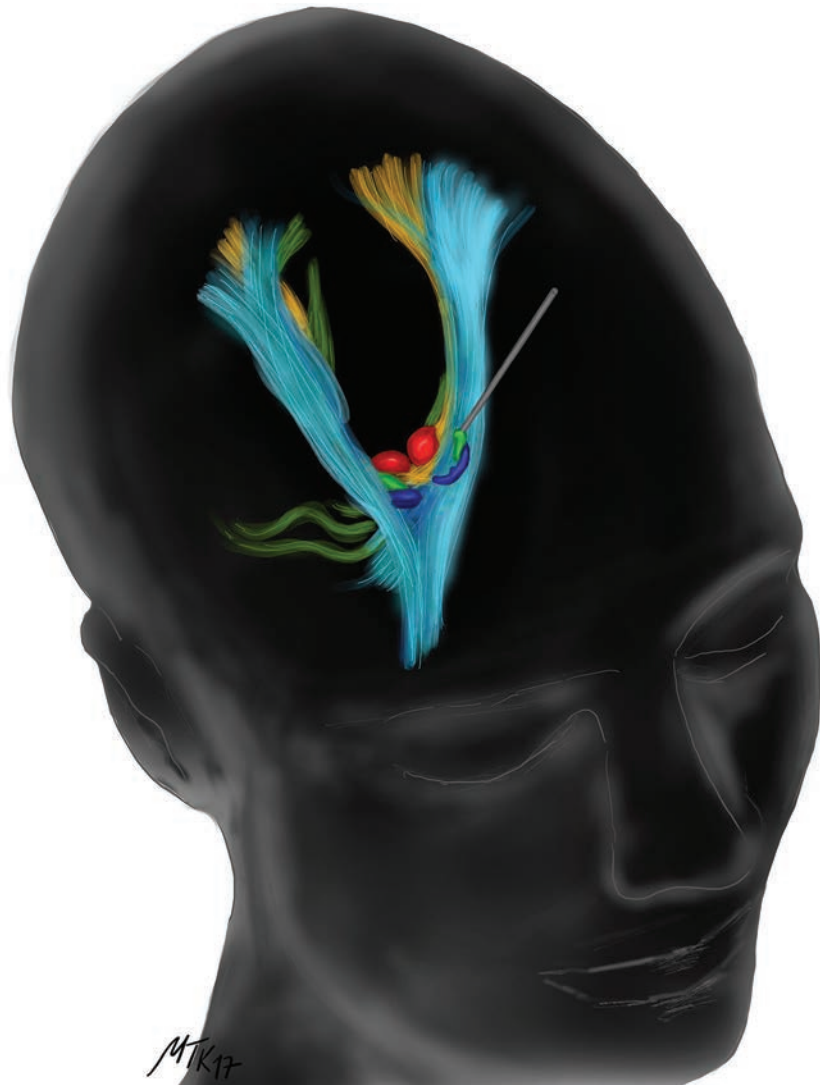
Editors Emeriti  
Mauricio Castillo, Robert I. Grossman,  
Michael S. Huckman, Robert M. Quencer

Managing Editor  
Karen Halm

Assistant Managing Editor  
Laura Wilhelm

Communications Coordinator  
Rebecca Artz

Executive Director, ASNIR  
Mary Beth Hepp



**Title:** Deep Brain Stimulation. This is an artistically modified illustration based on a real patient dataset. It depicts functional structures such as nuclei and white matter fibers as well as the human being itself. By stimulating these deep structures in the brain, an improvement of the quality of life can be achieved for many patients. The illustration was painted using Procreate software on an iPad Pro, based on a dataset from the Brainlab Elements software (Brainlab, Munich, Germany).

*Marie T. Krüger, MD, and Peter C. Reinacher, MD, Freiburg Medical Center and Faculty of Medicine, University of Freiburg, Freiburg, Germany*

# Non-Contrast-Enhancing Tumor: A New Frontier in Glioblastoma Research

 A. Lasocki and  F. Gaillard



## ABSTRACT

**SUMMARY:** There is a growing understanding of the prognostic importance of non-contrast-enhancing tumor in glioblastoma, and recent attempts at more aggressive management of this component using neurosurgical resection and radiosurgery have been shown to prolong survival. Optimizing these therapeutic strategies requires an understanding of the features that can distinguish non-contrast-enhancing tumor from other processes, in particular vasogenic edema; however, the limited and heterogeneous manner in which it has been defined in the literature limits clinical translation. This review covers pertinent literature on our growing understanding of non-contrast-enhancing tumor and focuses on key conventional MR imaging features for improving its delineation. Such features include subtle differences in the degree of FLAIR hyperintensity, gray matter involvement, and focal mass effect. Improved delineation of tumor from edema will facilitate more aggressive management of this component and potentially realize associated survival benefits.

**ABBREVIATIONS:** CET = contrast-enhancing tumor; FET = [<sup>18</sup>F]-fluoroethyl-L-tyrosine; GBM = glioblastoma; nCET = non-contrast-enhancing tumor

The molecular characterization of gliomas has been the focus of recent glioma research. While our growing understanding of the genetics of gliomas, now reflected in the updated World Health Organization classification, provides great hope, it is easy to forget that currently, this does not substantially affect treatment options. For example, glioblastomas (GBMs) have recently been subclassified into those with a mutation in the *isocitrate dehydrogenase (IDH)* gene and those without a mutation (known as *IDH* wild-type).<sup>1</sup> While *IDH* mutant GBMs have a significantly better prognosis than *IDH* wild-type tumors,<sup>1,2</sup> conventional treatment for both subtypes currently remains the same.<sup>3</sup> Unlike the treatment of many extracranial malignancies, which has been revolutionized by the development of immunotherapy<sup>4</sup> and monoclonal antibodies against key drivers of tumorigenesis,<sup>5</sup> progress in the treatment of diffuse gliomas has been slower and they remain largely incurable. Until new treatment

options enter clinical practice, it is, therefore, important to optimize existing therapies. This is arguably of greater importance now than ever before because with longer survival, also comes the growing prospect of living long enough to benefit from new emerging therapeutic options.

GBM is the most aggressive—and, unfortunately, most common—form of diffuse glioma.<sup>1</sup> The treatment of GBM typically consists of maximal safe neurosurgical resection followed by adjuvant chemoradiotherapy.<sup>3</sup> Gross macroscopic resection of the contrast-enhancing tumor (CET) component of GBMs is associated with longer survival<sup>6–8</sup> and thus represents the neurosurgical standard of care. Despite satisfactory resection and adjuvant chemoradiotherapy, however, local recurrence of GBM is almost inevitable due to tumor cells infiltrating beyond the CET component.<sup>9</sup> Often, at least a portion of the tumor extending beyond the contrast-enhancing margin is visible with MR imaging and is known as non-contrast-enhancing tumor (nCET), usually best visualized on T2-weighted FLAIR imaging.

The frequency with which complete or near-complete resection of the CET component can be achieved is increasing due to technologic advances, including neuronavigation techniques, fluorescence-guided surgery, and intraoperative MR imaging, which are translating into improved survival.<sup>10–12</sup> The potential gains from improved resection of the CET component are thus plateauing, increasing the importance of residual nCET. Historically, nCET in the context of a GBM has been thought to be of a lower grade. This view is being refuted because such nCET frequently progresses faster than one would expect purely on the basis of

Received December 8, 2018; accepted after revision February 5, 2019.

From the Department of Cancer Imaging (A.L.), Peter MacCallum Cancer Centre, Melbourne, Victoria, Australia; Sir Peter MacCallum Departments of Oncology (A.L.) and Radiology (F.G.), University of Melbourne, Parkville, Victoria, Australia; and Department of Radiology (F.G.), Royal Melbourne Hospital, Parkville, Victoria, Australia.

Paper previously presented, in part, at: Annual Meeting of the European Society of Neuroradiology, September 19–23, 2018; Rotterdam, the Netherlands.

Please address correspondence to Arian Lasocki, MD, Department of Cancer Imaging, Peter MacCallum Cancer Centre, Grattan St, Melbourne, Victoria, Australia 3000; e-mail: arian.lasocki@petermac.org

 Indicates open access to non-subscribers at [www.ajnr.org](http://www.ajnr.org)

<http://dx.doi.org/10.3174/ajnr.A6025>

imaging appearances, with even distant areas of nCET rapidly evolving to CET in patients with *IDH* wild-type GBM.<sup>13</sup> The high malignant potential of the nCET component is supported by our growing understanding of the genetics of gliomas, with *IDH* wild-type grade II and III tumors typically behaving more like GBMs than their *IDH* mutant counterparts of equivalent grade,<sup>1</sup> leading to the colloquial term “stealth glioblastomas.” If anything, the nCET component of a GBM could be expected to be more advanced genetically than in lower grade *IDH* wild-type tumors because dedifferentiation has already occurred in another portion of the tumor. The nCET component is also typically highly cellular. Eidel et al<sup>14</sup> recently showed that nCET had the highest content of viable tumor cells—higher than that present within the CET or necrotic components.

### **Non-Contrast-Enhancing Tumor Affects Prognosis**

It is increasingly being recognized that the nCET component of a GBM affects prognosis. Jain et al<sup>15</sup> showed that both nCET crossing the midline and elevated relative cerebral blood volume within the nCET component are associated with shorter survival. Similarly, Lasocki et al<sup>16</sup> found that those with peripheral GBMs with substantial cortical nCET (a subset of the total nCET) have shorter survival than those with peripheral tumors without this component. These findings are supported by studies assessing the postoperative residual nCET component. Grabowski et al<sup>17</sup> found that T2/FLAIR residual volume was a significant predictor of survival on both univariate and multivariate analysis. These results have recently been validated by a multicenter study showing that high postoperative residual nonenhancing volume conveyed a worse prognosis.<sup>18</sup>

*IDH* wild-type GBMs are much more common than their *IDH* mutant counterparts<sup>1</sup> and almost certainly accounted for most tumors in the above studies. Thus, prognostic significance can most confidently be attached to residual nCET for an *IDH* wild-type GBM, but it is less clear for *IDH* mutant GBMs. The association between a greater proportion of nCET and the presence of an *IDH* mutation was first described by Carrillo et al.<sup>19</sup> Substantial nCET is more common in *IDH* mutant GBMs, though also relatively common in *IDH* wild-type GBMs, limiting the strength of this association.<sup>20</sup> Specifically, *IDH* mutations are present in only about 5% of all glioblastomas,<sup>2</sup> while substantial (>33%) nCET is present in about 21% of *IDH* wild-type glioblastomas.<sup>20</sup> Thus, a glioblastoma with substantial nCET is nevertheless more likely to be *IDH* wild-type than *IDH* mutant.<sup>20</sup> Knowledge of the *IDH* status is, therefore, important in determining the significance of nCET. While greater residual nCET generally conveys a worse prognosis provided it is not simply related to *IDH* mutant status, the survival benefit conferred by an *IDH* mutation is likely to substantially outweigh the detrimental effect of greater residual nCET.

### **The Effect of Antiangiogenic Therapy**

Antiangiogenic agents such as bevacizumab and cediranib often produce a rapid decrease in the degree of contrast enhancement as a result of reconstitution of the disrupted blood-brain barrier. This does not represent a true response, however; thus, the phenomenon is known as a pseudoresponse.<sup>21</sup> Assessment of CET is less reliable in these patients, and monitoring nCET takes on

greater importance. This is reflected in the updated Response Assessment in Neuro-Oncology criteria,<sup>22</sup> and inclusion of T2/FLAIR imaging in patients treated with bevacizumab has been shown to improve the prediction of survival beyond that achieved by assessment based solely on postcontrast imaging.<sup>23,24</sup> Because T2 hyperintensity can have many contributors, assessment of nCET requires determining that the increase in T2 hyperintensity is attributable to tumor progression.<sup>24</sup> Thus, knowledge of the features of nCET is critical. The morphology of nCET in patients treated with antiangiogenic agents may also be important, with Nowosielski et al<sup>25</sup> having shown that a circumscribed pattern of progressive T2 hyperintensity in patients treated with bevacizumab is associated with shorter survival compared with a diffuse pattern.

### **Neurosurgical Resection of Non-Contrast-Enhancing Tumor**

A growing appreciation of the importance of nCET in GBM has led some authors to suggest extending the surgical resection to the nCET component, rather than solely focusing on CET.<sup>15,16</sup> The goal, at this stage, remains to delay progression and the development of symptomatic recurrence rather than provide a cure. A similar strategy was successfully used in grade II gliomas by Yordanova et al,<sup>26</sup> who performed “supratotal resection” in 15 cases. This was defined as extension of the resection beyond the area of signal abnormality visible on MR imaging, compared with confining the resection to the region of abnormal signal.<sup>26</sup> This cohort had a lower rate of anaplastic transformation and a lower rate of requiring adjuvant treatment compared with a control cohort.<sup>26</sup>

Recent effort to more aggressively resect nCET in GBM has also shown additional prognostic benefit over that achieved by gross macroscopic resection of the CET component alone. Li et al<sup>27</sup> showed that in patients in whom total resection of the CET component was achieved, resection of  $\geq 53.21\%$  of the surrounding FLAIR abnormality conveyed an additional survival benefit. These patients had a median survival of 20.7 months, compared with 15.5 months when  $< 53.21\%$  of the surrounding FLAIR abnormality was resected.<sup>27</sup> Pessina et al<sup>28</sup> had similar results, though they examined the extent of resection differently. Patients who had undergone supratotal resection, namely those in whom the entirety of the CET component and the surrounding FLAIR hyperintensity were resected, had an impressive median survival of 29 months.<sup>28</sup> Of note, this definition varies from that used by Yordanova et al<sup>26</sup> because they did not aim to extend the resection beyond the area of FLAIR hyperintensity.<sup>28</sup> In contrast, patients with gross total resection (defined as  $\geq 90\%$ ) of the CET component and variable resection of the infiltrative tumor component had a median survival of 16 months. For patients with gross total resection of the CET component, 45% resection of the infiltrative tumor component was the threshold that conveyed a survival benefit, achieving a 2-year survival rate of 54% compared with 12% when resection of the infiltrative component was less extensive.<sup>28</sup> The thresholds identified by these authors are somewhat arbitrary, and in practice, the extent will be limited by the neurosurgeon’s ability to visualize and safely resect the nCET component. Most interesting, Beiko et al<sup>29</sup> found that greater resection

of nCET was associated with improved prognosis only in *IDH* mutant malignant astrocytomas (grades III and IV), but not in *IDH* wild-type tumors of the same grades.

Although the results of these neurosurgical studies are impressive, the limited and heterogeneous manner in which the nCET component was defined in these studies raises questions. The definition of Li et al<sup>27</sup> was simply that of the “surrounding FLAIR abnormality,” and this is overly simplistic on the basis of our knowledge of gliomas. GBMs are typically associated with at least some surrounding edema; thus, it is difficult to determine how much of the nCET component was truly resected, and this will have been dependent on the relative contributions of nCET and edema to the overall area of FLAIR abnormality. While one can assume that some effort was made to target areas that were thought to represent nCET, presumably based on the MR imaging appearances, the limited description of the methods of Li et al limits translation into clinical practice. The description provided by Pessina et al<sup>28</sup> is similarly unclear. While they do discuss the surrounding FLAIR abnormality representing infiltrative tumor, there is no indication as to how or if this was differentiated from vasogenic edema.

Similar limitations are present in the aforementioned studies assessing postoperative residual FLAIR hyperintensity. Grabowski et al<sup>17</sup> acknowledged that a portion of the residual FLAIR hyperintensity may represent edema, both persisting after resection of the tumor (because this takes a variable time to resolve) and related to the surgery itself. The possibility of persistent edema is also relevant to the association with prognosis because Pope et al<sup>30</sup> have shown that more pronounced edema at diagnosis is associated with worse survival. Thus, unless effort has been made to specifically distinguish nCET from edema, part of the worse prognosis related to a greater amount of residual FLAIR hyperintensity postoperatively could simply relate to a tumor that induces more edema, rather than necessarily residual nCET.

The patterns of nCET vary substantially among patients,<sup>31</sup> though the literature on this topic is limited. These patterns themselves may have prognostic implications<sup>31</sup> that have not been accounted for in the above studies. For example, nCET having a masslike morphology or preferentially involving the gray matter may be associated with a better prognosis than a pattern infiltrating the white matter.<sup>31</sup> These more favorable morphologies are also generally easier to delineate, which is important if one is planning more aggressive resection. Furthermore, their typically more superficial location (compared with nCET involving the white matter) is likely to be associated with less surgical morbidity, again assisting surgical resection. There is thus the potential for selection bias in the above neurosurgical studies because more aggressive resection may have been facilitated by the nCET having a morphology that, in itself, conveyed an improved prognosis, compared with patients with a more infiltrative—and thus more difficult to resect—pattern of nCET.

Such considerations are supported by the results of Baldock et al,<sup>32</sup> who divided GBMs into “nodular” and “diffuse” based on a mathematic calculation of “relative invasiveness.” This study found that nodular tumors received a significant survival benefit from gross total resection of CET over subtotal resection or biopsy, but diffuse tumors did not. While this study examined re-

section of CET rather than nCET, the morphologic patterns assessed are equally relevant to nCET. Similarly, *IDH* mutant malignant astrocytomas (grades III and IV) have been shown to be more amenable to complete resection of CET than their *IDH* wild-type counterparts.<sup>29</sup> *IDH* status was not disclosed in the study by Li et al<sup>27</sup>; thus, a component of the improved prognosis attributed to more extensive resection could have related to a greater proportion of *IDH* mutant tumors, which will in itself have conveyed a better prognosis. Nevertheless, the effect of the potential for a greater proportion of *IDH* mutant tumors is likely to have been small, given the low frequency of *IDH* mutations in glioblastoma,<sup>2</sup> well-demonstrated by the cohort of Pessina et al<sup>28</sup> (with only 3.2% of tumors being *IDH* mutant).

Despite these potential confounders, the size of the survival benefit described is such that there is nevertheless likely to be true benefit to more aggressive resection, and this benefit is intuitive given our knowledge of the growth patterns of GBM. The same neurosurgical advances aiding resection of CET, as briefly outlined above, will also facilitate more aggressive resection of nCET. As a result, the identification and delineation of nCET are likely to become an increasingly important element of the preoperative MR imaging assessment of all diffuse gliomas, irrespective of grade.

### **New Avenues in Radiation Oncology**

Aggressive resection of CET is not always possible, however, for example, due to the proximity to eloquent structures and the associated risks of operative morbidity. Such considerations are amplified if aiming to extend the resection to nCET because functioning brain tissue is potentially embedded with the nCET component. This feature highlights the important role of optimal adjuvant radiation therapy. Postoperative radiation therapy, according to the protocol of Stupp et al,<sup>33</sup> has been the standard of care for GBM for many years, though tumor recurrence remains largely inevitable. This has prompted investigation into more aggressive management of the nCET component with radiation therapy, and this has also been shown to convey a survival benefit.<sup>34</sup> Duma et al<sup>34</sup> have described a technique of performing radiosurgery to the “leading edge” of a GBM, namely the migratory white matter pathways adjacent to and leading away from the CET component. The patients in their series had a median overall survival of 23 months, which is substantially longer than that in other comparable series.<sup>33,34</sup> These results provide further evidence supporting aggressive management of nCET in GBMs and again highlight the importance of not only high-quality pretreatment imaging but also careful re-imaging shortly before commencing radiation therapy. Edema related to CET may have receded, aiding delineation of nCET. Volumetric FLAIR imaging is likely to be of particular value in this context.

### **Identification of Non-Contrast-Enhancing Tumor**

To facilitate more aggressive management of nCET, there is a need to improve its accurate identification. In the preoperative setting, the main contributors to the FLAIR hyperintensity surrounding the CET component of a glioma are nCET and vasogenic edema. It is well-accepted that there is some overlap of these 2 etiologies, in particular adjacent to the CET component, but often a confident distinction of the dominant process is possible

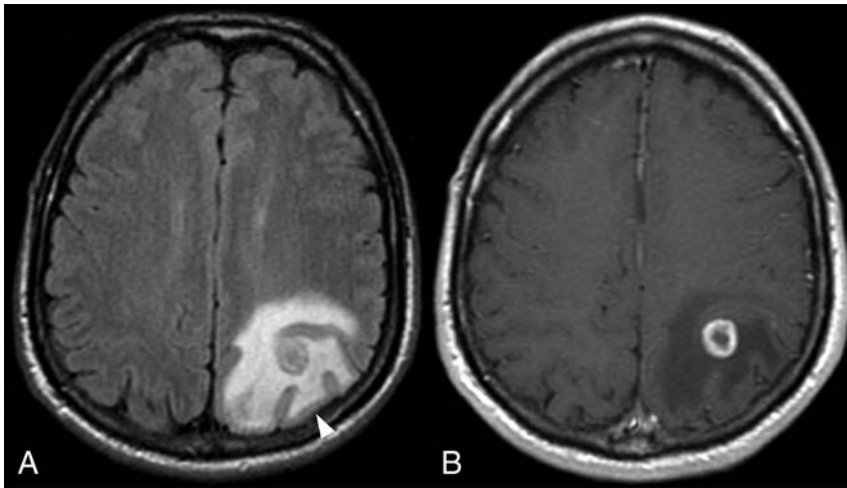


**FIG 1.** FLAIR imaging (A) showing edema around the CET component (B) sparing the cortex (arrowhead), producing the characteristic fingerlike appearance.

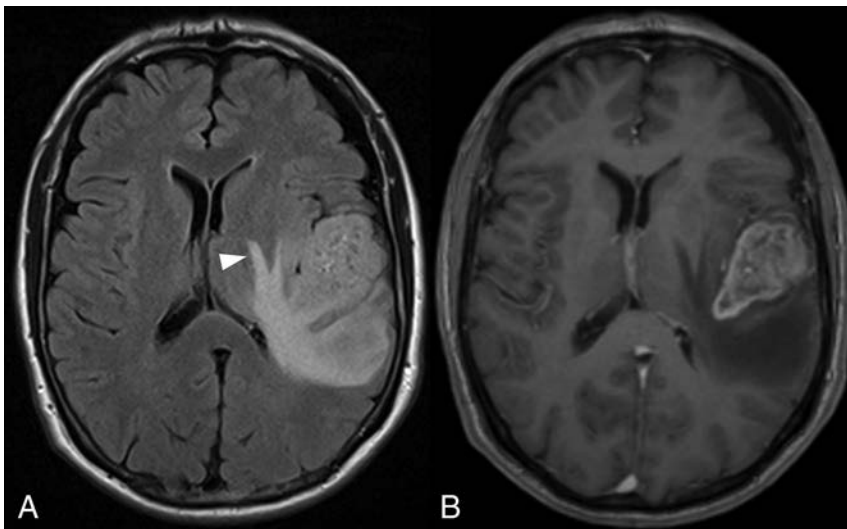


**FIG 2.** FLAIR imaging (A) showing edema extending around the left lentiform nucleus. The CET component is shown in B.

for at least a portion of the signal abnormality. We aimed, therefore, to provide and illustrate criteria that can help distinguish nCET and edema. Confirming that an abnormality on MR imaging correlates with nCET histopathologically is problematic because it is frequently not resected or separately biopsied. Even a comprehensive postmortem examination is limited by difficulties with coregistration and sampling error. As a result, these imaging criteria have been developed, in part, on the basis of knowledge of the imaging appearances and evolution, but they are nevertheless well accepted as evidenced by the description of similar strategies in the widely used Visually Accessible Rembrandt Images set of MR imaging features of glioma.<sup>35</sup> As technology improves, these principles are increasingly being validated by studies correlating imaging-guided biopsies with colocalized MR imaging metrics.

Although advanced MR imaging techniques such as MR spectroscopy and perfusion have value in determining the extent of nCET preoperatively, they are not universally available and are time-consuming and operator-dependent. These practical considerations are particularly relevant given the increasing use of

intraoperative MR imaging because assessment of residual nCET intraoperatively is based on conventional sequences. Even when advanced sequences are used preoperatively, it is useful to correlate these with the appearance on conventional sequences. For example, if CBV is elevated outside the CET component, there may be correlative features on T2WI and FLAIR.

Edema has several characteristic features. Edema is typically confined to the white matter, sparing the cortical ribbon and thus producing the characteristic fingerlike appearance (Fig 1).<sup>30</sup> Correlating with standard T2WI is useful for identifying this appearance because the cortex is usually better visualized.<sup>16,30</sup> Similar gray matter sparing of deep gray matter nuclei is also seen, with edema extending along the internal and external capsules (Fig 2). In contrast, gliomas frequently involve gray matter,<sup>16,36-38</sup> and such involvement can be confidently diagnosed as nCET (Figs 3 and 4).<sup>16</sup>

The white matter involvement of edema is typically relatively concentric around the enhancing lesions, other than where hindered by the relative barrier afforded by the gray matter. In contrast, eccentric extension of FLAIR hyperintensity, not accounted for by anatomic constraints, is highly suggestive of nCET. Wallerian degeneration is the main differential to consider for FLAIR hyperintensity along the course of the corticospinal tract, but this is most commonly seen in the context of a resection cavity or large necrotic tumor involving

the precentral gyrus. There is also usually appreciable volume loss, aiding the distinction. Parenchymal expansion, conversely, is a useful feature to confirm nCET, particularly in the corpus callosum (Fig 4).

Another useful differentiating feature is that edema is typically associated with more marked T2 and FLAIR hyperintensity than nCET,<sup>30</sup> often fading somewhat toward the periphery of the edema. In contrast, FLAIR hyperintensity related to nCET is usually more subtle. The relatively mild FLAIR hyperintensity of nCET is well-demonstrated in the gray matter where the distinction is simpler but can also be seen in the white matter, for example with an eccentric tongue of nCET extending beyond an area that has the typical appearance of edema. This finding has recently been supported by a study correlating radiographically localized biopsies with multiparametric MR imaging, which found that T2 FLAIR was inversely correlated with cell density.<sup>39</sup> These results support mild FLAIR hyperintensity being a feature of nCET, while greater hyperintensity indicates that edema dominates.

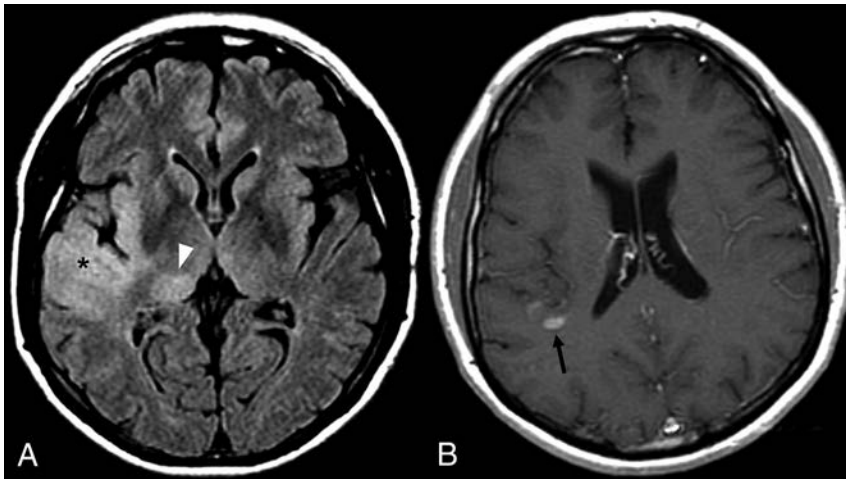


**FIG 3.** FLAIR imaging (A) demonstrating nCET involving the anterior right temporal cortex (*asterisk*), insula, and thalamus (*arrowhead*). A narrow window width has been used to improve conspicuity. The small CET component lies further superiorly (B, *arrow*).

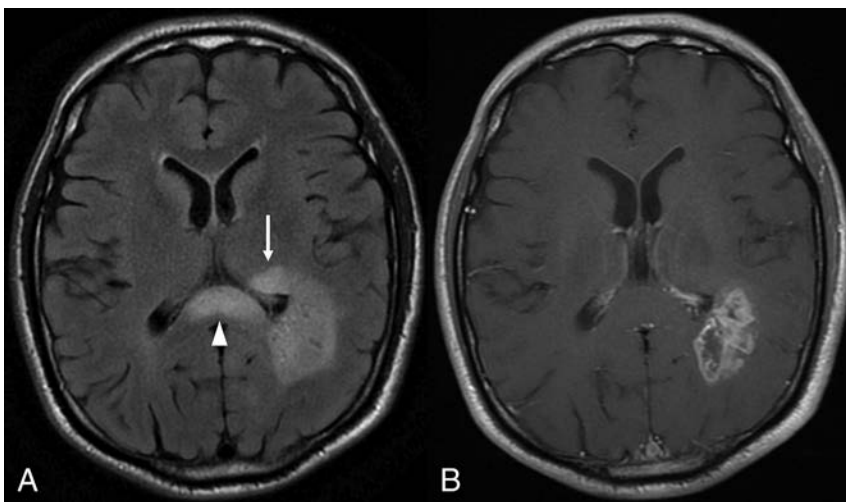


**FIG 4.** FLAIR imaging (A) showing eccentric extension of nCET across the corpus callosum, with associated expansion (*arrowhead*). Rounded hyperintensity in the left thalamus (*arrow*) is also consistent with nCET. Note the paucity of edema in the white matter immediately adjacent to the CET component (B).

**Conventional and advanced MRI features useful for differentiating between nCET and edema**

nCET	Edema
Conventional MRI features	
Gray matter involvement	Sparses the gray matter
Eccentric	Relatively concentric around enhancing lesions
Relatively mild FLAIR and T2 hyperintensity	More marked FLAIR and T2 hyperintensity
Focal parenchymal expansion	More diffuse mass effect if marked edema
Advanced MRI sequences	
Relative diffusion restriction	Facilitated diffusion
Choline elevation, NAA depletion	Normal MRS findings
Elevated rCBV around CET	rCBV elevation confined to CET

**Note:**—rCBV indicates relative cerebral blood volume.

A final conventional MR imaging feature useful for identifying nCET is mass effect. The edema surrounding CET may be extensive and may produce generalized mass effect, though often this is less pronounced. In contrast, the mass effect from nCET is often more focal, with parenchymal expansion and distortion rather than compression. Edema can thin the cortex and thus mimic cortical involvement, but relative expansion of the cortex, even mild, is convincing evidence of nCET. Expansion of nCET may be more rounded and mass-like,<sup>31</sup> and this appearance is perhaps most easily identified as nCET. A white matter infiltration pattern of nCET is typically associated with less mass effect, but other features, as described above, usually allow this distinction. Multifocality, in which there is evidence of a communication between enhancing lesions, most commonly on FLAIR imaging,<sup>40</sup> can also be used to infer intervening nCET.

Despite our best effort, we acknowledge that the above criteria do not allow the complete differentiation between nCET and edema in many patients. In particular, even when effort is made to identify areas confidently diagnosable as nCET, this will underestimate its true extent. Areas of FLAIR hyperintensity that have the typical appearance of edema will almost inevitably contain some nCET to a degree that is both variable and difficult to determine. Advanced MR imaging sequences are thus most useful in the white matter and are well-established. With the growing

number of available techniques, a comprehensive review of these is beyond of the scope of this article, but the key features are discussed briefly below. Both the conventional and advanced MR imaging features for identifying nCET are summarized in the Table.

The potential use of DWI for identifying nCET is based on the correlation between ADC values and tumor cellularity.<sup>41-43</sup> This association suggests that relative diffusion restriction (lower ADC values) is a marker of nCET, in contrast to the facilitated diffusion occurring with edema.<sup>44</sup> Published results have been conflicting,<sup>41,44-46</sup> but reassuring results have been obtained with newer techniques. For example, Price et al<sup>47</sup> have suggested value in DTI, with infiltrating tumor suggested by the presence of an increase in the isotropic component of the diffusion tensor and a marginal increase in the anisotropic component. Stadlbauer et al<sup>48</sup> have suggested that fractional anisotropy correlates better with histopathologic parameters than mean diffusivity. Functional diffu-

sion maps and high-b-value DWI have also been suggested as useful tools for identifying nCET.<sup>49,50</sup>

On MR perfusion imaging, nCET can be identified by relative CBV elevation outside the CET component, and again it is relative to normal parenchyma. Although relative CBV elevation may be a marker more of tumor vascularity than cellularity,<sup>51</sup> a correlation with both microvascular density and cell density has been suggested.<sup>52</sup> Identifying nCET based on diffusion restriction and elevated relative CBV may be particularly important because both features predict the subsequent development of enhancement.<sup>53,54</sup> It is possible, however, that a confident diagnosis of nCET on conventional sequences also predicts transformation to a higher grade; indeed, this seems to be the case for visible cortical nCET,<sup>13</sup> though the literature on this topic is limited.

The use of MR spectroscopy for identifying nCET is based on the presence of a “glioma trace,” with choline elevation (denoting increased membrane turnover) and decreased NAA. It is not clear, however, whether such MR spectroscopy changes necessarily imply that nCET is the dominant process (above edema), a finding important when weighing the risks and benefits of more aggressive resection. Greater degrees of choline elevation and/or NAA depletion are associated with higher histologic grades of glioma<sup>55,56</sup>; thus, it may be useful to use an MR spectroscopy threshold to predict value in resection.

In some cases, there will be overlap between features (both conventional and advanced); while in others, nCET will be identifiable by only a single MR imaging sequence or specific MR imaging feature. It is, therefore, important to use a multiparametric approach to improve both sensitivity and specificity for identifying nCET and to confirm that it is the dominant process within a given area of signal abnormality. This approach is not limited to MR imaging, and the addition of PET has the potential to provide complementary information. The most commonly used PET tracer, FDG, has limited use in the brain due to high uptake in normal brain tissue. This has, however, been overcome by the introduction of novel PET tracers, such as the amino acid tracer [<sup>18</sup>F]-fluoroethyl-L-tyrosine (FET), and FET-PET can be combined with MR imaging to improve delineation of nCET and thus aid radiation therapy planning.<sup>57,58</sup>

Computational methods are also being investigated. For example, Artzi et al<sup>59</sup> have suggested that combining radiomic texture analysis with machine learning may improve the delineation of nCET. The authors themselves concede that histologic validation remains a limitation, though some of this concern has been overcome by Hu et al,<sup>60</sup> who correlated similar techniques with image-guided biopsies and were able to identify nCET with an accuracy of 88% in both the training and validation cohorts. Nevertheless, specificity remains a consideration when identifying subtle differences not readily discernible by the human eye. Such subtle nCET would be expected to contain a lower proportion of tumor cells than areas identified by a neuroradiologist, and a neurosurgeon may hesitate to extend the resection. With time, quantification of such techniques can be expected to improve, and the combination of computational techniques with a growing armamentarium of MR imaging sequences likely represents the future of this field. It will be some time until such techniques are disseminated into routine clinical practice, however, and optimizing the

use and interpretation of conventional sequences remain a priority.

## CONCLUSIONS

There is a growing understanding of the prognostic importance of nCET in GBM. Extending neurosurgical resection beyond CET to the nCET component is associated with improved survival, as is more aggressive targeting of nCET with radiosurgery. Optimizing these therapeutic strategies requires an understanding of the features that can differentiate nCET from other causes of signal abnormality, in particular edema. Improved delineation of nCET from edema will facilitate more aggressive management of nCET and the associated survival benefits.

## REFERENCES

1. Louis DN, Ohgaki H, Wiestler OD, et al. *World Health Organization Histological Classification of Tumors of the Central Nervous System*. Lyon: International Agency for Research on Cancer; 2016
2. Yan H, Parsons DW, Jin G, et al. **IDH1 and IDH2 mutations in gliomas.** *N Engl J Med* 2009;360:765–73 CrossRef Medline
3. Weller M, van den Bent M, Tonn JC, et al; European Association for Neuro-Oncology (EANO) Task Force on Gliomas. **European Association for Neuro-Oncology (EANO) guideline on the diagnosis and treatment of adult astrocytic and oligodendroglial gliomas.** *Lancet Oncol* 2017;18:e315–29 CrossRef Medline
4. Karachaliou N, Gonzalez-Cao M, Sosa A, et al. **The combination of checkpoint immunotherapy and targeted therapy in cancer.** *Ann Transl Med* 2017;5:388 CrossRef Medline
5. Lee YT, Tan YJ, Oon CE. **Molecular targeted therapy: treating cancer with specificity.** *Eur J Pharmacol* 2018;834:188–96 CrossRef Medline
6. Hardesty DA, Sanai N. **The value of glioma extent of resection in the modern neurosurgical era.** *Front Neurol* 2012;3:140 CrossRef Medline
7. Lacroix M, Abi-Said D, Fourney DR, et al. **A multivariate analysis of 416 patients with glioblastoma multiforme: prognosis, extent of resection, and survival.** *J Neurosurg* 2001;95:190–98 CrossRef Medline
8. Stummer W, Reulen HJ, Meinel T, et al; ALA-Glioma Study Group. **Extent of resection and survival in glioblastoma multiforme: identification of and adjustment for bias.** *Neurosurgery* 2008;62:564–76; discussion 564–76 CrossRef Medline
9. Chamberlain MC. **Radiographic patterns of relapse in glioblastoma.** *J Neurooncol* 2011;101:319–23 CrossRef Medline
10. Kubben PL, ter Meulen KJ, Schijns OE, et al. **Intraoperative MRI-guided resection of glioblastoma multiforme: a systematic review.** *Lancet Oncol* 2011;12:1062–70 CrossRef Medline
11. Schulz C, Waldeck S, Mauer UM. **Intraoperative image guidance in neurosurgery: development, current indications, and future trends.** *Radiol Res Pract* 2012;2012:197364 CrossRef Medline
12. Zhao S, Wu J, Wang C, et al. **Intraoperative fluorescence-guided resection of high-grade malignant gliomas using 5-aminolevulinic acid-induced porphyrins: a systematic review and meta-analysis of prospective studies.** *PLoS One* 2013;8:e63682 CrossRef Medline
13. Lasocki A, Gaillard F, Tacey MA, et al. **The incidence and significance of multicentric noncontrast-enhancing lesions distant from a histologically-proven glioblastoma.** *J Neurooncol* 2016;129:471–78 CrossRef Medline
14. Eidel O, Burth S, Neumann JO, et al. **Tumor infiltration in enhancing and non-enhancing parts of glioblastoma: a correlation with histopathology.** *PLoS One* 2017;12:e0169292 CrossRef Medline
15. Jain R, Poisson LM, Gutman D, et al. **Outcome prediction in patients with glioblastoma by using imaging, clinical, and genomic biomarkers: focus on the nonenhancing component of the tumor.** *Radiology* 2014;272:484–93 CrossRef Medline
16. Lasocki A, Gaillard F, Tacey M, et al. **Incidence and prognostic sig-**

- nificance of non-enhancing cortical signal abnormality in glioblastoma. *J Med Imaging Radiat Oncol* 2016;60:66–73 CrossRef Medline
17. Grabowski MM, Recinos PF, Nowacki AS, et al. Residual tumor volume versus extent of resection: predictors of survival after surgery for glioblastoma. *J Neurosurg* 2014;121:1115–23 CrossRef Medline
  18. Kotrotsou A, Elakkad A, Sun J, et al. Multi-center study finds post-operative residual non-enhancing component of glioblastoma as a new determinant of patient outcome. *J Neurooncol* 2018;139:125–33 CrossRef Medline
  19. Carrillo JA, Lai A, Nghiemphu PL, et al. Relationship between tumor enhancement, edema, IDH1 mutational status, MGMT promoter methylation, and survival in glioblastoma. *AJNR Am J Neuroradiol* 2012;33:1349–55 CrossRef Medline
  20. Lasocki A, Tsui A, Gaillard F, et al. Reliability of noncontrast-enhancing tumor as a biomarker of IDH1 mutation status in glioblastoma. *J Clin Neurosci* 2017;39:170–75 CrossRef Medline
  21. Hygino da Cruz LC Jr, Rodriguez I, Domingues RC, et al. Pseudoprogression and pseudoreponse: imaging challenges in the assessment of posttreatment glioma. *AJNR Am J Neuroradiol* 2011;32:1978–85 CrossRef Medline
  22. Wen PY, Macdonald DR, Reardon DA, et al. Updated response assessment criteria for high-grade gliomas: Response Assessment in Neuro-Oncology Working Group. *J Clin Oncol* 2010;28:1963–72 CrossRef Medline
  23. Boxerman JL, Zhang Z, Safriel Y, et al. Prognostic value of contrast enhancement and FLAIR for survival in newly diagnosed glioblastoma treated with and without bevacizumab: results from ACRIN 6686. *Neuro Oncol* 2018;20:1400–10 CrossRef Medline
  24. Huang RY, Rahman R, Ballman KV, et al. The impact of T2/FLAIR evaluation per RANO criteria on response assessment of recurrent glioblastoma patients treated with bevacizumab. *Clin Cancer Res* 2016;22:575–81 CrossRef Medline
  25. Nowosielski M, Wiestler B, Goebel G, et al. Progression types after antiangiogenic therapy are related to outcome in recurrent glioblastoma. *Neurology* 2014;82:1684–92 CrossRef Medline
  26. Yordanova YN, Moritz-Gasser S, Duffau H. Awake surgery for WHO grade II gliomas within “noneloquent” areas in the left dominant hemisphere: toward a “supratotal” resection: clinical article. *J Neurosurg* 2011;115:232–39 CrossRef Medline
  27. Li YM, Suki D, Hess K, et al. The influence of maximum safe resection of glioblastoma on survival in 1229 patients: can we do better than gross-total resection? *J Neurosurg* 2016;124:977–88 CrossRef Medline
  28. Pessina F, Navarria P, Cozzi L, et al. Maximize surgical resection beyond contrast-enhancing boundaries in newly diagnosed glioblastoma multiforme: is it useful and safe? A single institution retrospective experience. *J Neurooncol* 2017;135:129–39 CrossRef Medline
  29. Beiko J, Suki D, Hess KR, et al. IDH1 mutant malignant astrocytomas are more amenable to surgical resection and have a survival benefit associated with maximal surgical resection. *Neuro Oncol* 2014;16:81–91 CrossRef Medline
  30. Pope WB, Sayre J, Perlina A, et al. MR imaging correlates of survival in patients with high-grade gliomas. *AJNR Am J Neuroradiol* 2005;26:2466–74 Medline
  31. Lasocki A, Gaillard F, Tacey M, et al. Morphologic patterns of non-contrast-enhancing tumor in glioblastoma correlate with IDH1 mutation status and patient survival. *J Clin Neurosci* 2018;47:168–73 CrossRef Medline
  32. Baldock AL, Ahn S, Rockne R, et al. Patient-specific metrics of invasiveness reveal significant prognostic benefit of resection in a predictable subset of gliomas. *PLoS One* 2014;9:e99057 CrossRef Medline
  33. Stupp R, Mason WP, van den Bent MJ, et al; European Organisation for Research and Treatment of Cancer Brain Tumor and Radiotherapy Groups, National Cancer Institute of Canada Clinical Trials Group. Radiotherapy plus concomitant and adjuvant temozolomide for glioblastoma. *N Engl J Med* 2005;352:987–96 CrossRef Medline
  34. Duma CM, Kim BS, Chen PV, et al. Upfront boost gamma knife “leading-edge” radiosurgery to FLAIR MRI-defined tumor migration pathways in 174 patients with glioblastoma multiforme: a 15-year assessment of a novel therapy. *J Neurosurg* 2016;125(Suppl 1):40–49 CrossRef Medline
  35. Wiki for the VASARI feature set. The National Cancer Institute. 2015. <https://wiki.cancerimagingarchive.net/display/Public/VASARI+Research+Project>. Accessed November 22, 2018
  36. Muccio CF, Tarantino A, Esposito G, et al. Differential diagnosis by unenhanced FLAIR T2-weighted magnetic resonance images between solitary high grade gliomas and cerebral metastases appearing as contrast-enhancing cortico-subcortical lesions. *J Neurooncol* 2011;103:713–17 CrossRef Medline
  37. Stuckey SL, Wijedeera R. Multicentric/multifocal cerebral lesions: can fluid-attenuated inversion recovery aid the differentiation between glioma and metastases? *J Med Imaging Radiat Oncol* 2008;52:134–39 CrossRef Medline
  38. Tang YM, Ngai S, Stuckey S. The solitary enhancing cerebral lesion: can FLAIR aid the differentiation between glioma and metastasis? *AJNR Am J Neuroradiol* 2006;27:609–11 Medline
  39. Chang PD, Malone HR, Bowden SG, et al. A multiparametric model for mapping cellularity in glioblastoma using radiographically localized biopsies. *AJNR Am J Neuroradiol* 2017;38:890–98 CrossRef Medline
  40. Lasocki A, Gaillard F, Tacey M, et al. Multifocal and multicentric glioblastoma: improved characterisation with FLAIR imaging and prognostic implications. *J Clin Neurosci* 2016;31:92–98 CrossRef Medline
  41. Brandão LA, Shiroishi MS, Law M. Brain tumors: a multimodality approach with diffusion-weighted imaging, diffusion tensor imaging, magnetic resonance spectroscopy, dynamic susceptibility contrast and dynamic contrast-enhanced magnetic resonance imaging. *Magn Reson Imaging Clin N Am* 2013;21:199–239 CrossRef Medline
  42. Guo AC, Cummings TJ, Dash RC, et al. Lymphomas and high-grade astrocytomas: comparison of water diffusibility and histologic characteristics. *Radiology* 2002;224:177–83 CrossRef Medline
  43. Kono K, Inoue Y, Nakayama K, et al. The role of diffusion-weighted imaging in patients with brain tumors. *AJNR Am J Neuroradiol* 2001;22:1081–88 Medline
  44. Tien RD, Felsberg GJ, Friedman H, et al. MR imaging of high-grade cerebral gliomas: value of diffusion-weighted echoplanar pulse sequences. *AJR Am J Roentgenol* 1994;162:671–77 CrossRef Medline
  45. Castillo M, Smith JK, Kwock L, et al. Apparent diffusion coefficients in the evaluation of high-grade cerebral gliomas. *AJNR Am J Neuroradiol* 2001;22:60–64 Medline
  46. Holodny AI, Makeyev S, Beattie BJ, et al. Apparent diffusion coefficient of glial neoplasms: correlation with fluorodeoxyglucose-positron-emission tomography and gadolinium-enhanced MR imaging. *AJNR Am J Neuroradiol* 2010;31:1042–48 CrossRef Medline
  47. Price SJ, Jena R, Burnet NG, et al. Improved delineation of glioma margins and regions of infiltration with the use of diffusion tensor imaging: an image-guided biopsy study. *AJNR Am J Neuroradiol* 2006;27:1969–74 Medline
  48. Stadlbauer A, Ganslandt O, Buslei R, et al. Gliomas: histopathologic evaluation of changes in directionality and magnitude of water diffusion at diffusion-tensor MR imaging. *Radiology* 2006;240:803–10 CrossRef Medline
  49. Ellingson BM, Malkin MG, Rand SD, et al. Validation of functional diffusion maps (fDMs) as a biomarker for human glioma cellularity. *J Magn Reson Imaging* 2010;31:538–48 CrossRef Medline
  50. Zeng Q, Ling C, Shi F, et al. Glioma infiltration sign on high b-value diffusion-weighted imaging in gliomas and its prognostic value. *J Magn Reson Imaging* 2018 Mar 1. [Epub ahead of print] CrossRef Medline
  51. Price SJ, Green HA, Dean AF, et al. Correlation of MR relative cerebral blood volume measurements with cellular density and proliferation for glioblastoma. *N Engl J Med* 2005;352:987–96 CrossRef Medline

- eration in high-grade gliomas: an image-guided biopsy study. *AJNR Am J Neuroradiol* 2011;32:501–06 CrossRef Medline
52. Sadeghi N, D'Haene N, Decaestecker C, et al. **Apparent diffusion coefficient and cerebral blood volume in brain gliomas: relation to tumor cell density and tumor microvessel density based on stereotactic biopsies.** *AJNR Am J Neuroradiol* 2008;29:476–82 CrossRef Medline
  53. Gupta A, Young RJ, Karimi S, et al. **Isolated diffusion restriction precedes the development of enhancing tumor in a subset of patients with glioblastoma.** *AJNR Am J Neuroradiol* 2011;32:1301–06 CrossRef Medline
  54. Danchaivijitr N, Waldman AD, Tozer DJ, et al. **Low-grade gliomas: do changes in rCBV measurements at longitudinal perfusion-weighted MR imaging predict malignant transformation?** *Radiology* 2008;247:170–78 CrossRef Medline
  55. Stadlbauer A, Gruber S, Nimsy C, et al. **Preoperative grading of gliomas by using metabolite quantification with high-spatial-resolution proton MR spectroscopic imaging.** *Radiology* 2006;238:958–69 CrossRef Medline
  56. Castillo M, Smith JK, Kwock L. **Correlation of myo-inositol levels and grading of cerebral astrocytomas.** *AJNR Am J Neuroradiol* 2000;21:1645–49 Medline
  57. Nowosielski M, DiFranco MD, Putzer D, et al. **An intra-individual comparison of MRI, [18F]-FET and [18F]-FLT PET in patients with high-grade gliomas.** *PLoS One* 2014;9:e95830 CrossRef Medline
  58. Lopez WO, Cordeiro JG, Albicker U, et al. **Correlation of (18)F-fluoroethyl tyrosine positron-emission tomography uptake values and histomorphological findings by stereotactic serial biopsy in newly diagnosed brain tumors using a refined software tool.** *Oncotargets Ther* 2015;8:3803–15 CrossRef Medline
  59. Artzi M, Liberman G, Blumenthal DT, et al. **Differentiation between vasogenic edema and infiltrative tumor in patients with high-grade gliomas using texture patch-based analysis.** *J Magn Reson Imaging* 2018 Jan 3. [Epub ahead of print] CrossRef Medline
  60. Hu LS, Ning S, Eschbacher JM, et al. **Multi-parametric MRI and texture analysis to visualize spatial histologic heterogeneity and tumor extent in glioblastoma.** *PLoS One* 2015;10:e0141506 CrossRef Medline

# Chimeric Antigen Receptor T-Cell Therapy: What the Neuroradiologist Needs to Know

H.A. Valand, F. Huda, and R.K. Tu

## ABSTRACT

**SUMMARY:** Chimeric antigen receptor T-cell therapy is an exciting and rapidly emerging “fifth pillar” treatment for hematologic cancers. Unique treatment-related toxicities and cost remain a major hindrance to its widespread application. The commonly faced challenges with this innovative therapy, its neurotoxicity, and manifestation on neuroimaging studies, are reviewed.

**ABBREVIATIONS:** CAR = chimeric antigen receptor; CRS = cytokine release syndrome; CRES = CAR-T-cell–related encephalopathy syndrome

## WHAT ARE CHIMERIC ANTIGEN RECEPTOR T-CELLS?

Two major types of immunotherapies have been developed during the past decade; 1) monoclonal antibodies agents specific to target tumor, and 2) adoptive T-cell therapy, agents that mount an immune response against tumor cells. Chimeric antigen receptor (CAR) T-cells are the adoptive T-cell therapy agents that are genetically engineered to produce an immune response against tumor cells.<sup>1,2</sup>

## WHO BENEFITS FROM CAR T-CELL THERAPY?

Since 2017, the US Food and Drug Administration has approved 2 CAR T-cell agents for 3 indications: 1) axicabtagene ciloleucel for relapsed/refractory diffuse large B-cell lymphoma, 2) tisagenlecleucel for pediatric and young adult leukemia, and 3) tisagenlecleucel for adult non-Hodgkin lymphoma. These therapies target, bind, and destroy cluster of differentiation 19 antigen, predominantly found in B-cell tumors.<sup>3-6</sup>

## HOW IS CAR T-CELL THERAPY DELIVERED TO PATIENTS?

Manufacturing of CAR T-cells involves 5 phases: 1) extraction of T-cells with an apheresis technique; 2) reprogramming of T-cells by disabled virus vectors, which genetically modify T-cells to

produce artificial protein receptors called chimeric antigen receptors, used to locate and bind the targeted tumor; 3) expansion and mass production of CAR T-cells and freezing when sufficient numbers are produced; 4) lymphodepletion, a reduction of the white blood cell load, making space for incoming reprogrammed CAR T-cells; and 5) infusion/treatment with CAR T-cells, in which cells multiply and mount an immune response against the targeted cancer cells. According to the current guidelines, patients are required to stay in the hospital from a few days to several weeks depending on their adverse effects profile. Posttreatment recovery time is approximately 2–3 months.<sup>7-10</sup>

## WHAT ARE THE MAJOR TOXICITIES OF CAR T-CELL THERAPY AND HOW ARE THEY GRADED?

Cytokine release syndrome (CRS) is the most commonly occurring toxicity in patients receiving CAR T-cell therapy followed by CAR-T-cell–related encephalopathy syndrome (CRES).

CRS results from immune activation resulting in elevated inflammatory cytokines. CRS-associated symptoms can range from fever, malaise, anorexia, and myalgias to end-organ dysfunction. There are 4 grades of CRS toxicity. Grade 1 comprises constitutional symptoms. Grade 2 includes hypotension that responds to fluids or low-dose vasopressors, hypoxia that responds to <40% O<sub>2</sub>, and grade 2 organ toxicities. Grade 3 encompasses hypotension requiring high-dose vasopressors, hypoxia requiring >40% O<sub>2</sub>, and grades 3 and 4 organ toxicities. Grade 4 also includes hypoxia requiring mechanical ventilation and grade 4 organ toxicities.<sup>11,12</sup> Severe CRS toxicity can rarely progress into fulminant hemophagocytic lymphohistiocytosis.<sup>12</sup>

CRES-associated symptoms can range from mild neurotoxicity to more severe forms such as seizures, paralysis, raised intracranial pressure (ICP), papilledema, and cerebral edema. CRES is

Received February 17, 2019; accepted after revision March 6.

From the American University of Integrative Sciences (H.A.V.), Brampton, Ontario, Canada; Department of Radiology (F.H.), George Washington University Hospital, Washington, DC; and Progressive Radiology (R.K.T.), George Washington University, Washington, DC.

Please address correspondence to Raymond K. Tu, MD, MS, FACR, Progressive Radiology, George Washington University, United Medical Center, 2121 K St NW, Suite 100, Washington, DC 20037; e-mail: Raymond.Tu@progressiveradiology.net; @RayTu10

<http://dx.doi.org/10.3174/ajnr.A6042>

categorized into 4 grades based on neurologic assessment (orientation, naming of objects, ability to write a standard sentence, and counting backwards), raised ICP, and the presence of seizures or motor weakness. Grading of neurologic assessment is as follows: mild (grade 1), moderate (grade 2), severe (grade 3), and critical/obtunded (grade 4). The presence of raised ICP, seizures, or motor weakness comprise grades 3 and 4.<sup>13-15</sup>

A study conducted by Gofshteyn et al<sup>16</sup> concluded that the incidence of neurotoxicity in pediatric and young adult populations (~45%) is similar to that found in the adult population (~40%–42%). The study demonstrated that the occurrence of life-threatening neurotoxicity was lower in comparison with adults and all patients had neurologic recovery with no fatal outcomes.

### WHAT ARE THE NEURORADIOLOGIC FINDINGS IN PATIENTS RECEIVING CAR T-CELL THERAPY?

A study conducted by Davila et al<sup>17</sup> at the National Institutes of Health showed that patients who underwent neuroimaging had unremarkable examination findings.

Santomasso et al<sup>13</sup> described 2 forms of neurotoxicity: mild and severe. Mild neurotoxicity comprises delirium, tremor, and headaches. Severe neurotoxicity ranges among disorientation, loss of attention, partial-to-global aphasia, myoclonus, and seizures. All patients with mild neurotoxicity had unremarkable MR imaging findings of the brain. In addition, of the 14 patients with severe neurotoxicity, 9 patients also had unremarkable changes. Patients with positive MR imaging findings showed a nonspecific pattern of predominantly white matter involvement extending to the brain stem. These nonspecific changes can also be seen with migraines and chronic microvascular ischemia resulting from common conditions such as hypertension among others.<sup>18</sup> Following symptom resolution, 2 of the remaining 5 patients with MR imaging–positive findings had reversal of the MR imaging changes.

### WHAT ARE THE NEURORADIOLOGIC RECOMMENDATIONS IN PATIENTS RECEIVING CAR T-CELL THERAPY?

Given the wide range of nonspecific brain findings and etiologies, the authors suggest a baseline pretreatment MR imaging to document any treatment-related changes. Given their immunocompromised state, these patients are prone to infections, which can result in the release of septic emboli into the bloodstream. This can lead to cerebritis and could further progress to abscess, advocating the use of contrast-enhanced MR imaging.<sup>19</sup>

### WHAT ARE THE CHALLENGES IN IMPLEMENTING CAR T-CELL THERAPY?

Despite its promising treatment response, health plan coverage and drug costs are barriers to access CAR T-cell therapy. Axicabtagene ciloleucel and tisagenlecleucel treatment costs are estimated at \$373,000 and \$475,000, respectively.<sup>20,21</sup> The nondrug costs due to adverse effects, apheresis, and lymphodepletion therapy are not part of these drug regimens and can cost from \$30,000 to \$56,000.<sup>22</sup> In addition, the facility costs to process and produce the final product, along with the use of cell therapy experts are

enormous; treatment delivery, risk assessment, and legal counseling teams are important, costly, and essential.<sup>23</sup> Currently, CAR T-cell therapy is not approved for Medicare patients. However, recently the US Centers for Medicare and Medicaid Services has proposed comprehensive nationwide coverage for CAR T-cell therapy.<sup>24</sup>

### REFERENCES

1. Sathyanarayanan V, Neelapu SS. **Cancer immunotherapy: strategies for personalization and combinatorial approaches.** *Mol Oncol* 2015; 9:2043–53 CrossRef Medline
2. Khalil DN, Smith EL, Brentjens RJ, et al. **The future of cancer treatment: immunomodulation, CARs and combination immunotherapy.** *Nat Rev Clin Oncol* 2016;13:273–90 CrossRef Medline
3. Ruella M, Xu J, Barrett DM, et al. **Induction of resistance to chimeric antigen receptor T cell therapy by transduction of a single leukemic B cell.** *Nat Med* 2018;24:1499–1503 CrossRef Medline
4. U.S. Food and Drug Administration. STN: BL 125646/0. <https://www.fda.gov/downloads/BiologicsBloodVaccines/CellularGeneTherapyProducts/ApprovedProducts/UCM574106.pdf>. Accessed January 30, 2019
5. U.S. Food and Drug Administration. BL 125646/76. <https://www.fda.gov/downloads/BiologicsBloodVaccines/CellularGeneTherapyProducts/ApprovedProducts/UCM606523.pdf>. Accessed January 28, 2019
6. U.S. Food and Drug Administration. BL 125643/0 <https://www.fda.gov/downloads/BiologicsBloodVaccines/CellularGeneTherapyProducts/ApprovedProducts/UCM581259.pdf>. Accessed January 28, 2019
7. Chemical & Engineering News. Controlling CAR-T: How scientists plan to make the engineered T cell therapy safer, and work for more cancers. <https://cen.acs.org/pharmaceuticals/oncology/Controlling-CAR-T-scientists-plan/96/119>. Accessed February 5, 2019
8. Leukemia and Lymphoma Society. Chimeric Antigen Receptor (CAR) T-Cell Therapy. <https://www.lls.org/treatment/types-of-treatment/immunotherapy/chimeric-antigen-receptor-car-t-cell-therapy>. Accessed February 6, 2019
9. National Cancer Institute. NCI Dictionary of Cancer Terms. <https://www.cancer.gov/publications/dictionaries/cancer-terms/def/car-t-cell-therapy>. Accessed February 6, 2019
10. Dana Farber Cancer Institute. How CAR T-cell works. <https://www.dana-farber.org/cellular-therapies-program/car-t-cell-therapy/how-car-t-cell-therapy-works/>. Accessed February 6, 2019
11. Lee DW, Gardner R, Porter DL, et al. **Current concepts in the diagnosis and management of cytokine release syndrome.** *Blood* 2014; 124:188–95 CrossRef Medline
12. Neelapu SS, Tummala S, Kebriaei P, et al. **Chimeric antigen receptor T-cell therapy: assessment and management of toxicities.** *Nat Rev Clin Oncol* 2018;15:47–62 CrossRef Medline
13. Santomasso BD, Park JH, Salloum D, et al. **Clinical and biological correlates of neurotoxicity associated with CAR T-cell therapy in patients with B-cell acute lymphoblastic leukemia.** *Cancer Discov* 2018;8:958–71 CrossRef Medline
14. Gust J, Hay KA, Hanafi LA, et al. **Endothelial activation and blood-brain barrier disruption in neurotoxicity after adoptive immunotherapy with CD19 CAR-T cells.** *Cancer Discov* 2017;7:1404–19 CrossRef Medline
15. MD Anderson Cancer Center. Chimeric Antigen Receptor (CAR) Cell Therapy Toxicity Assessment and Management—Adult. <https://www.mdanderson.org/documents/for-physicians/algorithms/clinical-management/clin-management-cytokine-release-web-algorithm.pdf>. Accessed February 18, 2019
16. Gofshteyn JS, Shaw PA, Teachey DT, et al. **Neurotoxicity after CTL019 in a pediatric and young adult cohort.** *Ann Neurol* 2018;84: 537–46 CrossRef Medline
17. Davila ML, Riviere I, Wang X, et al. **Efficacy and toxicity manage-**

- ment of 19–28z CAR T cell therapy in B cell acute lymphoblastic leukemia. *Sci Transl Med* 2014;6:224ra25 CrossRef Medline
18. Trauninger A, Leél-Ossy E, Kamson DO, et al. **Risk factors of migraine-related brain white matter hyperintensities: an investigation of 186 patients.** *J Headache Pain* 2011;12:97–103 CrossRef Medline
  19. Smirniotopoulos JG, Murphy FM, Rushing EJ, et al. **Patterns of contrast enhancement in the brain and meninges.** *Radiographics* 2007; 27:525–51 CrossRef Medline
  20. Lin JK, Lerman BJ, Barnes JL, et al. **Cost effectiveness of chimeric antigen receptor T-cell therapy in relapsed or refractory pediatric B-cell acute lymphoblastic leukemia.** *J Clin Oncol* 2018 Sep 13. [Epub ahead of print] CrossRef Medline
  21. Hao Y, Eldjerou LK, Yang H, et al. **Cost-effectiveness analysis of CTL019 for the treatment of pediatric and young adult patients with relapsed or refractory B-cell acute lymphoblastic leukemia in the United States.** In: *Proceedings of the American Society of Hematology Annual Meeting and Exposition*, Atlanta, Georgia. December 9–12, 2017; abstract 609
  22. Hernandez I, Prasad V, Gellad WF. **Total costs of chimeric antigen receptor T-cell immunotherapy.** *JAMA Oncol* 2018;4:994–96 CrossRef Medline
  23. Managed Health Care Executive. CAR T-cell therapy life-saving treatment, huge price tag. [https://www.managedhealthcareexecutive.com/sites/default/files/legacy/mm/digital/media/mhe1118\\_ezine\\_R1.pdf](https://www.managedhealthcareexecutive.com/sites/default/files/legacy/mm/digital/media/mhe1118_ezine_R1.pdf). Accessed February 6, 2019
  24. Centers for Medicare & Medicaid Services. Proposed Decision Memo for Chimeric Antigen Receptor (CAR) T-cell Therapy for Cancers (CAG-00451N). Last Updated February 15, 2019. <https://www.cms.gov/medicare-coverage-database/details/nca-proposed-decision-memo.aspx?NCAId=291>. Accessed February 15, 2019

# Predicting Motor Outcome in Acute Intracerebral Hemorrhage

J. Puig, G. Blasco, M. Terceño, P. Daunis-i-Estadella, G. Schlaug, M. Hernandez-Perez, V. Cuba, G. Carbó, J. Serena, M. Essig, C.R. Figley, K. Nael, C. Leiva-Salinas, S. Pedraza, and Y. Silva



## ABSTRACT

**BACKGROUND AND PURPOSE:** Predicting motor outcome following intracerebral hemorrhage is challenging. We tested whether the combination of clinical scores and DTI-based assessment of corticospinal tract damage within the first 12 hours of symptom onset after intracerebral hemorrhage predicts motor outcome at 3 months.

**MATERIALS AND METHODS:** We prospectively studied patients with motor deficits secondary to primary intracerebral hemorrhage within the first 12 hours of symptom onset. Patients underwent multimodal MR imaging including DTI. We assessed intracerebral hemorrhage and perihematomal edema location and volume, and corticospinal tract involvement. The corticospinal tract was considered affected when the tractogram passed through the intracerebral hemorrhage or/and the perihematomal edema. We also calculated affected corticospinal tract-to-unaffected corticospinal tract ratios for fractional anisotropy, mean diffusivity, and axial and radial diffusivities. Motor impairment was graded by the motor subindex scores of the modified NIHSS. Motor outcome at 3 months was classified as good (modified NIHSS 0–3) or poor (modified NIHSS 4–8).

**RESULTS:** Of 62 patients, 43 were included. At admission, the median NIHSS score was 13 (interquartile range = 8–17), and the median modified NIHSS score was 5 (interquartile range = 2–8). At 3 months, 13 (30.23%) had poor motor outcome. Significant independent predictors of motor outcome were NIHSS and modified NIHSS at admission, posterior limb of the internal capsule involvement by intracerebral hemorrhage at admission, intracerebral hemorrhage volume at admission, 72-hour NIHSS, and 72-hour modified NIHSS. The sensitivity, specificity, and positive and negative predictive values for poor motor outcome at 3 months by a combined modified NIHSS of >6 and posterior limb of the internal capsule involvement in the first 12 hours from symptom onset were 84%, 79%, 65%, and 92%, respectively (area under the curve = 0.89; 95% CI, 0.78–1).

**CONCLUSIONS:** Combined assessment of motor function and posterior limb of the internal capsule damage during acute intracerebral hemorrhage accurately predicts motor outcome.

**ABBREVIATIONS:** CST = corticospinal tract; FA = fractional anisotropy; ICC = intraclass correlation coefficient; ICH = intracerebral hemorrhage; IQR = interquartile range; PHE = perihematomal edema; PLIC = posterior limb of the internal capsule; rFA = FA ratio

More than half of patients with intracerebral hemorrhage (ICH) have residual motor deficits at 6-month follow-up.<sup>1</sup> Although the severity of the initial motor deficit is one of the most

important determinants of motor recovery after stroke, growing evidence shows that motor outcome after stroke is heavily dependent on the integrity of the corticospinal tract (CST).<sup>2–8</sup> Outcome predictions after ICH might be more difficult compared with outcome after ischemic stroke because the damage from ICH includes not only the mass effect but also inflammation and perihematomal edema (PHE), leading to fiber deformations, demyelination,

Received December 18, 2018; accepted after revision March 15, 2019.

From the Department of Radiology (J.P., M.E., C.R.F.), University of Manitoba. Winnipeg, Manitoba, Canada; Department of Radiology (J.P., G.B., V.C., G.C., S.P.), Biomedical Research Institute Imaging Research Unit, Diagnostic Imaging Institute, Dr Josep Trueta University Hospital, Girona, Spain; Department of Neurology (M.T., J.S., Y.S.), Girona Biomedical Research Institute, Dr Josep Trueta University Hospital, Girona, Spain; Department of Computer Science (P.D.-i.-E.), Applied Mathematics and Statistics, University of Girona, Girona, Spain; Neuroimaging and Stroke Recovery Laboratory (G.S.), Department of Neurology, Beth Israel Deaconess Medical Center and Harvard Medical School, Boston, Massachusetts; Department of Neurosciences (M.H.-P.), Germans Trias i Pujol University Hospital, Autonomous University of Barcelona, Badalona, Spain; Department of Radiology (K.N.), Icahn School of Medicine at Mount Sinai, New York; and Department of Radiology (C.L.-S.), University of Missouri, Columbia, Missouri.

This work was partially supported by a grant from the Spanish Ministry of Health, Instituto de Investigación Carlos III (grant No. 367823–764)

Please address correspondence to Josep Puig, MD, PhD, Department of Radiology, University of Manitoba, 820 Sherbrook St GA216, Winnipeg, MB R3T 2N2, Canada; e-mail: jpuig@hsc.mb.ca

Indicates open access to non-subscribers at [www.ajnr.org](http://www.ajnr.org)

Indicates article with on-line tables.

<http://dx.doi.org/10.3174/ajnr.A6038>

nation, and axonal shearing.<sup>9</sup> Wallerian degeneration in the CST both near and remote from the hematoma is common following ICH.<sup>10</sup> Whereas conventional MR imaging sequences such as FLAIR and gradient recalled-echo can show the hemorrhage and PHE, DTI depicts and quantifies white matter microstructure by measuring the diffusion of water in tissue.<sup>11</sup> Lower fractional anisotropy (FA) values along the affected CST remote from the infarct, interpreted as Wallerian degeneration, are associated with greater motor deficit 2–4 weeks after the onset of symptoms and worse motor outcome.<sup>12–14</sup> Damage to specific CST regions on diffusion tensor tractography can predict limb motor outcome: Involvement of the posterior limb of the internal capsule (PLIC) within the first 12 hours after symptom onset is strongly associated with unfavorable motor outcome at 3 months.<sup>15</sup> Moreover, the degree of motor deficit correlates higher with lesion-CST overlap than with the lesion size per se.<sup>7</sup>

Although several studies have examined whether DTI-derived data can predict motor outcome in patients with ICH, the results are inconsistent.<sup>16–22</sup> Both the FA ratio (rFA) remote from the lesion and the integrity of the CST in the subacute-to-chronic period of ICH have been associated with functional motor outcome.<sup>19–23</sup> An accurate method to individually predict motor outcome within a few hours after ICH would enable realistic goal setting and efficient resource allocation by clinicians, patients, and families, providing them with information that might help choose more efficient rehabilitation programs. Given the lack of studies in the acute phase, we aimed to determine whether combining clinical scores or motor impairment and DTI-derived data of tissue impairment from the first 12 hours after symptom onset allows prediction of motor outcome in patients with ICH.

## **MATERIALS AND METHODS**

### **Patients**

We studied consecutive patients with spontaneous primary ICH admitted to the Stroke Unit of Dr. Josep Trueta University Hospital from January 2012 through December 2014. Inclusion criteria were the following: 1) patient older than 18 years, 2) first-ever stroke, 3) supratentorial primary intraparenchymal hematoma, 4) presence of motor deficit, 5) MR imaging performed within 12 hours from symptom onset, and 6) clinical follow-up at 90 days. Exclusion criteria were the following: 1) secondary ICH due to vascular malformation, cranial trauma, or tumor; 2) poor pre-morbid functional status (mRS > 2); 3) dementia or terminal illness; 4) coma; 5) poor image quality; 6) primary intraventricular hemorrhage; or 7) infratentorial hemorrhage; 8) any contraindications for MR imaging; and 9) surgical treatment. All patients were managed according to recent published guidelines.<sup>24</sup> Standard rehabilitation programs were initiated once patients were clinically stable. Our institutional ethics committee approved the study, and all patients or their relatives provided written informed consent.

### **Clinical Examination**

A senior certified staff neurologist used the NIHSS to assess clinical deficits at admission, day 3, and 3 months. Limb motor performance was evaluated by the mNIHSS subindex (5a, 5b, 6a, 6b).

The scores were summed and defined with paresis grading ranging from zero, no motor weakness, to 8, hemiplegia in 2 limbs. Motor outcome at 3 months was classified as good (mNIHSS 0–3) or poor (mNIHSS 4–8).<sup>20</sup> The mRS was used to measure patients' functional disability at 3 months. Poor functional outcome was defined as mRS > 2.<sup>25</sup> All clinical assessments were blinded to the MR imaging findings.

### **MR Imaging Protocol**

All scans were performed with a whole-body 1.5T MR imaging system (Gyrosan Intera; Philips Healthcare, Best, the Netherlands) with a sensitivity encoding head coil. The protocol included FLAIR, gradient recalled-echo, TOF angiography, axial trace DWI, and DTI sequences. DTI was performed using a single-shot echo-planar imaging sequence with the sensitivity encoding parallel-imaging scheme (acceleration factor, 2) after contrast agent administration for angiography. A single diffusion-weighted  $B_0$  acquisition was obtained, and diffusion-sensitized gradients were applied along 15 noncollinear directions with a b-value of 1000 s/mm<sup>2</sup>. Other acquisition parameters were the following: TR/TE, 6795/72 ms; FOV, 230 × 230 mm; matrix size, 112 × 112. DTI voxel size was 2.05 × 2.0 × 3 mm. Forty sections covering the brain were obtained parallel to the bicommissural line without intersection gaps. DTI acquisition took 3 minutes 10 seconds. Parameters for FLAIR were the following: TR/TE, 7569/115 ms; flip angle, 90°; section thickness, 5 mm; intersection gap, 1 mm; FOV, 230 × 180 mm; and brain coverage, 120 mm. Parameters for gradient recalled echo were TR/TE, 1000/30 ms; and the others were the same as for FLAIR.

### **Diffusion Tensor Tractography Processing and Assessment of CST Involvement by ICH**

Deterministic diffusion tensor tractography was performed using Philips Research Integrated Development Environment (PRIDE; Philips Healthcare) software. Anisotropy maps were obtained using orientation-independent FA, and color FA maps were generated following the standard convention (red, left-right; green, anteroposterior; and blue, superoinferior). Tractography was based on a diffusion tensor deflection algorithm.<sup>26</sup> The threshold for stopping fiber propagation was FA < 0.2 and angle < 70°. The seeding method put 1 starting seed randomly inside each voxel with an FA of >0.4. To reconstruct the CST, we placed ROIs at the level of the cerebral peduncle and around the corona radiata in the direction-coded color axial sections. Fiber tracts passing through both ROIs were designated as tracts of interest. Exclusion ROIs were drawn around the superior and middle cerebellar peduncles to exclude fibers to the cerebellum, and around a midline sagittal section covering the brain stem and corpus callosum to exclude interhemispheric fibers.<sup>15,27</sup> The CST depicted was validated using landmarks from neuroanatomy atlases.<sup>28</sup> To determine which structures had ICH and PHE, we evaluated the centrum semiovale, corona radiata, and PLIC on tractograms superimposed on gradient recalled-echo and FLAIR. The CST was considered affected only when the tractogram passed through the ICH or/and PHE (Fig 1). In those patients in whom the tractogram was bent over or displaced by the ICH, the CST was considered not affected. These regions were scored on 2 separate occasions 8 weeks

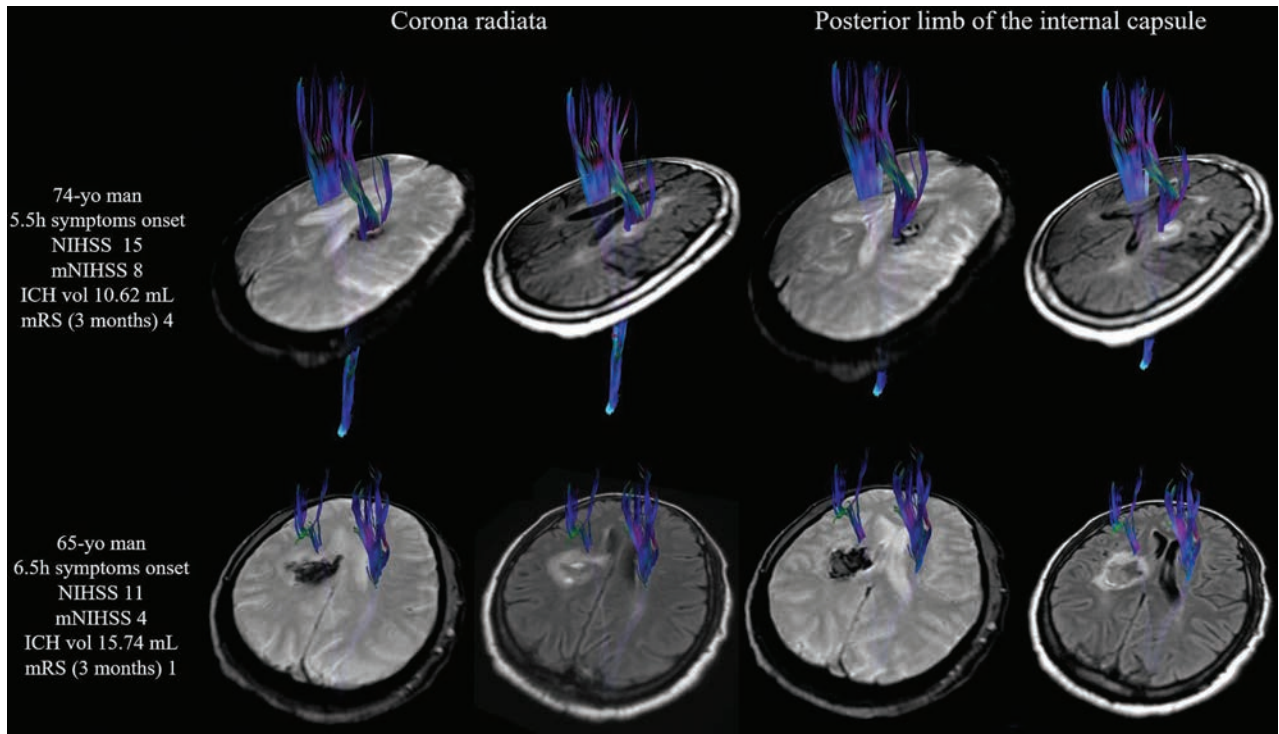


**FIG 1.** Assessing corticospinal tract involvement with diffusion tensor tractography superimposed on gradient recalled echo and FLAIR images. In the upper row, the corticospinal tract was affected by ICH (passes through it) at the level of the corona radiata and posterior limb of the internal capsule. Note that in lower row, the corticospinal tract was displaced slightly forward but preserved around the intracerebral hematoma. Vol indicates volume.

apart by 1 rater with 14 years' experience and once by 2 raters (14 and 5 years' experience); all raters were blinded to the clinical data. Discordant ratings were resolved by consensus.

#### Measurement of the CST DTI

Diffusion-sensitized image sets were analyzed off-line. One reader with 5 years' experience blinded to the clinical scores used Olea Sphere, Version 3.0 software (Olea Medical, La Ciotat, France) to calculate the following DTI measures on 2 separate occasions 4 weeks apart: radial diffusivity, axial diffusivity, mean diffusivity, and FA. The ipsilesional-to-contralateral CST ratios were calculated on axial sections of affected and unaffected CST at the level of the PLIC and at the level of the rostral pons (rDTI-Metric =  $\text{DTI-Metric}_{\text{affected side}} / \text{DTI-Metric}_{\text{unaffected side}}$ ). In each patient, the DTI measures of the CST were derived from the mean value of 3 contiguous sections. The results of the 2 assessments were averaged. Analyzing diffusion tensor tractography took 4 minutes and 30 seconds on average.

#### Measurement of the ICH and PHE Volumes

Two independent raters blinded to the clinical data measured ICH and PHE volumes on baseline MR imaging and 72-hour post-ICH CT scans using a semiautomated method (Olea Sphere, Version 3.0). At admission, ICH and PHE volumes were outlined on gradient recalled-echo sequences and FLAIR, respectively.<sup>29</sup> At 72 hours, PHE was delineated with the additional guideline that it should be more hypodense than the corresponding area in the contralateral hemisphere and most hypodense immediately surrounding the ICH.<sup>30</sup> Figure 2 de-

picts a representative example of a patient's ICH and PHE measurements. The results of the 2 assessments were averaged.

#### Statistical Analysis

Descriptive statistics are expressed as medians (interquartile range [IQR]) for continuous variables and as frequencies (percentages) for categorical variables. We compared baseline data, clinical variables at admission and at 72 hours, volumes of ICH and PHE, and DTI data between patients with good-versus-poor motor outcome at 3-month follow-up and between patients with  $\text{mRS} \leq 2$  and  $\text{mRS} > 2$ . For univariate comparison, we used *t* tests for numeric data and the  $\chi^2$  test for proportions. We used receiver operating characteristic curves to determine cutoffs for variables discriminating motor outcome. Multiple logistic regression was used to define independent predictors of motor outcome (mNIHSS score at 3 months). Several combinations of independent *P* values to ascertain the value of adding CST involvement to the mNIHSS score. We used the Cohen  $\kappa$  coefficient to assess intraobserver and interobserver reliability for the assessment of CST involvement by ICH. Intra- and interobserver agreement was classified as slight ( $\kappa = 0.0-0.20$ ), fair ( $\kappa = 0.21-0.40$ ), moderate ( $\kappa = 0.41-0.60$ ), substantial ( $\kappa = 0.61-0.80$ ), or almost perfect ( $\kappa = 0.81-1.00$ ) according to the scale proposed by Landis and Koch.<sup>31</sup> To compare first and second measurements of DTI measures, we used the intraclass correlation coefficient (ICC). The level of intra- and interobserver consistency was classified as fair

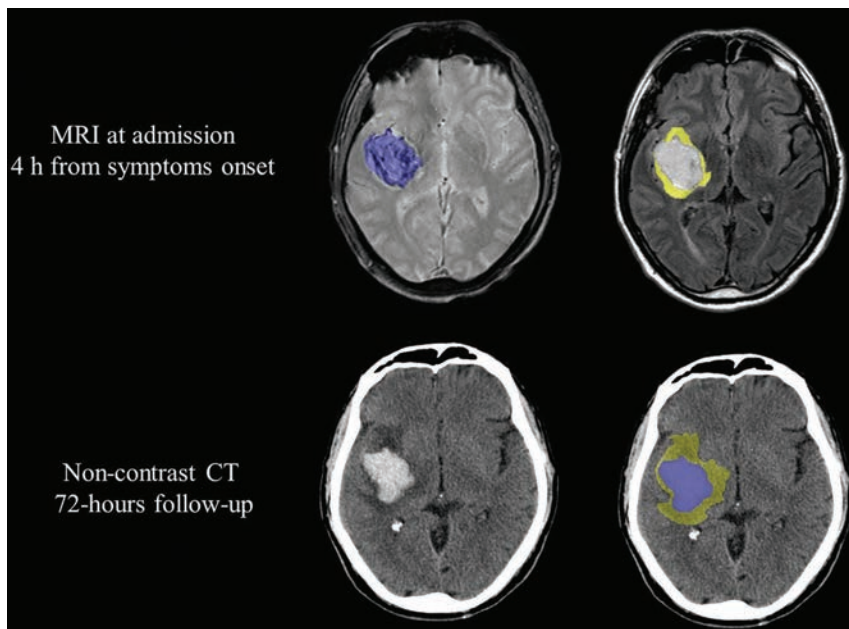


**FIG 2.** Example of ROI object maps used to measure intracerebral hematoma (blue) and perihematomal edema (yellow) volumes.

(ICC = 0.5–0.7), good (0.7–0.9), or almost perfect (>0.90). All statistical analyses were performed with R, Version 3.0.2 (<http://www.r-project.org/>).

## RESULTS

### Patients

Among 62 consecutive patients admitted with supratentorial primary ICH conforming to our inclusion criteria, 6 were excluded for not having motor deficits at admission; 6, for poor image quality due to motion artifacts; and 7 died within 72 hours of symptom onset. Therefore, the study population consisted of 43 patients (31 men; mean age 68 years; IQR = 57–76 years).

### Clinical and Neuroimaging Characteristics

On-line Table 1 summarizes patients' clinical and imaging data according to motor outcomes at 3 months. There were no differences in sex, age, presence of vascular risk factors, and laboratory parameters between 2 groups. At admission, most patients had moderate-to-severe neurologic deficits (NIHSS = 13, IQR = 8–17), and 26 (60.46%) of these had moderate-severe motor deficits (mNIHSS = 4–8). At 3 months, 13 (30.23%) patients had poor motor outcome. Time from ICH onset to MR imaging was 407 minutes (IQR = 238–559 minutes). The most frequent ICH location was the lenticulostriate territory (88.1%). The pre-morbid mRS was 0 for all patients. CST affected by ICH was present in 24 (55.8%) patients; and the PLIC, in 14 (32.5%) of these patients. All patients with CST affected by ICH had motor deficits at admission. Intrarater and interrater agreement about the CST-involvement region was almost perfect ( $\kappa = 0.89$  and  $\kappa = 0.82$ , respectively). The intraobserver consistency showed good agreement for CST DTI measures (ICC = 0.81; 95% CI, 0.78–0.86). For ICH and PHE volume assessment, all interrater ICCs were almost perfect at both baseline and 72-hour follow-up

(ICC<sub>ICH-baseline</sub> = 0.96; 95% CI, 0.94–1.00; ICC<sub>PHE-baseline</sub> = 0.95; 95% CI, 0.92–1.00; ICC<sub>ICH-72 hours</sub> = 0.98; 95% CI, 0.96–1.00; ICC<sub>PHE-72 hours</sub> = 0.98; 95% CI, 0.97–1.00).

### Analysis of Variables Associated with Clinical Outcome

In the 13 patients with poor motor outcome at 3 months, NIHSS and mNIHSS scores were higher at admission and at 72 hours than for patients with a good motor outcome (On-line Table 1). Patients with poor motor outcome had higher ICH volume at admission (10.45 mL; IQR = 5.07–15.74 mL versus 22.74 mL; IQR = 10.3–30;  $P = .034$ ) (On-line Table 1). At admission, ICH involved the CST in 11 (84.61%) patients with poor motor outcome and in 13 (43.33%) patients with good motor outcome ( $P = .016$ ); ICH involved the PLIC in 9 (69.23%) patients with poor motor outcome ( $P = .001$ ). Poor motor outcome at 3 months correlated with functional outcome (mRS) at 3 months ( $P < .001$ ). Patients with poor functional outcome had higher NIHSS and mNIHSS scores at admission and follow-up than patients with good outcome, as well as higher volumes of ICH (On-line Table 2). Poor functional outcome was also associated with CST affected by ICH. CST affected by PHE and quantitative DTI measures did not influence a patient's outcome (On-line Tables 1 and 2).

ICH involved the CST in 11 (84.61%) patients with poor motor outcome and in 13 (43.33%) patients with good motor outcome ( $P = .016$ ); ICH involved the PLIC in 9 (69.23%) patients with poor motor outcome ( $P = .001$ ). Poor motor outcome at 3 months correlated with functional outcome (mRS) at 3 months ( $P < .001$ ). Patients with poor functional outcome had higher NIHSS and mNIHSS scores at admission and follow-up than patients with good outcome, as well as higher volumes of ICH (On-line Table 2). Poor functional outcome was also associated with CST affected by ICH. CST affected by PHE and quantitative DTI measures did not influence a patient's outcome (On-line Tables 1 and 2).

### Predictive Models for Functional Motor Outcome

The best model was obtained by combining the mNIHSS score at 72 hours and PLIC affected by ICH at <12 hours (Table). The sensitivity, specificity, and positive and negative predictive values for poor motor outcome at 3 months by combined 72-hour mNIHSS scores of >3 and PLIC affected by ICH at ≤12 hours were 92%, 86%, 75%, and 96%, respectively (area under the curve = 0.94; 95% CI, 0.86–1.00). Additionally, the sensitivity, specificity, and positive and negative predictive values for poor motor outcome at 3 months by combined acute mNIHSS of >6 and PLIC involvement of <12 hours were 84%, 79%, 65%, and 92%, respectively (area under the curve = 0.89; 95% CI, 0.78–1).

## DISCUSSION

In this observational study, we analyzed DTI datasets acquired in patients with ICH within 12 hours of symptom onset. We tested whether the combination of clinical scores and DTI-based assessment of CST damage predicts motor function at 3 months in acute ICH. In the first 12 hours of symptom onset, our results suggest that patients with mNIHSS scores of >6 and any PLIC affected by ICH will most probably have poor motor outcome. Kuzu et al<sup>20</sup> demonstrated that an mNIHSS score of ≥6 was a strong predictor of motor outcome at 3 months and suggested that patients with an mNIHSS score of ≥6 might be considered

**Functional motor outcome prediction: summary of class performance and odds ratios for univariate and multivariate analyses at admission and at 72 hr**

Variables	Cutoff	AUC (95% CI)	Sensitivity	Specificity	Positive Predictive Value	Negative Predictive Value	P Value	Odds Ratio (95% CI)
NIHSS score at admission	15	0.77 (0.62–0.93)	0.69	0.77	0.56	0.85	.011	1.23 (1.05–1.43)
mNIHSS score at admission	6	0.79 (0.64–0.94)	0.77	0.77	0.59	0.88	.007	1.65 (1.15–2.36)
ICH volume at admission	17.08	0.71 (0.54–0.90)	0.38	0.86	0.50	0.80	.047	1.05 (1.00–1.10)
CST involvement by ICH at admission	Present	0.70 (0.56–0.84)	0.84	0.55	0.46	0.89	.025	6.77 (1.27–36.14)
PLIC involvement by ICH at admission	Present	0.76 (0.61–0.91)	0.69	0.83	0.64	0.86	.002	10.80 (2.36–49.46)
NIHSS score at 72 hr	8	0.88 (0.77–0.99)	0.92	0.67	0.54	0.95	<.001	1.31 (1.12–1.52)
mNIHSS score at 72 hr	5	0.91 (0.82–1.00)	0.92	0.83	0.71	0.96	<.001	2.10 (1.36–3.26)
NIHSS score at admission, PLIC involvement by ICH at admission	16 Present	0.87 (0.75–0.98)	0.85	0.86	0.73	0.93	.014 .005	1.25 (1.05–1.49), 14.21 (2.23–90.60)
mNIHSS score at admission, PLIC involvement by ICH at admission	6 Present	0.89 (0.78–1.00)	0.84	0.79	0.65	0.92	.009 .005	1.86 (1.17–2.94), 20.99 (2.52–174.80)
NIHSS score at 72 hr, PLIC involvement by ICH at admission	14 Present	0.93 (0.84–1.00)	0.85	0.93	0.85	0.93	.003 .017	1.32 (1.10–1.58), 13.73 (1.60–117.65)
mNIHSS score at 72 hr, PLIC involvement by ICH at admission	3 Absent	0.94 (0.86–1.00)	0.92	0.86	0.75	0.96	.005 .020	2.08 (1.25–3.50), 17.04 (1.56–186.18)

**Note:**—AUC indicates area under the curve.

for surgical evacuation of the hematoma. They also reported that absolute FA values of the cerebral peduncle at day 3 were 9% lower in patients with poor-rather than-good recovery. However, they did not combine the 2 variables to better predict motor outcome. On the other hand, Tao et al<sup>27</sup> recently demonstrated that the prognostic value of the ICH score surpassed that of FA values in the CST at the cerebral peduncle within the first 4 days after symptom onset. Combining the FA data with the ICH score did not improve prognostication, probably because 4 days are not enough to detect early Wallerian degeneration in the cerebral peduncle.<sup>32</sup>

We found that ICH volume was a poor predictor of motor outcome at day 90, and motor deficit was present only when critical motor regions were involved, suggesting that large lesions do not necessarily predict poor motor outcome. Thus, growing evidence shows that the preservation and recovery of the CST are crucial for good functional motor outcome. However, we noted that some patients with CST involvement had no motor deficits, presumably due to compensation by alternate motor fibers that contribute to motor control.<sup>8</sup> In ischemic stroke, functional outcome correlates with the extent of Wallerian degeneration remote from the lesion. In the subacute and the chronic phases of ischemic stroke, FA in the ipsilateral CST decreases progressively in correlation with motor functional outcome. A few studies have demonstrated that reductions in FA values in the acute phase correlate with clinical signs and can predict functional outcome in ICH.<sup>19–22</sup> Unlike other authors, we found no changes in anisotropy in the cerebral peduncle. Kusano et al<sup>16</sup> reported that rFA in the cerebral peduncle correlated negatively with paresis grade and differed significantly at 2 days between patients with good and poor motor outcomes at 28 days. One explanation for these discrepancies is that we examined changes in diffusivity in the first few hours and this time window was too short to detect early signs of Wallerian degeneration.<sup>31</sup> A recent meta-analysis showed that

the studies reported so far on the correlation between FA values and upper extremity motor recovery in patients with ICH are few with small sample sizes.<sup>33</sup> This meta-analysis found a strong correlation between FA and upper extremity motor recovery, though the authors concluded that further well-designed prospective studies with larger sample sizes are needed to confirm these findings.<sup>33</sup>

Several limitations warrant comment. This single-center study included too few patients to draw definite conclusions. Future studies with larger samples will enable regression analyses to assess associations in greater detail. We considered clinical follow-up at 3 months because motor recovery seems to occur predominantly in the first few months after stroke; however, some patients with ICH may show further recovery in later phases.<sup>2</sup> However, an advantage of using a relatively short follow-up is to reduce the possibility of losing patients. The NIHSS is widely used for evaluating patients with acute stroke but might not be good for a fine-grained assessment of motor impairment. The DTI metrics would be difficult to assess, especially when ICH or PHE or both compress the CST, and this may result in variability in location, size, and shape. DTI reflects the averaged water diffusion property within a voxel, which is considered an indirect indicator of the axons; therefore, this model may oversimplify axonal structures. More diffusion gradients would reduce artifacts and increase signal-to-noise ratios. However, increasing the number of directions would have increased the scanning time and decreased the number of patients with a DTI scan without motion artifacts. The diffusion properties of tissues are independent of magnetic field strength. However, the field strength affects the signal-to-noise ratio and artifacts of diffusion-weighted images, which influence the quantitative and spatial accuracy of DTI.

The increased SNR at 3T may be useful for obtaining more accurate diffusion measurements, shortening examination times,

or improving the spatial resolution. Along this line, DTI studies at 3T using parallel imaging have provided significantly improved DTI measurements relative to studies at 1.5T.<sup>34</sup> Deterministic fiber-tracking methods use a linear propagation approach, proceeding according to the principal eigenvector direction.<sup>35</sup> This method has poor sensitivity to reconstruct the tracts through regions of crossing fibers.<sup>36</sup> The presence of the ICH and/or the PHE could affect the appearance of the CST. By means of probabilistic approaches, the CST would be delineated more extensively.<sup>37</sup> In fact, the streamline method provides a single estimate of a virtual fiber tract without incorporating the uncertainty introduced by noise, whereas probabilistic approaches attempt to address this limitation by providing a confidence measure. Probabilistic methods provide an arbitrary number of virtual fiber tracts that are reconstructed.<sup>38</sup> Combining other imaging modalities, such as functional MR imaging or transcranial magnetic stimulation, would increase the accuracy of assessing the neural tracts, therefore, compensating for the limitations of DTI.

We did not assess the impact of the CST distortion of its natural course or whether the additional bending of the CST affected the DTI measures. Secondary lesions due to local intracranial hypertension could be omitted in early DTI scans. Therefore, delineation of the mass effect of PHE and ICH on a later scan performed at around 1 week and used as a covariable could help limit this problem in further studies.

## CONCLUSIONS

Combining mNIHSS and PLIC affected by ICH in the first 12 hours of onset can accurately predict motor outcome. The reliability of DTI in denoting very early damage to the CST could make it a prognostic biomarker useful for determining management strategies to improve outcome in the hyperacute stage. Our approach eliminates the need for advanced postprocessing techniques that are time-consuming and require greater specialization, so it can be applied more widely and benefit more patients. Prospective large-scale studies are warranted to validate these findings and determine whether this information could be used to stratify risk in patients with ICH.

Disclosures: Chase R. Figley—UNRELATED: Employment: University of Manitoba; Grants/Grants Pending: Brain Canada, Health Sciences Centre Foundation, MS Society of Canada, Natural Sciences and Engineering Research Council of Canada Discovery.\* Kambiz Nael—UNRELATED: Board Membership: Olea Medical, Comments: Medical Advisory Board. Salvador Pedraza—RELATED: Grant: Fondo de Inversión Sanitaria. Spanish government.\* Yolanda Silva—RELATED: Grant: Acadèmia de Ciències Mèdiques de Girona, Comments: I received a grant for €6000 from the Acadèmia de Ciències Mèdiques de Girona. Josep Puig—RELATED: Grant: Spanish Ministry of Health, Instituto de Investigación Carlos III, Comments: This work was partially supported by a grant from the Spanish Ministry of Health, Instituto de Investigación Carlos III (grant No. 367823–764).\* Mikel Terceño—RELATED: Grant: Acadèmia Ciències Mèdiques.\* \*Money paid to the institution.

## REFERENCES

- Daverat P, Castel JP, Dartigues JF, et al. **Death and functional outcome after spontaneous intracerebral hemorrhage: a prospective study of 166 cases using multivariate analysis.** *Stroke* 1991;22:1–6 CrossRef Medline
- Hendricks HT, van Limbeek J, Geurts AC, et al. **Motor recovery after stroke: a systematic review of the literature.** *Arch Phys Med Rehabil* 2002;83:1629–37 CrossRef Medline
- Feng W, Wang J, Chhatbar PY, et al. **Corticospinal tract lesion load: an imaging biomarker for stroke motor outcomes.** *Ann Neurol* 2015;78:860–70 CrossRef Medline
- Byblow WD, Stinear CM, Barber PA, et al. **Proportional recovery after stroke depends on corticomotor integrity.** *Ann Neurol* 2015;78:848–59 CrossRef Medline
- Pineiro R, Pendlebury ST, Smith S, et al. **Relating MRI changes to motor deficit after ischemic stroke by segmentation of functional motor pathways.** *Stroke* 2000;31:672–79 CrossRef Medline
- Pendlebury ST, Blamire AM, Lee MA, et al. **Axonal injury in the internal capsule correlates with motor impairment after stroke.** *Stroke* 1999;30:956–62 CrossRef Medline
- Zhu LL, Lindenberg R, Alexander MP, et al. **Lesion load of the corticospinal tract predicts motor impairment in chronic stroke.** *Stroke* 2010;41:910–15 CrossRef Medline
- Lindenberg R, Renga V, Zhu LL, et al. **Structural integrity of corticospinal motor fibers predicts motor impairment in chronic stroke.** *Neurology* 2010;74:280–87 CrossRef Medline
- Zhou Y, Wang Y, Wang J, et al. **Inflammation in intracerebral hemorrhage: from mechanisms to clinical translation.** *Prog Neurobiol* 2014;115:25–44 CrossRef Medline
- Venkatasubramanian C, Kleinman JT, Fischbein NJ, et al. **Natural history and prognostic value of corticospinal tract Wallerian degeneration in intracerebral hemorrhage.** *J Am Heart Assoc* 2013;2:e000090 CrossRef Medline
- Chaudhary N, Pandey AS, Gemmete JJ, et al. **Diffusion tensor imaging in hemorrhagic stroke.** *Exp Neurol* 2015;272:88–96 CrossRef Medline
- Puig J, Pedraza S, Blasco G, et al. **Wallerian degeneration in the corticospinal tract evaluated by diffusion tensor imaging correlates with motor deficit 30 days after middle cerebral artery ischemic stroke.** *AJNR Am J Neuroradiol* 2010;31:1324–30 CrossRef Medline
- Thomalla G, Glauche V, Weiller C, et al. **Time course of Wallerian degeneration after ischaemic stroke revealed by diffusion tensor imaging.** *J Neurol Neurosurg Psychiatry* 2005;76:266–68 CrossRef Medline
- Lindenberg R, Zhu LL, Rüber T, et al. **Predicting functional motor potential in chronic stroke patients using diffusion tensor imaging.** *Hum Brain Mapp* 2012;33:1040–51 CrossRef Medline
- Puig J, Pedraza S, Blasco G, et al. **Acute damage to the posterior limb of the internal capsule on diffusion tensor tractography as an early imaging predictor of motor outcome after stroke.** *AJNR Am J Neuroradiol* 2011;32:857–63 CrossRef Medline
- Kusano Y, Seguchi T, Horiuchi T, et al. **Prediction of functional outcome in acute cerebral hemorrhage using diffusion tensor imaging at 3T: a prospective study.** *AJNR Am J Neuroradiol* 2009;30:1561–65 CrossRef Medline
- Yoshioka H, Horikoshi T, Aoki S, et al. **Diffusion tensor tractography predicts motor functional outcome in patients with spontaneous intracerebral hemorrhage.** *Neurosurgery* 2008;62:97–103 CrossRef Medline
- Wang DM, Li J, Liu JR, et al. **Diffusion tensor imaging predicts long-term motor functional outcome in patients with acute supratentorial intracranial hemorrhage.** *Cerebrovasc Dis* 2012;34:199–205 CrossRef Medline
- Cheng CY, Hsu CY, Huang YC, et al. **Motor outcome of deep intracerebral haemorrhage in diffusion tensor imaging: comparison of data from different locations along the corticospinal tract.** *Neurol Res* 2015;37:774–81 CrossRef Medline
- Kuzu Y, Inoue T, Kanbara Y, et al. **Prediction of motor function outcome after intracerebral hemorrhage using fractional anisotropy calculated from diffusion tensor imaging.** *Cerebrovasc Dis* 2012;33:566–73 CrossRef Medline
- Koyama T, Tsuji M, Miyake H, et al. **Motor outcome for patients with acute intracerebral hemorrhage predicted using diffusion tensor imaging: an application of ordinal logistic modeling.** *J Stroke Cerebrovasc Dis* 2012;21:704–11 CrossRef Medline
- Koyama T, Uchiyama Y, Domen K. **Associations of diffusion-tensor fractional anisotropy and FIM outcome assessments after intracerebral hemorrhage.** *Stroke* 2013;44:1000–05 CrossRef Medline

- rebral hemorrhage. *J Stroke Cerebrovasc Dis*. 2018;27:2869–76 CrossRef Medline
23. Koyama T, Tsuji M, Nishimura H, et al. **Diffusion tensor imaging for intracerebral hemorrhage outcome prediction: comparison using data from the corona radiata/internal capsule and the cerebral peduncle.** *J Stroke Cerebrovasc Dis* 2013;22:72–79 CrossRef Medline
  24. Steiner T, Al-Shahi Salman R, Beer R, et al; European Stroke Organisation. **European Stroke Organisation (ESO) guidelines for the management of spontaneous intracerebral hemorrhage.** *Int J Stroke* 2014;9:840–55 CrossRef Medline
  25. Sulter G, Steen C, De Keyser J. **Use of the Barthel index and modified Rankin scale in acute stroke trials.** *Stroke* 1999;30:1538–41 CrossRef Medline
  26. Lazar M, Weinstein DM, Tsuruda JS, et al. **White matter tractography using diffusion tensor deflection.** *Hum Brain Mapp* 2003;18:306–21 CrossRef Medline
  27. Tao WD, Wang J, Schlaug G, et al. **A comparative study of fractional anisotropy measures and ICH score in predicting functional outcomes after intracerebral hemorrhage.** *Neurocrit Care* 2014;21:417–25 CrossRef Medline
  28. Wakana S, Jiang H, Nagae-Poetscher LM, et al. **Fiber tract-based atlas of human white matter anatomy.** *Radiology* 2004;230:77–87 CrossRef Medline
  29. Martin RM, Wright MJ, Lutkenhoff ES, et al. **Traumatic hemorrhagic brain injury: impact of location and resorption on cognitive outcome.** *J Neurosurg* 2017;126:796–804 CrossRef Medline
  30. Urday S, Beslow LA, Goldstein DW, et al. **Measurement of PHE in intracerebral hemorrhage.** *Stroke* 2015;46:1116–19 CrossRef Medline
  31. Landis JR, Koch GG. **The measurement of observer agreement for categorical data.** *Biometrics* 1977;33:159–74 CrossRef Medline
  32. Doughty C, Wang J, Feng W, et al. **Detection and predictive value of fractional anisotropy changes of the corticospinal tract in the acute phase of a stroke.** *Stroke* 2016;47:1520–26 CrossRef Medline
  33. Kumar P, Yadav AK, Misra S, et al. **Prediction of upper extremity motor recovery after subacute intracerebral hemorrhage through diffusion tensor imaging: a systematic review and meta-analysis.** *Neuroradiology* 2016;58:1043–50 CrossRef Medline
  34. Alexander AL, Lee JE, Wu YC, et al. **Comparison of diffusion tensor imaging measurements at 3.0 T versus 1.5 T with and without parallel imaging.** *Neuroimaging Clin N Am* 2006;16:299–309, xi CrossRef Medline
  35. Mori S. **Fiber tracking: principles and strategies—a technical review.** *NMR Biomed* 2002;15:468–80 CrossRef Medline
  36. Mandelli ML, Berger MS, Bucci M, et al. **Quantifying accuracy and precision of diffusion MR tractography of the corticospinal tract in brain tumors.** *J Neurosurg* 2014;121:349–58 CrossRef Medline
  37. Chung S, Lu Y, Henry RG. **Comparison of bootstrap approaches for estimation of uncertainties of DTI parameters.** *Neuroimage* 2006;33:531–41 CrossRef Medline
  38. Alexander AL, Lee JE, Lazar M, et al. **Diffusion tensor imaging of the brain.** *Neurotherapeutics* 2007;4:316–29 CrossRef Medline

# The Central Vein Sign in Radiologically Isolated Syndrome

S. Suthiphosuwana, P. Sati, M. Guenette, X. Montalban, D.S. Reich, A. Bharatha, and J. Oh

## ABSTRACT

**BACKGROUND AND PURPOSE:** Radiologically isolated syndrome describes asymptomatic individuals with incidental radiologic abnormalities suggestive of multiple sclerosis. Recent studies have demonstrated that >40% of white matter lesions in MS (and often substantially more) have visible central veins on MR imaging. This “central vein sign” reflects perivenous inflammatory demyelination and can assist in differentiating MS from other white matter disorders. We therefore hypothesized that >40% of white matter lesions in cases of radiologically isolated syndrome would show the central vein sign.

**MATERIALS AND METHODS:** We recruited 20 participants diagnosed with radiologically isolated syndrome after evaluation by a neurologist. We performed 3T MR imaging of the brain and cervical spinal cord. White matter lesions were analyzed for the central vein sign.

**RESULTS:** Of 391 total white matter lesions, 292 (75%) demonstrated the central vein sign (central vein sign+). The median proportion of central vein sign+ lesions per case was 87% (range, 29%–100%). When the “40% rule” that has been proposed to distinguish MS from other disorders was applied, of 20 participants, 18 cases of radiologically isolated syndrome (90%) had  $\geq$ 40% central vein sign+ lesions (range, 55%–100%). Two participants (10%) had <40% central vein sign+ lesions (29% and 31%). When the simpler “rule of 6” was applied, 19 participants (95%) met these criteria. In multivariable models, the number of spinal cord and infratentorial lesions was associated with a higher proportion of central vein sign+ lesions ( $P = .002$ ;  $P = .06$ , respectively).

**CONCLUSIONS:** Most cases of radiologically isolated syndrome had a high proportion of central vein sign+ lesions, suggesting that lesions in these individuals reflect perivenous inflammatory demyelination. Moreover, we found correlations between the proportion of central vein sign+ lesions and spinal cord lesions, a known risk factor for radiologically isolated syndrome progressing to MS. These findings raise the possibility, testable prospectively, that the central vein sign may have prognostic value in distinguishing patients with radiologically isolated syndrome at risk of developing clinical MS from those with white matter lesions of other etiologies.

**ABBREVIATIONS:** CVS = central vein sign; RIS = radiologically isolated syndrome

Multiple sclerosis is an inflammatory demyelinating disease of the central nervous system characterized by relapsing or progressive neurologic symptoms and focal white matter lesions.<sup>1</sup> Histopathologic studies have shown that these WM lesions, when

they first form, arise from inflammatory infiltrates around small veins, or “perivascular cuffs.”<sup>2</sup> On conventional MR imaging, MS lesions typically manifest as focal areas of high signal on T2-weighted images of the brain and spinal cord. However, focal T2-hyperintense WM lesions can be seen in a variety of settings, including normal aging, migraines, microangiopathy, and CNS vasculitis. Misinterpretation of such lesions is the most common cause of incorrect MS diagnosis,<sup>3</sup> and partly to address this issue, one can only apply the current MS diagnostic criteria in the setting of typical clinically isolated syndrome.<sup>4–6</sup> Diagnosing MS when such a syndrome is not present is therefore challenging.

Recent studies using high-resolution, susceptibility-based MR imaging sequences have demonstrated an identifiable vein inside

Received January 28, 2019; accepted after revision March 25.

From the Division of Neuroradiology (S.S., A.B.), Division of Neurology (S.S., M.G., X.M., J.O.), Department of Medicine, and Division of Neurosurgery (A.B.), Department of Surgery, St. Michael's Hospital, University of Toronto, Toronto, Ontario, Canada; Translational Neuroradiology Section (P.S., D.S.R.), National Institute of Neurological Disorders and Stroke, National Institutes of Health, Bethesda, Maryland; and Department of Neurology (D.S.R., J.O.), Johns Hopkins University, Baltimore, Maryland.

This work was supported by the MS Society of Canada and the St. Michael's Hospital Foundation Love/Barford Endowment.

The funders had no role in the design and conduct of the study; collection, management, analysis, and interpretation of the data; preparation, review, or approval of the manuscripts; and the decision to submit the manuscript for publication.

Paper previously presented at: American Society of Neuroradiology Annual Meeting and the Foundation of the ASNR Symposium, June 2–7, 2018, Vancouver, British Columbia, Canada (abstract No. O-70).

Please address correspondence to Jiwon Oh, MD, FRCPC, PhD, 30 Bond St, Shuter 3–019, Toronto, ON, M4K 1Z1 Canada; e-mail: ohjiw@smh.ca

<http://dx.doi.org/10.3174/ajnr.A6045>

WM lesions, called the “central vein sign” (CVS).<sup>3,7-21</sup> On these scans, the CVS is typically visible as a hypointense line that is centered within the lesion; the hypointensity reflects the presence of a paramagnetic substance, either deoxyhemoglobin or, in some circumstances, a gadolinium-based contrast agent.<sup>9,11,12</sup> Previous studies assessing the CVS in MS have reported that a high frequency of WM lesions in MS demonstrate the CVS compared with WM lesions seen in microangiopathic disease, migraines, CNS inflammatory vasculopathies, and neuromyelitis optica spectrum disorders.<sup>3,8,10,13-17,19-23</sup> On the basis of these studies, a cutoff threshold of 40% (in which  $\geq 40\%$  of WM lesions demonstrate the CVS) has been proposed to distinguish MS from non-MS disease.<sup>8</sup> More recent studies have proposed more simplified criteria, such as the “rule of 6,” whereby if  $>6$  WM lesions demonstrate the CVS, MS can be distinguished from other WM disorders.<sup>10,21,23</sup>

Radiologically isolated syndrome (RIS) describes asymptomatic individuals or those with neurologic symptoms that are not typical of MS, whose MR imaging scans show abnormalities typical of those seen in clinical MS.<sup>24</sup> Individuals with RIS have an increased risk of eventually developing clinical MS, but long-term prospective studies are lacking. The largest, multicenter, retrospective study has shown that 34% of patients with RIS eventually manifest clinically definite MS during 4.4 years.<sup>25</sup> Factors that increase the risk of conversion to MS include the following: male sex, younger age (younger than 37 years of age), and the presence of  $\geq 1$  spinal cord lesion on MR imaging.<sup>25,26</sup> Another study demonstrated that among individuals with RIS who develop MS, 11.7% develop primary-progressive MS, and these individuals are more likely to be older and male and have spinal cord lesions.<sup>27</sup> These data suggest that at least a portion of patients with RIS have a subclinical form of MS; of these, many may never develop clinical MS.

Currently, there is no consensus on the optimal clinical management of RIS because the natural history remains unclear and there are no evidence-based treatment or management guidelines. Moreover, the current diagnostic criteria for RIS<sup>24</sup> likely result in a heterogeneous group of participants being designated as such, including those who are at risk of developing MS and those who have a minimal risk. This result is likely because the diagnostic criteria for RIS are based entirely on lesion number and distribution (Barkhof<sup>28</sup> criteria for dissemination in space), criteria that were originally intended to be applied to individuals with symptomatology clinically suggestive of demyelinating disease. As a result, the current RIS criteria<sup>24</sup> have limited ability to reflect underlying subclinical demyelinating pathology, which represents individuals at high risk of developing MS.<sup>29</sup> Accordingly, assessing the CVS in WM lesions of RIS may be helpful to better evaluate the underlying pathologic processes of this entity and determine which individuals are at risk of eventually developing clinical MS.<sup>30</sup> To date, the presence of the CVS has not been evaluated in RIS, to our knowledge. Therefore, the objective of this study was to determine whether adults with RIS have similar proportions of lesions positive for CVS (CVS+ lesions) compared with those previously reported in clinical MS.

## MATERIALS AND METHODS

### Standard Protocol Approvals, Registrations, and Patient Consent

This study was approved by the institutional review board of St. Michael's Hospital. All participants provided written informed consent.

### Participants

Twenty adults diagnosed with RIS by a neurologist at the St. Michael's Hospital MS Clinic were recruited for prospective clinical and MR imaging evaluation between July 2017 and December 2017. Because RIS is a rare entity<sup>31</sup> and the central vein sign has not yet been evaluated in RIS, we were not able to perform sample size calculations of power analyses. Inclusion criteria were 18 years of age and older and meeting previously published clinical and MR imaging criteria for RIS,<sup>24</sup> which include the presence of asymptomatic WM abnormalities that are ovoid, well-circumscribed,  $\geq 3$  mm in maximal diameter, and fulfilling 3 of 4 Barkhof criteria<sup>28</sup> for dissemination in space (lesions in the periventricular, juxtacortical, infratentorial, or spinal cord regions). Brain MRIs were reviewed by experienced neuroradiologists (S.S. and A.B.) and a neurologist (J.O.) to confirm inclusion criteria. Individuals who had vascular risk factors and a history of substance abuse or toxic exposure were excluded.<sup>24</sup>

### Clinical Assessment

Within 30 days of MR imaging, study participants underwent an examination by a neurologist. None of the participants experienced a clinical relapse or neurologic symptoms suggestive of MS between recruitment and the study visit.

### MR Imaging

MR imaging was performed on a 3T scanner (Magnetom Skyra; Siemens, Erlangen, Germany) with a 20-channel head-neck coil and a 16-channel spine-array coil.

### Brain MR Imaging

The following parameters were used for brain sequences—3D T1-weighted MPRAGE: TR/TE/flip angle = 1900/2.52 ms/9°, number of averages = 1, slice thickness = 1 mm, in-plane resolution =  $1 \times 1$  mm<sup>2</sup>, and number of slices = 176; 3D T2-FLAIR: TR/TE/TI/flip angle = 4800/353/1800 ms/120°, number of averages = 1, slice thickness = 1 mm, in-plane resolution =  $1 \times 1$  mm<sup>2</sup>, and number of slices = 176; sagittal 3D T2\*-weighted multishot echo-planar imaging:<sup>9</sup> TR/TE/flip angle = 64/35 ms/10°, number of averages = 1, slice thickness = 0.65 mm, in-plane resolution =  $0.65 \times 0.65$  mm<sup>2</sup>, and number of slices = 265.

### Cervical Spinal Cord MR Imaging

The following parameters were used for cervical spinal cord sequences—sagittal 2D-T1-weighted phase-sensitive inversion recovery of the cervical spine:<sup>32</sup> TR/TE/TI = 2400/9.4/400 ms, number of averages = 2, slice thickness = 3 mm, in-plane resolution =  $0.7 \times 0.7$  mm<sup>2</sup>, and number of slices = 15. A T2-weighted sequence of the cervical spine was not performed.

## Image Analysis

Images were evaluated for the presence of the CVS by 3 reviewers: a neuroradiologist (S.S.), a medical physicist (P.S.), and a neurologist (J.O.). All reviewers completed training in CVS assessment according to the consensus criteria of the North America Imaging in Multiple Sclerosis Cooperative.<sup>11</sup>

## White Matter Lesion Evaluation

3D-T1-MPRAGE and 3D-T2-FLAIR images were evaluated for the number, location, and size of WM lesions by a neuroradiologist (S.S.). WM lesion locations were classified into 4 typical locations of MS-related lesions in the brain, including cortical/juxtacortical (involving or touching the cortex), subcortical/deep, periventricular (touching 1 of the ventricles), and infratentorial. The size of the WM lesion was determined by assessing the largest diameter of the lesion across all planes. The WM lesions with hypointense signal lower than that on the cortex on T1-MPRAGE, so called T1 black holes, were recorded.

The Multi-Atlas Cortical Reconstruction Using Implicit Surface Evolution<sup>33</sup> was used to acquire volumes of brain substructures, total lesion volume, and intracranial volume. The cerebral volume fraction was calculated by dividing total brain volume by intracranial volume.

## CVS Assessment

3D-T2\* EPI magnitude images with multiplanar reconstruction were viewed in 3 orthogonal planes to assess the presence of the CVS using recently published guidelines.<sup>11</sup> Specifically, identified central veins had to meet the following criteria: have a small apparent diameter (<2 mm); appear as a thin hypointense line or small hypointense dot; be visible in at least 2 perpendicular planes and appear as a thin hypointense line in 1 plane, run partially or entirely through the lesion; and be positioned approximately in the center of the WM lesion. WM lesions of <3 mm in maximum diameter, confluent or contiguous lesions, lesions containing >1 vein, and poorly visible lesions were excluded from this analysis.

Two reviewers (S.S. and P.S.) independently evaluated brain MRIs and assessed each WM lesion that was designated as being positive for the CVS (CVS+), or not. If there was discordance between the 2 reviewers, a third reviewer (J.O.) assessed the lesion and a consensus was reached by discussion. The proportion of CVS+ WM lesions in each participant was expressed as a percentage of the total WM lesions in each participant. The CVS assessment was performed blinded to the presence of spinal cord lesions and clinical information.

We applied 2 previously published criteria using the CVS to distinguish MS from other WM disorders: the “40% rule,” whereby a diagnosis of MS is likely if an individual has  $\geq 40\%$  CVS+ WM lesions;<sup>9</sup> and the “rule of 6,” whereby a diagnosis of MS is likely if an individual has  $\geq 6$  CVS+ WM lesions. For the rule of 6, if an individual has fewer than 6 CVS+ WM lesions, but CVS+ WM lesions outnumber non-CVS WM lesions, a diagnosis of MS can still be considered. If neither of these conditions is met, the diagnosis of MS is unlikely.<sup>10</sup>

## Cervical Spinal Cord Lesion Count

Sagittal 2D phase-sensitive inversion recovery images of the cervical spine,<sup>32</sup> which have been shown to have higher sensitivity for cervical spinal cord lesions over T2-based imaging,<sup>32,34</sup> were used

to assess for cervical spinal cord lesions. Phase-sensitive inversion recovery images were reviewed by 1 reviewer (S.S.), and the number of the cervical spinal cord lesions was evaluated, while the reviewer was blinded to the CVS analysis and clinical information.

## Statistical Analysis

Statistical calculations were performed using SPSS (Version 23.0; IBM, Armonk, New York). Univariable and multivariable linear regression was used to identify independent variables associated with the proportion of CVS+ WM lesions. Statistical significance was defined as  $P < .05$ .

## RESULTS

### Clinical Characteristics of Participants with RIS

This study included 20 adults with RIS. Fifteen participants (75%) were women, and the mean age was 46.3 years (range, 25–62 years). None of the participants had any current or prior neurologic symptoms suggestive of demyelinating disease. The neurologic examination findings were normal in all except 4 subjects: Three had a mildly diminished vibration sensation in the distal lower limbs, and 1 subject had mild horizontal gaze-evoked nystagmus without diplopia. Headache was the most common reason (9/20, 45%) for the initial brain MR imaging being performed. CSF studies were available in 6 of 20 participants with RIS, and CSF-specific oligoclonal bands were detected in 5 participants. Alternative diagnoses were clinically excluded by the treating neurologist and included a negative systemic autoimmune screen in 18 of 20 participants. None of the subjects had undergone disease-modifying treatment used in MS. Table 1 summarizes clinical and MR imaging characteristics, and Table 2 lists the reasons for the initial brain MR imaging.

### MR Imaging Findings

**White Matter Lesions.** A total of 997 WM lesions were identified. The median number of WM lesions per participant with RIS was 33 (range, 9–165). Two hundred six WM lesions (21%) were T1 black holes. The number of WM lesions in specific brain regions was as follows: 193 cortical/juxtacortical lesions (19%), 562 subcortical/deep WM lesions (56%), 203 periventricular WM lesions (20%), and 39 infratentorial lesions (4%).

Nine participants with RIS (45%) had lesions in the infratentorial brain. There were 16 participants with RIS (80%) who had WM lesions involving the corpus callosum (49 WM lesions). T1 black hole lesions were found in 15 participants with RIS (75%).

Automated brain segmentation<sup>33</sup> was performed in 18 participants with RIS. The median brain volume was 1208 cm<sup>3</sup> (range, 1066–1468 cm<sup>3</sup>), the median total brain lesion volume was 3.9 cm<sup>3</sup> (range, 0.3–17.9 cm<sup>3</sup>), and the median cerebral volume fraction was 0.9 (range, 0.88–0.91). Of note, the automated brain segmentation<sup>34</sup> failed in 2 cases (Table 1).

**Cervical Spinal Cord Lesions.** Thirteen participants (65%) had at least 1 lesion in the cervical spinal cord. The median number of lesions within the cervical spinal cord was 1 (range, 0–4) (Table 1).

**Central Vein Sign Assessment.** Of 997 WM lesions, 606 (61%) were excluded from analysis according to previously published

**Table 1: Clinical and MRI characteristics of RIS participants**

Clinical Characteristics	
Participants (No.)	20
Age (mean) (SD) (yr)	46 (11)
Female (No.) (%)	15 (75%)
No. of cases with positive oligoclonal band (No.) (%) <sup>a</sup>	5 (83%)
MRI characteristics	
Brain lesions	
Total brain lesion count (No.)	997
No. of brain lesions per case (median) (range)	33 (9–165)
Total brain lesion volume (median) (range) (cm <sup>3</sup> ) <sup>b</sup>	3.9 (0.3–17.9)
No. of cases with T1 black hole lesions (No.) (%)	15 (75%)
No. of T1 black hole lesion count	206 (21%)
No. of T1 black hole lesions per case (median) (range)	3.5 (0–43)
No. of brain lesions included in the analysis (No.) (%)	391 (39%)
No. of brain lesions excluded from analysis (No.) (%)	606 (61%)
Brain volume (median) (range) (cm <sup>3</sup> ) <sup>b</sup>	1208 (1066–1468)
Cerebral volume fraction (median) (range) <sup>b</sup>	0.90 (0.88–0.91)
No. of assessed brain lesion/total brain lesion by region (%)	
Cortical/juxtacortical	90/193 (47%)
Subcortical/deep	228/562 (40%)
Periventricular	60/203 (30%)
Infratentorial	13/39 (33%)
Cervical spinal cord lesions	
No. of cases with spinal cord lesions (No.) (%)	13 (65%)
Total spinal cord lesion count	30
No. of spinal cord lesions per case (median) (range)	1 (0–4)

<sup>a</sup> CSF analysis for oligoclonal bands was available in 6 of 20 cases.

<sup>b</sup> Automated brain lesion volume measurements were obtained from 18 cases ( $n = 18$ ). Automated brain segmentation failed in 2 cases.

**Table 2: Reasons for performing initial brain MRI**

Reasons	(No.) (%)
Headache	9 (45%)
Work-up for pituitary adenoma	2 (10%)
Transient paraphasic symptoms atypical for demyelinating disease	2 (10%)
Intermittent subjective cognitive symptoms	1 (5%)
Intermittent nocturnal tremor	1 (5%)
Pars planitis	1 (5%)
Sinusitis	1 (5%)
Back pain	1 (5%)
Dental pain	1 (5%)
Tinnitus	1 (5%)

CVS criteria,<sup>11</sup> leaving 391 WM lesions (39%) for analysis. Of these, 292 (75%) were CVS+, whereas 99 (25%) did not demonstrate the CVS.

One hundred fourteen of 391 assessed WM lesions were T1 black holes. Of these, 106 T1 black hole lesions (93%) were CVS+. Conversely, 106 of 292 CVS+ WM lesions (36%) were T1 black holes.

The median proportion of CVS+ WM lesions per participant was 87% (range, 29%–100%). When we applied the 40% rule,<sup>8</sup> 18 (90%) had  $\geq 40\%$  CVS+ WM lesions (range: 55%–100%) and 2 (10%) had  $< 40\%$  CVS+ WM lesions (29% and 31%) (Figs 1 and 2). Of note, the 2 individuals who did not meet the 40% rule did not have any visible infratentorial lesions or spinal cord lesions. These 2 individuals underwent initial brain MR imaging for work-up of pituitary adenoma and headache, which allowed identification of the WM lesions. When the WM lesions in these 2 individuals were scrutinized retrospectively, most were small ( $< 3$  mm), punctate, rarely confluent, and located predominantly in the anterior subcortical and deep WM. Furthermore, these indi-

viduals did not have WM lesions with T1 black holes or WM lesions involving the corpus callosum.

Nineteen individuals with RIS (95%) fulfilled the rule of 6 criteria.<sup>10</sup> The single individual who did not meet the rule of 6 also failed to meet the 40% rule (CVS+ WM lesions, 31%). There was 1 participant who fulfilled the rule of 6 but failed to meet 40% rule (CVS+ WM lesions = 29%) (Table 3).

All the infratentorial lesions evaluated were CVS+ (13/13, 100%). Ninety-three percent (56/60) of periventricular WM lesions were CVS+, 78% (70/90) of cortical/juxtacortical WM lesions were CVS+, and 67% (153/228) of subcortical/deep WM lesions were CVS+ (Fig 3).

### Correlations between the Proportion of CVS + WM Lesions and Clinical/MR Imaging Variables

Univariable regression analyses showed that the number of cervical spinal cord lesions was associated with a higher proportion of CVS+ WM lesions ( $P = .04$ ).

In multivariable regression models, including age, sex, number of brain WM lesions, cervical spinal cord lesions, and infratentorial lesions, age and the number of cervical spinal cord lesions showed a significant relationship with the proportion of CVS+ WM lesions ( $P = .01$  and  $.002$ , respectively), and the number of infratentorial lesions showed a trend toward a significant relationship ( $P = .06$ ). On the other hand, the total number of baseline WM lesions did not show a significant association with the proportion of CVS+ WM lesions ( $P = .29$ ) (Table 4).

## DISCUSSION

In this study, we found that nearly all participants with RIS in our cohort had a high proportion of CVS+ WM lesions, similar to that previously been reported in MS.<sup>3,8,13–23,35</sup> Furthermore, a large proportion of our RIS cohort (18/20, 90%) met the 40% rule (Fig 1 and Table 3),<sup>8</sup> which has previously been proposed to distinguish WM lesions observed in MS from other WM disorders.<sup>8</sup>

This is the first study assessing those with the CVS in RIS, a valuable population to evaluate because RIS is currently the earliest detectable stage of MS. Historically, asymptomatic inflammatory demyelinating lesions have been identified in postmortem series, with the estimated prevalence ranging from 0.08% to 0.2%.<sup>36–38</sup> However, the true prevalence and natural history of RIS remain unknown, making this entity challenging to manage from a clinical perspective. The largest retrospective study to date suggests that 34% of individuals with RIS develop clinical MS during a follow-up of  $\sim 5$  years.<sup>25</sup>

This study suggests that most MR imaging-visible lesions in RIS are consistent with perivenous demyelination, corroborating the notion that most of these individuals have typical MS pathol-

ogy and are at risk of converting to MS. Identifying large proportions of CVS+ WM lesions may have significant clinical implications for monitoring these participants and potentially initiating disease-modifying treatment. Prospective follow-up of this cohort will test the hypothesis that the proportion of CVS+ WM lesions in RIS has (either positive or negative) prognostic value. Furthermore, we also found T1 black holes in most subjects, and most T1 black holes demonstrated the CVS, suggesting that the observed WM lesions include destructive axonal pathology. It will also be of interest to evaluate the prognostic value of T1 black holes in RIS prospectively.

Current diagnostic criteria for MS emphasize lesion location as a helpful factor in the differential diagnosis of clinically isolated

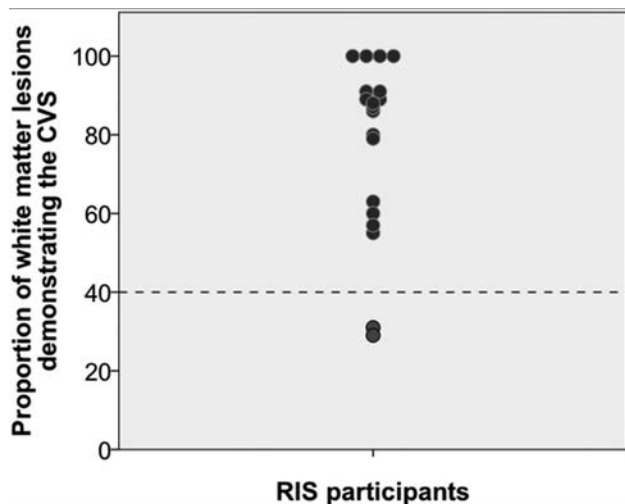


**FIG 1.** Proportion of white matter lesions demonstrating the central vein sign per case and the 40% rule. Eighteen patients with RIS (90%) met the 40% rule, whereas 2 did not.

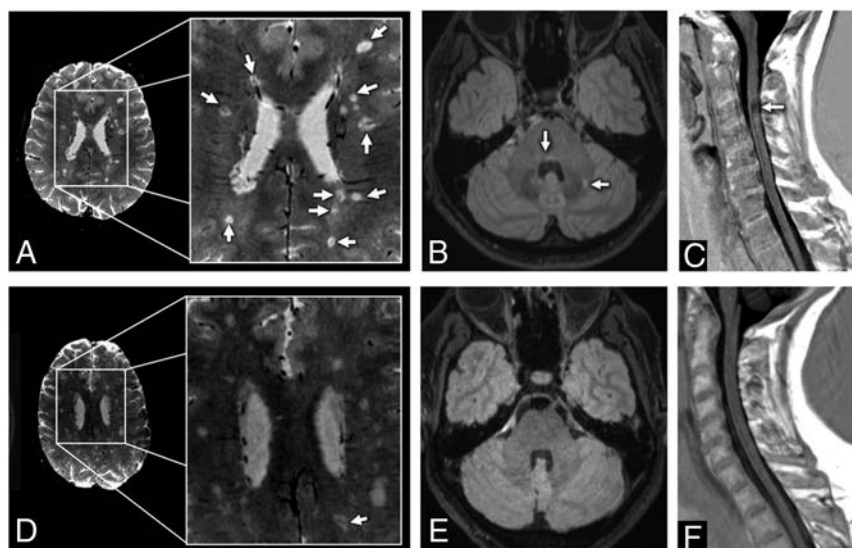


**FIG 2.** White matter lesions with evident central vein signs in 2 different radiologically isolated syndrome cases, as seen on axial reconstructed 3D-T2\*-weighted segmented echo-planar imaging sequences and 3D-T2-weighted FLAIR sequences of the brain, and sagittal T1-weighted phase-sensitive inversion recovery of the cervical spinal cord. A 50-year-old woman in whom most (90%) of the white matter lesions demonstrate the central vein sign (A, arrows). This individual also has evident infratentorial (B, arrows) and cervical spinal cord lesions (C, arrow). A 53-year-old woman with a small proportion (29%) of white matter lesions demonstrating the central vein sign (D, arrow). This individual did not have any infratentorial (E) or cervical spinal cord lesions (F).

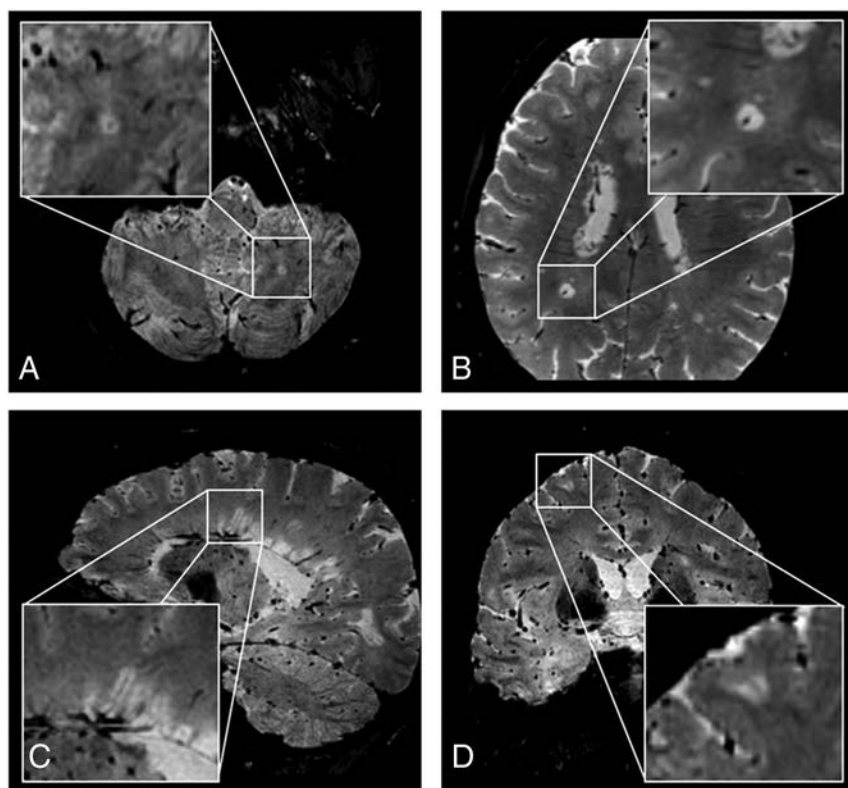
syndrome. When the WM lesions in our participants with RIS were classified by location, we found that the posterior fossa had the highest frequency of CVS+ lesions, followed by periventricular and cortical/juxtacortical locations. On the other hand, subcortical and deep WM lesions had the lowest frequency of CVS+ lesions (Fig 3). Previous studies that assessed only supratentorial lesions<sup>8,35</sup> found that the periventricular location had a high prevalence of CVS+ lesions. Our observation of a very high proportion of CVS+ lesions in the infratentorial region is of interest and is likely because lesions in the infratentorial region are not commonly seen with microangiopathy or migraines, common mimics of MS on MR imaging scans. The high prevalence of infratentorial CVS+ lesions observed in our study highlights the importance of assessing lesions in this region of the brain when evaluating RIS and in patients in whom the diagnosis of MS is a possibility.

We found a significant correlation between the number of spinal cord lesions and the proportion of CVS+ WM lesions (Table 4). Given that previous studies have shown that the presence of a spinal cord lesion is one of the strongest predictors of RIS converting to MS,<sup>25,26,39</sup> this finding raises the possibility that the proportion of CVS+ WM lesions may similarly be a predictor of RIS conversion to MS. In addition, the number of infratentorial lesions in participants with RIS also showed a trend toward correlating with the proportion of CVS+ WM lesions, which, together with the observation that the infratentorial region has the highest proportion of CVS+ lesions, suggests that assessing lesions in this region for the CVS may be of value from a prognostic standpoint. Given the cross-sectional nature of this study, however, these observations simply raise plausible hypotheses. Prospective follow-up of this cohort will be important to test these hypotheses before any definitive conclusions can be drawn.

A small proportion (2/20, 10%) of our RIS cohort had a low proportion of CVS+ WM lesions and failed to meet the 40% rule (Fig 1 and Table 3).<sup>8</sup> Notably, both of these individuals had no observable infratentorial or cervical spinal cord lesions identified on MR imaging (Fig 2D–F). Taken together, these findings suggest that the WM lesions observed in these patients lack perivenous demyelination and that there is therefore a lower risk of developing clinical MS. Although these individuals were considered to have RIS based on the applied consensus criteria, in retrospect, the imaging pattern was more “nonspecific”: Few lesions had the typical ovoid configuration of MS lesions. This finding highlights an important caveat of current RIS criteria, that lesions be typical of MS in the eyes of an expert observer. The determination of “typical” is necessarily subjective and explains why RIS cohorts may be heterogeneous.<sup>40,41</sup> In other words, it is not surprising, given current criteria, that some individuals diagnosed with RIS

**Table 3: Comparison of CVS criteria for MS diagnosis in the RIS cohort**

MS Diagnostic Criteria Using the CVS	No. of RIS Participants	
	Positive for CVS	Negative for CVS
40% rule	18 (90%)	2 (10%)
Rule of 6	19 (95%)	1 (5%)

**FIG 3.** White matter lesions demonstrating the central vein sign in different brain regions, using 3D-T2\*-weighted echo-planar imaging. A, Infratentorial. B, Deep white matter. C, Periventricular. D, juxtacortical.**Table 4: Relationships between the proportion of white matter lesions demonstrating the central vein sign and demographic and MRI variables in cases of RIS**

Variables	Univariable Regression (P Value)	Multivariable Regression (P Value)
Age	.27	.01
Sex	.30	.12
Total No. of brain lesions	.33	.29
No. of infratentorial lesions	.21	.06
No. of cervical spinal cord lesions	.04	.002

may, in fact, have WM lesions related to other entities, such as migraines, microangiopathy related to vascular risk factors, or even other inflammatory disorders of the central nervous system. Recent studies that have evaluated the CVS in other inflammatory disorders, including neuromyelitis optica<sup>23</sup> and central nervous system inflammatory vasculopathies,<sup>22</sup> have shown a significantly higher proportion of CVS+ WM lesions in MS. Thus, the availability of an imaging sign that is pathologically specific for MS-type lesions, such as the CVS, should improve the diagnosis of RIS and allow appropriate identification of individuals who are truly at risk of developing MS, rather than other disorders.

The other studies have proposed other cutoff thresholds, including 45%,<sup>10,21</sup> 50%,<sup>22</sup> and 54%,<sup>23</sup> of which the proportion of CVS+ WM lesions  $\geq 45\%$ ,  $\geq 50\%$ , and  $\geq 54\%$  can be used to

distinguished MS from non-MS diseases, respectively. Because the lowest proportion of these 18 participants with RIS with  $\geq 40\%$  CVS+ WM lesions was 55%, applying either the 45% or 50% rule led to the same observation, highlighting that most participants with RIS had high CVS+ WM lesions similar to those in MS.

When we applied the rule of 6,<sup>10</sup> the more simplified method to assess the CVS to our cohort, similar results were observed with most RIS participants, with the exception of 1 case. Only 1 case did not fulfill the rule of 6, and this case similarly failed to meet the 40% rule. However, there was 1 case that failed to meet the 40% rule but met the rule of 6. On further scrutiny, this participant had 16 CVS+ WM lesions of the 61 WM lesions (29%). By way of comparison, the individual who did not meet both sets of criteria had 5 CVS+ WM lesions of a total 16 WM lesions (31%).<sup>10</sup> These observations suggest that although there is general agreement between the 2 sets of criteria, the 40% rule may be more specific to individuals at risk of developing MS and the rule of 6 may need to be applied with caution in individuals with a large number of WM lesions. In line with this observation, another recent study in MS has shown that the rule of 6 has lower specificity for MS.<sup>21</sup> Although applying the rule of 6 has the benefit of efficiency and simplicity over the 40% rule, in cases with high WM lesion loads, applying the 40% rule may prevent false-positive conclusions. Given the practical difficulty of computing the CVS proportion in such cases, future directions may include the development of automated CVS detection algorithms<sup>42</sup> that can be rapidly applied in clinical settings. A recent study reported a promising automated CVS-detection program that was able to distinguish MS from non-MS disease; however, the sensitivity and specificity of this program were lower than those in manually obtained CVS proportions, suggesting that refinements need to be made before such programs can be practically used in clinical settings.

This study has a number of limitations. First, the sample size was relatively small because RIS is a rare entity. Second, a significant proportion of WM lesions were excluded from CVS analysis in our RIS cohort (61%), which is in accordance with current CVS identification criteria.<sup>11</sup> In addition, due to the potential risks of gadolinium (ie, gadolinium retention and nephrogenic systemic fibrosis), our MR imaging protocol did not include a gadolinium-based contrast agent, which has been demonstrated to increase

visualization of central veins within small WM lesions on the 3D-T2\* EPI sequence due to its paramagnetic properties.<sup>9,11,12</sup> Nevertheless, the observed prevalence of CVS in our RIS individuals was high, and in light of our detailed findings in the 2 individuals with <40% CVS+ lesions, the administration of gadolinium would not likely have changed our conclusions. Furthermore, we were not able to compare the CVS in RIS with that in a healthy control group or with a group of patients with WM disorders other than MS; this comparison would have been of interest. However, a number of prior studies using similar methodologies have clearly demonstrated that the CVS is rarely found in healthy controls<sup>9,23,35,43</sup> and to a much lower proportion in other WM disorders.<sup>3,8,11,15,21–23</sup> Because this study was performed using sequences identical to those in recent studies and the CVS was evaluated by experienced investigators who coauthored prior studies,<sup>3,9,11,12,15,21,22,42,43</sup> the lack of a control group would probably not have changed our conclusions. Finally, due to the cross-sectional nature of this study, we were unable to evaluate the prognostic value of the CVS in RIS. However, prospective follow-up of this cohort is planned, which will be informative and may eventually help guide clinical management.

## CONCLUSIONS

In this study, we found that most individuals with RIS based on current diagnostic criteria have a high proportion of lesions demonstrating the CVS, similar to that seen in clinical MS. This finding suggests that most patients with RIS have perivenous demyelinating pathology typical of MS. Moreover, we found significant correlations between the proportion of CVS+ WM lesions and spinal cord lesions in RIS, suggesting, by inference, that the CVS may have prognostic value in RIS. This raises the possibility that the CVS may be useful to distinguish patients with RIS at high risk of developing clinical MS from those with truly nonspecific WM lesions and therefore at minimal risk of developing clinical symptoms. Prospective follow-up of this cohort is planned, which will enable a better understanding of the diagnostic and predictive value of the CVS in RIS and of the natural history of RIS.

Disclosures: Suradech Suthiphosuwana—UNRELATED: Grants/Grants Pending: Sanofi Genzyme, Comments: I received fellowship educational support from an unrestricted educational grant. Xavier Montalban—UNRELATED: X.M. Consultancy: Biogen, Celgene, Sanofi Genzyme, Merck, Novartis, Roche and Teva Pharmaceutical. Daniel S. Reich—UNRELATED: Expert Testimony: Leventhal & Puga, P.C. Jiwon Oh—RELATED: Grant: MS Society of Canada and Love/Barford Endowment\*; UNRELATED: Consultancy: Biogen Idec, Roche, EMD Serono, Sanofi Genzyme, Celgene; Grants: Brain Canada, MS Society of Canada, Biogen Idec, Roche.\* \*Money paid to the institution.

## REFERENCES

- Thompson AJ, Baranzini SE, Geurts J, et al. **Multiple sclerosis.** *Lancet* 2018;391:1622–36 CrossRef Medline
- Adams CW, Abdulla YH, Torres EM, et al. **Periventricular lesions in multiple sclerosis: their perivenous origin and relationship to granular ependymitis.** *Neuropathol Appl Neurobiol* 1987;13:141–52 CrossRef Medline
- Solomon AJ, Schindler MK, Howard DB, et al. **“Central vessel sign” on 3T FLAIR\* MRI for the differentiation of multiple sclerosis from migraine.** *Ann Clin Transl Neurol* 2016;3:82–87 CrossRef Medline
- Polman CH, Reingold SC, Edan G, et al. **Diagnostic criteria for multiple sclerosis: 2005 revisions to the “McDonald Criteria.”** *Ann Neurol* 2005;58:840–46 CrossRef Medline
- Polman CH, Reingold SC, Banwell B, et al. **Diagnostic criteria for multiple sclerosis: 2010 revisions to the McDonald criteria.** *Ann Neurol* 2011;69:292–302 CrossRef Medline
- Thompson AJ, Banwell BL, Barkhof F, et al. **Diagnosis of multiple sclerosis: 2017 revisions of the McDonald criteria.** *Lancet Neurol* 2018;17:162–73 CrossRef Medline
- Tallantyre EC, Brookes MJ, Dixon JE, et al. **Demonstrating the perivascular distribution of MS lesions in vivo with 7-Tesla MRI.** *Neurology* 2008;70:2076–78 CrossRef Medline
- Tallantyre EC, Dixon JE, Donaldson I, et al. **Ultra-high-field imaging distinguishes MS lesions from asymptomatic white matter lesions.** *Neurology* 2011;76:534–39 CrossRef Medline
- Sati P, Thomasson DM, Li N, et al. **Rapid, high-resolution, whole-brain, susceptibility-based MRI of multiple sclerosis.** *Mult Scler* 2014;20:1464–70 CrossRef Medline
- Mistry N, Abdel-Fahim R, Samaraweera A, et al. **Imaging central veins in brain lesions with 3-T T2\*-weighted magnetic resonance imaging differentiates multiple sclerosis from microangiopathic brain lesions.** *Mult Scler* 2016;22:1289–96 CrossRef Medline
- Sati P, Oh J, Constable RT, et al. **The central vein sign and its clinical evaluation for the diagnosis of multiple sclerosis: a consensus statement from the North American Imaging in Multiple Sclerosis Cooperative.** *Nat Rev Neurol* 2016;12:714–22 CrossRef Medline
- Sati P, George IC, Shea CD, et al. **FLAIR\*: a combined MR contrast technique for visualizing white matter lesions and parenchymal veins.** *Radiology* 2012;265:926–32 CrossRef Medline
- Kau T, Taschwer M, Deutschmann H, et al. **The “central vein sign”: is there a place for susceptibility weighted imaging in possible multiple sclerosis?** *Eur Radiol* 2013;23:1956–62 CrossRef Medline
- Samaraweera AP, Clarke MA, Whitehead A, et al. **The central vein sign in multiple sclerosis lesions is present irrespective of the T2\* sequence at 3 T.** *J Neuroimaging* 2017;27:114–21 CrossRef Medline
- Solomon AJ, Watts R, Ontaneda D, et al. **Diagnostic performance of central vein sign for multiple sclerosis with a simplified three-lesion algorithm.** *Mult Scler* 2018;24:750–57 CrossRef Medline
- Sparacia G, Agnello F, Gambino A, et al. **Multiple sclerosis: high prevalence of the ‘central vein’ sign in white matter lesions on susceptibility-weighted images.** *Neuroradiol J* 2018;31:356–61 CrossRef Medline
- Miller AE, Calabresi PA. **Central vein sign in multiple sclerosis: ready for front and center?** *Neurology* 2018;90:631–32 CrossRef Medline
- Inglese M, Fleysher L, Oesingmann N, et al. **Clinical applications of ultra-high field magnetic resonance imaging in multiple sclerosis.** *Expert Rev Neurother* 2018;18:221–30 CrossRef Medline
- Hosseini Z, Matusinec J, Rudko DA, et al. **Morphology-specific discrimination between MS white matter lesions and benign white matter hyperintensities using ultra-high-field MRI.** *AJNR Am J Neuroradiol* 2018;39:1473–79 CrossRef Medline
- Lamot U, Avsenik J, Segal S, et al. **Presence of central veins and susceptibility weighted imaging for evaluating lesions in multiple sclerosis and leukoaraosis.** *Mult Scler Relat Disord* 2017;13:67–72 CrossRef Medline
- Campion T, Smith RJP, Altmann DR, et al. **FLAIR\* to visualize veins in white matter lesions: a new tool for the diagnosis of multiple sclerosis?** *Eur Radiol* 2017;27:4257–63 CrossRef Medline
- Maggi P, Absinta M, Grammatico M, et al. **Central vein sign differentiates multiple sclerosis from central nervous system inflammatory vasculopathies.** *Ann Neurol* 2018;83:283–94 CrossRef Medline
- Cortese R, Magnollay L, Tur C, et al. **Value of the central vein sign at 3T to differentiate MS from seropositive NMOSD.** *Neurology* 2018;90:e1183–90 CrossRef Medline
- Okuda DT, Mowry EM, Beheshtian A, et al. **Incidental MRI anomalies suggestive of multiple sclerosis: the radiologically isolated syndrome.** *Neurology* 2009;72:800–05 CrossRef Medline
- Okuda DT, Siva A, Kantarci O, et al. **Radiologically Isolated Syndrome Consortium (RISC), Club Francophone de la Sclérose en Plaques (CFSEP). Radiologically isolated syndrome: 5-year risk for an initial clinical event.** *PLoS One* 2014;9:e90509 CrossRef Medline
- Okuda DT, Mowry EM, Cree BA, et al. **Asymptomatic spinal cord**

- lesions predict disease progression in radiologically isolated syndrome. *Neurology* 2011;76:686–92 CrossRef Medline
27. Kantarci OH, Lebrun C, Siva A, et al. **Primary progressive multiple sclerosis evolving from radiologically isolated syndrome.** *Ann Neurol* 2016;79:288–94 CrossRef Medline
  28. Barkhof F, Filippi M, Miller DH, et al. **Comparison of MRI criteria at first presentation to predict conversion to clinically definite multiple sclerosis.** *Brain* 1997;120(Pt 11):2059–69 CrossRef Medline
  29. Filippi M, Rocca MA, Ciccarelli O, et al; MAGNIMS Study Group. **MRI criteria for the diagnosis of multiple sclerosis: MAGNIMS consensus guidelines.** *Lancet Neurol* 2016;15:292–303 CrossRef Medline
  30. De Stefano N, Giorgio A, Tintoré M, et al. **Radiologically isolated syndrome or subclinical multiple sclerosis: MAGNIMS consensus recommendations.** *Mult Scler* 2018;24:214–21 CrossRef Medline
  31. Forslin Y, Granberg T, Jumah AA, et al. **Incidence of radiologically isolated syndrome: a population-based study.** *AJNR Am J Neuroradiol* 2016;37:1017–22 CrossRef Medline
  32. Alcaide-Leon P, Pauranik A, Alshafai L, et al. **Comparison of sagittal FSE T2, STIR, and T1-weighted phase-sensitive inversion recovery in the detection of spinal cord lesions in MS at 3T.** *AJNR Am J Neuroradiol* 2016;37:970–75 CrossRef Medline
  33. Huo Y, Carass A, Resnick SM, et al. **Combining multi-atlas segmentation with brain surface estimation.** *Proc SPIE Int Soc Opt Eng* 2016; 9784 Medline
  34. Nair G, Absinta M, Reich DS. **Optimized T1-MPRAGE sequence for better visualization of spinal cord multiple sclerosis lesions at 3T.** *AJNR Am J Neuroradiol* 2013;34:2215–22 CrossRef Medline
  35. Kilsdonk ID, Lopez-Soriano A, Kuijjer JP, et al. **Morphological features of MS lesions on FLAIR\* at 7 T and their relation to patient characteristics.** *J Neurol* 2014;261:1356–64 CrossRef Medline
  36. Engell T. **A clinical patho-anatomical study of clinically silent multiple sclerosis.** *Acta Neurol Scand* 1989;79:428–30 CrossRef Medline
  37. Gilbert JJ, Sadler M. **Unsuspected multiple sclerosis.** *Arch Neurol* 1983;40:533–36 CrossRef Medline
  38. Castaigne P, Lhermitte F, Escourolle R, et al. **Asymptomatic multiple sclerosis: 3 cases (author's transl) [in French].** *Rev Neurol (Paris)* 1981;137:729–39 Medline
  39. Granberg T, Martola J, Kristoffersen-Wiberg M, et al. **Radiologically isolated syndrome: incidental magnetic resonance imaging findings suggestive of multiple sclerosis—a systematic review.** *Mult Scler* 2013;19:271–80 CrossRef Medline
  40. Labiano-Fontcuberta A, Benito-Leon J. **Radiologically isolated syndrome: an update on a rare entity.** *Mult Scler* 2016;22:1514–21 CrossRef Medline
  41. Liu S, Kullnat J, Bourdette D, et al. **Prevalence of brain magnetic resonance imaging meeting Barkhof and McDonald criteria for dissemination in space among headache patients.** *Mult Scler* 2013;19: 1101–05 CrossRef Medline
  42. Dworkin JD, Sati P, Solomon A, et al. **Automated integration of multimodal MRI for the probabilistic detection of the central vein sign in white matter lesions.** *AJNR Am J Neuroradiol* 2018;39: 1806–13 CrossRef Medline
  43. Gaitiá MI, de Alwis MP, Sati P, et al. **Multiple sclerosis shrinks intralesional, and enlarges extralesional, brain parenchymal veins.** *Neurology* 2013;80:145–51 CrossRef Medline

# Increased Water Content in Periventricular Caps in Patients without Acute Hydrocephalus

T. Sichter mann, J.K. Furtmann, S. Dekeyzer, G. Gilmour, A.M. Oros-Peusquens, J.P. Bach, M. Wiesmann, N.J. Shah, and O. Nikoubashman

## ABSTRACT

**BACKGROUND AND PURPOSE:** Periventricular caps are a common finding on MR imaging and are believed to reflect focally increased interstitial water content due to dysfunctional transependymal transportation rather than ischemic-gliotic changes. We compared the quantitative water content of periventricular caps and microvascular white matter lesions, hypothesizing that periventricular caps associated with increased interstitial fluid content display higher water content than white matter lesions and are therefore differentiable from microvascular white matter lesions by measurement of the water content.

**MATERIALS AND METHODS:** In a prospective study, we compared the water content of periventricular caps and white matter lesions in 50 patients using a quantitative multiple-echo, gradient-echo MR imaging water-mapping sequence.

**RESULTS:** The water content of periventricular caps was significantly higher than that of white matter lesions ( $P = .002$ ). Compared with normal white matter, the mean water content of periventricular caps was  $17\% \pm 5\%$  higher and the mean water content of white matter lesions was  $11\% \pm 4\%$  higher. Receiver operating characteristic analysis revealed that areas in which water content was 15% higher compared with normal white matter correspond to periventricular caps rather than white matter lesions, with a specificity of 93% and a sensitivity of 60% ( $P < .001$ ). There was no significant correlation between the water content of periventricular caps and whole-brain volume ( $P = .275$ ), white matter volume ( $P = .243$ ), gray matter volume ( $P = .548$ ), lateral ventricle volume ( $P = .800$ ), white matter lesion volume ( $P = .081$ ), periventricular cap volume ( $P = .081$ ), and age ( $P = .224$ ).

**CONCLUSIONS:** Quantitative MR imaging allows differentiation between periventricular caps and white matter lesions. Water content quantification of T2-hyperintense lesions may be a useful additional tool for the characterization and differentiation of T2-hyperintense diseases.

**ABBREVIATIONS:** iNPH = idiopathic normal pressure hydrocephalus; PVC = periventricular cap; WML = white matter lesions

Periventricular caps (PVCs), smooth T2-hyperintense areas around the lateral ventricles (mostly the frontal and posterior horns, Fig 1), are a common finding on cranial MR imaging, especially in elderly patients. Pathologic studies have shown that PVCs do not correspond to ischemic-gliotic changes, but rather to an area of finely textured myelin associated with denudation of the ventricular ependymal lining.<sup>1</sup> Because the ependyma provides a bidirectional barrier and transport system for CSF and

interstitial fluid exchange, age-related ependymal denudation might impair normal transportation of interstitial fluid into the ventricles, leading to an accumulation of interstitial fluid, which converges from the surrounding white matter, around the frontal horns of both lateral ventricles.<sup>1</sup> According to this theory, the increased T2 signal intensity in PVCs would reflect, at least in part, edematous rather than pure gliotic white matter changes. However, gliotic white matter changes caused by microvascular disease are also a frequent occurrence in the general population.<sup>2</sup> Because conventional T2-weighted sequences do not allow one to differentiate between those 2 types of lesions, alternative imaging sequences are necessary to differentiate these 2 pathologies. Quantitative MR imaging allows the quantification of water content of brain lesions within a clinically acceptable acquisition time of a few minutes.<sup>3,4</sup> For instance, it has been shown that quantitative water mapping allows one to detect an increase in cerebral water content in hepatic encephalopathy and to evaluate the surrounding edema in brain tumors.<sup>5,6</sup>

Received January 9, 2019; accepted after revision March 11.

From the Departments of Diagnostic and Interventional Neuroradiology (T.S., J.K.F., S.D., G.G., M.W., O.N.) and Neurology (J.P.B., N.J.S.), University Hospital, RWTH Aachen University, Aachen, Germany; Department of Radiology (S.D.), Antwerp University Hospital (UZA), Antwerp, Belgium; and Institute of Neuroscience and Medicine (A.M.O.-P., N.J.S.), Jülich, Germany.

Please address correspondence to Thorsten Sichter mann, MD, Klinik für Diagnostische und Interventionelle Neuroradiologie, Universitätsklinikum Aachen, Pauwelsstr 30, 52074 Aachen, Germany; e-mail: tsichter mann@ukaachen.de

<http://dx.doi.org/10.3174/ajnr.A6033>

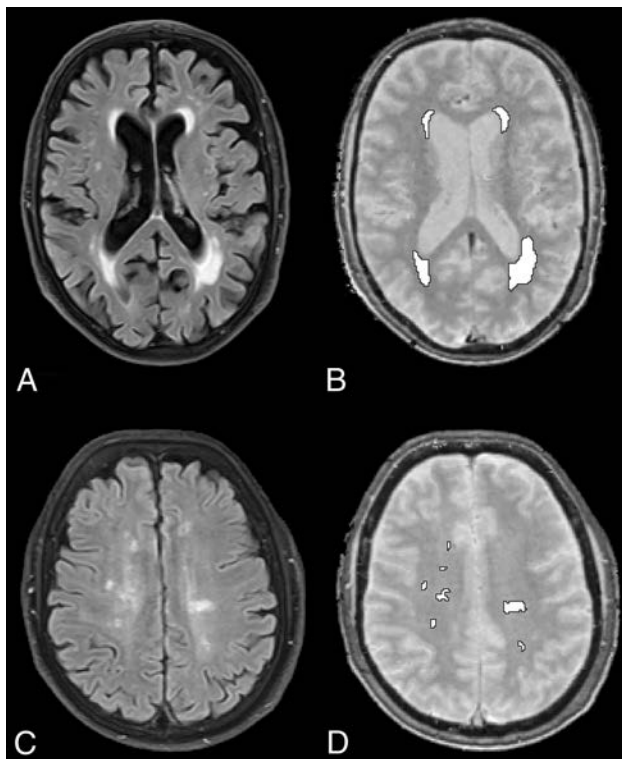


**FIG 1.** MR imaging acquisitions and segmentations. Exemplary T2-FLAIR (left) and water mapping (right) acquisitions and final segmentation (white ROIs). Periventricular caps (A and B) and gliotic white matter lesions (C and D) in 2 different patients.

We hypothesized that quantitative MR imaging allows differentiation between PVCs and microvascular white matter lesions (WML). Hence, the aim of this study was to investigate whether PVCs, representing interstitial fluid due to dysfunctional transpendymal transportation, contain an increased water content compared with gliotic microvascular deep white matter lesions, using a quantitative water-mapping sequence.

## MATERIALS AND METHODS

After approval from our local ethics board (faculty of medicine, RWTH Aachen University), we prospectively scanned all patients who presented with neurovascular symptoms between May 2014 and February 2017 and who agreed to participate in our study ( $n = 177$ ). For this analysis, we included all patients who had both PVCs and WML with a volume of at least  $.1 \text{ cm}^3$ . This cutoff was chosen to address lesions that are clearly assessable on clinical MR imaging with a typical slice thickness of 3–5 mm, thereby reducing partial volume effects on our measurements. We excluded patients with acute or subacute stroke adjacent to the investigated areas and patients with pathologies other than PVCs and WML, such as brain tumors or inflammation. This exclusion left 50 patients included in our study. No patient had clinical or radiologic signs of acute hydrocephalus or idiopathic normal pressure hydrocephalus (iNPH).

Our standard MR imaging protocol consisted, among others, of the following MR imaging sequences: DWI, FLAIR, T2\*-weighted, T2-weighted (sagittal), and T1-weighted (coronal). All MR images were acquired on a 3T scanner (Magnetom Prisma; Siemens; Erlangen, Germany).

Specifications of our T2-FLAIR sequence were as follows: TR, 9000 ms; TE, 98 ms; flip angle,  $150^\circ$ ; FOV, 230 mm; section thickness, 3 mm; matrix,  $256 \times 192$ ; acquisition time, 3 minutes and 2 seconds.

For quantitative water content measurements, we used the manufacturer's 2D multiple-echo gradient-echo sequence acquired with TR = 5000 ms and a nominal flip angle of  $25^\circ$ . By using an acceleration factor for parallel imaging of integrated Parallel Acquisition Techniques ("iPAT" = 2), the acquisition time (TA) for whole-brain coverage was 4 minutes and 12 seconds. Other relevant parameters were the following: TE1, 3.34 ms; deltaTE, 2.85 ms; 12 echoes; resolution,  $1 \times 1 \times 1.5 \text{ mm}$  (50% slice gap); bandwidth, 510 Hz/px; partial Fourier factor, 6/8; number of slices, 84.<sup>3</sup>

## Analysis

To delineate PVCs and WML, we used a semiautomatic segmentation approach to allow objective segmentation. Initially, we used the open-source deep learning framework DeepMedic (Version 0.6.1; <https://biomedica.doc.ic.ac.uk/software/deepmedic/>), which is used for automated segmentation, to segment the hyperintensities in the T2-FLAIR sequence.<sup>7</sup> We trained the neural network with 30 cases of voxelwise manually annotated ROIs as "PVCs" and "WML," depending on their morphology and location. We defined PVCs as smooth periventricular caps at the frontal and posterior horns of the lateral ventricles (grade 1 PVCs according to Thomas et al<sup>8</sup>), whereas irregular T2-hyperintense periventricular regions were not regarded as PVCs. WML were defined as patchy or confluent T2-hyperintense areas in the deep cerebral white matter. Areas where we could not clearly distinguish PVCs and WML were excluded altogether from our analysis. For our final analysis, 2 independent observers examined all segmented areas and adjusted the ROIs manually in a consensus reading, for example, to modify ROIs contiguous with the ventricles that could have been affected by partial volume effects. The final ROIs were then used in the water-mapping acquisitions to measure the quantitative water content of PVCs and WML. In addition, we investigated whether there was a gradient of water content from central periventricular white matter to more peripheral subcortical white matter by measuring 3 ROIs in the periventricular white matter, the centrum semiovale, and the subcortical white matter. Thus, we manually placed 3 respective ROIs in normal white matter on 1 axial slice adjacent to the examined T2 hyperintensities.

## Statistical Analysis

After testing for data distribution with a Shapiro-Wilk test, we performed a paired Student  $t$  test to determine whether the water content between areas of PVCs and WML differed significantly. We conducted an ANOVA to assess whether there was a gradient between the central and peripheral water content. We performed a receiver operating characteristic analysis to determine the sensitivity and specificity of water content measurements for PVCs and WML distinction. We examined correlations between PVC water content and brain volume, lateral ventricle volume, lesion volume, and age using the Pearson correlation coefficient. Continuous parametric variables are presented as mean  $\pm$  SD, and  $P$  values with an  $\alpha$  level  $<.05$  were considered statistically signifi-

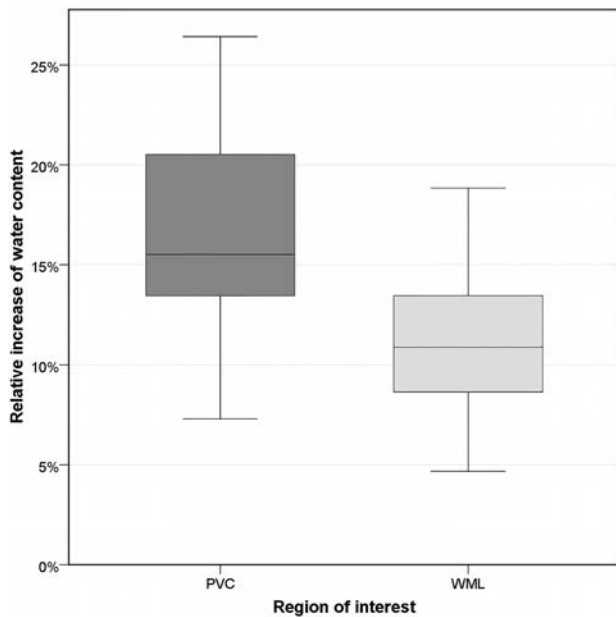


**FIG 2.** Relative increase of water content. The boxplot illustrates the relative increase of water content for periventricular caps and gliotic white matter lesions.

cant. All statistical analyses were calculated using the SPSS software package, Version 25 (IBM, Armonk, New York).

## RESULTS

The mean age of our 50 patients (21 women) was  $74 \pm 10$  years (median, 74 years; range, 45–94 years). The average volume of the measured PVC ROIs was  $2.3 \pm 1.5$  cm<sup>3</sup> (median, 1.9 cm<sup>3</sup>; range, .6–7.3 cm<sup>3</sup>). The average volume of the measured white matter lesion ROIs was  $4.6 \pm 7.6$  cm<sup>3</sup> (median, 2.0 cm<sup>3</sup>; range, .2–46.3 cm<sup>3</sup>). The mean water content of healthy white matter was  $69\% \pm 2\%$  (median, 69.6%; range 65%–74%). There was no gradient between central and peripheral water content in healthy white matter, with a water content of  $70\% \pm 3\%$  (median, 70%; range, 65%–80%) in the periventricular white matter,  $69\% \pm 2\%$  (median, 69%; range, 64%–73%) at the centrum semiovale, and  $69\% \pm 3\%$  (median, 69%; range, 63%–74%) in the subcortical white matter ( $P = .122$ ).

The absolute water content and the relative increase of water content of PVCs was significantly higher than that of WML ( $P = .002$ ). The mean absolute water content in PVCs was  $81\% \pm 2\%$  (median, 81%; range, 77%–85%). The water content in PVCs was  $17\% \pm 5\%$  (median, 16%; range, 7%–26%) higher than that of normal white matter (Fig 2). The mean absolute water content in WML was  $77\% \pm 2\%$  (median, 77%; range, 71%–81%). The water content in WML was  $11\% \pm 4\%$  (median, 11%; range, 5%–19%) higher than that of normal white matter (Fig 2). The water content of PVCs was higher than that of WML in all patients. Lesion volume had no significant impact on water content in PVCs and WML ( $P = .953$ ). Receiver operating characteristic analysis revealed that a 15% higher water content corresponded to PVCs rather than WML with a specificity of 93% and a sensitivity of 60% ( $P < .001$ , area under the curve = .842).

There was no significant correlation between the water content of PVCs and whole-brain volume ( $P = .275$ ), white matter

volume ( $P = .243$ ), gray matter volume ( $P = .548$ ), lateral ventricle volume ( $P = .800$ ), WML volume ( $P = .081$ ), PVC volume ( $P = .081$ ), and age ( $P = .224$ ).

## DISCUSSION

The microscopic nature of PVCs in patients without acute hydrocephalus is not fully understood. The literature suggests that PVCs might be secondary to dysfunctional transependymal transportation of interstitial fluid into the ventricles; thus, accordingly, it is expected that PVCs show higher water content compared with gliotic deep white matter lesions.<sup>1</sup>

In our study, we found that the water content of PVCs was indeed significantly higher than that of deep WML. Our receiver operating characteristic analysis revealed that a lesion with a 15% or higher water content compared with normal white matter corresponds to PVCs rather than deep WML, with an acceptable sensitivity and specificity. There was no significant correlation between the water content of PVCs and brain volume, lateral ventricle volume, lesion volume, and age. Because PVCs are located around the ventricles and WML are located peripherally, we investigated whether the water content difference was due to a water content gradient in healthy white matter with high water content in the periventricular areas and low content in the periphery. We assessed the water content in the respective regions and did not detect any such gradient, suggesting that the high water content in PVCs is, in fact, evidence of a histopathologic difference between deep WML and PVCs. Our study does not allow determining the exact pathophysiology of PVCs, in particular because our study lacks longitudinal imaging that could elucidate the etiology of PVCs. Hence, water content serves as a surrogate imaging marker that confirms pathologic studies that showed that there is increased water content accumulating from white matter surroundings or the intense venous network in this region.<sup>9,10</sup> This work, therefore, serves as an *in vivo* validation of previous pathologic studies.

The results of this study may be translated to patients with iNPH and may help understand the pathophysiology of that disease: For instance, it is still unclear whether periventricular changes in patients with iNPH represent transependymal edema or ischemic gliosis. In fact, it has been suggested that iNPH is primarily driven by gliotic white matter infarction, which diminishes brain tissue compliance, especially because iNPH is associated with vascular risk factors such as diabetes and arterial hypertension.<sup>11–13</sup> On the other hand, abnormalities of CSF circulation are believed to be the primary cause of iNPH,<sup>14–16</sup> supported by the fact that clinical symptoms and the degree of white matter lesions improve in some patients after ventricular shunting, the latter possibly depending on whether these lesions were gliotic or edematous.<sup>17–19</sup> Theoretically, quantitative water mapping could be used in these patients to distinguish periventricular gliotic-ischemic from edematous white matter changes in an attempt to elucidate the underlying nature of these changes and eventually predict shunt-responsiveness.

## Limitations

A major limitation of our study is the lack of an *in vivo* criterion standard for the distinction between gliotic and edematous T2

hyperintensities, which leads, to some extent, to a speculative interpretation of our data. In addition, it is not evident whether the presumably gliotic WML in our included patients are, in fact, caused by ischemia. To address this issue, we included only patients in whom microvascular ischemic gliosis was the most probable cause for their WML. Due to the study design, our study population consists solely of patients with neurovascular symptoms; inclusion of healthy, asymptomatic controls or patients presenting a wider range of symptoms would allow a better generalization of the findings. A strength of our study is the inclusion of patients with both PVCs and WML, which allows an intraindividual analysis. The fact that the water content of PVCs surpassed the water content of WML in every single patient underlines that averaging effects had no major impact on our results.

## CONCLUSIONS

We found that the water content of periventricular caps was significantly higher than that of deep white matter lesions; the latter were most probably of microvascular origin. Our results show that a lesion with a 15% or higher water content compared with normal white matter corresponds to PVCs rather than WML. Inversely, this finding also implies that it is possible to use quantitative water mapping to distinguish gliotic white matter lesions from other T2-hyperintense lesions. Quantifying the water content of periventricular T2-hyperintense white matter changes may be a useful additional tool for the differentiation of T2 hyperintensities in iNPH or other diseases such as multiple sclerosis.

Disclosures: Martin Wiesmann—UNRELATED: Consultancy: Stryker Neurovascular; Grants/Grants Pending: Stryker Neurovascular\*; Payment for Lectures Including Service on Speakers Bureaus: Bracco Imaging, Medtronic, Siemens, Stryker Neurovascular; Payment for Development of Educational Presentations: Abbott, ab medica, Acandis, Bayer Healthcare AG, Bracco Imaging, B. Braun Medical, Codman Neurovascular, Kaneka Pharma, Medtronic, Dahlhausen, MicroVention, Nvidia, Penumbra, phenox, Philips Healthcare, Route 92 Medical, Siemens, Silk Road Medical, St. Jude, Stryker Neurovascular.\* \*Money paid to the institution.

## REFERENCES

- Schmidt R, Schmidt H, Haybaeck J, et al. **Heterogeneity in age-related white matter changes.** *Acta Neuropathol* 2011;122:171–85 CrossRef Medline
- Jones DK, Lythgoe D, Horsfield MA, et al. **Characterization of white matter damage in ischemic leukoaraiosis with diffusion tensor MRI.** *Stroke* 1999;30:393–97 CrossRef Medline
- Oros-Peusquens AM, Louçao R, Zimmermann M, et al. **Methods for molecular imaging of brain tumours in a hybrid MR-PET context: water content, T2\*, diffusion indices and FET-PET.** *Methods* 2017;130:135–51 CrossRef Medline
- Shah NJ, Ermer V, Oros-Peusquens AM. **Measuring the absolute water content of the brain using quantitative MRI.** *Methods Mol Biol* 2011;711:29–64 CrossRef Medline
- Shah NJ, Neeb H, Kircheis G, et al. **Quantitative cerebral water content mapping in hepatic encephalopathy.** *Neuroimage* 2008;41:706–17 CrossRef Medline
- Neeb H, Zilles K, Shah NJ. **A new method for fast quantitative mapping of absolute water content in vivo.** *Neuroimage* 2006;31:1156–68 CrossRef Medline
- Kamnitsas K, Ledig C, Newcombe VFJ, et al. **Efficient multi-scale 3D CNN with fully connected CRF for accurate brain lesion segmentation.** *Med Image Anal* 2017;36:61–78 CrossRef Medline
- Thomas AJ, O'Brien JT, Barber R, et al. **A neuropathological study of periventricular white matter hyperintensities in major depression.** *J Affect Disord* 2003;76:49–54 CrossRef Medline
- Fazekas F, Kleinert R, Offenbacher H, et al. **Pathologic correlates of incidental MRI white matter signal hyperintensities.** *Neurology* 1993;43:1683–89 CrossRef Medline
- Sze G, De Armond SJ, Brant-Zawadzki M, et al. **Foci of MRI signal (pseudo lesions) anterior to the frontal horns: histologic correlations of a normal finding.** *AJR Am J Roentgenol* 1986;147:331–37 CrossRef Medline
- Krauss JK, Regel JP, Vach W, et al. **Vascular risk factors and arteriosclerotic disease in idiopathic normal-pressure hydrocephalus of the elderly.** *Stroke* 1996;27:24–29 CrossRef Medline
- Silverberg GD. **Normal pressure hydrocephalus (NPH): ischaemia, CSF stagnation or both.** *Brain* 2004;127:947–48 CrossRef Medline
- Silverberg GD, Mayo M, Saul T, et al. **Alzheimer's disease, normal-pressure hydrocephalus, and senescent changes in CSF circulatory physiology: a hypothesis.** *Lancet Neurol* 2003;2:506–11 CrossRef Medline
- Bradley WG Jr, Whittemore AR, Watanabe AS, et al. **Association of deep white matter infarction with chronic communicating hydrocephalus: implications regarding the possible origin of normal-pressure hydrocephalus.** *AJNR Am J Neuroradiol* 1991;12:31–39 Medline
- Symon L, Dorsch NW. **Use of long-term intracranial pressure measurement to assess hydrocephalic patients prior to shunt surgery.** *J Neurosurg* 1975;42:258–73 CrossRef Medline
- Bradley WG Jr, Scalzo D, Queralt J, et al. **Normal-pressure hydrocephalus: evaluation with cerebrospinal fluid flow measurements at MR imaging.** *Radiology* 1996;198:523–29 CrossRef Medline
- Tullberg M, Jensen C, Ekholm S, et al. **Normal pressure hydrocephalus: vascular white matter changes on MR images must not exclude patients from shunt surgery.** *AJNR Am J Neuroradiol* 2001;22:1665–73 Medline
- Krauss JK, Droste DW, Vach W, et al. **Cerebrospinal fluid shunting in idiopathic normal-pressure hydrocephalus of the elderly: effect of periventricular and deep white matter lesions.** *Neurosurgery* 1996;39:292–99; discussion 299–300 CrossRef Medline
- Damasceno BP. **Neuroimaging in normal pressure hydrocephalus.** *Dement Neuropsychol* 2015;9:350–55 CrossRef Medline

# *GJA1* Variants Cause Spastic Paraplegia Associated with Cerebral Hypomyelination

L. Saint-Val,<sup>1</sup> T. Courtin,<sup>1</sup> P. Charles,<sup>1</sup> C. Verny,<sup>1</sup> M. Catala,<sup>1</sup> R. Schiffmann,<sup>1</sup> O. Boespflug-Tanguy,<sup>1</sup> and F. Mochel<sup>1</sup>



## ABSTRACT

**SUMMARY:** Oculodentodigital dysplasia is an autosomal dominant disorder due to *GJA1* variants characterized by dysmorphic features. Neurologic symptoms have been described in some patients but without a clear neuroimaging pattern. To understand the pathophysiology underlying neurologic deficits in oculodentodigital dysplasia, we studied 8 consecutive patients presenting with hereditary spastic paraplegia due to *GJA1* variants. Clinical disease severity was highly variable. Cerebral MR imaging revealed variable white matter abnormalities, consistent with a hypomyelination pattern, and bilateral hypointense signal of the basal ganglia on T2-weighted images and/or magnetic susceptibility sequences, as seen in neurodegeneration with brain iron accumulation diseases. Patients with the more prominent basal ganglia abnormalities were the most disabled ones. This study suggests that *GJA1*-related hereditary spastic paraplegia is a complex neurodegenerative disease affecting both the myelin and the basal ganglia. *GJA1* variants should be considered in patients with hereditary spastic paraplegia presenting with brain hypomyelination, especially if associated with neurodegeneration and a brain iron accumulation pattern.

**ABBREVIATIONS:** Cx43 = connexin 43; Cx47 = connexin 47; ODDD = oculodentodigital dysplasia

Oculodentodigital dysplasia (ODDD, Online Mendelian Inheritance in Man, No. 164200) is an autosomal dominant disorder due to *GJA1* variants<sup>1</sup> and characterized by dysmorphic features involving the eyes (microphthalmia and microcornea), the nose (narrow, pinched nose with hypoplastic alae nasi), the teeth (small and carious), and limb extremities (syndactyly, camptodactyly). Some patients may present with neurosensory deficits such as spastic paraplegia, ataxia, decreased visual acuity,

and hearing loss, possibly associated with white matter and/or basal ganglia signal abnormalities on brain MR imaging.<sup>2,3</sup> However, there is no comprehensive overview of the neuroimaging features of ODDD besides isolated case reports. Therefore, to improve the accuracy of clinical diagnosis and better understand the pathophysiology underlying neurologic symptoms in ODDD, we wished to define key brain imaging findings in 8 consecutive patients presenting with spastic paraplegia due to *GJA1* variants.

## MATERIALS AND METHODS

We retrospectively studied 8 patients from 5 families presenting with hereditary spastic paraplegia. Patients were referred to reference centers for neurogenetic and neurometabolic diseases. Patients were informed and gave their consent to this study.

*GJA1* variants were suspected on the basis of the co-occurrence of hereditary spastic paraplegia with dysmorphic features in all patients. These dysmorphic features included ocular abnormalities (short palpebral fissures, microphthalmia), nasal abnormalities (long and narrow nose, hypoplastic alae nasi), dental abnormalities (microdontia, abnormal coloration of the enamel, multiple caries), and bone extremity abnormalities (syndactyly of the fourth and fifth fingers, clinodactyly, camptodactyly, and aphyalangia). Clinical examination was performed by experts in rare neurologic diseases (P.C., C.V., M.C., and F.M.). Disease severity was estimated by a disability stage index: 0, no functional handicap; 1, no functional handicap but signs at examination; 2,

Received November 26, 2018; accepted after revision February 27, 2019.

From the Department of Genetics (L.S.-V., T.C., P.C., F.M.), Reference Center for Adult Neurometabolic Diseases (F.M.), and Department of Neurology (M.C.), Assistance Publique-Hôpitaux de Paris, La Pitié-Salpêtrière University Hospital, Paris, France; Department of Neurology and Reference Center for Neurogenetic Diseases (C.V.), Angers University Hospital, Angers, France; Sorbonne Université (M.C.), Centre National de la Recherche Scientifique UMR 7622, Institut National de la Santé et de la Recherche Médicale ERL 1156, Institut de Biologie Paris-Seine, Paris, France; Baylor Scott & White Research Institute (R.S.), Dallas, Texas; Department of Neuropediatrics and Reference Center for Leukodystrophy and Leukoencephalopathy (O.B.-T.), Assistance Publique-Hôpitaux de Paris, Robert-Debré University Hospital, Paris, France; Groupe de Recherche Clinique No. 13, Neurométabolisme (F.M.), Sorbonne Université, Paris, France; and Sorbonne Université (F.M.), Université Pierre-et-Marie-Curie-Paris 6, UMR S 1127 and Institut National de la Santé et de la Recherche Médicale U 1127, and Centre National de la Recherche Scientifique UMR 7225, and Brain and Spine Institute, F-75013, Paris, France.

Please address correspondence to Fanny Mochel, MD, Reference Center for Adult Neurometabolic Diseases, Department of Genetics, La Pitié-Salpêtrière University Hospital, 47 Boulevard de l'Hôpital 75013 Paris, France; e-mail: fanny.mochel@upmc.fr

 Indicates article with supplemental on-line photo.

<http://dx.doi.org/10.3174/ajnr.A6036>

**Table 1: Clinical and molecular characteristics of 8 patients with *GJA1* variants<sup>a</sup>**

	Patient 1#	Patient 2#	Patient 3	Patient 4*	Patient 5*	Patient 6*	Patient 7	Patient 8
Sex/age at examination (yr)	Male/64	Female/34	Female/25	Female/49	Female/22	Female/19	Female/49	Male/56
Family history	Dominant	Dominant	None	Dominant	Dominant	Dominant	None	Dominant
ODDD dysmorphia	Yes	Yes	Yes	Yes	Yes	Yes	Yes	Yes
Age (yr)/symptom at onset	50/Gait	28/Gait	18/Urinary	14/Urinary	14/Urinary	16/Urinary	15/Gait	50/Gait
Current disability stage	1	3	3	3	1	1	6	1
LL reduced strength	None	Prox.	Prox.	Prox.	None	None	Prox./dist.	None
LL spasticity	Yes	Yes	Yes	Yes	No	No	Yes	Yes
UL/LL reflexes	↑/↑	↑/↑	↑/↑	↑/↑	↑/↑	↑/↑	↑/↑	↑/↑
Plantar reflexes	Indifferent	Extensor	Extensor	Extensor	Extensor	Extensor	Extensor	Extensor
UL/LL vibration sense	N/↓	N/↓	N/↓	↓/↓	N/N	N/N	N/↓	N/↓
Romberg sign	No	Yes	Yes	No	No	No	Yes	No
Oculomotor signs	Hypermetric saccades	Saccadic pursuit	None	Saccadic pursuit	Hypermetric saccades	None	None	Saccadic pursuit
Dysmetria/dysarthria	Yes/No	Yes/No	No/No	Yes/No	Yes/No	No/No	No/No	No/No
Urinary symptoms	No	+	+++	+++	++	++	++	No
Cognition	Dysexec.	Normal	Normal	Normal	Normal	Normal	Normal	Normal
<i>GJA1</i> variant	c.93T>G	c.93T>G	c.443G>A	c.428G>A	c.428G>A	c.428G>A	c.412G>A	c.634T>A
Amino acid change	p.I31M	p.I31M	p.R148Q	p.G143D	p.G143D	p.G143D	p.G138S	p.F212I

**Note:**—\* and # indicate patients belonging to the same family; UL, upper limbs; LL, lower limbs; Prox., proximal; dist., distal; ↑, increased; ↓, decreased; Dysexec., dysexecutive syndrome; N, normal; +, mild; ++, moderate; +++, severe.

<sup>a</sup> Disability stage index: 1, no functional handicap but signs at examination; 3, moderate, unable to run, limited walking without aid; 6, unable to walk, requiring wheelchair.

mild, able to run, walking unlimited; 3, moderate, unable to run, limited walking without aid; 4, severe, walking with 1 cane; 5, walking with 2 canes; 6, unable to walk, requiring a wheelchair; 7, confined to bed.

MR imaging was performed with a 1.5T (patients 1, 3, 5, 7, 8) or 3T (patients 2, 4, and 6) magnetic field and included at least 1 axial T1- and T2-weighted sequence and 1 sagittal sequence. CT scans were obtained in all patients except patients 1 and 3. Cerebral MR imaging and CT scans were qualitatively reviewed by 3 leukodystrophy experts (R.S., O.B.-T., and F.M.). Visual, brain stem auditory, and somatosensory and motor-evoked potentials were available for 4 patients.

## RESULTS

Clinical findings are presented in Table 1. Most patients were women (6/8) and had a family history of the disease (5/8). The age at onset was variable, from 14 to 50 years of age, and symptoms at onset were gait difficulties (4/8) and urinary dysfunction (4/8). Disease severity was highly variable with a disability stage index ranging from 1 to 6. All patients presented with spastic paraplegia associated with reduced muscle strength in 4 patients and decreased vibration sense, more pronounced in the lower limbs, in 6 patients. Six patients presented with signs of neurogenic bladder with variable severity: mild (1/8), moderate (3/8), and severe (2/8). One patient required self-catheterization several times a day (patient 3), and 1 had a cystectomy with enterocystoplasty (patient 4). Five patients had mild cerebellar signs.

Cerebral MR imaging revealed white matter abnormalities in all patients, consisting mainly of mild-to-moderate symmetric and diffuse hyperintensities of the corticospinal tracts on T2- and FLAIR-weighted sequences associated with hyper- or isointense T1-weighted signal (Table 2 and Fig 1), consistent with a hypomyelination pattern.<sup>4</sup> Most patients also presented with variable degrees of cerebral and cerebellar atrophy (Table 2 and Fig 1). Furthermore, all patients presented with basal ganglia abnormalities—that is, bilateral T2-hypointense signal of the pallidum and, in some instances, substantia nigra, red nucleus, and dentate nu-

cleus, associated with bilateral hypointense signal of the pallidum on T2\*- or magnetic susceptibility-weighted images (Table 2, Fig 2, and On-line Figure) as seen in neurodegeneration with brain iron accumulation diseases. One patient presented with a central region of hyperintensity within the T2-weighted hypointense signal in the globus pallidus, the so-called eye of the tiger sign (Table 2 and Fig 2). CT showed bilateral or unilateral calcifications of the basal ganglia in 2 of 5 patients (Table 2 and Fig 2). Patients with the more prominent basal ganglia abnormalities were the most disabled ones. When performed, visual, brain stem auditory, and somatosensory and motor-evoked potentials showed diffuse and pronounced central conduction anomalies (4/4), compatible with a hypomyelinating process.

Molecular analyses revealed 4 previously reported *GJA1* variants (c.93T>G, c.412G>A, c.428G>A, and c.443G>A)<sup>5</sup> and one novel heterozygous *GJA1* variant (c.634T>A). Of note, the mother of patient 4 carried the heterozygous c.428 G>A variant but without any ODDD symptoms, including normal bone extremities.

## DISCUSSION

This series of 8 patients with ODDD presenting with hereditary spastic paraplegia shows that the neurologic symptoms associated with *GJA1* variants are related to a complex neurodegenerative process affecting both the white matter and the basal ganglia. Therefore, *GJA1* variants should be considered in all patients with hereditary spastic paraplegia presenting with brain hypomyelination, especially when associated with neurodegeneration with a brain iron accumulation pattern. The early occurrence of urinary symptoms in more than half of the patients suggests an ascending process affecting the corticospinal tracts. Of note, most patients were female, while men presented with a later onset of disease.

Indeed, the *GJA1* gene encodes connexin 43 (Cx43), a transmembrane protein acting in intercellular communication.<sup>1</sup> Cx43 is expressed in astrocytes and plays a role in astrocyte-oligodendrocyte communication by heterotypic Cx43/connexin 47 (Cx47) channels. Some studies have suggested that Cx43/Cx47 channels

**Table 2: Brain imaging characteristics of 8 patients with *GJA1* variants<sup>a</sup>**

	Patient 1	Patient 2	Patient 3	Patient 4	Patient 5	Patient 6	Patient 7	Patient 8
Age (yr)/disability stage	64/1	34/3	25/3	49/3	22/1	19/1	49/6	56/1
WM T1 signal (relative to the cortex gray matter)	Iso	Hyper	Hyper	Iso	Iso	Hyper	Iso	Hyper
WM T2-hyperintense signal								
Periventricular	–	++	+	++	+	+	++	+
Internal capsule (posterior limb)	+	+	+	+	+	+/-	+	+
Corpus callosum	–	–	–	+	–	+	–	–
Cerebellar peduncles	–	+	+	+	+	+	–	+
Ventral pons	–	+	–	+	–	–	–	+
Globus pallidus								
Hypointensity on T2*/-susceptibility-weighted imaging	ND	++	+	++	+/-	+	++	+
Eye of the tiger	–	–	–	+	–	–	–	–
Calcifications	ND	–	ND	+(Unilat.)	–	–	++(Bilat.)	–
Atrophy								
Ventricle/subarachnoid space	+++/>+++	++/>++	+++/>++	-/>-	+/>-	-/>-	+++/>++	+++/>++
Corpus callosum	++	++	+/>-	–	–	+/>-	+++	+
Cerebellar vermis/hemisphere	+/>-	+++/>++	-/>-	+/>-	+/>-	+/>-	+++/>++	+++/>++

**Note:**—Iso indicates isointense; Hyper, hyperintense; ND, not done; Unilat., unilateral; Bilat., bilateral; –, absence of abnormalities; +/-, very mild; +, mild; ++, moderate; +++, severe.

<sup>a</sup>Disability stage index: 1, no functional handicap but signs at examination; 3, moderate, unable to run, limited walking without aid; 6, unable to walk, requiring wheelchair.

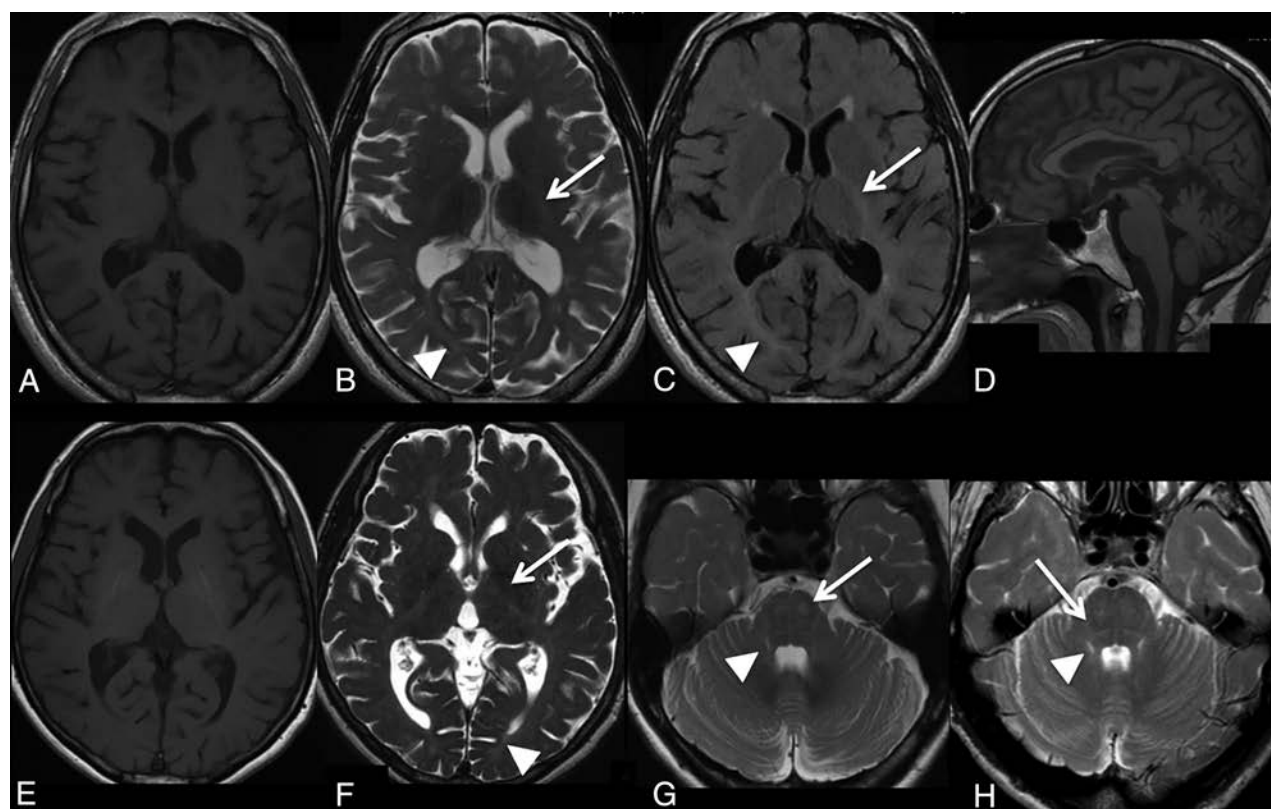


**FIG 1.** Axial scans of patients 8 (A–C) and 7 (E and F) show isointense-to-mild hyperintense T1-weighted signal (A and E) associated with mild-to-moderate hyperintense T2- (B and F) and FLAIR-weighted (C) signal of the white matter, especially the internal capsules (arrows) and optic radiations (arrowheads). Sagittal T1-weighted image of patient 8 (D) shows atrophy of the corpus callosum and the vermis. T2-weighted images of patients 2 (G) and 4 (H) show mild hyperintense signal of the corticospinal tract in the ventral pons (arrows) and cerebellar peduncles (arrowheads).

participate in myelin maintenance.<sup>6,7</sup> Cx47, encoded by *GJA12*, is deficient in Pelizaeus-Merzbacher-like disease,<sup>8</sup> a hypomyelinating disorder characterized by nystagmus, delayed psychomotor development, and cerebellospastic signs. Some data suggest that the total loss of function of Cx47/Cx43 is implicated in the pathophysiology of part of *GJA12* variants.<sup>6,7</sup> Similarities among

neurologic and imaging characteristics between Pelizaeus-Merzbacher-like disease and ODDD could underlie common molecular mechanisms involving the Cx43/Cx47 channels. However, unlike most hypomyelinating disorders such as Pelizaeus-Merzbacher-like disease, the perception of neurologic symptoms by patients with *GJA1* variants usually occurs in adulthood, which

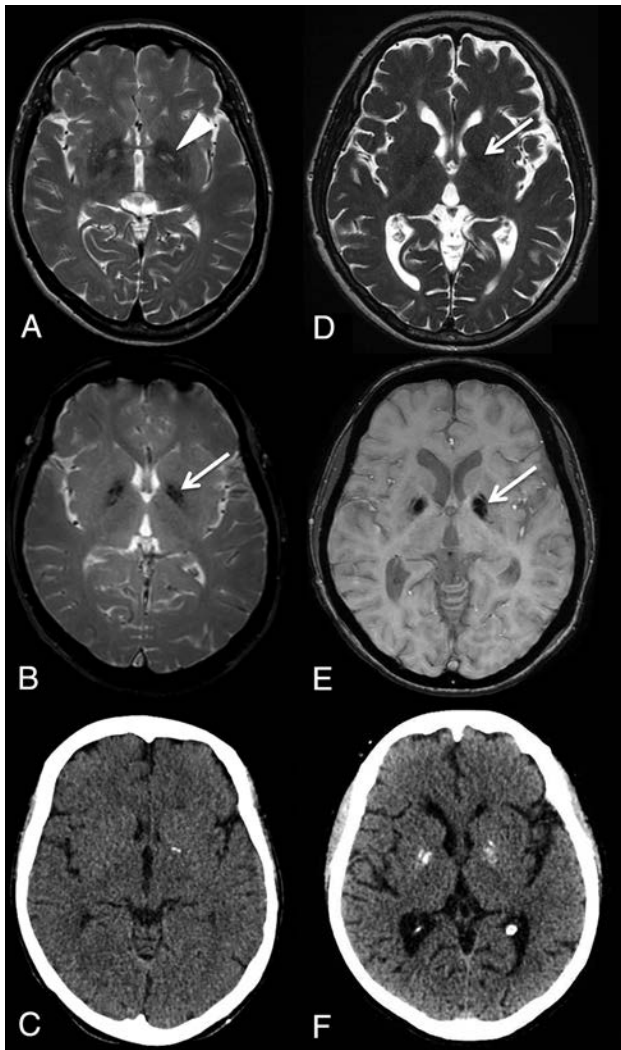


**FIG 2.** Basal ganglia abnormalities of patients 4 (A–C) and 7 (D–F). Axial T2- (A and D) and magnetic susceptibility- (B and E) weighted images show bilateral hypointensities of the pallidum (arrows) and the eye-of-the-tiger sign (arrowhead). Axial CT scans (C and F) show unilateral (C) and bilateral (F) calcifications.

may be related to the haploinsufficiency (instead of a loss of function) of Cx43 in ODDD.

In our series, all patients had abnormal MR imaging signal of the basal ganglia, as seen in neurodegeneration with brain iron accumulation disorders. We also observed calcifications of the basal ganglia as previously reported.<sup>9,10</sup> One patient even had an eye of the tiger sign described as a hallmark of pantothenate kinase-associated neurodegeneration.<sup>11</sup> Basal ganglia involvement is observed in other hypomyelinating leukodystrophies, including patients with *POLR3A/B* and *TUBB4* variants.<sup>12,13</sup> In our series, the extent of basal ganglia abnormalities was associated with the degree of the patient's disability. Given our limited number of patients, this observation requires further validation in a larger group of patients.

Disease severity was extremely variable with symptom onset from adolescence to adulthood and pyramidal symptoms ranging from very mild to very disabling. In addition, the mother of pa-

tient 4 - bearing the *c.428 G>A* variant - had a complete normal phenotype despite the penetrance of ODDD is classically qualified as high.<sup>1</sup> These findings emphasize that intra- and interfamilial expression of the disease is highly variable, without genotype-phenotype correlation. Therefore, it appears difficult to predict the risk of developing neurologic symptoms in patients with *GJA1* variants, a major pitfall for genetic counseling.

#### ACKNOWLEDGMENTS

We thank all our colleagues who provided the radiologic data used in this study. We thank Dr Pascal Hilbert (Institut de Pathologie et Génétique, Gosselies, Belgique) for performing the genetic analyses of patients 1, 2, 4, 5, and 6, as well as Dr Corinne Magdelaine (Centre Hospitalier Universitaire, Limoges, France) for performing the genetic analyses of patients 3 and 7.

Disclosures: Martin Catala—UNRELATED: Expert Testimony: Agence Nationale de Sécurité du Médicament.

#### REFERENCES

- Paznekas WA, Boyadjiev SA, Shapiro RE, et al. **Connexin 43 (GJA1) mutations cause the pleiotropic phenotype of oculodentodigital dysplasia.** *Am J Hum Genet* 2003;72:408–18 CrossRef Medline
- Gutmann DH, Zackai EH, McDonald-McGinn DM, et al. **Oculodentodigital dysplasia syndrome associated with abnormal cerebral white matter.** *Am J Med Genet* 1991;41:18–20 CrossRef Medline
- Loddenkemper T, Grote K, Evers S, et al. **Neurological manifestations of the oculodentodigital dysplasia syndrome.** *J Neurol* 2002; 249:584–95 CrossRef Medline
- Vanderver A, Prust M, Tonduti D, et al; GLIA Consortium. **Case definition and classification of leukodystrophies and leukoencephalopathies.** *Mol Genet Metab* 2015;114:494–500 CrossRef Medline
- Paznekas WA, Karczeski B, Vermeer S, et al. **GJA1 mutations, variants, and connexin 43 dysfunction as it relates to the oculodentodigital dysplasia phenotype.** *Hum Mutat* 2009;30:724–33 CrossRef Medline
- Orthmann-Murphy JL, Salsano E, Abrams CK, et al. **Hereditary spastic paraplegia is a novel phenotype for GJA12/GJC2 mutations.** *Brain* 2009;132(Pt 2):426–38 CrossRef Medline
- May D, Tress O, Seifert G, et al. **Connexin47 protein phosphorylation and stability in oligodendrocytes depend on expression of connexin43 protein in astrocytes.** *J Neurosci* 2013;33:7985–96 CrossRef Medline
- Uhlenberg B, Schuelke M, Rüschemdorf F, et al. **Mutations in the gene encoding gap junction protein alpha 12 (connexin 46.6) cause Pelizaeus-Merzbacher-like disease.** *Am J Hum Genet* 2004;75: 251–60 CrossRef Medline
- Furuta N, Ikeda M, Hirayanagi K, et al. **A novel GJA1 mutation in oculodentodigital dysplasia with progressive spastic paraplegia and sensory deficits.** *Intern Med* 2012;51:93–98 CrossRef Medline
- Tumminelli G, Di Donato I, Guida V, et al. **Oculodentodigital dysplasia with massive brain calcification and a new mutation of GJA1 gene.** *J Alzheimers Dis* 2016;49:27–30 CrossRef Medline
- Hayflick SJ. **Unraveling the Hallervorden-Spatz syndrome: pantothenate kinase-associated neurodegeneration is the name.** *Curr Opin Pediatr* 2003;15:572–77 CrossRef Medline
- La Piana R, Tonduti D, Gordish Dressman H, et al. **Brain magnetic resonance imaging (MRI) pattern recognition in Pol III-related leukodystrophies.** *J Child Neurol* 2014;29:214–20 CrossRef Medline
- Curjel J, Rodríguez Bey G, Takanohashi A, et al. **TUBB4A mutations result in specific neuronal and oligodendrocytic defects that closely match clinically distinct phenotypes.** *Hum Mol Genet* 2017;26: 4506–18 CrossRef Medline

# Susceptibility-Weighted Angiography for the Follow-Up of Brain Arteriovenous Malformations Treated with Stereotactic Radiosurgery

S. Finitis, R. Anxionnat, B. Gory, S. Planel, L. Liao, and S. Bracad

## ABSTRACT

**SUMMARY:** The criterion standard for assessing brain AVM obliteration postradiosurgery is DSA. To explore the value of susceptibility-weighted angiography, we followed 26 patients with brain AVMs treated by radiosurgery using susceptibility-weighted angiography and DSA. Studies were evaluated by 2 independent readers for residual nidi. Susceptibility-weighted angiography demonstrated good intermodality ( $\kappa = 0.71$ ) and interobserver ( $\kappa = 0.64$ ) agreement, and good sensitivity (85.7%) and specificity (85.7%). Susceptibility-weighted angiography is a useful radiation- and contrast material-free technique to follow-up brain AVM obliteration postradiosurgery.

**ABBREVIATIONS:** bAVM = brain AVM; SRS = stereotactic radiosurgery; SWAN = susceptibility-weighted angiography

Brain AVMs (bAVMs) may be treated by either surgical resection, embolization, or radiosurgery. Following treatment, confirmation of complete obliteration is imperative because the risk of bleeding in incompletely obliterated lesions persists.<sup>1-3</sup> After AVM radiosurgery, occlusion is usually achieved after 2-4 years, with regular imaging follow-up performed every 6-12 months until complete bAVM obliteration is documented.<sup>1,2</sup>

The criterion standard for evaluating post-stereotactic radiosurgery (SRS) bAVM obliteration is DSA because of its high spatial and temporal resolution.<sup>4,5</sup> However, DSA is a high-cost, invasive procedure involving radiation and contrast media exposure, with a 1% morbidity.<sup>6-9</sup> Noninvasive alternatives such as 3D-TOF-MRA, 3D contrast-enhanced MRA,<sup>10-12</sup> and, lately, 4D time-resolved MRA<sup>11,13,14</sup> have shown inferior diagnostic accuracy compared to DSA. Moreover, most entail intravenous administration of contrast material with additional cost and potential toxicity.<sup>15,16</sup>

Susceptibility-weighted angiography (SWAN) is a promising new technology that indirectly evaluates the amount of oxygen within blood vessels. As bAVMs shunt oxygenated blood from arteries to veins, bAVM draining veins appear hyperintense,<sup>17</sup> while normal veins containing deoxygenated blood appear hypointense.<sup>18,19</sup> SWAN demonstrates high spatial resolution that allows small normal draining veins with a diameter inferior to the

size of the voxel to be visualized and is highly sensitive to small, low-flow shunts.<sup>19</sup> Moreover, SWAN does not require administration of intravenous contrast material. We aimed to evaluate the performance of SWAN for the follow-up of patients with bAVMs treated with SRS.

## MATERIALS AND METHODS

### Inclusion Criteria

After institutional review board approval, all patients with bAVMs treated with SRS at the University Hospital of Nancy, France were prospectively included in a database. For the present study, patients imaged between March 2012 and May 2018 were included if they met the following criteria: 1) They had a bAVM treated by embolization and radiosurgery or radiosurgery only, 2) they were imaged during follow-up with SWAN at 1.5T or 3T and DSA, 3) both examinations were performed within a time interval of <6 months and without another treatment session in between, and 4) both examinations were performed at least 12 months after SRS.

The treatment strategy for each patient was based on multidisciplinary decisions involving neurosurgeons, radiotherapists, and neuroradiologists. For each patient, demographics, bleeding history, comorbidities, location of the nidus, Spetzler-Martin grade, previous treatment history, clinical symptoms, and radiosurgical parameters were recorded in a prospective database. The time intervals between SRS and SWAN imaging, SWAN imaging and DSA control were also recorded.

### Imaging

After SRS treatment, each patient underwent clinical evaluation and MR imaging at 6-month intervals on either 1.5T or 3T scan-

Received December 17, 2018; accepted after revision March 10, 2019.

From the Department of Neuroradiology (R.A., B.G., S.P., L.L., S.B.), Centre Hospitalier Universitaire de Nancy, Nancy, France; and AHEPA Hospital (S.F.), Aristotle University of Thessaloniki, Thessaloniki, Greece.

Please address correspondence to Stephanos Finitis, MD, AHEPA Hospital, Aristotle University of Thessaloniki, Thessaloniki, Greece; e-mail: stefanosfin@yahoo.com; @StephanosFinitis

<http://dx.doi.org/10.3174/ajnr.A6053>

ners (Signa 1.5T and 3T; GE Healthcare, Milwaukee, Wisconsin). The MR imaging SWAN protocol was fairly consistent: At 1.5T, the SWAN scanning parameters were the following: flip angle, 12°; TE, 80 ms; TR, 78.3 ms; slice thickness, 2.4 mm; FOV, 24 cm. At 3T, the SWAN scanning parameters were the following: flip angle, 15°; TE, 25 ms; number of echoes, 6; TR, minimum; slice thickness, 0.8 mm reconstructed in 2-mm MIP; FOV, 24 cm. DSA was performed on a biplane angiography unit (Innova; GE Healthcare) with selective contrast injections of intracranial vessels in standard projections.

### Image Analysis

Two independent senior readers (S.B. and R.A.), with >20 years of experience in diagnostic and interventional neuroradiology each, reviewed the axial SWAN examinations randomly and confirmed the presence or absence of a remaining arteriovenous shunt, that is, the presence of hypersignal within the nidus or a draining vein. Readers were blinded to baseline and follow-up clinical data, DSA imaging, bAVM location, and treatments received. In case of disagreement, consensus was reached by a third senior neuroradiologist (S.F.). Results were recorded separately and used to determine interobserver and intermodality agreement.

DSA studies were reviewed in consensus by 2 other senior readers. Total obliteration of the bAVM was defined as the complete absence of the nidus, normalization of the afferent and efferent vessels, and a normal circulation time. Any remaining nidus, regardless of its size, was considered “patent,” including the existence of early-filling draining veins.

### Statistical Analysis

Quantitative variables were described as median and interquartile ranges, whereas qualitative variables were described as numbers and percentages. Intermodality and interobserver agreement was calculated using the  $\kappa$  statistic. All analyses were completed using commercial statistical software (SPSS, Version 23.0; IBM, Armonk, New York).

## RESULTS

Twenty-six patients fulfilled the inclusion criteria (Fig 1). Patient demographics are shown in Table 1. Two patients underwent 2 sets of imaging at different time points that were included in the analysis. Before SRS, 23 patients were embolized with a mixture of *n*-BCA and glue; and 1, with Onyx (Covidien, Irvine, California).

### Interobserver Agreement

For SWAN examinations, the 2 observers agreed on the existence of a residual nidus in 23 of 28 cases (82.1%), resulting in good interobserver agreement ( $\kappa = 0.64$ ; 95% CI, 0.36–0.92) (Figs 2 and 3). Table 2 shows the interpretations according to the 2 readers and the consensus reading. Two disagreements corresponded to nidus remnants of millimetric size. Three more disagreements corresponded to occluded nidi that contained faint hyperintense spots.

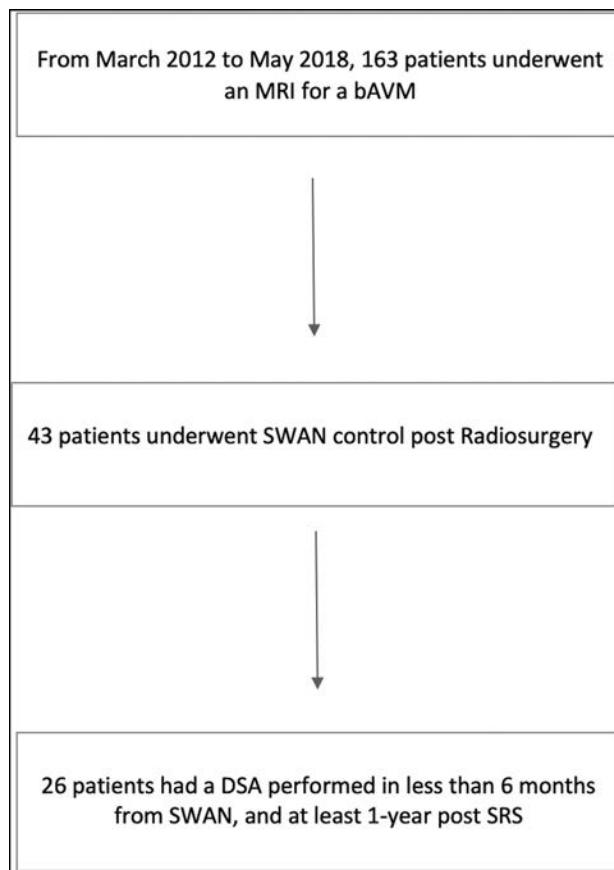


FIG 1. Patient flow chart.

Table 1: Characteristics of the 26 patients<sup>a</sup>

Characteristics	
Age (yr)	33 (22–42)
Sex, male	17 (65.4%)
bAVM location	
Supratentorial	24 (92.3%)
Infratentorial	2 (7.7%)
Spetzler-Martin grade	1 (I–II)
Presentation	
Hemorrhage	20 (76.9%)
Seizure	4 (15.4%)
Headache	5 (19.2%)
Neurologic symptoms	1 (3.8%)
Type of treatment	
Embolization then radiosurgery	22 (84.6%)
Radiosurgery	2 (7.7%)
Surgery then embolization then radiosurgery	2 (7.7%)
Time intervals	
Delay between last treatment and SWAN (mo) <sup>b</sup>	34 (27.7–46.8)
Delay between SWAN and DSA (days) <sup>b</sup>	3 (3–65)

<sup>a</sup> Continuous variables are presented as proportion and percentage; categorical variables are described as median and first and third quartiles.

<sup>b</sup> Calculated for 28 datasets because 2 patients had 2 separate SWAN/DSA follow-ups.

### Intermodality Agreement

The consensus reading for SWAN showed agreement regarding residual nidi in 24/28 (85.7%) cases, resulting in good intermodality agreement ( $\kappa = 0.71$ ; 95% CI, 0.455–0.974). Two unseen nidi (false-negative cases) were very small (Fig 4). One false-positive case was due to a large intranidal calcification that was obvious on plain CT (Fig 5). Another false-positive case was a corpus

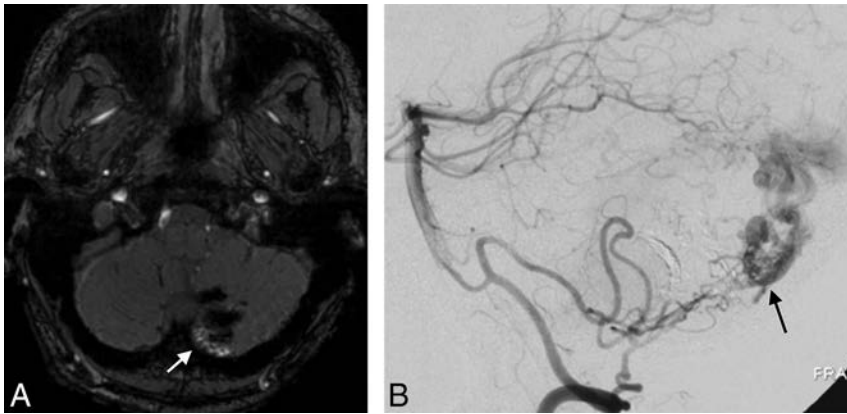


**FIG 2.** A 42-year-old man with a left cerebellar AVM, partially embolized with glue. A, SWAN imaging 3 years after SRS shows hyperintense vessels (white arrow) in the posterior part of the nidus that correspond to a nidus remnant confirmed by DSA (black arrow, B).

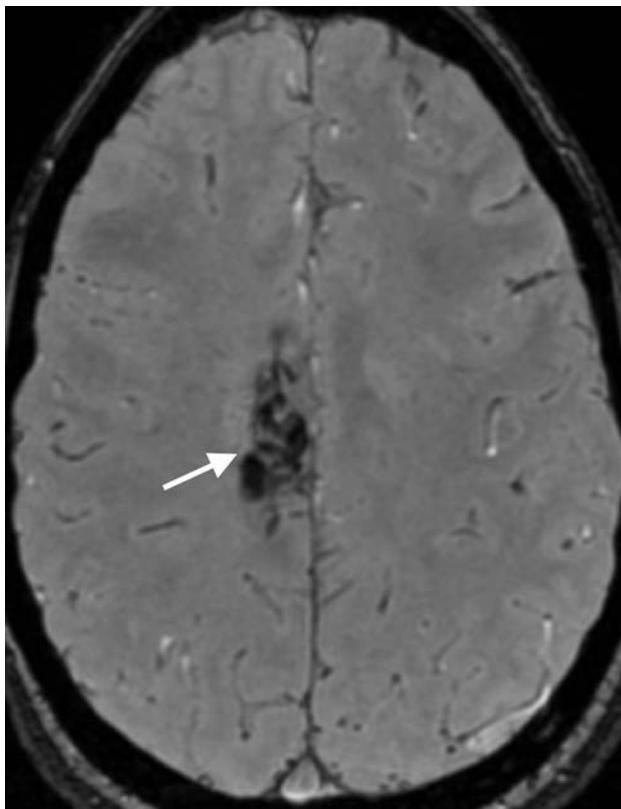


**FIG 3.** A 19-year-old woman with a right posterior frontal AVM with hemorrhagic presentation, partially embolized with glue. SWAN imaging 2.5 years after SRS shows the complete occlusion of the nidus (white arrow) confirmed by DSA (not shown).

callosum AVM with multiple adjacent arteries that gave the impression of hyperintense draining veins (Fig 6). Univariate statistics failed to show any association between false diagnostic results and Spetzler-Martin grade ( $P = .6$ ), AVM location ( $P = .6$ ), previous hemorrhage ( $P = 1$ ), and previous embolization ( $P = .27$ ).

#### Diagnostic Value of SWAN

The diagnostic accuracy of SWAN for a residual nidus reached a sensitivity of 85.7%, a specificity of 85.7%, a positive predictive value of 85.7%, and a negative predictive value of 85.7%.

#### DISCUSSION

The role of SWAN in the post-SRS follow-up of bAVMs has not been studied, to our knowledge. Our results show that SWAN has good intermodality ( $\kappa = 0.71$ ; 95% CI, 0.45–0.97) and interobserver ( $\kappa = 0.64$ ; 95% CI, 0.37–0.92) agreement compared with DSA, with a sensitivity of 85.7%, specificity of 85.7%, positive predictive value of 85.7%, and negative predictive value of 85.7%.

Although SWAN has good diagnostic accuracy, given its actual limitations, a negative SWAN finding cannot assert with certainty whether a bAVM is completely obliterated. However, it may guide imaging follow-up of patients

with bAVMs treated with SRS without the need for intravenous injection of gadolinium and may potentially help avoid some unnecessary DSA examinations. After bAVM SRS, SWAN may be performed annually until the findings become negative (ie, until there is no residual shunt visible) and the final result can be confirmed by DSA.

Using SWAN, we found spots of increased signal intensity for residual arteriovenous shunts and patent draining veins in 12 of 14 (85.7%) residual nidi diagnosed by DSA (Fig 2). This hyperintense pattern has been noted in previous SWAN studies of non-treated bAVMs. At high blood velocities, the hypersignal within the nidus and the venous drainage are partially related to an inherent TOF effect of SWAN at 1.5T and 3T.<sup>19,20</sup> At lower blood velocities, higher blood-oxygen levels and a lack of paramagnetic phase shift linked to direct arterial-to-venous shunt inside the nidus appears to be mainly responsible for the hyperintensity.<sup>19</sup>

False-negative diagnoses of a residual nidus on SWAN occurred in 2 cases of residual nidi of millimetric size (Fig 4). False-positive diagnoses of a nidus remnant occurred in 2 patients. In one, a hyperintense signal in a fully occluded nidus was produced by susceptibility artifacts from a large calcified area visible on plain CT (Fig 5). In the other patient, multiple hyperintense normal vessels near the occluded bAVM that proved to be normal arteries gave the false impression of hyperintense small draining veins (Fig 6). This pitfall may be avoided by the use of multiplanar reformations to distinguish draining veins and arteries.<sup>19</sup>

In the present study, 20 of 26 (76.9%) bAVMs had previously bled and contained hemosiderin. However, this was not found to be detrimental to the diagnosis of a residual bAVM nidus ( $P = 1$ ). *n*-BCA glue was used as an embolic agent in 23 of 26 bAVMs before SRS. When injected, *n*-BCA glue is mixed with Lipiodol (Guerbet, Roissy, France), an oil-based contrast agent that could exhibit high signal on T1- and T2-weighted images. However, in the present series, previous embolization was not related to the false diagnosis of a nidus remnant ( $P = .27$ ). One patient had been embolized with Onyx, but the remaining bAVM nidus was correctly diagnosed as patent. Previous embolizations could obscure the margin of the nidus or result in a fragmented nidus and thereby mislead to a false negative diagnosis. Although, in the present series, glue did not interfere with the diagnostic accuracy

**Table 2: Detection of nidus remnant on SWAN compared with DSA<sup>a</sup>**

DSA	SWAN Reader 1		SWAN Reader 2		Consensus Reading	
	Patent	Obliterated	Patent	Obliterated	Patent	Obliterated
Patent (n = 14)	11	3	11	2	12	2
Obliterated (n = 14)	5	9	3	12	2	12
Sensitivity (%)		68.7		78.6		85.7
Specificity (%)		75		85.7		85.7
PPV (%)		78.6		84.6		85.7
NPV (%)		64.3		80		85.7

**Note:**—PPV indicates positive predictive value; NPV, negative predictive value.

<sup>a</sup> Prevalence of nidus remnant after SRS for bAVM.

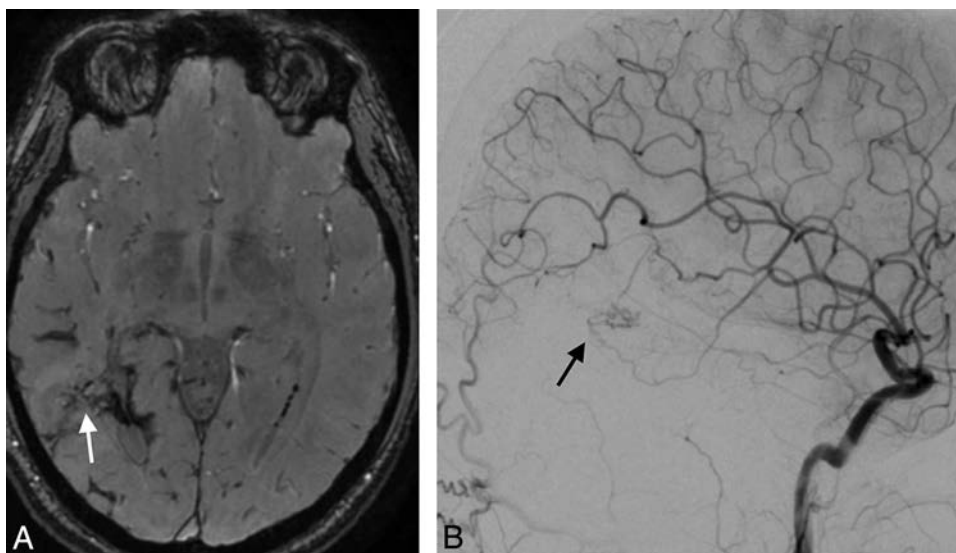


**FIG 4.** A 32-year-old man with a right parietal AVM with hemorrhagic presentation, partially embolized with glue. SWAN imaging 3.5 years after SRS (*white arrow, A*) fails to show a very small residual nidus that was depicted by DSA (*black arrow, B*).

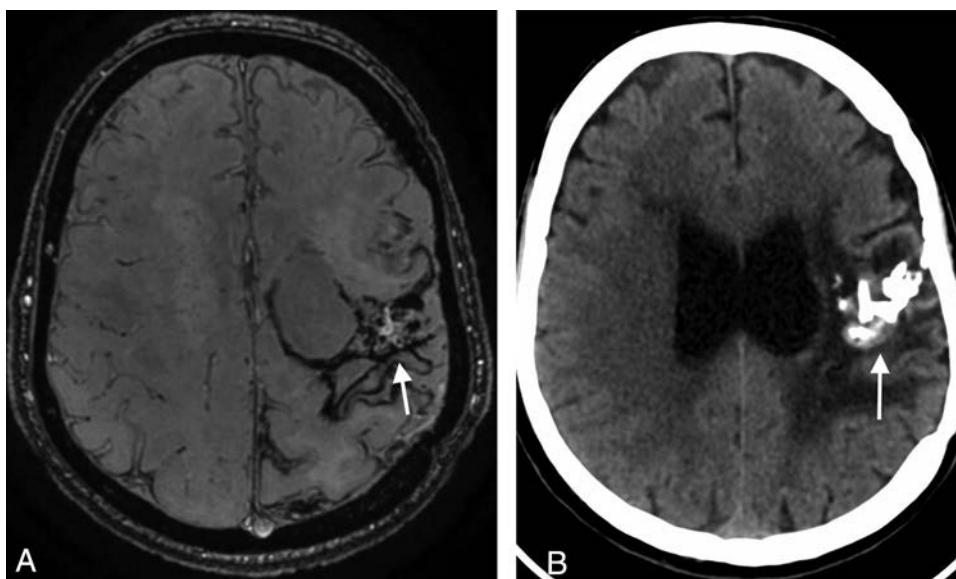


**FIG 5.** A 60-year-old man with a left parietal AVM with hemorrhagic presentation that was partially embolized with glue. A, SWAN imaging 4 years after SRS shows an amorphous area of hyperintensity within the nidus (*white arrow*) that was diagnosed as a nidus remnant, but the DSA findings were negative. B, CT shows extensive calcification (*white arrow*) inside the AVM scar.

of SWAN, the potential for diagnostic pitfalls related to the use of ethylene copolymer-based embolic agents should be investigated in larger series.

Lee et al<sup>21</sup> assessed the diagnostic accuracy of 3D-TOF and T1

postcontrast MR imaging for the diagnosis of residual post-SRS treated bAVMs and found sensitivities ranging from 76.7% to 84.9% and specificities from 88.9% to 95%. Other authors have studied the accuracy of time-resolved MRA and have found sen-

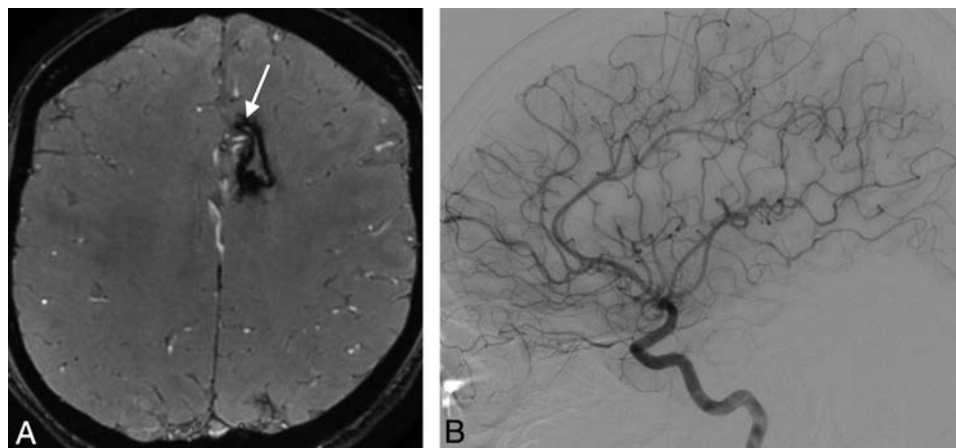


**FIG 6.** A 19-year-old man with a left frontal AVM with hemorrhagic presentation that was partially embolized with glue. **A**, SWAN imaging 5 years after SRS shows hyperintense vessels (white arrow) near the AVM that were mistakenly diagnosed as a nidus remnant. **B**, Digital subtraction angiography findings were negative.

sitivities, specificities, positive and negative predictive values ranging from 64.3% to 79.6%, 90.6% to 100%, 84.6% to 100%, and 78.3% to 90% respectively.<sup>11,21</sup> The clear advantage of SWAN compared to these techniques is the absence of contrast material administration, which represents added cost and entails potential toxicity.<sup>15,16</sup> Compared to 3D-TOF techniques or the detection of T2-weighted flow voids, SWAN has the potential to be more sensitive to small, slow-flow shunts.<sup>19</sup> Nevertheless, a head-to-head comparison with these techniques is warranted.

SWAN is a susceptibility weighted imaging technique available exclusively on GE scanners. Therefore, caution should be used when extrapolating the present findings to susceptibility weighted imaging sequences of other MR imaging machine vendors, where venous drainage may appear hypointense<sup>22-24</sup> or hyperintense.<sup>17,25</sup>

During the study period, a substantial number of patients did not undergo SWAN. This may have introduced bias in our study. Also, studies were performed on MR imaging machines with 2 different field strengths (1.5T and 3T). However, follow-up protocols were consistent. Moreover, readers were not allowed to use MIP or reformatted images, or consult baseline SWAN or DSA studies which, if available, may have improved diagnostic accuracy.

## CONCLUSIONS

SWAN is a useful radiation- and contrast material-free technique for the follow-up of patients with brain AVMs treated by SRS. It has the potential to reduce the number of DSA controls after SRS. However, given the actual limitations of SWAN, DSA remains mandatory for the final assessment of brain AVM cure.

## REFERENCES

1. Pierot L, Cognard C, Spelle L. **Cerebral arteriovenous malformations: evaluation of the hemorrhagic risk and its morbidity [in French].** *J Neuroradiol* 2004;31:369–75 CrossRef Medline
2. Novakovic RL, Lazzaro MA, Castonguay AC, et al. **The diagnosis and management of brain arteriovenous malformations.** *Neurol Clin* 2013;31:749–63 CrossRef Medline
3. Maruyama K, Kawahara N, Shin M, et al. **The risk of hemorrhage**

**after radiosurgery for cerebral arteriovenous malformations.** *N Engl J Med* 2005;352:146–53 CrossRef Medline

4. Oppenheim C, Meder JF, Trystram D, et al. **Radiosurgery of cerebral arteriovenous malformations: is an early angiogram needed?** *AJNR Am J Neuroradiol* 1999;20:475–81 Medline
5. Steiner L, Lindquist C, Adler JR, et al. **Clinical outcome of radiosurgery for cerebral arteriovenous malformations.** *J Neurosurg* 1992; 77:1–8 CrossRef Medline
6. Dawkins AA, Evans AL, Wattam J, et al. **Complications of cerebral angiography: a prospective analysis of 2,924 consecutive procedures.** *Neuroradiology* 2007;49:753–59 CrossRef Medline
7. Heiserman JE, Dean BL, Hodak JA, et al. **Neurologic complications of cerebral angiography.** *AJNR Am J Neuroradiol* 1994;15:1401–07; discussion 1408–11 Medline
8. Earnest F 4th, Forbes G, Sandok BA, et al. **Complications of cerebral angiography: prospective assessment of risk.** *AJR Am J Roentgenol* 1984;142:247–53 Medline
9. Bendszus M, Koltzenburg M, Burger R, et al. **Silent embolism in diagnostic cerebral angiography and neurointerventional procedures: a prospective study.** *Lancet* 1999;354:1594–97 CrossRef Medline
10. Heidenreich JO, Schilling AM, Unterharnscheidt F, et al. **Assessment of 3D-TOF-MRA at 3.0 Tesla in the characterization of the angioarchitecture of cerebral arteriovenous malformations: a preliminary study.** *Acta Radiol* 2007;48:678–86 CrossRef Medline
11. Lim HK, Choi CG, Kim SM, et al. **Detection of residual brain arteriovenous malformations after radiosurgery: diagnostic accuracy of contrast-enhanced four-dimensional MR angiography at 3.0 T.** *Br J Radiol* 2012;85:1064–69 CrossRef Medline
12. Unlu E, Temizoz O, Albayram S, et al. **Contrast-enhanced MR 3D angiography in the assessment of brain AVMs.** *Eur J Radiol* 2006;60: 367–78 CrossRef Medline
13. Soize S, Bouquigny F, Kadziolka K, et al. **Value of 4D MR angiography at 3T compared with DSA for the follow-up of treated brain arteriovenous malformation.** *AJNR Am J Neuroradiol* 2014;35: 1903–09 CrossRef Medline
14. Hadizadeh DR, Kukuk GM, Steck DT, et al. **Noninvasive evaluation of cerebral arteriovenous malformations by 4D-MRA for preoperative planning and postoperative follow-up in 56 patients: comparison with DSA and intraoperative findings.** *AJNR Am J Neuroradiol* 2012;33:1095–101 CrossRef Medline
15. Kanda T, Ishii K, Kawaguchi H, et al. **High signal intensity in the dentate nucleus and globus pallidus on unenhanced T1-weighted MR images: relationship with increasing cumulative dose of a gadolinium-based contrast material.** *Radiology* 2014; 270:834–41 CrossRef Medline

16. Mawad H, Laurin LP, Naud JF, et al. **Changes in urinary and serum levels of novel biomarkers after administration of gadolinium-based contrast agents.** *Biomark Insights* 2016;11:91–94 CrossRef Medline
17. Jagadeesan BD, Delgado Almandoz JE, Moran CJ, et al. **Accuracy of susceptibility-weighted imaging for the detection of arteriovenous shunting in vascular malformations of the brain.** *Stroke* 2011;42:87–92 CrossRef Medline
18. Hodel J, Rodallec M, Gerber S, et al. **Susceptibility weighted magnetic resonance sequences “SWAN, SWI and VenoBOLD”: technical aspects and clinical applications [in French].** *J Neuroradiol* 2012;39:71–86 CrossRef Medline
19. Hodel J, Blanc R, Rodallec M, et al. **Susceptibility-weighted angiography for the detection of high-flow intracranial vascular lesions: preliminary study.** *Eur Radiol* 2013;23:1122–30 CrossRef Medline
20. Schmitz BL, Aschoff AJ, Hoffmann MHK, et al. **Advantages and pitfalls in 3T MR brain imaging: a pictorial review.** *AJNR Am J Neuroradiol* 2005;26:2229–37 Medline
21. Lee KE, Choi CG, Choi JW, et al. **Detection of residual brain arteriovenous malformations after radiosurgery: diagnostic accuracy of contrast-enhanced three-dimensional time of flight MR angiography at 3.0 Tesla.** *Korean J Radiol* 2009;10:333–39 CrossRef Medline
22. Saini J, Thomas B, Bodhey NK, et al. **Susceptibility-weighted imaging in cranial dural arteriovenous fistulas.** *AJNR Am J Neuroradiol* 2009;30:E6 CrossRef Medline
23. Noguchi K, Kuwayama N, Kubo M, et al. **Intracranial dural arteriovenous fistula with retrograde cortical venous drainage: use of susceptibility-weighted imaging in combination with dynamic susceptibility contrast imaging.** *AJNR Am J Neuroradiol* 2010;31:1903–10 CrossRef Medline
24. Gasparetto EL, Pires CE, Domingues RC. **Susceptibility-weighted MR phase imaging can demonstrate retrograde leptomeningeal venous drainage in patients with dural arteriovenous fistula.** *AJNR Am J Neuroradiol* 2011;32:E54 CrossRef Medline
25. Letourneau-Guillon L, Krings T. **Simultaneous arteriovenous shunting and venous congestion identification in dural arteriovenous fistulas using susceptibility-weighted imaging: initial experience.** *AJNR Am J Neuroradiol* 2012;33:301–07 CrossRef Medline

# Image Processing to Improve Detection of Mesial Temporal Sclerosis in Adults

F. Dahi, M.S. Parsons, H.L.P. Orlowski, A. Salter, S. Dahiya, and A. Sharma

## ABSTRACT

**SUMMARY:** In this retrospective case-control study, we investigated whether an image-processing algorithm designed to exaggerate the intensity of diseased hippocampi on FLAIR images can improve the diagnostic accuracy and interobserver reliability of radiologists in detecting mesial temporal sclerosis–related hippocampal signal alteration. Herein, we share the results of this study that showed that the image processing improved the confidence of radiologists in detecting mesial temporal sclerosis–related signal alteration, allowing an improved sensitivity, specificity, and interobserver reliability.

**ABBREVIATIONS:** MTS = mesial temporal sclerosis; SI = signal intensity

**A** confident identification of mesial temporal sclerosis (MTS) based on hippocampal volume loss, signal abnormality, and architectural distortion on MR imaging is important for timely surgical management of refractory epilepsy.<sup>1–4</sup> Because signal abnormalities may precede volume loss in MTS, improved detection of hippocampal signal abnormalities may help in its early diagnosis and treatment.<sup>5</sup> Recently, an image-processing algorithm using correlative properties of neighboring pixels has shown promise in selectively enhancing the visual conspicuity of diseased hippocampi.<sup>6,7</sup> Here we share the results of a retrospective case-control study testing whether this image processing could translate into an improved diagnostic performance of radiologists in detecting MTS in adults.

## MATERIALS AND METHODS

### Image Processing and Review

A blinded coinvestigator processed coronal FLAIR images from 51 subjects with MTS and 51 healthy controls (Table 1) with a proprietary image-processing algorithm (Correlative Image Enhancement) using a custom plug-in for OsiriX Lite ([https://www.downloadthat.com/windows/search/osirix\\_lite\\_for\\_windows](https://www.downloadthat.com/windows/search/osirix_lite_for_windows)).

Received October 26, 2018; accepted after revision January 18, 2019.

From the Progressive Physicians Association (F.D.), Bethlehem, Pennsylvania; and Mallinckrodt Institute of Radiology (M.S.P., H.L.P.O., A.Sharma), Department of Biostatistics (A.Salter), and Department of Pathology and Immunology (S.D.), Washington University School of Medicine, Washington University in St Louis, St Louis, Missouri.

Please address correspondence to Matthew Parsons, MD, Mallinckrodt Institute of Radiology, Washington University School of Medicine, Campus Box 8131, 510 S Kingshighway Blvd, St. Louis, MO 63110; e-mail: parsonsms@wustl.edu; @MattParsonsMD

<http://dx.doi.org/10.3174/ajnr.A6022>

The algorithm exaggerated the hippocampal signal intensity (SI) if it was considerably higher than that of the normal gray matter as defined by an ROI drawn over the normal-appearing insular cortex. Processed images were saved as a separate DICOM series. Six readers with varied experience levels reviewed baseline and processed images separately, rating the SI of each hippocampus on a 5-point scale: 1, definitely normal; 2, probably normal; 3, possibly normal; 4, probably abnormal; and 5, definitely abnormal. They also indicated whether the hippocampal SI was unusually high, suggesting the effect of processing.

### Data Analysis

Differences among the median SI ratings across all readers for baseline and processed images were computed and compared using a paired *t* test or signed rank test. If one considered the SI ratings of 1–3 as normal and 4–5 as abnormal, the effects of processing on the sensitivity, specificity, positive predictive value, negative predictive value, and accuracy of each reader and for all readers were assessed. Sensitivity was additionally assessed for a subgroup of patients in whom the MR imaging findings were originally reported as normal. The effect of processing on the interobserver reliability of identifying hippocampal signal abnormality (SI ratings) was computed using a model-based measure of agreement, which is robust to the underlying disease prevalence.<sup>8</sup>

## RESULTS

All readers reported confluent areas of markedly increased signal (Fig 1) in processed images of 37 (72.5%) diseased hippocampi. Individual readers reported processing-related foci of markedly

**Table 1: Details of cases and controls**

	Subjects	Controls
Mean age (range) (yr)	34.6 (18–58)	42.8 (21–79)
Men	24	13
Women	27	38
Selection source	Pathology database	RIS search and review
Inclusion criteria	Age older than 18 yr Pathologically proven MTS	Age older than 18 yr Brain and orbital MRI Coronal FLAIR images extending across hippocampi
Exclusion criteria	Preoperative coronal FLAIR through hippocampi not available	Seizures Known or imaging suspicion of neurologic disease known to affect hippocampus Reported hippocampal abnormalities
Indication for MRI	Refractory epilepsy	Diplopia, cranial neuropathy, visual dysfunction, optic neuropathy, papilledema, retrobulbar pain, ptosis, ocular findings
MR imaging magnet strength (No.)	3T (36) 1.5T (15)	3T (6) 1.5T (45)
Coronal 2D FLAIR parameters		
Thickness (mm)	3	3
FOV (mm)	180 × 180	166 × 190
TR (ms)	9000–11,000	9000–10,000
TE (ms)	80–110	80–110
TI (ms)	2500	2500
Matrix	256 × 256	256 × 224

**Note:**—RIS indicates radiology information system.

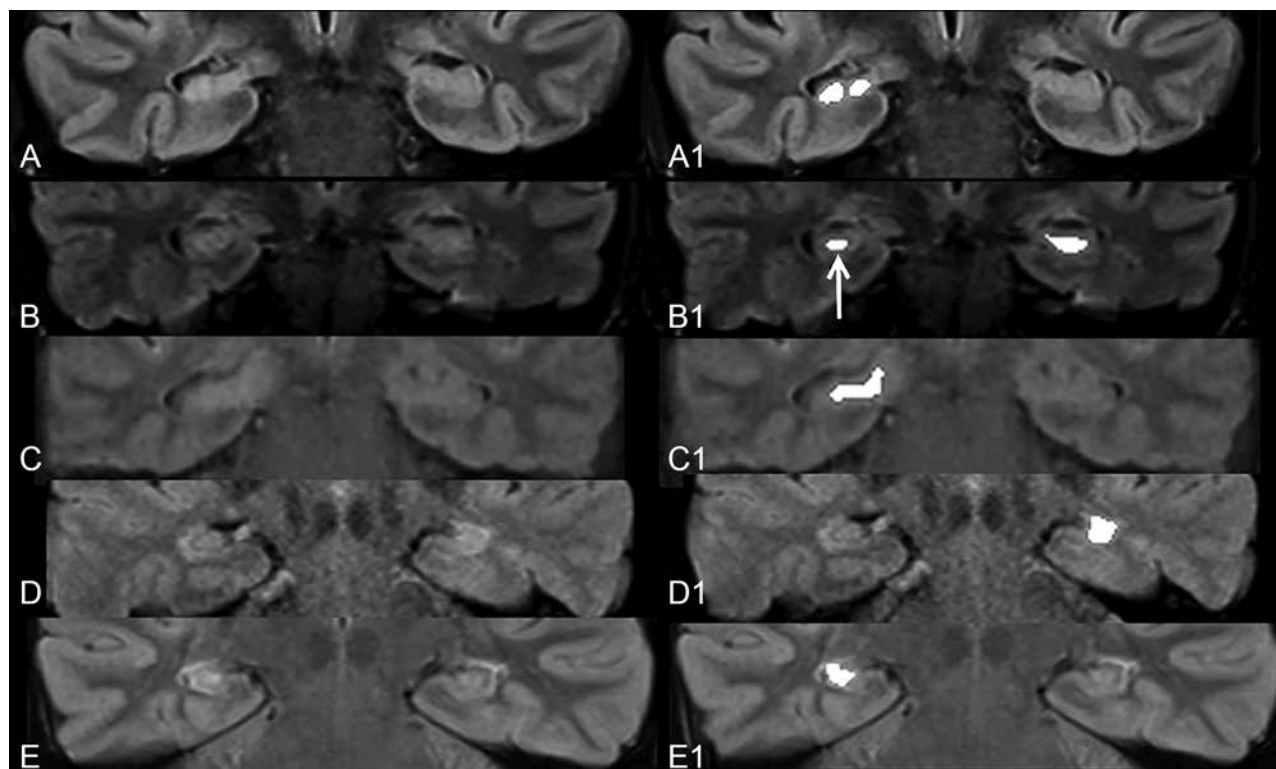


**FIG 1.** Coronal FLAIR images (A–E) across the medial temporal lobes in patients with pathologically confirmed right-sided (A, C, and E) and left-sided (B and D) MTS. Corresponding images following image processing (A1–E1) demonstrate confluent areas of marked exaggeration of signal intensity of the diseased hippocampi. Note a similar exaggeration of signal intensity to a smaller extent in the right hippocampus (arrow) in B1, presumably indicating bilateral disease.

increased SI in 2%–4.9% (average, 3.6%) of control hippocampi (Fig 2).

#### **Effect on Confidence Ratings**

Image processing resulted in an increase in median SI rating for diseased hippocampi ( $P < .001$ , Table 2) and a decrease in the

median SI rating for both left- ( $P = .03$ ) and right-sided ( $P = .003$ ) hippocampi in controls.

#### **Effect on Readers' Diagnostic Performance**

An improvement in the average sensitivity, specificity, positive predictive value, negative predictive value, and accuracy was seen

after processing (Table 3). The average sensitivity increased by >10% (Table 3), and readers were able to detect hippocampal signal abnormality in 4/10 (40%) cases reported as having normal findings on the original clinical reports.

### Effect on Interobserver Reliability

Processing resulted in an improvement in the interobserver agreement in SI ratings for cases of MTS from moderate (Fleiss  $\kappa = 0.4$ ; 95% CI, 0.2–0.56) to almost perfect (Fleiss  $\kappa = 0.88$ ; 95% CI, 0.80–0.97).<sup>9</sup> For control hippocampi, interobserver agreement improved from slight to moderate.<sup>9</sup>

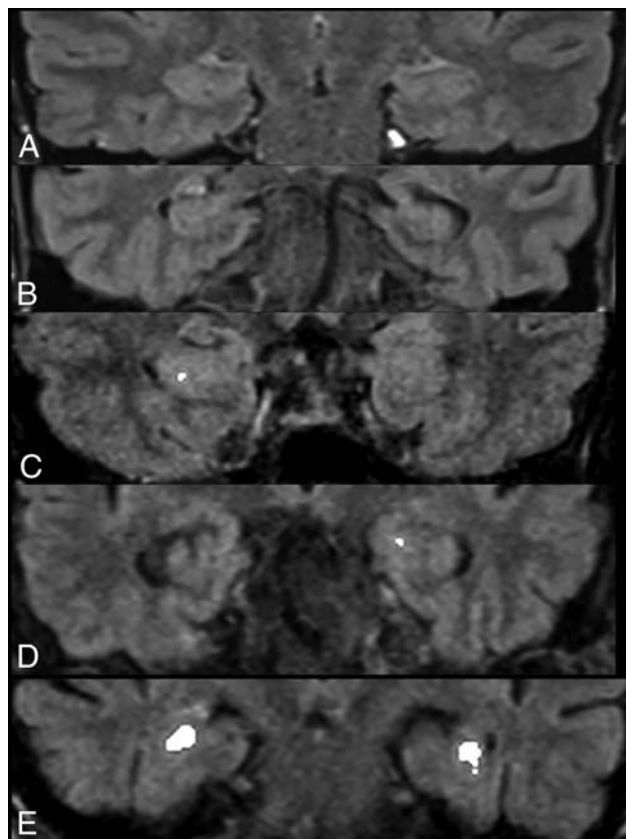


**FIG 2.** Representative postprocessed coronal FLAIR images across the medial temporal lobes of 5 controls without seizures. Processing did not result in any alteration of hippocampal signal (A and B) for most control hippocampi. While punctate (C and D) foci of signal exaggeration were noted in some control hippocampi, false-positive confluent regions of increased intensity mimicking MTS (E) were observed in the bilateral hippocampi of 1 (2%) control.

**Table 2: Effect of image processing on signal intensity ratings for subjects with MTS, right-sided control hippocampi, and left-sided control hippocampi on a 5-point scale<sup>a</sup>**

	Median	Minimum	25th Percentile	75th Percentile	Maximum	P
Subjects	4.00	1.00	1.00	2.00	4.00	<.001
Subjects (processed)	5.00	1.00	1.00	2.00	5.00	
Controls (R)	1.00	1.00	1.00	1.50	3.50	<.01
Controls (R, processed)	1.00	1.00	1.00	1.00	5.00	
Controls (L)	1.00	1.00	1.00	1.50	2.00	.03
Controls (L, processed)	1.00	1.00	1.00	1.00	5.00	

**Note:**—R indicates right; L, left.

<sup>a</sup>1, Definitely normal; 2, probably normal; 3, possibly normal; 4, probably abnormal; 5, definitely abnormal.

## DISCUSSION

In our study, an easily recognizable increase in the contrast-to-noise ratio of diseased hippocampi by the image processing<sup>6,7</sup> translated into substantial improvement in sensitivity when present and slight improvement in specificity when absent. Our results indicate that this processing may help detect MTS in some patients with focal epilepsy with otherwise normal MR imaging findings,<sup>10</sup> thereby allowing earlier diagnosis and treatment. An improvement in interobserver agreement may make this processing particularly helpful for nonexpert readers, prompting a timely referral to experts.

Unlike volumetry-based techniques,<sup>11,12</sup> the image processing used in our study relies on highlighting MTS-related signal abnormality. Thus, it is similar to other techniques such as T2 relaxometry and automated FLAIR analysis but may be more generalizable because it does not require comparison with normative data.<sup>13–16</sup>

## CONCLUSIONS

The image-processing algorithm tested by us can improve detection of MTS on MR imaging. In view of a small possibility of false-positive effects of processing, this technique should serve as a complement to a complete epilepsy protocol MR imaging, interpreted in the context of clinical history.

Disclosures: Amber Salter—UNRELATED: Consultancy: Circulation Cardiovascular Imaging. Aseem Sharma—RELATED: Other: Correlative Enhancement LLC, Comments: I hold the intellectual property rights to the image-processing algorithms

**Table 3: Diagnostic performance of 6 blinded readers in detection of MTS-related hippocampal signal alteration before and after image processing with a proprietary algorithm**

Reader	Sensitivity	Specificity	PPV	NPV	Accuracy
Before processing					
R1	72.55	98.04	97.37	78.13	0.85
R2	60.78	98.04	96.88	71.43	0.79
R3	43.14	100.00	100.00	63.75	0.72
R4	58.82	92.16	88.24	69.12	0.75
R5	86.27	80.39	81.48	85.42	0.83
R6	66.67	100.00	100.00	75.00	0.83
Mean (SD)	64.71 (14.46)	94.77 (7.61)	93.99 (7.50)	73.81 (7.53)	0.80 (0.05)
After Processing					
R1	74.51	96.08	95.00	79.03	0.85
R2	78.43	98.04	97.56	81.97	0.88
R3	72.55	98.04	97.37	78.13	0.85
R4	78.43	92.16	90.91	81.03	0.85
R5	72.55	98.04	97.37	78.13	0.85
R6	74.51	98.04	97.44	79.37	0.86
Mean (SD)	75.16 (2.68)	96.73 (2.37)	95.94 (2.65)	79.61 (1.57)	0.86 (0.01)

**Note:**—R1 and R2 indicate radiology residents; R3 and R4, neuroradiology fellows; R5 and R6, attending neuroradiologists; PPV, positive predictive value; NPV, negative predictive value.

used in this study. I have founded a company (Correlative Enhancement LLC) with the aim of future commercialization of this intellectual property. I am the sole proprietor of the company, and since the inception of the company until now (including the time during which I processed the images for this study), this company has not received funding from any external source. While I used the algorithms to process the images for this study, I did not participate in patient selection, image review, image analysis, or the subsequent statistical analysis; *UNRELATED: Consultancy*: Biomedical Systems, *Comments*: As a consultant, I serve as an independent reviewer for imaging studies performed for research by third parties; *Patents (Planned, Pending or Issued)*: I have been issued the patent for the method of image processing used in this and other studies; *Stock/Stock Options*: GE Healthcare, *Comments*: I hold approximately \$10,000 worth of publicly traded GE stocks. Sonika Dahiya—*UNRELATED: Employment*: Washington University School of Medicine.

## REFERENCES

1. Kuzniecky RI, Bilir E, Gilliam F, et al. **Multimodality MRI in mesial temporal sclerosis: relative sensitivity and specificity.** *Neurology* 1997;49:774–78 CrossRef Medline
2. Janszky J, Janszky I, Schulz R, et al. **Temporal lobe epilepsy with hippocampal sclerosis: predictors for long-term surgical outcome.** *Brain* 2005;128:395–404 Medline
3. Thom M, Mathern GW, Cross JH, et al. **Mesial temporal lobe epilepsy: how do we improve surgical outcome?** *Ann Neurol* 2010; 68:424–34 CrossRef Medline
4. Malmgren K, Thom M. **Hippocampal sclerosis—origins and imaging.** *Epilepsia* 2012;53(Suppl 4):19–33 CrossRef Medline
5. Provenzale JM, Barboriak DP, VanLandingham K, et al. **Hippocampal MRI signal hyperintensity after febrile status epilepticus is predictive of subsequent mesial temporal sclerosis.** *AJR Am J Roentgenol* 2008;190:976–83 CrossRef Medline
6. Parsons MS, Sharma A, Hildebolt C. **Using correlative properties of neighboring pixels to enhance contrast-to-noise ratio of abnormal hippocampus in patients with intractable epilepsy and mesial temporal sclerosis.** *Acad Radiol* 2018 Jun 12. [Epub ahead of print] CrossRef Medline
7. Orłowski HL, Smyth MD, Parsons MS, et al. **Enhancing contrast to noise ratio of hippocampi affected with mesial temporal sclerosis: a case-control study in children undergoing epilepsy surgeries.** *Clin Neurol Neurosurg* 2018;174:144–48 CrossRef Medline
8. Nelson KP, Edwards D. **Measures of agreement between many raters for ordinal classifications.** *Stat Med* 2015;34:3116–32 CrossRef Medline
9. Landis JR, Koch GG. **An application of hierarchical kappa-type statistics in the assessment of majority agreement among multiple observers.** *Biometrics* 1977;33:363–74 CrossRef Medline
10. Kwan P, Brodie MJ. **Early identification of refractory epilepsy.** *N Engl J Med* 2000;342:314–19 CrossRef Medline
11. Guzmán Perez-Carrillo GJ, Owen C, Schwetye KE, et al. **The use of hippocampal volumetric measurements to improve diagnostic accuracy in pediatric patients with mesial temporal sclerosis.** *J Neurosurg Pediatr* 2017;19:720–28 CrossRef Medline
12. Silva G, Martins C, Moreira da Silva N, et al. **Automated volumetry of hippocampus is useful to confirm unilateral mesial temporal sclerosis in patients with radiologically positive findings.** *Neuroradiol J* 2017;30:318–23 CrossRef Medline
13. Huppertz HJ, Wagner J, Weber B, et al. **Automated quantitative FLAIR analysis in hippocampal sclerosis.** *Epilepsy Res* 2011;97: 146–56 CrossRef Medline
14. Bernasconi A, Bernasconi N, Caramanos Z, et al. **T2 relaxometry can lateralize mesial temporal lobe epilepsy in patients with normal MRI.** *Neuroimage* 2000;12:739–46 CrossRef Medline
15. Pell GS, Briellmann RS, Waites AB, et al. **Voxel-based relaxometry: a new approach for analysis of T2 relaxometry changes in epilepsy.** *Neuroimage* 2004;21:707–13 CrossRef Medline
16. Focke NK, Bonelli SB, Yogarajah M, et al. **Automated normalized FLAIR imaging in MRI-negative patients with refractory focal epilepsy.** *Epilepsia* 2009;50:1484–90 CrossRef Medline

# Visualization of Aneurysmal Neck and Dome after Coiling with 3D Multifusion Imaging of Silent MRA and FSE-MR Cisternography

T. Satoh, T. Hishikawa, M. Hiramatsu, K. Sugiu, and I. Date



## ABSTRACT

**BACKGROUND AND PURPOSE:** Our aim was to visualize the precise configuration of the aneurysmal neck and dome with/without remnants combined with a coiled dome after coiling treatment for cerebral aneurysms. We developed 3D multifusion imaging of silent MRA and FSE-MR cisternography.

**MATERIALS AND METHODS:** We examined 12 patients with 3D multifusion imaging by composing 3D images reconstructed from TOF-MRA, silent MRA, and FSE-MR cisternography. The influence of magnetic susceptibility artifacts caused by metal materials affecting the configuration of the aneurysmal complex with coiling was assessed in a single 3D image.

**RESULTS:** In all cases, TOF-MRA failed to depict the aneurysmal neck complex precisely due to metal artifacts, whereas silent MRA delineated the neck and parent arteries at the coiled regions without serious metal artifacts. FSE-MR cisternography depicted the shape of the coiled aneurysmal dome and parent artery complex together with the brain parenchyma. With the 3D multifusion images of silent MRA and FSE-MR cisternography, the morphologic status of the coiled neck and parent arteries was clearly visualized with the shape of the dome in a single 3D image.

**CONCLUSIONS:** Silent MRA is a non-contrast-enhanced form of MRA. It depicts the coiled neck complex without serious metal artifacts. FSE-MR cisternography can delineate the shape of the coiled dome. In this small feasibility study, 3D multifusion imaging of silent MRA and FSE-MR cisternography allowed good visualization of key features of coiled aneurysms. This technique may be useful in the follow-up of coiled aneurysms.

**ABBREVIATIONS:** AComA = anterior communicating artery; MRC = MR cisternography

In the follow-up after the endovascular treatment of a cerebral aneurysm, the precise visualization of the shape of the neck and dome with/without remnants from coiling is necessary.<sup>1-11</sup> X-ray DSA is a reference standard to examine the above-described configuration, but it is invasive and presents certain risks related to the catheter procedure, contrast media,

and radiation.<sup>2,5-7,9,10</sup> As a noninvasive substitute for DSA, 3D TOF-MRA with/without contrast media is widely used, but this method presents some difficulty regarding magnetic susceptibility artifacts from the coils.<sup>2,4,5,7-11</sup>

With some recent advances in MR imaging, it has been speculated that silent MRA with zero-TE and arterial spin-labeling tagging may overcome the above problems by delineating flowing blood at the neck with minimal artifacts from metal substances.<sup>2,7,9,10,12</sup> In addition, MR cisternography (MRC) with a heavily T2-weighted 3D FSE sequence can depict the shape of the aneurysmal dome together with perianeurysmal anatomic structures, including the brain parenchyma and cranial nerves.<sup>13-15</sup> In the present study, we used 3D multifusion imaging with silent MRA—instead of TOF-MRA—and FSE-MRC to delineate the configuration of the aneurysmal neck and dome after coiling treatment of cerebral aneurysms. To the best of our knowledge, the delineation of the coiled neck with 3D silent MRA and the dome with 3D FSE-MRC, and 3D multifusion imaging of these structures in a single 3D image has not been described.

Received December 8, 2018; accepted after revision March 11, 2019.

From the Department of Neurological Surgery (T.S.), Ryofukai Satoh Neurosurgical Hospital, Fukuyama, Hiroshima, Japan; and Department of Neurological Surgery (T.H., M.H., K.S., I.D.), Okayama University Graduate School of Medicine, Okayama, Okayama, Japan.

Paper previously presented, in part, at: Scientific Conference on Neurosurgical Topics of Okayama University Neurosurgical Alumni Association, November 11, 2017; Okayama, Japan; and the Chugoku-Shikoku Scientific Meeting of the Japan Neurosurgical Society, December 8, 2018; Ehime, Japan.

Please address correspondence to Toru Satoh, MD, Department of Neurological Surgery, Ryofukai Satoh Neurosurgical Hospital, 5-23-23 Matsunaga, Fukuyama, Hiroshima 729-0104, Japan; e-mail: ucsfbtrc@urban.ne.jp

Indicates open access to non-subscribers at [www.ajnr.org](http://www.ajnr.org)

Indicates article with supplemental on-line table.

<http://dx.doi.org/10.3174/ajnr.A6026>

## MATERIALS AND METHODS

This retrospective study was approved by the ethics committee of Ryofukai Satoh Neurosurgical Hospital. Informed consent was obtained from all patients for the use of their clinical data.

### Patient Population

Between July 2017 and June 2018, twelve patients were examined by TOF-MRA, silent MRA, and FSE-MRC for the follow-up of endovascular treatment of a ruptured and/or unruptured cerebral aneurysm at Ryofukai Satoh Neurosurgical Hospital and Okayama University Hospital (On-line Table). The aneurysm location was the anterior communicating artery (AComA) in 5 patients, the distal anterior cerebral artery in 1 patient, the internal carotid–posterior communicating artery in 1 patient, the internal carotid–anterior choroidal artery in 1 patient, the middle cerebral artery in 1 patient, and the top of the basilar artery in 3 patients.

### Imaging Procedures

The imaging by TOF-MRA, silent MRA, and FSE-MRC was performed in the same session on a 3T unit (Signa Pioneer; GE Healthcare, Milwaukee, Wisconsin). The TOF-MRA was performed with the following parameters: TR/TE, 25/3.4 ms; flip angle, 20°; FOV, 180 × 180 mm; matrix, 288 × 192; section thickness, 1.2 mm; NEX, 1; bandwidth, 35.71 kHz; acquisition time, 5 minutes 41 seconds. A total of 144 continuous axial source images were acquired.

The silent MRA was performed by a silent scan with the following parameters: TR/TE, 880/0.016 ms; flip angle, 5°; FOV, 180 × 180 mm; matrix, 200 × 200; spokes per segment, 320; section thickness, 1.0 mm; NEX, 1.5; bandwidth, 31.25 kHz; acquisition time, 12 minutes 48 seconds. A total of 400 continuous axial source images were acquired.

The heavily T2-weighted 3D FSE-MRC was performed with the following parameters: TR/TE, 1900/100 ms; FOV, 180 × 180 mm; matrix, 356 × 256; section thickness, 1.2 mm; NEX, 1; bandwidth, 31.25 kHz; echo-train length, 128; acquisition time, 5 minutes 53 seconds. A total of 60 continuous axial source images were acquired.

### Image Processing

Volumetric datasets from the source images of the TOF-MRA, silent MRA, and FSE-MRC were transferred to a workstation (Ziostation-2; Ziosoft/AMIN, Tokyo, Japan) as described by Satoh et al.<sup>13-15</sup> For the 3D TOF-MRA and silent MRA, the vessel configurations were reconstructed by a perspective volume-rendering algorithm, and the arterial lumen was selected from the opacity chart of the datasets with higher MR signal intensity of arteries (threshold, >400 for TOF-MRA and >300 for silent MRA, respectively) compared with the background. Thus, the 3D image of parent arteries and aneurysmal neck after coiling was depicted by the 2 types of MRA.

The perspective volume-rendering image of the 3D FSE-MRC was reconstructed from the entire dataset with a lower signal intensity of CSF (threshold, <1200) so that the shape of the coiled aneurysmal dome and parent artery complex was delineated with its perianeurysmal anatomic structures, including the brain parenchyma and cranial nerves.

To visualize the 2 types of MRA images in combination with MRC images in a single 3D image, we used 3D multifusion imaging by compositing the above-described reconstructed 3D images of TOF-MRA, silent MRA, and FSE-MRC. The overall time required to reconstruct a picture of 3D multifusion imaging was within 120 seconds per image. We were thus able to directly compare the shape of the aneurysmal neck complex with/without neck remnants depicted by the 2 types of MRA combined with the coiled dome shown by MRC. The difference between the TOF-MRA and silent MRA, in combination with FSE-MRC, was directly compared in each case.

### Image-Quality Analysis of TOF-MRA and Silent MRA

The source images, MIP, 3D perspective volume-rendering, and 3D multifusion images between the TOF-MRA and the silent MRA combined with FSE-MRC were compared with respect to the configuration of the coiled aneurysmal complex depicted by DSA obtained after the completion of the coiling. The 2 types of MRA images were independently reviewed by 2 board-certified neurosurgeons (T.H. and M.H.). The quality of the visualization of the coiled aneurysmal complex including the neck and parent arteries obtained by the TOF-MRA and silent MRA in conjunction with the FSE-MRC was rated subjectively on the following 4-point scale: 1, not visible (no signal or gap in the parent artery or the neck); 2, poor (visible, but incomplete with artifacts); 3, good (good quality with minimal artifacts); 4, excellent (excellent quality without artifacts). The scores obtained by the 2 observers were averaged for each of the 2 types of MRA, and the statistical analysis was performed by a Wilcoxon signed rank test. A *P* value < .05 was considered significant. Interobserver agreement between the 2 observers' scores for each type of MRA was tested by intraclass correlation coefficient statistics.

### Size and Volume Analysis of Coiled Aneurysms

We measured the maximum size (*x*, *y*, *z*) of the aneurysmal neck remnants based on the source images obtained by TOF-MRA and silent MRA and the dome from FSE-MRC in each case. The volume of the remnant was calculated on the basis of ROIs drawn on the source images of TOF-MRA and silent MRA, where the contours of each remnant were respectively serially masked. The voxel volume was determined by a pixel size on the source image and the slice pitch, and the number of voxels within the masked region was counted. The volume of the masked region was then calculated as the number of voxels multiplied by the volume of voxels within the region using a workstation. Similarly, the volume of the dome was calculated on the source images of FSE-MRC. Each numeric value was determined as the mean of 3 measurements performed by the senior author (T.S.).

## RESULTS

### Quality Assessment

The On-line Table provides the data of the 12 patients, including age ( $62.8 \pm 8.9$  years; range, 51–78 years) and sex (4 men and 8 women), location of aneurysms, symptoms, time interval between DSA and MRA ( $8.5 \pm 4.4$  months; range, 3–12 months), and the scores for TOF-MRA and silent MRA (TOF/silent MRAs) obtained by the 2 observers. In all cases, the Wilcoxon signed rank

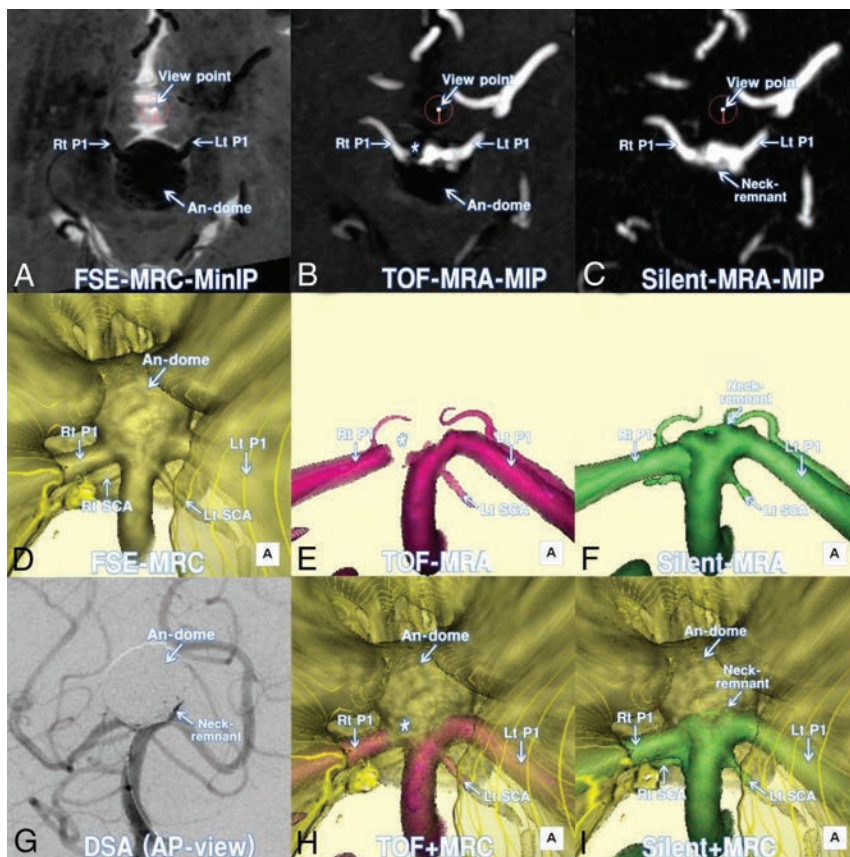


**FIG 1.** A 69-year-old woman (patient 10) treated by coiling for a large unruptured top of the basilar artery (BA-top) aneurysm. *A*, Axial minimum intensity projection (MinIP) image of postcoiling FSE-MRC. The encircled arrow indicates the viewing position for the following 3D images. *B*, Axial MIP image of postcoiling TOF-MRA. *C*, Axial MIP image of postcoiling silent MRA. *D*, Postcoiling 3D FSE-MRC image. *E*, Postcoiling 3D TOF-MRA image. Note the gap (asterisk) of the parent artery and irregularity of the neck. *F*, Postcoiling 3D silent MRA image. Parent arteries and the coiled neck are clearly visualized. *G*, DSA image at the completion of coiling. Note that the configuration of the neck complex with remnants and parent arteries is depicted with the shadow of the coiled dome. *H*, *I*, A 3D multifusion image of postcoiling TOF-MRA and FSE-MRC. *I*, A 3D multifusion image of postcoiling silent MRA and FSE-MRC. Note that the coiled neck complex with remnants is clearly visualized together with the coiled dome and adjacent brain parenchyma. P1 indicates the first segment of posterior cerebral artery; Lt, left; Rt, right; AP, anteroposterior; An, aneurysm.

test revealed that the visualization score of parent arteries and neck status for the silent MRA ( $3.75 \pm 0.5$ ) was significantly higher than that for TOF-MRA ( $1.5 \pm 1.25$ ) ( $P < .01$ ). The interobserver agreement tested by the intraclass correlation coefficient was 0.955 for TOF-MRA and 0.941 for silent MRA and was interpreted as excellent.

### 3D Visualization of the Aneurysmal Neck and Dome Complex

With the use of TOF-MRA, the coiled neck and parent arteries were depicted but not precisely visualized, apparently due to metal artifacts. In contrast, the silent MRA clearly delineated the aneurysmal neck with/without remnants and afferent and efferent parent arteries without serious metal artifacts. Additionally, the shape of the dome treated and packed by coils was depicted by the FSE-MRC with perianeurysmal anatomic structures including the brain parenchyma and cranial nerves.

With the 3D multifusion images reconstructed and composed of 3D silent MRA and 3D FSE-MRC, the morphologic status of the neck and parent arteries of the coiled aneurysm

was visualized with the dome, together with adjacent brain parenchyma (Figs 1–3).

### Size and Volume of the Neck Remnants and Coiled Domes

The On-line Table also provides the size and volume of the neck remnants obtained by TOF-MRA and silent MRA and the coiled domes from FSE-MRC. With TOF-MRA, the sizes of the remnants were not measured accurately due to an incomplete depiction of the neck or parent arteries due to metal artifacts. In contrast, the size and volume of the remnants were obtained by silent MRA, and the size and volume of the domes were obtained by FSE-MRC. Although potential remodeling after coiling during the mean time interval between the MRA/MRC and the DSA ( $8.5 \pm 4.4$  months) may have affected the findings, the neck and dome complex was not visualized identically but was similar to that provided by the DSA obtained at the time of coiling. Neck remnants were depicted in 10 of the 12 cases, and we calculated the percentage of the remnant volume (ie, the residual filling volume at the neck) measured by the silent MRA to the dome volume (the whole volume of the coiled dome) by the FSE-MRC in each case: 2.3%–36.7%. The clinical results showed complete cure in 2 patients, follow-up with remnants in 8 patients, and re-treatment in 2 patients.

### DISCUSSION

Endovascular treatment involving coil embolization has been performed widely for cerebral aneurysms, but coil compaction and the recanalization of a coiled aneurysm frequently occur after this treatment.<sup>1,5,6,8</sup> The remnants of the dome may be at risk of growing, and they thus require long-term vascular follow-up.<sup>1,3,8</sup> When retreatment is being considered, the clear visualization of the neck remnants and the dome configuration is necessary in the follow-up examination.<sup>3,4,6,8,11</sup>

In the present study, we used silent MRA for the follow-up in patients with coil treatment for cerebral aneurysms. Silent MRA may provide a clear depiction of flowing blood within the vessels (eg, the aneurysmal neck with/without remnants and parent arteries) with minimal artifacts caused by metal substances so that the aneurysmal complex can be delineated without serious susceptibility artifacts.<sup>2,7,9,10,12</sup> With the currently available imaging software, the entire shape of an aneurysm (including the neck, parent arteries, and dome) treated by coiling can be reconstructed and depicted in a single 3D image by

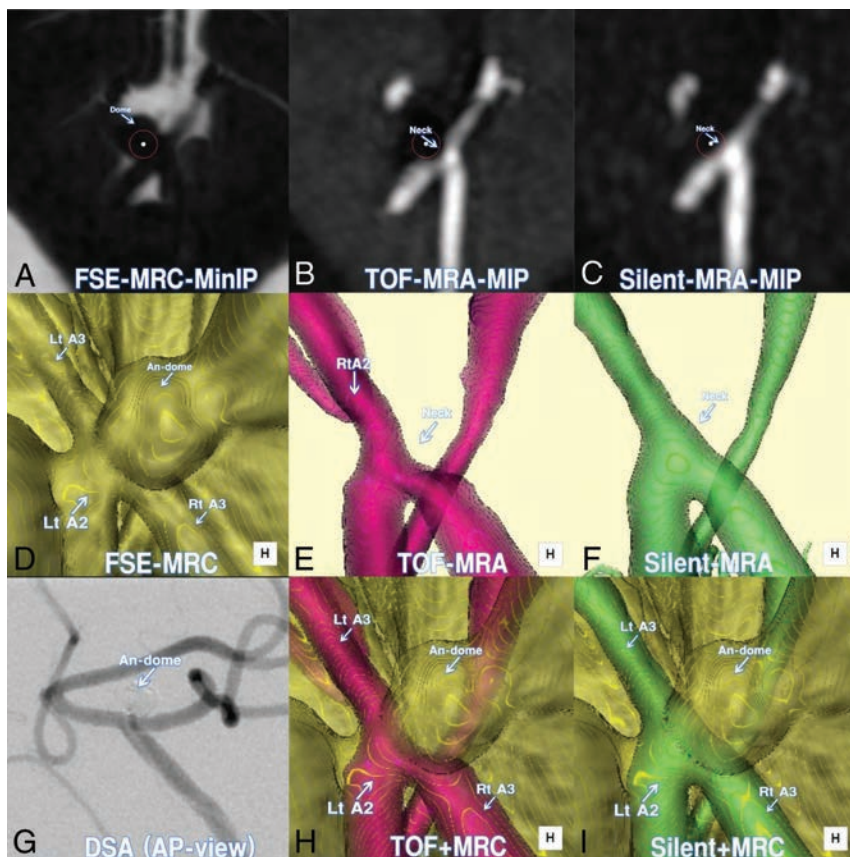


**FIG 2.** A 78-year-old woman (patient 6) treated by coiling for an unruptured distal anterior cerebral artery (A2–A3) aneurysm. *A*, Axial minimum intensity projection (MinIP) image of postcoiling FSE-MRC. *B*, Axial MIP image of postcoiling TOF-MRA. *C*, Axial MIP image of postcoiling silent MRA. *D*, Postcoiling 3D FSE-MRC image. *E*, Postcoiling 3D TOF-MRA image. Note the defects of the parent artery and the neck. *F*, Postcoiling 3D silent MRA image. Note that the parent arteries and coiled neck without remnants are clearly visualized. *G*, DSA image at the completion of coiling. Note that the configuration of the neck complex without remnants is depicted with the shadow of the coiled dome. *H*, A 3D multifusion image of postcoiling TOF-MRA and FSE-MRC. *I*, A 3D multifusion image of postcoiling silent MRA and FSE-MRC. Note the complete occlusion of the neck without remnants together with the coiled dome. A2 indicates the second segment of the anterior cerebral artery; A3, the third segment of the anterior cerebral artery; An, aneurysm; Lt, left; Rt, right; AP, anteroposterior.

the 3D multifusion imaging in combination with silent MRA and FSE-MRC described herein.

### Disadvantages of TOF-MRA

TOF-MRA is a noninvasive technique used to obtain vessels-to-soft-tissue contrast by the flow of the spins within the blood vessels. The arterial geometry and patency obtained by TOF-MRA with/without contrast media do not represent the luminal morphology as depicted by DSA and CTA, but they do represent the flow voids caused by an inflow effect that are related mainly to peak systolic flow velocities within the vessel lumen during data acquisition.<sup>13–15</sup> TOF-MRA may be affected by several factors, such as the loss of signal intensity that occurs from spin saturation effects due to slow flow and/or phase dispersion due to disturbed and complex flow. Magnetic susceptibility and radiofrequency-shielding artifacts from metal substances inevitably occur.<sup>10,16</sup> As a result, it may be difficult to depict the precise configuration of the neck and parent artery of coiled aneurysms with TOF-MRA with/without contrast media.

### Merits of Silent MRA

Silent MRA is also known as zero-TE MRA or arterial spin-labeling MRA,<sup>2,7,9,10,12</sup> and the environmental noise during acquisition is <3 dB (compared with >100 dB with TOF-MRA). Silent MRA is a non-contrast-enhanced form of MRA, and its use may eliminate the acute and late possible adverse events of the administration of gadolinium-based contrast agents in the body and brain.<sup>17,18</sup> In contrast to TOF-MRA, silent MRA depicts the configuration of flowing blood within the arteries so that the angioarchitecture of the aneurysmal neck complex is depicted without the contamination of veins, cranial base bones, and serious metal artifacts from coil materials.<sup>2,7,9,10</sup> It is reported that silent MRA can visualize the flow in an intracranial stent more effectively than TOF-MRA.<sup>2</sup> The details of the algorithm of silent MRA using the Silenz sequence were not disclosed by GE Healthcare; however, an ultrashort TE (0.016 ms) is used with arterial spin-labeling tagging and many spokes per segment for scanning. A preparation pulse is used at the carotid artery, and the data acquisition of the whole brain is based on a 3D radial scan. Before the labeling pulse, a control image without labeling is scanned first, followed by the labeled image. Subtraction of the control from the labeled image creates an angiogram (T1WI) that consists of pure flowing blood within the vessels.

In silent MRA, the ultrashort TE can minimize the phase dispersion of the labeled blood flow signal in the voxel space and decrease magnetic susceptibility artifacts.<sup>2,7,9,10</sup> Consequently, silent MRA has much merit for depicting the arterial geometry at the neck as the flowing blood signal within the vessels with minimal metal artifacts. Additionally, due to the reduction of the blood flow saturation effect, silent MRA can depict slow flows, multidirectional flows, whirlpools, and turbulence flows more clearly compared with TOF-MRA.

Regarding the image processing, the maximum intensity projection images reconstructed from silent MRA usually show blurred margins of the vessels compared with TOF-MRA. The volumetric dataset must be selected using a distinct threshold that corresponds to the size of the vessels and borderline in the process of reconstructing 3D images.<sup>13–15</sup> In the present study, a signal intensity threshold of >300 was used for the arteries. With this selected dataset, the outer wall configuration of the aneurysmal neck complex with coils can be depicted clearly without serious metal artifacts.

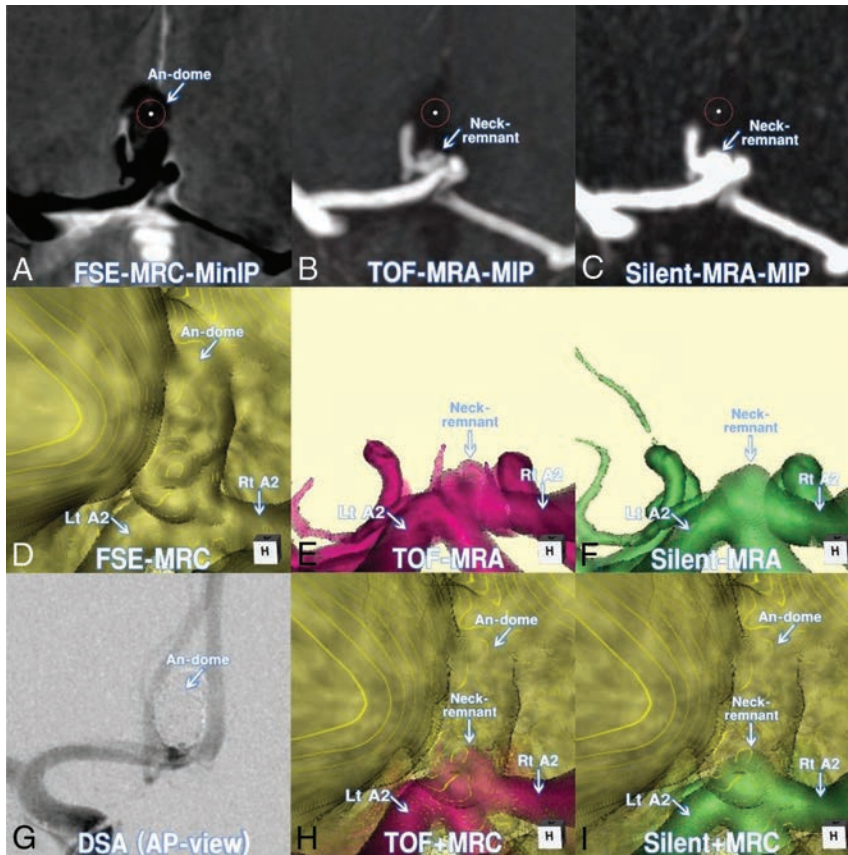


**FIG 3.** A 58-year-old man (patient 3) treated by endovascular coiling for an unruptured AComA aneurysm. *A*, Axial minimum intensity projection (MinIP) image of postcoiling FSE-MRC. *B*, Axial MIP image of postcoiling TOF-MRA. *C*, Axial MIP image of postcoiling silent MRA. *D*, Postcoiling 3D FSE-MRC image. *E*, Postcoiling 3D TOF-MRA image. Note the minor defects at the parent artery and the neck. *F*, Postcoiling 3D silent MRA image. Note that the parent arteries and coiled neck are clearly visualized. *G*, DSA image at the completion of coiling. Note the configuration of the neck complex with the shadow of the coiled dome. *H*, A 3D multifusion image of postcoiling TOF-MRA and FSE-MRC. *I*, A 3D multifusion image of postcoiling silent MRA and FSE-MRC. Note the clear visualization of the coiled neck complex with remnants, together with the coiled dome and adjacent brain parenchyma. Rt indicates right; Lt, left; AP, anteroposterior.

### Merits of FSE-MRC

We did not use so-called T2 high-resolution images such as the FIESTA sequence for MRC.<sup>19</sup> Because all the intracisternal anatomic structures are uniformly depicted as low signal intensity, it may be difficult to distinguish the boundary of an aneurysmal dome from the adjacent brain parenchyma and cranial nerves.

In the present study, we used FSE-MRC, a traditional heavily T2-weighted 3D FSE sequence, with a relatively short TR/TE (1900/100 ms). FSE-MRC obtained by a 3T unit with a wide bandwidth can depict the outer wall configuration of the intracisternal aneurysmal complex and perianeurysmal anatomic structures with thin sections and a high signal-to-noise ratio.<sup>13-15</sup> An aneurysmal dome and parent arteries are depicted as a heavily dark area, and brain parenchyma and cranial nerves are depicted as a moderately dark area. These are well-contrasted to the surrounding CSF as a profoundly bright area. With FSE-MRC, the entire aspect of the aneurysmal dome and neck complex treated by coils is clearly visualized without metal artifacts. The contour of the coiled dome can thus be distinguished from the surrounding

structures including adjacent brain parenchyma and cranial nerves.

### Merits of 3D Multifusion Imaging with Silent MRA and FSE-MRC

Instead of using TOF-MRA and FIES-TA-MRC, we reconstructed and combined silent MRA and FSE-MRC images by means of 3D multifusion imaging.<sup>13-15</sup> Because the anatomic structure of a coiled aneurysm is complicated, it may be difficult to acquire a precise understanding of the architecture of the aneurysmal neck and parent arteries by simply reviewing  $\geq 1$  of the source images displayed in 2D. Silent MRA may depict the coiled neck with/without remnants, and FSE-MRC delineates the dome and adjacent brain parenchyma after coiling treatment for cerebral aneurysms. The 3D reconstruction of silent MRA in combination with FSE-MRC may provide the clear visualization of the aneurysmal complex with the coiled neck and dome in a single 3D image.

Our present results indicate that 3D multifusion images with silent MRA and FSE-MRC can provide the residual filling volume at the neck (remnant) with respect to the whole volume of the coiled dome (dome volume). This finding could be used in the decision regarding whether to conduct re-embolization. The size and volume of the remnant together with the coiled dome may also distinguish coil compaction from regrowth of the aneurysm. Consequently, visualization of the neck and dome with this imaging is useful for follow-up evaluations of patients treated with coiling for cerebral aneurysms.

### Limitations and Perspectives Regarding 3D Multifusion Imaging with Silent MRA and FSE-MRC

Several limitations may exist in the application of 3D multifusion imaging with silent MRA and FSE-MRC. The sample size in the present study was small ( $n = 12$ ), and the cases were limited to those of simple coil embolization. Cases with various types of stent- or flow-diverter-assisted coil embolization should be tested. In addition, silent MRA can depict the coiled aneurysmal neck complex with minimal metal artifacts via an ultrashort TE. However, a potential limitation is the occurrence of magnetic susceptibility and radiofrequency-shielding artifacts due to certain materials containing pure ferromagnetic substances such as a platinum alloy.<sup>7,11,16</sup>

Moreover, in the process of reconstructing 3D multifusion imaging, the size and volume of the neck and dome rendered for each 3D image may change according to the threshold value se-

lected from an opacity chart of the datasets.<sup>13-15</sup> It may be difficult to decide the optimal threshold values for the geometry of the aneurysmal neck for silent MRA and the dome for FSE-MRC in each individual subject. In this study, we determined the shape of arteries using the signal intensity threshold of >300 for silent MRA, >400 for TOF-MRA, and <1200 for FSE-MRC. By means of 3D multifusion imaging, an appropriate threshold for each TOF-MRA, silent MRA, and FSE-MRC can be determined by adjusting the shape of the objects, including parent arteries, neck, and dome of the coiled aneurysm by fusing 3 different images. In addition to the images of simple TOF-MRA, silent MRA, and FSE-MRC, 3D multifusion imaging may make a contribution by allowing the incorporation of all the views in a single 3D fused image.

Prospectively, we suggest that 3D multifusion imaging obtaining the pre- and posttreatment images with silent MRA and FSE-MRC may be useful to confirm the initial success of coiling for cerebral aneurysms. Additionally, sequential follow-ups may depict changes in the shape of the coiled neck and dome, which may inform the timing of retreatment. More research is required to refine and validate the imaging techniques described herein.

## CONCLUSIONS

Silent MRA can depict the configuration of the coiled neck and parent arteries without serious susceptibility artifacts. FSE-MRC can delineate the shape of the coiled dome together with adjacent brain parenchyma. In this small feasibility study, 3D multifusion imaging of silent MRA and FSE-MRC provided good visualization of key features of coiled aneurysms. This technique may be useful in the follow-up of coiled aneurysms.

## ACKNOWLEDGMENTS

We thank Ms Megumi Sasaki, radiologic technician, and Ms Kana Murakami, laboratory technologist, Ryofukai Satoh Neurosurgical Hospital, for conducting the MR imaging examinations.

## REFERENCES

- Binning MJ, Veznedaroglu E. **Aneurysm remnants after coiling and clipping: considerations in surgical and endovascular treatment options.** *Neurosurgery* 2015;62:103–06 CrossRef Medline
- Irie R, Suzuki M, Yamamoto M, et al. **Assessing blood flow in an intracranial stent: a feasibility study of MR angiography using a silent scan after stent-assisted coil embolization for anterior circulation aneurysms.** *AJNR Am J Neuroradiol* 2015;36:967–70 CrossRef Medline
- Jabbarli R, Pierscianek D, Wrede K, et al. **Aneurysm remnant after clipping: the risks and consequences.** *J Neurosurg* 2016;125:1249–55 CrossRef Medline
- Kaufmann TJ, Huston J 3rd, Cloft HJ, et al. **A prospective trial of 3T and 1.5T time-of-flight and contrast-enhanced MR angiography in the follow-up of coiled intracranial aneurysms.** *AJNR Am J Neuroradiol* 2010;31:912–18 CrossRef Medline
- Pierot L, Portefaix C, Gauvrit JY, et al. **Follow-up of coiled intracranial aneurysms: comparison of 3D time-of-flight MR angiography at 3T and 1.5T in a large prospective series.** *AJNR Am J Neuroradiol* 2012;33:2162–66 CrossRef Medline
- Serafin Z, Strzeńiewski P, Lasek W, et al. **Comparison of remnant size in embolized intracranial aneurysms measured at follow-up with DSA and MRA.** *Neuroradiology* 2012;54:1381–88 CrossRef Medline
- Shang S, Ye J, Luo X, et al. **Follow-up assessment of coiled intracranial aneurysms using zTE MRA as compared with TOF MRA: a preliminary image quality study.** *Eur Radiol* 2017;27:4271–80 CrossRef Medline
- Shankar JJS, Lum C, Parikh N, et al. **Long-term prospective follow-up of intracranial aneurysms treated with endovascular coiling using contrast-enhanced MR angiography.** *AJNR Am J Neuroradiol* 2010;31:1211–15 CrossRef Medline
- Takano N, Suzuki M, Irie R, et al. **Usefulness of non-contrast-enhanced MR angiography using a silent scan for follow-up after Y-configuration stent-assisted coil embolization for basilar tip aneurysms.** *AJNR Am J Neuroradiol* 2017;38:577–81 CrossRef Medline
- Takano N, Suzuki M, Irie R, et al. **Non-contrast-enhanced silent scan MR angiography of intracranial anterior circulation aneurysms treated with a low-profile visualized intraluminal support device.** *AJNR Am J Neuroradiol* 2017;38:1610–16 CrossRef Medline
- Wallace RC, Karis JP, Partovi S, et al. **Noninvasive imaging of treated cerebral aneurysms, Part I: MR angiographic follow-up of coiled aneurysms.** *AJNR Am J Neuroradiol* 2007;28:1001–08 CrossRef Medline
- Alibek S, Vogel M, Sun W, et al. **Acoustic noise reduction in MRI using silent scan: an initial experience.** *Diagn Interv Radiol* 2014;20:360–63 CrossRef Medline
- Satoh T, Onoda K, Tsuchimoto S. **Visualization of intraaneurysmal flow patterns with transluminal flow images of 3D MR angiograms in conjunction with aneurysmal configurations.** *AJNR Am J Neuroradiol* 2003;24:1436–45 Medline
- Satoh T, Omi M, Osako C, et al. **Visualization of aneurysmal contours and perianeurysmal environment with conventional and transparent 3D MR cisternography.** *AJNR Am J Neuroradiol* 2005;26:313–18 Medline
- Satoh T, Omi M, Osako C, et al. **Influence of perianeurysmal environment on the deformation and bleb formation of the unruptured cerebral aneurysm: assessment with fusion imaging of 3D MR cisternography and 3D MR angiography.** *AJNR Am J Neuroradiol* 2005;26:2010–18 Medline
- McFadden JT. **Magnetic resonance imaging and aneurysm clips: a review.** *J Neurosurg* 2012;117:1–11 CrossRef Medline
- Kanda T, Ishii K, Kawaguchi H, et al. **High signal intensity in the dentate nucleus and globus pallidus on unenhanced T1-weighted MR images: relationship with increasing cumulative dose of a gadolinium-based contrast material.** *Radiology* 2014;270:834–41 CrossRef Medline
- Quattrocchi CC, van der Molen AJ. **Gadolinium retention in the body and brain: is it time for an international joint research effort?** *Radiology* 2017;282:12–16 CrossRef Medline
- Chávez GC, De Salles AAF, Solberg TD, et al. **Three-dimensional fast imaging employing steady-state acquisition magnetic resonance imaging for stereotactic radiosurgery of trigeminal neuralgia.** *Neurosurgery* 2005;56:E628 CrossRef Medline

# Usefulness of Silent MR Angiography for Intracranial Aneurysms Treated with a Flow-Diverter Device

H. Oishi, T. Fujii, M. Suzuki, N. Takano, K. Teranishi, K. Yatomi, T. Kitamura, M. Yamamoto, S. Aoki, and H. Arai



## ABSTRACT

**BACKGROUND AND PURPOSE:** The flow-diverter device has been established as a treatment procedure for large unruptured intracranial aneurysms. The purpose of this study was to compare the usefulness of Silent MR angiography and time-of-flight MRA to assess the parent artery and the embolization state of the aneurysm after a flow-diverter placement.

**MATERIALS AND METHODS:** Seventy-eight large, unruptured internal carotid aneurysms in 78 patients were the subjects of this study. After 6 months of treatment, they underwent follow-up digital subtraction angiography, Silent MRA, and TOF-MRA, performed simultaneously. All images were independently reviewed by 2 neurosurgeons and 1 radiologist and rated on a 4-point scale from 1 (not visible) to 4 (excellent) to evaluate the parent artery. The aneurysmal embolization status was assessed with 2 ratings: complete or incomplete occlusion.

**RESULTS:** The mean scores of Silent MRA and TOF-MRA regarding the parent artery were  $3.18 \pm 0.72$  and  $2.31 \pm 0.86$ , respectively, showing a significantly better score with Silent MRA ( $P < .01$ ). In the assessment of the embolization of aneurysms on Silent MRA and TOF-MRA compared with DSA, the percentages of agreement were 91.0% and 80.8%, respectively.

**CONCLUSIONS:** Silent MRA is superior for visualizing blood flow images inside flow-diverter devices compared with TOF-MRA. Furthermore, Silent MRA enables the assessment of aneurysmal embolization status. Silent MRA is useful for assessing the status of large and giant unruptured internal carotid aneurysms after flow-diverter placement.

The advancement of endovascular treatment devices for intracranial aneurysms has been remarkable. In the treatment of large and giant intracranial aneurysms, a flow-diverter device with a high metal coverage ratio is placed in the parent artery so that it decreases blood flow into aneurysms, promotes thrombosis, and thereby prevents rupture. The usefulness of the flow-diverter device has become apparent by various large-scale studies, and its adoption is consistently increasing.<sup>1-6</sup> However, due to the characteristics of the device, which divert the blood flow and promote thrombosis, careful radiologic follow-up observation is required, and periodic checkups on the status of the aneurysmal embolization and patency of the parent artery are essential. The standard test of follow-up for endovascular treatment of intracra-

nial aneurysms is digital subtraction angiography. Because DSA itself is invasive and involves the risk of complications and adverse effects caused by contrast agents and radiation exposure, less invasive and simple examination procedures are warranted.<sup>7-10</sup> In recent years, the usefulness of contrast-enhanced MR angiography has often been reported,<sup>11,12</sup> though using gadolinium carries the risk of serious complications such as nephrogenic systemic fibrosis.<sup>13</sup> Therefore, time-of-flight MRA has been gaining attention as a viable imaging procedure without having to use a contrast agent.<sup>14,15</sup> However, there have been some skeptical views regarding its accuracy.<sup>11,12</sup>

We have reported the usefulness of Silent MRA (GE Healthcare, Milwaukee, Wisconsin) as a radiologic follow-up procedure after coil embolization for intracranial aneurysms.<sup>16-18</sup> Silent MRA is a procedure using an ultrashort TE and arterial spin-labeling techniques, which efficiently visualizes the status after the treatment of intracranial aneurysms. In Silent MRA, the 3D image is reconstructed by subtracting the control image from the image obtained by the labeling pulse. At the beginning of its development, although it was a procedure that literally silences the noise of the MR imaging, Silent MRA was attracting attention because its imaging capability after endovascular treatment is superior to

Received February 1, 2019; accepted after revision March 25.

From the Departments of Neuroendovascular Therapy (H.O., T.F., T.K.), Neurosurgery (H.O., K.T., K.Y., M.Y., H.A.), and Radiology (M.S., N.T., S.A.), Juntendo University Faculty of Medicine, Tokyo, Japan.

This work was supported by Medtronic.

Please address correspondence to Takashi Fujii, MD, Department of Neuroendovascular Therapy, Juntendo University Faculty of Medicine, 2-1-1 Hongo, Bunkyo-ku, Tokyo 113-8421, Japan; e-mail: takashigreengreen@yahoo.co.jp

<http://dx.doi.org/10.3174/ajnr.A6047>

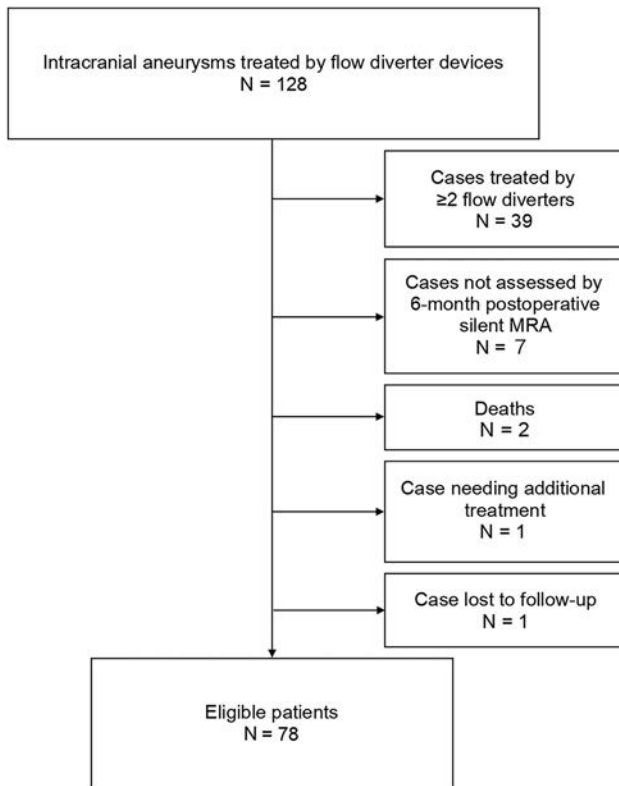


**FIG 1.** A flowchart of eligible patients assessed by Silent MR angiography after Pipeline Flex placement for intracranial aneurysms.

that of other modalities. To date, there have been several reports on the comparison of the assessment procedures between TOF-MRA and contrast-enhanced MRA after flow-diverter placement therapy.<sup>12,19,20</sup> To our knowledge, this is the first study of the comparison of Silent MRA and TOF-MRA after flow-diverter placement in intracranial aneurysms, in as much as we searched medical search engines using the key words “Silent MRA,” “TOF-MRA” and “flow diverter.” We report here the posttreatment assessment of flow-diverter therapy by Silent MRA in a study with a population of 78 patients along with the bibliographic consideration of the relevant literature.

## MATERIALS AND METHODS

### Patient and Aneurysm Characteristics

We retrospectively studied aneurysms treated with 1 flow-diverter device (Pipeline Flex Embolization Device; Covidien, Irvine, California) between June 2015 and February 2018. The patients treated with  $\geq 2$  flow-diverter devices were excluded to avoid the effects of excess metal artifacts. Among the 128 patients treated with flow-diverter devices during the study, there were 78 patients, excluding 39 patients who were treated with  $\geq 2$  flow diverter devices, 7 patients who did not undergo Silent MRA at the 6-month follow-up, 2 patients who were not examined due to postoperative death, 1 patient who needed additional treatment, and 1 patient who dropped out of the study for personal reasons (Fig 1).

Because this study was noninvasive and retrospective, patients’ informed consent was not required. We obtained approval for this study from the ethics review board.

**Table 1: Characteristics of the patients assessed by DSA, Silent MRA, and TOF-MRA after placement of flow-diverter devices**

Parameters	Data
Age (mean) (range) (yr)	61.4 $\pm$ 13.3 (19–82)
Sex (M/F)	6:72
Side (R/L)	36:42
Location (cavernous segment/paraclinoid segment)	52:26
Aneurysmal size (mean) (range) (mm)	14.8 $\pm$ 5.5 (10.0–32.5)
Aneurysmal neck diameter (mean) (range) (mm)	6.5 $\pm$ 2.2 (2.8–15.3)
Symptomatic cases (No.) (%)	23 (29.5%)
Additional coiling (No.) (%)	39 (50%)
Pipeline diameter (mean) (range) (mm)	4.2 $\pm$ 0.6 (3–5)
Pipeline length (mean) (range) (mm)	21.8 $\pm$ 6.3 (16–35)
In-stent percutaneous transluminal angioplasty (No.) (%)	52 (66.7%)
In-stent stenosis (No.) (%)	
None (0%)	28 (38.9%)
Mild (0–25%)	41 (52.6%)
Moderate ( $\geq 25\%$ )	9 (11.5%)
Duration of follow-up (mean) (range) (mo)	6.1 $\pm$ 0.6 (4–8)

**Note:**—R indicates right; L, left.

The patients’ characteristics are summarized in Table 1. We evaluated all patients on the basis of Silent MRA, TOF-MRA, and DSA, which were undergone postoperatively at approximately 6 months. DSA was performed for endovascular treatment and for postoperative assessment using the Artis Q BA Twin biplane system (Siemens, Erlangen, Germany).

### Endovascular Procedure

Preoperative loading of antiplatelet agents began at least 10 days before with a dose of 100 mg of aspirin and 50–75 mg of clopidogrel, with the dose determined according to body weight. For patients who might possibly have late-onset rupture of intracranial aneurysms, additional coil embolization was performed to promote thrombosis.<sup>21–23</sup> Additional in-stent percutaneous transluminal angioplasty was performed if the patients were found to have poor adhesion of the Pipeline Flex from the results of intraoperative DSA and conebeam CT. All the patients continuously received postoperative administration of dual-antiplatelet therapy until the 6-month Silent MRA follow-up was performed. All treatments for all patients were performed by one of the authors (H.O.), who has >20 years of experience conducting endovascular procedures.

### MRA Scan Parameters

TOF-MRA and Silent MRA were performed with 3T MRA (Discovery MR750w; GE Healthcare). Imaging parameters for Silent MRA were the following: TR/TE, 642.8/0.016 ms; flip angle, 5°; FOV, 180  $\times$  180 mm; matrix, 150  $\times$  150; section thickness, 1.0 mm; NEX, 1; bandwidth,  $\pm 31.2$  kHz; acquisition time, 12 minutes 13 seconds. Imaging parameters for TOF-MRA were the following: TR/TE, 20/2.9 ms; flip angle, 18°; FOV, 200  $\times$  200 mm; matrix, 416  $\times$  224; section thickness, 1.0 mm; NEX, 1; bandwidth,  $\pm 41.7$  kHz; acquisition time, 4 minutes 45 seconds. Although the detailed algorithm for Silent MRA has not been disclosed, the arterial spin-labeling technique was used as a preparation pulse, and data were obtained by a 3D radial scan.<sup>24</sup>

### Image Analysis

Images in DSA, Silent MRA, and TOF-MRA before treatment and after 6 months were reviewed independently by 2 neurosurgeons (H.O. and T.F.) and 1 radiologist (M.S.). Assessment parameters were location of the aneurysm, size, and neck diameter. The per-

centage of in-stent stenosis was measured at the narrowest site in DSA. It was classified into 3 levels: none (0%), mild (0%–25%), and moderate (25%–50%). In-stent blood flow was rated on a 4-point scale: 1, not visible (signal alteration not detected or cannot be assessed); 2, poor (blood flow slightly visible, but not adequate for diagnosis); 3, acceptable (blood flow roughly visible, diagnosable images); and 4, excellent (images almost equal to DSA). Scores of in-stent signals were calculated as the mean of those assessed by the 3 observers. Mean scores of the high- and the low-score groups were  $>2$  and  $\leq 2$ , respectively. Scores for Silent MRA and TOF-MRA were assessed. The percentage of agreement of scores by 3 observers was also assessed. The status of embolization of aneurysms observed by DSA, Silent MRA, and TOF-MRA was assessed with a 2-point rating scale: 1, incomplete occlusion (intra-aneurysmal signal alteration recognized); and 2, complete occlusion (no intra-aneurysmal signal alterations recognized). In case of discrepancy among the 3 observers, the images were reviewed by 3 other observers (K.T., K.Y., and M.Y.) to confirm the embolization status of all the aneurysms, determining whether complete or incomplete occlusion was achieved by rechecking the DSA, Silent MRA, and TOF-MRA. The rate of agreement of the embolization status between DSA and Silent MRA and TOF-MRA was also assessed.

### Thrombosis after Pipeline Flex Placement

When an intra-aneurysmal signal alteration after the treatment of an aneurysm was not observed by Silent MRA, but was observed

**Table 2: Comparison of correlations between Silent MRA and TOF-MRA from the viewpoint of all parameters for Silent MRA ( $3.18 \pm 0.72$ )**

	High Score ( $>2$ , $n = 66$ )	Low Score ( $\leq 2$ , $n = 12$ )	P Value
Aneurysmal size (mean) (mm)	14.8 $\pm$ 5.4	15.0 $\pm$ 6.6	.91
Aneurysmal neck diameter (mean) (mm)	6.5 $\pm$ 2.2	6.4 $\pm$ 2.3	.79
Pipeline diameter (mean) (mm)	4.3 $\pm$ 0.6	4.1 $\pm$ 0.6	.27
Pipeline length (mean) (mm)	21.7 $\pm$ 6.3	22.0 $\pm$ 6.8	.90
In-stent stenosis (No.) (%)	42/66 (63.6%)	8/12 (66.7%)	.84
Location (paraclinoid/cavernous)	44:22	8:4	1.00
Additional coiling (No.) (%)	33/66 (50.0%)	7/12 (58.3%)	.60

**Table 3: Comparison of correlations between Silent MRA and TOF-MRA from the viewpoint of all parameters for TOF-MRA ( $2.31 \pm 0.86$ )**

	High Score ( $>2$ , $n = 44$ )	Low Score ( $\leq 2$ , $n = 34$ )	P Value
Aneurysmal size (mean) (mm)	13.5 $\pm$ 4.3	16.6 $\pm$ 6.5	<.05
Aneurysmal neck diameter (mean) (mm)	6.0 $\pm$ 1.6	7.2 $\pm$ 2.7	<.05
Pipeline diameter (mean) (mm)	4.2 $\pm$ 0.6	4.3 $\pm$ 0.5	.61
Pipeline length (mean) (mm)	20.8 $\pm$ 5.8	23.0 $\pm$ 6.9	.13
In-stent stenosis (No.) (%)	28/44 (63.6%)	22/34 (65.9%)	.92
Location (paraclinoid/cavernous)	35:9	17:17	<.01
Additional coiling (No.) (%)	26/44 (59.1%)	14/34 (41.2%)	.12

**Table 4: Comparison of correlation between Silent MRA and TOF-MRA from the viewpoint of intra-aneurysmal thrombosis after flow-diverter device placement**

	Intra-Aneurysmal Thrombosis (+) ( $n = 13$ )	Intra-Aneurysmal Thrombosis (-) ( $n = 65$ )	P Value
Location (paraclinoid segment/cavernous segment)	2:11	63:2	<.01
Aneurysmal size (mean) (range) (mm)	21.7 $\pm$ 5.3 (12.6–32.5)	13.4 $\pm$ 4.4 (8.1–28.7)	<.01
Aneurysmal neck diameter (mean) (range) (mm)	7.8 $\pm$ 3.1 (2.8–15.3)	6.3 $\pm$ 1.9 (3.3–13.9)	<.05
Additional coiling (No.) (%)	2 (15.4%)	37 (56.9%)	<.01
Pipeline diameter (mean) (range) (mm)	4.21 $\pm$ 0.5 (3–5)	4.23 $\pm$ 0.6 (3–5)	.91
Pipeline length (mean) (range) (mm)	27.5 $\pm$ 7.2 (18–35)	20.6 $\pm$ 5.4 (16–35)	<.01
Silent MRA score (mean)	3.5 $\pm$ 0.5	3.1 $\pm$ 0.7	.10
TOF-MRA score (mean)	2.0 $\pm$ 0.8	2.3 $\pm$ 0.8	.20

**Note:**—+ indicates present; —, absent.

by TOF-MRA, the status was interpreted as intra-aneurysmal thrombosis after the Pipeline Flex placement. Thrombosis was reported as a region showing a high-intensity signal on both TOF-MRA and a T1-weighted image<sup>25</sup>; and it was confirmed that in all cases, the signal in the aneurysm was a high-intensity signal on a T1-weighted image. It has been reported that assessment of the status of the parent artery and intra-aneurysmal status revealed on TOF-MRA are more difficult in the event of an intra-aneurysmal thrombosis.<sup>12,17</sup> Aneurysms treated with Pipeline Flex placement were divided into 2 groups, those with and those without thromboses. The assessment items were the following: location, aneurysmal size and neck diameter, presence or absence of additional coiling, diameter and length of Pipeline Flex, and the difference in the scores between Silent MRA and TOF-MRA.

### Statistical Analysis

Each value was expressed by mean  $\pm$  SD and range. The difference between 2 groups was assessed by a *t* test or the  $\chi^2$  test.  $P < .05$  was considered to indicate statistical significance. The rate of agreement among the 3 observers was expressed by the Fleiss  $\kappa$  coefficient.

### RESULTS

The patients' characteristics are summarized in Table 1.

The mean score of Silent MRA,  $3.18 \pm 0.72$ , was significantly higher than that of TOF-MRA,  $2.31 \pm 0.86$  ( $P < .01$ ). The Fleiss  $\kappa$  coefficient was 0.408. In Tables 2 and 3, correlation between Silent MRA and TOF-MRA was shown from the viewpoint of parameters in the groups with high ( $>2$ ) and low ( $\leq 2$ ) mean scores. The scores of Silent MRA were not influenced by any of these parameters, whereas the scores of TOF-MRA were statistically significantly low when the aneurysmal size and neck diameter were large and the aneurysm was located in the cavernous segment.

Comparisons of the correlation between Silent MRA and TOF-MRA from the viewpoint of intra-aneurysmal thrombosis after Pipeline Flex placement are summarized in Table 4. Thrombosis occurred frequently after Pipeline Flex placement in a statistically significant manner under the following conditions: Aneurysms were located in the cavernous segment, the aneurysm was large, there was an absence of additional coiling, and the Pipeline was long.

Embolization of aneurysms was assessed in comparisons of DSA, Silent MRA, and TOF-MRA by dividing the patients with complete or incomplete occlusion of aneurysms (Table 5). The rate of agreement between Silent MRA and DSA and TOF-MRA and DSA was 91.0% and 80.8%, respectively.

### DISCUSSION

In the present study, we used the flow-diverter device, Pipeline Flex, with a high metal coverage ratio. Consequently, Silent MRA was better in terms of visualizing in-stent blood flow and the embolic state of aneurysms compared with TOF-MRA in a statistically significant manner. Particularly, Silent MRA showed superior visualization regardless of the maximum size of the aneurysmal diameter, diameter and length of the Pipeline Flex itself, the location of the aneurysms, the degree of

in-stent stenosis, and the presence or absence of additional coiling. On the other hand, TOF-MRA showed significantly poor visualization of large aneurysms and those located in the cavernous segment (Fig 2).

With TOF-MRA, it has become known that within an artery, such as in the cavernous segment with considerable bends and meandering, there are often signal losses due to turbulent and/or slow flow.<sup>26-29</sup> The TOF-MRA score tended to be lower when the neck diameter was larger and the Pipeline Flex was longer, though it was not statistically significant. One of the causes of these results was the effect of the metal artifacts of the Pipeline Flex. On the other hand, although artifacts due to additional coiling were speculated to be the cause of poor imaging, such an effect was not observed. The cause was thought to be that during the Pipeline placement, because the purpose of coil embolization was not complete occlusion but to promote thrombosis, coiling induced only rough packing, and consequently the metal surface area was small.

In the present study, in TOF-MRA images after Pipeline Flex placement, there were cases in which occlusion of the parent artery was difficult and which were mistakenly diagnosed as incomplete intra-aneurysmal occlusion due to the intra-aneurysmal thrombosis signals (Fig 3). The aneurysm will be completely oc-

cluded by promoting intra-aneurysmal thrombosis after flow-diverter placement. It is reported that TOF-MRA shows a high-intensity signal from an acute-to-subacute phase of thrombus formation.<sup>25</sup> The thrombosis signal change of TOF-MRA was particularly frequent in the cavernous segment, the segment in which additional coiling was not required, presumably because the thrombosis occurred slowly and it was easy to pick up the signal change in TOF-MRA. The Silent MRAs and the 3D images were reconstituted by subtraction of data from the control image of those obtained by labeling pulse, signals of thrombosis after the flow-diverter placement can be removed. This means that Silent MRA does not pick up a thrombosis signal, but, like DSA, it shows only a blood flow signal into the aneurysm as a signal change. Similarly, in contrast-enhanced MRA, signals of thrombosis can be eliminated by the subtraction between control and contrast-enhanced images. However, it is possible that false-positive alterations of intra-aneurysmal signals such as venous contamination and enhancement of the aneurysmal wall were observed with contrast-enhanced MRA.<sup>30</sup> In any event, postoperative assessment of a flow-diverter device that promotes aneurysmal thrombosis may be difficult by TOF-MRA. In the present study, signal alterations due to thrombosis were examined in chronologic order (Fig 3). Immediately after the treatment, there was no area with high-intensity signals on the T1-weighted image. Six months later, signals due to thrombosis reached a peak, and 1 year later the signals slightly decreased. Immediately after the treatment, Silent MRA visualized intra-aneurysmal signal alteration due to the remaining blood, while at 6 months and again at 1 year later, no signal alterations were observed. Furthermore, it was found that the percentage of agreement in the assessment of intra-aneurysmal embolization on Silent MRA was higher than that on TOF-MRA.

**Table 5: Comparison of embolization assessment among DSA, Silent MRA, and TOF-MRA after flow-diverter device placement**

		DSA	
		CO (n = 55)	IO (n = 23)
Silent MRA	CO (n = 58)	53	5
	IO (n = 20)	2	18
TOF-MRA	CO (n = 52)	47	7
	IO (n = 26)	8	16

**Note:**—CO indicates complete occlusion; IO, incomplete occlusion.

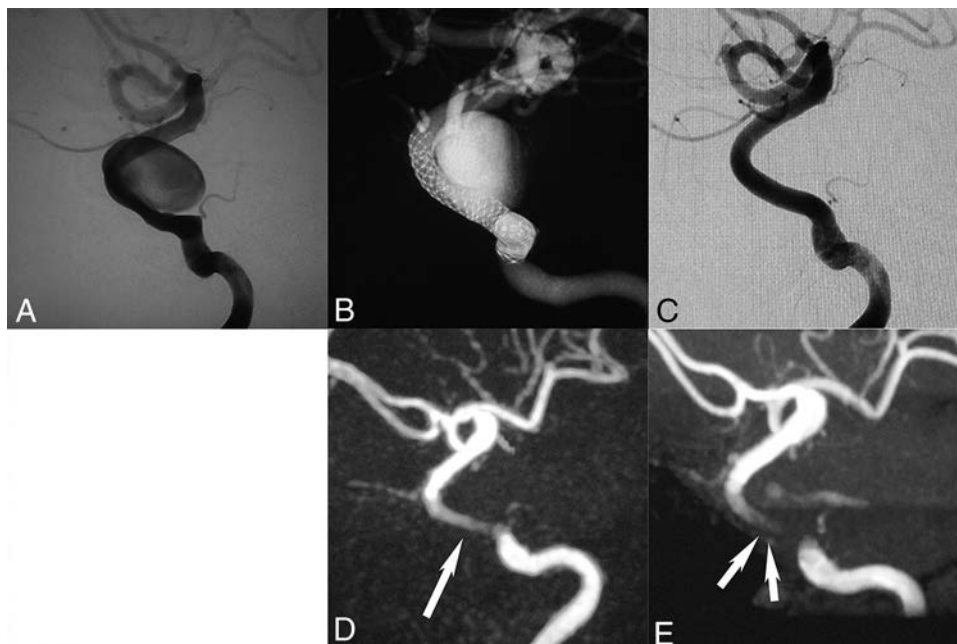


**FIG 2.** A, An 82-year-old woman. Flow-diverter placement in the left internal carotid artery cavernous segment aneurysm (20.1 × 6.3 mm) was performed with the Pipeline Flex (4.5 × 25 mm). B, Digital subtraction angiography shows the location of the Pipeline Flex by conebeam CT. C, The 6-month follow-up DSA shows complete occlusion of the aneurysm. D, This Silent MRA shows an excellent signal flow in the Pipeline Flex (arrow) but no intra-aneurysmal signal. E, This time-of-flight MRA almost lost the signal in the Pipeline Flex (double arrows) and has a faint signal in the aneurysm. The scores of the Silent MRA by 3 observers were 4, 3, and 4, and those of the TOF-MRA were 2, 2, and 2.

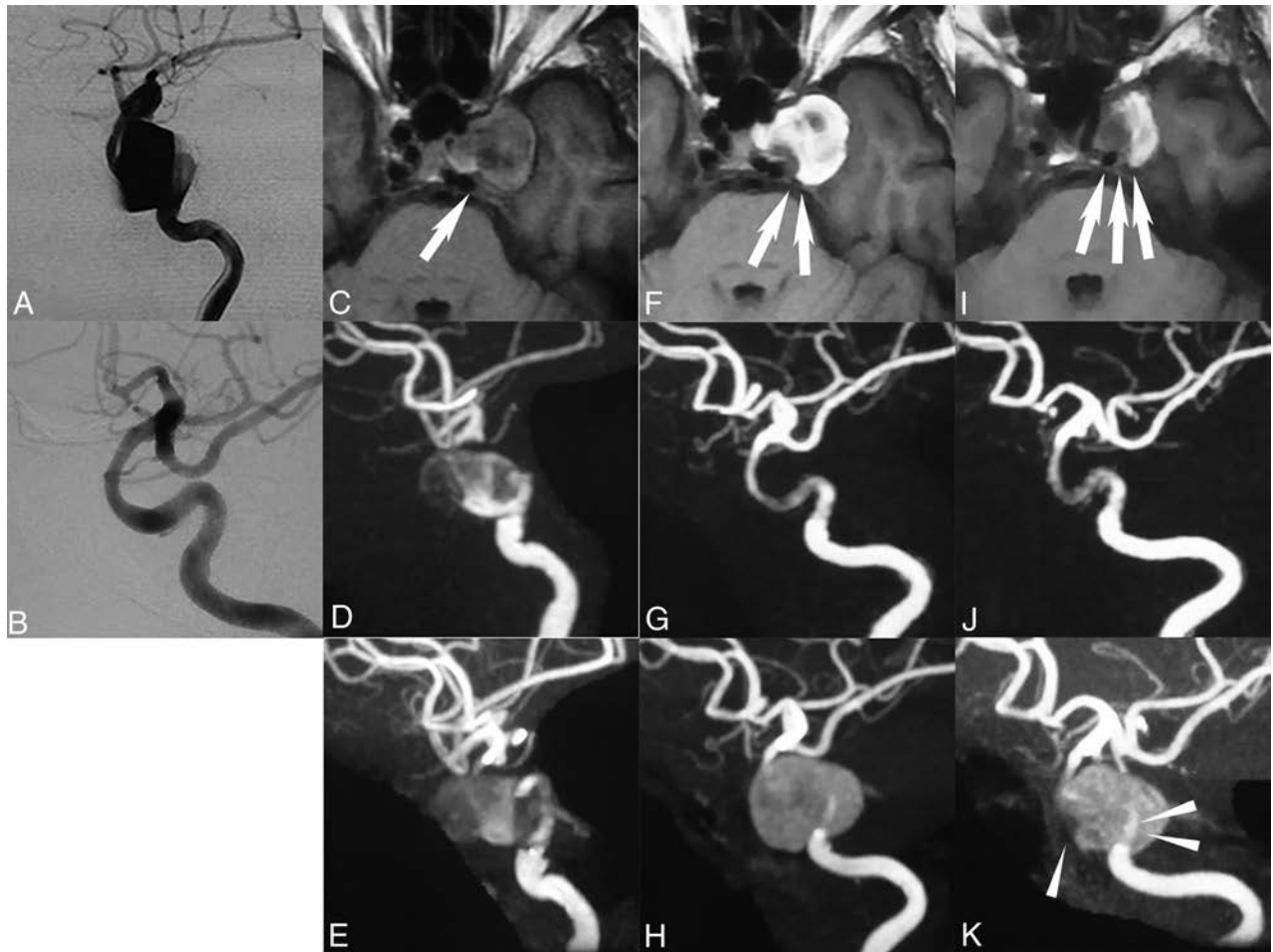


**FIG 3.** A 75-year-old woman. *A*, The aneurysm (26.2 × 6.1 mm) was located in the left internal carotid artery paraclinoid segment. *B*, A 6-month follow-up DSA shows almost complete occlusion of the aneurysm. *C*, The MRA T1-weighted image immediately after the operation shows an intra-aneurysmal isointensity signal (arrow). *D* and *E*, Both Silent MRA and TOF-MRA show an intra-aneurysmal signal that had a negative influence on the parent artery assessment. *F*, A 6-month follow-up T1-weighted image shows an intra-aneurysmal high-intensity signal, which means thrombosis (double arrows). *G*, A 6-month follow-up, Silent MRA shows excellent signal flow in the Pipeline Flex. *H*, A 6-month follow-up TOF-MRA shows that the image could not be assessed by the intra-aneurysmal thrombosed signal. *I*, The 1-year follow-up T1-weighted MR image shows a lower intra-aneurysmal high-intensity signal decrease than at the 6-month follow-up (triple arrows). *J*, The 1-year follow-up findings on the Silent MRA signal flow were the same as at the 6-month follow-up. *K*, The 1-year follow-up on TOF-MRA shows a better signal flow than at the 6-month follow-up TOF-MRA (arrowhead) by improvement of the thrombosed aneurysm (double arrowheads), but the signal flow on the Silent MRA is better than that on the TOF-MRA. The scores of the 6-month follow-up Silent MRA by 3 independent observers were 4, 4, and 4. The scores of the TOF-MRA were 1, 1, and 1.

Especially, intra-aneurysmal thrombosis was likely to contribute to the high rate of false-positive signals on TOF-MRA.

In the present study, there were 2 cases in which TOF-MRA showed significantly better images than Silent MRA (Fig 4). In 1 patient, a 65-year-old woman, the images were not clear, probably due to artifacts caused by the woman's denture. Because the arterial spin-labeling technique was used for Silent MRA, a labeling pulse was performed through the patient's cervical region. Therefore, although Silent MRA is useful even if there are intracranial metal artifacts, cervical artifacts such as a denture could possibly influence the image. The other case was that of a 73-year-old woman. This patient was claustrophobic and could not stay still during the MR imaging examination. As a result, visualization was poor due to motion artifacts. Silent MRA imaging takes 12 minutes 13 seconds, which is significantly longer than the 4 minutes 45 seconds needed for a TOF-MRA. Therefore, for claustro-

phobic patients, children, or elderly and postoperatively restless patients, TOF-MRA is preferable.

There are some limitations to the present study. First, we have not assessed contrast-enhanced MRA. There have been some studies that report that contrast-enhanced MRA is excellent for the postoperative assessment of stent placement and flow-diverter placement. Although Silent MRA was found to be superior to TOF-MRA in the present study, comparison with contrast-enhanced MRA is warranted. Second, the present assessment was limited to internal carotid aneurysms. Recently, flow-diverter devices for the posterior circulation have been developed, and their usefulness has been demonstrated.<sup>31</sup> In the future, the assessment of the posterior circulation should be performed. Third, the present study was retrospective. A prospective study with a high level of evidence-based medicine would be desirable.

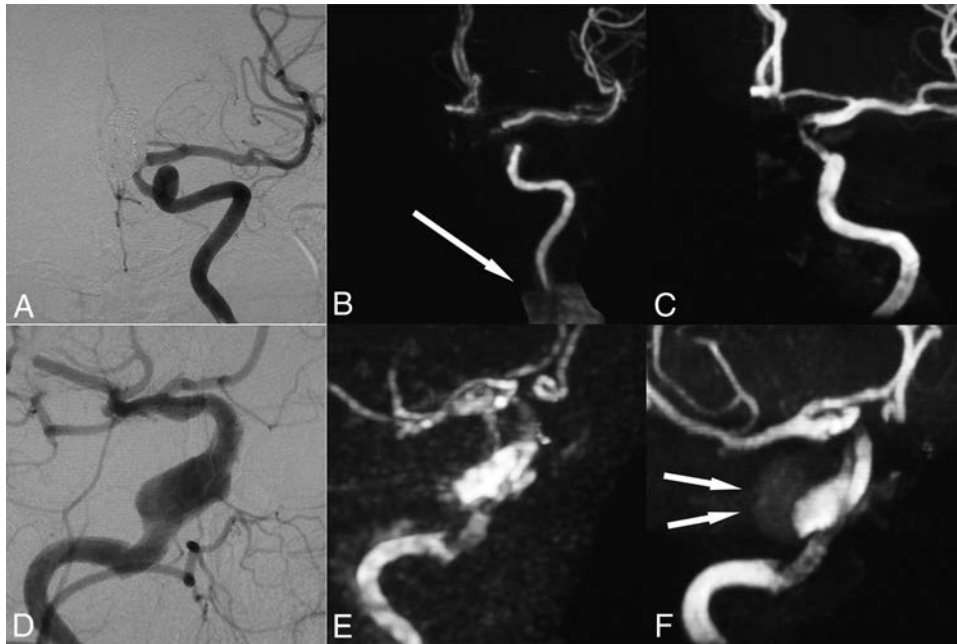


**FIG 4.** A–C, A 62-year-old woman. A, The 6-month follow-up DSA shows complete occlusion and good patency in the Pipeline Flex. B and C, The 6-month follow-up Silent MRA shows a worse signal flow than the TOF-MRA due to artifacts caused by the left denture (arrow). The Silent MRA scores by 3 independent observers were 2, 1, and 2, while the TOF-MRA scores were 3, 2, and 3. D–F, A 73-year-old woman. D, The 6-month follow-up DSA shows complete occlusion and good patency in the Pipeline Flex. E and F, The 6-month follow-up Silent MRA shows a poor signal caused by motion artifacts because the patient was claustrophobic and moved during the procedure, and TOF-MRA also shows a poor signal flow caused by an intra-aneurysmal thrombosis after the Pipeline Flex placement (double arrows). The scores of Silent MRA by 3 independent observers were 3, 3, and 3. The scores of TOF-MRA were 2, 3, and 4.

## CONCLUSIONS

In the postoperative assessment of Pipeline Flex placement for large and giant unruptured internal carotid aneurysms after 6 months, Silent MRA showed superior visualization of both in-stent signals and the status of intra-aneurysmal embolization compared with TOF-MRA. Given these results, Silent MRA techniques to assess intra-aneurysmal blood flow after Pipeline Flex placement will become more effective.

Disclosures: Hidenori Oishi—RELATED: Grant: Medtronic, Comments: a donation in the form of a research fund to the endowed chair; Consulting Fee or Honorarium: Medtronic, Comments: More than one million Japanese yen. Shigeki Aoki—UNRELATED: Grants/Grants Pending: Mediphsysics, Toshiba, Bayer AG, Daiichi Sankyo, Eisai, Fujiyaku, Fujifilm RI, Guerbet, Comments: grant for diagnostic radiology\*; Payment for Lectures Including Service on Speakers Bureaus: Mediphsysics, Toshiba, Bayer AG, Daiichi Sankyo, Eisai, Fujiyaku, Fujifilm RI, Canon, Guerbet, Comments: grant for diagnostic radiology; Payment for Manuscript Preparation: honorarium for lectures/chair from GE Healthcare, Toshiba/Canon, Hitachi, Siemens, Bayer AG, Daiichi Sankyo, Eisai, Fujiyaku, Fujifilm RI, Mediphsysics, Novartis, Takeda Pharmaceutical Company, Biogen, Chugai Pharmaceutical Co was paid to individual; Payment for Development of Educational Presentations: Gakken Medical Shujunsha, Miwa Shoten Publishers. \*Money paid to the institution.

## REFERENCES

- Nelson PK, Lylyk P, Szikora I, et al. **The Pipeline Embolization Device for the intracranial treatment of aneurysms trial.** *AJNR Am J Neuroradiol* 2011;32:34–40 CrossRef Medline
- Becske T, Kallmes DF, Saatci I, et al. **Pipeline for uncoilable or failed aneurysms: results from a multicenter clinical trial.** *Radiology* 2013; 267:858–68 CrossRef Medline
- Kallmes DF, Hanel R, Lopes D, et al. **International retrospective study of the Pipeline Embolization Device: a multicenter aneurysm treatment study.** *AJNR Am J Neuroradiol* 2015;36:108–15 CrossRef Medline
- Liu JM, Zhou Y, Li Y, et al; PARAT investigators. **Parent artery reconstruction for large or giant cerebral aneurysms using the Tubridge Flow Diverter: a multicenter, randomized, controlled clinical trial (PARAT).** *AJNR Am J Neuroradiol* 2018;39:807–16 CrossRef Medline
- Keskin F, Erdi F, Kaya B, et al. **Endovascular treatment of complex intracranial aneurysms by Pipeline flow-diverter embolization device: a single-center experience.** *Neurol Res* 2015;37:359–65 CrossRef Medline
- Lubicz B, Van der Elst O, Collignon L, et al. **Silk flow-diverter stent for the treatment of intracranial aneurysms: a series of 58 patients with emphasis on long-term results.** *AJNR Am J Neuroradiol* 2015; 36:542–46 CrossRef Medline
- Ferns SP, Sprengers ME, van Rooij WJ, et al. **Coiling of intracranial aneurysms: a systematic review on initial occlusion and reopening and retreatment rates.** *Stroke* 2009;40:e523–29 CrossRef Medline
- Kanaan H, Jankowitz B, Aleu A, et al. **In-stent thrombosis and stenosis after neck-remodeling device-assisted coil embolization of intracranial aneurysms.** *Neurosurgery* 2010;67:1523–32; discussion 1532–33 CrossRef Medline
- Mocco J, Fargen KM, Albuquerque FC, et al. **Delayed thrombosis or stenosis following Enterprise-assisted stent-coiling: is it safe? Mid-term results of the interstate collaboration of Enterprise stent coiling.** *Neurosurgery* 2011;69:908–13; discussion 913–14 CrossRef Medline
- Briganti F, Leone G, Marseglia M, et al. **Endovascular treatment of cerebral aneurysms using flow-diverter devices: a systematic review.** *Neuroradiol J* 2015;28:365–75 CrossRef
- Agid R, Schaaf M, Farb R. **CE-MRA for follow-up of aneurysms post stent-assisted coiling.** *Interv Neuroradiol* 2012;18:275–83 CrossRef Medline
- Boddu SR, Tong FC, Dehkharghani S, et al. **Contrast-enhanced time-resolved MRA for follow-up of intracranial aneurysms treated with the Pipeline Embolization Device.** *AJNR Am J Neuroradiol* 2014;35: 2112–18 CrossRef Medline
- Penfield JG, Reilly RF. **Nephrogenic systemic fibrosis risk: is there a**

- difference between gadolinium-based contrast agents? *Semin Dial* 2008;21:129–34 CrossRef Medline
14. Cho WS, Kim SS, Lee SJ, et al. **The effectiveness of 3T time-of-flight magnetic resonance angiography for follow-up evaluations after the stent-assisted coil embolization of cerebral aneurysms.** *Acta Radiol* 2014;55:604–13 CrossRef Medline
  15. Cho YD, Kim KM, Lee WJ, et al. **Time-of-flight magnetic resonance angiography for follow-up of coil embolization with Enterprise stent for intracranial aneurysm: usefulness of source images.** *Korean J Radiol* 2014;15:161–68 CrossRef Medline
  16. Irie R, Suzuki M, Yamamoto M, et al. **Assessing bold flow in an intracranial stent: a feasibility study of MR angiography using a Silent scan after stent-assisted coil embolization for anterior circulation aneurysms.** *AJNR Am J Neuroradiol* 2015;36:967–70 CrossRef Medline
  17. Takano N, Suzuki M, Irie R, et al. **Usefulness of non-contrast-enhanced MR angiography using a Silent scan for follow-up after Y-configuration stent-assisted coil embolization for basilar tip aneurysms.** *AJNR Am J Neuroradiol* 2017;38:577–81 CrossRef Medline
  18. Takano N, Suzuki M, Irie R, et al. **Non-contrast-enhanced Silent scan MR angiography of intracranial anterior circulation aneurysms treated with a low-profile visualized intraluminal support device.** *AJNR Am J Neuroradiol* 2017;38:1610–16 CrossRef Medline
  19. Attali J, Benaissa A, Soize S, et al. **Follow-up of intracranial aneurysms treated by flow diverter: comparison of three-dimensional time-of-flight MR angiography (3D-TOF-MRA) and contrast-enhanced MR angiography (CE-MRA) sequences with digital subtraction angiography as the gold standard.** *J Neurointerv Surg* 2016;8:81–86 CrossRef Medline
  20. Patzig M, Forbrig R, Ertl L, et al. **Intracranial aneurysms treated by flow-diverting stents: long-term follow-up with contrast-enhanced magnetic resonance angiography.** *Cardiovasc Intervent Radiol* 2017;40:1713–22 CrossRef Medline
  21. Benaissa A, Tomas C, Clarençon F, et al. **Retrospective analysis of delayed intraparenchymal hemorrhage after flow-diverter treatment: presentation of a retrospective multicenter trial.** *AJNR Am J Neuroradiol* 2016;37:475–80 CrossRef Medline
  22. Cruz JP, Chow M, O’Kelly C, et al. **Delayed ipsilateral parenchymal hemorrhage following flow diversion for the treatment of anterior circulation aneurysms.** *AJNR Am J Neuroradiol* 2012;33:60–68 CrossRef Medline
  23. Kulcsár Z, Houdart E, Bonafe A, et al. **Intra-aneurysmal thrombosis as a possible cause of delayed aneurysm rupture after flow-diversion treatment.** *AJNR Am J Neuroradiol* 2011;32:20–25 CrossRef Medline
  24. Alibek S, Vogel M, Sun W, et al. **Acoustic noise reduction in MRI using Silent Scan: an initial experience.** *Diagn Interv Radiol* 2014;20:360–63 CrossRef Medline
  25. Renard D, Le Bars E, Arquizan C, et al. **Time-of-flight MR angiography in cerebral venous sinus thrombosis.** *Acta Neurol Belg* 2017;117:837–40 CrossRef Medline
  26. Wall A, Kugel H, Bachman R, et al. **3.0 T vs. 1.5 T MR angiography: in vitro comparison of intravascular stent artifacts.** *J Magn Reson Imaging* 2005;22:772–79 CrossRef Medline
  27. Wang Y, Truong TN, Yen C, et al. **Quantitative evaluation of susceptibility and shielding effects of nitinol, platinum, cobalt-alloy, and stainless steel stents.** *Magn Reson Med* 2003;49:972–76 CrossRef Medline
  28. Majoie CB, Sprengers ME, van Rooij WJ, et al. **MR angiography at 3T versus digital subtraction angiography in the follow-up of intracranial aneurysms treated with detachable coils.** *AJNR Am J Neuroradiol* 2005;26:1349–56 Medline
  29. Wallace RC, Karis JP, Partovi S, et al. **Noninvasive imaging of treated cerebral aneurysms, part 1: MR angiographic follow-up of coiled aneurysms.** *AJNR Am J Neuroradiol* 2007;28:1001–08 CrossRef Medline
  30. Choi JW, Roh HG, Moon WJ, et al. **Time-resolved 3D contrast-enhanced MRA on 3.0T: a non-invasive follow-up technique after stent-assisted coil embolization of the intracranial aneurysm.** *Korean J Radiol* 2011;12:662–70 CrossRef Medline
  31. Leucking H, Engelhorn T, Lang S, et al. **FRED flow diverter: a study on safety and efficacy in a consecutive group of 50 patients.** *AJNR Am J Neuroradiol* 2017;38:596–02 CrossRef Medline

# Pointwise Encoding Time Reduction with Radial Acquisition with Subtraction-Based MRA during the Follow-Up of Stent-Assisted Coil Embolization of Anterior Circulation Aneurysms

Y.J. Heo, H.W. Jeong, J.W. Baek, S.T. Kim, Y.G. Jeong, J.Y. Lee, and S.-C. Jin

## ABSTRACT

**BACKGROUND AND PURPOSE:** Time-of-flight MR angiography, though widely used after coil embolization, is associated with limitations owing to magnetic susceptibility and radiofrequency shielding following stent-assisted coil embolization. We evaluated the pointwise encoding time reduction with radial acquisition (PETRA) sequence in subtraction-based MRA (qMRA) using an ultrashort TE relative to TOF-MRA during the follow-up of stent-assisted coil embolization for anterior circulation aneurysms.

**MATERIALS AND METHODS:** Twenty-five patients (3 men and 22 women; mean age,  $59.1 \pm 14.0$  years) underwent stent-assisted coil embolization for anterior circulation aneurysms and were retrospectively evaluated using TOF-MRA and PETRA qMRA data from the same follow-up session. Two neuroradiologists independently reviewed both MRA findings and subjectively graded flow within the stents (relative to the latest DSA findings) and occlusion status (complete occlusion or neck/aneurysm remnant). Interobserver and intermodality agreement for TOF-MRA and PETRA qMRA were evaluated.

**RESULTS:** The mean score for flow visualization within the stents was significantly higher in PETRA qMRA than in TOF-MRA ( $P < .001$  for both observers), and good interobserver agreement was reported ( $\kappa = 0.63$ ). The aneurysm occlusion status of PETRA qMRA (observer 1, 92.0%; observer 2, 88.0%) was more consistent with DSA than with TOF-MRA (observer 1, 76.0%; observer 2, 80.0%), and there was a better intermodality agreement between DSA and PETRA qMRA than between DSA and TOF-MRA.

**CONCLUSIONS:** These findings indicate that PETRA qMRA is a useful follow-up technique for patients who have undergone stent-assisted coil embolization for anterior circulation aneurysms.

**ABBREVIATIONS:** PETRA = pointwise encoding time reduction with radial acquisition; qMRA = subtraction-based MRA

Stent-assisted coil embolization has been widely used for cases in which conventional coil embolization is considered difficult, such as in wide-neck aneurysms. Considering the possibility of recanalization, follow-up imaging is important even after complete occlusion has been achieved. DSA is considered the criterion standard for follow-up to evaluate intra-aneurysmal flow or in-stent restenosis; however, this technique has risks associated with contrast media, procedural invasiveness, and radiation exposure. Contrast-enhanced MRA provides visualization of the remnant neck and stented segments that is similar to that of DSA.<sup>1-3</sup> How-

ever, contrast-enhanced MRA has contrast-associated risks, including nephrogenic systemic fibrosis, anaphylaxis, gadolinium deposition, and the potential for misdiagnosing perianeurysmal enhancement as recanalization.

Nonenhanced TOF-MRA is another established technique used for follow-up after coil embolization. Specifically, it is useful for the evaluation of the residual lumen of aneurysms.<sup>4</sup> However, this approach is difficult in cases with stent-assisted coil embolization because visualizing blood flow within intracranial stents and the parent artery is complicated by radiofrequency shielding and susceptibility artifacts.<sup>2,5</sup> These can obscure the neck remnant and adjacent structures as a result of signal loss. Several trials have attempted to overcome these problems when using MRA after stent-assisted coil embolization.<sup>6-10</sup> For example, ultrashort-TE MRA is known to decrease the susceptibility artifacts caused by metallic devices and to increase the signal intensity within the stent.<sup>11,12</sup> Recently, a few studies<sup>7-9</sup> have highlighted the efficacy of Silent MRA (GE Healthcare, Milwaukee, Wisconsin) using an ultrashort TE after stent-assisted coil embolization.

Received November 23, 2018; accepted after revision March 11, 2019.

From the Departments of Radiology (Y.J.H., H.W.J., J.W.B.), Neurosurgery (S.T.K., Y.G.J.), and Internal Medicine (J.Y.L.), Inje University Busan Paik Hospital, Busan, Korea; and Department of Neurosurgery (S.-C.J.), Inje University Haeundae Paik Hospital, Busan, Korea.

This work was supported by the 2018 Inje University research grant.

Please address correspondence to Hae Woong Jeong, MD, PhD, Department of Radiology, Inje University Busan Paik Hospital, Bokji-ro 75, Busanjin-Gu, Busan, Korea, 47392; e-mail: hwjeong2000@hanmail.net

<http://dx.doi.org/10.3174/ajnr.A6035>

The present study evaluated another nonenhanced MRA technique using ultrashort TE, known as pointwise encoding time reduction with radial acquisition (PETRA). Our results indicate that PETRA showed a higher SNR compared with the conventional ultrashort TE. This was due to a shorter encoding time for whole  $k$ -space, which was required before the signal decayed.<sup>13</sup> To the best of our knowledge, PETRA with subtraction-based MRA (qMRA) has not been studied following stent-assisted coil embolization. Therefore, we aimed to evaluate its utility relative to TOF-MRA during follow-up after stent-assisted coil embolization for anterior circulation aneurysms.

## MATERIALS AND METHODS

### Patients

This retrospective study evaluated 25 patients (22 women and 3 men; mean age,  $59.1 \pm 14.0$  years) who underwent stent-assisted coil embolization for unruptured aneurysms in the anterior circulation (24 cases in the paraclinoid segment of the ICA, 1 case in the anterior communicating artery) between September 2017 and October 2018. All subjects underwent TOF-MRA and PETRA qMRA during the same follow-up session. The retrospective protocol of the study was approved by the Inje University Busan Paik Hospital institutional review board.

Eighteen patients were treated using a Neuroform stent (Stryker Neurovascular, Kalamazoo, Michigan), 6 patients were treated with an Enterprise stent (Codman & Shurtleff, Raynham, Massachusetts), and 1 patient was treated using both stents. Endovascular therapy and DSA were performed using a biplane angiographic unit (Integris V, Philips Healthcare, Best, the Netherlands; or Artis zee biplane system, Siemens, Erlangen, Germany). Complete occlusion was identified in 15 cases, and a residual neck was observed in 10 cases, based on the latest DSA findings.

### Imaging Acquisition

Intracranial TOF-MRA and PETRA qMRA were performed during the same follow-up session using 3T MR imaging (Magnetom Skyra; Siemens) with a 64-channel head-neck coil. The PETRA qMRA technique has been described previously<sup>14</sup> and is commercially available. Briefly, labeled and control data were obtained; the labeled data were applied to the slice-selective saturation pulse for the carotid artery (ie, arterial inflow appears dark). The saturation pulse of control data was applied to the 10 mm above the vertex of the head, and the subtracted MRA showed dark background tissue and suppressed venous flow. The detailed scan parameters for PETRA qMRA: TR/TE, 3.52/0.07 ms; flip angle, 6°; FOV, 230 × 230 mm; matrix, 320 × 320; radial sampling, 20,000 radial spokes; voxel size,  $0.72 \times 0.72 \times 0.72$  mm<sup>3</sup>; section thickness, 0.72 mm; NEX, 1; bandwidth, 363 Hz/pixel; slice-selective saturation pulse applied once per 20 TRs; and acquisition time, 2 minutes 10 seconds. The detailed scan parameters for TOF-MRA: TR/TE, 24/3.99 ms; flip angle, 20°; FOV, 220 × 177 mm; matrix, 576 × 302; voxel size,  $0.38 \times 0.38 \times 0.38$  mm<sup>3</sup>; section thickness, 0.6 mm; NEX, 1; bandwidth, 185 Hz/pixel; acquisition time, 6 minutes 40 seconds; number of slab, 6. The maximum intensity projections for both sequences were reconstructed in the same manner as the DSA images.

### Image Analysis

Two neuroradiologists independently reviewed both MRA findings at 2-week intervals and subjectively graded the visualization of flow within each stent (relative to the latest DSA findings) using the following scale: 1, no signal within the stent; 2, slightly visible but not of diagnostic quality due to image blurring; 3, good quality with minimal blurring; or 4, excellent quality. The occlusion status of the coiled aneurysm was also evaluated. The locations of the aneurysms were provided to the observers, but they were blinded to the DSA results. However, observers were not blinded to the type of MR images because the 2 MR images are distinctively different in appearance. One experienced interventional neuroradiologist also assessed the occlusion status of the coiled aneurysm using the Montreal Neurological Institute scale.<sup>15</sup> Specifically, patients were rated as having complete occlusion, subtotal occlusion (residual neck, residual aneurysm), or incomplete occlusion. The latest DSA images were used as references, and the average interval between the latest DSA and the MRA follow-up was 16 months, with a range of 1 day to 127 months.

### Statistical Analyses

Continuous variables are presented as mean  $\pm$  SD. We compared the mean scores for each MRA technique and type of intracranial stent using the Wilcoxon signed rank test and the Mann-Whitney test. Weighted  $\kappa$  coefficients were used to evaluate the interobserver and intermodality agreement for TOF-MRA and PETRA qMRA. The results were classified as poor ( $<0.20$ ), fair (0.21–0.40), moderate (0.41–0.60), good (0.61–0.80), or excellent (0.81–1.00).<sup>16</sup> All statistical analyses were performed using SPSS software (Version 24.0; IBM, Armonk, New York) and MedCalc for Windows (Version 18.11.3; MedCalc Software, Mariakerke, Belgium).  $P$  values  $< .05$  were considered statistically significant.

## RESULTS

The mean score for assessing blood flow within the intracranial stent was significantly higher in the PETRA qMRA than in the TOF-MRA (observer one:  $3.40 \pm 0.87$  for PETRA qMRA and  $2.20 \pm 0.87$  for TOF-MRA,  $P < .001$ ; observer two:  $3.60 \pm 0.76$  for PETRA qMRA and  $2.44 \pm 0.77$  for TOF-MRA,  $P < .001$ ) with good interobserver agreement for both MRA techniques ( $\kappa = 0.63$  for PETRA qMRA, 95% CI, 0.35–0.90;  $\kappa = 0.63$  for TOF-MRA, 95% CI, 0.43–0.83). The Neuroform stents (open-cell design) were associated with higher scores than the Enterprise stents (closed-cell design) for both PETRA qMRA and TOF-MRA; however, no significant differences were detected between the 2 intracranial stents (Table 1). On the basis of the latest DSA findings, complete occlusion was achieved in 15 cases (60.0%) and a residual neck was observed in 10 cases (40.0%). PETRA qMRA findings were consistent with DSA findings in 23 cases (92.0%) according to observer 1 and 22 cases (88.0%) according to observer 2. Therefore, the intermodality agreement between PETRA qMRA and DSA was excellent according to observer 1 (weighted  $\kappa = 0.83$ ; 95% CI, 0.60–1.00) and good according to observer 2 (weighted  $\kappa = 0.73$ ; 95% CI, 0.47–1.00) (Table 2). However, only 19 cases (76.0%) of TOF-MRA findings were consistent with DSA according to observer 1 and 20 cases (80.0%) according to ob-

server 2. Thus, the intermodality agreement between TOF-MRA and DSA was moderate in both observer 1 (weighted  $\kappa = 0.44$ ; 95% CI, 0.12–0.77) and observer 2 (weighted  $\kappa = 0.55$ ; 95% CI, 0.23–0.86) (Figs 1 and 2).

## DISCUSSION

The present study revealed that PETRA qMRA provided better visualization of intracranial stent flow than TOF-MRA, regardless of stent type. Furthermore, PETRA qMRA showed higher intermodality agreement with DSA than TOF-MRA. In the 2 cases in which PETRA qMRA failed to detect the residual neck, the intervals between the last DSA and the MRA were 31 and 15 months. Santillan et al<sup>17</sup> reported cumulative occlusion after the first treatment, and our cases may have involved progressive occlusion within the aneurysms. In cases in which PETRA qMRA identified the residual neck, its configuration was more similar to DSA find-

ings than to TOF-MRA findings. These results suggest that PETRA qMRA could be a useful imaging technique following stent-assisted coil embolization.

The increased use of intracranial stent placement has also increased the difficulty of using follow-up imaging to assess the recanalization status or stability of the stent. Although DSA is an established technique for follow-up, it also has risks related to contrast media (eg, nephrogenic systemic fibrosis), neurologic complications (eg, embolic infarction),<sup>18</sup> and radiation exposure. Contrast-enhanced MRA provides better delineation of the parent artery and is correlated with DSA findings; however, it can also cause contrast-related complications. Furthermore, contrast-enhanced MRA can produce a false-positive result that indicates a residual neck, which is caused by peripheral enhancement of the thrombus or vasa vasorum within the aneurysmal wall.<sup>19,20</sup> In contrast, TOF-MRA is a noninvasive imaging technique that is used following intracranial stent insertion. However, TOF-MRA is prone to susceptibility artifacts, which can generate false-positive or false-negative results at the stent insertion site. Various trials have attempted to overcome these problems.<sup>4,10,21</sup> Additionally, some reports have described the value of the ultrashort-TE technique in this setting,<sup>4,6–9</sup> which can significantly reduce susceptibility artifacts and decrease the phase dispersion of labeled flow.<sup>22,23</sup>

Irie et al<sup>6</sup> reported that Silent MRA with an ultrashort TE is useful for visualizing flow within an intracranial stent and the occlusion status of aneurysms. Furthermore, there is a strong positive correlation between the results obtained using Silent MRA and DSA. PETRA qMRA also uses an ultrashort TE, and our findings indicate that the results from this technique are strongly correlated with those from Silent MRA. Similar to Silent MRA, PETRA qMRA uses subtraction of scanned images from before and after labeling. This makes it difficult to assess static tissue and may prevent detection of in-stent thrombus, which is visualized as a high-intensity signal during TOF-MRA. Although in-stent thrombosis can occasionally occur after stent insertion for atherosclerotic stenosis, it is uncommon and usually asymptomatic or it spontaneously regresses in patients who undergo stent-assisted coil embolization.<sup>17,24</sup> PETRA qMRA is associated with poorer

**Table 1: Comparison of PETRA qMRA and TOF-MRA according to stent design<sup>a</sup>**

	Enterprise (n = 6)	Neuroform (n = 18)	P Value
PETRA qMRA			
Observer 1	2.83 ± 1.17	3.50 ± 0.71	.224
Observer 2	3.33 ± 0.82	3.89 ± 0.32	.156
Mean for 2 observers	3.08 ± 0.97	3.69 ± 0.42	.177
TOF-MRA			
Observer 1	2.00 ± 0.90	2.33 ± 0.84	.454
Observer 2	2.17 ± 0.41	2.61 ± 0.78	.137
Mean for 2 observers	2.08 ± 0.58	2.47 ± 0.78	.224

<sup>a</sup>Data are presented as means.

**Table 2: Comparison of occlusion status of coiled aneurysms between PETRA qMRA and TOF-MRA<sup>a</sup>**

	PETRA qMRA	TOF-MRA
Observer 1		
Complete occlusion	100.0% (17/15)	100.0% (21/15)
Residual neck	80.0% (8/10)	40.0% (4/10)
Observer 2		
Complete occlusion	100% (17/15)	100.0% (20/15)
Residual neck	70.0% (7/10)	50.0% (5/10)
Interobserver agreement	0.90 (95% CI, 0.72–1.00)	0.86 (95% CI, 0.61–1.00)

<sup>a</sup>Data represent sensitivity (number of cases).



**FIG 1.** A 54-year-old man with a left paraclinoid internal carotid artery aneurysm who underwent stent-assisted coil embolization using a Neuroform stent. A, The follow-up DSA reveals the neck remnant (arrow). B, The PETRA qMRA reveals minimal signal loss at the stent insertion site, and the neck remnant is clearly visible (arrow). C, The TOF-MRA reveals mild signal loss at the stent insertion site and a less prominent neck remnant relative to the PETRA qMRA.

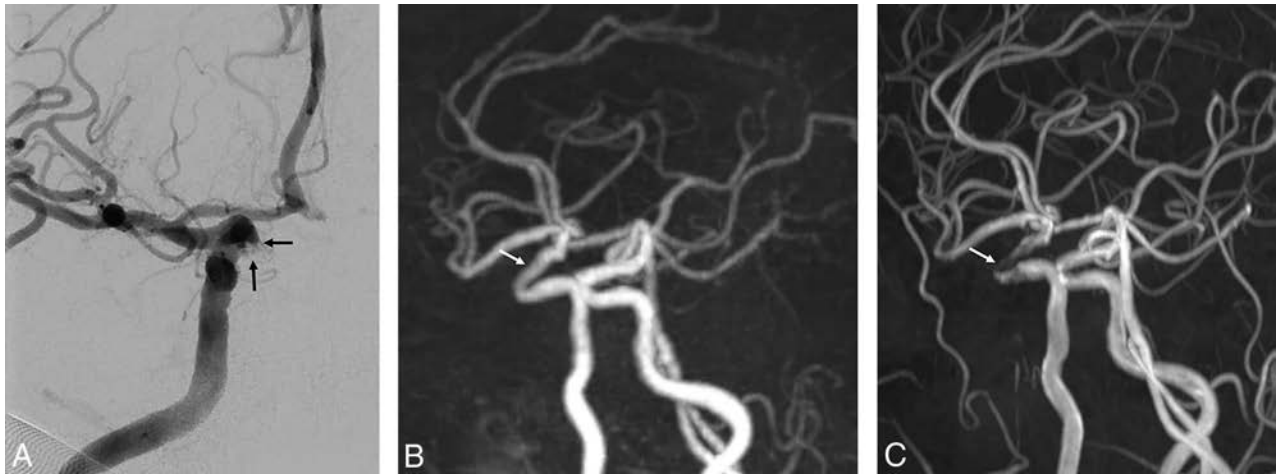


**FIG 2.** A 70-year-old woman with a right paraclinoid internal carotid artery aneurysm who underwent stent-assisted coil embolization using an Enterprise stent. *A*, The follow-up DSA reveals the neck remnant (arrows), and the neck remnant is clearly visible. *B*, The PETRA qMRA reveals minimal signal loss at the stent-injection-site remnant (arrow), and the neck remnant is clearly visible. *C*, The TOF-MRA reveals marked signal loss at the stent-injection-site remnant (arrow) and poor differentiation of the prominent neck remnant relative to PETRA qMRA.

imaging quality than TOF-MRA, which is another disadvantage of PETRA qMRA, like Silent MRA. Although, Silent MRA is associated with better background suppression, it has been reported that it showed more blurring and a lower SNR than TOF-MRA because of its longer readout time.<sup>25</sup> Conversely, PETRA qMRA had a shorter acquisition time (approximately 2 minutes) than Silent MRA and TOF-MRA (approximately 6–7 minutes) using a highly undersampled outer  $k$ -space.<sup>13</sup>

The degree of artifacts associated with an intracranial stent can vary according to the material, cell design, and strut thickness. For example, previous reports have indicated that stents made using stainless steel or cobalt are associated with more artifacts than nitinol stents.<sup>10,26,27</sup> The present study included only patients who were treated with nitinol stents, albeit with different cell designs (open cell versus closed cell) and strut thicknesses. Although the Neuroform stent has an open-cell design, thinner struts, and better intrastent flow than the Enterprise stent (a closed-cell design with thicker struts), there were no significant differences between the 2 intracranial stents according to the analyses of the 2 observers. We believe that this was due to the small sample size of this study. Similarly, previous studies<sup>5,21,28</sup> have demonstrated that the Neuroform stent generated fewer artifacts than the Enterprise stent because the thinner struts generated less radiofrequency shielding.<sup>5,7,11</sup>

The present study has several limitations. First, the retrospective design is prone to selection bias. Second, there was a long interval between the latest DSA and MRA, which may indicate that the patients were evaluated with MRA when they were at a slightly different status from that in their last DSA. However, we do not regularly perform DSA for patients who do not show evidence of recanalization during follow-up MRA due to the invasiveness of the procedure and the possibility of neurologic complications. Therefore, shorter intervals between the latest DSA and MRA could not be achieved. Additionally, we did not compare our results with those of contrast-enhanced MRA, which is considered a useful follow-up technique for stent-assisted coil embolization.<sup>21,29</sup> Thus, future studies comparing PETRA qMRA with contrast-enhanced MRA are necessary. Furthermore, we

evaluated cases that involved nitinol stents, which have fewer artifacts than stents made using other materials. Further studies should be conducted to determine whether our findings are consistent with the use of stainless steel, platinum, and cobalt stents. Finally, this study had a small sample size; future studies should include a large sample size to confirm the effectiveness of PETRA qMRA.

## CONCLUSIONS

Our results show that PETRA qMRA provides clear visualization of intracranial stent flow in the anterior circulation. Additionally, PETRA qMRA was more similar to the occlusion status of DSA than TOF-MRA. Overall, it appears that PETRA qMRA could be a useful follow-up technique for patients who have undergone stent-assisted coil embolization for anterior circulation aneurysms.

## ACKNOWLEDGMENTS

The authors thank Kang Soo Kim (Siemens Healthcare, Korea) for technical advice.

Disclosures: Young Jin Heo—RELATED: Grant: 2018 Inje University research grant.

## REFERENCES

1. Agid R, Willinsky R, Lee SK, et al. **Characterization of aneurysm remnants after endovascular treatment: contrast-enhanced MR angiography versus catheter digital subtraction angiography.** *AJNR Am J Neuroradiol* 2008;29:1570–74 CrossRef Medline
2. Lubicz B, Levivier M, Sadeghi N, et al. **Immediate intracranial aneurysm occlusion after embolization with detachable coils: a comparison between MR angiography and intra-arterial digital subtraction angiography.** *J Neuroradiol* 2007;34:190–97 CrossRef Medline
3. Kaufmann TJ, Huston J 3rd, Cloft HJ, et al. **A prospective trial of 3T and 1.5T time-of-flight and contrast-enhanced MR angiography in the follow-up of coiled intracranial aneurysms.** *AJNR Am J Neuroradiol* 2010;31:912–18 CrossRef Medline
4. Gönner F, Heid O, Remonda L, et al. **MR angiography with ultra-short echo time in cerebral aneurysms treated with Guglielmi detachable coils.** *AJNR Am J Neuroradiol* 1998;19:1324–28 Medline
5. Cho WS, Kim SS, Lee SJ, et al. **The effectiveness of 3T time-of-flight magnetic resonance angiography for follow-up evaluations after**

- the stent-assisted coil embolization of cerebral aneurysms. *Acta Radiol* 2014;55:604–13 CrossRef Medline
6. Irie R, Suzuki M, Yamamoto M, et al. Assessing blood flow in an intracranial stent: a feasibility study of MR angiography using a silent scan after stent-assisted coil embolization for anterior circulation aneurysms. *AJNR Am J Neuroradiol* 2015;36:967–70 CrossRef Medline
  7. Takano N, Suzuki M, Irie R, et al. Usefulness of non-contrast-enhanced MR angiography using a silent scan for follow-up after Y-configuration stent-assisted coil embolization for basilar tip aneurysms. *AJNR Am J Neuroradiol* 2017;38:577–81 CrossRef Medline
  8. Takano N, Suzuki M, Irie R, et al. Non-contrast-enhanced silent scan MR angiography of intracranial anterior circulation aneurysms treated with a low-profile visualized intraluminal support device. *AJNR Am J Neuroradiol* 2017;38:1610–16 CrossRef Medline
  9. Ye J, Luo X, Qu J, et al. Follow-up assessment of coiled intracranial aneurysms using zTE MRA as compared with TOF MRA: a preliminary image quality study. *Eur Radiol* 2017;27:4271–80 CrossRef Medline
  10. Meyer JM, Buecker A, Spuentrup E, et al. Improved in-stent magnetic resonance angiography with high flip angle excitation. *Invest Radiol* 2001;36:677–81 CrossRef Medline
  11. Choi JW, Roh HG, Moon WJ, et al. Optimization of MR parameters of 3D TOF-MRA for various intracranial stents at 3.0T MRI. *Neurointervention* 2011;6:71–77 CrossRef Medline
  12. Ikushima Y, Hashido T, Watanabe Y, et al. Effects of imaging parameters on the quality of contrast-enhanced MR angiography of cerebral aneurysms treated using stent-assisted coiling: a phantom study. *Magn Reson Med Sci* 2017;16:146–51 CrossRef Medline
  13. Grodzki DM, Jakob PM, Heismann B. Ultrashort echo time imaging using pointwise encoding time reduction with radial acquisition (PETRA). *Magn Reson Med* 2012;67:510–18 CrossRef Medline
  14. Yutaka Natsuaki RG, Grimm R, Grodzki D, et al. PETRA quiet MRA: improved robustness with 3D elastic cross-registration. In: *Proceedings of the Annual Meeting and Exhibition of the International Society for Magnetic Resonance in Medicine*, Singapore. May 7–8, 2016
  15. Raymond J, Guilbert F, Weill A, et al. Long-term angiographic recurrences after selective endovascular treatment of aneurysms with detachable coils. *Stroke* 2003;34:1398–403 CrossRef Medline
  16. Landis JR, Koch GG. The measurement of observer agreement for categorical data. *Biometrics* 1977;33:159–74 Medline
  17. Santillan A, Greenberg E, Patsalides A, et al. Long-term clinical and angiographic results of Neuroform stent-assisted coil embolization in wide-necked intracranial aneurysms. *Neurosurgery* 2012;70:1232–37; discussion 1237 CrossRef Medline
  18. Willinsky RA, Taylor SM, terBrugge K, et al. Neurologic complications of cerebral angiography: prospective analysis of 2,899 procedures and review of the literature. *Radiology* 2003;227:522–28 CrossRef Medline
  19. Gauvrit JY, Leclerc X, Pernodet M, et al. Intracranial aneurysms treated with Guglielmi detachable coils: usefulness of 6-month imaging follow-up with contrast-enhanced MR angiography. *AJNR Am J Neuroradiol* 2005;26:515–21 Medline
  20. Gauvrit JY, Leclerc X, Caron S, et al. Intracranial aneurysms treated with Guglielmi detachable coils: imaging follow-up with contrast-enhanced MR angiography. *Stroke* 2006;37:1033–37 CrossRef Medline
  21. Choi JW, Roh HG, Moon WJ, et al. Time-resolved 3D contrast-enhanced MRA on 3.0T: a non-invasive follow-up technique after stent-assisted coil embolization of the intracranial aneurysm. *Korean J Radiol* 2011;12:662–70 CrossRef Medline
  22. Schmalbrock P, Yuan C, Chakeres DW, et al. Volume MR angiography: methods to achieve very short echo times. *Radiology* 1990;175:861–65 CrossRef Medline
  23. Robson MD, Gatehouse PD, Bydder M, et al. Magnetic resonance: an introduction to ultrashort TE (UTE) imaging. *J Comput Assist Tomogr* 2003;27:825–46 CrossRef Medline
  24. Fiorella D, Albuquerque FC, Woo H, et al. Neuroform in-stent stenosis: incidence, natural history and treatment strategies. *Neurosurgery* 2006;59:34–42 CrossRef
  25. Holdsworth SJ, Macpherson SJ, Yeom KW, et al. Clinical evaluation of Silent T1-weighted MRI and Silent MR angiography of the brain. *AJR Am J Roentgenol* 2018;210:404–11 CrossRef Medline
  26. Bartels LW, Bakker CJ, Viergever MA. Improved lumen visualization in metallic vascular implants by reducing RF artifacts. *Magn Reson Med* 2002;47:171–80 CrossRef Medline
  27. Bartels LW, Smits HF, Bakker CJ, et al. MR imaging of vascular stents: effects of susceptibility, flow, and radiofrequency eddy currents. *J Vasc Interv Radiol* 2001;12:365–71 CrossRef Medline
  28. Lövblad KO, Yilmaz H, Chouiter A, et al. Intracranial aneurysm stenting: follow-up with MR angiography. *J Magn Reson Imaging* 2006;24:418–22 CrossRef Medline
  29. Agid R, Schaaf M, Farb R. CE-MRA for follow-up of aneurysms post stent-assisted coiling. *Interv Neuroradiol* 2012;18:275–83 CrossRef Medline

# Treatment of Wide-Neck Intracranial Aneurysms with the Woven EndoBridge Device Associated with Stenting: A Single-Center Experience

 F. Cagnazzo,  R. Ahmed,  C. Dargazanli,  P.-H. Lefevre,  G. Gascou,  I. Derraz,  S.A. Kalmanovich,  C. Riquelme,  A. Bonafe, and  V. Costalat



## ABSTRACT

**BACKGROUND AND PURPOSE:** The intrasaccular flow disruptor, the Woven EndoBridge device, is increasingly used for the treatment of wide-neck intracranial aneurysms. Due to unfavorable anatomy, additional stent placement is sometimes required to avoid Woven EndoBridge protrusion into bifurcation branches. We report our experience with the Woven EndoBridge associated with stent placement for the treatment of complex intracranial aneurysms.

**MATERIALS AND METHODS:** Patients with aneurysms treated with the Woven EndoBridge Single-Layer plus stent placement were evaluated retrospectively with prospectively maintained data. The technical feasibility, procedural complications, aneurysm occlusion, and clinical outcome were studied.

**RESULTS:** Seventeen patients and aneurysms treated with the Woven EndoBridge plus stent placement were included. The mean aneurysm size was  $7 \pm 3.1$  mm. Aneurysm locations were the following: MCA (10 patients), anterior communicating artery (3 patients), basilar tip (3 patients), and posterior communicating artery (1 patient). Two lesions were ruptured and treated in the acute phase. The Woven EndoBridge and stent placement were successfully delivered in all cases. There were no permanent/major complications. Among the 2 patients with SAH, minor and completely reversible in-stent thrombosis occurred during treatment. An asymptomatic occlusion of the angular artery with a distal nonbifurcation aneurysm was discovered during the angiographic follow-up. Long-term (10.4 months) angiographic complete (Raymond-Roy I) and near-complete (Raymond-Roy II) occlusion was obtained in 11 (69%) and 2 (12.5%) aneurysms, respectively. The mean sizes of aneurysms showing Raymond-Roy I/Raymond-Roy II and Raymond-Roy III occlusion were  $5.5 \pm 2.1$  mm and  $10 \pm 1$  mm, respectively ( $P = .003$ ). The mean fluoroscopy time was  $35 \pm 14$  minutes.

**CONCLUSIONS:** Aneurysm embolization with the Woven EndoBridge device associated with stent placement appears technically feasible and effective for the treatment of lesions with unfavorable anatomy. In our study, this strategy was relatively safe with a low rate of relevant procedure-related adverse events.

**ABBREVIATIONS:** AcomA = anterior communicating artery; PcomA = posterior communicating artery; RR = Raymond-Roy; SL = Single-Layer

Despite the increased operator experience and the improvement of available devices, the endovascular treatment of wide-neck intracranial aneurysms, especially at bifurcation points, remains challenging. Accordingly, more complex endovascular techniques have been developed such as balloon-assisted coiling, stent-assisted coiling, and flow diversion.<sup>1,2</sup> The intrasaccular flow disruptor, the Woven EndoBridge device (WEB; Se-

quent Medical, Aliso Viejo, California), is now a well-established option for the treatment of wide-neck bifurcation aneurysms.<sup>3-6</sup> However, although the WEB treatment procedure is usually a single-step technique, additional stent placement can sometimes be required to prevent the protrusion of the device into the bifurcation arteries.<sup>7</sup> To date, there are no series specifically evaluating treatment-related outcomes of the WEB associated with additional stent placement, to our knowledge. We present a retrospective series of 17 consecutive aneurysms treated with WEB plus stent placement at our institution, discussing the safety and efficacy of this treatment strategy.

## MATERIALS AND METHODS

### Patient Selection

Our hospital institutional review board approved this retrospective study. The prospectively maintained data bases of WEB de-

Received January 3, 2019; accepted after revision March 11.

From the Neuroradiology Department, University Hospital Gui De Chauliac, Centre Hospitalier Universitaire de Montpellier, Montpellier, France.

Please address correspondence to Federico Cagnazzo, MD, Neuroradiology Department, CHU Gui De Chauliac, 80 Ave Augustin Fliche, 34000 Montpellier, France; e-mail: f.cagnazzo86@gmail.com

<http://dx.doi.org/10.3174/ajnr.A6032>

 Indicates article with supplemental on-line tables.

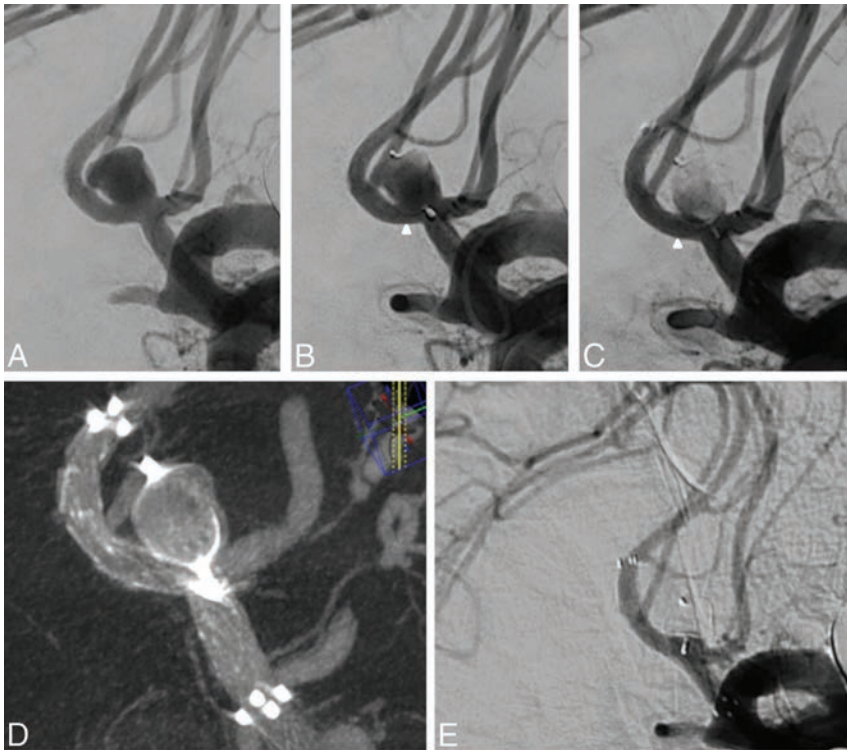


**FIG 1.** A, Patient 5 with a 6 × 4 mm unruptured AcomA aneurysm. B, A WEB-SL (7 × 3 mm) is opened inside the sac, with good aneurysm wall apposition and without impacting the branching vessels. However, after deployment, a protrusion occurred in the right A2 segment, leading to a stenosis (white arrowhead). C, A laser-cut Neuroform Atlas stent (3 × 20 mm) is then delivered to protect the caliber of the artery (white arrowhead). D, A final VasoCT confirms the satisfactory position and wall apposition of the stent and the WEB. E, Twelve-month DSA follow-up shows complete occlusion of the aneurysm.

vices (from January 2014 to December 2018) at our institution were retrospectively reviewed by 2 and, in case of inconsistency, by 3 investigators independently to identify patients with intracranial aneurysms treated with the WEB and requiring additional stent placement to protect the vessel. We included aneurysms embolized with the WEB plus a stent in the same treatment session, excluding lesions in which stent placement was performed in a second treatment. Data collection included the following: demographics, aneurysm characteristics, clinical presentation, details of the treatment, follow-up imaging, and clinical outcome. Treatment strategy was decided by multidisciplinary consensus (vascular neurosurgeons, interventional neuroradiologists). The decision to treat with the WEB plus stent placement was made on the basis of the following situations: 1) planned stent placement: wide-neck lesions with branching vessels coming from the aneurysm for which treatment with adjunctive stent placement was planned beforehand because of the risk of WEB protrusion into the vessel; and 2) unplanned stent placement: slow flow or narrowing of the bifurcation vessel after WEB deployment due to the protrusion of the device into the artery.

#### **Antiplatelet Therapy**

For unruptured aneurysms, antiplatelet therapy included daily dual-antiplatelet medication with aspirin (Kardelic), 75 mg, and clopidogrel (Plavix), 75 mg, starting 5 days before treat-

ment. The therapy was maintained for 3 months. In general, on the basis of the clinical and radiologic evaluations, the patients were switched to aspirin. The VerifyNow P2Y12 assay (Accumetrics, San Diego, California) was used to test the platelet inhibition: Both the P2Y12 and aspirin reaction units were tested. When stents and the WEB were used in patients with acutely ruptured aneurysms, an intravenous bolus of abciximab (0.125 mg/kg) was administered before stent deployment, and standard dual-antiplatelet therapy was started the day after. Concurrent with the procedure, in both unruptured and ruptured aneurysms, intravenous heparinization was performed (activated clotting time maintained above 250 seconds).

#### **Description of Technique**

All patients were treated under general anesthesia via a transfemoral approach. Access to the target aneurysm was obtained in a triaxial fashion. Through a long femoral sheath, a 6F guiding catheter was advanced into the carotid artery. Vessel and aneurysm features were analyzed via biplane and 3D rotational angiography. Size selection of the WEB was derived from the measurements of the aneurysm (width and

height of the dome, width of the neck) based on a 3D rotational angiographic dataset. In general, the device was chosen adding 1 mm to the average width (to assure good wall apposition) and subtracting 1 mm from the average height of the aneurysm (to adjust for the longitudinal increase caused by the horizontal compression).<sup>8</sup> An appropriate VIA Microcatheter (Sequent Medical) was placed inside the aneurysmal fundus followed by the deployment of the WEB under roadmap guidance.

The stent was selected on the basis of the diameter of the artery and was unsheathed under roadmap guidance through an appropriate microcatheter navigated beyond the aneurysm neck. Immediately postdeployment, VasoCT (Philips Healthcare, Best, the Netherlands) with diluted iodinated contrast medium was used to assess both the WEB and stent apposition.

#### **Clinical and Imaging Assessment**

Clinical evaluation was performed preoperatively, postprocedure, throughout the following days, and at discharge. The modified Rankin Scale was used for outcome assessment. Clinical follow-up evaluation was performed at 3, 6, 12, and 24 months. Usually, the degree of aneurysm occlusion was evaluated with MR angiography or digital subtraction angiography at 6 months, followed by long-term (12 and 24 months) DSA follow-up. The aneurysm occlusion rate was defined on the basis of the Raymond-Roy (RR) classification: complete occlu-

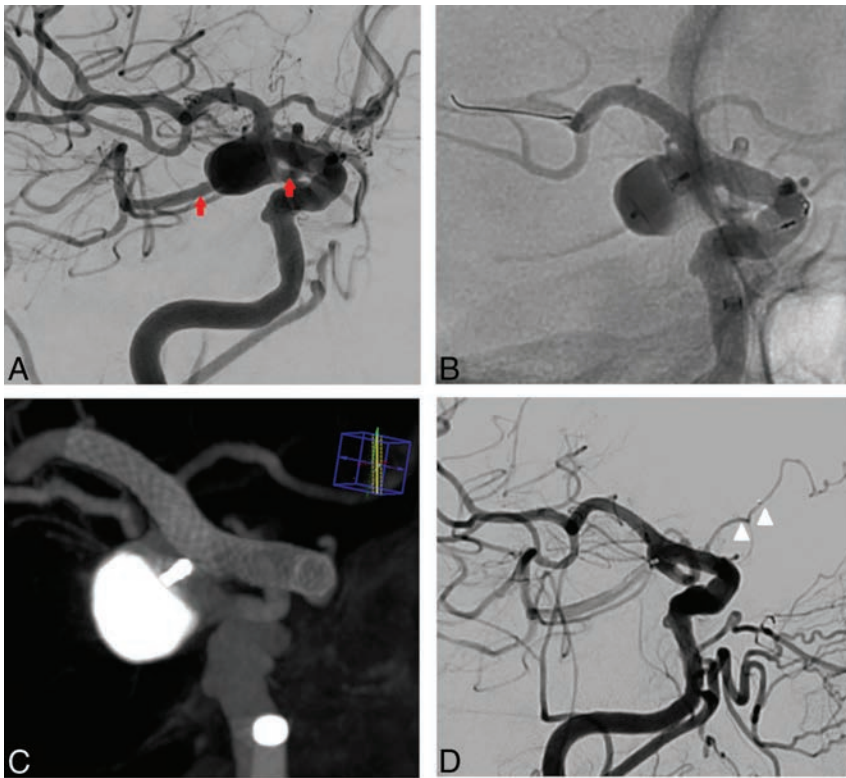


**FIG 2.** A, Right ICA angiography depicting a 9 × 10 mm PcomA unruptured aneurysm. A fetal variant of the PcomA arises from the aneurysm (red arrows). B, A WEB-SL (10 × 5 mm) was delivered inside the sac, intentionally undersized with respect to the origin of the fetal PcomA. Subsequently, a PED, 3.5 × 18 mm, was implanted from the right ICA to the right M1, covering the aneurysm neck, the PcomA, and the right A1. C, Flat panel CT reconstruction shows successful WEB and flow-diverter implantation and correct vessel wall apposition. D, Fifteen-month DSA follow-up shows complete occlusion of the aneurysm and the narrowing of the covered right A1 (white arrowheads).

sion (class I), residual neck (class II), and incomplete occlusion or residual aneurysm (class III).<sup>9</sup>

### Statistical Analysis

All statistical analyses were performed with SPSS, Version 24 (IBM, Armonk, New York). Summary statistics are presented for all data available using means ± SDs for continuous variables and frequency tabulations for categorical variables.

## RESULTS

### Baseline Population Characteristics

Population characteristics are summarized in On-line Table 1. In the 4-year period, 102 consecutive patients with unruptured and ruptured intracranial aneurysms were treated with the WEB. We extracted 17 patients treated with WEB plus stent placement (12 women, 5 men; mean age, 62 ± 8.9 years; range, 39–75 years). The pretreatment mRS score was 0 for 15 patients (88%), 1 for 1 patient (6%), and 4 for 1 patient (6%). Overall, 14 patients showed vascular risk factors: Two patients were hypertensive (14%), 5 patients were smokers (36%), and 7 patients were hypertensive and smokers (50%). Two patients were treated in the setting of acute SAH (patients 4 and 7).

### Aneurysm Characteristics

The mean size of the aneurysms was 7 ± 3.1 mm (range, 3–11 mm). All the aneurysms arose from a bifurcation point or pre-

sented with a branching vessel coming from the neck. Only 1 patient (patient 13) presented with an aneurysm with a fusiform aspect arising along the wall of the angular artery (M3). The most common location was the MCA (10 patients), followed by the anterior communicating artery (AcomA) (3 patients), basilar tip (3 patients), and posterior communicating artery (PcomA) (1 patient). Fifteen aneurysms were unruptured (88%), whereas 2 (12%) lesions were acutely ruptured. Among the unruptured group, 1 aneurysm (6%) was previously coiled, and WEB plus stent placement was used because of recanalization after coiling (patient 17).

### Treatment Characteristics and Technical Results

The Single-Layer (SL) WEB device was used in all the reported cases (On-line Table 2). Stent placement was performed with the Neuroform Atlas (Stryker Neurovascular, Kalamazoo, Michigan) in 14 cases (illustrative case in Fig 1) and with the LEO baby stent (Balt Extrusion, Montmorency, France) in 2 cases. One case of a large unruptured PcomA aneurysm was treated with the WEB plus the Pipeline Embolization Device (PED; Covidien, Irvine, California)

(patient 6 and Fig 2). Among 10 patients (58%), stent and WEB were planned before the treatment. A single stent was used in all except 2 cases (patients 3 and 17 treated with Y-stent placement) (illustrative case in Fig 3). In all cases, the WEB and stent were successfully navigated to the target area and deployed inside the sac and across the aneurysm neck, respectively. The mean intervention time was 78 ± 19 minutes (range, 50–105 minutes). The mean fluoroscopy time was 35 ± 14 minutes (range, 17–70 minutes).

### Clinical Outcome and Procedure-Related Complications

Treatment-related complications and clinical outcomes are summarized in On-line Table 2. There were no permanent complications. Overall, 2 patients showed mild intraprocedural in-stent thrombosis completely reversible after abciximab injection (0.125 mg/kg). In these 2 cases, stent placement was performed in the setting of acute SAH: The bifurcation vessel presented slow flow due to a mild WEB protrusion, and the stent was placed to protect the branch (patients 4 and 7). During follow-up, patient 13, with a distal nonbifurcation MCA aneurysm, presented with a completely asymptomatic occlusion of the vessel after 12 months of DSA follow-up (Fig 4).

The mean fluoroscopy time among patients reporting intraprocedural ischemic events versus patients without intraprocedural complications was 51.5 ± 18.5 minutes versus 33 ± 3.1 minutes, respectively ( $P = .08$ ), whereas the mean intervention time was

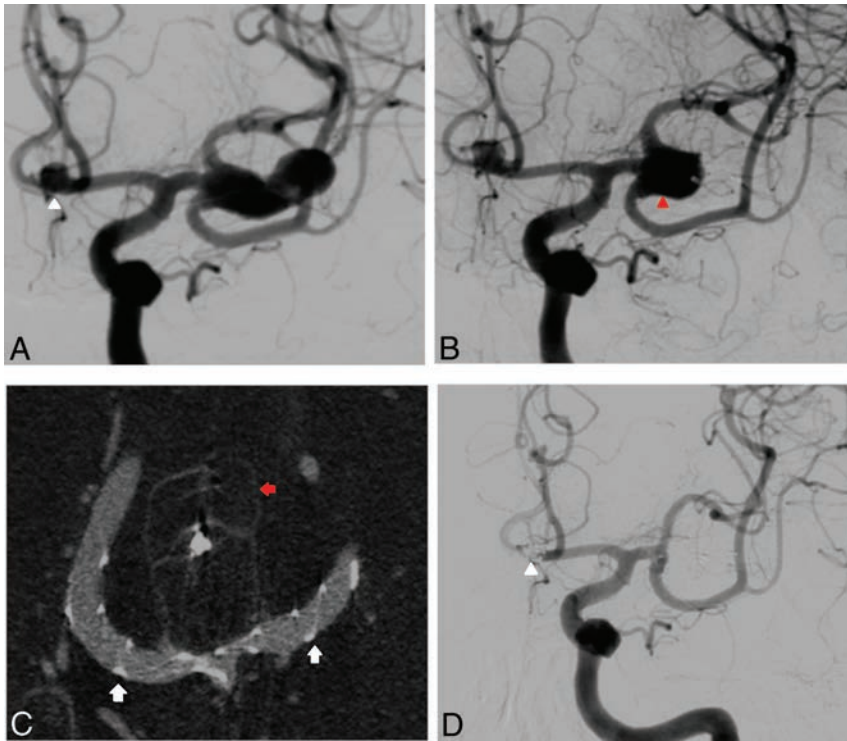


**FIG 3.** A, Patient 3 with a left large (14 × 7 mm) unruptured aneurysm originating from the MCA bifurcation and another small unruptured aneurysm of the AcomA (white arrowhead). B, The MCA aneurysm, initially treated with a WEB-SL (9 × 6 mm), presents with a large recanalization (red arrowhead) due to WEB compaction. C, VasoCT shows the retreatment with a second WEB-SL (9 × 6 mm) associated with 2 Y-configured LEO baby stents (2 × 18 mm) deployed from the M1 to the superior and inferior M2 branches (small white arrows). The first WEB appears compacted (small red arrow). D, Thirty-six-month DSA follow-up shows complete occlusion of the aneurysm. Both M2 branches are normal in caliber. The small AcomA aneurysm was coiled in another treatment session (white arrowhead).

100 ± 0 minutes and 76 ± 18.5 minutes, respectively ( $P = .09$ ). During long-term clinical follow-up (mean clinical follow-up, 11 months; range, 6–36 months), there were no modifications of the mRS related to the treatment. Overall, 14 patients presented with mRS 0, one patient presented with mRS 1, one patient (with a previous SAH from another aneurysm) presented with mRS 4, and 1 patient died due to the complications of the SAH.

#### Angiographic Outcome of Aneurysms

The mean radiologic follow-up was 10.4 months (range, 6–36 months) (On-line Table 2). Immediate complete occlusion (Raymond-Roy [RR] I) after treatment was achieved in 6 aneurysms (35%); 1 aneurysm (6%) showed a neck remnant (RR II), whereas 10 aneurysms (59%) were incompletely occluded (RR III). Sixteen patients were available for long-term angiographic follow-up. Overall, 11 (69%) aneurysms were completely occluded, 2 lesions presented with neck remnants (12.5%), and 3 aneurysms (18.5%) showed incomplete occlusion and were retreated with Y-stent-assisted coiling.

The mean sizes of aneurysms with occlusion RR I/RR II and RR III were 5.5 ± 2.1 mm (range, 3–9 mm) and 10 ± 1 mm (range, 9–11 mm), respectively ( $P = .003$ ). Immediately after treatment, 90% (9 of 10) of aneurysms showing RR III occlusion presented with contrast agent stagnation inside the sac. Of them, 77% (7 of 9) progressed to RR I/II occlusion during follow-up. There were no cases of aneurysm rupture during long-term follow-up. Three cases of asymptomatic

mild stent stenosis (<50%) were observed and were related to in-stent intimal hyperplasia. In case of mild stent stenosis, aspirin was usually prolonged until the next radiologic follow-up.

#### DISCUSSION

The safety and efficacy of the WEB device for the treatment of wide-neck intracranial aneurysms, particularly for lesions challenging to treat with standard coiling, have been reported in several studies.<sup>5,6,10,11</sup> However, treatment-related outcomes after intrasaccular flow-disruption with the WEB used with stents were not evaluated. We report the first series of a “stent-assisted WEB” used for the treatment of intracranial aneurysms in different locations.

#### Technical and Angiographic Outcomes

The WEB and the stent were successfully deployed inside the aneurysm and the artery in all cases, highlighting the feasibility of this technique. Consistent with the literature of WEB devices,<sup>5,10</sup> initial complete/near-complete occlusion immediately after WEB and stent deployment was obtained in 41% of patients, whereas long-term adequate occlusion (RR I/RR II) was 81%. These results appear

quite comparable with the angiographic outcome of other endovascular treatment modalities. In a meta-analysis of nearly 1900 aneurysms treated with stent-assisted coiling, the rates of immediate and long-term complete/near-complete occlusion were 54% and 73%, respectively.<sup>12</sup> However, in our study, 3 aneurysms (18%) were incompletely occluded at follow-up and required retreatment with Y-stent-assisted coiling. Although the rate of retreatment was quite high, all of these were large aneurysms located at the basilar tip (On-line Tables 1 and 2). In a recent series of 79 endovascularly treated basilar tip aneurysms, the rate of incomplete occlusion was close to 40%, and large aneurysm size was reported as an independent risk factor for incomplete occlusion.<sup>13</sup> Similarly, Abecassis et al<sup>14</sup> reported a retreatment rate close to 40% among basilar tip aneurysms treated with endovascular techniques. Accordingly, in our experience, the stent-assisted WEB technique was associated with good angiographic results, except for large aneurysms of the basilar tip, where the bifurcation configuration and the hemodynamic forces may play an important role in the aneurysm recanalization.<sup>15</sup>

Among the published series of the WEB, the rate of treatment with the WEB and additional stent placement ranged between 5%<sup>6</sup> and 18%.<sup>7,16</sup> In general, the stents were implanted due to a suboptimal placement of the WEB inside the sac with a protrusion

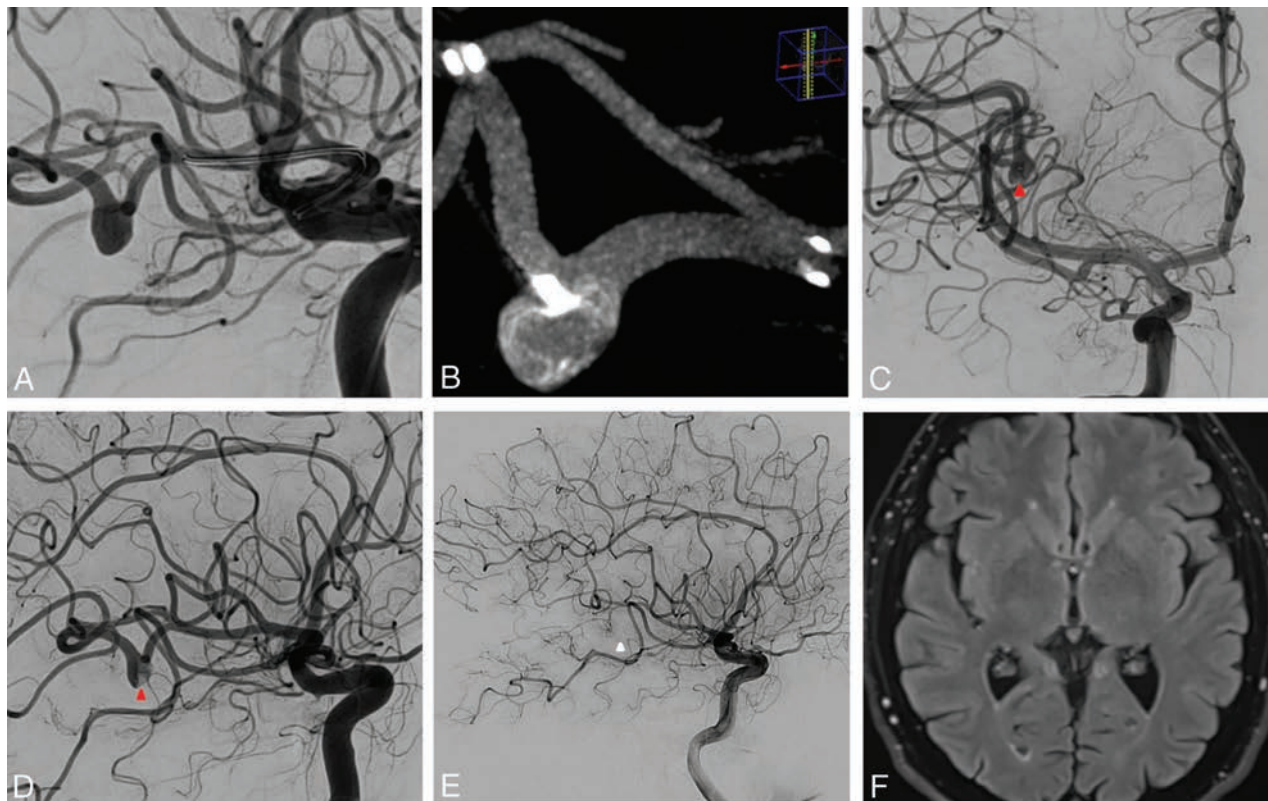


**FIG 4.** A, Patient 13 with a 5 × 4 mm unruptured nonbifurcation aneurysm arising from the wall of the distal portion of the angular artery (right MCA). B, VasoCT depicts the correct deployment of a WEB-SL (6 × 3 mm) into the sac associated with a Neuroform Atlas, 3 × 24 mm, delivered into the artery. Anteroposterior (C) and lateral (D) posttreatment angiograms show contrast agent stagnation into the aneurysm (red arrowhead). E, Twelve-month DSA follow-up (lateral view) shows the asymptomatic occlusion of the parent artery (white arrowhead). F, A FLAIR brain MR imaging sequence shows no associated ischemic lesions.

of the device inside the artery. Kabbasch et al,<sup>16</sup> in a series of 114 intracranial aneurysms treated with the WEB, described 14% of cases requiring additional stent placement, reporting 69% adequate occlusion during follow-up.

In our series, as reported above, the decision to stent the artery was planned before or was made during treatment after deployment of the WEB. In the first situation, during the preoperative planning, the main morphologic factors indicating the need for additional stent placement were the presence of a wide neck and a vessel arising from the aneurysm sac. Thus, the possibility of WEB protrusion into the artery was considered not negligible, and stent placement was planned beforehand. An example is reported in Fig 4, in which a case of nonbranching 5 × 4 mm aneurysm arising from the wall of the angular artery is depicted. The strategy was to exclude the aneurysm with a WEB-SL (6 × 3 mm) and to protect the artery with a Neuroform Atlas (3 × 24 mm). Fig 2 shows another example of planned WEB plus stent placement. The WEB was intentionally undersized to avoid the coverage of the fetal PcomA coming from the aneurysm; accordingly, due to a large basal aneurysm remnant, a PED was deployed from the internal carotid artery to the M1 segment to cause a diversion of the flow from the residual aneurysm. In our opinion, given the undersized device, the risk of WEB compaction and aneurysm recanalization during follow-up was high; consequently, we decided to use a flow-diversion device in the same treatment session.

A third example is reported in Fig 3, depicting a large MCA bifurcation aneurysm recanalized after treatment with a WEB-SL. When we opened the first WEB, an immediate complete aneurysm exclusion was noticed, and no additional devices were used in the first session. However, likely due to the undersized WEB, the aneurysm was recanalized and the WEB was compacted at the mid-term follow-up. A second WEB was deployed covering the aneurysm neck, while the M2 branches arising from the sac were protected with a Y-stent placement with 2 LEO baby stents. Complete aneurysm occlusion was achieved during follow-up.

On the other hand, when stent placement was not planned, the decision to stent the artery was because of the WEB protrusion into the bifurcation vessel. Fig 1 shows a wide-neck 6 × 4 mm AcomA aneurysm treated with a WEB-SL (7 × 3 mm). The WEB was protruding into the right A2, leading to a severe stenosis. Accordingly, a laser-cut stent was delivered to restore the caliber of the artery.

In general, larger aneurysms treated endovascularly are associated with lower rates of angiographic occlusion and a higher risk of recurrence.<sup>17</sup> Accordingly, we found a significantly higher mean size among aneurysms incompletely occluded compared with those showing complete occlusion during follow-up (10 versus 5.5 mm,  $P = .003$ ). This finding is line with a recent series investigating factors related to aneurysm occlusion after the WEB: The authors reported, in the multivariate analysis, that aneurysm

size (OR = 1.2; 95% CI, 1.01–1.38;  $P = .034$ ) was an independent morphologic risk factor for aneurysm remnants.<sup>16</sup>

### Treatment-Related Complications

A recent large series and meta-analysis of the WEB for the treatment of intracranial aneurysms showed variable rates of treatment-related morbidity (between 2% and 10%).<sup>5,10</sup> In our series, there were no permanent events or major neurologic complications. We describe 2 cases (patients 4 and 7) of intraprocedural complications after stent placement during acute SAH: A mild in-stent thrombosis was reported after stent deployment and was completely resolved after abciximab injection. During follow-up, only 1 patient (patient 13) had an asymptomatic parent vessel occlusion (angular artery) that was discovered during the angiographic long-term follow-up. It is likely that the artery was moderately stenosed by the WEB, and due to the collateral circulation, it became occluded without radiologic (the FLAIR findings were negative) and clinical sequelae (Fig 4).

Treatment with the WEB is, in general, a straightforward strategy, and this is mainly reflected by the brevity of the total fluoroscopic time reported in the literature. Fiorella et al<sup>3</sup> in the WEB Intra-saccular Therapy Study (WEB-IT) reported a mean fluoroscopy time of  $30 \pm 15.7$  minutes. Similarly, in a recent series of ruptured aneurysms treated with the WEB, the mean fluoroscopy time was 24 minutes (range, 8–40 minutes).<sup>18</sup> It has been reported that longer intervention time (>120 minutes) is a risk factor associated with ischemic events after endovascular treatment of intracranial aneurysms.<sup>19</sup> In our series, although some aneurysms required more complex treatment such as Y-stent placement plus a WEB, the mean intervention and fluoroscopy times were relatively low (78 and 35 minutes, respectively). Consistent with the literature, among patients reporting intraprocedural ischemic events, the mean fluoroscopy (51.5 versus 33 minutes) and intervention (100 versus 76 minutes) times were higher compared with those without complications.

### Limitations of the Study

Our study has limitations intrinsic to single-center series. The number of patients is relatively small, though it is the first larger series investigating WEB-plus-stent placement. The data, though prospectively collected, were analyzed retrospectively. In addition, the imaging outcome was assessed by operators and not independently. There was a lack of standardization of radiologic follow-up.

### CONCLUSIONS

Aneurysm embolization with WEB devices in association with stent placement appears both technically feasible and effective for the treatment of lesions with unfavorable anatomy, allowing high rates of long-term occlusion. In our study, this strategy was relatively safe with a low rate of relevant procedure-related adverse events.

Disclosures: Pierre-Henri Lefevre—UNRELATED: Payment for Development of Educational Presentations: Medtronic. Alain Bonafe—UNRELATED: Consultancy: Stryker Neurovascular, MicroVention. Vincent Costalat—UNRELATED: Consul-

tancy: Medtronic, Stryker Neurovascular, Balt Extrusion, MicroVention; Grants/Grants Pending: Medtronic, Balt Extrusion\*; Payment for Development of Educational Presentations: Medtronic, Balt Extrusion, Stryker Neurovascular. \*Money paid to the institution.

### REFERENCES

1. Shapiro M, Becske T, Sahlein D, et al. **Stent-supported aneurysm coiling: a literature survey of treatment and follow-up.** *AJNR Am J Neuroradiol* 2012;33:159–63 CrossRef Medline
2. Pierot L, Cognard C, Spelle L, et al. **Safety and efficacy of balloon remodeling technique during endovascular treatment of intracranial aneurysms: critical review of the literature.** *AJNR Am J Neuroradiol* 2012;33:12–15 CrossRef Medline
3. Fiorella D, Molyneux A, Coon A, et al; WEB-IT Study Investigators. **Demographic, procedural and 30-day safety results from the WEB Intra-saccular Therapy Study (WEB-IT).** *J Neurointerv Surg* 2017;9:1191–96 CrossRef Medline
4. Tau N, Sadeh-Gonik U, Aulagner G, et al. **The Woven EndoBridge (WEB) for endovascular therapy of intracranial aneurysms: update of a systematic review with meta-analysis.** *Clin Neurol Neurosurg* 2018;166:110–15 CrossRef Medline
5. Pierot L, Gubucz I, Buhk JH, et al. **Safety and efficacy of aneurysm treatment with the WEB: results of the WEBCAST 2 study.** *AJNR Am J Neuroradiol* 2017;38:1151–55 CrossRef Medline
6. Caroff J, Mihalea C, Klisch J, et al. **Single-layer WEBS: intrasaccular flow disrupters for aneurysm treatment—feasibility results from a European study.** *AJNR Am J Neuroradiol* 2015;36:1942–46 CrossRef Medline
7. Kabbasch C, Mpotsaris A, Reiner M, et al. **WEB as part of a multimodality treatment in complex, large, and partially thrombosed intracranial aneurysms: a single-center observational study of technical success, safety, and recurrence.** *J Neurointerv Surg* 2016;8:1235–39 CrossRef Medline
8. Lescher S, du Mesnil de Rochemont R, Berkefeld J. **Woven Endo-bridge (WEB) device for endovascular treatment of complex unruptured aneurysms—a single center experience.** *Neuroradiology* 2016;58:383–90 CrossRef Medline
9. Roy D, Milot G, Raymond J. **Endovascular treatment of unruptured aneurysms.** *Stroke* 2001;32:1998–2004 CrossRef Medline
10. Asnafi S, Rouchaud A, Pierot L, et al. **Efficacy and safety of the Woven EndoBridge (WEB) device for the treatment of intracranial aneurysms: a systematic review and meta-analysis.** *AJNR Am J Neuroradiol* 2016;37:2287–92 CrossRef Medline
11. van Rooij SB, van Rooij WJ, Peluso JP, et al. **WEB treatment of ruptured intracranial aneurysms: a single-center cohort of 100 patients.** *AJNR Am J Neuroradiol* 2017;38:2282–87 CrossRef Medline
12. Zhao B, Yin R, Lanzino G, et al. **Endovascular coiling of wide-neck and wide-neck bifurcation aneurysms: a systematic review and meta-analysis.** *AJNR Am J Neuroradiol* 2016;37:1700–05 CrossRef Medline
13. Ge H, Lv X, Jin H, et al. **The role of endovascular treatment in unruptured basilar tip aneurysms.** *Interv Neuroradiol* 2017;23:8–13 CrossRef Medline
14. Abecassis IJ, Sen RD, Barber J, et al. **Predictors of recurrence, progression, and retreatment in basilar tip aneurysms: a location-controlled analysis.** *Oper Neurosurg (Hagerstown)* 2019;16:435–44 CrossRef Medline
15. Sugiyama S, Niizuma K, Sato K, et al. **Blood flow into basilar tip aneurysms: a predictor for recanalization after coil embolization.** *Stroke* 2016;47:2541–47 CrossRef Medline
16. Kabbasch C, Goertz L, Siebert E, et al. **Factors that determine aneurysm occlusion after embolization with the Woven EndoBridge (WEB).** *J Neurointerv Surg* 2018 Oct 24. [Epub ahead of print] CrossRef Medline

17. Cagnazzo F, Mantilla D, Rouchaud A, et al. **Endovascular treatment of very large and giant intracranial aneurysms: comparison between reconstructive and deconstructive techniques—a meta-analysis.** *AJNR Am J Neuroradiol* 2018;39:852–58 CrossRef Medline
18. Da Ros V, Bozzi A, Comelli C, et al. **Ruptured intracranial aneurysms treated with Woven EndoBridge intrasaccular flow disruptor: a multicenter experience.** *World Neurosurg* 2019;122:e498–505 CrossRef Medline
19. Hahnemann ML, Ringelstein A, Sandalcioglu IE, et al. **Silent embolism after stent-assisted coiling of cerebral aneurysms: diffusion-weighted MRI study of 75 cases.** *J Neurointerv Surg* 2014;6:461–65 CrossRef Medline

# Image Quality of Low-Dose Cerebral Angiography and Effectiveness of Clinical Implementation on Diagnostic and Neurointerventional Procedures for Intracranial Aneurysms

J. Choi, B. Kim, Y. Choi, N.Y. Shin, J. Jang, H.S. Choi, S.L. Jung, and K.J. Ahn

## ABSTRACT

**BACKGROUND AND PURPOSE:** Awareness of the potential for exposure to high doses of radiation from interventional radiologic procedures has increased. The purpose of this study was to evaluate image quality and dose reduction of low-dose cerebral angiography during diagnostic and therapeutic procedures for intracranial aneurysms.

**MATERIALS AND METHODS:** A retrospective review of 1137 prospectively collected patients between January 2012 and June 2014 was performed. Beginning in April 2013, a dose-reduction strategy was implemented. Subjective image-quality assessment of 506 standard and 540 low-dose cerebral angiography images was performed by 2 neuroradiologists using a 5-point scale and was tested using noninferiority statistics. Radiation dose-area product and air kerma of 1046 diagnostic and 317 therapeutic procedures for intracranial aneurysms were analyzed and compared between groups before (group 1) and after (group 2) clinical implementation of a dose-reduction strategy.

**RESULTS:** The image quality of the low-dose cerebral angiography was not inferior on the basis of results from the 2 readers. For diagnostic cerebral angiography, the mean dose-area product and air kerma were  $140.8 \text{ Gy} \times \text{cm}^2$  and 1.0 Gy, respectively, in group 1 and  $82.0 \text{ Gy} \times \text{cm}^2$  and 0.6 Gy in group 2 ( $P < .001$ ,  $P < .001$ ). For the neurointerventional procedure, the mean dose-area product and air kerma were  $246.0 \text{ Gy} \times \text{cm}^2$  and 3.7 Gy, respectively, in group 1 and  $169.8 \text{ Gy} \times \text{cm}^2$  and 3.3 Gy in group 2 ( $P < .001$ ,  $P = .291$ ).

**CONCLUSIONS:** With low-dose cerebral angiography, image quality was maintained, and implementation of dose-reduction strategies reduced radiation doses in patients undergoing diagnostic and neurointerventional procedures for intracranial aneurysms.

**ABBREVIATIONS:** AK = air kerma; DAP = dose-area product

Although CT and MR angiography are performed frequently to diagnose cerebrovascular diseases, cerebral angiography is still the criterion standard for the evaluation of the vasculature in cerebrovascular disease, especially when therapeutic procedures are anticipated. The potential for high radiation doses from interventional radiologic procedures is well-known; thus, such procedures should only be performed with adequate justification.<sup>1,2</sup> The adverse health effects of radiation exposure can be divided into 2 categories: deterministic effects and stochastic effects. Skin dose is related to deterministic effects such as skin erythema, necrosis, ulceration, cataract, and permanent epilation.<sup>1,3</sup> Although

direct measurement of the skin radiation dose using thermoluminescent dosimeters is the most accurate, it is not practical because it is a cumbersome procedure with limitations.<sup>4,5</sup> Dose-area product (DAP) and air kerma (AK) are alternative indirect measurements of a patient dose and are the most convenient and currently most widely used parameters for monitoring it.<sup>4,6-10</sup>

With increased awareness of the need for reduction of the radiation dose during cerebral angiography, many techniques and strategies have reduced unnecessary radiation doses while maintaining image quality needed to perform procedures.<sup>7-12</sup> At Seoul St. Mary's Hospital, we have recorded radiation parameters for each procedure since 2009, and our early experience has shown that the proportion of the radiation dose in terms of DAP from angiographic acquisitions was 88.6% for diagnostic cerebral angiography and 49.5% for neurointerventional procedures.<sup>6</sup> Thus, low-dose angiography provides good image quality and may be an effective way to reduce the radiation dose to patients undergoing diagnostic or neurointerventional procedures. Although there have been several reports showing the effectiveness of low-dose cerebral angiography, little work has been done to study the ap-

Received November 22, 2018; accepted after revision February 27, 2019.

From the Department of Radiology (J.C.), St. Vincent's Hospital, College of Medicine, The Catholic University of Korea, Gyeonggi-do, Republic of Korea; and Department of Radiology (B.K., Y.C., N.Y.S., J.J., H.S.C., S.L.J., K.J.A.), Seoul St. Mary's Hospital, College of Medicine, The Catholic University of Korea, Seoul, Republic of Korea.

Please address correspondence to Bum-soo Kim, MD, Department of Radiology, Seoul St. Mary's Hospital, The Catholic University of Korea, 505, Banpo-dong, Seocho-gu, Seoul, 133-701, Korea; e-mail: bumrad@catholic.ac.kr

<http://dx.doi.org/10.3174/ajnr.A6029>

plication and its effectiveness in a clinical setting with a large volume of patients.<sup>8,9,13-15</sup>

Since April 2013, our clinic has implemented the following new dose-reduction strategy: 1) low-dose angiographic protocol (from 3.6  $\mu\text{Gy}/\text{frame}$  to 1.8  $\mu\text{Gy}/\text{frame}$ ) for cerebral angiography, and 2) a roadmap image saved for evaluation of the femoral arterial puncture site, instead of femoral angiography. The purpose of this study was to evaluate image quality of low-dose cerebral angiography and the effectiveness of the clinical implementation of our dose-reduction strategies in diagnostic and neurointerventional procedures for intracranial aneurysms.

### MATERIALS AND METHODS

This study was approved by Seoul St. Mary's Hospital institutional review board. A waiver of the need for consent was obtained for this Health Insurance Portability and Accountability Act-compliant retrospective study. Retrospective review of the prospectively collected data base of 1137 patients (799 females, 338 males; median age, 56 years; range, 13–88 years) between January 2012 and June 2014 was performed. All procedures were per-

formed by a team of 2 experienced neurointerventionalists. A clinical fellow with >300 previous cases performed the diagnostic angiographic procedures, while embolizations were performed by a radiologist with >20 years of experience in aneurysm embolization. Diagnostic procedures performed for follow-up after clipping of an aneurysm were excluded. There were, in total, 1046 diagnostic and 317 therapeutic procedures.

The angiographic system used was a biplane angiographic unit (Axiom Artis dBA; Siemens, Erlangen, Germany) with a flat panel detector: A and B planes (48 cm) with variable FOVs of 42 to 32–22 to 16 cm. The total filtration was 2.5 mm Al. The angiography unit had 3 pulsed fluoroscopy modes of 10, 15, and 30 P/s, of which 15 P/s was used most frequently with variable copper filtration of up to 0.9 mm. The system had a DAP meter, including a verification of the AK and DAP displayed values against an external dosimeter during the quality-assurance process at least once a year.

Since April 2013, our institution has applied the following dose-reduction strategy: 1) low-dose angiographic protocol (from 3.6  $\mu\text{Gy}/\text{frame}$  to 1.8  $\mu\text{Gy}/\text{frame}$ ) for cerebral angiography, and 2) a roadmap image saved for evaluation of the femoral artery puncture site, instead of femoral angiography. Angiographic procedures were the same as those used in a previous protocol, including acquisition of internal carotid and vertebral arteriographies in anteroposterior and lateral views, and rotational angiog-

**Table 1: Mean image quality of angiography by 2 separate readers before and after the low-dose angiographic protocol**

	Reader 1	Reader 2
Phase 1	4.94 $\pm$ 0.32	4.91 $\pm$ 0.33
Phase 2	4.95 $\pm$ 0.32	4.94 $\pm$ 0.23

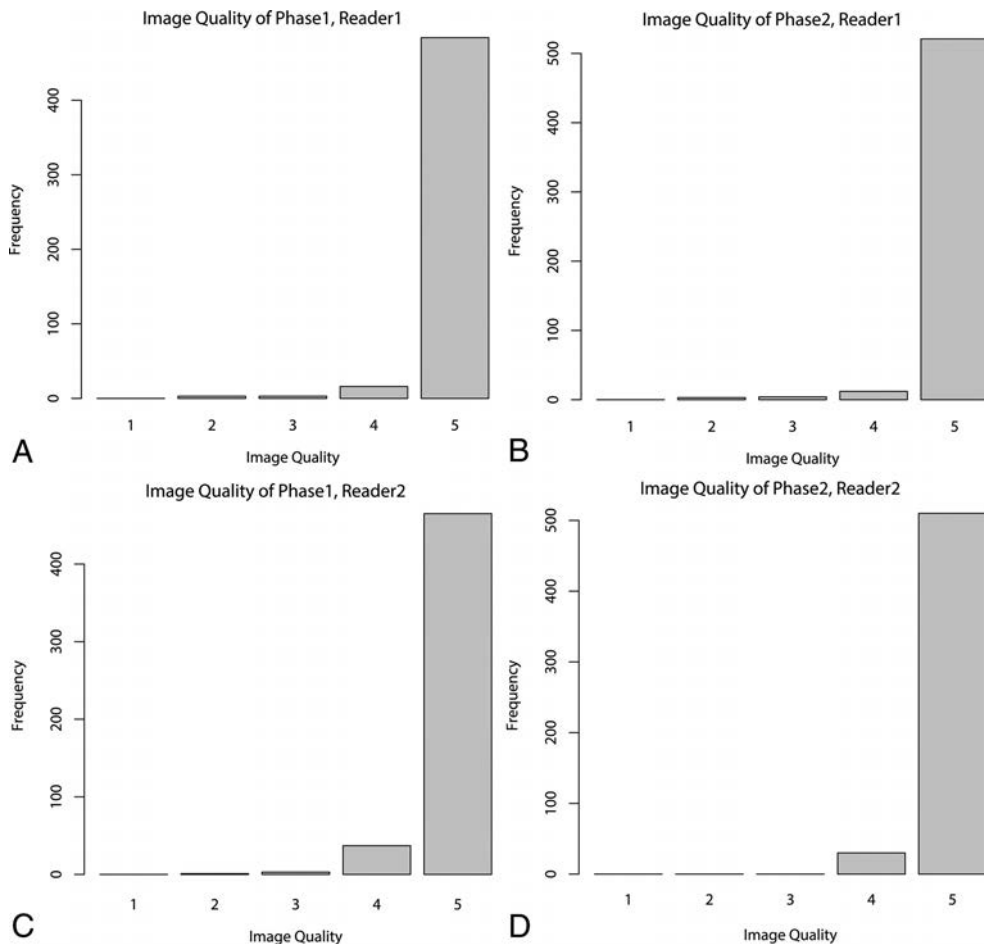


**FIG 1.** Image quality of angiography by 2 separate readers before (Phase 1) and after (Phase 2) the low-dose angiographic protocol.

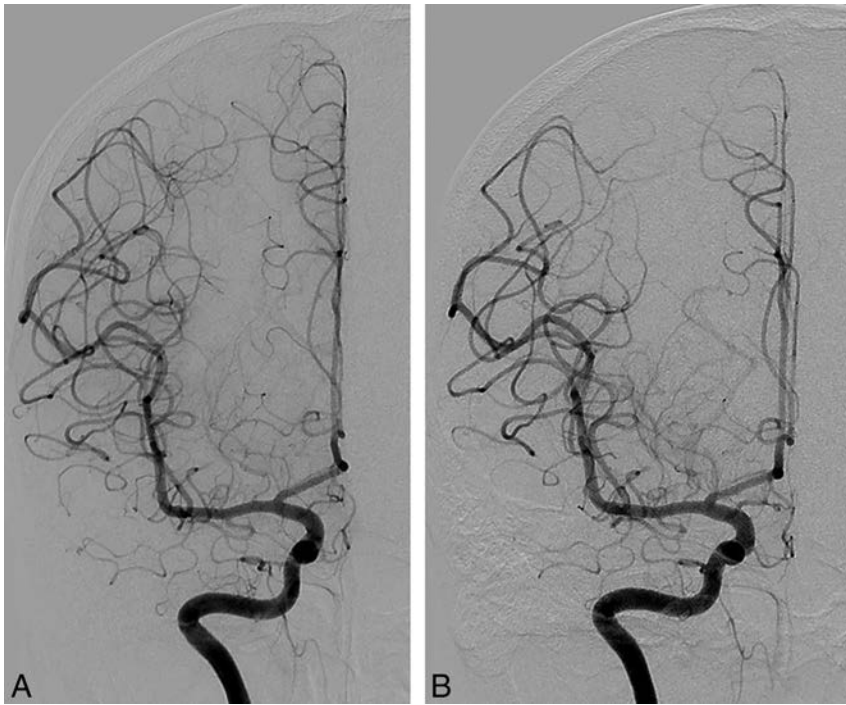


**FIG 2.** Representative examples of angiographic images before (A) and after (B) the low-dose angiographic protocol. These are cerebral angiograms of a patient who underwent diagnostic angiography to determine the cause of perimesencephalic subarachnoid hemorrhage.

**Table 2: Mean and third quartile results for fluoroscopic time, DAP, AK, and image frames for diagnostic and therapeutic procedures before and after the low-dose angiographic protocol**

	Fluoroscopic Time (min)	DAP (Gy×cm <sup>2</sup> )	AK (Gy)	Image Frames
<b>Diagnostic</b>				
Phase 1				
Mean	13.0 ± 7.9	140.8 ± 48.1	1.02 ± 0.42	251.2 ± 72
3rd quartile	14.4	160.8	1.18	273
Phase 2				
Mean	11.9 ± 6.9	82.0 ± 30.0	0.61 ± 0.33	222.6 ± 52
3rd quartile	13.8	94.1	0.69	246
P value	.012	<.001	<.001	<.001
<b>Therapeutic</b>				
Phase 1				
Mean	53.5 ± 34.1	246.0 ± 148.3	3.67 ± 2.66	287.6 ± 150
3rd quartile	64.5	301.4	4.42	341
Phase 2				
Mean	49.1 ± 32.2	169.8 ± 111.6	3.31 ± 3.21	260.2 ± 128
3rd quartile	60.0	206.2	4.24	334
P value	.237	<.001	.291	.080

raphy was performed using 5-second dual runs with 0.36  $\mu\text{Gy}/\text{frame}$  when an intracranial aneurysm was suspected on 2D cerebral angiography.<sup>6</sup>

Two experienced neuroradiologists with >15 years of experience evaluated the quality of the images, which had been arranged in a random order. They reviewed all DSA series, and they were blinded to the examination date to avoid knowing the dose category. They analyzed the image quality on a scale of 5, with the higher number indicating better image quality: 1 (nondiagnostic), 2 (poor: compromised large and small vessel visualization), 3 (average: diagnostic value for large vessel but compromised small vessel visualization), 4 (good: excellent large vessel and minimal compromise of small vessel visualization), 5 (very good: excellent large and small vessel visualization).

The parameters measured were DAP, AK, fluoroscopy exposure time, and the number of angiographic image acquisitions for all procedures. Image quality was also obtained for 1046 diagnostic procedures (506 procedures before the low-dose protocol and 540 procedures after the low-dose protocol).

A noninferiority test was used for the image quality of diagnostic procedures before and after dose reduction, and interrater reliability was tested using the Cronbach  $\alpha$ . The difference in parameters before and after the dose-reduction protocol was tested with a Student *t* test. SPSS (IBM, Armonk, New York) was used for statistical analysis. Statistical significance was defined as  $P < .05$ .

## RESULTS

The subjective data for the quality of images before and after the low-dose protocol by 2 radiologists are presented in Table 1 and Fig 1. The image-quality score was well-correlated between the 2 observers (Cronbach  $\alpha = 0.853$ ). The

diagnostic noninferiority of the angiography with 1.8  $\mu\text{Gy}/\text{frame}$  was demonstrated using the noninferiority test because the upper margin of the 1-sided 97.5% confidence interval did not cross the predefined noninferiority margin of  $-0.2$ . Figure 2 shows representative examples of the 2 cohorts.

The quantitative data are shown in Table 2 and Fig 3. Before application of the low-dose angiographic protocol (Phase 1), mean fluoroscopic time, total mean DAP, total AK, and total angiographic image frames were  $13.0 \pm 7.9$  minutes,  $140.8 \pm 48.1 \text{ Gy} \times \text{cm}^2$ ,  $1.02 \pm 0.42 \text{ Gy}$ , and  $251.2 \pm 72$  frames for diagnostic procedures, respectively, and  $53.5 \pm 34.1$  minutes,  $246.0 \pm 148.3 \text{ Gy} \times \text{cm}^2$ ,  $3.67 \pm 2.66 \text{ Gy}$ , and  $287.6 \pm 150$  frames for therapeutic procedures. The third quartiles, which may be used as a dose reference level, were 14.4 and 64.5 minutes for fluoroscopy times, 160.8 and 301.4  $\text{Gy} \times \text{cm}^2$  for DAP, 1.18 and 4.42 Gy for AK, and 273 and 341 image frames in diagnostic and therapeutic procedures, respectively. After application of the low-dose angiographic protocol (Phase 2), mean fluoroscopic time, total mean DAP, total AK, and total angiographic image frames were  $11.9 \pm 6.9$  minutes,  $82.0 \pm 30.0 \text{ Gy} \times \text{cm}^2$ ,  $0.61 \pm 0.33 \text{ Gy}$ , and  $222.6 \pm 52$  frames for diagnostic procedures, respectively, and  $49.1 \pm 32.2$  minutes,  $169.8 \pm 111.6 \text{ Gy} \times \text{cm}^2$ ,  $3.31 \pm 3.21 \text{ Gy}$ , and  $260.2 \pm 128$  frames for therapeutic procedures. The third quartiles, which may be used as a dose reference level, were 13.8 and 60.0 minutes for fluoroscopy times, 94.1 and 206.2  $\text{Gy} \times \text{cm}^2$  for DAP, 0.69 and 4.24 Gy for AK, and 246 and 334 image frames in diagnostic and therapeutic procedures, respectively. There was a significant difference between the mean parameters of fluoroscopic time ( $P = .012$ ), DAP ( $P < .001$ ), AK ( $P < .001$ ), and image frames ( $<.001$ ) before and after dose reduction for

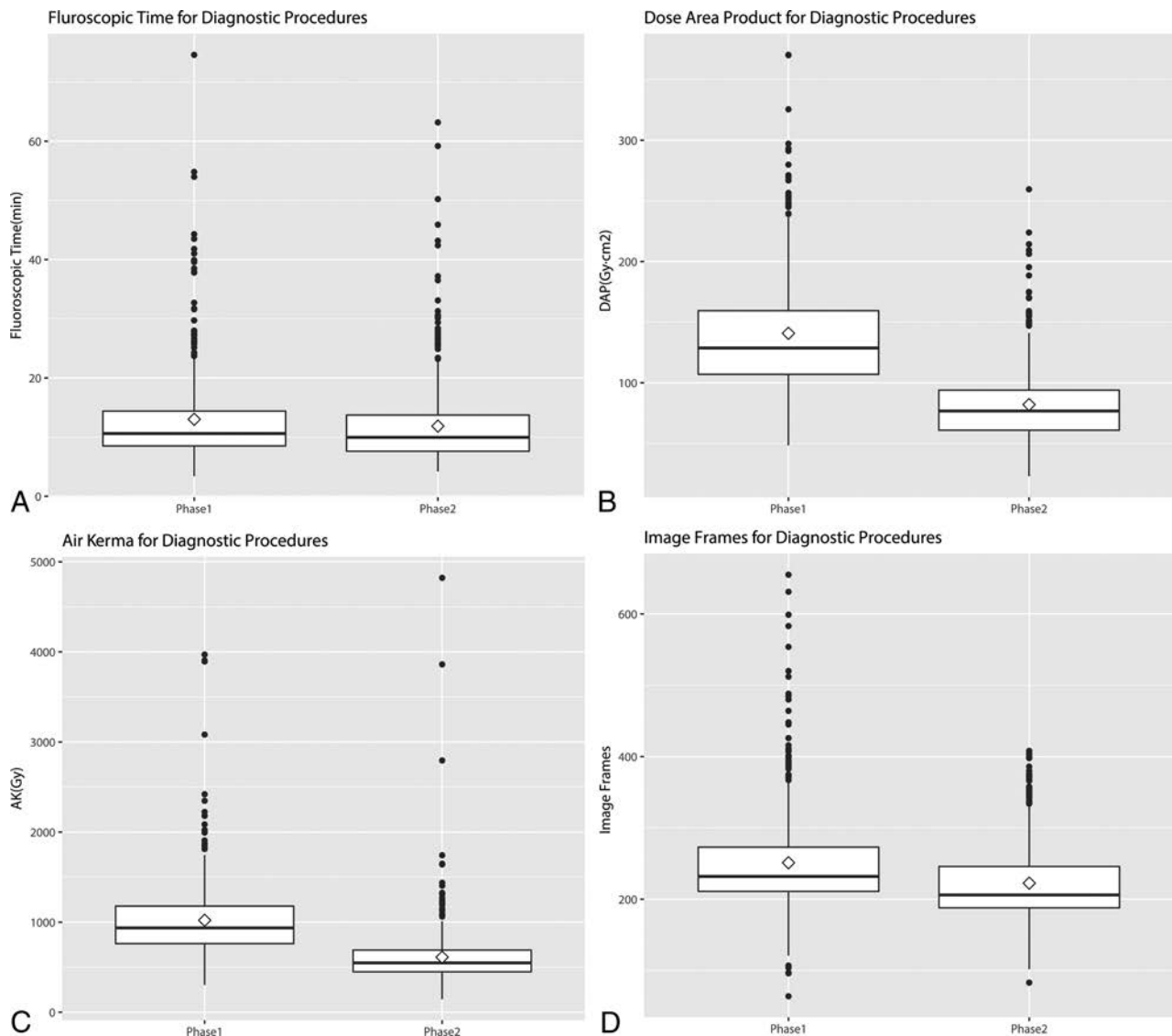


**FIG 3.** Boxplots of fluoroscopic time, DAP, AK, and image frames for diagnostic and therapeutic procedures before (Phase 1) and after (Phase 2) the low-dose angiographic protocol. *Thick horizontal lines* indicate median values, and *diamonds* indicate mean values.

diagnostic procedures. For therapeutic procedures, only the DAP showed a statistically significant difference before and after the dose-reduction protocol ( $P < .001$ ).

## DISCUSSION

In this study, the subjective image quality of cerebral angiography with  $1.8 \mu\text{Gy}/\text{frame}$  was not inferior to that with  $3.6 \mu\text{Gy}/\text{frame}$ . Furthermore, low-dose angiography showed clinically acceptable images with very good image quality of 4.9 of 5. As in our experience, simple modifications of the default radiation dose have effectively reduced the radiation dose delivered by neurointerventional procedures, but thorough evaluation of image quality in a clinical setting has not been performed.<sup>13-15</sup> Reducing the radiation dose generally leads to more quantum noise artifacts and edge blurring, which deteriorate image quality. We found that other factors such as blurring caused by patient motion had a greater effect on degradation of image quality than the protocol itself.

Our results showed that the  $1.8 \mu\text{Gy}/\text{frame}$  protocol can re-

duce DAP and AK by 41.8% and 40.0%, respectively, for diagnostic procedures and by 31.0% and 10.0% for therapeutic procedures. They also showed that roadmap saving can reduce the fluoroscopic time and the number of image frames by 8.46% and 11.39%, respectively, for diagnostic procedures and by 8.22% and 9.53% for therapeutic procedures. Our results showed a statistically significant difference of DAP and AK during diagnostic procedures but failed to show a statistically significant difference of AK for therapeutic procedures. This result might be because of the effect of different backscatter radiation, which is sensitive to patient habitus and the effect of different angles of the x-ray beams. The proportion of angiography performed during therapeutic procedures is lower than that during diagnostic procedures (49.5% versus 88.6%), and this can neutralize the effect of the low-dose protocol.<sup>16</sup>

Tables 3 and 4 summarize the mean and third quartile data of DAP, fluoroscopic time, and the number of image frames for diagnostic and therapeutic procedures for intracranial aneurysms by various authors. Fluoroscopic time, DAP, and the number of

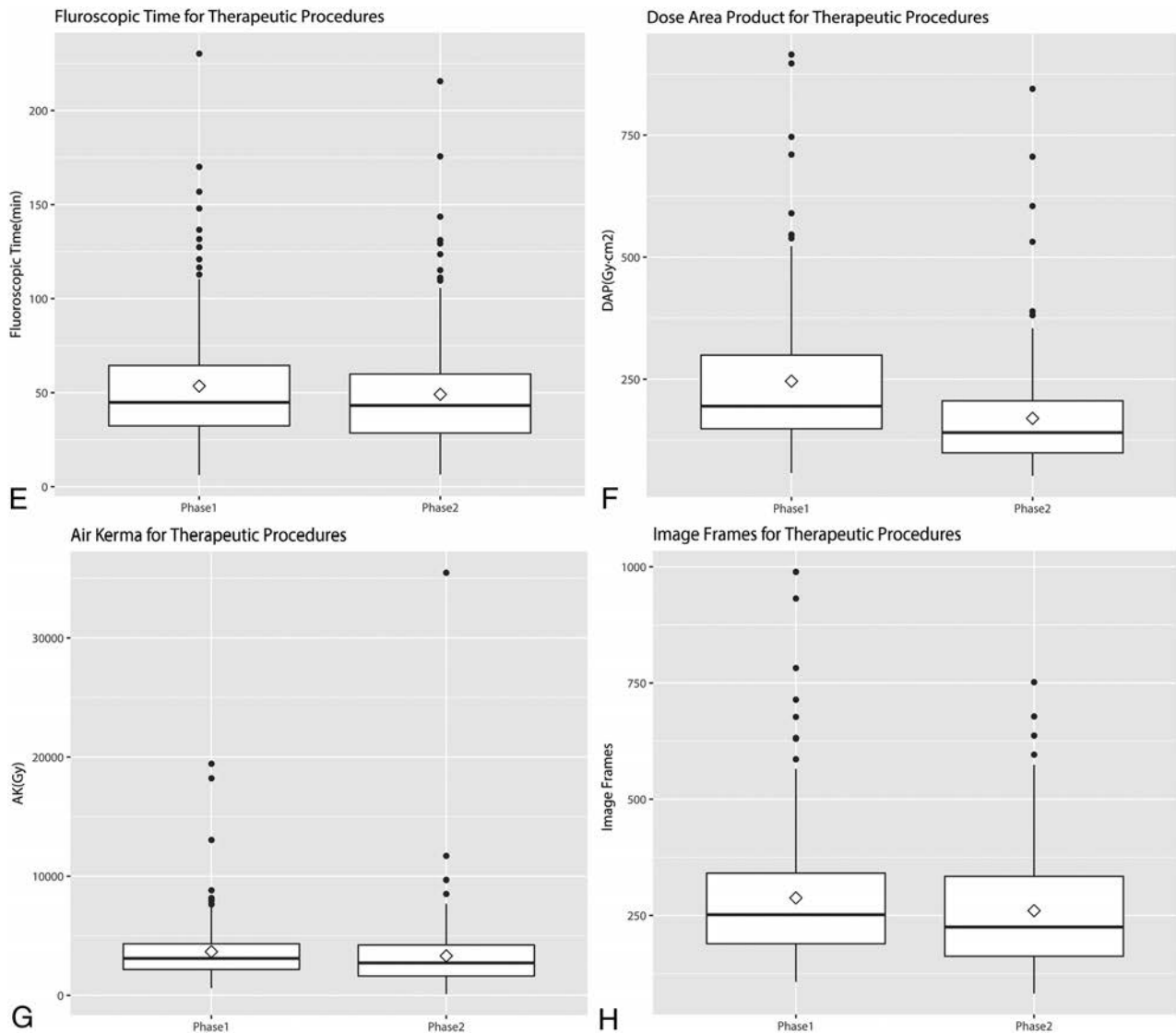


FIG 3. Continued.

**Table 3: Summary of mean and third quartile data of DAP, fluoroscopic time, and number of image frames acquired during diagnostic cerebral angiography for intracranial aneurysms**

Reference	No. of Patients	DAP (Gy×cm <sup>2</sup> )		Fluoroscopy Time (min)		No. of Frames	
		Mean	3rd Quartile	Mean	3rd Quartile	Mean	3rd Quartile
Phase 1	506	140.8	160.8	13.0	14.4	251.2	273
Phase 2	540	82.0	94.1	11.9	13.8	222.6	246
Hassan and Amelot <sup>17</sup>	398	43.1	59.7	5.6	7.5	245	314
Chun et al <sup>6</sup>	439	136.6	154.2	12.6	14.0	251	273
D'Ercole et al <sup>18</sup>	100	142.1	180	9.9	12.3	220	317
Aroua et al <sup>19</sup>	91	121	125	12.6	15	679	480
Verdun et al <sup>20</sup>	91	107	124				
Brambilla et al <sup>21</sup>	188	158	198	13.7	17.5		

image frames before the low-dose protocol of this study are similar to those from the previous results, except for the report of Hassan and Amelot,<sup>17</sup> in which the most recent angiographic system was used.<sup>6,18-21</sup> Our study is especially meaningful in that dose reduction was achieved without purchasing a new angiographic system with sophisticated functions.

We evaluated the DAP instead of the entrance skin dose in our

study. The DAP is the absorbed radiation dose multiplied by the size of the area irradiated.<sup>22</sup> This value can be used to monitor radiation exposure levels and is readily available because it can be easily measured using an ionization chamber in fluoroscopic and angiographic units, and the effective dose can be calculated from it using conversion factors.<sup>22</sup> Even though the precise prediction of the skin dose using DAP is difficult because x-ray beams enter

**Table 4: Summary of mean and third quartile data of DAP, fluoroscopic time, and number of image frames acquired during therapeutic cerebral angiography for intracranial aneurysms**

Reference	No. of Patients	DAP (Gy×cm <sup>2</sup> )		Fluoroscopy Time (min)		No. of Frames	
		Mean	3rd Quartile	Mean	3rd Quartile	Mean	3rd Quartile
Phase 1	144	246.0	301.4	53.5	64.5	287.6	341
Phase 2	173	169.8	206.2	49.1	60.0	260.2	334
Hassan and Amelot <sup>17</sup>	71	78.7	111.9	25.7	34.8	300	428
Chun et al <sup>6</sup>	111	226.0	272.8	52.9	61.1	241	276
D'Ercole et al <sup>18</sup>	72	382.2	487	37.2	46.3	558	717
Aroua et al <sup>19</sup>	52	335	440	36.5	50	760	800
Verdun et al <sup>20</sup>	58	335	352				
Brambilla et al <sup>21</sup>	356	319.9		87.1		1053	

**Table 5: The proportion of DAP contributed by rotational angiography before and after the low-dose protocol<sup>a</sup>**

	Phase 1	Phase 2
Diagnostic		
Total DAP (Gy×cm <sup>2</sup> )	140.8 ± 48.1	82.0 ± 30.0
Rotation DAP (Gy×cm <sup>2</sup> )	26.3 ± 13.4	28.0 ± 13.7
Rotations/total DAP	18.7 %	34.1 %
No. of rotations	1.49 ± 2.60	1.44 ± 0.68
Therapeutic		
Total DAP (Gy×cm <sup>2</sup> )	246.0 ± 148.3	169.8 ± 111.6
Rotation DAP (Gy×cm <sup>2</sup> )	30.8 ± 17.0	25.6 ± 14.3
Rotations/total DAP	12.5 %	15.1 %
No. of rotations	1.58 ± 0.79	1.33 ± 0.68

<sup>a</sup> Data are means and percentages.

the patient in many directions, there is a good correlation between skin dose and DAP.<sup>5</sup> Thus, DAP can be used to set the action level of radiation that indicates skin exposures necessitating medical follow-up for possible radiation injuries and to refine the nationwide reference level as well.<sup>16,23</sup>

The reduction in the number of image frames in our study was largely due to the use of roadmap saving instead of angiography for femoral arteries. Greater reduction of the radiation dose by reducing the number of frames can be achieved using lower frame rates that still produce acceptable image quality.

Some factors can be adjusted to reduce the radiation dose. Fluoroscopic time is directly related to the radiation dose and is dependent on the operators. We think proficiency in cerebral angiography can reduce fluoroscopic time, especially for therapeutic procedures. Rotational angiography is another factor that can be adjusted. When the radiation dose by angiographic procedures was reduced, the proportion of the radiation dose by rotational angiography increased (Table 5). We think we can further reduce the radiation dose using a low-dose protocol for rotational angiography, the feasibility of which was shown by Pearl et al.<sup>11</sup> Last, strict control of the FOV to contain only vascular structures can also contribute to reduction of the radiation dose.

There are some limitations in our study. First, it was retrospective. Even though the data base was built prospectively, the study was retrospective and vulnerable to selection bias and information bias. We think that the large number of samples tested overcomes this limitation. Second, the cases analyzed were limited to aneurysms. We used only aneurysms because they are the most frequent vascular disease and can be used as representative cases. However, limiting cases makes it difficult to generalize the results of this study. Third, the DAP we used was a simple summation of angiographic DAP, fluoroscopic DAP, and rotational angio-

graphic DAP. In this study, we did not evaluate acquisition and fluoroscopic doses separately because we concentrated on only the effect of the low-dose angiography on the total patient dose. Further studies separately analyzing the 2D angiographic dose, 3D rotational angiographic dose, and fluoroscopic dose would have meaningful results. Fourth, we did not evaluate the radiation dose according to the mode of treatment. Cheung et al<sup>24</sup> showed that the mode of treatment can affect the radiation dose, and this might have had a confounding effect on our results.

## CONCLUSIONS

Low-dose cerebral angiography maintained image quality, and implementation of dose-reduction strategies contributed to reduced radiation doses of patients undergoing diagnostic and neurointerventional procedures for intracranial aneurysms.

## REFERENCES

- Valentin J. Avoidance of radiation injuries from medical interventional procedures, ICRP Publication 85. *Ann ICRP* 2000;30:7–67 CrossRef
- Food U, Administration D. Avoidance of serious X-ray-induced skin injuries to patients during fluoroscopically-guided procedures. *Med Bull* 1994;24:7–17
- Wagner LK, Eifel PJ, Geise RA. Potential biological effects following high X-ray dose interventional procedures. *J Vasc Interv Radiol* 1994;5:71–84 CrossRef Medline
- Mahesh M. Fluoroscopy: patient radiation exposure issues. *Radiographics* 2001;21:1033–45 CrossRef Medline
- Suzuki S, Furui S, Matsumaru Y, et al. Patient skin dose during neuroembolization by multiple-point measurement using a radiosensitive indicator. *AJNR Am J Neuroradiol* 2008;29:1076–81 CrossRef Medline
- Chun CW, Kim BS, Lee CH, et al. Patient radiation dose in diagnostic and interventional procedures for intracranial aneurysms: experience at a single center. *Korean J Radiol* 2014;15:844–49 CrossRef Medline
- Söderman M, Holmin S, Andersson T, et al. Image noise reduction algorithm for digital subtraction angiography: clinical results. *Radiology* 2013;269:553–60 CrossRef Medline
- Söderman M, Mauti M, Boon S, et al. Radiation dose in neuroangiography using image noise reduction technology: a population study based on 614 patients. *Neuroradiology* 2013;55:1365–72 CrossRef Medline
- Schneider T, Wyse E, Pearl MS. Analysis of radiation doses incurred during diagnostic cerebral angiography after the implementation of dose reduction strategies. *J Neurointerv Surg* 2017;9:384–88 CrossRef Medline
- Honarmand AR, Shaibani A, Pashae T, et al. Subjective and objective evaluation of image quality in biplane cerebral digital subtraction angiography following significant acquisition dose reduction

- in a clinical setting. *J Neurointerv Surg* 2017;9:297–301 CrossRef Medline
11. Pearl MS, Torok C, Katz Z, et al. **Diagnostic quality and accuracy of low dose 3D-DSA protocols in the evaluation of intracranial aneurysms.** *J Neurointerv Surg* 2015;7:386–90 CrossRef Medline
  12. Vano E, Fernandez JM, Sanchez RM, et al. **Patient radiation dose management in the follow-up of potential skin injuries in neuroradiology.** *AJNR Am J Neuroradiol* 2013;34:277–82 CrossRef Medline
  13. Yi HJ, Sung JH, Lee DH, et al. **Analysis of radiation doses and dose reduction strategies during cerebral digital subtraction angiography.** *World Neurosurg* 2017;100:216–23 CrossRef Medline
  14. Schneider T, Wyse E, Pearl MS. **Analysis of radiation doses incurred during diagnostic cerebral angiography after the implementation of dose reduction strategies.** *J Neurointerv Surg* 2017;9:384–88 CrossRef Medline
  15. Kahn EN, Gemmete JJ, Chaudhary N, et al. **Radiation dose reduction during neurointerventional procedures by modification of default settings on biplane angiography equipment.** *J Neurointerv Surg* 2016;8:819–23 CrossRef Medline
  16. Ihn YK, Kim BS, Byun JS, et al. **Patient radiation exposure during diagnostic and therapeutic procedures for intracranial aneurysms: a multicenter study.** *Neurointervention* 2016;11:78–85 CrossRef Medline
  17. Hassan AE, Amelot S. **Radiation exposure during neurointerventional procedures in modern biplane angiographic systems: a single-site experience.** *Interv Neurol* 2017;6:105–16 CrossRef Medline
  18. D’Ercole L, Thyron FZ, Bocchiola M, et al. **Proposed local diagnostic reference levels in angiography and interventional neuroradiology and a preliminary analysis according to the complexity of the procedures.** *Phys Med* 2012;28:61–70 CrossRef Medline
  19. Aroua A, Rickli H, Stauffer JC, et al. **How to set up and apply reference levels in fluoroscopy at a national level.** *Eur Radiol* 2007;17:1621–33 CrossRef Medline
  20. Verdun FR, Aroua A, Trueb PR, et al. **Diagnostic and interventional radiology: a strategy to introduce reference dose level taking into account the national practice.** *Radiat Prot Dosimetry* 2005;114:188–91 CrossRef Medline
  21. Brambilla M, Marano G, Dominiotto M, et al. **Patient radiation doses and reference levels in interventional radiology.** *Radiol Med* 2004;107:408–18 Medline
  22. Nickoloff EL, Lu ZF, Dutta AK, et al. **Radiation dose descriptors: BERT, COD, DAP, and other strange creatures.** *Radiographics* 2008;28:1439–50 CrossRef Medline
  23. Bogaert E, Bacher K, Lemmens K, et al. **A large-scale multicentre study of patient skin doses in interventional cardiology: dose-area product action levels and dose reference levels.** *Br J Radiol* 2009;82:303–12 CrossRef Medline
  24. Cheung NK, Boutchard M, Carr MW, et al. **Radiation exposure, and procedure and fluoroscopy times in endovascular treatment of intracranial aneurysms: a methodological comparison.** *J Neurointerv Surg* 2018;10:902–06 CrossRef Medline

# Differences in Cerebral Aneurysm Rupture Rate According to Arterial Anatomies Depend on the Hemodynamic Environment

 S. Fukuda,  Y. Shimogonya, and  N. Yonemoto, on behalf of the CFD ABO Study Group



## ABSTRACT

**BACKGROUND AND PURPOSE:** Cerebral aneurysms have significantly different rupture rates depending on their size and location. The mechanisms underlying these differences are unclear. We examined whether anatomic rupture risks are dependent on the hemodynamic environment on the aneurysmal surface.

**MATERIALS AND METHODS:** Patient-specific geometries and flow rates of 84 cerebral aneurysms (42 anterior communicating artery and 42 MCA aneurysms) were acquired from our clinical study, the Computational Fluid Dynamics Analysis of Blood Flow in Cerebral Aneurysms: Prospective Observational Study. Pulsatile blood flow was simulated to calculate hemodynamic metrics with special attention to wall shear stress magnitude and temporal disturbance. Multivariate analyses were performed to identify associations between hemodynamic metrics and known rupture predictors (age, sex, hypertension, smoking history, location, and size).

**RESULTS:** All the wall shear stress magnitude–based metrics showed a significant negative association with size and location ( $P < .03$ ), but not other risk factors. All the wall shear stress disturbance–based metrics were significantly related to size ( $P < .001$ ). Only normalized transverse wall shear stress, a metric for multidirectional wall shear stress disturbance, was related to location ( $P = .03$ ). The normalized transverse wall shear stress had the highest odds ratio for location and size among hemodynamic metrics (odds ratios, 1.275 and 1.579; 95% confidence intervals, 1.020–1.693 and 1.238–2.219, respectively). Among the arterial geometric parameters, the aspect ratio had the second strongest association with all hemodynamic metrics, after our newly proposed aspect ratio–asphericity index.

**CONCLUSIONS:** The differences in aneurysm rupture rates according to size and location may reflect differences in hemodynamic environments in qualitatively different ways. An enhanced multidirectional wall shear stress disturbance may be especially associated with aneurysm rupture.

**ABBREVIATIONS:** AAI = aspect ratio–asphericity index; AcomA = anterior communicating artery;  $\beta$  = regression coefficient; CFD = computational fluid dynamics; GON = gradient oscillatory number; NtransWSS = normalized transverse wall shear stress; NWSS = normalized wall shear stress; NWSSG = normalized wall shear stress gradient; OSI = oscillatory shear index; TAWSS = time-averaged wall shear stress; TAWSSG = time-averaged wall shear stress gradient; WSS = wall shear stress

Cerebral aneurysm rupture is a major cause of life-threatening SAH, with high mortality and disability rates. Although sev-

eral known risk factors exist, including size, location, sex, age, history of hypertension, and smoking, it remains difficult to predict which cerebral aneurysms are more likely to rupture.<sup>1-4</sup> New predictors of cerebral aneurysm rupture are thus needed.

Aneurysm ruptures are mainly attributable to the biologic process of the progressive degradation of vessel wall structure and strength, in which hemodynamic stress and inflammation are thought to be closely involved.<sup>1,5-7</sup> We have focused on the role of hemodynamics and are using computational fluid dynamics

Received November 26, 2018; accepted after revision March 11, 2019.

From the Department of Neurosurgery (S.F.), National Hospital Organization Kyoto Medical Center, Kyoto, Japan; College of Engineering (Y.S.), Nihon University, Koriyama, Japan; and Department of Biostatistics (N.Y.), Kyoto University, Kyoto, Japan

Shunichi Fukuda and Yuji Shimogonya contributed equally to this work.

The CFD ABO Study Group Member List is in the On-line Appendix.

This work is supported by a grant-in-aid for the Japanese National Hospital Organization Multi-Center Clinical Research, AMED, under grant No. JP15gm0810006h0301, and JSPS KAKENHI grant No. 15K10323.

Paper previously presented, in part, at: International Stroke Conference 2018, January 23–25, 2018; Los Angeles, California.

Please address correspondence to Shunichi Fukuda, MD, Department of Neurosurgery, National Hospital Organization Kyoto Medical Center, 1-one Mukaihata-cho,

Fukakusa, Fushimi-ku, Kyoto City, Kyoto, Japan 612-8555; e-mail: fukudashunichi@gmail.com

 Indicates open access to non-subscribers at [www.ajnr.org](http://www.ajnr.org)

 Indicates article with supplemental on-line appendix and tables.

 Indicates article with supplemental on-line photos.

<http://dx.doi.org/10.3174/ajnr.A6030>

(CFD) techniques to clarify hemodynamics-related factors of cerebral aneurysm ruptures. We are currently conducting the Computational Fluid Dynamics Analysis of Blood Flow in Cerebral Aneurysms: Prospective Observational Study (the CFD ABO Study) as a multi-institutional prospective observational clinical study of the National Hospital Organization in Japan (UMIN000013584). Individual flow rates and arterial geometries were acquired from 461 registered patients to provide realistic patient-specific CFD models.

Among the known predictors of rupture, cerebral artery anatomic parameters such as size and location are the most significant.<sup>1-4</sup> The rupture rate of aneurysms with sizes of 7–10 mm is approximately 3 times higher than that of 3–5 mm aneurysms.<sup>2</sup> The rupture rate of anterior communicating artery (AcomA) aneurysms is approximately twice that of MCA aneurysms.<sup>2</sup> Several researchers have reported that low wall shear stress (WSS) and disturbed WSS are significantly associated with aneurysm rupture.<sup>1,6,8,9</sup> However, the relationships between these anatomic risk factors and the hemodynamic environment and the underlying mechanisms remain unclear. A better understanding of these phenomena could improve the prediction of aneurysm ruptures.

Given the above-described background, we hypothesized that rupture risks based on arterial anatomic parameters are determined by the hemodynamics—that is, the hemodynamic environment on the aneurysmal surface may vary depending on the size and location of the aneurysm, and changes in the hemodynamic environments may cause differences in the rupture-risk rate. We examined the associations between known risk factors and hemodynamic metrics on the aneurysmal surface, and we considered the mechanisms from the point of view of fluid mechanics. We applied CFD and multivariate analysis to 84 cases of bifurcation-type aneurysms located at 2 representative and frequently involved sites, the MCA and AcomA, from the CFD ABO Study. We also explored which geometry-related metrics of aneurysms (among size and 8 other known geometric parameters) were best correlated with the detected hemodynamics metrics.

## MATERIALS AND METHODS

See the On-line Appendix for details of the CFD ABO study methodology.

### Data Sources

3D-CTA images and patient-specific physiologic data, including the flow rate, were acquired from patients who consented to participate in either the CFD ABO Study approved by the National Hospital Organization, Japan, or the pilot study approved by the Ethics Committee of the Kyoto Medical Center, Japan. We analyzed 84 bifurcation-type aneurysms (42 AcomA and 42 MCA aneurysms). A flow chart of the method used is provided in On-line Fig 1.

### CFD Modeling and Postprocessing

Pulsatile blood flow was simulated using the CFD software package ANSYS CFX (ANSYS, Canonsburg, Pennsylvania). We then calculated 7 hemodynamic metrics and 9 geometric parameters during postprocessing for use in statistical analy-

## Characteristics of the cases with cerebral aneurysms<sup>a</sup>

Characteristics	
Women (No.) (%)	43 (51.2%)
Age (yr)	70.4 ± 9.0
Age 70 yr or older	46 (54.8%)
Hypertension (No.) (%)	62 (73.8%)
Smoking history (No.) (%)	49 (58.3%)
AcomA (No.) (%)	42 (50.0%)
Size (mm)	5.64 ± 2.04
Surface area (mm <sup>2</sup> )	60.0 ± 44.8
Volume (mm <sup>3</sup> )	45.5 ± 48.8
Size ratio	2.42 ± 1.08
Area ratio	14.9 ± 14.1
Aspect ratio	0.93 ± 0.39
Aspect ratio—sphericity index	0.565 ± 0.246
Parent artery diameter (mm)	2.45 ± 0.53
Aneurysm surface-averaged TAWSS (Pa)	4.68 ± 4.96
Aneurysm surface-averaged NWSS	5.88 ± 6.58
Aneurysm surface-averaged TAWSSG (Pa/mm)	5.15 ± 6.14
Aneurysm surface-averaged NWSSG	16.0 ± 19.9
Aneurysm surface-averaged OSI	0.0169 ± 0.0144
Aneurysm surface-averaged GON	0.0664 ± 0.0523
Aneurysm surface-averaged NtransWSS	0.130 ± 0.059

<sup>a</sup> Data are mean ± SD unless otherwise indicated.

ses. The CFD modeling and postprocessing details are described in the On-line Appendix.

### Statistical Analysis

The continuous data are reported as means ± SDs and were analyzed using the Wilcoxon rank sum test. A multivariate regression analysis was performed to investigate the influence of known risk factors for rupture—ie, size (the maximum diameter of the cerebral aneurysm), location (AcomA versus MCA), sex, age, history of hypertension and smoking—on the 7 hemodynamic metrics: the time-averaged wall shear stress (TAWSS), normalized WSS (NWSS), time-averaged WSS gradient (TAWSSG), normalized WSS gradient (NWSSG), oscillatory shear index (OSI), gradient oscillatory number (GON), and normalized transverse WSS (NtransWSS).

We performed a multivariate logistic analysis to determine the effects of the 7 hemodynamic metrics on size (<7 versus ≥7 mm) and location. We also performed a multivariate regression analysis to determine the associations between the known arterial geometric parameters and hemodynamic metrics after adjustment for age, sex, hypertension, smoking history, and aneurysm location. The rationales for risk-factor selection are described in the On-line Appendix. We computed regression coefficients with 95% CIs and *P* values for the models. Differences with *P* < .05 were considered significant. All analyses were performed using JMP, Version 11.0.0 software (SAS Institute, Cary, North Carolina).

## RESULTS

### Characteristics

The case characteristics are summarized in the Table.

### Association of Known Rupture Risk Factors with Hemodynamic Metrics

To investigate whether known rupture risk factors are hemodynamically involved in rupture, we examined the association be-

tween each rupture risk factor and hemodynamic metrics using a multivariate regression analysis (On-line Table 1 and On-line Fig 3). The size and WSS magnitude–based metrics, TAWSS, NWSS, TAWSSG, and NWSSG, were significantly negatively correlated, indicated by the following: TAWSS regression coefficient ( $\beta$ ),  $-0.561$  (95% CI,  $-1.064$  to  $-0.058$ )  $P = .02$ ; NWSS  $\beta$ ,  $-0.867$  (95% CI,  $-1.510$  to  $-0.224$ )  $P = .008$ ; TAWSSG  $\beta$ ,  $-0.868$  (95% CI,  $-1.486$  to  $-0.249$ )  $P = .006$ ; NWSSG  $\beta$ ,  $-3.22$  (95% CI,  $-5.16$  to  $-1.28$ )  $P = .001$ . The WSS disturbance–based metrics, OSI, GON, and NtransWSS, were significantly positively correlated as indicated by the following: OSI  $\beta$ ,  $0.00332$  (95% CI,  $0.00191$ – $0.00472$ )  $P < .001$ ; GON  $\beta$ ,  $0.0145$  (95% CI,  $0.0097$ – $0.0193$ )  $P < .001$ ; NtransWSS  $\beta$ ,  $0.0145$  (95% CI,  $0.0089$ – $0.0200$ )  $P < .001$ .

In contrast, a significant negative association was observed between the location (MCA versus AcomA aneurysms) and each of the WSS magnitude–based metrics: TAWSS  $\beta$ ,  $-1.82$  (95% CI,  $-2.84$  to  $-0.80$ )  $P < .001$ ; NWSS  $\beta$ ,  $-2.45$  (95% CI,  $-3.75$  to  $-1.15$ )  $P < .001$ ; TAWSSG  $\beta$ ,  $-2.05$  (95% CI,  $-3.31$  to  $-0.80$ )  $P = .001$ ; NWSSG  $\beta$ ,  $-6.91$  (95% CI,  $-10.84$  to  $-2.98$ )  $P < .001$ . A significant positive association with the location was found in only NtransWSS as a metric for multidirectional WSS disturbance among all of the WSS disturbance–based metrics examined ( $\beta$ ,  $0.0119$ ; 95% CI,  $0.0006$ – $0.0232$ ;  $P = .03$ ).

#### **Association of Hemodynamic Metrics with the Size and Location of Cerebral Aneurysms**

Using a multivariate logistic analysis, we sought to identify which hemodynamic metric was most strongly related to the size ( $<7$  versus  $\geq 7$  mm) and location in which significant hemodynamic involvement was observed. Although all of the hemodynamic metrics showed a significant association with both size and location, the NtransWSS had the highest OR and the strongest association with both size (OR,  $1.579$ ; 95% CI,  $1.238$ – $2.128$ ) and location (OR,  $1.275$ ; 95% CI,  $1.020$ – $1.639$ ) (On-line Table 1).

#### **Association between Aneurysm Arterial Geometric Parameters and Hemodynamic Metrics**

Several arterial geometric parameters have been reported as predictors of aneurysm rupture, such as size, size ratio, and aspect ratio. We therefore examined which arterial geometric parameter most strongly reflects each hemodynamic metric by performing a multivariate regression analysis. Among the known arterial geometric rupture risk factors, the aspect ratio showed the strongest association with all hemodynamic metrics as shown in On-line Table 2: TAWSS  $\beta$ ,  $-2.46$  (95% CI,  $-5.12$  to  $-0.21$ )  $P = .07$ ; NWSS  $\beta$ ,  $-3.20$  (95% CI,  $-6.65$  to  $0.25$ )  $P = .06$ ; TAWSSG  $\beta$ ,  $-2.92$  (95% CI,  $-6.26$  to  $-0.42$ )  $P = .08$ ; NWSSG  $\beta$ ,  $-10.5$  (95% CI,  $-21.1$  to  $-0.2$ )  $P = .05$ ; OSI  $\beta$ ,  $0.00799$  (95% CI,  $0.00017$ – $0.01616$ )  $P = .05$ ; GON  $\beta$ ,  $0.0352$  (95% CI,  $0.0057$ – $0.0648$ )  $P = .02$ ; NtransWSS  $\beta$ ,  $0.0379$  (95% CI,  $0.0052$ – $0.0707$ )  $P = .02$ .

However, the aspect ratio–sphericity index (AAI), our newly proposed geometric parameter, was more strongly correlated with all the hemodynamic metrics than the aspect ratio: TAWSS  $\beta$ ,  $-4.02$  (95% CI,  $-8.23$  to  $-0.19$ )  $P = .06$ ; NWSS  $\beta$ ,  $-5.46$  (95% CI,  $-10.90$  to  $-0.01$ )  $P = .04$ ; TAWSSG  $\beta$ ,  $-4.72$  (95% CI,  $-9.99$  to  $-0.56$ )  $P = .07$ ; NWSSG  $\beta$ ,  $-17.3$  (95% CI,  $-34.0$  to

$-0.5$ )  $P = .04$ ; OSI  $\beta$ ,  $0.0121$  (95% CI,  $0.0008$ – $0.0250$ )  $P = .06$ ; GON  $\beta$ ,  $0.0559$  (95% CI,  $0.0092$ – $0.1027$ )  $P = .01$ ; NtransWSS  $\beta$ ,  $0.0558$  (95% CI,  $0.0038$ – $0.1079$ )  $P = .03$ . Here, AAI is defined as  $(H/N) \times (d^2/S)$ , where  $H$  is the height,  $N$  the neck width,  $d$  the size, and  $S$  the surface area.

#### **Differences in Flow Rates in Parent Vessels and Size between the AcomA and MCA Aneurysms**

The anterior cerebral artery flow rate ( $90.9 \pm 41.9$  mL/min) was significantly lower than the MCA flow rate ( $123.0 \pm 50.9$  mL/min) ( $P < .001$ ; On-line Table 3). The size was slightly, but not significantly, larger in the AcomA aneurysms ( $5.82 \pm 2.10$  mm) than the MCA aneurysms ( $5.46 \pm 2.00$  mm).

#### **Differences in Flow Rates in Parent Vessels and Size Between the 2 Different Size Groups**

The parent vessel flow rate was not significantly different between the large ( $\geq 7$  mm;  $92.2 \pm 41.9$  mL/min) and small aneurysm groups ( $<7$  mm;  $112.8 \pm 50.8$  mL/min; On-line Table 4). The size was significantly greater in the large ( $8.28 \pm 1.16$  mm) than in the small ( $4.58 \pm 1.17$  mm) aneurysm group ( $P < .001$ ).

#### **Differences in Hemodynamic Metrics between Size Groups with a Threshold of 5 or 7 mm**

Using a multivariate regression analysis, we examined the differences in hemodynamic metrics between the 2 different size groups with a threshold of 5 or 7 mm (On-line Table 5). The WSS magnitude–based metrics and size were better correlated in the 5–than the 7–mm threshold ( $\beta$ , 5 versus 7 mm; TAWSS,  $-1.27$  versus  $-1.20$ ; NWSS,  $-2.37$  versus  $-1.48$ ; TAWSSG,  $-1.89$  versus  $-1.70$ ; NWSSG,  $-7.97$  versus  $-5.20$ ), whereas in the WSS disturbance–based metrics, the association was stronger in the 7–than the 5–mm threshold ( $\beta$ , 5 versus 7 mm; OSI,  $0.00367$  versus  $0.00648$ ; GON,  $0.0207$  versus  $0.0260$ ; NtransWSS,  $0.0176$  versus  $0.0274$ ).

#### **Flow Rates and TAWSS on the ICA in MCA Aneurysm Cases**

In the MCA aneurysm cases, both the flow rate and the TAWSS on the ICA on the side where the aneurysm was present were significantly higher in the large ( $\geq 5$  mm) than the small ( $<5$  mm) aneurysm group ( $P = .03$  and  $.03$ , respectively; On-line Table 6).

## **DISCUSSION**

Hemodynamics is likely involved in cerebral aneurysm ruptures, and some of the rupture predictors become significant risk factors due to the influence of hemodynamics.<sup>1,5–7</sup> Several studies have quantitatively examined hemodynamic metrics in ruptured and unruptured cerebral aneurysms.<sup>7,10</sup> These reports examined the degree of association between hemodynamic metrics and aneurysm rupture and demonstrated that ruptured and unruptured aneurysms had significantly different hemodynamic characteristics.<sup>10</sup> Therefore, it is presumed that some of the known rupture risks become significant by reflecting the influence of these hemodynamic environments. However, to our knowledge, no report has described the significance of the association between hemodynamic parameters as independent variables and the rupture risks, such as size and location, or conversely, how much the rup-

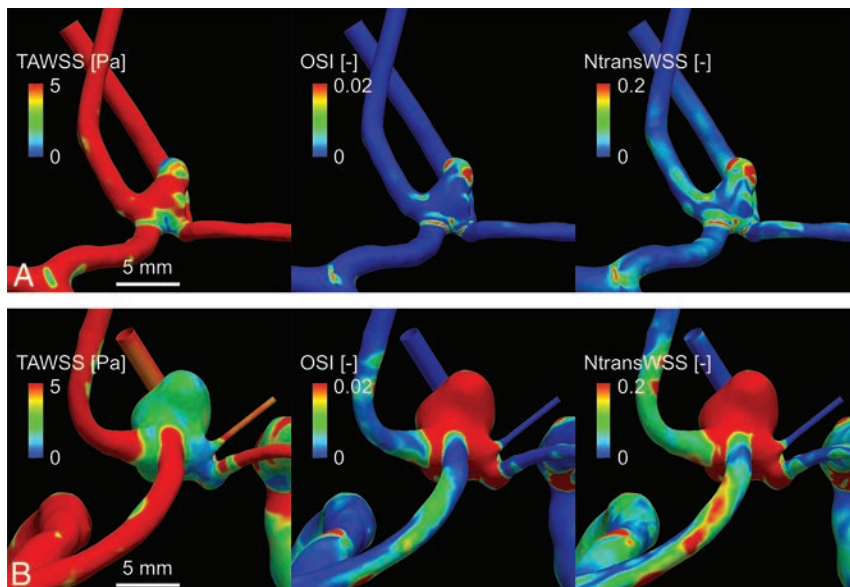


**FIG 1.** Comparisons of hemodynamic metrics between a representative small aneurysm (A) and a large aneurysm (B).

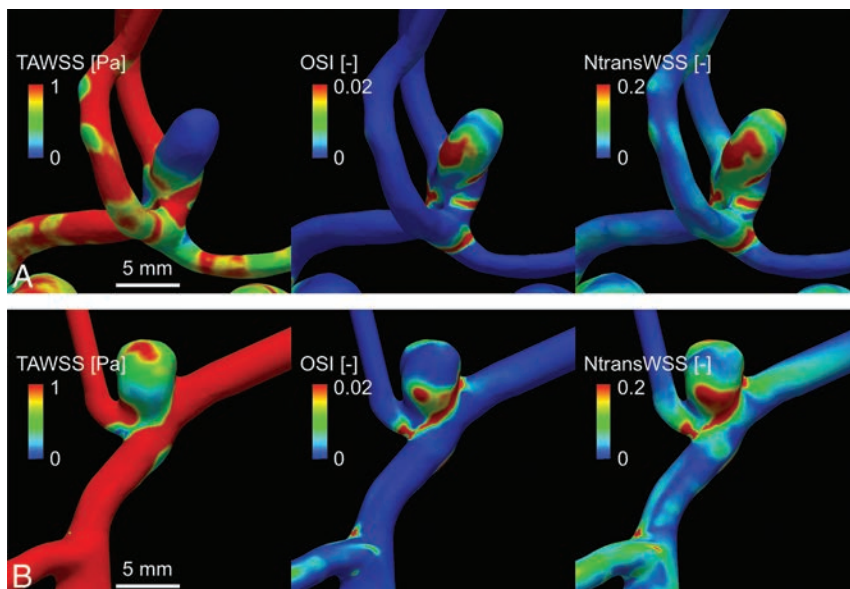


**FIG 2.** Comparisons of hemodynamic metrics between a representative anterior communicating artery aneurysm (A) and an MCA aneurysm (B).

ture risks as independent variables are related to hemodynamic environments, though several reports have examined the association between hemodynamic factors and rupture itself.<sup>7,10</sup> Therefore, we statistically examined the mutual relationship between hemodynamic parameters and representative risk factors such as age, sex, smoking history, and hypertension in addition to size and location. This is thus the first examination of this type. The results of our analyses indicate that arterial anatomic parameters (size and location of aneurysms) and hemodynamic metrics characterizing the WSS magnitude and disturbance were significantly associated; both the associations of the arterial anatomic parameters with the hemodynamic metrics and the associations of the hemodynamic metrics with the arterial anatomic parameters were statistically significant (On-line Table 1 and On-line Fig 3), sug-

gesting that rupture risks based on arterial anatomic parameters are determined by the hemodynamic environment.

Larger and Acoma aneurysms have higher rupture rates than smaller and MCA aneurysms, respectively.<sup>2</sup> The present results show that the TAWSS on the aneurysmal surface was significantly negatively associated with size and location (On-line Table 1 and Figs 1 and 2 and On-line Figs 3–5). This finding is consistent with studies showing that a significant decrease in the magnitude of the WSS on the aneurysmal surface is closely associated with the aneurysm rupture status.<sup>1,6,8,9</sup>

This leads us to ask what mechanisms cause the WSS to become low or disturbed depending on the size and location. Are the mechanisms different between size and location? Based on the present data, we considered the mechanisms from the point of view of fluid mechanics. The finding that the TAWSS was significantly decreased on Acoma aneurysms compared with MCA aneurysms could be explained qualitatively. It is hemodynamically clear that the TAWSS on the aneurysmal surface is affected principally by the size of the aneurysm and the inflow rate into the aneurysm.<sup>11</sup> The larger the size of the aneurysm (ie, the larger the open space inside the aneurysm) and the lower the inflow rate, the lower the TAWSS will be.

Because it was difficult to measure the inflow rate into the aneurysm for all the cases, we use the flow rate in the parent vessel, the anterior cerebral artery or MCA, in the following discussion. In our results, the anterior cerebral artery flow rate was significantly lower than the MCA flow rate, whereas the aneurysmal size showed no significant difference between the Acoma and MCA aneurysm groups (On-line Table 3). Therefore, the significant difference in TAWSS between the 2 groups was due mainly to the difference in flow rates. In contrast, the decrease in the TAWSS with increasing aneurysm size may be explained simply by the effect of size because the flow rate in the parent vessel showed no difference between the 2 size groups (On-line Table 4).

A significant positive association was observed between each of the WSS disturbance-based metrics (the OSI, GON, and NtransWSS) and the size of the aneurysm (On-line Table 1, Fig 1, and On-line Fig 4). With respect to location, however, only NtransWSS differed significantly among the different locations (On-line Table 1, Fig 2, and On-line Fig 5). These findings suggest that aneurysm size and location both contribute significantly to

the hemodynamic disturbance, but in qualitatively different ways. In the present study, we defined a new metric, the NtransWSS, by dividing the nodal transverse WSS<sup>12</sup> by the TAWSS at the same node because this normalization allowed us to compare the transverse WSS among multiple cases on the same basis. The OSI can distinguish between purely forward (low OSI) and reversing unidirectional (high OSI) flow, but the NtransWSS cannot (low NtransWSS in both cases). In contrast, the NtransWSS can distinguish between reversing unidirectional (low NtransWSS) and multidirectional (high NtransWSS) flow, but the OSI cannot (high OSI in both cases).<sup>12</sup>

It thus seems reasonable to infer that the hemodynamic environments of small and large aneurysms are characterized in part by purely forward and multidirectional WSS, respectively, because both the OSI and NtransWSS were significantly different. In contrast, the hemodynamic environment of the MCA and AcomA aneurysms may be characterized in part by reversing unidirectional and multidirectional WSS, respectively, because significant variations were observed in the NtransWSS, but not in the OSI. The more disturbed hemodynamic stress at AcomA aneurysms compared with MCA aneurysms may be because AcomA, but not MCA, aneurysms are positioned along the circle of Willis.

Among the hemodynamic metrics, the NtransWSS had the highest OR for both size and location (On-line Table 1). This suggests that rupture rates in aneurysms of different sizes and locations are most strongly influenced by the multidirectional disturbance in WSS. Several experimental studies have reported that low WSS or disturbed WSS without a clear direction, ie, multidirectional WSS, or both cause sustained molecular signaling of proinflammatory and proliferative pathways of vascular endothelial cells.<sup>13,14</sup> The inflammatory processes in vessel walls play a critical role in the pathogenesis of cerebral aneurysms.<sup>15-17</sup> Therefore, the clinical evidence of higher rupture rates in AcomA aneurysms and larger aneurysms might be associated, in part, with the inflammation in the vessel walls enhanced by the low WSS and the multidirectionally disturbed WSS detected by the NtransWSS.<sup>7,18</sup>

Several researchers have proposed various aneurysmal geometric parameters for predicting rupture risk.<sup>19-21</sup> The use of surrogate geometric parameters of the hemodynamic environment with high rupture risk would be of great clinical value because geometric parameters can be measured more easily than hemodynamic metrics at clinical sites. We thus investigated which previously proposed geometric parameters of aneurysms best correlated with the TAWSS and NtransWSS. Our analyses revealed that the aspect ratio was most strongly correlated with both the TAWSS and NtransWSS, followed by the size ratio. The aspect ratio has been reported to play a greater role than the size in the rupture of AcomA and MCA aneurysms.<sup>19,20</sup> The size ratio has been reported to be a useful rupture risk predictor, particularly for small aneurysms of <5 mm.<sup>21</sup>

However, the correlation between some geometric parameters, including size ratio and aspect ratio, and aneurysm rupture is still controversial.<sup>22</sup> This is presumably because these geometric parameters only partially reflect hemodynamic environments (On-line Table 2). Therefore, we defined a novel geometric parameter, the AAI, which serves as a special refined geometric marker for the nonsphericity of aneurysmal shapes.

The AAI best reflected both the TAWSS and the NtransWSS among all of the geometric parameters examined (On-line Table 2). The AAI is thus a potentially useful geometric parameter for predicting the rupture risk of aneurysms. We will validate its usefulness on completion of the ABO study. Because CFD analyses currently take time and effort, it is clinically impractical to conduct them for all unruptured aneurysm cases. Thus, the use of arterial geometric parameters may be more convenient at the clinical level. Indeed, it might be reasonable to first perform a screening with useful arterial geometric parameters and then to examine the detailed hemodynamics using a CFD analysis for essential cases.

To better understand how the hemodynamic metrics change with increasing aneurysm size, we examined the threshold size at which the hemodynamic metrics changed notably. The difference in the WSS magnitude–based metrics between the 2 different size groups with a threshold of 5 mm was larger than that with a threshold of 7 mm, whereas the difference in the WSS disturbance–based metrics between the 2 different size groups with a threshold of 7 mm was larger than that when the threshold was 5 mm (On-line Table 6). In other words, as the aneurysm size increases, the magnitude of the WSS declines first, and then the WSS disturbance occurs. Cerebral aneurysms may have at least 2 different critical sizes at which the rupture risk is heightened.

In the CFD ABO study, individual flow rates and arterial geometries have been acquired from each registered patient to provide realistic patient-specific CFD models. In most hemodynamic cohort studies using CFD analyses, the inlet boundary conditions are based on a typical flow velocity or flow rate of healthy subjects.<sup>7,18</sup> Alternatively, in other studies, the inlet boundary conditions were set so that the mean WSS at the ICA was equal to 1.5 Pa.<sup>23</sup> However, we found that the mean flow rate and the WSS at the ICA of the large MCA cases ( $\geq 5$  mm) were significantly higher than those of the small MCA cases (<5 mm; On-line Table 6). Thus, the mean WSS at the ICA is not constant but strongly depends on characteristics of the individual case. Because such substantial differences are thought to have a non-negligible impact on hemodynamic characteristics,<sup>10</sup> it is essential to use patient-specific inflow boundary conditions in combination with patient-specific arterial geometry in these types of statistical analyses.

The present study has some limitations. First, we did not directly measure the rupture risk, but we measured recognized risk factors for rupture. Second, it remains unclear whether the NtransWSS can further help to stratify the rupture risk of aneurysms with similar sizes and locations, though the results suggest that an enhanced NtransWSS may be strongly associated with aneurysm rupture. Third, we cannot conclude that the NtransWSS is superior to other hemodynamic metrics in terms of the risk assessment of aneurysm rupture. Fourth, only AcomA and MCA aneurysms were examined. It is unclear how the present results would change if aneurysms at other locations were included. These limitations may be resolved by a statistical hemodynamic comparison between unruptured and ruptured/enlarged aneurysms at various locations, which will be made in our ongoing clinical study.

## CONCLUSIONS

In the analysis of AcomA and MCA aneurysms, the arterial anatomic parameters (size and location) and hemodynamic metrics characterizing the WSS magnitude and disturbance were significantly associated. Therefore, the differences in the rupture rate of aneurysms for various arterial anatomic parameters may reflect the differences in the hemodynamic environment. Our results also suggest that a CFD analysis is a useful simulation that matches epidemiologic data. Although both low WSS and enhanced disturbed flow may be involved in aneurysm ruptures, an enhanced disturbance of multidirectional WSS may be most strongly associated with aneurysm ruptures; the NtransWSS, a refined hemodynamic metric proposed in the present study, had the highest OR for size and location among all the examined hemodynamic metrics including OSI. Size and location had significant effects on the hemodynamic environment in qualitatively different ways; thus, the decrease in the WSS with increasing aneurysm size may be explained by the effect of size itself, whereas the significant difference in the WSS according to location may be due to the difference in the flow rate of the parent artery. Our novel geometric parameter, the AAI, may be useful for predicting the rupture risk of aneurysms.

## ACKNOWLEDGMENTS

We thank Dr Geert W. Schmid-Schönbein, Chair of the Department of Bioengineering, University of California, San Diego, for his valuable advice. We also thank Mr Yasuhide Imoto for his assistance.

Disclosures: Shunichi Fukuda—RELATED: Grant: grant-in-aid from the Japanese National Hospital Organization Multi-Center Clinical Research, AMED, and a JSPS KAKENHI grant, Comments: This study was supported by a grant-in-aid from the Japanese National Hospital Organization Multi-Center Clinical Research, AMED, under grant No. JP15gm0810006h0301 and a JSPS KAKENHI grant No. 15K10323.

## REFERENCES

1. Etminan N, Rinkel GJ. **Unruptured intracranial aneurysms: development, rupture and preventive management.** *Nat Rev Neurol* 2016; 12:699–713 CrossRef Medline
2. Morita A, Kirino T, Hashi K, et al; the UCAS Japan Investigators. **The natural course of unruptured cerebral aneurysms in a Japanese cohort.** *N Engl J Med* 2012;366:2474–82 CrossRef Medline
3. Greving JP, Wermer M, Brown RD Jr, et al. **Development of the PHASES score for prediction of risk of rupture of intracranial aneurysms: a pooled analysis of six prospective cohort studies.** *Lancet Neurol* 2014;13:59–66 CrossRef Medline
4. Cebal JR, Raschi M. **Suggested connections between risk factors of intracranial aneurysms: a review.** *Ann Biomed Eng* 2013;41:1366–83 CrossRef Medline
5. Kayembe KN, Sasahara M, Hazama F. **Cerebral aneurysms and variations in the circle of Willis.** *Stroke* 1984;15:846–50 CrossRef Medline
6. Shimogonya Y, Fukuda S. **Computational and experimental studies into the hemodynamics of cerebral aneurysms.** *Journal of Biomechanical Science and Engineering* 2016;11:15–00488 CrossRef
7. Xiang J, Natarajan SK, Tremmel M, et al. **Hemodynamic-morphologic discriminants for intracranial aneurysm rupture.** *Stroke* 2011; 42:144–52 CrossRef Medline
8. Signorelli F, Sela S, Gesualdo L, et al. **Hemodynamic stress, inflammation, and intracranial aneurysm development and rupture: a systematic review.** *World Neurosurg* 2018;115:234–44 CrossRef Medline
9. Takao H, Murayama Y, Otsuka S, et al. **Hemodynamic differences between unruptured and ruptured intracranial aneurysms during observation.** *Stroke* 2012;43:1436–39 CrossRef Medline
10. Cebal JR, Mut F, Weir J, et al. **Quantitative characterization of the hemodynamic environment in ruptured and unruptured brain aneurysms.** *AJNR Am J Neuroradiol* 2011;32:145–51 CrossRef Medline
11. Jansen IG, Schneiders JJ, Potters WV, et al. **Generalized versus patient-specific inflow boundary conditions in computational fluid dynamics simulations of cerebral aneurysmal hemodynamics.** *AJNR Am J Neuroradiol* 2014;35:1543–48 CrossRef Medline
12. Peiffer V, Sherwin SJ, Weinberg PD. **Computation in the rabbit aorta of a new metric: the transverse wall shear stress—to quantify the multidirectional character of disturbed blood flow.** *J Biomech* 2013; 46:2651–58 CrossRef Medline
13. Aoki T, Yamamoto K, Fukuda M, et al. **Sustained expression of MCP-1 under low wall shear stress concomitant with turbulent flow in endothelial cells of intracranial aneurysm.** *Acta Neuropathol Commun* 2016;4:48 CrossRef Medline
14. Chien S. **Effects of disturbed flow on endothelial cells.** *Ann Biomed Eng* 2008;36:554–62 CrossRef Medline
15. Aoki T, Kataoka H, Shimamura M, et al. **NF- $\kappa$ B is a key mediator of cerebral aneurysm formation.** *Circulation* 2007;116:2830–40 CrossRef Medline
16. Nuki Y, Tsou TL, Kurihara C, et al. **Elastase-induced intracranial aneurysms in hypertensive mice.** *Hypertension* 2009;54:1337–44 CrossRef Medline
17. Aoki T, Fukuda M, Nishimura M, et al. **Critical role of TNF- $\alpha$ -TNFR1 signaling in intracranial aneurysm formation.** *Acta Neuropathol Commun* 2014;2:34 CrossRef Medline
18. Shojima M, Oshima M, Takagi K, et al. **Magnitude and role of wall shear stress on cerebral aneurysm: computational fluid dynamic study of 20 middle cerebral artery aneurysms.** *Stroke* 2004;35: 2500–05 CrossRef Medline
19. Lin N, Ho A, Gross BA, et al. **Differences in simple morphological variables in ruptured and unruptured middle cerebral artery aneurysms.** *J Neurosurg* 2012;117:913–19 CrossRef Medline
20. Maiti TK, Bir SC, Patra DP, et al. **158 Morphological parameters for anterior communicating artery aneurysm rupture risk assessment.** *Neurosurgery* 2016;63:163–64 CrossRef
21. Kashiwazaki D, Kuroda S; Sapporo SAH Study Group. **Size ratio can highly predict rupture risk in intracranial small (<5 mm) aneurysms.** *Stroke* 2013;44:2169–73 CrossRef Medline
22. Lauric A, Baharoglu MI, Gao BL, et al. **Incremental contribution of size ratio as a discriminant for rupture status in cerebral aneurysms: comparison with size, height, and vessel diameter.** *Neurosurgery* 2012; 70:944–51; discussion 951–52 CrossRef Medline
23. Sugiyama S, Niizuma K, Sato K, et al. **Blood flow into basilar tip aneurysms: a predictor for recanalization after coil embolization.** *Stroke* 2016;47:2541–47 CrossRef Medline

# Impact of Balloon-Guiding Catheter Location on Recanalization in Patients with Acute Stroke Treated by Mechanical Thrombectomy

 D.E. Jeong,  J.W. Kim,  B.M. Kim,  W. Hwang, and  D.J. Kim

## ABSTRACT

**BACKGROUND AND PURPOSE:** Mechanical thrombectomy with proximal flow control and forced aspiration may improve the outcome of endovascular revascularization therapy for patients with acute stroke. The purpose of this study was to compare the impact of balloon-guiding catheter locations in patients treated for anterior circulation acute ischemic stroke using mechanical thrombectomy.

**MATERIALS AND METHODS:** The influence of the balloon-guiding catheter location (proximal, balloon-guiding catheter tip proximal to C1 vertebral body; distal, between the skull base and the C1 vertebral body) was analyzed in patients with acute anterior circulation stroke treated with stent-retriever thrombectomy. The baseline angiographic/clinical characteristics, time intervals, recanalization rates, and clinical outcomes were compared.

**RESULTS:** The clinical analysis included 102 patients (mean age,  $69.5 \pm 12.8$  years; male/female ratio = 52:50). The balloon-guiding catheter was located distally in 49 patients and proximally in 53 patients for flow control and forced aspiration during stent retrieval. The puncture-to-recanalization time was shorter in the distal group than in the proximal group (40 versus 56 minutes,  $P = .02$ ). Successful and complete recanalizations were more frequently achieved in the distal group compared with the proximal group (98.0% versus 75.5%,  $P = .003$ ; 67.3% versus 45.3%,  $P = .04$ , respectively). Multivariate analysis showed that the distal catheterization location was independently associated with successful recanalization (adjusted OR, 13.4; 95% CI, 2.4–254.8;  $P = .02$ ).

**CONCLUSIONS:** Location of the balloon-guiding catheter has a significant impact on recanalization in patients with acute stroke. The balloon-guiding catheter should be positioned as distally as safely possible in the cervical ICA for maximally effective thrombectomy.

**ABBREVIATION:** BGC = balloon-guiding catheter

The successful recanalization and better clinical outcome of endovascular revascularization therapy in acute ischemic stroke have been proved in several randomized clinical trials.<sup>1–5</sup> Recently, various methods using balloon-guiding catheters, intermediate catheters, and stent-deployment techniques have been introduced that may improve the efficacy of mechanical thrombectomy.<sup>6–8</sup> Proximal flow control with a balloon-guiding catheter (BGC) using stent retrievers has been shown to improve recanalization rates with shorter procedural times.<sup>9–11</sup> Despite the improved outcome, some cases still show

less-than-optimal results with prolonged procedural time and unsuccessful/incomplete recanalization.

It is intuitive that the effects of flow arrest and forced aspiration would be most effective when the distance between the thrombus and the site of balloon occlusion is short (ie, the balloon is catheterized as distally as possible). However, the actual clinical impact of achieving distal balloon catheterization is not well-known. In addition, there may be concerns for complications such as dissection related to distal navigation of the BGC into the distal cervical ICA.<sup>12,13</sup>

The purpose of this study was to compare the impact of BGC locations in patients treated for anterior circulation acute ischemic stroke by mechanical thrombectomy.

## MATERIALS AND METHODS

### Patient Analysis

The patients were collected from a prospectively maintained stroke registry. Between July 2014 and June 2018, three hundred thirty-two patients were referred for endovascular revascularization therapy of acute ischemic stroke in Severance Hospital. The inclusion criteria for the study were as follows: 1) patients pre-

Received December 28, 2018; accepted after revision March 7, 2019.

From the Department of Radiology (D.E.J., J.W.K., B.M.K., D.J.K.), Yonsei University College of Medicine, Severance Hospital, Seoul, South Korea; Department of Neurology (D.E.J.), YeongNam University College of Medicine, Daegu, South Korea; and Department of Mechanical and Aerospace Engineering (W.H.), Seoul National University, Seoul, South Korea.

This study was supported by a grant from the Research Institute of Radiological Science, Yonsei University College of Medicine (grant No. 4-2017-0877).

Please address correspondence to Dong Joon Kim, MD, PhD, Department of Radiology, Yonsei University College of Medicine, 50-1 Yonsei-ro, Seodaemun-gu, Seoul 03722, South Korea; e-mail: djkimmd@yuhs.ac

<http://dx.doi.org/10.3174/ajnr.A6031>

senting within 8 hours from symptom onset of an anterior circulation large-vessel occlusion on CT angiography, 2) ASPECTS of 4 or more, 3) treated by stent-retriever (Solitaire, 4 × 20 mm; Covidien, Irvine, California) thrombectomy with a BGC (Cello 95 cm; Covidien). The exclusion criteria of this study were the following: 1) posterior circulation occlusion ( $n = 61$ ), 2) dissection ( $n = 1$ ) as the etiology of stroke, and 3) ipsilateral stenosis or occlusion of the proximal ICA ( $n = 29$ ). Other reasons for exclusion were the following: primary contact aspiration ( $n = 18$ ), different-profile BGC/stent retriever ( $n = 106$ ), no BGC use ( $n = 6$ ), primary angioplasty ( $n = 4$ ), failed access ( $n = 2$ ), and multiple cerebral artery occlusions ( $n = 3$ ). In total, 102 patients who met the criteria were included in this study. The anteroposterior and lateral DSA images were reviewed for analysis of the imaging findings, including the cervical ICA tortuosity, occlusion site, BGC location, recanalization, and number of thrombectomies.

The locations of the BGCs were defined and grouped as follows: the distal balloon-guiding group, the balloon-guiding tip catheterization approaches the entrance of the petrous ICA—ie, balloon inflation between the skull base and the lower margin of the C1 vertebral body; and the proximal BGC group, balloon inflation proximal to lower margin of the C1 vertebral body for flow control and forced aspiration during stent retrieval. Tortuosity of the cervical ICA was defined as an angulation of  $\geq 90^\circ$  of the main flow axes of the cervical ICA. Modified TICI scores of 2b or 3 were defined as successful recanalization.<sup>14</sup> A modified TICI score of 3 was defined as complete recanalization. Embolization to a new territory was defined as emboli observed within the previously unaffected territory on postthrombectomy angiography.<sup>15</sup>

Clinical information including sex, age, vascular risk factors (hypertension, diabetes mellitus, atrial fibrillation, previous ischemic stroke), NIHSS score, intravenous rtPA therapy, time intervals (onset, puncture, recanalization time), hemorrhage, 3-month mRS score, and mortality was analyzed. The recanalization time was defined as the time to final recanalization in successful recanalizations and the time of the last angiographic series in patients with unsuccessful recanalizations. An intracerebral hemorrhage was classified according to the second European-Australasian Acute Stroke Study classification, and symptomatic intracerebral hemorrhage was defined as any hemorrhage associated with an NIHSS score increase of  $\geq 4$  within 24 hours.<sup>16</sup> Good clinical outcome was defined as 3-month mRS scores of 0–2. The images and clinical information were compared between the distal and proximal BGC groups.

### Procedure

All procedures were performed by the femoral artery approach. In general, an 8F sheath (Radifocus; Terumo, Tokyo, Japan or Flexor Shuttle-SL; Cook, Bloomington, Indiana) and an 8F BGC were introduced into the cervical ICA coaxially with a 5F diagnostic catheter. Distal access to the cervical ICA with the BGC was preferred, but the decision was made at the discretion of the operator. A microcatheter over a microguidewire was used in all cases for catheterization of the occluded intracranial vessel. After we placed the microcatheter distal to the thrombus, the microguidewire was replaced by a stent retriever. After stent deployment, antegrade

reperfusion was maintained for 3–4 minutes before retrieval. After proximal flow control with balloon inflation, the stent retriever and the microcatheter were retrieved together under continuous forced aspiration using 20-mL syringes. After mechanical thrombectomy, 15- to 20-minute delayed angiograms were obtained to detect re-occlusion of the target vessel.

### Statistical Analysis

The data were analyzed using the R statistical and computing software (Version 3.5.1; <http://www.r-project.org/>). The continuous variables were analyzed with the 2-sample *t* test and presented as mean  $\pm$  SD when normal distribution could be assumed; otherwise, the Mann-Whitney *U* test was used and presented as a median (minimum, maximum). Categorical variables were compared using the Pearson  $\chi^2$  or Fisher exact test as appropriate. Multivariate logistic analyses were performed for variables including sex, age, hypertension, initial NIHSS score, IV rtPA therapy, tortuosity of the ICA, and BGC location. A *P* value  $< .05$  was considered statistically significant.

The study was approved by the Severance Hospital institutional review board with a waiver of informed consent due to its retrospective design.

### RESULTS

The mean age of the patients was  $69.5 \pm 12.8$  years (male/female ratio = 52:50). The median initial NIHSS score was 15. The baseline characteristics of the distal and proximal BGC groups are summarized in Table 1. Hypertension was more frequent in the proximal BGC group than in the distal BGC group. Other factors did not show statistically significant differences between the groups.

Overall successful recanalization was achieved in 88 of 102 (86.3%) patients. The puncture-to-recanalization time was significantly shorter in the distal BGC group than in the proximal BGC group (56 versus 40 minutes,  $P = .02$ ). Successful recanalization was more frequently achieved in the distal BGC group compared with the proximal BGC group (98.0% versus 75.5%,  $P = .003$ ; Table 2). Complete recanalization was also more frequently achieved with a distal BGC (67.3% versus 45.3%,  $P = .04$ ). The good long-term outcome rates were more favorable in the distal BGC group but did not reach statistical significance (57.1% versus 45.3%,  $P = .32$ ).

In the multivariate logistic regression analysis (adjusted for age, sex, initial NIHSS score, IV-rtPA use, ICA tortuosity, and hypertension), the BGC location was the only independent factor of successful recanalization (adjusted odds ratio, 13.399; 95% confidence interval, 2.369–254.815;  $P = .02$ ; Table 3).

Successful recanalization was highest in patients with nontortuous cervical ICAs and distal balloon-guiding catheterization (100%) and lowest in patients with tortuous cervical ICAs and proximal balloon-guiding catheterization (70.6%, Table 4).

There were 2 cases of iatrogenic proximal common carotid artery dissection in patients with left distal ICA and M2 occlusions, respectively. Both dissections occurred in cases of distal BGC location and were discovered during reselection of the affected carotid artery with a 5F diagnostic catheter for delayed angiograms after mechanical thrombectomy. In the former case,

**Table 1: Comparison of the baseline characteristics of distal and proximal BGC groups**

	Distal BGC (n = 49)	Proximal BGC (n = 53)	P Value
Age (yr) <sup>a</sup>	70 (37–96)	72 (24–87)	.32
Female	23 (46.9%)	27 (50.9%)	.84
Atrial fibrillation	26 (53.1%)	21 (39.6%)	.25
Hypertension	27 (55.1%)	41 (77.4%)	.03
Diabetes mellitus	12 (24.5%)	11 (20.8%)	.91
Ischemic stroke <sup>b</sup>	4 (8.2%)	4 (7.5%)	<.99
Smoking <sup>b</sup>	4 (8.2%)	3 (5.7%)	.71
Initial NIHSS score (mean)	13.9 ± 5.5	14.5 ± 5.4	.58
IV rtPA use	20 (40.8%)	20 (37.7%)	.91
Onset-to-puncture time (min) <sup>a</sup>	195 (90–758)	200 (75–1185)	.41
Occlusion location			
M1	22 (44.9%)	31 (58.5%)	.24
M2	13 (26.5%)	10 (18.9%)	.49
ICA	14 (28.6%)	12 (22.6%)	.65
Tortuous ICA	11 (22.4%)	17 (32.1%)	.39

<sup>a</sup> Mann-Whitney *U* test. Data are medians, and numbers in parentheses are interquartile range.

<sup>b</sup> Fisher exact test.

**Table 2: Comparison of the results between the distal and proximal BGC groups**

	Distal BGC (n = 49)	Proximal BGC (n = 53)	P Value
Puncture-to-recanalization time (min) <sup>a</sup>	40 (14–133)	56 (15–204)	.02
Puncture-to-recanalization time (mean) (min)	47.8 ± 7.6	67.9 ± 12.4	.01
No. of passes <sup>a</sup>	2 (1–7)	2 (1–12)	.32
No. of passes (mean)	2.3 ± 0.4	3.1 ± 0.8	.07
Emboli to new territory <sup>b</sup>	2 (4.1%)	3 (5.7%)	>.99
Successful recanalization	48 (98.0%)	40 (75.5%)	.003
Complete recanalization	33 (67.3%)	24 (45.3%)	.04
Cervical artery dissection <sup>b</sup>	2 (4.1%)	0	.23
Symptomatic hemorrhage <sup>b</sup>	4 (8.2%)	3 (5.7%)	.71
Discharge NIHSS score <sup>a</sup>	6 (0–42)	6 (0–42)	.28
Mortality	5 (10.2%)	10 (18.9%)	.34
Good clinical outcome	28 (57.1%)	24 (45.3%)	.32

<sup>a</sup> Mann-Whitney *U* test. Data are medians, and numbers in parentheses are interquartile range.

<sup>b</sup> Fisher exact test.

**Table 3: Predictors of successful recanalization**

Variable	Univariable Analysis		Multivariable Analysis	
	Odds Ratio (95% CI)	P Value	Adjusted Odds Ratio (95% CI)	P Value
Age	0.99 (0.95–1.04)	.94	1.03 (0.97–120.01)	.38
Sex	0.49 (0.14–1.52)	.23	0.50 (0.12–1.88)	.32
Hypertension	0.29 (0.04–1.16)	.12	0.36 (0.04–1.98)	.28
Initial NIHSS score	0.99 (0.89–1.10)	.80	1.01 (0.89–1.15)	.84
IV rtPA use	1.19 (0.38–4.14)	.77	0.97 (0.26–3.86)	.97
ICA tortuosity	0.44 (0.14–1.48)	.17	0.51 (0.14–1.89)	.30
Distal/proximal BGC location	15.6 (2.92–289.52)	.01	13.40 (2.37–254.82)	.02

**Table 4: Recanalization rates according to ICA tortuosity<sup>a</sup>**

	Total	Tortuosity (+)	Tortuosity (-)
Total	86/102 (84.3%)	22/28 (78.6%)	64/74 (86.5%)
Distal BGC	48/49 (98.0%)	10/11 (90.9%)	38/38 (100%)
Proximal BGC	38/53 (71.7%)	12/17 (70.6%)	26/36 (72.2%)

<sup>a</sup> + indicates present; –, absent.

modified TICI 3 recanalization had been achieved for intracranial occlusion with contrast stagnation at the common carotid artery dissection site but with no flow compromise; thus, no further treatment was performed. In the latter case, modified TICI 2b recanalization had been achieved for the intracranial occlusion.

Slight flow reduction at the common carotid artery dissection site was seen, but intracranial flow was preserved from good anterior communicating artery cross-flow; thus, no further treatment was performed for the dissection. Both patients showed good clinical outcome.

## DISCUSSION

Our results show that the location of the BGC may have a significant impact on the mechanical thrombectomy treatment result in patients with acute stroke. When we compared distal with proximal BGC location, flow control and aspiration at the distal cervical ICA were associated with significantly improved successful and complete recanalization rates during mechanical thrombectomy with stent retrievers.

### Improved Efficacy of Mechanical Thrombectomy

Currently, clot capture with a stent retriever and contact aspiration with a distal aspiration catheter are the 2 main concepts of mechanical thrombectomy.<sup>9,11,17,18</sup> Various improvised techniques for improved flow control and aspiration are being introduced. The bare wire thrombectomy technique involves removal of the microcatheter before stent retrieval for increased aspiration force.<sup>8</sup> The concurrent use of the stent retriever with distal aspiration catheters may have a synergistic effect of local aspiration and thrombus entrapment by the stent.<sup>19,20</sup> Continuous aspiration before stent deployment and during distal navigation of the aspiration catheter and retrieval may decrease the incidence of clot fragment emboli and increase the near-complete recanalization rates.<sup>7</sup>

Proximal flow control with a BGC and forced aspiration are also an adjuvant method for improved efficacy. Analysis of

the North American Solitaire Acute Stroke Registry has shown that the use of a BGC with a Solitaire stent-retriever device is associated with superior revascularization results (modified TICI grade, 3; 53.7% versus 32.5%), shorter procedure time (120 ± 28.5 versus 161 ± 35.6 minutes), and improved clinical outcome (discharge NIHSS score 12 ± 14.5 versus 17.5 ± 16) compared with patients without a BGC.<sup>11</sup> However, to the best of our knowledge, there are no reports analyzing the impact of location of the BGC. Thus, our study shows that the effects of proximal flow control and forced aspiration can be maximized without an increase in complications by achieving distal catheterization with the BGC.

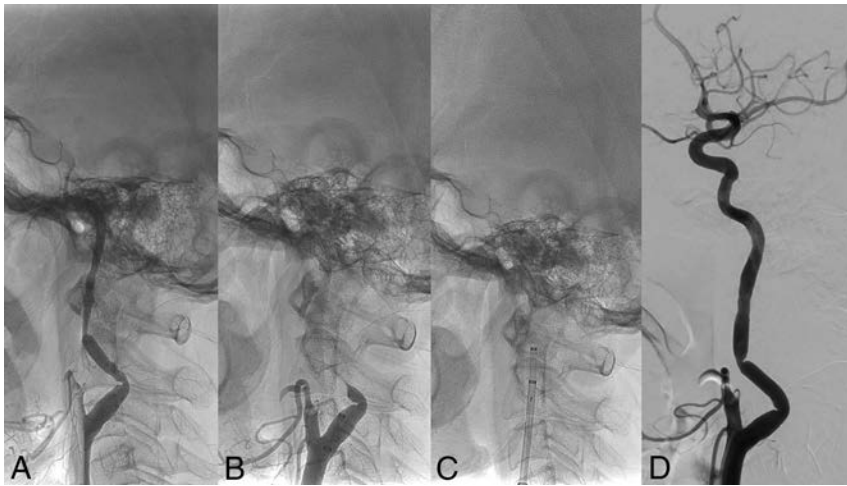


**FIGURE.** A 53-year-old woman who presented with acute stroke and an initial NIHSS score of 7. Delayed-phase nonsubtracted lateral DSA image shows occlusion of the left supraclinoid ICA. Acute angulation of the proximal cervical ICA is seen at the lower C2 vertebral level (A). The tip of the BGC is located at the C3 vertebral level proximal to the angulation of the cervical ICA (B). Careful balloon-guiding catheterization was successfully performed into the distal cervical ICA despite the tortuous artery. The tip of the BGC is now located at the C1 vertebral level (C). Stent-retriever thrombectomy with proximal flow control and continuous forced aspiration through the distally located BGC was performed. Subtracted lateral DSA image shows complete recanalization after thrombectomy. The cervical ICA shows no signs of dissection (D). The patient showed good clinical outcome on 3-month follow-up.

#### **Factors Associated with Improved Efficacy of Distal Balloon-Guiding Catheterization**

A number of factors including the diameter of the vessel, length, tortuosity, surface roughness, and flow velocity can influence the forced aspiration pressure.

For a straight pipe, the Darcy Weisbach equation states

$$\Delta P = f_D \frac{\rho V^2 L}{2 D},$$

Where  $\Delta P$  is the pressure difference across the pipe,  $\rho$  is the density of the fluid,  $V$  is the average velocity in the pipe,  $f_D$  is the friction factor,  $L$  is the length of the pipe, and  $D$  is the diameter of the pipe.<sup>21</sup> Shortening of the length correlates with distal location of the BGC. Thus, distal BGC location will result in a theoretic decrease in the pressure difference within the system and an increase in the aspiration force. Our results support the theoretic advantages of distal balloon-guiding catheterization with significant improvement in recanalization rates. From the equation, we can also postulate that using a BGC with a larger inner diameter will result in an increased aspiration force; however, the feasibility and risks of navigating a larger profile BGC to the distal ICA have to be considered.

Another potential factor for improved recanalization in the distal BGC group may be related to the extravascular anatomy of the ICA. The cervical ICA is encased by the soft tissues of the neck. There may be concerns for collapse of the cervical ICA during forced aspiration of the proximally positioned BGC.<sup>18</sup> On the other hand, the petrous ICA may be more resistant to collapse due to the thick periosteal layer attached to the vessel and petrous bone.<sup>22</sup> Collapse of the cervical ICA may result in decreased suction force and dissection. It may also cause shearing of the clot captured by the stent and result in distal emboli during retrieval. These concerns may be reflected in the significantly lower incidence of successful and complete recanalizations with proximal balloon-guiding catheterization in our series.

#### **Risks and Other Factors Associated with Distal Balloon-Guiding Catheterization**

Although achieving distal location of the BGC is favorable in terms of recanalization efficacy, this may not always be feasible. One of the main causes of failure of distal access may be the tortuosity and/or the diameter of the cervical ICA. The tortuous vessel hinders safe balloon-guiding catheterization. However, our series shows that although tortuosity can preclude distal BGC access, it may be overcome in some cases (Figure). Distal catheterization was achieved in 11 of the 28 cases with cervical ICA tortuosity, and 10 of these 11 cases (90.9%) resulted in successful recanalization compared with 12 of 17 cases (70.6%) with proximal catheterization in patients with tortuous cervical ICAs. The tortuous vessel may be straightened by carefully navigating the guidewire or using coaxial catheters. Distal access with a coaxial intermediate catheter may

reduce the gap between the 2 catheters, thus reducing the risk of dissection, and may also provide support for advancement of the BGC. Selection of a BGC with a soft distal tip may also aid in safe distal catheterization.

Another cause of failure of distal access may be length incompatibility of the BGC. In tall patients or patients with very tortuous aortas, the BGC may not be long enough to reach the distal ICA, especially when the shorter length BGC is selected. On the other hand, a longer length BGC may not always be advantageous in patients with severely tortuous cervical ICAs. Sufficient access of the distal cervical ICA with the BGC may not be achieved in these cases; this issue may impede sufficient distal access of the microcatheter to the occluded artery. Careful investigation of the cervical vessels on the preprocedural CT angiography, the tortuosity of the aorta during sheath introduction, and the habitus of the patient before selection of the length of the BGCs may aid in selecting the appropriate-length devices. Other causes may include oversight of the BGC location by the operator and kickback of the BGC during microcatheter navigation.

In our retrospective analysis, the BGC was positioned proximally in almost half of the patients (36/74 patients) despite the nontortuous cervical ICA. The difference in recanalization rates between patients with a distal-versus-proximal BGC in nontortuous ICA cases was about 30% (100% versus 72.2%, Table 4). Considering the significant impact on recanalization, the operator should be alert to confirming the location of the BGC throughout the procedure.

Despite the improved outcome from distal balloon-guiding catheterization, its benefits should be carefully weighed against the potential risks. We experienced 2 cases of left proximal common carotid artery dissection during reselection of the carotid artery with a diagnostic catheter for delayed angiograms. Although the location of the dissections was localized in the com-

mon carotid artery without ICA extension, suggesting that it was not directly related to BGC navigation in the cervical ICA, endothelial injury may have occurred during initial navigation of the Shuttle sheath and BGC into the acutely angulated left common carotid artery and may have been discovered during reselection for the delayed angiogram. Fortunately, these patients did not have any serious complications associated with the dissections. However, such risks should be carefully avoided, especially in patients with severely tortuous cervical ICAs. Our results also call for the development of softer tipped and flexible BGCs, which can be safely navigated distally into the cervical ICA.

In our study, the puncture-to-recanalization time was significantly shorter in the distal than in the proximal BGC group. This feature may be due to the tendency for a decreased mean number of passes in the distal BGC group ( $2.3 \pm 0.4$  versus  $3.1 \pm 0.8$ ,  $P = .07$ ). Also, the higher incidence of hypertension in the proximal BGC group may have been associated with more tortuous arteries, including the aorta, resulting in increased procedural time.<sup>23</sup>

This study is limited by the retrospective nature of the analysis. To analyze and prove the concept of BGC location and its impact on recanalization, we limited the patients in this series to those treated with a specific type of stent retriever and BGC; thus, there may be bias. It remains to be clarified whether devices with different profiles such as a longer stent retriever would compensate for the effect of the BGC position because longer stent retrievers may enhance thrombectomy performance.<sup>24</sup> Also, despite the significantly higher recanalization rates with distal balloon-guiding catheterization, the difference in the long-term good outcome rate did not reach statistical significance, probably due to the small size of the cohort. Future prospective studies in a larger cohort are warranted.

## CONCLUSIONS

In patients with acute stroke treated with short stent retrievers and without contact aspiration, the location of the BGC has a significant impact on the recanalization of occluded arteries. The BGC should be navigated as distally as safely possible in the cervical ICA for maximally effective thrombectomy.

## ACKNOWLEDGMENTS

The authors thank Professor Kyunghwa Han, PhD, Department of Radiology, Yonsei University College of Medicine, for the statistical analysis.

Disclosures: Dong Joon Kim—UNRELATED: Consultancy: Stryker Pacific Limited.

## REFERENCES

- Berkhemer OA, Fransen PS, Beumer D, et al. **A randomized trial of intraarterial treatment for acute ischemic stroke.** *N Engl J Med* 2015; 372:11–20 CrossRef Medline
- Campbell BC, Mitchell PJ, Kleinig TJ, et al; EXTEND-IA Investigators. **Endovascular therapy for ischemic stroke with perfusion-imaging selection.** *N Engl J Med* 2015;372:1009–18 CrossRef Medline
- Goyal M, Demchuk AM, Menon BK, et al; ESCAPE Trial Investigators. **Randomized assessment of rapid endovascular treatment of ischemic stroke.** *N Engl J Med* 2015;372:1019–30 CrossRef Medline
- Jovin TG, Chamorro A, Cobo E, et al; REVASCAT Trial Investigators. **Thrombectomy within 8 hours after symptom onset in ischemic stroke.** *N Engl J Med* 2015;372:2296–306 CrossRef Medline
- Saver JL, Goyal M, Bonafe A, et al; SWIFT PRIME Investigators. **Stent-retriever thrombectomy after intravenous t-PA vs. t-PA alone in stroke.** *N Engl J Med* 2015;372:2285–95 CrossRef Medline
- Haussen DC, Rebello LC, Nogueira RG. **Optimizing clot retrieval in acute stroke: the push and fluff technique for closed-cell stent-retrievers.** *Stroke* 2015;46:2838–42 CrossRef Medline
- McTaggart RA, Tung EL, Yaghi S, et al. **Continuous aspiration prior to intracranial vascular embolectomy (CAPTIVE): a technique which improves outcomes.** *J Neurointerv Surg* 2017;9:1154–59 CrossRef Medline
- Nikoubashman O, Alt JP, Nikoubashman A, et al. **Optimizing endovascular stroke treatment: removing the microcatheter before clot retrieval with stent-retrievers increases aspiration flow.** *J Neurointerv Surg* 2017;9:459–62 CrossRef Medline
- Chueh JY, Kühn AL, Puri AS, et al. **Reduction in distal emboli with proximal flow control during mechanical thrombectomy: a quantitative in vitro study.** *Stroke* 2013;44:1396–401 CrossRef Medline
- Chueh JY, Puri AS, Wakhloo AK, et al. **Risk of distal embolization with stent retriever thrombectomy and ADAPT.** *J Neurointerv Surg* 2016;8:197–202 CrossRef Medline
- Nguyen TN, Malisch T, Castonguay AC, et al. **Balloon guide catheter improves revascularization and clinical outcomes with the Solitaire device: analysis of the North American Solitaire Acute Stroke Registry.** *Stroke* 2014;45:141–45 CrossRef Medline
- Paramasivam S, Leesch W, Fifi J, et al. **Iatrogenic dissection during neurointerventional procedures: a retrospective analysis.** *J Neurointerv Surg* 2012;4:331–35 CrossRef Medline
- Akpınar S, Yılmaz G. **Dissection of extracranial internal carotid artery due to balloon guiding catheter resulting in asymptomatic internal carotid artery occlusion.** *Iran J Radiol* 2016;13:e28209 CrossRef Medline
- Zaidat OO, Yoo AJ, Khatri P, et al; Cerebral Angiographic Revascularization Grading (CARG) Collaborators, STIR Revascularization Working Group, STIR Thrombolysis in Cerebral Infarction (TICI) Task Force. **Recommendations on angiographic revascularization grading standards for acute ischemic stroke: a consensus statement.** *Stroke* 2013;44:2650–63 CrossRef Medline
- Mokin M, Setlur Nagesh SV, Ionita CN, et al. **Comparison of modern stroke thrombectomy approaches using an in vitro cerebrovascular occlusion model.** *AJNR Am J Neuroradiol* 2015;36:547–51 CrossRef Medline
- Hacke W, Kaste M, Fieschi C, et al. **Randomised double-blind placebo-controlled trial of thrombolytic therapy with intravenous alteplase in acute ischaemic stroke (ECASS II): Second European-Australasian Acute Stroke Study Investigators.** *Lancet* 1998;352:1245–51 CrossRef Medline
- Velasco A, Buerke B, Stracke CP, et al. **Comparison of a balloon guide catheter and a non-balloon guide catheter for mechanical thrombectomy.** *Radiology* 2016;280:169–76 CrossRef Medline
- Klinger-Gratz PP, Schroth G, Gralla J, et al. **Protected stent retriever thrombectomy prevents iatrogenic emboli in new vascular territories.** *Neuroradiology* 2015;57:1045–54 CrossRef Medline
- Jindal G, Serulle Y, Miller T, et al. **Stent retrieval thrombectomy in acute stroke is facilitated by the concurrent use of intracranial aspiration catheters.** *J Neurointerv Surg* 2017;9:944–47 CrossRef Medline
- Humphries W, Hoit D, Doss VT, et al. **Distal aspiration with retrievable stent assisted thrombectomy for the treatment of acute ischemic stroke.** *J Neurointerv Surg* 2015;7:90–94 CrossRef Medline
- White FM. *Fluid Mechanics*. 8th Edition. New York: McGraw-Hill Education; 2016
- Sekhar LN, Schramm VL Jr, Jones NF, et al. **Operative exposure and management of the petrous and upper cervical internal carotid artery.** *Neurosurgery* 1986;19:967–82 CrossRef Medline
- Dobrin PB, Schwarcz TH, Baker WH. **Mechanisms of arterial and aneurysmal tortuosity.** *Surgery* 1988;104:568–71 Medline
- Haussen DC, Al-Bayati AR, Grossberg JA, et al. **Longer stent retrievers enhance thrombectomy performance in acute stroke.** *J Neurointerv Surg* 2019;11:6–8 CrossRef Medline

# Angiographic and Clinical Features of Noninvoluting Congenital Hemangiomas

A. Patel, R. De Leacy, and A. Berenstein



## ABSTRACT

**SUMMARY:** While infantile hemangiomas are very common, congenital hemangiomas are rare and less understood. Congenital hemangiomas are present at birth. They fall into 2 major categories: rapidly involuting congenital hemangioma and noninvoluting congenital hemangioma. Noninvoluting congenital hemangioma is the rarer of the 2 entities. If not recognized and treated appropriately, noninvoluting congenital hemangioma can lead to considerable morbidity. There is a paucity of literature regarding noninvoluting congenital hemangiomas. In this article, we will outline our experience with this condition, focusing on clinical and angiographic features. There is a distinct angiographic appearance of noninvoluting congenital hemangiomas involving an arterial-capillary web, a dense tumor blush with identifiable feeding arteries, no arteriovenous shunting, and variably present draining veins. Our experience with endovascular embolization and direct percutaneous treatment is the largest for this entity to date. Endovascular embolization and/or direct percutaneous sclerotherapy of this lesion may obviate subsequent surgical resection.

**ABBREVIATION:** NICH = noninvoluting congenital hemangioma

Hemangiomas are vascular tumors that enlarge through proliferation of endothelial cells. Infantile hemangiomas are common lesions, occurring in up to 10% of infants and young children.<sup>1</sup> These tumors generally appear in the first 6 weeks of life and subsequently undergo a spontaneous involution phase. Digital subtraction angiography, if performed, will demonstrate dilated feeding arteries, organized arterial angioarchitecture, a dense parenchymal blush, and drainage into dilated draining veins.<sup>1</sup> Infantile hemangiomas may demonstrate rapid venous filling, indicating arteriovenous shunting.

Congenital hemangiomas are much rarer lesions. Physicians caring for pediatric patients with hemangiomas have long noted that infants would occasionally present with congenital hemangiomas.<sup>2</sup> These hemangiomas undergo their proliferative phase in utero. Therefore, while they can still grow proportionally as the

patient ages, these hemangiomas will not demonstrate accelerated or disproportionate postnatal growth. The pathologic characteristic distinguishing these lesions from the more common infantile hemangioma is the lack of expression of *glucose transporter isoform 1 (GLUT1)*.<sup>3</sup>

There are 2 types of congenital hemangiomas: rapidly involuting congenital hemangiomas and noninvoluting congenital hemangiomas (NICHs). These lesions rarely coexist with the more common infantile hemangiomas and are usually solitary. As the name implies, rapidly involuting congenital hemangioma lesions undergo a rapid involuting phase, and most cases demonstrate complete involution within the first 6–14 months of life.<sup>4</sup> Management of these lesions is straightforward if the patient presents typically. Observation is, in general, the initial approach. Lesions that do not involute may need biopsy to exclude a tumor such as rhabdomyosarcoma or congenital fibrosarcoma.

Noninvoluting congenital hemangiomas are even rarer than rapidly involuting congenital hemangioma lesions. Most lesions occur in the head and neck, trunk, or limbs. These lesions tend to be plaque-like, pink-to-purple with telangiectasia on the surface. They are often warm to touch. Noninvoluting congenital hemangiomas stain negative for *GLUT1*, and a characteristic hobnailed appearance is often seen on pathology. As their name implies, these lesions will never disappear or involute. Imaging often demonstrates hyperintensity on T2-weighted images with flow voids similar to those in infantile hemangiomas. A limited description of the angiographic features of these lesions and endovascular

Received November 16, 2018; accepted after revision March 2, 2019.

From the Department of Radiology (A.P.), New York Presbyterian-Weill Cornell Medical Center, New York, New York; and Cerebrovascular Center (R.D.L., A.B.), Icahn School of Medicine at Mount Sinai, New York, New York.

Previously presented at: American Society of Neuroradiology Annual Meeting and the Foundation of the ASNR Symposium, June 2–7, 2018; Vancouver, British Columbia, Canada.

Please address correspondence to Anant Patel, MD, Department of Radiology, New York Presbyterian-Weill Cornell Medical Center, 520 E 70th Street, Starr 8a, New York, New York 10021; e-mail: arp9071@med.cornell.edu; @AnantPatelMD

Indicates article with on-line table.

<http://dx.doi.org/10.3174/ajnr.A6044>

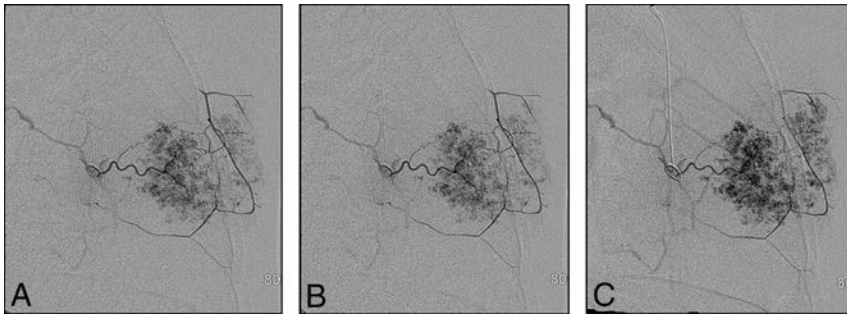


**FIG 1.** Left internal maxillary artery injection of a NICH of the left anterior chest wall. The lesion was initially treated with QuadraSphere Microspheres; the treatment was not successful. Subsequent treatment with an ethanol injection led to involution.

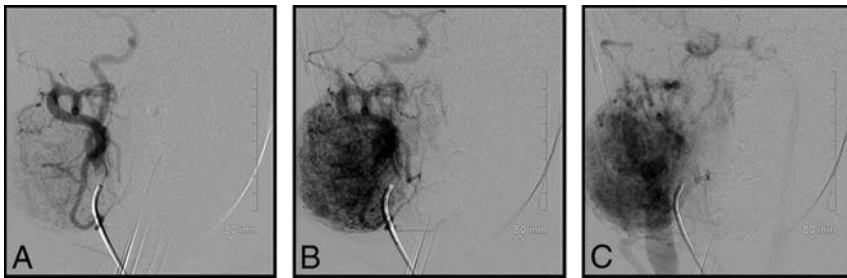


**FIG 2.** Right external carotid artery injection of a right facial NICH. Again, there is a discrete angiographic appearance involving an arteriocapillary web, no arteriovenous shunting, and identifiable draining veins. This lesion was treated successfully with polyvinyl alcohol particles.

approaches for treating them is available.<sup>5</sup> The literature focuses on resection as the mainstay of treatment. Previous, limited reports of endovascular embolization are only in the context of a preoperative setting to control bleeding in larger lesions during subsequent resection. Here, we report our experience with this entity and demonstrate that endovascular embolization and/or direct percutaneous sclerotherapy can be an effective treatment strategy in well-selected cases.

### Case Series

**Case Selection.** Using Mount Sinai institutional review board-approved protocol, all cases of noninvolving congenital hemangiomas from 1990 to present were identified for this retrospective study. Ten patients were identified from the January 1990 to May 2017. All cases were patients who had been referred for endovascular embolization and/or direct percutaneous sclerotherapy. All patients were treated. Indications for treating NICH included cosmetic deformity, location not suitable for gross resection, lesions previously treated but not regressing, or the need to shrink the size of the lesion so that it could be amenable to a subsequent resection.

Lesion location, clinical scenario, patient age, angiographic features, embolization technique, postembolization angiography, need for multiple treatments (if applicable), complications, and long-term clinical follow-up were recorded. Comparison with any prior or subsequent imaging after angiography was performed to document stability. When possible, we accessed pathology reports confirming *GLUT1* negativity in these patients with NICH.

### Angiography and Endovascular Embolization

For patients undergoing angiography and embolization, the right common femoral artery was accessed. A 4F sheath was placed. A 4F Berenstein catheter (Boston Scientific, Fremont, California) and/or Prowler 10 microcatheter (Codman & Shurtleff, Raynham, Massachusetts) was used to superselect the vessel of interest. Superselective injections with the microcatheter along the arcade of the vascular lesion would be performed to confirm an angiographic appearance of the NICH.

Embolization was performed once distal catheterization was achieved and it was determined that the patient's lesion was suitable for treatment. In most cases, we used *n*-BCA. Specifically, we generally used 0.7 mL of 25% *n*-BCA (1 mL of *n*-BCA mixed with 3 mL of Ethiodol [Andre Guerbet, Melville, New York]) for injection. The relatively small volume of *n*-BCA reflects the relative overall volumes of these lesions (most patients were small children), limited

number of pedicles in most lesions, and the primary objective of the *n*-BCA often being to slow down the flow in the main pedicle.

### Direct Percutaneous Sclerotherapy

Patients presenting with very large hemangiomas undergoing direct percutaneous sclerotherapy were also reviewed. This technique was used more frequently across time as the practice of our primary operator evolved. Under direct fluoroscopic monitoring, direct percutaneous puncture of the lesion of interest at multiple locations was performed. Following establishment of blood flow, a small amount of contrast material was injected to confirm the intravascular location of our angiocatheter. Subsequently, we would sclerose the hemangioma with progressive small injections of 98% ethanol. Given the nature of the lesions, we would inject either in the central portion of the mass or in separate compartments to decrease the overall size. Many cases indeed used multiple, separate puncture sites in which ethanol was injected followed by ~5 mL of Avitene microfibrillar collagen hemostat suspension (Bard Davol, Warwick, Rhode Island) for hemostasis.

### Outcomes

We identified 10 patients who underwent 25 total treatments. The On-line Table summarizes the key clinical and angiographic features of our patients. Most of our patients presented between 2 and 8 years of age. One patient underwent treatment at 44 years of age. Seven patients were female, and 3 were male. Five patients were treated with endovascular embolization, 2 patients were treated with percutaneous sclerotherapy, and 3 patients were

treated with a combination of the 2 approaches as the practice of our primary operator evolved.

Patients were seen in clinic between 1 and 2 months after treatment and at 12 months. As shown in the On-line Table, most patients required between 1 and 2 treatments to achieve 12 months without lesion recurrence or progression. One of our patients did require a total of 12 treatments (in addition to 3 prior endovascular treatments at a peer institution) before surgical resection. Another patient required 2 treatments before surgical resection. The remaining 8 patients did not need an operation.

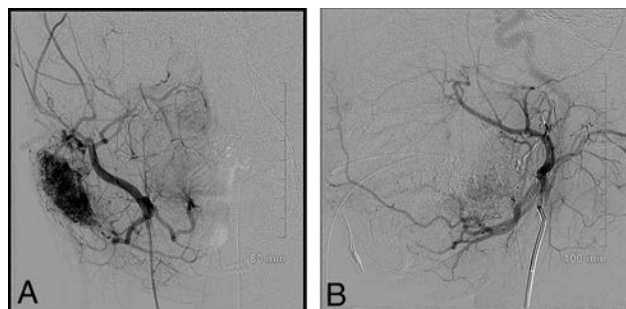


**FIG 3.** Pre- and postembolization images of a right parotid NICH treated with *n*-BCA. There were 5 vascular pedicles seen on angiography, and each was injected with 25% *n*-BCA (0.15–0.45 mL per pedicle).

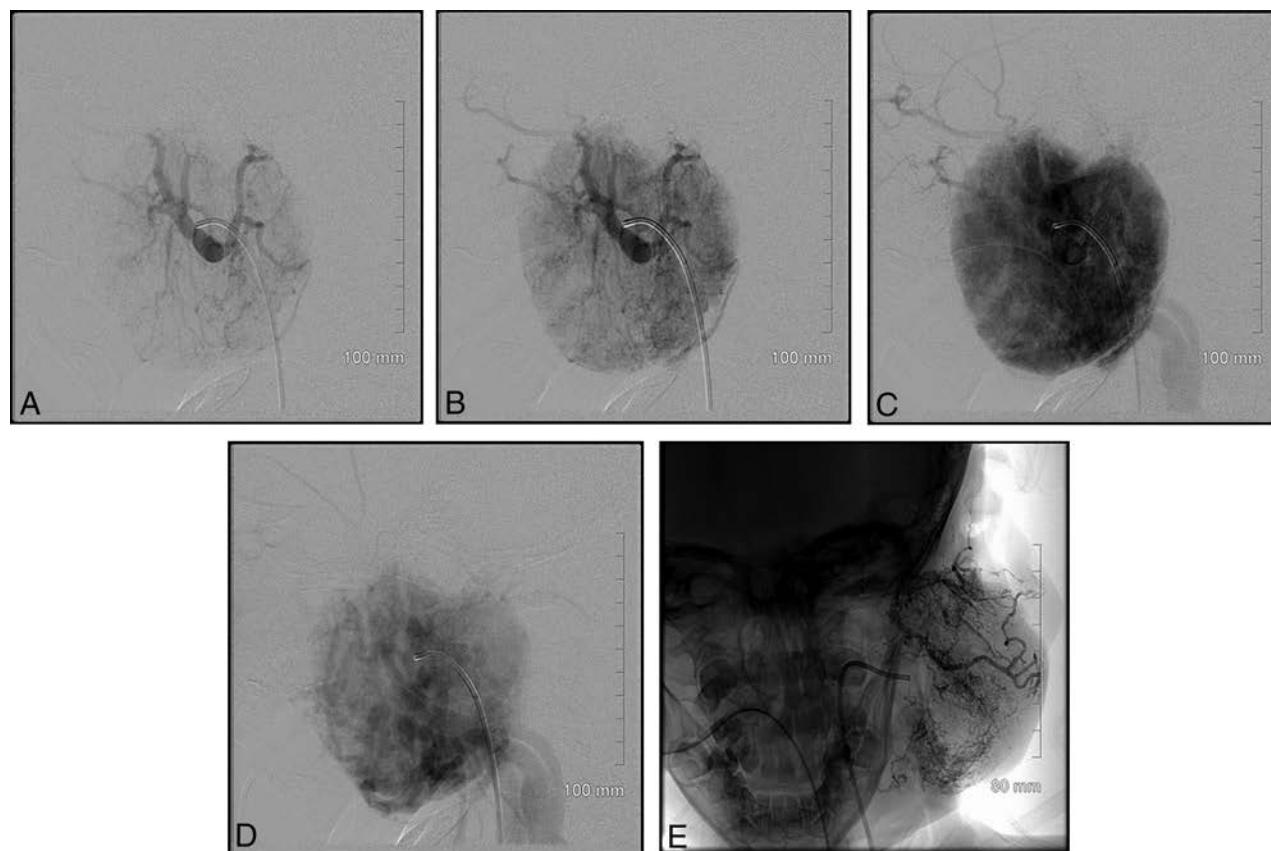


**FIG 4.** An incredibly vascular left parotid lesion. This lesion was treated with both endovascular embolization and direct percutaneous sclerotherapy. Postembolization image (E) from this case shows a markedly reduced vascular supply.

## DISCUSSION

Our cases highlight several important points: noninvoluting congenital hemangiomas have the same angiographic appearance throughout the body. Figure 1 of a case involving an NICH in the anterior chest wall shows the same features as a facial NICH, including a discrete arterial-capillary web, homogeneous tumor blush, no arteriovenous shunting, and draining veins. This lesion was initially treated with QuadraSphere Microspheres (Merit Medical, South Jordan, Utah) (and did not significantly involute). The lesion was subsequently successfully treated with ethanol. Figure 2 highlights a right facial NICH with similar angiographic features. This lesion was successfully treated with polyvinyl alcohol particles, 45–120  $\mu$ m. Markedly enlarged draining veins are noted in this example.

Contrary to previous reports, our experience shows that in some cases, endovascular embolization or direct percutaneous sclerotherapy can obviate surgical resection. The largest previous case series on NICH identified 53 patients across 3 large vascular anomaly centers.<sup>5</sup> However, this study had a limited description of angiographic features, and only 7 of 53 patients underwent embolization, which was performed explicitly to possibly decrease bleeding in a subsequent resection. This article goes on to say that “embolization is unnecessary.” Two of our cases showed that preprocedural embolization can considerably decrease intraoperative bleeding. More important, 6 of our cases suggest that effective endovascular embolization and/or direct sclerotherapy can entirely obviate a resection.

Indeed, we have seen that endovascular embolization and/or direct sclerotherapy can effectively decrease the vascular supply, lead to involution, and, in appropriately selected cases, be a definitive treatment.

Another important observation from our experience is that both endovascular embolization and direct percutaneous sclerotherapy are effective. Figure 3 highlights a right parotid NICH in a 4-year-old patient. The lesion was not regressing. A dense tumor stain was observable as well as 5 discrete vascular pedicles feeding the lesion. The lesion was successfully treated with *n*-BCA.

Direct percutaneous sclerotherapy is another technique that can be used. Our group's experience is that this technique works well in select cases. Moreover, use of this procedure increased with time, mirroring the evolution of our primary operator's practice. Figure 4 highlights a case using both endovascular embolization and direct percutaneous sclerotherapy with Avitene. This was an extremely vascular tumor, and the combination of both techniques led us to achieve occlusion of approximately 80% of the tumor.

Our study has some limitations. Our case series includes only 10 patients. However, this mainly underscores the rare incidence of this condition. Only 2 patients had a biopsy before our intervention, which showed *GLUT1* negativity, confirming NICH. The remaining patients did not have a preprocedural biopsy but were noted to have a clinical scenario reliably demonstrating an NICH lesion. Moreover, because a subsequent operation was not necessary, no sample of tissue was sent for *GLUT1* staining.

Five of our patients needed only 1 treatment. One patient was noted to have undergone 12 embolizations with us, many of which were after surgical resection. Additionally, this patient had 3 prior embolizations at Johns Hopkins.

## CONCLUSIONS

Our study is the largest case series of embolization and/or direct sclerotherapy for NICH and the most thorough evaluation of angiographic features associated with these lesions. NICHs have distinguishing angiographic and clinical features. Endovascular or direct percutaneous embolization or both are effective treatment strategies that may obviate surgical resection.

Disclosures: Reade De Leacy—UNRELATED: Board Membership: Asahi Intecc, Comments: research grant\*; Consultancy: Siemens, Penumbra. Alejandro Berenstein—RELATED: Grant: MicroVention; Consulting Fee or Honorarium: MicroVention, Mivi Neuroscience, Scientia Vascular, Endostream Medical LTD, Bendit Technologies, Magneto Thrombectomy Solutions; UNRELATED: Royalties: AngioDynamics; Stock/Stock Options: Mivi Neuroscience, Endostream Medical LTD, Scientia Vascular, Bendit Technologies, Magneto Thrombectomy Solutions. \*Money paid to the institution.

## REFERENCES

1. Song JK, Niimi Y, Berenstein A. **Endovascular treatment of hemangiomas.** *Neuroimaging Clin N Am* 2007;17:165–73 CrossRef Medline
2. Krol A, MacArthur CJ. **Congenital hemangiomas: rapidly involuting and noninvoluting congenital hemangiomas.** *Arch Facial Plast Surg* 2005;7:307–11 CrossRef Medline
3. North PE, Warner M, Mizeracki A, et al. **GLUT1: a newly discovered immunohistochemical marker for juvenile hemangiomas.** *Hum Pathol* 2000;31:11–22 CrossRef Medline
4. Mulliken JB, Enjoiras O. **Congenital hemangiomas and infantile hemangioma: missing links.** *J Am Acad Dermatol* 2004;50:875–82 CrossRef Medline
5. Enjolras O, Mulliken JB, Boon LM, et al. **Noninvoluting congenital hemangioma: a rare cutaneous vascular anomaly.** *Plast Reconstr Surg* 2001;107:1647–54 CrossRef Medline

# Reduced Jet Velocity in Venous Flow after CSF Drainage: Assessing Hemodynamic Causes of Pulsatile Tinnitus

H. Haraldsson, J.R. Leach, E.I. Kao, A.G. Wright, S.G. Ammanuel, R.S. Khangura, M.K. Ballweber, C.T. Chin, V.N. Shah, K. Meisel, D.A. Saloner, and M.R. Amans



## ABSTRACT

**BACKGROUND AND PURPOSE:** Idiopathic intracranial hypertension is commonly associated with transverse sinus stenosis, a venous cause of pulsatile tinnitus. In patients with idiopathic intracranial hypertension, CSF drainage via lumbar puncture decreases intracranial pressure, which relieves the stenosis, and may provide at least temporary cessation of pulsatile tinnitus. The objective of this study was to evaluate changes in venous blood flow caused by lowered intracranial pressure in patients with pulsatile tinnitus to help identify the cause of pulsatile tinnitus.

**MATERIALS AND METHODS:** Ten patients with suspected transverse sinus stenosis as a venous etiology for pulsatile tinnitus symptoms underwent MR imaging before and after lumbar puncture in the same session. The protocol included flow assessment and rating of pulsatile tinnitus intensity before and after lumbar puncture and MR venography before lumbar puncture. Post-lumbar puncture MR venography was performed in 1 subject.

**RESULTS:** There was a lumbar puncture–induced reduction in venous peak velocity that correlated with the opening pressure ( $r = -0.72$ ,  $P = .019$ ) without a concomitant reduction in flow rate. Patients with flow jets had their peak velocity reduced by  $0.30 \pm 0.18$  m/s ( $P = .002$ ), correlating with a reduction in CSF pressure ( $r = 0.82$ ,  $P = .024$ ) and the reduction in subjectively scored pulsatile tinnitus intensity ( $r = 0.78$ ,  $P = .023$ ). The post-lumbar puncture MR venography demonstrated alleviation of the stenosis.

**CONCLUSIONS:** Our results show a lumbar puncture–induced reduction in venous peak velocity without a concomitant reduction in flow rate. We hypothesize that the reduction is caused by the expansion of the stenosis after lumbar puncture. Our results further show a correlation between the peak velocity and pulsatile tinnitus intensity, suggesting the flow jet to be instrumental in the development of sound.

**ABBREVIATIONS:** CE = contrast-enhanced; 2Dflow = time-resolved MR velocimetry in a 2D plane; 4Dflow = time-resolved MR velocimetry in a 3D volume; IIH = idiopathic intracranial hypertension; LP = lumbar puncture; MRV = MR venography; PT = pulsatile tinnitus

**P**ulsatile tinnitus (PT) is the auditory perception of a rhythmic, cardiac-synchronized, “whooshing” sound in the absence of an external source, which affects nearly 3 million

Americans.<sup>1–4</sup> The impact of PT is high due to difficulties in diagnosis, the health risks associated with the underlying causative diseases, and extremely common comorbid debilitating psychiatric illnesses. In addition, several of the anomalies that cause PT can have serious sequelae such as ischemic stroke, blindness, or intracranial hemorrhage.<sup>5–7</sup> PT is often related to abnormal flow, including turbulence, in the blood vessels near the cochlea, but the exact mechanism of sound production remains elusive.

Idiopathic intracranial hypertension (IIH) is 1 cause of PT that carries a risk of developing blindness. Many patients with IIH have stenosis of 1 or both transverse sinuses at the junction with the sigmoid sinus, which may be caused by increased curvature of the tentorium cerebelli.<sup>8–10</sup> Stent placement in usually 1 of these stenoses has been shown in prospective trials to both treat IIH and resolve patients’ pulsatile tinnitus.<sup>11–14</sup> In addition, lumbar puncture (LP) with removal of CSF temporarily decreases intracranial pressure and re-

Received August 1, 2018; accepted after revision March 18, 2019.

From the Departments of Radiology and Biomedical Imaging (H.H., J.R.L., E.I.K., A.G.W., S.G.A., R.S.K., M.K.B., C.T.C., V.N.S., D.A.S., M.R.A.) and Neurology (K.M.), University of California, San Francisco, San Francisco, California; and Radiology Service (D.A.S.), VA Medical Center, San Francisco, California.

This work was supported by National Institutes of Health, R21DC016087 (M.R.A./D.A.S.).

Paper previously presented, in part, at: Annual Meeting of the Society for Magnetic Resonance Angiography, August 28–31, 2018; Glasgow, Scotland; and American Society of Neuroradiology Annual Meeting and the Foundation of the ASNR Symposium, June 2–7, 2018; Vancouver, British Columbia, Canada.

Please address correspondence to Matthew R. Amans, MD, MSc, Department of Radiology and Biomedical Imaging, UCSF, 505 Parnassus Ave, Room L349, San Francisco, CA 94143; e-mail: Matthew.Amans@ucsf.edu

Indicates open access to non-subscribers at www.ajnr.org

<http://dx.doi.org/10.3174/ajnr.A6043>

**Table 1: MR imaging parameters**

Acquisition	Parameters
CE-MRV	FOV = 240 × 180 × 108 mm, acq. matrix = 400 × 286 × 90, acq. time = 66 sec, TR = 5.0 ms, TE = 1.8 ms, FA = 30°, SENSE = 2
4Dflow	FOV = 240 × 193 × 34 mm, acq. matrix = 184 × 149 × 24, acq. time = 12 min, TR = 6.5 ms, TE = 2.9 ms, FA = 8°, SENSE = 2, segments = 3, VENC = 1.5 m/s
2Dflow	FOV = 160 × 120 mm, acq. matrix = 160 × 120, acq. time = 73 sec, TR = 8.8 ms, TE = 5.4 ms, FA = 15°, segments = 2, VENC = 0.75 m/s

**Note:**—acq. indicates acquisition; SENSE, sensitivity encoding; FA, flip angle; VENC, velocity encoding.

sults in a temporary improvement in the patients' IIH symptoms, including PT.

Recent advances in measuring the velocity field of blood flow in a 3D volume through the cardiac cycle using phase contrast MR imaging, referred to as 4Dflow, have allowed depiction of blood flow in the main cerebral outflow veins of patients.<sup>15-17</sup> In this study, we used 4Dflow to try to determine the flow patterns that may be causing pulsatile tinnitus in patients with venous sinus stenoses who are suspected of having IIH. We performed flow analysis of the transverse sinus stenosis before and after removal of CSF via LP (which often at least temporarily resolves PT in patients with IIH). The aim of the study was the following: 1) to investigate whether flow jets, a potential source of turbulent flow, are present in symptomatic patients; 2) to see if these flow jets are reduced by reducing the intracranial pressure via LP; and 3) to determine whether the reduction in flow jets correlates with the improvement in PT sound intensity.

## MATERIALS AND METHODS

We prospectively performed MR imaging of adult patients with a suspected venous etiology of pulsatile tinnitus before and after MR imaging-guided LP with removal of as much as 20 mL of CSF using a study protocol approved by the Institutional Review Board at UCSF. All patients signed written informed consent to participate in this study.

### Patient Selection

Ten patients with PT and suspected IIH and venous etiology of PT were recruited from the University of California, San Francisco Pulsatile Tinnitus Clinic, a multispecialty clinic that evaluates patients with PT. PT was suspected to be of venous etiology if a patient described a low-pitched, pulse-synchronous sound that improved with ipsilateral neck compression, and potential arterial (or other) causes such as carotid atherosclerosis, fibromuscular dysplasia, tumor, or dural arteriovenous fistula were not identified on noninvasive imaging. Patients were suspected of having IIH if they had symptoms of IIH and an MR imaging that excluded intracranial mass, but had findings suggestive of IIH (including transverse sinus stenosis, optic nerve sheath distension or kinking, and a partially empty and expanded sella).

### Experimental Protocol

Pre-LP MR imaging, MR imaging-guided LP, and post-LP MR imaging were performed consecutively in an interventional MR imaging suite using a 1.5T MR imaging system. None of the subjects were administered anxiolytic or analgesic medications before the LP or MR imaging. A summary of the MR imaging parameters is shown in Table 1.

The pre-LP MR imaging examination started with a low-res-

olution timing run performed after a 2-mL Gd-DTPA bolus followed by a 20-mL saline flush (both administered at 2 mL/s) to determine the transit time from the injection site to the jugular vein. A contrast-enhanced MR venography (CE-MRV) was then acquired, timed to the venous phase as determined by the timing run. That study used a high-resolution CE-MR venogram with a 20-mL Gd-DTPA bolus followed by a 20-mL saline flush (both administered at 2 mL/s). For 1 patient, Gd-DTPA was replaced with ferumoxytol. In accordance with our institutional guidelines, 12 mL of ferumoxytol was infused slowly for 20 minutes before the MR imaging acquisition, and the timing run was not performed. Following the CE-MR venogram, sinus flow rates were acquired with time-resolved MR velocimetry in a 2D plane (2Dflow) in planes perpendicular to the sigmoid sinuses just distal to their junctions with the jugular veins. Finally, the velocities in the sinuses were measured using 4Dflow acquired in a slab covering the transverse and sigmoid sinuses.

Before LP, patients were asked to rate their PT symptoms on a 0–10 Likert scale. Ten was rated as the sound intensity of a passing train, 6 was the intensity of a typical conversation in a restaurant, and 0 was no symptoms at the time of evaluation. LP was performed under MR imaging guidance on the MR imaging table of the interventional MR imaging suite. Opening pressure was measured with subjects lying in the decubitus position with legs relaxed. IIH was diagnosed by the modified Dandy criteria as opening pressure of >25 cm H<sub>2</sub>O.<sup>18</sup> Patients had 20 mL of CSF withdrawn, which was sent for routine laboratory analysis if the opening pressure was ≥25 cm H<sub>2</sub>O. Closing pressure was measured after removal of CSF. Patients were asked to again rate their PT on the same 0–10 scale after CSF removal.

Following the LP, a post-LP MR imaging acquisition included 2D- and 4Dflow as previously described. Furthermore, the prolonged intravascular residence time of ferumoxytol of >12 hours<sup>19,20</sup> permitted a repeat post-LP CE-MR venogram for 1 patient without administration of an additional contrast agent.<sup>21</sup>

### Flow Postprocessing

The peak velocity at several locations along the ipsilateral sinuses was obtained using in-house software, schematically described in Fig 1. Postprocessing begins with contouring the transverse and sigmoid sinuses on the symptomatic side from the CE-MRV. This is followed by a phase-offset background correction to the 4Dflow and registering the CE-MRV contour to both the pre- and post-LP 4Dflow. Then, the centerline of the contoured lumen is extracted, and cross-sectional cut planes are generated at 1-mm intervals along the flow lumen. Last, peak velocities are extracted from each of the cut planes along the centerline across time. The

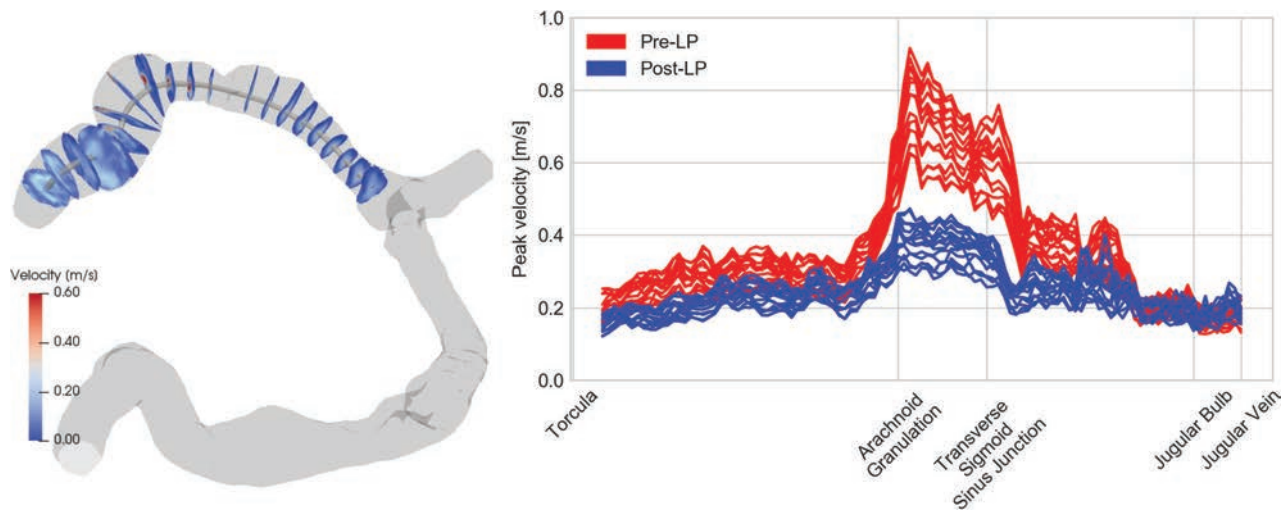


**FIG 1.** Left, MR venogram (gray) of the bilateral transverse and sigmoid sinuses showing the centerline and transverse cut planes. Right, The peak velocity along the centerline is plotted for different time points in the cardiac cycle before (red) and after (blue) LP.

**Table 2: Summary of patients<sup>a</sup>**

	Pre-LP	Post-LP	P Value
Pressure (cm H <sub>2</sub> O)	21.7 ± 5.2	8.9 ± 2.0	<.001
PT intensity	4.4 ± 3.2	1.7 ± 2.5	.020
Ipsilateral flow rate (mL/min)	393 ± 100	406 ± 92	.296
Ipsilateral peak velocity (m/s)	0.98 ± 0.37	0.73 ± 0.25	.003
CSF withdrawn (mL)		14.9 ± 6.4	
Severity of stenosis		77.9 ± 28.0	

<sup>a</sup> Data are means unless otherwise indicated.

peak velocity of >0.5 m/s visually matched the appearance of a flow jet, so this velocity was used as a threshold value to determine the presence of jets.

Flow rates were quantified using Segment (<http://segment.heiberg.se>)<sup>22</sup> to evaluate the 2Dflow data acquired through the sigmoid sinus.

### Statistical Analysis

Linear regression was performed to investigate the relation between the opening pressure and the change in peak velocity caused by the CSF drainage. To investigate potential confounding characteristics, we used ANOVA to test whether linear regression models with 2 variables were better than a model using the opening pressure alone. The additional variables investigated were flow rate, stenosis severity, change in CSF pressure, and the amount of CSF drained.

Statistical analysis was performed on both the group as a whole but also on the subgroup of patients with ipsilateral flow jets, which depict the impact for PT with suspected flow jet etiology.

Paired *t* tests were used to detect changes in intracranial pressure, flow rate, and velocities before and after lumbar puncture. The Pearson product momentum correlation was used to determine whether a reduction in peak velocity correlated with the reduction in intracranial pressure, and it was also used to determine whether the reduction in peak velocity correlated with the reduction in PT sound intensity.

## RESULTS

Ten patients were included in the study. Seven of the 10 patients did not meet the diagnostic criteria for IIH<sup>8</sup>; 2 were PT asymp-

tomatic at the time of the pre-LP query; an ipsilateral jet with peak velocity of >0.5 m/s was identified in 8 of the 10 patients; and 1 patient underwent placement of a lumbar drain preventing recording of the closing pressure. A summary of the patient information is provided in Table 2.

There was a correlation between the change in ipsilateral peak velocity and the opening pressure ( $r = -0.72$ ,  $P = .019$  for all patients, Fig 2, and  $r = -0.80$ ,  $P = .030$  for patients without IIH). No confounding characteristics were found by adding a second variable to the linear regression in addition to the opening pressure: flow rate ( $P = .208$ ), stenosis severity ( $P = .375$ ), change in CSF pressure ( $P = .543$ ), and the amount of CSF drained ( $P = .529$ ).

No correlation was found between opening pressure and the change in the ipsilateral flow rate ( $r = 0.21$ ,  $P = .564$ ). There was also a correlation between the change in the PT rating and the reduction in peak velocity ( $r = 0.67$ ,  $P = .035$ ). The severity of the stenosis was not found to correlate with peak velocity ( $r = 0.50$ ,  $P = .146$ ) or a change in peak velocity ( $r = -0.40$ ,  $P = .258$ ).

### Patients with an Ipsilateral Jet

Eight of 10 patients had an ipsilateral flow jet, as illustrated in Fig 3. Two of these were asymptomatic at the time of the pre-LP query. The lumbar puncture reduced CSF pressure by a mean of  $12.8 \pm 3.4$  cm H<sub>2</sub>O ( $P < .001$ ) without significant changes in the ipsilateral bulk flow rate ( $P = .479$ ). Nevertheless, the peak velocity was reduced by a mean of  $0.30 \pm 0.18$  m/s ( $P = .002$ ). The reduction in peak velocity correlated with the reduction in pressure ( $r = 0.82$ ,  $P = .024$ ) and with the reduction in subjectively scored PT intensity ( $r = 0.78$ ,  $P = .023$ ). The hemodynamic relations for these patients are illustrated in Fig 4.

The 6 patients experiencing pre-LP PT symptoms reported a mean PT intensity reduction of  $3.8 \pm 3.4$ .

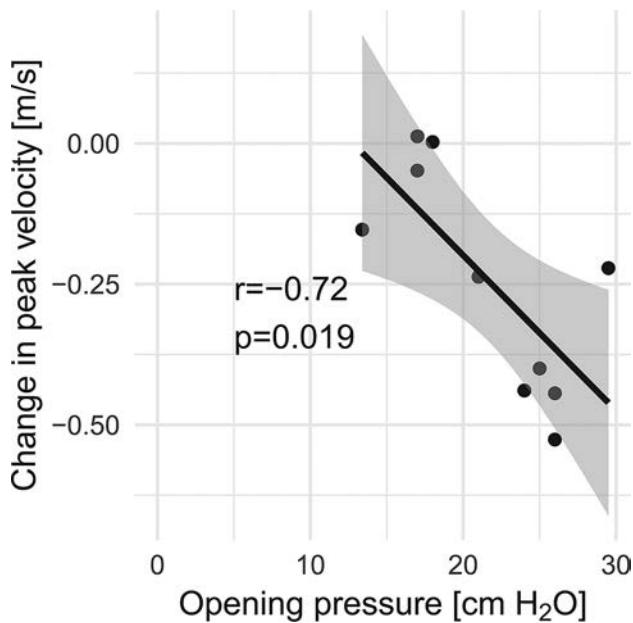


**FIG 2.** Lumbar puncture–induced change in ipsilateral peak velocity in relation to opening pressure.

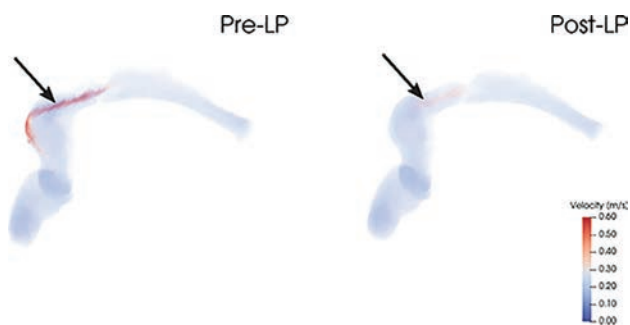


**FIG 3.** The *left side* shows an ipsilateral flow jet pre-LP that is weakened post-LP without a concomitant change in the flow rate (374–381 mL/min). The rating of PT intensity for this patient was reduced from 9 to 0.

### Patients without an Ipsilateral Jet

Two patients did not have an ipsilateral flow jet. The first of these patients had a contralateral jet of reduced peak velocity after lumbar puncture (0.61 m/s from 0.67 m/s pre-LP), matching the mild improvement of the PT intensity (4 to 3). The second patient had high velocities in the external carotid artery, which subsided after LP, qualitatively matching the reduction in PT intensity (decreasing from 3 to 0).

### Pre- and Post-LP MRV

The patient imaged using ferumoxytol contrast underwent both pre- and post-LP CE-MR venography studies, demonstrating near-complete resolution of transverse sinus stenosis at a lower CSF pressure (10 cm H<sub>2</sub>O from 25 cm H<sub>2</sub>O before LP) (Fig 5).

## DISCUSSION

The aim of this study was to investigate changes in venous sinus flow features and PT intensity in response to lumbar puncture. The key findings in this study were the following: 1) Flow jets were seen in most cases in this study; 2) lowering the CSF pressure

decreased the peak velocity of the flow jet in a venous sinus stenosis, without a concomitant reduction in the bulk flow rate; and 3) the reduction of peak velocity correlated with a reduced PT sound intensity. We thus hypothesize that the flow jet, and not the sinus bulk flow rate, is related to PT in patients with a transverse sinus stenosis.

The suspected cause of the decrease in peak jet velocity post-LP is an alleviation of transverse sinus stenosis as suggested by prior case reports.<sup>23–26</sup> We were able to directly demonstrate this with MR venography in 1 patient using a blood pool contrast agent, and we believe this study is the first to use MR venography to show an immediate resolution in venous sinus stenosis after LP.

The direct relationship between peak jet velocity and CSF pressure was maintained for patients in this series who met the Dandy criteria for IIH (CSF opening pressure of >25 cm H<sub>2</sub>O) and for patients not meeting the Dandy criteria. Of our subjects who had improvement in their PT after removal of CSF, 5 of 7 had an opening pressure of ≥20 cm H<sub>2</sub>O, a threshold for abnormal elevation proposed by Corbett and Mehta<sup>27</sup> for patients with a normal body mass index. Of note, venous sinus stenosis was observed in all patients in this series meeting or exceeding the 20-cm H<sub>2</sub>O threshold.

In a prospective trial, Boddu et al<sup>11</sup> showed that PT can be alleviated in patients with IIH with venous sinus stent placement, and our results suggest that broadening this therapy to patients with PT who do not have IIH may warrant consideration, at least for patients with a transverse sinus stenosis whose symptoms improve with LP reduction of CSF pressure.<sup>28</sup>

While this study suggests the flow jet to be critical in the development of sound, the mechanistic link between a flow jet and PT symptoms remains opaque. We hypothesize that the transition into turbulent flow that can occur during the deceleration of these jets immediately “downstream” from the stenosis is a probable cause of the sound that causes PT.<sup>29</sup> However, other anatomic variables may also play a role, such as sigmoid sinus diverticula, which can sometimes be seen in patients with transverse sinus stenosis.

At first glance, a finding that a reduction in symptoms following LP is not associated with a reduction in flow appears somewhat counterintuitive. Although not statistically significant, our data rather indicate that the flow rate might be slightly increased. On closer consideration however, it is known and expected that a vascular stenosis will, at first, have little effect on volume flow rates while peak velocities in the jet rise (and this feature forms the basis of Doppler sonography evaluation of stenoses of the extracranial carotid arteries). In carotid bruits, it is the disordered flow caused by the jet that is the source of sound, and that would be consistent with our observations reported here for PT. We also note that the reduced intracranial pressure seems to result in improvement in a very focal area of stenosis, and not the entirety of the sinus. In fact, most of the stenoses in this cohort were caused by compression from an arachnoid granulation as opposed to a smooth extrinsic stenosis. This discrepancy may help to explain the disparity between our results and prior work.

We hypothesized that the reduced peak velocities, without concomitant reduction in flow rates, primarily are the result of a reduction in the degree of stenosis. The stenoses caused by intra-

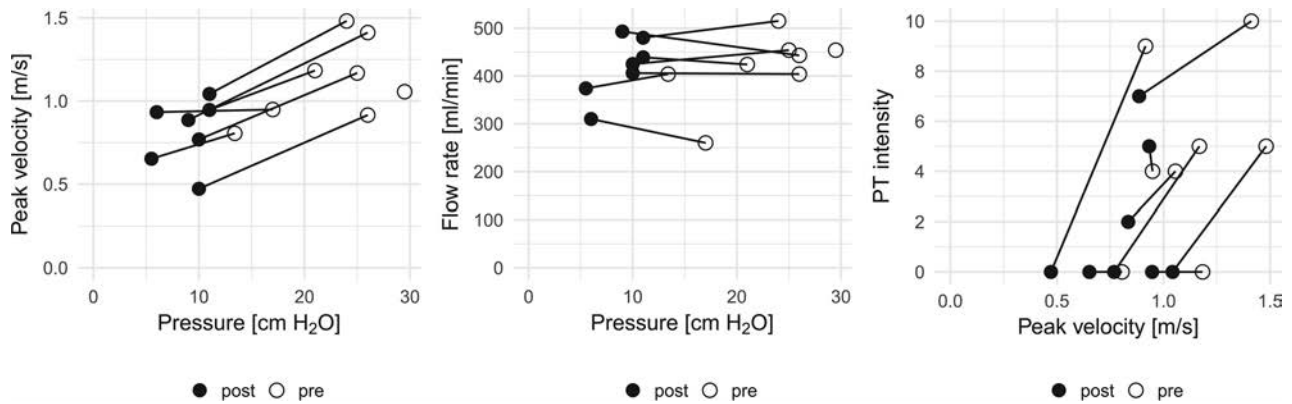


**FIG 4.** Lumbar puncture–induced hemodynamic changes for patients with ipsilateral jets. Note that reduced pressure lowered the ipsilateral peak velocity (*left panel*) without a concomitant reduction in flow rate (*middle panel*). Furthermore, PT intensity also decreased as the peak velocity was reduced.

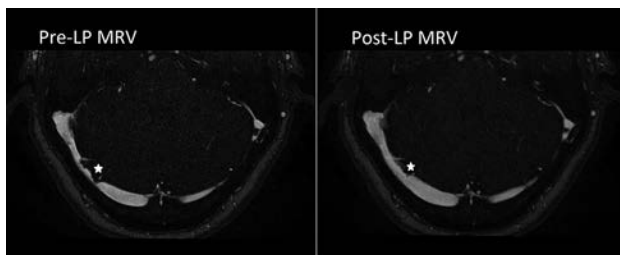


**FIG 5.** LP-induced change in lumen geometry. The pre-LP MRV lumen is shown on the *left side* (opening pressure of 25 cm H<sub>2</sub>O), whereas the post-LP lumen is seen in the *right side* (closing pressure of 10 cm H<sub>2</sub>O). Note the improved transverse sinus stenosis at a prominent arachnoid granulation in the right transverse sinus (*star*).

cranial hypertension of >20 cm H<sub>2</sub>O are alleviated by an LP-induced reduction in intracranial pressure resulting in a concomitant reduction in the jet velocities. This hypothesis is supported by the pre- and post-LP MRA seen in Fig 5, which clearly shows widening of the transverse sinus stenosis after the LP.

## CONCLUSIONS

The objective of this study was to evaluate changes in venous blood flow caused by lowered intracranial pressure in patients with PT after LP to help identify the cause of PT. Our results show an LP-induced reduction in venous peak velocity without a concomitant reduction in flow rate. We hypothesize that the reduction in jet velocity is caused by the alleviation of the transverse stenosis following LP. Our results further show a correlation between peak velocity and PT intensity, suggesting that flow jets are critical in the development of sound.

## ACKNOWLEDGMENTS

We thank Drs Wade Smith and Jonathan Horton for their helpful conversations in developing the concepts behind this work.

Disclosures: Henrik Haraldsson—*RELATED: Grant:* National Institutes of Health.\* David A. Saloner—*RELATED: Grant:* National Institutes of Health.\* Matthew R. Amans—*RELATED: Grant:* National Institutes of Health, *Comments:* R21DC016087\*; *UNRELATED: Consultancy:* Covidien, Stryker Neurovascular, *Comments:* minor financial compensation for consultant work. Alexandra G. Wright—*RELATED: Grant:* National Institutes of Health, R21DC016087.\* \*Money paid to the institution.

## REFERENCES

1. Krishnan A, Mattox DE, Fountain AJ, et al. **CT arteriography and venography in pulsatile tinnitus: preliminary results.** *AJNR Am J Neuroradiol* 2006;27:1635–38 *Medline*
2. Liyanage SH, Singh A, Savundra P, et al. **Pulsatile tinnitus.** *J Laryngol Otol* 2006;120:93–97 *CrossRef Medline*
3. Madani G, Connor SE. **Imaging in pulsatile tinnitus.** *Clin Radiol* 2009;64:319–28 *CrossRef Medline*
4. Harvey RS, Hertzano R, Kelman SE, et al. **Pulse-synchronous tinnitus and sigmoid sinus wall anomalies: descriptive epidemiology and the idiopathic intracranial hypertension patient population.** *Otol Neurotol* 2014;35:7–15 *CrossRef Medline*
5. Cognard C, Gobin YP, Pierot L, et al. **Cerebral dural arteriovenous fistulas: clinical and angiographic correlation with a revised classification of venous drainage.** *Radiology* 1995;194:671–80 *CrossRef Medline*
6. Chan CF, Gatehouse PD, Hughes R, et al. **Novel technique used to detect swallowing in volume-selective turbo spin-echo (TSE) for carotid artery wall imaging.** *J Magn Reson Imaging* 2009;29:211–16 *CrossRef Medline*
7. Olin JW, Froehlich J, Gu X, et al. **The United States Registry for Fibromuscular Dysplasia: results in the first 447 patients.** *Circulation* 2012;125:3182–90 *CrossRef Medline*
8. Morris PP, Black DF, Port J, et al. **Transverse sinus stenosis is the most sensitive MR imaging correlate of idiopathic intracranial hypertension.** *AJNR Am J Neuroradiol* 2017;38:471–77 *CrossRef Medline*
9. Morris PP, Lachman N, Black DF, et al. **Increased curvature of the tentorium cerebelli in idiopathic intracranial hypertension.** *AJNR Am J Neuroradiol* 2017;38:1789–93 *CrossRef Medline*
10. Farb RI, Vanek I, Scott JN, et al. **Idiopathic intracranial hypertension: the prevalence and morphology of sinovenous stenosis.** *Neurology* 2003;60:1418–24 *CrossRef Medline*
11. Boddu S, Dinkin M, Suurna M, et al. **Resolution of pulsatile tinnitus after venous sinus stenting in patients with idiopathic intracranial hypertension.** *PLoS One* 2016;11:e0164466 *CrossRef Medline*
12. Asif H, Craven CL, Siddiqui AH, et al. **Idiopathic intracranial hypertension: 120-day clinical, radiological, and manometric outcomes after stent insertion into the dural venous sinus.** *J Neurosurg* 2018;129:723–31 *CrossRef Medline*
13. Dinkin MJ, Patsalides A. **Venous sinus stenting in idiopathic intracranial hypertension: results of a prospective trial.** *J Neuroophthalmol* 2017;37:113–21 *CrossRef Medline*
14. Liu KC, Starke RM, Durst CR, et al. **Venous sinus stenting for reduction of intracranial pressure in IIH: a prospective pilot study.** *J Neurosurg* 2017;127:1126–33 *CrossRef Medline*
15. Kao E, Kefayati S, Amans MR, et al. **Flow patterns in the jugular veins of pulsatile tinnitus patients.** *J Biomech* 2017;52:61–67 *CrossRef Medline*

16. Kefayati S, Amans M, Faraji F, et al. **The manifestation of vortical and secondary flow in the cerebral venous outflow tract: an in vivo MR velocimetry study.** *J Biomech* 2017;50:180–87 CrossRef Medline
17. Acevedo-Bolton G, Amans MR, Kefayati S, et al. **Four dimensional magnetic resonance velocimetry for complex flow in the jugular vein.** *Quant Imaging Med Surg* 2015;5:635–37 CrossRef Medline
18. Smith JL. **Whence pseudotumor cerebri?** *J Clin Neuroophthalmol* 1985;5:55–56 Medline
19. Ittrich H, Peldschus K, Raabe N, et al. **Superparamagnetic iron oxide nanoparticles in biomedicine: applications and developments in diagnostics and therapy.** *Rofo* 2013;185:1149–66 CrossRef Medline
20. Weinstein JS, Varallyay CG, Dosa E, et al. **Superparamagnetic iron oxide nanoparticles: diagnostic magnetic resonance imaging and potential therapeutic applications in neurooncology and central nervous system inflammatory pathologies: a review.** *J Cereb Blood Flow Metab* 2010;30:15–35 CrossRef Medline
21. Hope MD, Hope TA, Zhu C, et al. **Vascular imaging with ferumoxytol as a contrast agent.** *AJR Am J Roentgenol* 2015;205:W366–73 CrossRef Medline
22. Heiberg E, Sjögren J, Ugander M, et al. **Design and validation of Segment: freely available software for cardiovascular image analysis.** *BMC Med Imaging* 2010;10:1 CrossRef Medline
23. Scoffings DJ, Pickard JD, Higgins JN. **Resolution of transverse sinus stenoses immediately after CSF withdrawal in idiopathic intracranial hypertension.** *J Neurol Neurosurg Psychiatry* 2007;78:911–12 CrossRef Medline
24. King JO, Mitchell PJ, Thomson KR, et al. **Manometry combined with cervical puncture in idiopathic intracranial hypertension.** *Neurology* 2002;58:26–30 CrossRef Medline
25. Baryshnik DB, Farb RI. **Changes in the appearance of venous sinuses after treatment of disordered intracranial pressure.** *Neurology* 2004;62:1445–46 CrossRef Medline
26. Onder H, Gocmen R, Gursoy-Ozdemir Y. **Reversible transverse sinus collapse in a patient with idiopathic intracranial hypertension.** *BMJ Case Rep* 2015;2015 CrossRef Medline
27. Corbett JJ, Mehta MP. **Cerebrospinal fluid pressure in normal obese subjects and patients with pseudotumor cerebri.** *Neurology* 1983;33:1386–88 CrossRef Medline
28. Lenck S, Labeyrie MA, Vallee F, et al. **Stent placement for disabling pulsatile tinnitus caused by a lateral sinus stenosis: a retrospective study.** *Oper Neurosurg (Hagerstown)* 2017;13:560–65 CrossRef Medline
29. Baomin L, Yongbing S, Xiangyu C. **Angioplasty and stenting for intractable pulsatile tinnitus caused by dural venous sinus stenosis: a case series report.** *Otol Neurotol* 2014;35:366–70 CrossRef Medline

# The Black Turbinate Sign, A Potential Diagnostic Pitfall: Evaluation of the Normal Enhancement Patterns of the Nasal Turbinates

Q. Han and E.J. Escott



## ABSTRACT

**BACKGROUND AND PURPOSE:** Lack of enhancement of a nasal turbinate on MR imaging, known as the black turbinate, has been reported as a finding highly suggestive of invasive fungal rhinosinusitis in immunocompromised patients. Our purpose was to investigate the normal enhancement pattern of nasal turbinates and to determine whether a black turbinate occurs in patients without invasive fungal rhinosinusitis and, if so, to distinguish differentiating features from pathologic enhancement.

**MATERIALS AND METHODS:** We examined patient medical records and available MR imaging, which included most nasal turbinates in more than 1 sequence. Imaging was performed with contrast, either with or without fat saturation, in patients without invasive fungal rhinosinusitis. All MR images were evaluated for a turbinate enhancement pattern and the presence of nonenhancing areas.

**RESULTS:** After we applied the exclusion criteria, 75 MR images from each group, with and without fat saturation, were included. Overall, the frequency of observed nonenhancing portions of turbinates, ie, black turbinates, was 30%. Most observed black turbinates were located in the posterior portion of inferior turbinates. Tiny areas of nonenhancement within turbinates were also a common finding.

**CONCLUSIONS:** A black turbinate is not uncommon on MR images in immunocompetent patients who have no chance of having invasive fungal rhinosinusitis. Benign turbinate nonenhancement improves over subsequent series, has preserved thin peripheral enhancement, and often has thin internal septa. Knowledge of this normal pattern of nasal turbinate enhancement can aid in the differentiation of the benign black turbinate in immunocompetent patients from the pathologic black turbinate seen in patients with invasive fungal rhinosinusitis.

**ABBREVIATIONS:** BT = black turbinate; IFRS = invasive fungal rhinosinusitis; NE = nonenhancing or nonenhancement

Lack of enhancement of a nasal turbinate on MR images (the “black turbinate [BT] sign”) has been reported as highly suggestive of invasive fungal rhinosinusitis (IFRS) in immunocompromised patients (Fig 1).<sup>1–5</sup> However, we have noticed nonenhancing (NE) turbinates in patients imaged for other indications, who have essentially no possibility of having IFRS. IFRS in the at-risk population is a rapidly progressive disease that frequently progresses to involve the orbit and brain. Although treated with aggressive surgical debridement, these patients usually have a poor prognosis.<sup>6,7</sup> On the other hand, no treatment would be

required if nonenhancement of a nasal turbinate could be a normal finding as well. Therefore, we sought to better understand what constitutes the normal enhancement pattern of the nasal turbinates on MR imaging and attempted to define differentiating features between the normal and pathologic enhancement patterns.

## MATERIALS AND METHODS

### Patient Selection

This was a retrospective institutional review board–approved study involving the examination of patient medical records, such as medical history and MR images obtained without and with (gadolinium-based) intravenous contrast. Patients were enrolled in the study via a reverse chronologic order search of the PACS for appropriate MR images. We obtained 2 groups of scans. The fat-saturation group included MR images using orbit, face, neck, or skull base protocols: postcontrast T1-weighted imaging with fat saturation, from May 9, 2016, through July 31, 2016. The brain group included MR images using brain protocols: postcontrast T1-weighted imaging that did not use fat-saturation, from July 1, 2016, through July 10, 2016. Both groups of patients were enrolled

Received March 28, 2018; accepted after revision March 18, 2019.

From the Departments of Radiology (Q.H.) and Radiology and Otolaryngology-Head and Neck Surgery (E.J.E.), University of Kentucky, Lexington, Kentucky.

Paper previously presented at: Annual Meeting of the American Society of Neuroradiology and the Foundation of the ASNR Symposium, April 22–27, 2017; Long Beach, California.

Please address correspondence to Qiong Han, MD, PhD, Department of Radiology, University of Kentucky, HX 319D, 800 Rose St, Lexington, KY 40506; e-mail: qiong.han@uky.edu

Indicates article with supplemental on-line table.

<http://dx.doi.org/10.3174/ajnr.A6037>

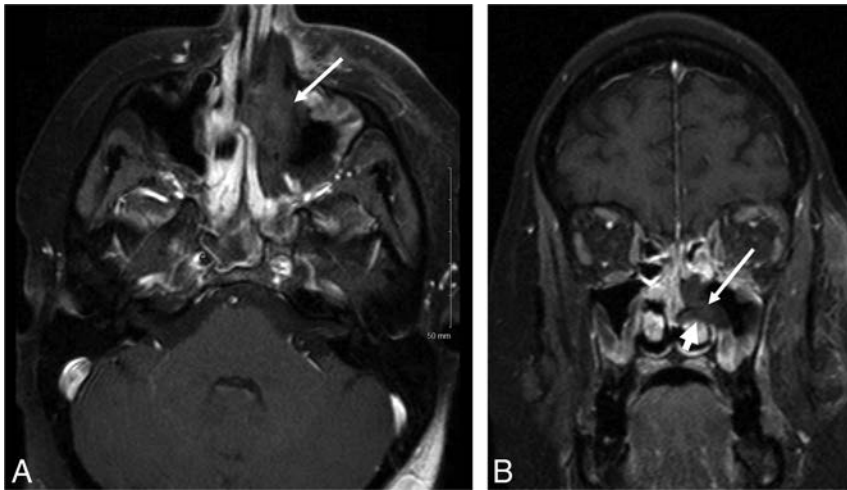


**FIG 1.** A 27-year-old woman with relapsed pre-B-cell acute lymphoblastic leukemia was admitted for chemotherapy. She had an MR imaging examination due to headache. Axial (A) and coronal (B) T1-weighted postcontrast images with fat saturation showed nonenhancement centered in the left middle turbinate (*long arrows*) with irregular and invasive borders extending into the left inferior turbinate (*short arrow*). The patient had tissue-proved invasive fungal rhinosinusitis and went through a series of 12 aggressive surgical debridements and eventually died.

in reverse chronologic order until the same number of patients (75) was enrolled for each group after applying the exclusion criteria. The medical records of all patients were evaluated to confirm that the enrolled patients were not likely to have IFRS.

#### Exclusion Criteria

Our exclusion criteria were specifically designed to ensure sufficient and reliable evaluation of the spatial and temporal enhancement pattern of the nasal turbinates. They were as follows:

- 1) Scans that did not include at least two-thirds of the concha of the inferior turbinate.
- 2) Scans with substantial postoperative or posttreatment changes in the sinonasal region.
- 3) If >1 scan was obtained at the same session, only the first scan was counted, and any additional scan was used as a further delayed series: If the brain was scanned first in a combined brain/orbit scan, the orbit scan was excluded from the fat-saturation group and only included in the brain group.
- 4) Scans with only 1 sequence routinely including the nasal turbinates, such as scans using our internal auditory canal, pituitary, or various research protocols.
- 5) Scans with significant motion or other artifacts.
- 6) Scans with any mass or destructive lesion in the sinonasal region.
- 7) Scans from outside or satellite hospitals were excluded as the index examinations but were used as prior comparison examinations.

#### MR Image Acquisition

MR images included in this study were obtained using various MR imaging scanners (Espree, Aera, Symphony, Skyra and Verio; Siemens, Erlangen, Germany). Our departmental protocols for the brain, orbit, face, neck, or skull base were used. There was some variation between pediatric and adult protocols and among different scanners. Some of the key technical parameters such as the length of time to acquire each sequence are summarized in the

On-line Table and Table 1. In general, there was a 25- to 30-second delay between intravenous contrast injection and imaging in the first postcontrast sequence.

#### MR Image Interpretation

MR images were evaluated for the presence of areas of NE within the nasal turbinates (ie, BT). Areas of NE must be confluent areas larger than  $4 \times 5$  mm to be called BTs. This criterion was specifically defined to differentiate between BT and scattered small NE foci that are commonly seen and would not likely be interpreted as potential IFRS.

Each patient with a nonenhancing turbinate was further evaluated for the location of NE within the turbinates and for whether the NE areas persisted but improved or resolved during the multiple postcontrast series. In addition, the

size symmetry of the turbinates, the overall enhancement degree, and associated signal intensity on the T2-weighted images were graded by a neuroradiologist with a Certificate of Added Qualification in neuroradiology and 24 years' experience and a senior resident radiologist-in-training. If there was any initial disagreement between the 2 observers, the final grading in each category was decided by further discussion and consensus (Tables 2–4 for the grading system and summary of the cases). A prior MR image, if available, was also thoroughly reviewed to evaluate any temporal variability of the enhancement pattern of the nasal turbinate.

#### Statistical Analysis

The Fisher exact test was used to determine whether there was a statistically significant difference between the sex and age composition of the 2 groups overall and the percentage of BT cases in each group.

#### RESULTS

One hundred sixty-two MR images from the fat-saturation group and 108 MR images from the brain group were evaluated, among which 87 MR images from the fat-saturation group and 33 MR images from the brain group were excluded per the exclusion criteria. Most of the excluded scans were orbit scans with insufficient inclusion of the nasal turbinates. A detailed breakdown of the excluded scans is shown in Fig 2. Seventy-five MR images were included in each group. The demographic information of all included scans and scans that demonstrated BT is summarized in Tables 6 and 7, respectively.

Overall, the observed rate of BT in both cohorts combined was 30% (45/150), with 21% (16/75) in the fat-saturation group and 39% (29/75) in the brain group, respectively. There was a discrepancy between the percentage of BT cases in the 2 groups, and such discrepancy was likely due to the technical differences, including the length of the scans and the greater conspicuity of enhancement on the images with fat saturation.

**Table 1: Timing guideline of postcontrast sequences for 3T scanners<sup>a</sup>**

Skyra adult protocols				
Orbit	Axial T1 FS	Coronal T1 FS	Cor MPRAGE (O)	
Timing	04:10	04:42	04:14	
Face	Coronal T1 FS	Axial T1 FS	Sagittal T1 FS	
Timing	03:58	04:31	05:03	
Neck	Sagittal T1 FS	Coronal T1 FS	Axial T1 FS	
Timing	06:43	04:39	08:02	
Skull base	Axial FLAIR	Axial T1 FS	Coronal T1 FS	Sagittal FLAIR FS
Timing	01:54	06:58	06:42	02:54
Brain	Axial T1 FLAIR	Coronal T1 FLAIR	Sagittal T1 FLAIR	
Timing	01:54	02:54	02:54	
Verio adult protocols				
Orbit	Axial T1 FS	Coronal T1 FS		
Timing	03:14	01:51		
Face	Coronal T1 FS	Axial T1 FS	Sagittal T1 FS	
Timing	04:00	04:00	05:04	
Neck	Axial T1 FS	Coronal T1 FS	Axial T1 FS	
Timing	03:56	04:04	05:03	
Skull base	Axial T1 FS	Coronal T1 FS	Axial T1	Sagittal T1 FS
Timing	05:13	05:13	01:41	05:07
Brain	Axial T1	Coronal T1	Sagittal T1 FLAIR	Cor MPRAGE (O)
Timing	01:21	01:45	01:39	04:18

**Note:**—Cor indicates coronal; FS, fat saturation; O, optional sequence; VIBE, volume interpolated gradient echo.

<sup>a</sup> Skyra and Verio scanners (Siemens, Erlangen, Germany). All timing is in minutes and seconds.

**Table 2: Grading criteria for imaging findings<sup>a</sup>**

Category	Grades		
	1	2	3
Size symmetry	Markedly asymmetric	Mildly-to-moderately asymmetric	Symmetric
Degree of enhancement	Less than extraocular muscle	Similar to extraocular muscle	Greater than extraocular muscle
T2 signal intensity	Similar to extraocular muscle	Similar to gray matter	Similar to vitreous

<sup>a</sup> Grading criteria for the symmetry of the size of the nasal turbinates, their overall degree of enhancement, and their signal intensity on the T2-weighted images. Scores range from 1 to 3, with scores of 1.5 or 2.5 representing the intermediate grade between 2 levels.

**Table 3: Imaging findings by group<sup>a</sup>**

	Grades				
	1	1.5	2	2.5	3
FS group (16 cases)					
Size symmetry			10		6
Enhancement level	12	1	2		1
T2 signal intensity			8	1	7
Brain group (29 cases)					
Size symmetry	3		8	1	17
Enhancement level	5		24		
T2 signal intensity			10	17	2

<sup>a</sup> Grading criteria for the symmetry of the size of the nasal turbinates, their overall degree of enhancement, and their signal intensity on the T2-weighted images. Scores range from 1 to 3, with scores of 1.5 or 2.5 representing the intermediate grade between 2 levels.

**Table 4: BT site of involvement and temporal characteristics<sup>a</sup>**

Groups	Superior	Middle	Inferior	Temporal-	Temporal-
				Improving <sup>b</sup>	Transient <sup>c</sup>
FS		6	16	5	11
Brain		8	28	13	16

<sup>a</sup> The location of the black turbinates and the change in enhancement during multiple series are shown. Because a patient can demonstrate BT in >1 turbinate (ie, both the middle and inferior turbinates can show BT simultaneously), the total number of turbinates seen with BT is larger than the number of cases in each group.

<sup>b</sup> BT persists across all sequences but improves gradually.

<sup>c</sup> BT resolves on later sequences.

The NE in the BT cases was confined within the turbinate, with regular and well-defined borders. Another common observation was thin rim enhancement around the NE areas (Figs 3 and 4),

**Table 5: Relationship of turbinate size to BT, presence of BT at 2 time points, and nasal cycling<sup>a</sup>**

Groups	Cases with BT	Cases with Size Asymmetry	BT Seen in Smaller Turbinates	Cases with Prior Exam	BT Seen on Prior Exam	Cases with Nasal Cycling
Brain	29	12	4	13	10	3

<sup>a</sup> The occurrence of BT relative to turbinate size shows that BT did not primarily occur in the smaller turbinate when size asymmetry was present. Patients who had a BT on 1 scan often did not always have a BT on a prior exam. Nasal cycling indicates a change in nasal turbinate symmetry between the index and prior study. This occurred relatively infrequently.

likely corresponding to normal mucosal enhancement. Faint septa could occasionally be seen in the NE areas. The NE areas were most commonly seen in the concha of the inferior turbinates, sparing the anterior aspects (Fig 3), with a similar distribution within the middle turbinates being the next most frequent site.

Another phenomenon we frequently observed was scattered small foci (usually much smaller than 4 × 5 mm) of NE, which either developed as a resolving stage of the BT or were present on the first postcontrast sequence. The scattered NE foci followed a distribution pattern similar to that of BTs (Figs 4 and 5).

### Size Asymmetry

In about half of the cases of BT (10 of 16 in the fat-saturation group and 12 of 29 in the brain group, or 22 of 45 cases in both

groups), there was a significant side-to-side size asymmetry between the bilateral turbinates. Among those 22 cases, approximately 45% of them (10/22) showed BTs or more prominent BTs (if bilateral) in the smaller turbinates (Table 5).

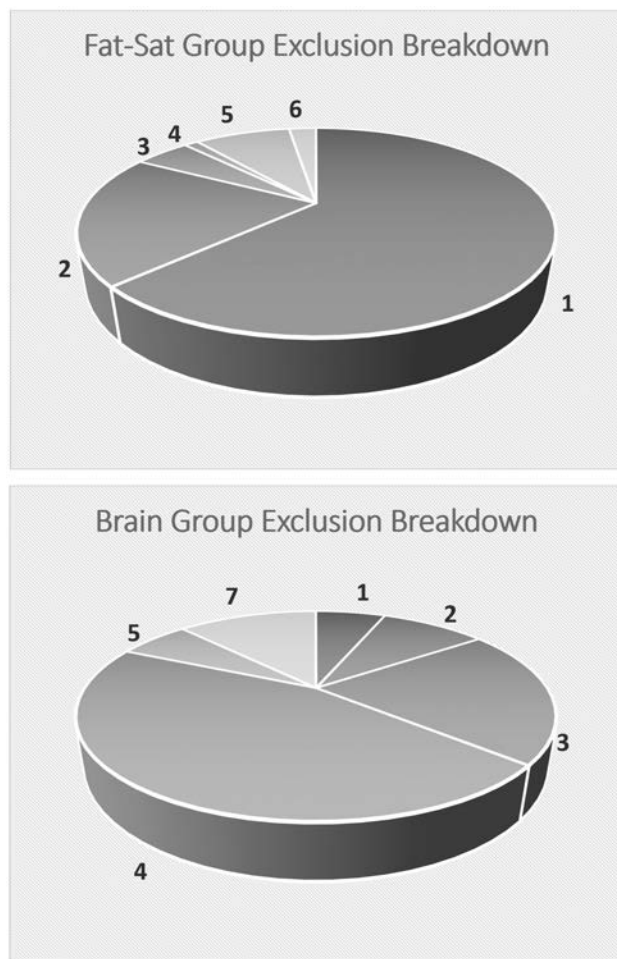


**FIG 2.** Breakdown of excluded cases: 1) insufficient inclusion of nasal turbinates, 2) significant postoperative or posttreatment changes involving the nasal cavity, 3) inappropriate scan sequence, 4) specific protocols, 5) significant motion or other artifacts, 6) significant nasal mass, and 7) scans from outside or satellite hospitals.

**Table 6: Demographic summary of the recruited patients<sup>a</sup>**

	Total	Female	Male	<i>P</i> (M vs F)	Pediatric Patients	Adult Patients	<i>P</i> (Adult vs Pediatric)
FS group	75	40 (53%)	35 (47%)	.74 <sup>b</sup>	16 (21%) (6 mo to 14 yr)	59 (79%) (range, 18–81 yr)	.74 <sup>b</sup>
Brain group	75	41 (55%)	34 (45%)	.62 <sup>b</sup>	17 (23%) (2 mo to 17 yr)	58 (77%) (range, 24–86 yr)	1.00 <sup>b</sup>
<i>P</i> FS vs Brain		1.00 <sup>c</sup>				1.00 <sup>c</sup>	

**Note:**—*P* indicates *P* value; M, male; F, female.

<sup>a</sup> All *P* values were calculated using the Fisher exact test.

<sup>b</sup> To compare the sex and age composition of each group with the general population, assuming even sex distribution and approximately 24% pediatric population.

<sup>c</sup> To compare the sex and age composition between the FS and brain groups.

**Table 7: Demographic summary of the patients with black turbinates<sup>a</sup>**

	Total	Female	Male	<i>P</i> (M vs F)	Pediatric Patients	Adult Patients	<i>P</i> (Adult vs Pediatric)
FS group	16	11 (69%)	5 (31%)	.28 <sup>b</sup>	2 (12%) (11 and 14 yr)	14 (88%) (range, 31–74 yr)	.73 <sup>b</sup>
Brain group	29	17 (59%)	12 (41%)	.83 <sup>b</sup>	1 (3%) (10 yr)	28 (97%) (range, 24–79 yr)	.02 <sup>b,c</sup>
<i>P</i> FS vs brain		.54 <sup>d</sup>				.28 <sup>d</sup>	

<sup>a</sup> All *P* values were calculated using the Fisher exact test.

<sup>b</sup> To compare the sex and age compositions of each BT group with the general population, assuming even sex distribution and approximately 24% pediatric population.

<sup>c</sup> Significant.

<sup>d</sup> To compare the sex and age composition between the FS and brain BT groups.

### Signal Intensity on T2-Weighted Imaging

On T2WI, the signal intensity of the BTs and turbinates in general was variable but was mostly intermediate to high (Table 3), without any case falling into the low category.

### Temporal Characteristics of Enhancement

Most cases of BT or scattered small foci of NE showed increasing enhancement with time. Most BT regions became scattered foci of NE with time (Fig 4), and 11 of 16 and 16 of 29 BTs in the fat-saturation and brain groups, respectively, showed resolution of BTs.

### Prior Examination

Nine of the 16 cases of BT in the fat-saturation group and 13 of the 29 cases of BT in the brain group had adequate prior examinations, per the same exclusion criteria (Table 5). Four of the 9 cases of BTs in the fat-saturation group and 10 of the 13 cases of BTs in the brain group also demonstrated BTs on the prior examinations, respectively.

If there was any change in size asymmetry between the index and prior examinations, we considered this as a surrogate for nasal cycling. In summary, no nasal cycling was seen in the fat-saturation group, while 3 cases in the brain group (of 10) showed evidence of nasal cycling:

**Case 1.** The larger turbinate switched from the right side to the left between the index and prior examinations, while BTs remained predominantly on the left side on both examinations.

**Case 2.** The larger turbinate switched from the right side to the left between the index and the prior examinations, while BTs were predominantly in the smaller turbinates.

**Case 3.** The turbinates were symmetric on the index examination and slightly larger on the left on the prior examination, while the BT was predominantly seen on the left side on both examinations.

For cases with BTs seen on both the index and prior examinations but without evidence of nasal cycling between the examinations, 1 of 4 cases in the fat-saturation group and 3 of 7 cases in the brain group had BTs on opposite sides between the index and prior examinations (if on the right on the index examination, then on the left on the prior examination, and vice versa), while the

remaining cases demonstrated BTs on the same side between the index and prior examinations.

In summary, benign BTs may not necessarily be present in the same patient at different time points and do not seem to be consistently influenced by nasal cycling.

## DISCUSSION

The vascular supply and complex microvascular anatomy of the nasal turbinates can partially explain our findings. The main arterial supplies to the nasal turbinates are the posterolateral (or lateral) branches of the sphenopalatine arteries.<sup>8-10</sup> Branches first supply the inferior turbinates, then the middle turbinates from their posterior aspects. Blood supply is supplemented by anastomotic branches from the anterior ethmoidal arteries that enter along the more anterior aspects of the turbinates.

The nasal tissues can vary in size, due to expansile or erectile tissues.<sup>11,12</sup> This feature is due to the complex microvascular anatomy, consisting of capillaries, arteriovenous anastomoses, capacitance vessels or sinusoids, and postcapillary venules. It is the capacitance vessels or sinusoids that are responsible for the ability of nasal structures to change size by virtue of the amount of blood within them increasing or decreasing by several mechanisms.<sup>11</sup> Ng et al<sup>12</sup> evaluated the distribution of these erectile or cavernous tissues using MR imaging. The authors found the greatest change in size in the inferior turbinate, followed by the middle turbinate (anterior third less than the remainder) and anterior nasal septum. They concluded that this distribution represented that of the cavernous tissues in the nose. This distribution seems to coincide somewhat with the distribution of the most common sites for BT and NE foci and may also explain the filling

in of these areas with time. Additionally, the scattered NE foci seen in most of the cases imply that this NE phenomenon might fall within a continuous spectrum, with the BT cases having the most confluent NE foci.

The findings of benign BT, which include nonenhancing areas with well-defined, noninvasive borders confined within a turbinate, are contrasted with the more extensive findings involving adjacent structures seen in our case of IFRS (Fig 1).

Common observations in our benign BT cases of thin rim enhancement around the nonenhancing areas (Figs 3 and 4) and intermediate and high signal intensity on the T2-weighted images were not consistently described in the cases of IFRS reported in the literature<sup>1-4,7</sup>

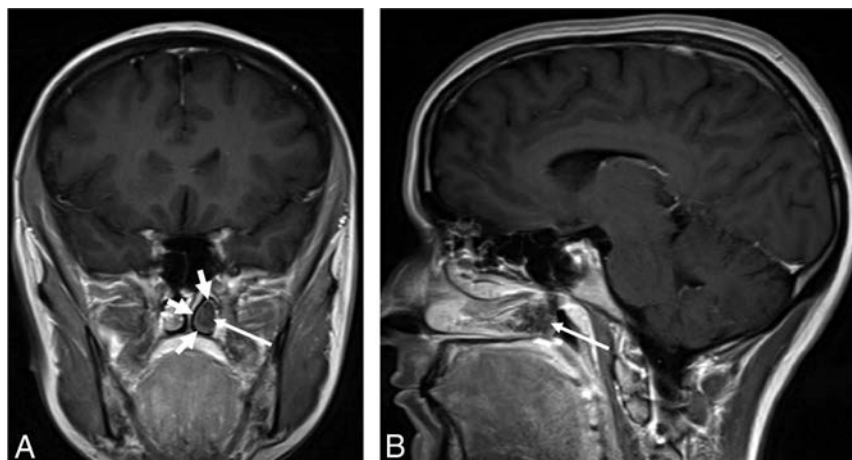


**FIG 3.** A 24-year-old immunocompetent woman with a history of a gestational trophoblastic neoplasm who had a brain MR imaging for a metastatic work-up. Coronal (A) and sagittal (B) postcontrast T1-weighted images show nonenhancement of the posterior aspect of the left inferior turbinate (*long arrows*) with thin rim enhancement (*short arrows*). The posterior aspect of the inferior turbinate is a common location of a black turbinate in immunocompetent patients.

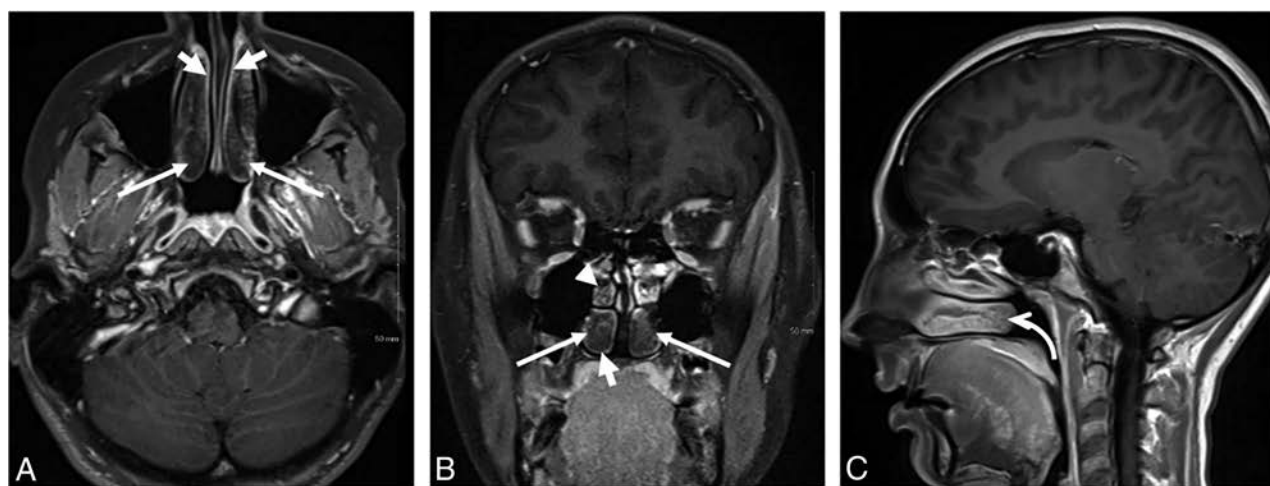


**FIG 4.** A 14-year-old immunocompetent adolescent girl with right-sided blurred vision, who had orbit and brain MR imaging for a multiple sclerosis work-up. The postcontrast images for the orbit MR imaging were obtained before those for the brain MR imaging. Axial (A) and coronal (B) postcontrast T1-weighted images with fat saturation show nonenhancement most pronounced in the posterior aspects of both inferior turbinates (*long arrows*) with thin rim enhancement (*short arrows*) and scattered nonenhancing foci in the right middle turbinate (*arrowhead*). The inferior turbinate, especially the posterior portion, is a common location of a BT in immunocompetent patients. The sagittal postcontrast image from the brain MR imaging (C), which is the last postcontrast sequence available, shows that the BT of the right inferior turbinate is almost completely resolved and has transitioned into mildly scattered nonenhancing foci (*curved arrow*).

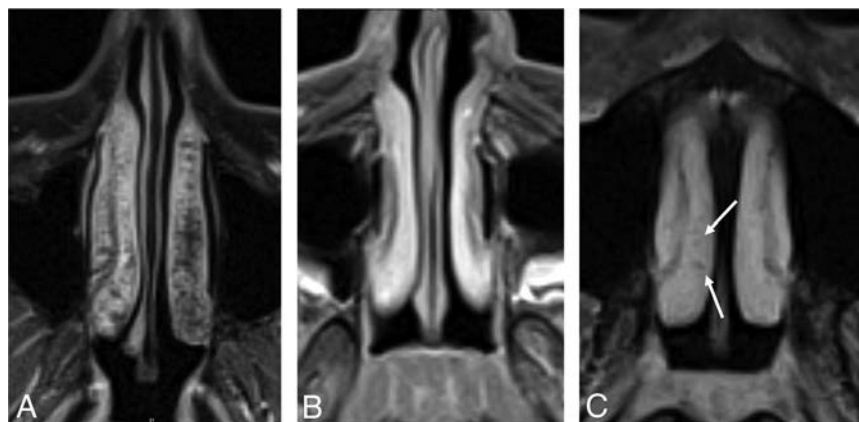


**FIG 5.** Axial postcontrast T1-weighted images with fat saturation from 3 different patients. A, A 43-year-old woman shows extensive nonenhancing “dots” in both inferior turbinates, left more than right, with relative sparing of the anterior aspects, which is a typical pattern of scattered nonenhancing foci. B, A 12-year-old girl shows the more homogeneous and intense enhancement of the nasal turbinates, which is typical of pediatric patients. C, A 36-year-old woman shows relatively homogeneous enhancement, but it is less intense than that in the pediatric patient, and there are a few small nonenhancing dots (arrows).

**Table 8: Imaging features of benign BT in immunocompetent patients compared with those of invasive fungal rhinosinusitis in immunocompromised patients**

	Incidental BT in Immunocompetent Patients	Patients with IFRS
Enhancement pattern	Nonenhancing centrally with smooth, thin peripheral enhancement, likely normal mucosal enhancement	Infiltrative nonenhancement extending into adjacent structures, without smooth, thin enhancing margin
T2 characteristic	Intermediate to hyperintense, but not hypointense	Variable: hypointense, intermediate, or hyperintense
Internal feature	Faint septa or confluent dots	Confluent nonenhancement
Most common location for BT	Posterior and midportions of inferior turbinate	Middle turbinate
NE confined to turbinate?	Yes	No
Temporal feature	Increased enhancement with time	Persistent nonenhancement

or seen in our case of IFRS. Choi et al<sup>4</sup> stated that in patients with IFRS, “Although LoCE (Lack of Contrast Enhancement) showed variable signal intensity (SI), homogeneously or heterogeneously enhancing lesions showed exclusively low SI (100%, 12/12) on T2WI.” Seo et al,<sup>3</sup> in their review of 23 patients with IFRS, found 17 patients who had nonenhancing areas in the sinonasal region (13 with extension into adjacent structures), and the signal intensity on the T2WI was variable, with most being hyperintense and many also having areas of iso- or hypointensity compared with the brain cortex.<sup>3</sup> Therefore, there is no consistent signal intensity on the T2WI suggesting the diagnosis of IFRS when an NE turbinate is encountered in high-risk patients. Conversely, low signal intensity on T2WI was not seen in any of our patients with benign BTs.

Diffusion-weighted imaging may have little utility and is only mentioned by the authors of several series in the literature, and not necessarily with respect to the nasal turbinates.<sup>2,4</sup> Safder et al<sup>2</sup> described restricted diffusion in 2 cases; however, Choi et al<sup>4</sup> described facilitated diffusion in 2 of their cases. Choi et al also

felt that the NE areas were due to coagulation necrosis rather than infarction, therefore explaining this imaging finding.

The most frequent locations of NE turbinates in IFRS are also different from the distribution of benign BTs. Gillespie et al,<sup>13</sup> in their retrospective study of 25 patients with IFRS, found that the most common site of involvement was the middle turbinate (62% of biopsied patients). Their hypothesis was that the middle turbinate filters the major volume of the nasal airflow and might have contributed to the predilection for fungal seeding in this region.

Compared with a true pathologic turbinate NE pattern in patients with IFRS, the NE turbinates in immunocompetent patients have the features summarized in Table 8. Overall, improving NE turbinates through the course of a scan with preserved peripheral (likely normal mucosal) enhancement and thin septa are the key features to differentiate benign BT from IFRS, which will more likely demonstrate persistent NE in affected turbinates; the NE of IFRS may extend into adjacent structures rather than having well-defined thin peripheral enhancement.

However, this comparison is itself limited by the relative rarity of cases of true pathologic turbinate NE both in the literature<sup>1-7</sup> and in daily practice.

There are several additional limitations to our study. We had a relatively small number of pediatric patients. In

both the fat-saturation and brain groups, the number of pediatric patients was significantly less than for the adult patients (Table 6). However, within the brain group, there was a statistically significant difference in the number of pediatric patients compared with adult patients demonstrating BTs (Table 7). While this could represent a true difference, we suspect it is due to the small pediatric sample size. Further investigation might be needed to definitively explain this finding and to better evaluate the pediatric population overall.

Additionally, the variable length of the sequences and the different protocols and scanners used could potentially affect the valuation of the temporal pattern of enhancement. However, we would suggest that similar scanner and protocol variability are present in many large practices and academic institutions, so this mix approximates the everyday scan variability that many radiologists will encounter.

Last, there was no pathologic proof of benignity of the BTs in our immunocompetent patients; however, evidence obtained from the patients’ electronic medical records supported this presumption.

## CONCLUSIONS

Although a sign suggesting IFRS in the appropriate clinical setting, areas of NE within the nasal turbinates are common on both MR imaging with or without fat saturation in immunocompetent patients who have little chance of having IFRS. This benign NE will improve over subsequent series, have preserved thin peripheral enhancement, and will often have thin internal septa. Knowledge of the normal patterns of nasal turbinate enhancement can help radiologists better differentiate findings suggestive of IFRS from normal variations and lead to a higher positive predictive value of the BT sign.

## REFERENCES

1. Nunes DM, Rocha AJ, Rosa Júnior M, et al. **“Black turbinate sign”: a potential predictor of mucormycosis in cavernous sinus thrombophlebitis.** *Arq Neuropsiquiatr* 2012;70:78 CrossRef Medline
2. Safder S, Carpenter JS, Roberts TD, et al. **The “Black Turbinate” sign: an early MR imaging finding of nasal mucormycosis.** *AJNR Am J Neuroradiol* 2010;31:771–74 CrossRef Medline
3. Seo J, Kim HJ, Chung SK, et al. **Cervicofacial tissue infarction in patients with acute invasive fungal sinusitis: prevalence and characteristic MR imaging findings.** *Neuroradiology* 2013;55:467–73 CrossRef Medline
4. Choi YR, Kim JH, Min HS, et al. **Acute invasive fungal rhinosinusitis: MR imaging features and their impact on prognosis.** *Neuroradiology* 2018;60:715–23 CrossRef Medline
5. Bae MS, Kim EJ, Lee KM, et al. **Rapidly progressive rhino-orbito-cerebral mucormycosis complicated with unilateral internal carotid artery occlusion: a case report.** *Neurointervention* 2012;7:45–49 CrossRef Medline
6. Monroe MM, McLean M, Sautter N, et al. **Invasive fungal rhinosinusitis: a 15-year experience with 29 patients.** *Laryngoscope* 2013;123:1583–87 CrossRef Medline
7. Groppo ER, El-Sayed IH, Aiken AH, et al. **Computed tomography and magnetic resonance imaging characteristics of acute invasive fungal sinusitis.** *Arch Otolaryngol Head Neck Surg* 2011;137:1005–10 CrossRef Medline
8. Som PM, Lawson W, Fatterpekar GM, et al. **Embryology, anatomy, physiology, and imaging of the sinonasal cavities.** In: Som PM, Curtin HD, eds. *Head and Neck Imaging*. 5th ed. St. Louis: Mosby; 2011:116–17
9. Osborn AG. **The nasal arteries.** *AJR Am J Roentgenol* 1978;130:89–97 CrossRef Medline
10. Strandling S. **Nose, nasal cavity and paranasal sinuses.** In: Birch R, Collins P, Gray H, et al, eds. *Gray’s Anatomy: The Anatomical Basis of Clinical Practice*. 2015. Philadelphia: Elsevier Limited; 2016:556–70
11. Widdicombe, J. **Microvascular anatomy of the nose.** *Allergy* 1997; 52(40 Suppl):7–11
12. Ng BA, Ramsey RG, Corey JP. **The distribution of nasal erectile mucosa as visualized by magnetic resonance imaging.** *Ear Nose Throat J* 1999;78:159, 163–66 Medline
13. Gillespie MB, O’Malley BW Jr, Francis HW. **An approach to fulminant invasive fungal rhinosinusitis in the immunocompromised host.** *Arch Otolaryngol Head Neck Surg* 1998;124:520–26 CrossRef Medline

# Neuroimaging Findings in Moebius Sequence

 D.A. Herrera,  N.O. Ruge,  M.M. Florez,  S.A. Vargas,  M. Ochoa-Escudero, and  M. Castillo

## ABSTRACT

**BACKGROUND AND PURPOSE:** Moebius sequence comprises a spectrum of brain congenital malformations predominantly affecting the function of multiple cranial nerves. Reported neuroimaging findings are heterogeneous and based on case reports or small case series. Our goal was to describe the neuroimaging findings of Moebius sequence in a large population of patients scanned with MR imaging.

**MATERIALS AND METHODS:** An observational cross-sectional study was performed to assess brain MR imaging findings in 38 patients with Moebius syndrome studied between 2013 and 2016.

**RESULTS:** Retrospective analysis of MR imaging studies showed flattening of the floor of the fourth ventricle floor secondary to a bilateral absent facial colliculus in 38 patients (100%) and unilateral absence in 1. A hypoplastic pons was found in 23 patients (60.5%). Mesencephalic malformations consisted of tectal beaking in 15 patients (39.5%) and increased anteroposterior midbrain diameter with a shallow interpeduncular cistern in 12 (31.6%). Infratentorial arachnoid cysts were found in 5 patients (13.2%), and cerebellar vermis hypoplasia, in 2 (5.3%). Supratentorial findings included the following: thalamic fusion (26.3%), periventricular nodular heterotopias (26.3%), ventriculomegaly (26.3%), callosal abnormalities (23.7%), and hippocampal malrotations (23.7%).

**CONCLUSIONS:** Findings seen in this large patient cohort agreed with previously published reports. Flattening of the fourth ventricle floor secondary to a bilaterally absent facial colliculus was the most frequent MR imaging finding. The presence of other brain stem and cerebellar malformations as well as supratentorial abnormalities may help explain clinical symptoms and achieve a correct diagnosis.

Moebius sequence comprises a spectrum of congenital malformations that mainly affect the function of cranial nerves.<sup>1</sup> The estimated incidence of Moebius sequence is 1:250,000 live births with no sex differences.<sup>2</sup> This syndrome is clinically characterized by unilateral or bilateral congenital facial paralysis and the failure of ocular abduction with esotropia due to cranial nerve VI palsy.<sup>3,4</sup> Because of the predominant involvement of the cranial nerves, Moebius sequence has been classified as forming part of malformations of the midbrain and rhombencephalon.<sup>5</sup> Both genetic and nongenetic factors are believed to be important for the development of Moebius sequence.<sup>6</sup> Currently, the most accepted etiology of this syndrome is hypoxic-ischemic injury to the brain stem during development, which is supported by histo-

pathologic evaluation of postmortem Moebius sequence brains with evidence of focal necrosis with areas of gliosis and calcification in vascular territories of the brain stem.<sup>7</sup>

Moebius sequence diagnosis is based on clinical criteria after exclusion of similar syndromes such as congenital fibrosis of the extraocular muscles in which there is severe congenital strabismus, ptosis, and vertical gaze palsy.<sup>8,9</sup> MR imaging is helpful to exclude Moebius sequence mimickers and can be useful to confirm the diagnosis. Neuroimaging findings in Moebius sequence have been reported previously. However, reported findings are heterogeneous and based on case reports or small case series.<sup>9-13</sup> Consequently, our goal was to describe the neuroimaging findings of Moebius sequence in a large group of patients.

## MATERIALS AND METHODS

Institutional review board (Universidad de Antioquia) approval was obtained for this retrospective study. Between August 2013 and November 2016, a total of 43 patients with the clinical diagnosis of Moebius syndrome were studied with multiplanar non-contrast MR imaging, which included routine imaging sequences. Four patients with partial or complete fusion of the basal ganglia were excluded because a mutation in Tubulin-related genes could

Received December 7, 2018; accepted after revision March 12, 2019.

From the Department of Radiology (D.A.H., M.M.F., S.A.V.) and Grupo de Neurociencias (N.O.R.), Universidad de Antioquia, Medellín, Colombia; Department of Radiology (M.O.-E.), Hospital Pablo Tobón Uribe, Medellín, Colombia; and Department of Radiology (M.C.), University of North Carolina, Chapel Hill, North Carolina.

Please address correspondence to Diego A. Herrera, MD, Department of Radiology, Universidad de Antioquia UdeA, Calle 32D # 80B - 34, Medellín, Colombia 050030; e-mail: herrera.diego@gmail.com

<http://dx.doi.org/10.3174/ajnr.A6028>

not be ruled out. Another patient with neuroimaging features of pontine tegmental cap dysplasia was eliminated from the analysis as well. There were 24 males (63.2%) and 14 females (36.8%) with an average age of 4.1 years (range, 1 month to 25 years). MR imaging studies were independently reviewed by 2 neuroradiologists and 1 neuroradiology fellow. Conflicts among reviewer assessments were resolved by consensus. We analyzed the shape and size of the fourth ventricle, vermis, cerebellum, and cisterns. For the brain stem, we measured the length of the pons and midbrain and assumed that normal was when the former was at least twice the length of the latter. In the supratentorial region, we studied the corpus callosum, gray matter distribution (including the appearance of the basal ganglia), ventricular shape and size, hippocampal shape and size, and subarachnoid spaces.

Means and ranges were calculated for continuous variables. Descriptive statistics with the number of patients and percentages were used for results presentation. All analyses were performed using the software SPSS, Version 26 (IBM, Armonk, New York).

## RESULTS

### Infratentorial Findings

Flattening of the fourth ventricle floor secondary to an absent bilateral facial colliculus was present in 38 patients (100%). A hypoplastic pons was found in 23 patients (60.5%). Mesen-

#### Neuroimaging findings in 38 patients with Moebius sequence

Finding	No. (%)
Flattening of the floor of the fourth ventricle due to bilateral absence of facial colliculus	38 (100%)
Pons hypoplasia	23 (60.5%)
Tectal beaking	15 (39.5%)
Increased anteroposterior diameter of the mesencephalon	12 (31.6%)
Thalamic fusion	10 (26.3%)
Periventricular nodular heterotopia	10 (26.3%)
Middle cranial fossa arachnoid cysts	10 (26.3%)
Ventriculomegaly without obstructive hydrocephalus	10 (26.3%)
Dysplastic corpus callosum	9 (23.7%)
Hippocampal malrotation	9 (23.7%)
Infratentorial arachnoid cysts	5 (13.2%)
Frontal horn prominence	5 (13.2%)
Cerebellar vermis hypoplasia	2 (5.3%)
Mesencephalic aqueduct stenosis with hydrocephalus	2 (5.3%)

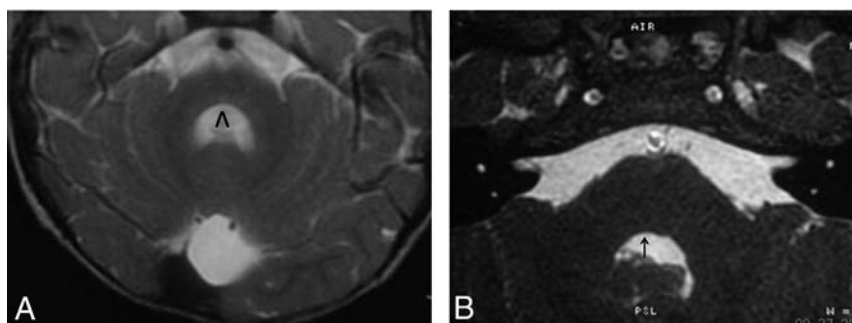


**FIG 1.** A, Axial T2-weighted image shows bilateral absence of the facial colliculus in the pontine tegmentum with a central depression of the dorsal brain stem. The fourth ventricle has a horseshoe or V shape (inverted V). Pons hypoplasia and a small retrocerebellar cyst are observed. B, A different patient shows absence of only the right facial colliculus (black arrow).

cephalic malformations consisted of tectal beaking in 15 patients (39.5%) and increased anteroposterior midbrain diameter with a shallow interpeduncular cistern, in 12 patients (31.6%). Infratentorial arachnoid cysts were found in 5 (13.2%), and cerebellar vermis hypoplasia, in 2 (5.3%).

### Supratentorial Findings

Fusion of the thalami was found in 10 patients (26.3%). Periventricular nodular heterotopia was found in 10 subjects (26.3%). Corpus callosum abnormalities were present in 9 patients (23.7%). Hippocampal malrotations were observed in 9 individuals (23.7%). Middle cranial fossa arachnoid cysts were present in 10 patients (26.3%). Ventriculomegaly without imaging criteria for obstructive hydrocephalus was observed in 10 patients (26.3%), and of these, 5 (13.2%) had mostly dilation of the frontal horns. Two patients (5.3%) had hydrocephalus secondary to stenosis of the cerebral aqueduct.

Above-mentioned neuroimaging findings are described in the Table and Figs 1–4.

## DISCUSSION

Moebius sequence refers to malformations arising during development of the mesencephalon-rhombencephalon and is classified within the group of early defects of the dorsoventral pattern.<sup>5</sup> The term “sequence” is preferred to “syndrome” because it defines a cascade of secondary events after an initial insult during the embryonic period.<sup>6</sup> In histopathologic studies of patients affected by Moebius sequence, the main abnormality is found in the pontine tegmentum where the nuclei for cranial nerve VI are located and the intra-axial fibers of the seventh cranial nerve are crossing posterior to these nuclei (the facial colliculus).<sup>14</sup>

Brain stem ischemia during embryogenesis is the most accepted cause of Moebius sequence. Distribution of branches of the embryonic basilar artery makes the dorsomedial aspect of the brain stem vulnerable to hypoxic-ischemic injury.<sup>15</sup> This feature probably explains why hemorrhage and uterine contractions produced by misoprostol have been associated with Moebius sequence.<sup>14</sup> Concerning the genetic etiology of Moebius sequence, 2 different loci at 3q21-q22 and 10q have been reported. Additionally, de novo mutations have also been reported affecting the *PLXND1* and *REV3L* genes. These result in a defect in facial branchiomotor neuron migration, supporting these genes as causative

for at least a portion of Moebius sequence cases.<sup>6</sup> Clinically, patients have unilateral or bilateral congenital facial paralysis and esotropia with preservation of the vertical gaze.

Known brain MR imaging findings in Moebius sequence are based on small case series. The present study includes the largest number of patients reported to date. In our series, the most frequent finding was bilateral absence of the facial colliculus in the pontine tegmentum with flattening of the floor of the fourth ventricle (100%). In axial images, patients showed depression of the floor of the fourth ventricle leading to a V or horse-

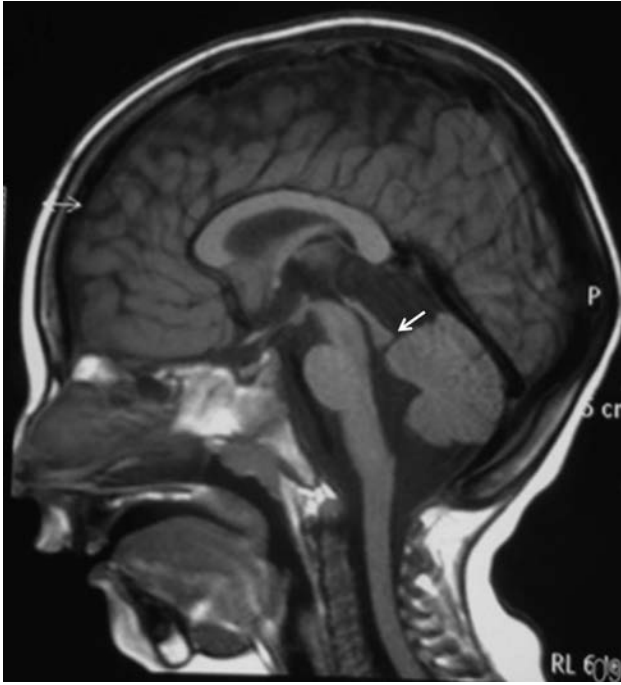


**FIG 2.** Sagittal T1-weighted image demonstrates a scalloped floor of the fourth ventricle, pontine hypoplasia (pontomesencephalic ratio,  $<2$ ), tectal beaking with fusion of the inferior colliculi (*white arrow*), a quadrigeminal arachnoid cyst, and micrognathia. We cannot exclude an abnormal tectum related to mechanical compression by the cyst rather than a malformation by itself.

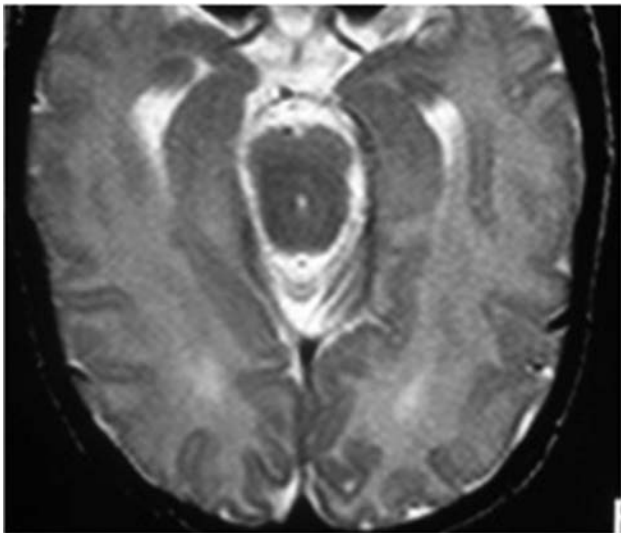


**FIG 3.** Axial T2-weighted image shows an increase in the anteroposterior diameter of the mesencephalon, fusion of the quadrigeminal inferior colliculi, a very shallow interpeduncular cistern, and ventriculomegaly.

shoe shape, a finding that agrees with reports from other authors (Fig 1).<sup>10,11,16</sup> One of our patients had unilateral absence of the facial colliculus, and this correlated with the clinical manifestation of unilateral facial paralysis.

The second most frequent finding was pons hypoplasia (60.5%), which, for the purpose of this study, was defined as a pontomesencephalic ratio of  $<2$  (craniocaudal pons length/craniocaudal midbrain length) (Fig 2). Pons and brain stem hyp-

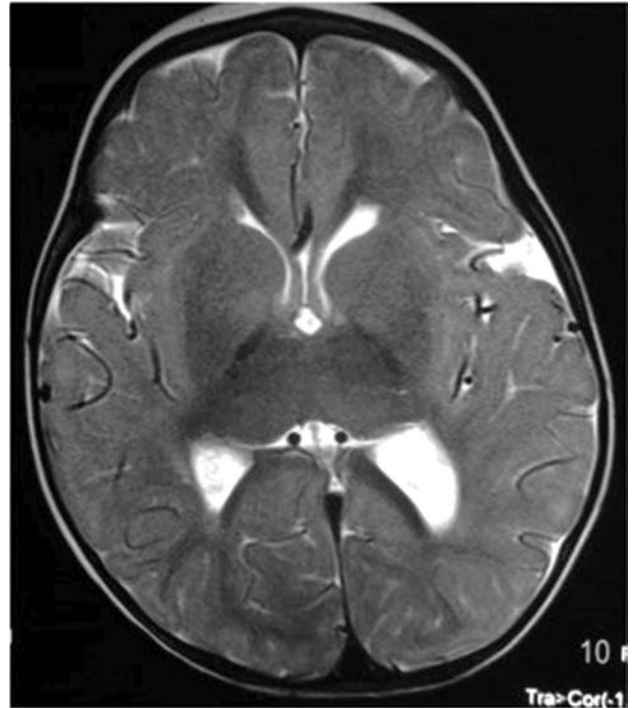


**FIG 4.** T2-weighted axial image shows thalamic fusion. Small frontal periventricular nodular heterotopias and mild ventriculomegaly are also present.

oplasia have been also described by other authors.<sup>10,12,13,17</sup> Tectal beaking was present in 39.5% of patients (Fig 2). This finding has only been previously reported in 1 patient and thus is more common than previously believed.<sup>12</sup>

In almost one-third of our patients, we observed a subjective increase in the anteroposterior diameter of the mesencephalon, similar to that described in the previously mentioned case report (Fig 3).<sup>12</sup> We speculate that this finding may be caused by fusion of the inferior mesencephalic tectum colliculus. Its association with a decrease in the amplitude of the interpeduncular cistern remains difficult to explain.

Dysplasia of the corpus callosum and ventriculomegaly were seen with a frequency of 23.7% and 26.3%, respectively. Ventriculomegaly in our study was a less frequent finding than reported by Matsui et al.<sup>17</sup> In that publication, 6 of 10 patients showed ventriculomegaly and 3 exhibited prominence of the frontal horns of the lateral ventricles. We found prominence of the frontal horns of the lateral ventricles in 5 (13.2%), and although we did not measure tissue volume, this finding could be explained by white matter volume loss.

Fusion of the thalami was present in 10 patients (26.3%) (Fig 4). This finding was previously described by Pirmez et al<sup>16</sup> in an isolated case. These authors found that partial fusion of the thalami was associated with agenesis of the septum pellucidum and frontal horns of the lateral ventricles, concluding that it represented a mild form of lobar holoprosencephaly in association with Moebius sequence. In our study, 1 patient who showed thalamic fusion also had agenesis of the septum pellucidum, but the findings did not fall into the spectrum of holoprosencephaly.

Arachnoid cysts are common in the general population and represent up to 1% of intracranial masses.<sup>18</sup> However, in our series,

middle cranial fossa and infratentorial arachnoid cysts were observed more frequently in 26.3% and 13.2% of patients with Moebius sequence, respectively. Although the pathogenesis of arachnoid cysts has not been completely elucidated, it has been hypothesized that they could be secondary to an early defect in fetal development coinciding with the appearance of the Moebius sequence.<sup>19</sup>

Isolated periventricular nodular heterotopia was observed in 26.3% of patients. These malformations of cortical development are the result of arrested neuronal migration. Clinically, patients with these sporadic malformations do not have major intellectual disabilities, and seizures may not appear until the second or third decade of life.<sup>20</sup> Our patients with periventricular nodular heterotopia did not have seizures, but because they are young, seizures may occur later in life.

The differential diagnosis of Moebius sequence includes the congenital cranial dysinnervation disorders. In these disorders, MR imaging can show diverse findings such as the absence of the abducens nerve on the affected side in Duane syndrome (related to mutations in *CHN1* or *SALL4* genes) or extraocular muscle volume loss in congenital fibrosis of the extraocular muscles (mutations in *KIF21A*, *PHOX2A*, and *TUBB3* genes).<sup>21</sup> In our series, we excluded 4 patients with cranial nerve VI and VII palsies because brain MR imaging showed fusion of basal ganglia due to dysgenesis of the anterior arm of the internal capsules, which is a characteristic finding described in the spectrum of tubulinopathies resulting from an abnormal axonal navigation/orientation caused by a mutation in the Tubulin genes.<sup>22</sup> Tubulinopathies could not be excluded in those patients because they were not genetically tested; thus, we did not include patients with dysmorphic basal ganglia in this analysis. Last, another condition that should be considered in the differential diagnosis of Moebius sequence is pontine tegmental cap dysplasia (we also excluded another patient with that disorder from the study after analyzing the MR imaging). In this malformation, neuroimaging shows pons hypoplasia associated with tegmental prominence projected into the fourth ventricle (tegmental “cap”) and middle cerebellar peduncle hypoplasia.<sup>23</sup> This malformation can be related to deficiencies of multiple cranial nerves and reorganization of white matter tracts.<sup>3</sup>

Our study has limitations: mainly its retrospective nature, nonquantitative nature, and the absence of a single researcher-defined protocol for imaging acquisition. Nevertheless, because of the relatively large (largest to date) number of patients, we believe our series is unique and important to report.

## CONCLUSIONS

Findings seen in this large patient cohort agreed with previously published reports. Flattening of the fourth ventricle floor secondary to a bilaterally absent facial colliculus was the most frequent MR imaging finding. The presence of other brain stem and cerebellar malformations as well as supratentorial abnormalities may help explain clinical symptoms and achieve a correct diagnosis.

## REFERENCES

- Abramson DL, Cohen MM Jr, Mulliken JB. **Mobius syndrome: classification and grading system.** *Plast Reconstr Surg* 1998;102:961–67 CrossRef Medline
- Picciolini O, Porro M, Cattaneo E, et al. **Moebius syndrome: clinical features, diagnosis, management and early intervention.** *Ital J Pediatr* 2016;42:56 CrossRef Medline
- Ouanounou S, Saigal G, Birchansky S. **Möbius syndrome.** *AJNR Am J Neuroradiol* 2005;26:430–32 Medline
- Budić I, Šurdilović D, Slavković A, et al. **Moebius syndrome: challenges of airway management.** *Acta Clin Croat* 2016;55(Suppl 1):94–97 Medline
- Jissendi-Tchofo P, Severino M, Nguema-Edzang B, et al. **Update on neuroimaging phenotypes of mid-hindbrain malformations.** *Neuroradiology* 2015;57:113–38 CrossRef Medline
- Pedersen LK, Maimburg RD, Hertz JM, et al. **Moebius sequence: a multidisciplinary clinical approach.** *Orphanet J Rare Dis* 2017;12:4 CrossRef Medline
- St Charles S, DiMario FJ Jr, Grunnet ML. **Möbius sequence: further in vivo support for the subclavian artery supply disruption sequence.** *Am J Med Genet* 1993;47:289–93 CrossRef Medline
- Whitman M, Hunter DG, Engle EC. **Congenital fibrosis of the extraocular muscles.** In: Adam MP, Ardinger HH, Pagon RA, et al, eds. *GeneReviews*® [Internet]. Seattle (WA): University of Washington, Seattle; 1993–2019
- McKay VH, Touil LL, Jenkins D, et al. **Managing the child with a diagnosis of Moebius syndrome: more than meets the eye.** *Arch Dis Child* 2016;101:843–46 CrossRef Medline
- Fons-Estupiñá MC, Póo P, Colomer J, et al. **Moebius sequence: clinico-radiological findings** [in Spanish]. *Rev Neurol* 2007;44:583–88 Medline
- Pedraza S, Gámez J, Rovira A, et al. **MRI findings in Möbius syndrome: correlation with clinical features.** *Neurology* 2000;55:1058–60 CrossRef Medline
- Lengyel D, Zaunbauer W, Keller E, et al. **Möbius syndrome: MRI findings in three cases.** *J Pediatr Ophthalmol Strabismus* 2000;37:305–08 Medline
- Verzijl HT, Valk J, De Vries R, et al. **Radiologic evidence for absence of the facial nerve in Möbius syndrome.** *Neurology* 2005;64:849–55 CrossRef Medline
- Marques-Dias MJ, Gonzalez CH, Rosemberg S. **Möbius sequence in children exposed in utero to misoprostol: neuropathological study of three cases.** *Birth Defects Res A Clin Mol Teratol* 2003;67:1002–07 CrossRef Medline
- Sarnat HB. **Watershed infarcts in the fetal and neonatal brainstem: an aetiology of central hypoventilation, dysphagia, Möbius syndrome and micrognathia.** *Eur J Paediatr Neurol* 2004;8:71–87 CrossRef Medline
- Pirmez R, Freitas ME, Gasparetto EL, et al. **Moebius syndrome and holoprosencephaly following exposure to misoprostol.** *Pediatr Neurol* 2010;43:371–73 CrossRef Medline
- Matsui K, Kataoka A, Yamamoto A, et al. **Clinical characteristics and outcomes of Möbius syndrome in a children’s hospital.** *Pediatr Neurol* 2014;51:781–89 CrossRef Medline
- Osborn AG, Preece MT. **Intracranial cysts: radiologic-pathologic correlation and imaging approach.** *Radiology* 2006;239:650–64 CrossRef Medline
- Conde Sardón R. **Arachnoid cysts: historical evolution of the concept and pathophysiological theories** [in Spanish]. *Neurocirugia (Astur)* 2015;26:192–95 CrossRef Medline
- Leventer RJ, Guerrini R, Dobyns WB. **Malformations of cortical development and epilepsy.** *Dialogues Clin Neurosci* 2008;10:47–62 Medline
- Gutowski NJ, Chilton JK. **The congenital cranial dysinnervation disorders.** *Arch Dis Child* 2015;100:678–81 CrossRef Medline
- Bahi-Buisson N, Poirier K, Fourniol F, et al. **The wide spectrum of tubulinopathies: what are the key features for the diagnosis?** *Brain* 2014;137:1676–700 CrossRef Medline
- Barth PG, Majoie CB, Caan MW, et al. **Pontine tegmental cap dysplasia: a novel brain malformation with a defect in axonal guidance.** *Brain* 2007;130:2258–66 CrossRef Medline

# Comparison of Iterative Model Reconstruction versus Filtered Back-Projection in Pediatric Emergency Head CT: Dose, Image Quality, and Image-Reconstruction Times

R.N. Southard, D.M.E. Bardo, M.H. Temkit, M.A. Thorkelson, R.A. Augustyn, and C.A. Martinot

## ABSTRACT

**BACKGROUND AND PURPOSE:** Noncontrast CT of the head is the initial imaging test for traumatic brain injury, stroke, or suspected nonaccidental trauma. Low-dose head CT protocols using filtered back-projection are susceptible to increased noise and decreased image quality. Iterative reconstruction noise suppression allows the use of lower-dose techniques with maintained image quality. We review our experience with children undergoing emergency head CT examinations reconstructed using knowledge-based iterative model reconstruction versus standard filtered back-projection, comparing reconstruction times, radiation dose, and objective and subjective image quality.

**MATERIALS AND METHODS:** This was a retrospective study comparing 173 children scanned using standard age-based noncontrast head CT protocols reconstructed with filtered back-projection with 190 children scanned using low-dose protocols reconstructed with iterative model reconstruction. ROIs placed on the frontal white matter and thalamus yielded signal-to-noise and contrast-to-noise ratios. Volume CT dose index and study reconstruction times were recorded. Random subgroups of patients were selected for subjective image-quality review.

**RESULTS:** The volume CT dose index was significantly reduced in studies reconstructed with iterative model reconstruction compared with filtered back-projection, (mean,  $24.4 \pm 3.1$  mGy versus  $31.1 \pm 6.0$  mGy,  $P < .001$ ), while the SNR and contrast-to-noise ratios improved 2-fold ( $P < .001$ ). Radiologists graded iterative model reconstruction images as superior to filtered back-projection images for gray-white matter differentiation and anatomic detail ( $P < .001$ ). The average reconstruction time of the filtered back-projection studies was 101 seconds, and with iterative model reconstruction, it was 147 seconds ( $P < .001$ ), without a practical effect on work flow.

**CONCLUSIONS:** In children referred for emergency noncontrast head CT, optimized low-dose protocols with iterative model reconstruction allowed us to significantly reduce the relative dose, on average, 22% compared with filtered back-projection, with significantly improved objective and subjective image quality.

**ABBREVIATIONS:** ASIR = adaptive statistical iterative reconstruction; CNR = contrast-to-noise ratio; CTDI<sub>vol</sub> = volume CT dose index; FBP = filtered back-projection; IMR = iterative model reconstruction; MBIR = model-based iterative reconstruction; IR = iterative reconstruction

Children younger than 18 years of age constitute approximately one-fifth of the 130 million annual visits to hospital-affiliated emergency departments in the United States.<sup>1</sup> Trauma is a leading cause of morbidity and mortality in children older than

1 year, with head trauma representing nearly 80% of these injuries. Noncontrast head CT is often the first-line study for evaluation of traumatic brain injury or suspected nonaccidental trauma in children.<sup>2</sup> Various dose-reduction strategies are used by vendors and radiologists to reduce CT radiation exposure in children.<sup>3,4</sup> Minimizing radiation exposure while maintaining image quality of brain CT is challenging because low-contrast lesion detectability, detection of subtle bleeds, and anatomic detail, especially in the posterior fossa, may be affected by noise, artifacts, and reduced contrast-to-noise ratio (CNR) that accompanies lower-dose techniques.<sup>5</sup> The use of lower-dose techniques by lowering the tube voltage or current, with filtered back image reconstruction, is susceptible to increased image noise, decreased spatial resolution, and low-contrast lesion detectability and overall reduced reader confidence.

Received October 15, 2018; accepted after revision February 27, 2019.

From the Departments of Medical Imaging (R.N.S., D.M.E.B., M.A.T., R.A.A., C.A.M.) and Clinical Research (M.H.T.), Phoenix Children's Hospital, Phoenix, Arizona.

Paper previously presented at: Society for Pediatric Radiology Annual Meeting and Postgraduate Course, May 15–19, 2018; Nashville, Tennessee.

Abstract reuse permission from Springer Nature/RightLink license No. 4366020744406, obtained June 11, 2018.

Please address correspondence to Richard N. Southard, MD, Vice Chair of Clinical Operations, Director of CT and Cardiac Imaging, Department of Medical Imaging, Phoenix Children's Hospital, 1919 East Thomas Rd, Main Tower/Radiology, Phoenix, AZ 85016; e-mail: rsouthard@phoenixchildrens.com

<http://dx.doi.org/10.3174/ajnr.A6034>

Image reconstruction with iterative reconstruction (IR) uncouples noise reduction and spatial resolution and allows the use of lower-dose techniques with maintained image quality.<sup>6,7</sup> There are different types of iterative reconstructions: those that denoise image domain space alone; those that denoise in both projection and image space; and pure, systems- or model-based iterative reconstruction (MBIR), which takes into consideration all aspects of the imaging chain including system optics and, by virtue of complex computational algorithms used, has longer reconstruction times, which may prevent its use in the emergency setting. Overuse of noise-suppression strength may also result in an undesirable overly smooth image texture with loss of anatomic edge detail presumably due to a shift in spatial frequency distribution of image noise. We review our experience with children undergoing emergency head CT examinations reconstructed using knowledge-based iterative model reconstruction (IMR; Philips Healthcare, Best, the Netherlands) versus standard filtered back-projection (FBP) reconstruction, comparing reconstruction times, radiation dose, and objective and subjective image quality.

## MATERIALS AND METHODS

### Design

This institutional review board–approved and Health Insurance Portability and Accountability Act–compliant retrospective review compared 400 nonrandomized consecutive patients referred from the emergency department for urgent head CT examinations between January and March 2016 performed using either standard age-based protocols and FBP image reconstruction or reduced-dose age-based protocols and IMR. The institutional review board waived the need for patient consent.

### Patient Groups

All children referred from the emergency department for urgent head CT without contrast + 3D reconstruction (Current Procedural Terminology: 70450/76376) in 2016 were identified in our image data base. The first 200 consecutive patients imaged on the 64-slice multidetector row CT scanner situated in the emergency department with FBP image reconstruction, and the first 200 consecutive patients imaged on the 256-slice multidetector row CT scanner in the main department with image reconstruction using IMR were eligible. Excluded were patients with repeat studies, marked motion, and multiple implanted metallic leads or when the incorrect age-based CT protocol was used. Patient age (months) and sex were recorded for each subject.

### Data Acquisition and Reconstruction

We used 4 age-based protocols for unenhanced CT head examinations: younger than 1.5 years, 1.5–6 years, 7–12 years, and older than 13 years. Image-acquisition parameters of the standard-dose studies performed on the emergency department scanner (Brilliance 64-Slice; Philips Healthcare) included a collimation of  $64 \times 0.625$  mm, pitch of 0.64, rotation time of 0.5 seconds, tube voltage of 120 kV, and tube currents corresponding to the 4 age-based protocols of 200, 225, 300, or 350 mAs. Scan parameters for the low-dose studies performed on the main department scanner (Brilliance iCT 256-Slice; Philips Healthcare) included collimation of  $64 \times 0.625$  mm, with a pitch of 0.39, rotation time of 0.4

seconds, and age-dependent tube currents of 160, 168, 200, or 210 mAs. The FBP standard-dose examinations were reconstructed with a UB (soft) convolution kernel, section-thickness of 3 mm with 3-mm increments, and high resolution, and the IR low-dose examinations were reconstructed with a mild noise-reduction IMR<sub>BRAIN 1</sub> routine convolution kernel, a section-thickness of 3 mm with 3-mm increments, and high resolution.

Both scanners were surveyed and tested by a certified medical CT physicist in accordance with the American College of Radiology CT Accreditation Program as part of our routine departmental quality-assurance program. Comparison of the calculated clinical examination dose estimate and the measured volume CT dose index (CTDI<sub>vol</sub>) reported by the scanner yielded a percentage difference of 11.86% for pediatric head (1 year of age) and 2.48% for adult head CT protocols on the iCT 256-Slice multidetector row CT scanner, and 0.80% and 2.60% on the Brilliance 64-Slice multidetector row CT scanner.

### Radiation Dose Measurement

The estimated radiation dose CTDI<sub>vol</sub> was recorded for each study.

### Reconstruction Time

Reconstruction times were determined by recording the millisecond image-creation times for the first image and the last image reconstructed for each examination, as obtained from the information tile available for each individual image on the PACS workstation.

### Quantitative Analysis

All images were viewed on a dedicated PACS on a calibrated dedicated diagnostic workstation in our department. For each study, a single representative image at the level of the lateral ventricles was selected to include both the thalamus and frontal white matter, and 1 radiologist with 25 years' experience who was not involved in the blinded subjective image-quality review placed equal ROIs measuring between 6 and 9 mm on the right thalamus deep gray matter and right frontal white matter to maintain uniformity. Measurements of mean CT density (Hounsfield unit) and SD yielded the signal-to-noise ratio for the white matter and thalamus (SNR<sub>White Matter</sub> and SNR<sub>Thalamus</sub>) using the formula  $SNR = HU / SD$ , and CNR using the formula  $CNR = (HU_{Thalamus} - HU_{White Matter}) / [(SD_{Thalamus} + SD_{White Matter}) / 2]$ .

### Qualitative Analysis

Subjective image quality was assessed by selecting a randomized de-identified age-group-matched subgroup from both the FBP and IR groups using a random number generator (<http://www.randomnumbergenerator.com/>) ( $n = 40$ ; power index,  $>80\%$ ). Qualitative analysis of the 3-mm images was independently performed by 2 board-certified, subspecialty-certified neuroradiology attending radiologists with 16 and 17 years' experience, and scores were reported assessing gray-white matter differentiation and anatomic detail using a 5-point scale of 1, poor; 2, fair; 3, average; 4, good; and 5, excellent. Reviewers were blinded to the scanner, scan parameters, reconstruction settings, and slice thickness.

## Statistical Analysis

Group comparisons were conducted using 2 independent-samples equal variances *t* tests for continuous variables and the  $\chi^2$  test for categorical variables. The Pearson correlation coefficient and the resulting *P* value for statistical significance were determined, with the significance level at *P* < .05. Subjective image-quality scores were combined as an average for each patient, and the intraclass correlation coefficient and correlation coefficient for the individual physician grades were calculated. Power and sample-size calculations for subjective image-quality scoring using a 2-group independent-samples *t* test were used to determine the required number of subjects needed to detect a mean difference of 1.0 between FBP and IR. The power calculations were conducted using the procedure Proc Power available in the SAS statistical software. Statistical analyses were performed using SAS 9.4 (SAS Institute, Cary North Carolina) and R Studio, Version 1.0.153 (<http://rstudio.org/download/desktop>).

## RESULTS

### Patient Groups

A total of 363 patients were enrolled in the study; 173 patients with a mean age of  $76.3 \pm 73.8$  months were imaged with standard dose protocols with FBP reconstruction, and 190 patients with a mean age  $67.6 \pm 67.9$  months were imaged with low-dose protocols with IR reconstruction. Thirty-seven patients were excluded due to excessive motion, multiple implanted leads, or incorrect protocol. Age group and age were not significantly different (Table 1), and although sex difference did not achieve statistical significance, approximately two-thirds of the patients were male.

### Radiation Dose

The use of IMR reconstructions allowed diagnostic images using lower dose parameters. The mean estimated CTDI<sub>vol</sub> was significantly reduced in the IMR group,  $24.4 \pm 3.1$  mGy versus the FBP

group,  $31.1 \pm 6.0$  mGy (*P* < .001). In addition, the CTDI<sub>vol</sub> was significantly reduced in each of the 4 individual age groups, 27%, 25%, 13%, and 12% (Table 2), with the largest dose savings observed in the younger-than-1.5 years and 1.5- to 6-year age groups.

### Reconstruction Times

The average study reconstruction time for the FBP-group was 100.9 seconds (range, 64–237 seconds), and for the IMR group, it was 147.0 seconds (range, 125–473 seconds) (*P* < .001).

### Quantitative Analysis

SNR<sub>Thalamus</sub>, SNR<sub>White Matter</sub>, and CNR were significantly improved in the IMR groups compared with the FBP groups approximately 2-fold, with representative images and sample measurements in Fig 1 and group results summarized in Table 2.

### Qualitative Analysis

A random number generator was used to select 5 patients from each of the age groups imaged on each scanner (*n* = 40). Subjective image quality, as it pertains to anatomic detail and gray-white matter differentiation, was scored, on average,  $2.3 \pm 0.6$  (fair-to-average) for those standard-dose studies reconstructed with FBP, and  $3.6 \pm 0.6$  (average-to-good) for those lower-dose studies reconstructed with IMR (*P* < .001). Each physician independently scored those studies reconstructed with IMR as superior to those reconstructed with FBP ( $3.6 \pm 0.8$  versus  $1.9 \pm 0.8$  and  $3.7 \pm 0.6$  versus  $2.8 \pm 0.6$  (*P* < .001). However, score agreement between the individual physicians was low, with an intraclass correlation coefficient of 0.399 and a correlation coefficient *r* = 0.43 for the FBP groups, and an intraclass correlation coefficient of 0.345 and *r* = 0.37 for the IMR groups (Table 3).

## DISCUSSION

In our patient population, we demonstrate statistically significant relative CTDI<sub>vol</sub> dose reduction in all 4 patient age groups undergoing emergency unenhanced head CT examinations, 1.5 years or younger, 1.5–6 years, 7–12 years, and 13 years and older, of 27%, 25%, 13%, and 12% respectively, using low-dose protocols with IMR image reconstruction, compared with patients imaged using standard protocols and FBP image reconstruction, with statistically improved quantitative and qualitative image quality (Fig 1). The

**Table 1: Patient demographics by age group, age, sex, and scanner<sup>a</sup>**

	IMR (n = 190)	FBP (n = 173)	Total (n = 363)	P Value
Age group				.50 <sup>b</sup>
Younger than 1.5 years	65 (34.2%)	48 (27.7%)	113 (31.1%)	
1.5–6 years	60 (31.6%)	58 (33.5%)	118 (32.5%)	
7–12 years	24 (12.6%)	29 (16.8%)	53 (14.6%)	
Older than 13 years	41 (21.6%)	38 (22.0%)	79 (21.8%)	
Age (mean) (SD) (months)	67.6 (67.9)	76.3 (73.8)	71.8 (70.8)	.24 <sup>c</sup>
Sex				.05 <sup>b</sup>
Female	81 (42.6%)	56 (32.4%)	137 (37.7%)	
Male	109 (57.4%)	117 (67.6%)	226 (62.3%)	

<sup>a</sup>Data are number (percentage) unless otherwise indicated.

<sup>b</sup> $\chi^2$  test.

<sup>c</sup>Equal variances *t* test.

**Table 2: Mean (SD) dose estimates and objective image-quality measures by age group and scanner**

	Younger Than 1.5 yr		1.5–6 yr		7–12 yr		Older Than 13 yr	
	FBP	IMR	FBP	IMR	FBP	IMR	FBP	IMR
CTDI <sub>vol</sub>	29.9 (5.5)	21.8 (0.1)	30.6 (5.5)	22.8 (0.0)	31.5 (6.2)	27.5 (0.0) <sup>a</sup>	33.3 (6.9)	29.2 (0.6) <sup>a</sup>
SNR <sub>THAL</sub>	9.3 (2.3)	22.0 (5.3)	8.6 (1.8)	20.2 (3.9)	8.8 (2.3)	18.7 (3.2)	8.6 (2.2)	17.9 (3.5)
SNR <sub>WM</sub>	8.3 (2.3)	16.5 (3.8)	8.2 (2.3)	15.8 (3.3)	7.8 (1.3)	16.9 (4.3)	7.9 (2.4)	14.9 (2.9)
CNR	2.1 (0.9)	4.9 (1.3)	2.1 (1.1)	4.4 (0.9)	2.0 (1.0)	3.7 (0.9)	1.8 (0.6)	3.6 (1.0)

**Note:**—THAL indicates thalamus; WM, white matter; vol, volume.

<sup>a</sup>*P* value < .003. For all other results, *P* value < .001, equal variances *t* test.

implication is that further dose reduction with even lower-dose techniques and maintained, rather than improved, image quality is possible with IMR.

The average reconstruction time with IMR was 46 seconds (46%) longer than with standard FBP reconstruction, but with no practical effect on work flow. Willemink et al<sup>8</sup> likewise reported a 35% increased reconstruction time of hybrid iDose4 (Philips Healthcare) in abdominal CT examinations. Reconstruction times can be expressed in slices per second; however, the number of slices per second is not a linear function because there is a longer lag time until the first image. In our study, the FBP reconstructions averaged 5.2–5.6 slices/second, and the IMR reconstructions, 3.4–3.6 slices/second. As computer-processing speeds improve, image-reconstruction times with IMR should continue to decrease.

Multiple studies have reported success in reducing relative radiation doses in pediatric cohorts undergoing head CT examinations, ranging from 24% to 48%, using low-dose protocols with hybrid IR image reconstruction versus standard-dose FBP protocols.<sup>9–15</sup> Vorona et al, 2013,<sup>16</sup> reported that 20% adaptive statistical iterative reconstruction (ASIR) could allow 22% relative dose reduction in pediatric head CT without affecting image quality. Kilic et al, 2013,<sup>17</sup> demonstrated a 29% dose reduction with low-dose 30% ASIR versus standard-dose FBP in 305 pediatric head CT examinations with maintained diagnostic quality and image sharpness, but they noted decreased SNR and increased white

matter noise in the IR images. McKnight et al, 2014,<sup>18</sup> showed a relative dose reduction of 28% and 48% in pediatric head CT examinations in patients 3–12 years of age and older than 12 years of age, respectively, using 30% ASIR. Thomas et al, 2018,<sup>19</sup> reported a relative dose reduction of 26% in pediatric head CT examinations using hybrid IR iDose4 strength level 2 reconstruction versus standard-dose FBP, with improved SNR and CNR. However, subjective image-quality reviewers preferred the FBP images for noise in the older-than-13-year group, and image sharpness in the 7- to 12-year and older-than-13-year groups.<sup>19</sup> Kim et al, 2017,<sup>20</sup> reported that the use of hybrid IR ASIR-V (GE Healthcare) allowed a 12.8%–34% dose reduction and lower noise and higher CNR in both supratentorial and posterior fossa structures in patients younger than 3 years of age and 3–15 years of age, with improved image sharpness on qualitative review. Ono et al, 2016,<sup>21</sup> reported 78 children 5 years of age and younger undergoing emergent noncontrast head CT reconstructed with FBP and 2 strengths of hybrid sinogram-affirmed iterative reconstruction. SNR and CNR were highest in the IR groups, as were subjective image-quality scores for gray-white matter differentiation and artifacts from the skull.

Relatively few studies have assessed IMR in pediatric head CT examinations. To our knowledge, no prior study has compared pediatric head CT examinations reconstructed using IMR and FBP. Notohamiprodjo et al, 2015,<sup>22</sup> reported improved subjective image quality, decreased artifacts, and significantly improved

SNR and CNR in head CT examinations reconstructed with MBIR compared with hybrid IR (ASIR) and proposed the potential of further reduction of the radiation dose with MBIR. den Harder et al, 2015,<sup>23</sup> reviewed hybrid and model-based IR in pediatric CT examinations and demonstrated improved noise reduction with MBIR and described variations of image textures depending on IR strength and reconstruction kernels.<sup>23</sup> Smith et al, 2014,<sup>24</sup> compared reduced-dose MBIR and hybrid IR 30% ASIR in pediatric body CT and reported decreased noise and improved spatial resolution with MBIR, but noted an altered texture and decreased sharpness of trabecular bone with MBIR. Cheng et al, 2018,<sup>25</sup> examined the image quality of head and neck CTA in pediatric patients scanned at a lowered radiation dose (80 kV) using decreased IV contrast volume and IMR image reconstruction and

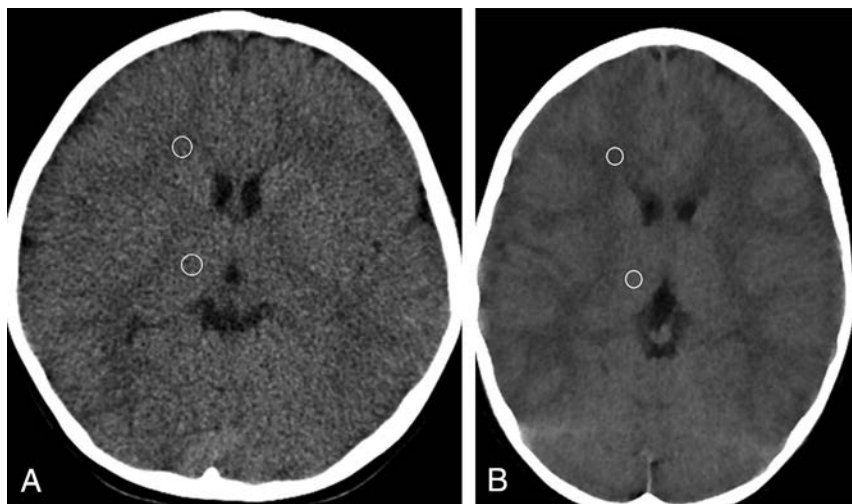


**FIG 1.** A, A 5-year-old girl bitten by a dog with scalp lacerations. Unenhanced head CT 3-mm axial image obtained using standard-dose protocol with FBP reconstruction. ROIs were placed on the thalamus and frontal white matter: thalamus,  $32.3 \pm 4.1$  HU; SNR, 7.9; white matter,  $26.8 \pm 3.9$  HU; SNR, 6.9; CNR, 1.4;  $CTDI_{vol}$ , 28.7 mGy. B, A 5-year-old boy who hit his head on concrete. Unenhanced head CT 3-mm axial image obtained using a low-dose age-based protocol with IMR reconstruction. ROIs were placed on the thalamus and frontal white matter: thalamus,  $31 \pm 1.5$  HU; SNR, 20.7; white matter,  $25 \pm 1.5$  HU; SNR, 16.7; CNR, 4.1;  $CTDI_{vol}$ , 22.8 mGy. SNR and CNR improved 2-fold with IMR, with a 21% decrease in  $CTDI_{vol}$ .

**Table 3: Mean subjective image-quality scores (SD) and average combined scores with frequency of image-quality scores given for FBP and IMR images<sup>a</sup>**

	Combined	DR1	DR2	DR1 (Frequency)	DR2 (Frequency)	r	ICC
FBP	2.3 (0.6)	1.9 (0.8)	2.8 (0.6)	6/11/2/1/0	0/6/13/4/0	0.43	0.399
IMR	3.6 (0.6)	3.6 (0.8)	3.7 (0.6)	0/1/10/6/3	0/1/4/15/0	0.37	0.345
P value	<.001	<.001	<.001				

**Note:**—ICC indicates intraclass correlation coefficient; DR1, radiologist 1; DR2, radiologist 2.

<sup>a</sup> Combined scores are in column 2. Scores are 1 (poor) to 5 (excellent).

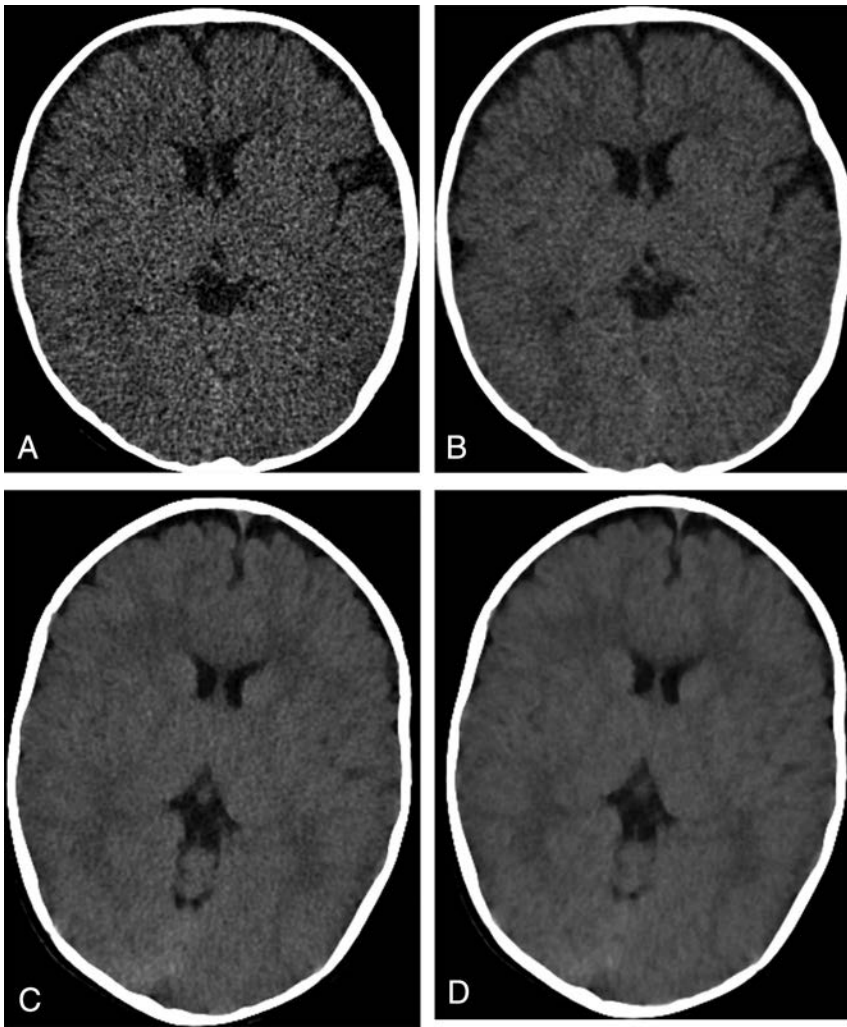


**FIG 2.** A 6-month-old female infant who fell from a couch. Axial noncontrast head CT using standard protocol and FBP reconstructed at 1-mm (*top left*) and 3-mm (*top right*) slice thickness. *A*, Thalamus,  $29 \pm 7.5$  HU; SNR, 3.9; WM,  $26 \pm 7.5$  HU; SNR, 3.5; CNR, 0.4;  $CTDI_{vol}$ , 25.5 mGy. *B*, Thalamus,  $29 \pm 3.9$  HU; SNR, 7.4; WM,  $24 \pm 4.0$  HU; SNR, 6.0; CNR, 1.3;  $CTDI_{vol}$ , 25.5 mGy. The 1-mm FBP image has noticeably increased noise and a 69% decrease in CNR compared with the 3-mm FBP image, which lessens the diagnostic quality. A 6-month-old female infant with altered loss of consciousness and “not acting normally.” Axial noncontrast images using low-dose protocol and IMR reconstructed at 1-mm (*bottom left*) and 3-mm (*bottom right*) slice thickness. *C*, Thalamus,  $29 \pm 2.7$  HU; SNR, 10.7; WM,  $25 \pm 2.2$  HU; SNR, 11.4; CNR, 1.6;  $CTDI_{vol}$ , 21.8 mGy. *D*, Thalamus,  $29 \pm 1.8$  HU; SNR, 16.1; WM,  $25 \pm 1.9$  HU; SNR, 13.1; CNR, 2.2;  $CTDI_{vol}$ , 21.8 mGy. The 1-mm IMR image has increased-but-acceptable noise, less than that in the 3-mm standard FBP image, and only a 27% decrease in CNR compared with the 3-mm IMR image. The 1-mm IMR has a more acceptable image texture and appears less waxy compared with the 3-mm IMR image.

found improved mean SNR and CNR, improved CT attenuation values of the arteries, and less noise compared with patients imaged at a higher 100 kV with images reconstructed with FBP. Improved vessel attenuation, CNR, and reduced noise with IMR lend themselves to improved spatial resolution and 3D volume-rendered models.

One common problem with model-based IR is altered image texture, which has been described as “waxy” or “glossy.” To minimize this effect, our neuroradiologists rely on the 1-mm image set for primary diagnostic interpretation. The use of thinner image sets lessens the undesirable overly smooth image texture of the thicker images reconstructed using IMR, with relative maintained SNR, CNR, and acceptable noise (Fig 2).

A limitation of our study is that it was a retrospective review of patients, and we were unable to randomize patients and scanners. Our results demonstrated an average dose reduction of 22% with the use of IMR, which agrees with findings of other studies using hybrid IR. However, the concept of dose reduction is relative depending on reference protocols. Individual institutional results will vary depending on current protocols used, availability and type of IR used, physician noise tolerance, and image-texture preferences.

There is an inherent limitation in assessing reconstruction times because the studies were performed on different scanners, and machine differences in hardware, processor clock speeds, and RAM could impact our observed reconstruction times.

Qualitative image-quality analysis may have been limited by the size of the random subsets evaluated. Lack of intra-class correlation coefficient agreement between our 2 reviewers may have been the result of how they were prepared to score image quality. Reviewers were only given a brief written and verbal guideline on how to rate the studies, but there was no hands-on prestudy training using case examples and no discussion on how to rate each parameter before conducting individual blinded reviews. Physician confidence and image-noise tolerance can be affected by experience, which we hoped to minimize by selecting radiologist reviewers, both with  $\geq 16$  years’ experience. Both reviewers individually scored the IMR images as superior to those reconstructed with FBP; however, 1 reviewer consistently scored comparable studies 1 full grade below that given by the second reviewer, also

contributing to lack of an intraclass correlation coefficient. We used a 5-point rather than 4-point scale to score image quality, which added potential variability of possible scores. In addition, given the altered image texture of the IMR images, the reviewers could conceivably learn which reconstruction algorithm was used, possibly introducing bias.

Reported IMR subjective image-quality scores may have been underestimated because we used the 3-mm FBP and 3-mm IMR images for review and grading, which likely affected subjective image-quality scores, because our neuroradiology physicians routinely use the thin 1-mm IMR images for clinical interpretation. Liu et al, 2017,<sup>26</sup> demonstrated that thin-slice 1-mm IMR images yielded the lowest noise, posterior fossa artifacts, and best CNR in

unenanced brain CT examinations, compared with 3-mm hybrid IR and 5-mm FBP reconstruction, and they had better sensitivity in the detection of small lacunar lesions. We did not examine posterior fossa image quality, which should be different from that in supratentorial measurements due to increased posterior fossa noise.

## CONCLUSIONS

Study reconstruction times of urgent head CT examinations using IMR were statistically longer than those using FBP by 46% ( $P < .001$ ), but without a practical effect on work flow. We demonstrated a relative dose reduction of 12%–27% using optimized low-dose head CT protocols with IMR, with the greatest dose savings seen in the youngest patient groups, with a 2-fold improvement of SNR and CNR and statistically improved subjective image quality. Results suggest that further potential dose savings with maintained image quality are possible with IMR.

Disclosures: Richard N. Southard—UNRELATED: Consultancy: Philips Healthcare; Payment for Lectures Including Service on Speakers Bureaus: Philips Healthcare; OTHER RELATIONSHIPS: Koninklijke Philips NV: Master Enterprise Agreement between Philips Healthcare and Phoenix Children's Hospital. Dianna M.E. Bardo—UNRELATED: Consultancy: Koninklijke Philips NV, Comments: Master Enterprise Agreement\*; Payment for Lectures Including Service on Speakers Bureaus: Koninklijke Philips NV, Comments: honoraria to my institution, travel support; Travel/Accommodations/Meeting Expenses Unrelated to Activities Listed: Koninklijke Philips NV; Other: Thieme Publishing, Comments: Royalties. \*Money paid to the institution.

## REFERENCES

- Wier LM, Hao Y, Owens PV, et al. Overview of Children in the Emergency Department, 2010. Statistical Brief #157. June 2013. Healthcare Cost and Utilization Project (HCUP) Statistical Briefs [Internet]. Agency for Healthcare Research and Quality, Rockville, Maryland. <https://www.ncbi.nlm.nih.gov/books/NBK154386/>. Accessed March 26, 2019
- Ryan M, Palasis S, Saigal G, et al. ACR Appropriateness Criteria head trauma: child. *J Am Coll Radiol* 2014;11:939–47 CrossRef Medline
- Coakley F, Gould R, Yeh B, et al. CT radiation dose: what can you do right now in your practice? *AJR Am J Roentgenol* 2011;196:619–25 CrossRef Medline
- Mahesh M. Advances in CT technology and application to pediatric imaging. *Pediatr Radiol* 2011;41(Suppl 2):493–97 CrossRef Medline
- Smith A, Dillon W, Gould R, et al. Radiation dose-reduction strategies for neuroradiology CT protocols. *AJNR Am J Neuroradiol* 2007;28:1628–32 CrossRef Medline
- Seibert J. Iterative reconstruction: how it works, how to apply it. *Pediatr Radiol* 2014;44(Suppl 3):431–39 CrossRef Medline
- Padole A, Khawaja DR, Kalra MK, et al. CT radiation dose and iterative reconstruction techniques. *AJR Am J Roentgenol* 2015;204:W384–92 CrossRef Medline
- Willeminck MJ, Schilham AM, Leiner T, et al. Iterative reconstruction does not substantially delay CT imaging in the emergency setting. *Insights Imaging* 2013;4:391–97 CrossRef Medline
- Mirro AE, Brady SL, Kaufman RA. Full dose-reduction potential of statistical iterative reconstruction for head CT protocols in a predominantly pediatric population. *AJNR Am J Neuroradiol* 2016;37:1199–205 CrossRef Medline
- Harris M, Huckle J, Anthony D, et al. The acceptability of iterative reconstruction algorithms in head CT: an assessment of Sinogram Affirmed Iterative Reconstruction (SAFIRE) vs. filtered back projection (FBP) using phantoms. *Journal of Medical Imaging and Radiation Sciences* 2017;48:259–69 CrossRef
- Ho C, Oberle R, Wu I, et al. Comparison of image quality in pediatric head computed tomography reconstructed using blended iterative reconstruction versus filtered back projection. *Clin Imaging* 2014;38:231–35 CrossRef Medline
- Korn A, Fenchel M, Bender B, et al. Iterative reconstruction in head CT: image quality of routine and low-dose protocols in comparison with standard filtered back-projection. *AJNR Am J Neuroradiol* 2012;33:218–24 CrossRef Medline
- Ren Q, Dewan SK, Li M, et al. Comparison of adaptive statistical iterative and filtered back projection reconstruction techniques in brain CT. *Eur J Radiol* 2012;81:2597–601 CrossRef Medline
- Bodelle B, Klein E, Naguib NN, et al. Acute intracranial hemorrhage in CT: benefits of sinogram affirmed iterative reconstruction techniques. *AJNR Am J Neuroradiol* 2014;35:445–49 CrossRef Medline
- Singh S, Kalra MK, Shenoy-Bhangle AS, et al. Radiation dose reduction with hybrid iterative reconstruction for pediatric CT. *Radiology* 2012;263:537–46 CrossRef Medline
- Vorona G, Zuccoli G, Sutcavage T, et al. The use of adaptive statistical iterative reconstruction in pediatric head CT: a feasibility study. *AJNR Am J Neuroradiol* 2013;34:205–11 CrossRef Medline
- Kilic K, Erbas G, Guryildirim M, et al. Quantitative and qualitative comparison of standard-dose and low-dose pediatric head computed tomography: a retrospective study assessing the effect of adaptive statistical iterative reconstruction. *J Comput Assist Tomogr* 2013;37:377–81 CrossRef Medline
- McKnight C, Watcharotone K, Ibrahim M, et al. Adaptive statistical iterative reconstruction: reducing dose while preserving image quality in the pediatric head CT examination. *Pediatr Radiol* 2014;44:997–1003 CrossRef Medline
- Thomas A, Southard R, Curran J, et al. Comparing fourth generation statistical iterative reconstruction technique to standard filtered back projection in pediatric head computed tomography examinations. *J Comput Assist Tomogr* 2018;42:475–81 CrossRef Medline
- Kim HG, Lee HJ, Lee SK, et al. Head CT: image quality improvement with ASIR-V using a reduced radiation dose protocol for children. *Eur Radiol* 2017;27:3609–17 CrossRef Medline
- Ono S, Niwa T, Yanagimachi N, et al. Improved image quality of helical computed tomography of the head in children by iterative reconstruction. *J Neuroradiol* 2016;43:31–36 CrossRef Medline
- Notohamprodo S, Deak Z, Meurer F, et al. Image quality of iterative reconstruction in cranial CT imaging: comparison of model-based iterative reconstruction (MBIR) and adaptive statistical iterative reconstruction (ASiR). *Eur Radiol* 2015;25:140–46 CrossRef Medline
- den Harder AM, Willeminck MJ, Budde RP, et al. Hybrid and model-based iterative reconstruction techniques for pediatric CT. *AJR Am J Roentgenol* 2015;204:645–53 CrossRef Medline
- Smith EA, Dillman JR, Goodsitt MM, et al. Model-based iterative reconstruction: effect on patient radiation dose and image quality in pediatric body CT. *Radiology* 2014;270:526–34 CrossRef Medline
- Cheng B, Xing H, Lei D, et al. Impact of iterative model reconstruction combined with dose reduction on the image quality of head and neck CTA in children. *Sci Rep* 2018;8:12613 CrossRef Medline
- Liu X, Chen L, Weiwei Q, et al. Thin-slice brain CT with iterative reconstruction algorithm for small lacunar lesions detection: image quality and diagnostic accuracy evaluation. *Medicine (Baltimore)* 2017;96:e9412 CrossRef Medline

# Pediatric Atypical Teratoid/Rhabdoid Tumors of the Brain: Identification of Metabolic Subgroups Using In Vivo <sup>1</sup>H-MR Spectroscopy

B. Tamrazi, S. Veneti, A. Margol, D. Hawes, S.Y. Cen, M. Nelson, A. Judkins, J. Biegel, and S. Blüml



## ABSTRACT

**BACKGROUND AND PURPOSE:** Atypical teratoid/rhabdoid tumors are rare, aggressive central nervous system tumors that are predominantly encountered in very young children. Our aim was to determine whether in vivo metabolic profiles correlate with molecular features of central nervous system pediatric atypical teratoid/rhabdoid tumors.

**MATERIALS AND METHODS:** Twenty confirmed patients with atypical teratoid/rhabdoid tumors who underwent MR spectroscopy were included in this study. In vivo metabolite levels of atypical teratoid/rhabdoid tumors were compared with molecular subtypes assessed by achaete-scute homolog 1 expression. Additionally, brain-specific creatine kinase levels were determined in tissue samples.

**RESULTS:** In vivo creatine concentrations were higher in tumors that demonstrated achaete-scute homolog 1 expression compared with those without achaete-scute homolog 1 expression ( $3.42 \pm 1.1$  versus  $1.8 \pm 0.8$  IU,  $P < .01$ ). Additionally, levels of myo-inositol (ml) ( $9.0 \pm 1.5$  versus  $4.7 \pm 3.6$  IU,  $P < .05$ ) were significantly different, whereas lipids approached significance ( $44 \pm 20$  versus  $80 \pm 30$  IU,  $P = .07$ ) in these 2 cohorts. Higher brain-specific creatine kinase levels were observed in the cohort with achaete-scute homolog 1 expression ( $P < .05$ ). Pearson correlation analysis showed a significant positive correlation of brain-specific creatine kinase with absolute creatine ( $P < .05$ ) and myo-inositol ( $P < .05$ ) concentrations.

**CONCLUSIONS:** In vivo MR spectroscopy may predict key molecular features of atypical teratoid/rhabdoid tumors at initial diagnosis, leading to timely patient risk stratification and accelerating the development of targeted therapies.

**ABBREVIATIONS:** ASCL1 = achaete-scute homolog 1; AT/RT = atypical teratoid/rhabdoid tumor; CKB = brain-specific creatine kinase; Cr = creatine; ml = myo-inositol; Cho = choline; SMARCB1 = SWI/SNF-related matrix-associated actin-dependent regulator of chromatin subfamily B member 1

Primary brain tumors are the most common pediatric solid tumors in children and the leading cause of death from childhood cancer.<sup>1,2</sup> Recently, through the emergence of molecular diagnostics and the growing field of pediatric molecular neuro-oncology, biologically distinct and clinically relevant molecular subtypes of pediatric brain tumors have been identified. These include atypical teratoid/rhabdoid tumors (AT/RTs), a group of rare, highly aggressive central nervous system tumors with poor

prognosis. The genetic hallmark of AT/RTs is the loss of protein expression of *SWI/SNF-related matrix-associated actin-dependent regulator of chromatin subfamily B member 1 (SMARCB1)*, a tumor-suppressor locus on chromosome 22q11.23.<sup>3,4</sup> Although these tumors are uniformly characterized by deletions and/or mutations in this locus, there is clinical and molecular heterogeneity among the patients. This suggests further underlying biologic heterogeneity,<sup>5,6</sup> which has been defined by recent multicenter studies.<sup>7,8</sup> Noninvasive imaging markers obtained at initial presentation can potentially serve as surrogates for these molecular subgroups or for specific clinically relevant molecular features that may lead to patient risk stratification and improved treatment strategies. Recently, an imaging study demonstrated significant differences in the location and conventional MR imaging characteristics of AT/RTs, which may potentially correlate with the different molecular features/subgroups.<sup>9</sup>

Among the molecular features that can be used to distinguish AT/RTs is a transcription factor known as achaete-scute homolog 1 (ASCL1). Patients whose tumors had expression of ASCL1 had improved overall survival.<sup>10</sup> In this study, we focused on this spe-

Received December 13, 2018; accepted February 27, 2019.

From the Departments of Radiology (B.T., M.N., S.B.) and Pediatrics (A.M.) and Division of Hematology Oncology, and Pathology (D.H., A.J., J.B.), Children's Hospital Los Angeles, Los Angeles, California; Department of Pathology (S.V.), University of Michigan, Ann Arbor, Michigan; Department of Radiology and Neurology (S.Y.C.), University of Southern California, Los Angeles, California; and Rudi Schulte Research Institute (S.B.), Santa Barbara, California.

Funding for this research provided by the American Society of Pediatric Neuro-radiology Research Award.

Please address correspondence to Benita Tamrazi, MD, Children's Hospital Los Angeles, Department of Radiology, 4650 Sunset Blvd, Los Angeles CA 90027 MS 81; e-mail: btamrazi@chla.usc.edu

<http://dx.doi.org/10.3174/ajnr.A6024>

**Table 1: Patient demographics and clinical and biologic lesion characterization**

Age (yr)	Sex	Overall Survival (mo)	Location	LM	ASCL1	CKB	Germline Mutation
0.15	F	0.5 <sup>a</sup>	Posterior fossa	0	Negative	5.05	
0.32	F	17.0	Posterior fossa	0	Positive	6.31	Yes
0.39	M	8.2 <sup>b</sup>	Posterior fossa	1	Positive		
0.64	M	7.0	Parietal lobe	0	Negative	5.10	
0.67	M	0.5 <sup>a</sup>	Posterior fossa	1	Positive		
0.68	M	5.1	Intraventricular	0	ND		
0.92	F	0.5 <sup>a</sup>	Posterior fossa	1	Positive		Yes
0.95	M	71.9 <sup>b</sup>	Posterior fossa	0	ND		
1.09	M	13.0	Posterior fossa	0	Negative	5.31	
1.14	M	7.0	Temporal lobe	0	Positive	6.05	Yes
1.15	M	59.0	Posterior fossa	0	Negative	6.31	
1.42	F	9.0	Posterior fossa	1	ND		
1.54	M	32.0	Temporal lobe	0	Positive	6.53	Yes
1.55	M	63.2 <sup>b</sup>	Posterior fossa	0	Negative		
1.73	M	13.0	Pineal	0	Positive		
1.84	F	18.0	Frontotemporal	0	Negative	5.21	
1.96	F	NA	Temporal lobe	1	ND		
2.86	M	18.0	Frontotemporal	1	Positive	6.61	
7.43	F	40.0	Frontotemporal	0	Positive	6.42	
13.72	M	40.0	Intraventricular	0	Positive	5.71	

**Note:**—NA indicates patient lost to follow up; LM, leptomeningeal disease present (1) versus absent (0) at presentation; ND, not determined.

<sup>a</sup> Patients who died from surgical/other complications with no MR imaging or clinical evidence of progressive tumor.

<sup>b</sup> Patients who were still alive at the time of the completion of this study.

cific molecular feature and explored whether in vivo <sup>1</sup>H-MR spectroscopy can distinguish ASCL1-expressing AT/RTs from those that do not express ASCL1. In an analysis of tissue samples, we observed different levels of brain-specific creatine kinase (CKB), with CKB being higher in ASCL1-expressing AT/RTs. Thus, our primary objective was to determine whether in vivo Cr concentrations were significantly higher in AT/RTs with ASCL1 expression versus tumors without ASCL1 expression. A secondary goal of this study was to review other metabolic features that are obtained simultaneously with the measurement of creatine to further differentiate these 2 cohorts using a metabolic/MR spectroscopy imaging approach.

## MATERIALS AND METHODS

### Patients

Our single-center, retrospective study was approved by our institutional review board (Children's Hospital Los Angeles) and was compliant with the Health Insurance Portability and Accountability Act. The requirement to obtain informed consent was waived. We accessed the pediatric oncology data base of our institution to identify patients with AT/RTs from 2000 to 2017 with MR spectroscopy and frozen tissue specimens obtained at our institution. All included patients had confirmed AT/RTs of the brain with patient characteristics summarized in Table 1.

### Imaging Protocol

All brain MR spectroscopy examinations were performed with 1.5T or 3T whole-body MR imaging systems in our institution (Achieva and Ingenia, Philips Healthcare, Best, the Netherlands; Signa HD 1.5, GE Healthcare, Milwaukee, Wisconsin). A single-voxel point-resolved spectroscopic sequence with TE = 35 ms, TR = 1.5 seconds (for 1.5T) and 2 seconds (for 3T), and 128 signal averages was used for all acquisitions. T2-weighted fast spin-echo, FLAIR, and T1-weighted FLAIR images were acquired in all instances before MR spectroscopy and were reviewed to determine

the extent of tumor lesions. We identified the ROIs for MR spectroscopy on the basis of MR images from all 3 planes centered in the solid parts of the tumors, excluding any surrounding normal brain tissue or edema and in a manner that minimized inclusion of cystic or necrotic areas. An attending pediatric neuroradiologist reviewed and approved the ROIs for each patient and confirmed that the MR spectroscopy profile was representative of tumor tissue only. The sizes and shapes of the ROIs were adjusted to lesion size and typically varied between 5 and 10 cm<sup>3</sup>. Spectra were processed using the fully automated LCModel, Version 6.1–1 L software (<http://www.lcmodel.com/>). Absolute concentrations (IU) of Cho, Cr, mI, lactate, and lipid, which all consistently have been reported to be abnormal in tumors, were analyzed. The unsuppressed water signal, assuming a water content of 75%, was used as an internal concentration reference.

### Molecular Diagnostic Analysis

**SMARCB1 Protocol.** SMARCB1 molecular genetic analysis by Sanger sequencing and multiplex ligation-dependent probe amplification were conducted on all tissue samples to confirm the diagnosis of AT/RT<sup>11</sup> per prior reported methodology.

**ASCL1 Protocol/Immunohistochemistry and Automated Scoring of CKB.** Immunohistochemical studies were performed as previously described.<sup>12</sup> The primary antibody (ASCL1) (Mouse Anti-MASH1, catalog No. 556604; BD Biosciences, San Jose, California) diluted 1:100 with Bond Primary Antibody Diluent (Leica Biosystems, Buffalo Grove, Illinois) was incubated for 30 minutes. The primary antibody was detected using the Bond Polymer Refine Detection kit (Leica Biosystems), which uses a peroxidase block, secondary antibodies, and 3, 3'-diaminobenzidine and was finally counter-stained with hematoxylin.

Immunohistochemical studies for CKB were performed on previously characterized rhabdoid tumor tissue microarrays as

previously described,<sup>13,14</sup> and full paraffin-embedded sections from all available tumor blocks were obtained from imaged patients. Quantification of immunohistochemical data was performed as previously described.<sup>15</sup> Blocker D, Streptavidin (HRP), and the DAB detection kit (Ventana Medical Systems, Tucson, Arizona) were used according to the manufacturer's instructions.

For automated scoring, each tissue microarray slide was scanned using a Scanscope Scanner (Aperio, Vista, California) and viewed through the ImageScope software program (Aperio). An individual blinded to the experimental design captured JPEG images from each core (circular area of 315 cm<sup>2</sup> corresponding to the entire core) at 10× magnification. For full sections, the same blinded individual captured 5 random areas (circular area of 315 cm<sup>2</sup> at 10× magnification). Quantification was conducted using an automated analysis program with the Matlab Image-Processing Toolbox (MathWorks, Natick, Massachusetts) based on previously described methodology.<sup>15</sup> The final score for a given case and marker was calculated by averaging the score of 2 cores (for each case) or from 5 areas per section for full slides. These raw CKB numbers were log-transformed ( $CKB = \log_{10} [CKB_{raw}]$ ) for statistical analysis.

### Data Collection

Frozen tumor tissue from 16 of 20 patients with AT/RTs and MR spectroscopy studies from all 20 patients diagnosed at Children's Hospital Los Angeles between 2000 and 2017 were available for analysis. Sufficient tissue samples available from 11 patients were examined for CKB.

### Statistical Analysis

Statistical analysis was informed by the previously reported finding of 2 distinct molecular subtypes defined by the expression of the molecular marker ASCL1.<sup>10</sup> For demographic measurements, the Fisher exact test was used to assess the difference in sex and lesion location (posterior fossa versus lesions outside the posterior fossa) between the 2 ATRT categories. A 2-sided exact test with a Wilcoxon score was used to examine the difference in continuous measurements, including the demographics, month of follow-up, and metabolic profiles. Because there were multiple outcomes, the sequential gatekeeper strategy<sup>16</sup> was used to control the family-wise type I error rate. In this strategy, the outcomes were grouped into primary, secondary, and tertiary families. The primary and secondary outcomes were CKB and Cr, respectively. The tertiary outcome family included Cho, lactate, mI, and lipids. We first gave the full  $\alpha$  of .05 to the primary outcome. If the primary outcome failed to reject the null hypothesis, the statistical test would stop at the primary level. Otherwise, the  $\alpha$  value would be fully passed to the secondary outcome. If it failed to reject the null hypothesis at the secondary family, the statistical test would stop; otherwise, it would proceed to the tertiary outcome family. Because the tertiary family had 4 outcome measurements, the Benjamini-Hochberg false discovery rate correction method was used to control the error introduced by multiple testing. Furthermore, Spearman correlation analysis was used to assess the correlation between CKB and Cr concentrations in AT/RTs. We have conducted an exploratory analysis of survival using the Kaplan-Meier curve with a log-rank test. Patients who died from causes not related to disease progression were excluded because the log-

rank test assumes noninformative right censoring. Patients at final follow-up were censored. SAS 9.4 (SAS Institute, Cary, North Carolina) was used for all statistical tests.

### RESULTS

In vivo MR spectra acquired from AT/RTs demonstrated considerable metabolic heterogeneity. For example, whereas in some patients signals from Cr and mI were readily detectable, these metabolites were essentially absent in other AT/RT cases (Fig 1).

CKB was analyzed independently for 11 AT/RTs, and significantly higher CKB levels were observed in the cohort with ASCL1 expression ( $P < .05$ , Table 2) in our patient population. The subsequent analysis of in vivo Cr concentrations demonstrated that Cr was significantly higher in tumors with ASCL1 expression than in tumors without ASCL1 expression ( $P < .05$ , Table 2). In addition, significantly different in these 2 subgroups was the metabolite mI ( $P < .05$ , Table 2), whereas lipid levels approached significance ( $P = .07$ , Table 2). Pearson correlation analysis showed statistically significant positive correlations of CKB with absolute Cr ( $P < .05$ ) and mI ( $P < .01$ ) concentrations.

AT/RTs located outside the posterior fossa more often expressed ASCL1 (6 versus 3 patients), whereas AT/RTs in the posterior fossa more often did not express ASCL1 (3 versus 4). Although this difference was not statistically significant in this small cohort of patients, the trend is consistent with the findings reported by Torchia et al.<sup>10</sup> Overall survival in the 2 AT/RT subgroups was not significantly different ( $P = .93$ ).

### DISCUSSION

AT/RTs are rare, aggressive central nervous system tumors that are predominantly encountered in very young children. These tumors have been considered incurable, with survival being typically <1 year after diagnosis for most patients. Although AT/RTs are uniformly defined by the loss of expression of *SMARCB1*, clinically there is considerable heterogeneity. While most children with these tumors have a very poor prognosis, a subset of patients experience distinctly prolonged survival, indicating epigenetic heterogeneity that potentially affects the response to treatment.<sup>6</sup> Indeed, current consensus from a large multicenter study is that there are at least 3 molecular subgroups, referred to as AT/RT-SHH, AT/RT-TYR, and AT/RT-MYC.<sup>8</sup> A second and independent consortium of investigators<sup>7</sup> also postulated 3 molecular subgroups of AT/RTs: Group 1 carried "neurogenic" signatures such as the expression of ASCL1 with clinically more favorable behavior, and groups 2A and 2B consisted of "mesenchymal" AT/RTs, which were more aggressive/treatment-resistant and did not express ASCL1. Richardson et al<sup>5</sup> suggested that AT/RT-SHH, AT/RT-TYR, and AT/RT-MYC subgroups may correspond with group 1, 2A, and 2B subgroups, respectively. However, this possibility has not been formally investigated and confirmed. In this study, to establish a clear separation of patients, we focused on the molecular feature of ASCL1 expression with our groups comprising AT/RTs that either expressed ASCL1 or did not express ASCL1.

When comparing in vivo MR spectroscopy measurements in AT/RTs, we observed significantly higher Cr concentrations in the ASCL1-expressing group versus the non-ASCL1-expressing group. Cr is an energy metabolite that is synthesized through a

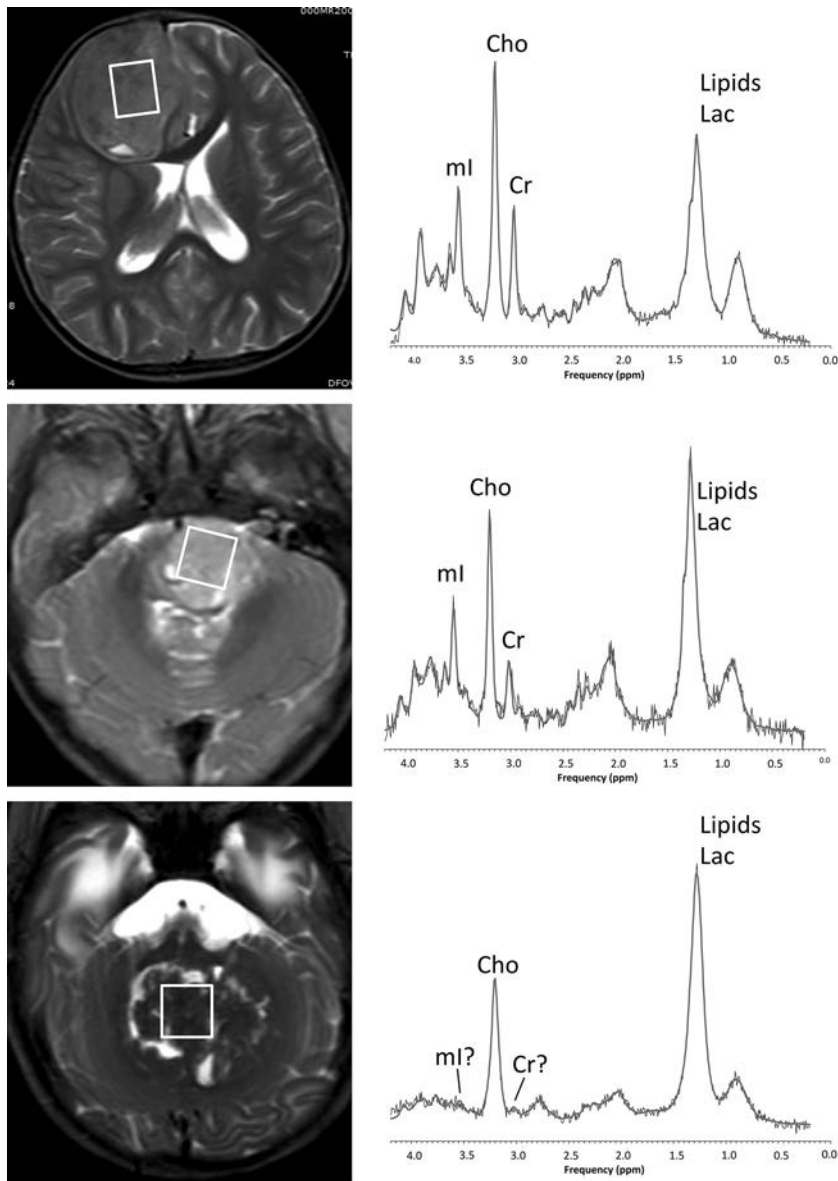


**FIG 1.** T2-weighted MR imaging and MR spectra of supratentorial AT/RTs with ASCL1 expression (upper row), a posterior fossa AT/RT with ASCL1 expression (middle row), and posterior fossa AT/RT without ASCL1 expression (lower row). Cr, Cho, and mI are readily detectable in the spectra of supratentorial and posterior fossa ASCL1-expressing AT/RTs, whereas only Cho is clearly detectable in the ASCL1-nonexpressing posterior fossa AT/RT. All spectra show prominent signal from lipids and lactate (Lac). Shown are the unprocessed data (thin black lines) with the superimposed fit (thick gray lines) used for quantification. The “box” seen in the images represents the voxel placement.

2-step process in the kidneys, pancreas, and liver. The brain then takes up Cr from the bloodstream by specific receptors known as SLC6A8, which are expressed in neurons and oligodendrocytes of the brain. Once Cr enters the CNS, it becomes part of the free creatine/phosphocreatine/creatine kinase system, which serves as an energy reservoir to maintain stable adenosine triphosphate levels.<sup>17,18</sup> Both free Cr and creatine/phosphocreatine contribute to the total Cr peak, which is quantified by MR spectroscopy.

For our cohort, the finding of higher levels of CKB in ASCL1-expressing AT/RTs provides additional evidence for considerable differences in Cr uptake and regulation in the ASCL1-expressing subgroup of AT/RTs. Furthermore, we have reviewed publicly

available data from the studies of Torchia et al<sup>7,10</sup> and have noted that in their dataset, both CKB and the creatine receptor (SLC6A8) were significantly higher in AT/RTs with ASCL1 expression compared with tumors without expression of ASCL1. Further studies are necessary to determine whether there is a direct relationship between ASCL1 expression and creatine metabolism. However, the above observations strongly indicate that the energy metabolism in the ASCL1-expressing subgroup could be different from that in the subgroup without ASCL1 expression. Therefore, we postulate that the molecular differences of the subgroups ultimately lead to differences in the underlying metabolism, which can be identified by noninvasive methods such as MR spectroscopy.

Myo-inositol was also significantly higher in ASCL1-expressing AT/RTs than in those without expression of ASCL1. Myo-inositol, a sugarlike molecule, is involved in signaling as part of the second messenger systems in the normal brain.<sup>19</sup> Similar to creatine, mI is not synthesized inside brain cells but is derived from the diet or is synthesized in the kidneys. Myo-inositol is believed to be a putative marker of glial cells, particularly of astrocytes.<sup>20,21</sup> It is thus generally high in astrocytomas but decreases when lesions transform to a higher grade.<sup>22,23</sup> Myo-inositol is involved in the activation of the protein kinase C, which leads to production of proteolytic enzymes that are found more often in malignant, aggressive primary cerebral tumors.<sup>22</sup> For AT/RTs, mI may potentially serve as a surrogate predictor of more aggressive lesions—that is, lower mI predicts the more aggressive AT/RTs without expression of ASCL1. The cause for low mI in these tumors may be the lack of uptake and transport; however, this was not specifically investigated in this study, and further validation studies are needed.

In contrast to Cr and mI, which were both lower in AT/RTs that did not demonstrate ASCL1 expression, lipids were more prominent, though statistical significance was not reached. There is some controversy about the origin of the lipid signal in tumors. Some groups suggested that the lipid signal originates from mobile lipid molecules as a result of tissue degradation and necrosis of aggressively growing lesions.<sup>24-26</sup> On the other hand, prominent lipid signal was also reported in spectra obtained from tumors without detectable necrosis.<sup>27</sup> In any case, there appears to

**Table 2: Features of AT/RTs with expression of ASCL1<sup>a</sup>**

	ASCL1 Pos.	ASCL1 Neg.	P Value
Age (mean) (yr)	3.4 ± 4.5	1.8 ± 0.8	NS
Sex (M/F)	6:3	5:2	NS
Location PF vs not PF	3 vs 6	4 vs 3	NS
Cr <sup>b</sup>	3.4 ± 1.1	1.8 ± 0.8	<.05
Cho <sup>b</sup>	3.2 ± 0.8	3.8 ± 2.1	NS
mI <sup>b</sup>	9.0 ± 1.5	4.7 ± 3.6	<.05
Lac <sup>b</sup>	5.0 ± 3.9	2.6 ± 2.6	NS
Lipids <sup>b</sup>	44 ± 20	80 ± 30	NS <sup>c</sup>
CKB (mean)	6.3 ± 0.3	5.4 ± 0.5	<.05
Months of follow-up (mean)	22 ± 14	32 ± 27	NS

**Note:**—NS indicates not significant; Pos., positive; Neg., negative; PF, posterior fossa.

<sup>a</sup> Tissue from 16 of 20 AT/RTs was available for testing of ASCL1 status.

<sup>b</sup> Means in IU.

<sup>c</sup> Approaching significance with  $P = .07$ .

be consensus that the presence of high lipids is generally an indicator of more malignant lesions.<sup>24</sup> The observed trend of higher lipid levels in AT/RTs without expression of ASCL1 would thus be consistent with a potentially worse prognosis.

Differences in our patient cohort in terms of germline-versus-sporadic *SMARCB1* mutations were also investigated. A total of 4 patients were identified with germline mutations (Table 1), all of which demonstrated expression of ASCL1. Although this is an interesting finding, more data are needed to investigate the clinical significance, if any, of this observation.

Overall survival in the 2 AT/RT subgroups in this study was not significantly different. This appears to be inconsistent with the study of Torchia et al,<sup>10</sup> which predicted a clinically more favorable outcome for AT/RTs with expression of ASCL1. However, treatment approaches for most patients included in this study were not consistent, likely playing a role in outcome/prognosis. Thus, the inability of this study to detect a difference in clinical outcomes of a small group of AT/RTs should not be overemphasized. Our study did, however, demonstrate a trend concordant with the findings of Torchia et al,<sup>7</sup> specifically that AT/RTs expressing ASCL1 are more often located outside the posterior fossa.

The question arises as to whether metabolic features of AT/RTs, obtained by noninvasive MR spectroscopy, form clusters and whether these clusters correlate with molecular subtypes or specific molecular features. Our analysis of the MR spectroscopy data available for this study is suggestive of the presence of 2 dominant metabolic clusters consisting of AT/RTs with significant differences in Cr and mI (relative to Cho) (Fig 2). However, given the broad heterogeneity of the larger metabolic group data points (dashed line circle in Fig 2), it is unclear whether these cases form a separate third group as predicted by the molecular phenotypes. Further, multicenter prospective trials with larger number of subjects using MR spectroscopy data are needed for analysis.

Our study had several limitations, including the single-center retrospective design. Our total number of patients is small. However, to our knowledge, this is the largest cohort of patients with AT/RTs with both molecular and metabolic (MR spectroscopy) data. No corrections of metabolite concentrations for T1 and T2 effects were applied because they are unknown in AT/RTs and it was not feasible to measure them in a clinical setting in patients. It is known that T1 times are longer at 3T than at 1.5T. The longer

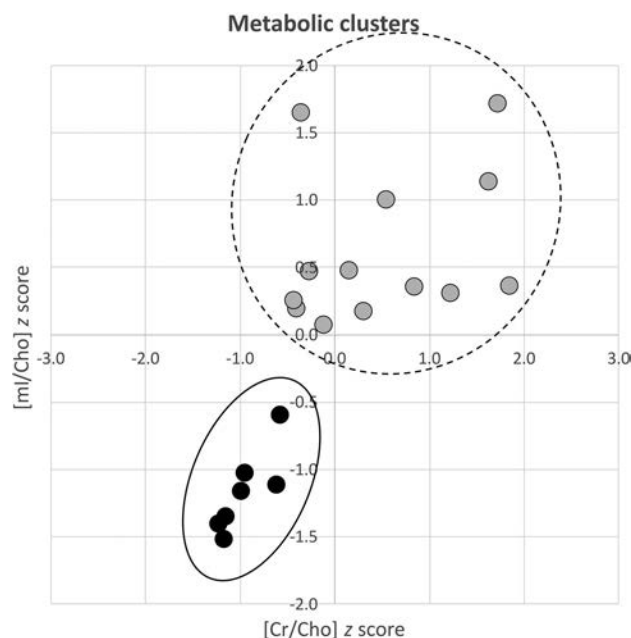


**FIG 2.** K-means cluster analysis graph demonstrating the metabolic clusters based on Cr/Cho and mI/Cho ratios. Ratios were transformed to z scores for better illustration. Findings suggest that a subgroup of AT/RTs (solid line) are homogeneously characterized by very low Cr and mI levels (relative to Cho) and are well-separated from other AT/RTs. It is, however, unclear whether the remaining larger cluster of AT/RTs (dashed line) forms a single group or multiple separate groups as suggested by the molecular data.

TR of our 3T studies (2.0 versus 1.5 seconds) partially corrects for this effect. Additionally, due to acquisition of the data at both 1.5 and 3T, differentiation of the mI and glycine peak proved to be challenging, particularly at 1.5T because both mI and glycine contribute to the peak at 3.5 ppm. Clinically, glycine and mI may have similar implications because prior studies have reported that glycine consumption and synthesis are correlated with rapid cancer cell proliferation<sup>28</sup>; therefore, glycine may serve as a marker for more aggressive tumors. Changes in glycine therefore can potentially coincide with and/or parallel those of mI in aggressive brain tumors. Further studies at 3T are warranted to investigate the role of glycine in aggressive pediatric brain tumors.

## CONCLUSIONS

Our study demonstrates that metabolic profiles as determined by MR spectroscopy can help predict molecular features of AT/RTs, potentially serving as in vivo biomarkers for the molecular subgroups. AT/RTs with and without expression of ASCL1 are currently treated using similar aggressive chemotherapy regimens, sometimes with added radiation therapy. However, it is expected that in the future, therapeutic options will be developed that will try to exploit unique biologic/molecular features in individual patients. A noninvasive method for early stratification would then be helpful clinically and is the ultimate goal for the current precision-based oncologic management of patients with brain tumors.

Disclosures: Benita Tamrazi—RELATED: Grant: American Society of Pediatric Neurology Research Grant, Comments: The grant supports research conducted for this article\*; UNRELATED: Consultancy: Bayer, Debra Hawes—UNRELATED: Employment: University of Southern California, Comments: primary employer Children's Hospital Los Angeles. Marvin Nelson—UNRELATED: Employment: Children's Hospi-

## REFERENCES

1. Ostrom QT, Gittleman H, Fulop J, et al. **CBTRUS Statistical Report: Primary Brain and Central Nervous System Tumors Diagnosed in the United States in 2008–2012.** *Neuro Oncol* 2015;17(Suppl 4): iv1–62 CrossRef Medline
2. Gurney J, Smith M, Bunin G. **CNS and miscellaneous intracranial and intraspinal neoplasms.** In: Ries L, Smith M, Gurney J, et al., eds. *Cancer Incidence and Survival among Children and Adolescents: United States SEER Program 1975–1995.* Bethesda: National Cancer Institute, SEER Program. NIH Pub. No. 99–4649; 1999
3. Biegel JA, Zhou JY, Rorke LB, et al. **Germ-line and acquired mutations of INI1 in atypical teratoid and rhabdoid tumors.** *Cancer Res* 1999;59:74–79 Medline
4. Versteeg I, Sévenet N, Lange J, et al. **Truncating mutations of hSNF5/INI1 in aggressive paediatric cancer.** *Nature* 1998;394: 203–06 CrossRef Medline
5. Richardson EA, Ho B, Huang A. **Atypical teratoid rhabdoid tumour: from tumours to therapies.** *J Korean Neurosurg Soc* 2018;61:302–11 CrossRef Medline
6. Ginn KF, Gajjar A. **Atypical teratoid rhabdoid tumor: current therapy and future directions.** *Front Oncol* 2012;2:114 CrossRef Medline
7. Torchia J, Golbourn B, Feng S, et al. **Integrated (epi)-genomic analyses identify subgroup-specific therapeutic targets in CNS rhabdoid tumors.** *Cancer Cell* 2016;30:891–908 CrossRef Medline
8. Johann PD, Erkek S, Zapatka M, et al. **Atypical teratoid/rhabdoid tumors are comprised of three epigenetic subgroups with distinct enhancer landscapes.** *Cancer Cell* 2016;29:379–93 CrossRef Medline
9. Nowak J, Nemes K, Hohm A, et al. **Magnetic resonance imaging surrogates of molecular subgroups in atypical teratoid/rhabdoid tumor.** *Neuro Oncol* 2018;20:1672–79 CrossRef Medline
10. Torchia J, Picard D, Lafay-Cousin L, et al. **Molecular subgroups of atypical teratoid rhabdoid tumours in children: an integrated genomic and clinicopathological analysis.** *Lancet Oncol* 2015;16: 569–82 CrossRef Medline
11. Eaton KW, Tooke LS, Wainwright LM, et al. **Spectrum of SMARCB1/INI1 mutations in familial and sporadic rhabdoid tumors.** *Pediatr Blood Cancer* 2011;56:7–15 CrossRef Medline
12. Panwalkar P, Clark J, Ramaswamy V, et al. **Immunohistochemical analysis of H3K27me3 demonstrates global reduction in group-A childhood posterior fossa ependymoma and is a powerful predictor of outcome.** *Acta Neuropathol* 2017;134:705–14 CrossRef Medline
13. Venneti S, Le P, Martinez D, et al. **Malignant rhabdoid tumors express stem cell factors, which relate to the expression of EZH2 and Id proteins.** *Am J Surg Pathol* 2011;35:1463–72 CrossRef Medline
14. Eaton BT, Hyatt AD, Brookes SM. **The replication of bluetongue virus.** *Curr Top Microbiol Immunol* 1990;162:89–118 Medline
15. Venneti S, Garimella MT, Sullivan LM, et al. **Evaluation of histone 3 lysine 27 trimethylation (H3K27me3) and enhancer of Zest 2 (EZH2) in pediatric glial and glioneuronal tumors shows decreased H3K27me3 in H3F3A K27M mutant glioblastomas.** *Brain Pathol* 2013;23:558–64 CrossRef Medline
16. FDA. **Multiple Endpoints in Clinical Trials.** 2017. <https://www.fda.gov/downloads/drugs/guidancecomplianceregulatoryinformation/guidances/ucm536750.pdf>. Accessed September 18, 2018
17. Hanna-El-Daher L, Braissant O. **Creatine synthesis and exchanges between brain cells: what can be learned from human creatine deficiencies and various experimental models?** *Amino Acids* 2016;48: 1877–95 CrossRef Medline
18. Braissant O, Henry H, Villard AM, et al. **Creatine synthesis and transport during rat embryogenesis: spatiotemporal expression of AGAT, GAMT and CT1.** *BMC Dev Biol* 2005;5:9 CrossRef Medline
19. Fisher SK, Novak JE, Agranoff BW. **Inositol and higher inositol phosphates in neural tissues: homeostasis, metabolism and functional significance.** *J Neurochem* 2002;82:736–54 CrossRef Medline
20. Isaacs RE, Bender AS, Kim CY, et al. **Osmotic regulation of myo-inositol uptake in primary astrocyte cultures.** *Neurochem Res* 1994; 19:331–38 CrossRef Medline
21. Brand A, Richter-Landsberg C, Leibfritz D. **Multinuclear NMR studies on the energy metabolism of glial and neuronal cells.** *Dev Neurosci* 1993;15:289–98 CrossRef Medline
22. Castillo M, Smith JK, Kwok L. **Correlation of myo-inositol levels and grading of cerebral astrocytomas.** *AJNR Am J Neuroradiol* 2000; 21:1645–49 Medline
23. Panigrahy A, Krieger MD, Gonzalez-Gomez I, et al. **Quantitative short echo time 1H-MR spectroscopy of untreated pediatric brain tumors: preoperative diagnosis and characterization.** *AJNR Am J Neuroradiol* 2006;27:560–72 Medline
24. Negendank W, Sauter R. **Intratumoral lipids in 1H MRS in vivo in brain tumors: experience of the Siemens cooperative clinical trial.** *Anticancer Res* 1996;16:1533–38 Medline
25. Kuesel AC, Sutherland GR, Halliday W, et al. **1H MRS of high grade astrocytomas: mobile lipid accumulation in necrotic tissue.** *NMR Biomed* 1994;7:149–55 CrossRef Medline
26. Rock JP, Hearshen D, Scarpace L, et al. **Correlations between magnetic resonance spectroscopy and image-guided histopathology, with special attention to radiation necrosis.** *Neurosurgery* 2002;51: 912–19, discussion 919–20 Medline
27. Kuesel AC, Donnelly SM, Halliday W, et al. **Mobile lipids and metabolic heterogeneity of brain tumours as detectable by ex vivo 1H MR spectroscopy.** *NMR Biomed* 1994;7:172–80 CrossRef Medline
28. Jain M, Nilsson R, Sharma S, et al. **Metabolite profiling identifies a key role for glycine in rapid cancer cell proliferation.** *Science* 2012; 336:1040–44 CrossRef Medline

# Intravoxel Incoherent Motion MR Imaging of Pediatric Intracranial Tumors: Correlation with Histology and Diagnostic Utility

K. Kikuchi, A. Hiwatashi, O. Togao, K. Yamashita, R. Kamei, D. Momosaka, N. Hata, K. Iihara, S.O. Suzuki, T. Iwaki, and H. Honda



## ABSTRACT

**BACKGROUND AND PURPOSE:** Intravoxel incoherent motion imaging, which simultaneously measures diffusion and perfusion parameters, is promising for brain tumor grading. However, intravoxel incoherent motion imaging has not been tested in children. The purpose of this study was to evaluate the correlation between intravoxel incoherent motion parameters and histology to assess the accuracy of intravoxel incoherent motion imaging for pediatric intracranial tumor grading.

**MATERIALS AND METHODS:** Between April 2013 and September 2015, 17 children (11 boys, 6 girls; 2 months to 15 years of age) with intracranial tumors were included in this retrospective study. Intravoxel incoherent motion parameters were fitted using 13 b-values for a biexponential model. The perfusion-free diffusion coefficient, pseudodiffusion coefficient, and perfusion fraction were measured in high- and low-grade tumors. These intravoxel incoherent motion parameters and the ADC were compared using the unpaired *t* test. The correlations between the intravoxel incoherent motion parameters and microvessel density or the MIB-1 index were analyzed using the Spearman correlation test. Receiver operating characteristic analysis was used to evaluate diagnostic performance.

**RESULTS:** The perfusion-free diffusion coefficient and ADC were lower in high-grade than in low-grade tumors (perfusion-free diffusion coefficient,  $0.85 \pm 0.40$  versus  $1.53 \pm 0.21 \times 10^{-3} \text{ mm}^2/\text{s}$ ,  $P < .001$ ; ADC,  $1.04 \pm 0.33$  versus  $1.60 \pm 0.21 \times 10^{-3} \text{ mm}^2/\text{s}$ ,  $P < .001$ ). The pseudodiffusion coefficient showed no difference between the groups. The perfusion fraction was higher in high-grade than in low-grade tumors ( $21.7 \pm 8.2\%$  versus  $7.6 \pm 4.3\%$ ,  $P < .001$ ). Receiver operating characteristic analysis found that the combined perfusion-free diffusion coefficient and perfusion fraction had the best diagnostic performance for tumor differentiation (area under the curve = 0.986).

**CONCLUSIONS:** Intravoxel incoherent motion imaging reflects tumor histology and may be a helpful, noninvasive method for pediatric intracranial tumor grading.

**ABBREVIATIONS:** D = perfusion-free diffusion coefficient; D\* = pseudodiffusion coefficient; f = perfusion fraction; IVIM = intravoxel incoherent motion; MVD = microvessel density; ROC = receiver operating characteristic; WHO = World Health Organization

Brain tumors are the second most common tumors in the pediatric population.<sup>1</sup> Each year, approximately 2500 children are diagnosed with brain tumors in the United States.<sup>2</sup>

Pediatric brain tumors are different from those of adults, with specific infantile subtypes and pathologic features that are widely heterogeneous.<sup>1</sup> Accurate preoperative diagnosis is beneficial for determining the appropriate therapeutic strategy; however, this remains challenging because of tumor variability and heterogeneity.

MR imaging plays an important role in the accurate diagnosis of brain tumors. Many attempts have been made to identify biomarkers on DWI<sup>3,4</sup> and PWI<sup>5,6</sup> that can be used to grade pediatric brain tumors and those found in adults.<sup>7,8</sup> In clinical practice, the ADC is usually calculated using 2 b-values (0 and 1000 s/mm<sup>2</sup>) and serves as a useful biomarker, reflecting cellular density.<sup>4,9</sup> Similar to the ADC, CBV and CBF are also useful biomarkers.<sup>5,6,10</sup> Measuring DSC-derived CBV requires an intravenous gadolinium-based contrast agent. Thus, this method can be difficult to implement in children.<sup>5</sup> DSC imaging often requires high-flow contrast injection by power injectors requiring large-bore intravenous access, which presents chal-

Received December 19, 2018; accepted after revision March 27, 2019.

From the Departments of Clinical Radiology (K.K., A.H., O.T., K.Y., R.K., D.M., H.H.), Neurosurgery (N.H., K.I.), and Neuropathology (S.O.S., T.I.), Graduate School of Medical Sciences, Kyushu University, Fukuoka, Japan.

This work was supported by JSPS KAKUNHI Grant Number 18H06164.

Paper previously presented, in part, at: Scientific Assembly and Annual Meeting of Radiological Society of North America, November 29 to December 4, 2015; Chicago, Illinois; No. VSPD11-03.

Please address correspondence to Akio Hiwatashi, MD, PhD, Department of Clinical Radiology, Graduate School of Medical Sciences, Kyushu University, 3-1-1 Maidashi, Higashi-ku, Fukuoka 812-8582, Japan; e-mail: hiwatashi@radiol.med.kyushu-u.ac.jp

 Indicates open access to non-subscribers at [www.ajnr.org](http://www.ajnr.org)

 Indicates article with supplemental on-line photos.

<http://dx.doi.org/10.3174/ajnr.A6052>

**Table 1: Patient demographics and tumor characteristics**

No.	Age, Sex	Histology				IVIM Parameters			
		Pathologic Diagnosis	WHO Grade	MIB-1 (%)	MVD	D ( $\times 10^{-3}$ mm <sup>2</sup> /s)	f (%)	D* ( $\times 10^{-3}$ mm <sup>2</sup> /s)	ADC ( $\times 10^{-3}$ mm <sup>2</sup> /s)
1	6 yr, M	Diffuse midline glioma, H3 K27M-mutant	IV	59.2	3.1	1.50	16.4	5.6	1.61
2	4 yr, M	Medulloblastoma, classic, histologically defined	IV	15.6	34.7	0.30	37.7	13.7	0.56
3	11 yr, M	Medulloblastoma, classic, histologically defined	IV	72.6	10.2	0.53	27.1	30.2	0.87
4	3 yr, M	Atypical teratoid/rhabdoid tumor	IV	50.0	11.0	0.86	14.1	9.0	0.98
5	2 yr, F	Anaplastic ependymoma	III	23.2	12.5	0.87	19.3	18.4	1.02
6	3 yr, M	Anaplastic ependymoma	III	19.6	4.3	1.15	16.8	5.5	1.30
7	6 yr, F	Anaplastic ependymoma	III	58.4	10.1	0.71	20.7	41.7	0.96
8	12 yr, M	Diffuse astrocytoma, IDH wild-type	II	2.1	2.1	1.22	8.4	33.3	1.29
9	1 yr, M	Pilocytic astrocytoma	I	4.4	5.8	1.45	3.5	5.5	1.50
10	3 yr, F	Pilocytic astrocytoma	I	6.7	4.0	1.82	7.2	10.2	1.88
11	3 yr, M	Pilocytic astrocytoma	I	8.0	4.7	1.52	10.0	48.3	1.64
12	6 yr, M	Pilocytic astrocytoma	I	6.0	3.2	1.72	4.2	58.4	1.78
13	11 yr, F	Pilocytic astrocytoma	I	4.0	5.6	1.55	5.5	12.8	1.61
14	2 yr, M	Subependymoma	I	0.1	1.9	1.58	5.1	11.3	1.60
15	2 mo, F	Choroid plexus papilloma	I	0.1	13.4	1.47	17.4	11.6	1.62
16	10 yr, M	Dysembryoplastic neuroepithelial tumor	I	2.7	1.3	1.76	10.9	4.3	1.82
17	15 yr, F	Ganglioglioma	I	1.0	1.1	1.21	3.6	22.4	1.24

Note.—IDH indicates isocitrate dehydrogenase.

lenges in young children and infants.<sup>5</sup> In contrast, measuring CBF with arterial spin-labeling does not require a contrast agent; this feature is beneficial for children.<sup>5,6</sup>

In 1988, Le Bihan et al<sup>11</sup> reported on an imaging technique depicting the molecular motion of water in tissue and used for distinguishing diffusion and perfusion components on the basis of the intravoxel incoherent motion (IVIM) model. The ADC contaminates contributions from capillary microcirculation because it cannot inherently separate the coherent motion of microperfusion with small b-values.<sup>11</sup> Therefore, the ADC is influenced by perfusion and could be overestimated, especially in hypervascular tumors. IVIM imaging fits the signal decay to a biexponential function using multiple b-values and then discriminates perfusion-free diffusion from capillary perfusion, allowing the simultaneous evaluation of diffusion and perfusion parameters. Furthermore, the perfusion-free diffusion coefficient (D) can reveal the state of diffusion more accurately than the ADC because it is based on a model that does not rely on the influence of perfusion. IVIM imaging has been used to evaluate malignant tumors in adults (eg, glioma or head, neck, rectal, or breast cancers),<sup>12–15</sup> and the IVIM perfusion parameter correlates with tumor histology in animals.<sup>16,17</sup> However, to date, few studies have evaluated IVIM imaging in children. The purpose of this study was to evaluate the correlation between IVIM parameters and histology to assess the accuracy of IVIM imaging for pediatric intracranial tumor grading.

## MATERIALS AND METHODS

This retrospective study was approved by our institutional review board, and the informed consent requirement was waived.

### Patients

The inclusion criteria for this study are outlined in On-line Fig 1. Twenty-one consecutive pediatric patients with intracranial tumors who underwent IVIM imaging examinations between April 2013 and September 2015 were identified. On the basis of the exclusion criteria (On-line Fig 1), 1 patient with an inadequate histologic specimen and 3 patients with non-neuroectodermal tumors were excluded. Therefore, data from 17 patients (11 boys,

6 girls; median age, 4 years; range, 2 months to 15 years) with 7 high-grade (World Health Organization [WHO] grades III and IV; 5 boys, 2 girls; median age, 4 years; range, 2–11 years) and 10 low-grade (WHO grades I and II; 6 boys, 4 girls; median age, 4.5 years; range, 2 months to 15 years) tumors were available for analysis.

### Histopathologic Diagnosis

Patient demographics and pathologic diagnoses based on the 2016 WHO classification<sup>18</sup> are shown in Table 1.

### IVIM MR Imaging

IVIM imaging was performed as previously described<sup>12,19</sup> using a 3T MR imaging scanner (Achieva 3T TX; Philips Healthcare, Best, the Netherlands) with an 8-channel head coil. The IVIM scans were obtained in the axial plane using a 2D single-shot spin-echo EPI diffusion sequence. We used 13 b-values (0, 10, 20, 30, 50, 80, 100, 200, 300, 400, 600, 800, and 1000 s/mm<sup>2</sup>) in 3 orthogonal directions. The other IVIM imaging parameters were as follows: TR/TE, 2500/82 ms; matrix, 128  $\times$  126 (reconstructed to 256  $\times$  256); NEX, 1; section thickness/gap, 5/1 mm; FOV, 230  $\times$  230 mm; number of sections, 11; sensitivity encoding factor, 1.5; and total scan time, 2 minutes 10 seconds. IVIM imaging was acquired before contrast agent injection. Several standard MR images (T1WI, T2WI, FLAIR, and contrast-enhanced T1WI) were also obtained for diagnostic purposes.

### Image Analysis

The IVIM parameters from each map with 13 b-values were generated using a commercially available workstation (SYNAPSE VINCENT; Fujifilm Medical, Tokyo, Japan).<sup>20</sup> For IVIM data analysis, the biexponential model was defined by the following equation:

$$1) \quad \frac{SI_b}{SI_0} = f \times \exp(-b \times D^*) + (1 - f) \times \exp(-b \times D),$$

where  $SI_0$  corresponds to the signal intensity without diffusion weighting ( $b = 0$  s/mm<sup>2</sup>) and  $SI_b$  is the  $SI$  acquired with different b-values. First, the  $D$  was determined from data with higher b-values ( $b = 300, 400, 600, 800,$  and  $1000$  s/mm<sup>2</sup>). When high b-val-

ues were used and the IVIM component was negligible, we used the following least-squares curve fit:

$$2) \quad \frac{SI_b}{SI_0} = \exp(-b \times D).$$

Second, the segmented method was used to calculate perfusion fraction ( $f$ ) according to the following equation:

$$3) \quad f = (SI_0 - SI_{inter}) / SI_0.$$

Here,  $SI_{inter}$  is the intersection point of the y-axis and a line through  $\log_e SI_{300}$  and  $\log_e SI_{1000}$ . Third, the pseudodiffusion coefficient ( $D^*$ ) was derived from the monoexponential fit to Equation (1). The ADC was also calculated with b-values of 0 and 1000 s/mm<sup>2</sup> using the following equation:

$$4) \quad \frac{SI_{1000}}{SI_0} = \exp(-b \times ADC).$$

Two board-certified neuroradiologists (K.K. and D.M., with 13 and 7 years of experience, respectively) evaluated each tumor using non-overlapping ROIs (area, >10 mm<sup>2</sup>). Three or more circular ROIs were placed on each tumor map. When placing the ROIs, we carefully avoided areas containing necrosis, hemorrhage, calcification, or blood vessels by referring to other sequences. The average ROI values were used as representative values for each parameter. D-map ROIs were copied to the corresponding ADC maps for comparison. Similarly, f-map ROIs were copied to the corresponding  $D^*$  maps.

### Histopathologic Evaluation

Histologic microvessel density (MVD) was evaluated as previously described.<sup>6</sup> Briefly, tissue sections were immunostained with anti-CD31 (Dako Japan, Tokyo, Japan). Stained vessels were viewed under a microscope using a  $\times 20$  objective field. The MVD was calculated using the following equation:

$$\text{MVD} = (\text{Anti-CD31 Immunostained Vascular Area}) \div (\text{Total Tissue Area}).$$

Three different fields were evaluated, and a mean representative value was calculated.

MIB-1 is a monoclonal antibody to the Ki-67 antigen, which is expressed in proliferating and dividing cells during all active phases of the cell cycle (ie, G<sub>1</sub>, S, G<sub>2</sub>, and M phases), but not during the G<sub>0</sub> phase.<sup>21</sup> The MIB-1 index is a marker of cell proliferation.<sup>22</sup> All specimens were evaluated by the Department of Neuropathology using this index.

### Statistical Analysis

We assessed the distribution of the data using the Shapiro-Wilk test. Each IVIM parameter (ie, D,  $D^*$ , and  $f$ ) and the ADC, MVD, and MIB-1 index were compared between high- and low-grade tumors using the unpaired  $t$  test. The D and ADC values were also compared within the high- and low-grade tumor groups by a paired  $t$  test. The Mann-Whitney  $U$  test was used when these data deviated from a normal distribution.

The relationships between the MIB-1 proliferation index and diffusion parameters (ie, D and ADC) were evaluated by the Pearson correlation test, and those between the MVD and IVIM perfusion

parameters (ie,  $D^*$  and  $f$ ) were evaluated by the Spearman correlation test.

The diagnostic performances of each IVIM parameter and the ADC were evaluated by receiver operating characteristic (ROC) curve analysis.

All the statistical analyses were performed using commercial software programs (JMP, Version 11.0.0; SAS Institute, Cary, North Carolina; GraphPad Prism 7.0, GraphPad Software, San Diego, California; MedCalc for Windows, Version 15.10.0, MedCalc Software, Mariakerke, Belgium). A  $P$  value < .05 was considered statistically significant.

## RESULTS

### Differentiation of High- and Low-Grade Tumors Using IVIM Parameters

Figure 1 and Table 2 summarize the parameter measurements for pediatric intracranial neuroectodermal tumor grading. The D and ADC were lower in high-grade than in low-grade tumors (D,  $0.85 \pm 0.40$  versus  $1.53 \pm 0.21 \times 10^{-3}$  mm<sup>2</sup>/s,  $P = .0003$ ; ADC,  $1.04 \pm 0.33$  versus  $1.60 \pm 0.21 \times 10^{-3}$  mm<sup>2</sup>/s,  $P = .0007$ ; Fig 1A and Table 2). The  $D^*$  showed wide variability and no significant differences between tumor grades ( $P = .8337$ ; Fig 1B and Table 2). The  $f$  was higher in high-grade than in low-grade tumors ( $21.7 \pm 8.2\%$  versus  $7.6 \pm 4.3\%$ ,  $P = .0003$ ; Fig 1C and Table 2).

### Comparison of the D and ADC Values

The D was significantly lower than the ADC in high- ( $P = .0010$ ) and low-grade ( $P = .0004$ ; Fig 1A) tumors. The percentage difference between the D and ADC was  $23.3\% \pm 22.0\%$  in the high-grade tumors and  $4.4\% \pm 18.9\%$  in the low-grade tumors.

### Relationship between the IVIM Parameters and MVD

On-line Figure 2 shows the relationship between each IVIM parameter and histology. There were strongly negative correlations between the MIB-1 proliferation index and D ( $r = -0.577$ ,  $P = .0154$ ; On-line Fig 2A) and ADC ( $r = -0.517$ ,  $P = .0334$ ; On-line Fig 2B). Notably, the correlation value of the D was higher than that of the ADC ( $-0.577$  versus  $-0.517$ ; On-line Fig 2A, -B). There was a strongly positive correlation between the  $f$  and MVD ( $\rho = 0.832$ ,  $P < .0001$ ; On-line Fig 2D). There was no significant correlation between the  $D^*$  and MVD ( $\rho = -0.088$ ,  $P = .7380$ ; On-line Fig 2C).

### ROC Analysis of Each IVIM Parameter for Grading Pediatric Intracranial Tumors

Table 3 and On-line Fig 3 show the ROC analysis results for the diagnostic performance of each IVIM parameter in differentiating high- and low-grade tumors. The combined D and  $f$  showed the best diagnostic performance (area under the curve = 0.986). The D, ADC, and  $f$  also showed robust diagnostic performance (area under the curve = 0.943, 0.907, and 0.957, respectively). The  $D^*$  showed low diagnostic performance (area under the curve = 0.536). The optimal diagnosis cutoff values for discriminating high- and low-grade tumors were  $\leq 1.50$  and  $> 16.4$  for the combined D and  $f$ , respectively ( $\leq 1.15$  for the D,  $\leq 1.02$  for the ADC, and  $> 14.1$  for the  $f$ ).

Figures 2 and 3 show representative patients with grades IV (medulloblastoma) and I (pilocytic astrocytoma) tumors, respectively.

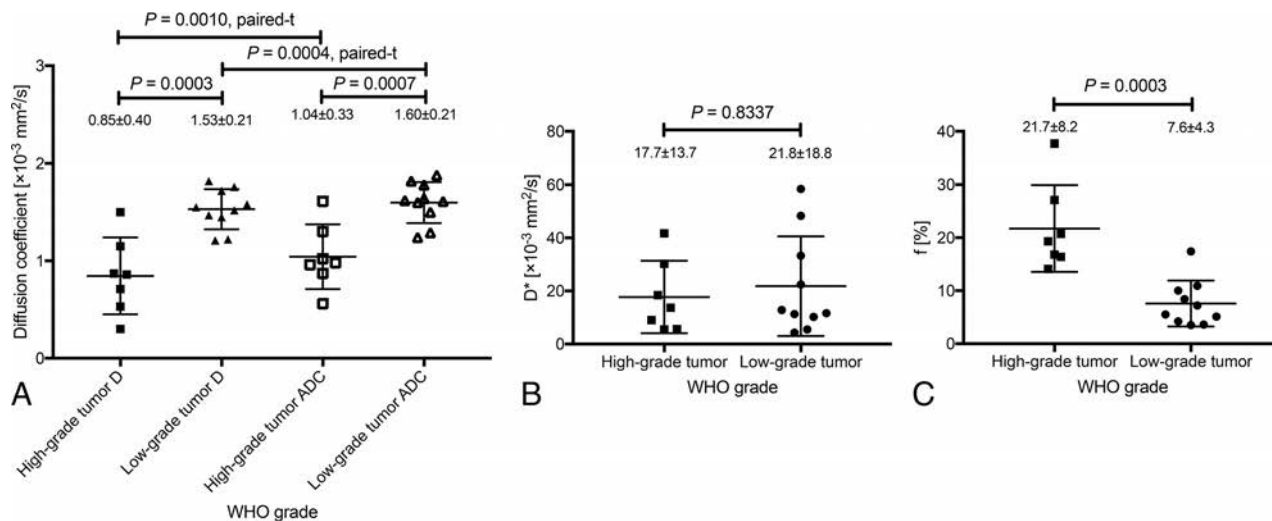


**FIG 1.** Comparison of the IVIM parameters of high- (WHO grades III and IV) and low-grade (WHO grades I and II) tumors. D and ADC were lower in high-grade than in low-grade tumors (D,  $0.85 \pm 0.40$  versus  $1.53 \pm 0.21 \times 10^{-3} \text{ mm}^2/\text{s}$ ,  $P = .0003$ ; ADC,  $1.04 \pm 0.33$  versus  $1.60 \pm 0.21 \times 10^{-3} \text{ mm}^2/\text{s}$ ,  $P = .0007$ ; A). D was significantly lower than the ADC in high- ( $P = .0010$ ) and low-grade ( $P = .0004$ ; A) tumors.  $D^*$  showed wide variability and no significant differences between the high- and low-grade groups ( $P = .8337$ ; B). The  $f$  was higher in high- than in low-grade tumors ( $21.7 \pm 8.2\%$  versus  $7.6 \pm 4.3\%$ ,  $P = .0003$ ; C).

**Table 2: Comparison of parameters between high- and low-grade tumors<sup>a</sup>**

Parameters	High-Grade Tumor	Low-Grade Tumor	P Value
D ( $\times 10^{-3} \text{ mm}^2/\text{s}$ )	0.30–1.50, 0.86, $0.85 \pm 0.40$	1.21–1.82, 1.54, $1.53 \pm 0.21$	.0003 <sup>b</sup>
ADC ( $\times 10^{-3} \text{ mm}^2/\text{s}$ )	0.56–1.61, 0.98, $1.04 \pm 0.33$	1.24–1.88, 1.62, $1.60 \pm 0.21$	.0007 <sup>b</sup>
$D^*$ ( $\times 10^{-3} \text{ mm}^2/\text{s}$ )	5.5–41.7, 13.7, $17.7 \pm 13.7$	4.3–58.4, 12.8, $21.8 \pm 18.8$	.8337 <sup>c</sup>
$f$ (%)	14.1–37.7, 19.3, $21.7 \pm 8.2$	3.5–17.4, 6.4, $7.6 \pm 4.3$	.0003 <sup>b</sup>
MVD (%)	3.1–34.7, 10.2, $12.3 \pm 10.5$	1.1–13.4, 3.6, $4.3 \pm 3.6$	.0431 <sup>c</sup>
MIB-1 (%)	15.6–72.6, 50.0, $42.7 \pm 22.8$	0.1–8.0, 3.4, $3.5 \pm 2.8$	<.0001 <sup>b</sup>

<sup>a</sup>Data are expressed as range, median, mean.

<sup>b</sup>Unpaired test.

<sup>c</sup>Mann-Whitney  $U$  test.

**Table 3: Diagnostic performance of parameters in differentiating high- and low-grade tumors**

Parameters	Cutoff Value	Sensitivity (%)	Specificity (%)	AUC
D ( $\times 10^{-3} \text{ mm}^2/\text{s}$ )	$\leq 1.15$	85.7	85.7	0.943
$D^*$ ( $\times 10^{-3} \text{ mm}^2/\text{s}$ )	$> 9.0$	42.9	22.9	0.536
$f$ (%)	$> 14.1$	100	90.0	0.957
ADC ( $\times 10^{-3} \text{ mm}^2/\text{s}$ )	$\leq 1.02$	71.4	71.4	0.907
D + $f$	$\leq 1.50, > 16.4$	100	90.0	0.986

**Note:**—AUC indicates area under the curve.

## DISCUSSION

We found significant correlations between the histology and IVIM parameters of different pediatric intracranial tumors. These results suggest that IVIM imaging reflects cell density and vascularity across different types of pediatric brain tumors. Our findings are consistent with those of previous studies showing a significant correlation between histology and IVIM parameters in animal models<sup>16,17</sup> and human patients.<sup>6,12,16,17</sup> To our knowledge, no previous study has evaluated the correlation between the IVIM parameters and the histology of intracranial tumors in children. Furthermore, we demonstrated that both the diffusion and perfusion parameters measured on IVIM imaging are useful for grading intracranial neuroectodermal tumors in pediatric patients.

Both of the diffusion parameters (ie, D and ADC) demonstrated good sensitivity and specificity for grading pediatric intra-

cranial tumors. Diffusion parameters reflect the movement of water molecules, which is hindered in some pathologic states (eg, intracellular edema). The ADC has been reported to have high sensitivity in detecting cell density.<sup>23–25</sup> The increased number of cell membranes in tumors leads to narrowing of the interstitial space as well as the reduction in the size of the intracellular space, which results in decreased water movement. Thus, the ADC has been used to evaluate cell density in many types of cancer. In previous studies, the ADC was typically calculated using 2 b-values (ie, 0 and 1000 s/mm<sup>2</sup>).<sup>3,4,24</sup> However, in the present study, the D values were significantly lower than the ADC values in both tumor groups. Moreover, there was a 23.3% difference between the D and ADC in high-grade tumors. This

difference most likely reflects the increased perfusion fraction of malignant tumors.<sup>12</sup> With small perfusion fractions, the following relationship applies:  $(ADC - D) \sim f/b$ . Applying the ADC and D values of low- and high-grade tumors found in this study to this relationship (ie,  $ADC - D$ ) produces values of  $1.9 \times 10^{-4} \text{ mm}^2/\text{s}$  (high-grade tumors) and  $0.6 \times 10^{-4} \text{ mm}^2/\text{s}$  (low-grade tumors). These values are very close to the  $f/b$  ( $b = 1000 \text{ s/mm}^2$ ) values of  $2.2 \times 10^{-4} \text{ mm}^2/\text{s}$  and  $0.8 \times 10^{-4} \text{ mm}^2/\text{s}$  for high- and low-grade tumors, respectively.

These findings provide strong support for the results and validate the method. Furthermore, the correlation value for the MIB-1 proliferation index and D was higher than for the MIB-1 proliferation index and ADC. This result indicates that D more precisely reflects the tumor cell density than the ADC. We also demonstrated that D had better diagnostic performance than the

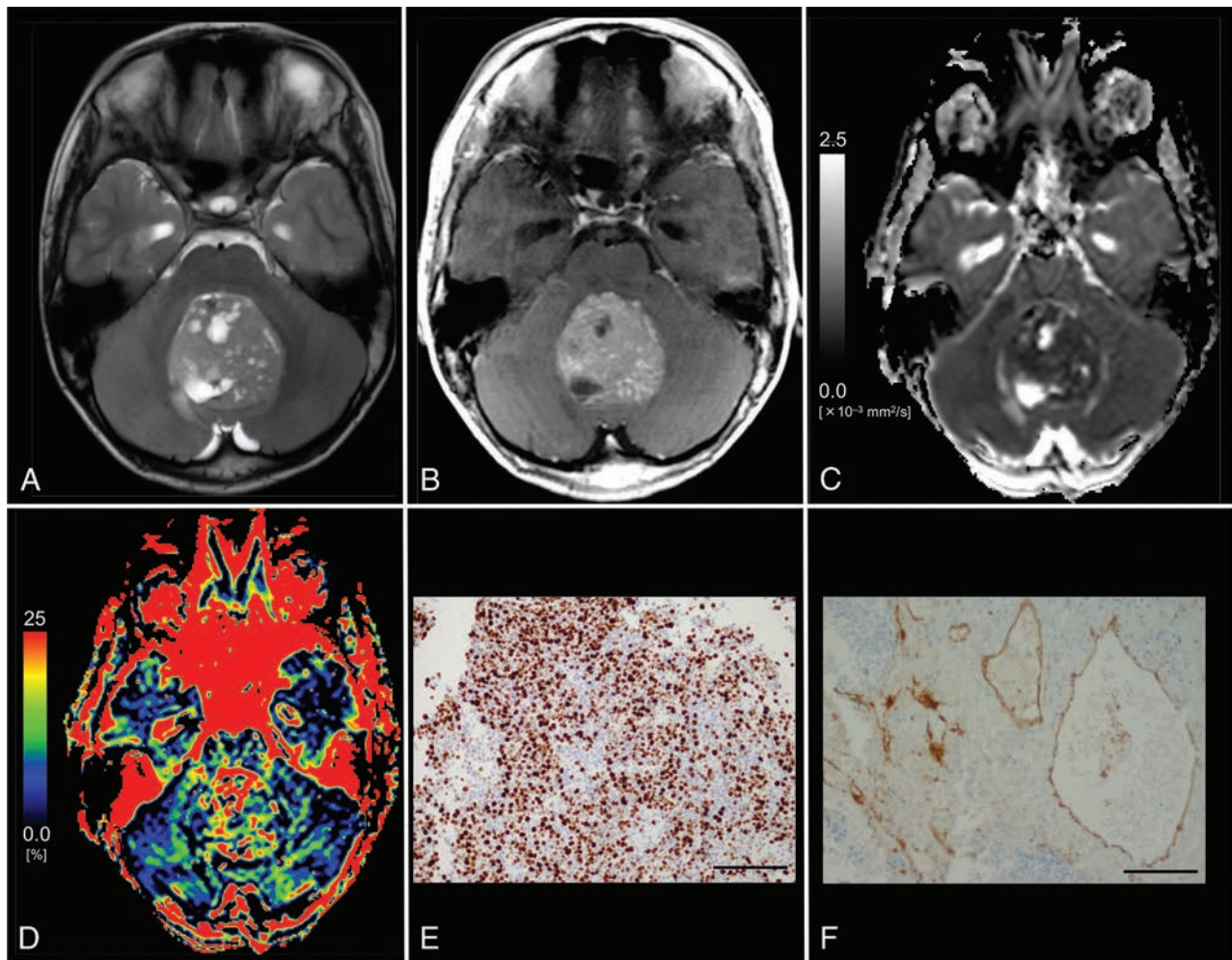


**FIG 2.** Images from an 11-year-old boy with histologically defined classic medulloblastoma (WHO grade IV). *A*, T2WI shows a heterogeneous, hyperintense mass in the vermis. *B*, Contrast-enhanced T1WI shows heterogeneous enhancement of the tumor. *C*, The D map shows the low D value ( $0.53 \times 10^{-3} \text{ mm}^2/\text{s}$ ) of the lesion, which is lower than the cutoff value ( $\leq 1.15 \times 10^{-3} \text{ mm}^2/\text{s}$ ; Table 3). *D*, The f map shows the f value (27.1%) of the lesion, which is higher than the cutoff value ( $>14.1\%$ ; Table 3). *E*, MIB-1 staining reveals a high MIB-1 index (72.6%). *F*, Immunohistochemical staining for anti-CD31 shows a high MVD (10.2%). Bar = 100  $\mu\text{m}$ .

ADC for differentiating high- and low-grade tumors. In this study, the ADC derived using a pair of b-values had acceptable diagnostic performance for grading; however, the diagnostic performance accuracy using D was an improvement over the conventional ADC.

Of the perfusion parameters, f may reflect tumor vascularity. In general, malignant tumors, in particular gliomas, are hypervascular. Hypervascularity is another important consideration for the histopathologic diagnosis of tumors because malignancy progression is accompanied by neoangiogenesis.<sup>26</sup> We demonstrated that the MVD reflects neoangiogenesis progression and its measured values correlated closely with those of f. The f was higher in high-grade than in low-grade tumors, a finding consistent with previous IVIM studies in adults.<sup>12,13</sup> Our study may be the first to demonstrate the value of IVIM imaging in pediatric patients with intracranial neuroectodermal tumors. Many researchers have used arterial spin-labeling to grade pediatric tumors because this method can evaluate cerebral blood flow without a contrast agent. Similar to arterial spin-labeling, f can also be measured without contrast agent.

This noninvasive feature is useful for children. However, D\* was not helpful for tumor grading. This finding has been previously reported in adult IVIM studies.<sup>12,19</sup> Moreover, other studies have suggested that D\* is poorly reproducible<sup>27,28</sup> and could be substantially affected by cardiac motion.<sup>29</sup> The cardiac-gating technique may improve D\* assessment in tumors.<sup>30</sup>

The combined D and f had the best diagnostic performance of all parameters investigated in our study. Combining D and f increased the area under the curve compared with each parameter alone. In combination, these 2 parameters can be used to evaluate different pathologic features of intracranial tumors. For example, some infantile tumors have high vascularity and low cell density (ie, hemangioblastoma or choroid plexus papilloma). IVIM imaging can simultaneously evaluate both diffusion and perfusion parameters in the same anatomic space; this feature improves diagnostic accuracy in such tumors. However, it is still difficult to differentiate high-grade tumors, such as medulloblastoma and atypical teratoid/rhabdoid tumor, which have the same pattern of high vascularity and cell density. In

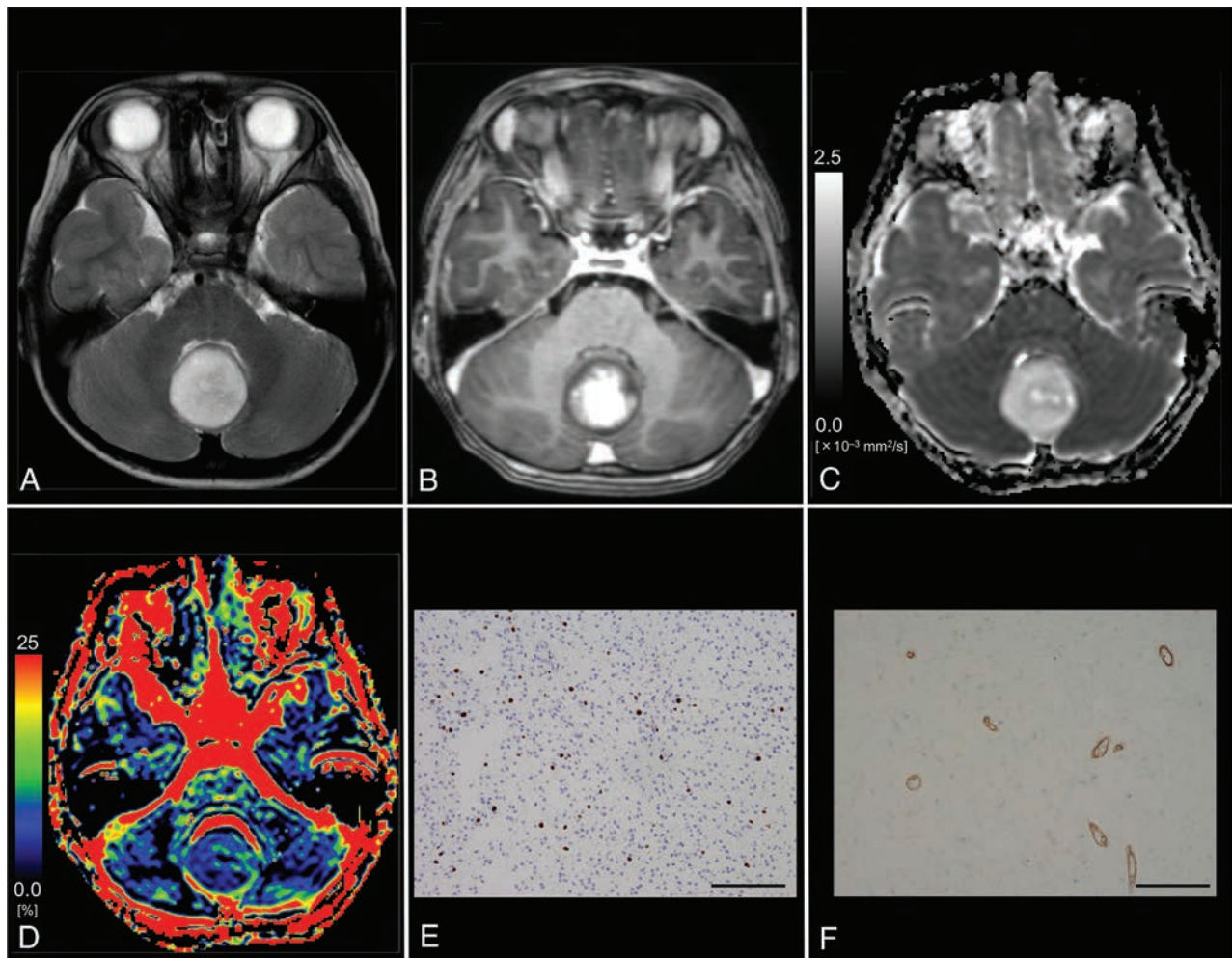


**FIG 3.** Images from a 6-year-old boy with pilocytic astrocytoma (WHO grade I). *A*, T2WI shows a homogeneous, hyperintense mass in the vermis. *B*, Contrast-enhanced T1WI shows mild, heterogeneous enhancement of the tumor. *C*, The D map shows the high D value ( $1.72 \times 10^{-3} \text{ mm}^2/\text{s}$ ) of the lesion, which is higher than the cutoff value ( $\leq 1.15 \times 10^{-3} \text{ mm}^2/\text{s}$ ; Table 3). *D*, The f map shows the low f value (4.2%) of the lesion, which is lower than the cutoff value ( $>14.1\%$ ; Table 3). *E*, MIB-1 staining reveals a low MIB-1 index (6.0%). *F*, Immunohistochemical staining for anti-CD31 reveals a low MVD (3.2%). Bar = 100  $\mu\text{m}$ .

such cases, basic information (ie, tumor location and patient age) is essential.

A strength of this study was that histologic diagnoses were available for all patients. However, this study also had some limitations. First, the sample size was very small, especially for patients with grade II glioma ( $n = 1$ ). Second, the ROI analyses were subjective, which may have introduced selection bias. However, in clinical practice, ROI analysis is often used for diagnosis.<sup>6,12,19</sup> Automatic tumor segmentation, which involves computer-aided segmentation and histogram analysis, could help address this issue. Third, the IVIM model used in this study does not account for non-Gaussian diffusion effects, which may lead to the overestimation of  $f$ .<sup>15</sup> Non-Gaussian fitting may improve the accuracy of  $f$ , especially with very high  $b$ -values. Fourth, we used only 3 perpendicular directions for diffusion encoding. In anisotropic tissues, (eg, white matter), anisotropic analysis via the diffusion tensor imaging method requires the use of at least 6 directions; however, in clinical practice, DWI averaged over 3 directions is often used during the diagnostic process.

## CONCLUSIONS

IVIM imaging reflected histology, which suggests that it may be a helpful noninvasive diagnostic method for intracranial neuroectodermal tumor grading in children.

Disclosures: Kazufumi Kikuchi—RELATED: Grant: Japan Society for the Promotion of Science KAKENHI, Comments: grant No. JP 18H06164.

## REFERENCES

- Pollack IF. Brain tumors in children. *N Engl J Med* 1994;331:1500–07 CrossRef Medline
- Gajjar A, Packer RJ, Foreman NK, et al. Children's Oncology Group's 2013 blueprint for research: central nervous system tumors. *Pediatr Blood Cancer* 2013;60:1022–26 CrossRef Medline
- Gauvain KM, McKinstry RC, Mukherjee P, et al. Evaluating pediatric brain tumor cellularity with diffusion-tensor imaging. *AJR Am J Roentgenol* 2001;177:449–54 CrossRef Medline
- Tzika AA, Zarifi MK, Goumnerova L, et al. Neuroimaging in pediatric brain tumors: Gd-DTPA-enhanced, hemodynamic, and diffusion MR imaging compared with MR spectroscopic imaging. *AJNR Am J Neuroradiol* 2002;23:322–33 Medline
- Yeom KW, Mitchell LA, Lober RM, et al. Arterial spin-labeled per-  
*AJNR Am J Neuroradiol* 40:878–84 May 2019 www.ajnr.org 883

- fusion of pediatric brain tumors. *AJNR Am J Neuroradiol* 2014;35:395–401 [CrossRef Medline](#)
6. Kikuchi K, Hiwatashi A, Togao O, et al. Correlation between arterial spin-labeling perfusion and histopathological vascular density of pediatric intracranial tumors. *J Neurooncol* 2017;135:561–69 [CrossRef Medline](#)
  7. Chang YW, Yoon HK, Shin HJ, et al. MR imaging of glioblastoma in children: usefulness of diffusion/perfusion-weighted MRI and MR spectroscopy. *Pediatr Radiol* 2003;33:836–42 [CrossRef Medline](#)
  8. Huisman TA, Sorensen AG. Perfusion-weighted magnetic resonance imaging of the brain: techniques and application in children. *Eur Radiol* 2004;14:59–72 [Medline](#)
  9. Sugahara T, Korogi Y, Kochi M, et al. Usefulness of diffusion-weighted MRI with echo-planar technique in the evaluation of cellularity in gliomas. *J Magn Reson Imaging* 1999;9:53–60 [CrossRef Medline](#)
  10. Sugahara T, Korogi Y, Kochi M, et al. Correlation of MR imaging-determined cerebral blood volume maps with histologic and angiographic determination of vascularity of gliomas. *AJR Am J Roentgenol* 1998;171:1479–86 [CrossRef Medline](#)
  11. Le Bihan D, Breton E, Lallemand D, et al. Separation of diffusion and perfusion in intravoxel incoherent motion MR imaging. *Radiology* 1988;168:497–505 [CrossRef Medline](#)
  12. Togao O, Hiwatashi A, Yamashita K, et al. Differentiation of high-grade and low-grade diffuse gliomas by intravoxel incoherent motion MR imaging. *Neuro Oncol* 2016;18:132–41 [CrossRef Medline](#)
  13. Sumi M, Nakamura T. Head and neck tumors: assessment of perfusion-related parameters and diffusion coefficients based on the intravoxel incoherent motion model. *AJNR Am J Neuroradiol* 2013;34:410–16 [CrossRef Medline](#)
  14. Surov A, Meyer HJ, Höhn AK, et al. Correlations between intravoxel incoherent motion (IVIM) parameters and histological findings in rectal cancer: preliminary results. *Oncotarget* 2017;8:21974–83 [CrossRef Medline](#)
  15. Iima M, Yano K, Kataoka M, et al. Quantitative non-Gaussian diffusion and intravoxel incoherent motion magnetic resonance imaging: differentiation of malignant and benign breast lesions. *Invest Radiol* 2015;50:205–11 [CrossRef Medline](#)
  16. Iima M, Reynaud O, Tsurugizawa T, et al. Characterization of glioma microcirculation and tissue features using intravoxel incoherent motion magnetic resonance imaging in a rat brain model. *Invest Radiol* 2014;49:485–90 [CrossRef Medline](#)
  17. Lee HJ, Rha SY, Chung YE, et al. Tumor perfusion-related parameter of diffusion-weighted magnetic resonance imaging: correlation with histological microvessel density. *Magn Reson Med* 2014;71:1554–58 [CrossRef Medline](#)
  18. Louis D, Ohgaki H, Wiestler O, et al. **WHO Classification of Tumours of the Central Nervous System, Revised**. Lyon: International Agency for Research on Cancer; 2016
  19. Yamashita K, Hiwatashi A, Togao O, et al. Diagnostic utility of intravoxel incoherent motion MR imaging in differentiating primary central nervous system lymphoma from glioblastoma multiforme. *J Magn Reson Imaging* 2016;44:1256–61 [CrossRef Medline](#)
  20. Mikayama R, Yabuuchi H, Sonoda S, et al. Comparison of intravoxel incoherent motion diffusion-weighted imaging between turbo spin-echo and echo-planar imaging of the head and neck. *Eur Radiol* 2018;28:316–24
  21. Gerdes J, Lemke H, Baisch H, et al. Cell cycle analysis of a cell proliferation-associated human nuclear antigen defined by the monoclonal antibody Ki-67. *J Immunol* 1984;133:1710–15 [Medline](#)
  22. McCormick D, Chong H, Hobbs C, et al. Detection of the Ki-67 antigen in fixed and wax-embedded sections with the monoclonal antibody MIB1. *Histopathology* 1993;22:355–60 [CrossRef Medline](#)
  23. Lyng H, Haraldseth O, Rofstad EK. Measurement of cell density and necrotic fraction in human melanoma xenografts by diffusion weighted magnetic resonance imaging. *Magn Reson Med* 2000;43:828–36 [CrossRef Medline](#)
  24. Chen L, Liu M, Bao J, et al. The correlation between apparent diffusion coefficient and tumor cellularity in patients: a meta-analysis. *PLoS One* 2013;8:e79008 [CrossRef Medline](#)
  25. Togao O, Doi S, Kuro-o M, et al. Assessment of renal fibrosis with diffusion-weighted MR imaging: study with murine model of unilateral ureteral obstruction. *Radiology* 2010;255:772–80 [CrossRef Medline](#)
  26. Winkler F, Kienast Y, Fuhrmann M, et al. Imaging glioma cell invasion in vivo reveals mechanisms of dissemination and peritumoral angiogenesis. *Glia* 2009;57:1306–15 [CrossRef Medline](#)
  27. Andreou A, Koh DM, Collins DJ, et al. Measurement reproducibility of perfusion fraction and pseudodiffusion coefficient derived by intravoxel incoherent motion diffusion-weighted MR imaging in normal liver and metastases. *Eur Radiol* 2013;23:428–34 [CrossRef Medline](#)
  28. Meeus EM, Novak J, Withey SB, et al. Evaluation of intravoxel incoherent motion fitting methods in low-perfused tissue. *J Magn Reson Imaging* 2017;45:1325–34 [CrossRef Medline](#)
  29. Federau C, Hagmann P, Maeder P, et al. Dependence of brain intravoxel incoherent motion perfusion parameters on the cardiac cycle. *PLoS One* 2013;8:e72856 [CrossRef Medline](#)
  30. Habib J, Auer DP, Morgan PS. A quantitative analysis of the benefits of cardiac gating in practical diffusion tensor imaging of the brain. *Magn Reson Med* 2010;63:1098–103 [CrossRef Medline](#)

# Brain and CSF Volumes in Fetuses and Neonates with Antenatal Diagnosis of Critical Congenital Heart Disease: A Longitudinal MRI Study

 N.H.P. Claessens,  N. Khalili,  I. Isgum,  H. ter Heide,  T.J. Steenhuis,  E. Turk,  N.J.G. Jansen,  L.S. de Vries,  J.M.P.J. Breur,  R. de Heus, and  M.J.N.L. Benders



## ABSTRACT

**BACKGROUND AND PURPOSE:** Fetuses and neonates with critical congenital heart disease are at risk of delayed brain development and neurodevelopmental impairments. Our aim was to investigate the association between fetal and neonatal brain volumes and neonatal brain injury in a longitudinally scanned cohort with an antenatal diagnosis of critical congenital heart disease and to relate fetal and neonatal brain volumes to postmenstrual age and type of congenital heart disease.

**MATERIALS AND METHODS:** This was a prospective, longitudinal study including 61 neonates with critical congenital heart disease undergoing surgery with cardiopulmonary bypass <30 days after birth and MR imaging of the brain; antenatally (33 weeks postmenstrual age), neonatal preoperatively (first week), and postoperatively (7 days postoperatively). Twenty-six had 3 MR imaging scans; 61 had at least 1 fetal and/or neonatal MR imaging scan. Volumes (cubic centimeters) were calculated for total brain volume, unmyelinated white matter, cortical gray matter, cerebellum, extracerebral CSF, and ventricular CSF. MR images were reviewed for ischemic brain injury.

**RESULTS:** Total fetal brain volume, cortical gray matter, and unmyelinated white matter positively correlated with preoperative neonatal total brain volume, cortical gray matter, and unmyelinated white matter ( $r = 0.5\text{--}0.58$ ); fetal ventricular CSF and extracerebral CSF correlated with neonatal ventricular CSF and extracerebral CSF ( $r = 0.64$  and  $0.82$ ). Fetal cortical gray matter, unmyelinated white matter, and the cerebellum were negatively correlated with neonatal ischemic injury ( $r = -0.46$  to  $-0.41$ ); fetal extracerebral CSF and ventricular CSF were positively correlated with neonatal ischemic injury ( $r = 0.40$  and  $0.23$ ). Unmyelinated white matter:total brain volume ratio decreased with increasing postmenstrual age, with a parallel increase of cortical gray matter:total brain volume and cerebellum:total brain volume. Fetal ventricular CSF:intracranial volume and extracerebral CSF:intracranial volume ratios decreased with increasing postmenstrual age; however, neonatal ventricular CSF:intracranial volume and extracerebral CSF:intracranial volume ratios increased with postmenstrual age.

**CONCLUSIONS:** This study reveals that fetal brain volumes relate to neonatal brain volumes in critical congenital heart disease, with a negative correlation between fetal brain volumes and neonatal ischemic injury. Fetal brain imaging has the potential to provide early neurologic biomarkers.

**ABBREVIATIONS:** CGM = cortical gray matter; CHD = congenital heart disease; ECSF = extracerebral CSF; ICV = intracranial volume; PMA = postmenstrual age; TBV = total brain volume; UWM = unmyelinated white matter; VCSF = ventricular CSF; WMI = white matter injury

Neurologic comorbidities are prevalent in neonates undergoing open heart surgery with the use of cardiopulmonary bypass for critical congenital heart disease (CHD) in the first weeks of life.<sup>1</sup> Ischemic brain injury is common before and after the surgical procedure and is associated with neurodevelopmental disabilities throughout school age.<sup>2,3</sup> In addition, delayed brain

growth with suggested antenatal onset has been reported in those with critical CHD.<sup>4,5</sup>

Antenatal studies have shown fetuses with critical CHD to demonstrate progressively reduced brain growth with enlarged CSF spaces compared with healthy fetuses.<sup>6</sup> Smaller brain volumes in fetuses with critical CHD are thought to be the result of reduced antenatal cerebral oxygen delivery and cerebral oxygen

Received November 11, 2018; accepted after revision February 27, 2019.

From the Departments of Neonatology (N.H.P.C., E.T., L.S.d.v., M.J.N.L.B.), Pediatric Cardiology (N.H.P.C., H.t.H., T.J.S., J.M.P.J.B.), Pediatric Intensive Care (N.H.P.C., N.J.G.J.), and Obstetrics (R.d.H.), Wilhelmina Children's Hospital, Utrecht, the Netherlands; Image Sciences Institute (N.K., I.I.), University Medical Center Utrecht, Utrecht, the Netherlands; and Department of Pediatrics (N.J.G.J.), Beatrix Children's Hospital, University Medical Center Groningen, Groningen, the Netherlands.

Roel de Heus and Manon J.N.L. Benders share last authorship.

Please address correspondence to Nathalie Claessens, MD, PhD, Department of Neonatology, University Medical Centre Utrecht, KE 04.123.1, PO Box 85090, 3508 AB Utrecht, the Netherlands; e-mail: n.h.p.claessens-2@umcutrecht.nl; @UMC utrecht; @hetWKZ

 Indicates article with supplemental on-line appendix and table.

 Indicates article with supplemental on-line photo.

<http://dx.doi.org/10.3174/ajnr.A6021>



**FIG 1.** Fetal and neonatal brain tissue segmentation. Coronal T2-weighted segmented fetal and neonatal image of the same individual with transposition of the great arteries at 30 weeks of gestation and before the operation.

consumption, a consequence of the anatomic changes from the cardiac defect.<sup>5,7,8</sup> The extent to which delayed fetal brain growth is transient or persists into the neonatal period remains undescribed. Revealing the association between fetal and neonatal delayed brain growth and acquired neonatal brain injury provides important information for the potential use of fetal brain imaging parameters as biomarkers for neurologic outcome in infants with critical CHD. This would also allow future implementation of interventions for improving brain growth before birth.

Using a prospective, longitudinal design, we investigated the correlation between fetal and neonatal preoperative and postoperative brain and CSF volumes, and the correlation of fetal brain and CSF volumes with neonatal ischemic brain injury. Our secondary aim was to examine trajectories of brain and CSF volumes in relation to postmenstrual age (PMA) during the third trimester of gestation and first weeks after birth in different cardiac defects.

## MATERIALS AND METHODS

This was a prospective, longitudinal observational cohort study.

### Study Population

Between May 2016 and December 2017, fetuses with an antenatal diagnosis of critical CHD requiring open heart surgery with the use of cardiopulmonary bypass at <30 days of life and referred to the Wilhelmina Children's Hospital Utrecht, a tertiary level hospital, underwent longitudinal MR imaging of the brain at 3 time points, antenatally (around 33 weeks PMA), neonatal preoperatively (within the first week of life), and neonatal postoperatively (around 7 days after the operation; range, 5–10 days). For this study, we excluded individuals with a genetic syndrome confirmed by antenatal karyotype or microarray (such as trisomy 21 or 22q11 deletion) or cerebral congenital malformations (such as corpus callosum agenesis). The local medical ethics board approved the study, and parental informed consent for the use of clinical data for research purposes was obtained.

### MR Imaging Acquisition

All fetuses and neonates were scanned on a 3T MR imaging system (Achieva, Philips Healthcare, Best, the Netherlands). Fetal and neonatal MR images were reviewed by 2 independent researchers for the presence of congenital anomalies, parenchymal hemorrhage, ischemic brain injury, and ventriculomegaly (atrial diameter, >10 mm).<sup>9,10</sup> Details are provided in the On-line Appendix.

### Quantitative 3D Volumetric Analysis

Fetal and neonatal coronal T2-weighted images were automatically segmented into different tissue classes: extracerebral CSF (ECSF), ventricular CSF (VCSF), unmyelinated white matter (UWM), cortical gray matter (CGM), cerebellum, basal ganglia and thalamus, brain stem, and myelinated white matter (Fig 1), using a further adjusted approach for neonatal MR images.<sup>11</sup> Volumes were calculated for all 8 tissue classes. All segmentations were manually checked for quality; no manual adjustments to the segmentations were made. Because basal ganglia, brain stem, and myelinated white matter were difficult to distinguish reliably on fetal T2-weighted images, these tissues were not taken into account for this study. Intracranial volume (ICV) was calculated as the sum of all 8 tissues classes; total brain volume (TBV), as the sum of UWM, CGM, cerebellum, basal ganglia and thalamus, brain stem, and myelinated white matter.

### Statistical Analysis

For statistical analysis, R statistical and computing software, Version 3.5.0 (<http://www.r-project.org/>) was used. Clinical variables were predominantly not normally distributed; therefore, nonparametric tests were performed and medians (25th/75th centiles) were presented for continuous data. Counts (percentage) were presented for categorical data. To test the differences in baseline characteristics between individuals with and without fetal MR imaging, we used Mann-Whitney *U* and Fisher exact tests. Univariable linear and nonlinear quadratic regression analysis was performed to examine the association between fetal brain and CSF volumes and neonatal (preoperative and postoperative) brain, and between CSF volumes and acquired neonatal brain injury, with correction for PMA at the time of scanning. Correlation coefficients with 95% confidence intervals were presented. Mixed-model analysis (R, nlme package 3.1–137) was performed to test the difference in brain and CSF volumes between different types of CHDs (fixed effect), including PMA (fixed effect), with the brain or CSF volume as dependent factors and individual subjects as random factors. A *P* value < .007 was considered significant with correction for multiple comparisons.

## RESULTS

### Study Population

In the study period, 71 neonates with an antenatal diagnosis of critical CHD were born, of whom 8 died without any MR imaging of the brain. Sixty-three neonates with an antenatal diagnosis of

**Table 1: Baseline and MRI characteristics of the study population<sup>a</sup>**

Characteristics	
Maternal characteristics (n = 29; fetal MRI)	
Maternal age (yr)	30.5 (27.8/35.3)
Maternal body mass index	22.8 (20.8/23.9)
Maternal smoking	3 (12%)
Placental weight (g)	455 (375/510)
Patient characteristics (n = 61; total study population)	
Female	18 (30)
CHD groups	
SVP	21 (34)
TGA	18 (30)
LVOTO	22 (36)
Antenatal CHD diagnosis	61 (100)
Twin	1 (2)
Genetic disorder	0 (0)
Additional congenital anomaly	3 (5)
Gestational age (wk)	39.1 (38.4/40.1)
Birth weight (g)	3320 (2970/3670)
Birth weight (z score)	-0.4 (-0.8/0.3)
Cesarean delivery	18 (31)
Neonatal death	6 (10)
MRI characteristics	
Fetal, PMA (wks)	33.4 (32.7/34.1)
Preoperative, days after birth	5 (3/6)
Preoperative, PMA (wks)	40.1 (39.1/41.0)
Postoperative, days after surgery	8 (7/9)
Postoperative, PMA (wks)	42.0 (40.6/43.0)

**Note:**—LVOTO indicates left ventricle outflow tract obstruction; SVP, single ventricle physiology; TGA, transposition of the great arteries.

<sup>a</sup> Median and interquartile range or number with percentage are shown. No significant differences were seen between the primary and secondary study populations.

critical CHD had cardiac surgery within 30 days after birth, of whom, 2 were excluded because of a genetic syndrome, leaving 61 neonates eligible for this study. Thirty-one neonates underwent all 3 MR imaging scans; however, 5 had poor fetal imaging quality, leaving 26 with all 3 MR imaging scans for the primary study aim. All 61 neonates were included for the secondary study aim: 26 plus an additional 21 with 2 MR imaging scans and 14 with 1 MR imaging scan (flowchart in On-line Figure). Baseline characteristics are presented in Table 1.

#### Fetal and Neonatal MR Imaging: Conventional Analysis

Two fetuses showed unilateral ventriculomegaly (atrial diameter, 10–15 mm). None of the fetuses showed parenchymal hemorrhage or ischemic brain injury.

At preoperative neonatal MR imaging, focal infarction was seen in 2 (8%) and WM injury (WMI) in 2 (8%). Punctate cerebellar hemorrhage was seen in 1 (4%). Cumulatively (at preoperative and postoperative MR imaging), focal infarction was present in 7 (28%) and WMI in 9 (38%). Hypoxic-ischemic watershed injury was not seen in any neonates.

#### Fetal Brain and CSF Volumes: Clinical Factors

Fetal UWM was positively associated with fetal CGM ( $r = 0.87$ ); fetal UWM, with fetal cerebellum ( $r = 0.60$ ); and fetal CGM, with fetal cerebellum ( $r = 0.56$ ). Fetal UWM:TBV (proportion of TBV occupied by UWM) was negatively associated with fetal CGM:TBV ( $r = -0.51$ ). Fetal VCSF and ECSF were negatively associated with fetal UWM:TBV ( $r = -0.39$  and  $-0.53$ , respectively).

Fetal brain and CSF volumes (corrected for PMA at scanning)

**Table 2: Association between fetal and neonatal MRI<sup>a</sup>**

Fetal Volume	Neonatal		
	Preoperative Volume	Postoperative Volume	Ischemic Brain Injury
TBV <sup>b</sup>	●	●	○
UWM <sup>b</sup>	●		□
CGM <sup>b</sup>	●	■	□
CB <sup>b</sup>	■		□
UWM:TBV <sup>c</sup>		●	■
CGM:TBV <sup>c</sup>	■		
CB:TBV <sup>c</sup>	●	●	■
TBV:ICV <sup>c</sup>	●	■	
VCSF <sup>c</sup>	●		
ECSF <sup>c</sup>	●	●	■
VCSF:ICV <sup>c</sup>	■	●	
ECSF:ICV <sup>c</sup>	●	■	

**Note:**—CB indicates cerebellum.

<sup>a</sup> Strength of correlation of fetal and neonatal preoperative volumes (first column); fetal and neonatal postoperative volumes (second column); fetal volumes and neonatal ischemic brain injury (third column). Square indicates moderate correlation (closed square,  $r = 0.3$ – $0.5$ ; open square  $r = -0.5$  to  $-0.3$ ). Circle indicates strong correlation (closed circle,  $r = 0.5$ – $0.8$ ; open circle,  $r = -0.8$  to  $-0.5$ ).

<sup>b</sup> Result of linear regression analysis with correction for PMA at scanning.

<sup>c</sup> Result of quadratic regression analysis. Correlation coefficient and 95% CI are in the On-line Table.

were not associated with maternal body mass index, maternal age, maternal smoking, placental weight, or birth weight z score (all  $P$  values  $> .007$  with Bonferroni correction for multiple comparisons). None of the mothers of the primary study population had preeclampsia or gestational diabetes.

#### Brain and CSF Volumes: Correlation between Fetal and Neonatal MR Imaging

Fetal volumes of CGM, UWM, and TBV correlated with preoperative neonatal volumes of CGM, UWM, and TBV, respectively (Table 2). Postoperatively, the association of fetal CGM and TBV with neonatal CGM and TBV, respectively, was still seen. Fetal VCSF, ECSF, VCSF:ICV, and ECSF:ICV correlated with preoperative neonatal VCSF, ECSF, VCSF:ICV, and ECSF:ICV, respectively. Postoperatively, the associations between fetal and neonatal MR imaging were still seen for ECSF and VCSF:ICV (Table 2 and On-line Table).

#### Fetal Brain and CSF Volumes: Correlation with Neonatal Ischemic Brain Injury

Baseline characteristics were not different between neonates with and without ischemic brain injury (data not shown). Both fetuses with antenatal ventriculomegaly had moderate-severe WMI before the operation (100%).

The fetal TBV, CGM, UWM, and cerebellum were negatively associated with the presence of neonatal (either preoperatively or postoperatively acquired) ischemic brain injury (Table 2), in which fetal ECSF was positively associated with neonatal ischemic brain injury. The rate of preoperative ischemic brain injury was low and consequently was not examined separately in relation to fetal brain and CSF volumes.

#### Fetal and Neonatal MR Imaging: Brain Volumes, PMA, and Type of CHD

For the secondary study aim, the total study population of 61 subjects was analyzed. ICV, TBV, UWM, CGM, and the cerebellum all showed a linear association with PMA (Fig 2). The pro-

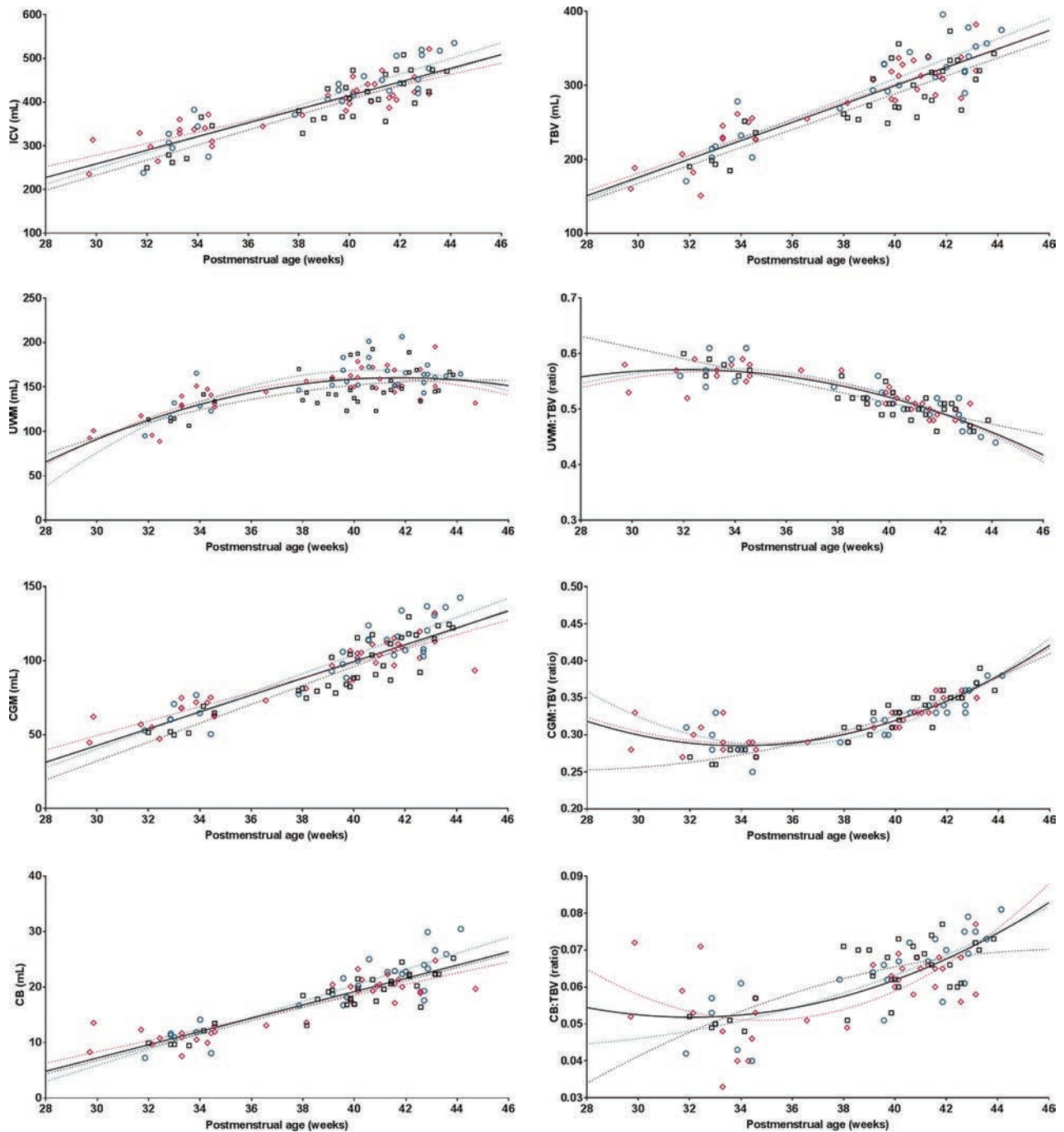


**FIG 2.** Fetal and neonatal brain volumes in relation to postmenstrual age. Plotted are brain volumes (y-axis) in relation to postmenstrual age at scanning (x-axis) for transposition of the great arteries (*pink diamonds*), left ventricle outflow tract obstruction (*green circles*), and single-ventricle physiology (*black squares*). Either the regression or quadratic line was fitted for each congenital heart defect separately (*dotted lines*), also as 1 line combining all subjects (*solid black line*).  $R^2$  values reflecting the goodness of fit: ICV, 0.76; TBV, 0.76; UWM, 0.53; CGM, 0.81; cerebellum, 0.79; CGM:TBV, 0.78; UWM:TBV, 0.77; cerebellum:TBV, 0.48.

portion of TBV occupied by UWM decreased with time, with a parallel increase of occupation of the TBV by CGM and the cerebellum. The proportions of VCSF: ICV and ECSF:ICV decreased during the fetal period with increasing PMA; however, it increased again in the neonatal period (Fig 3).

By means of mixed-model analysis, no differences in brain or CSF volumes were seen among CHD groups (all  $F$ -test  $P$  values  $> .007$ , with correction for multiple comparisons).

## DISCUSSION

Previous studies have reported smaller brain volumes in fetuses and neonates with critical CHD compared with healthy subjects. Linking longitudinal fetal and neonatal brain and CSF volumes, for the first time, this study reveals the strong relationship between brain volumes and postmenstrual age in individuals with critical CHD. Additionally, the results show a negative correlation between fetal brain volumes and neonatal ischemic brain injury.

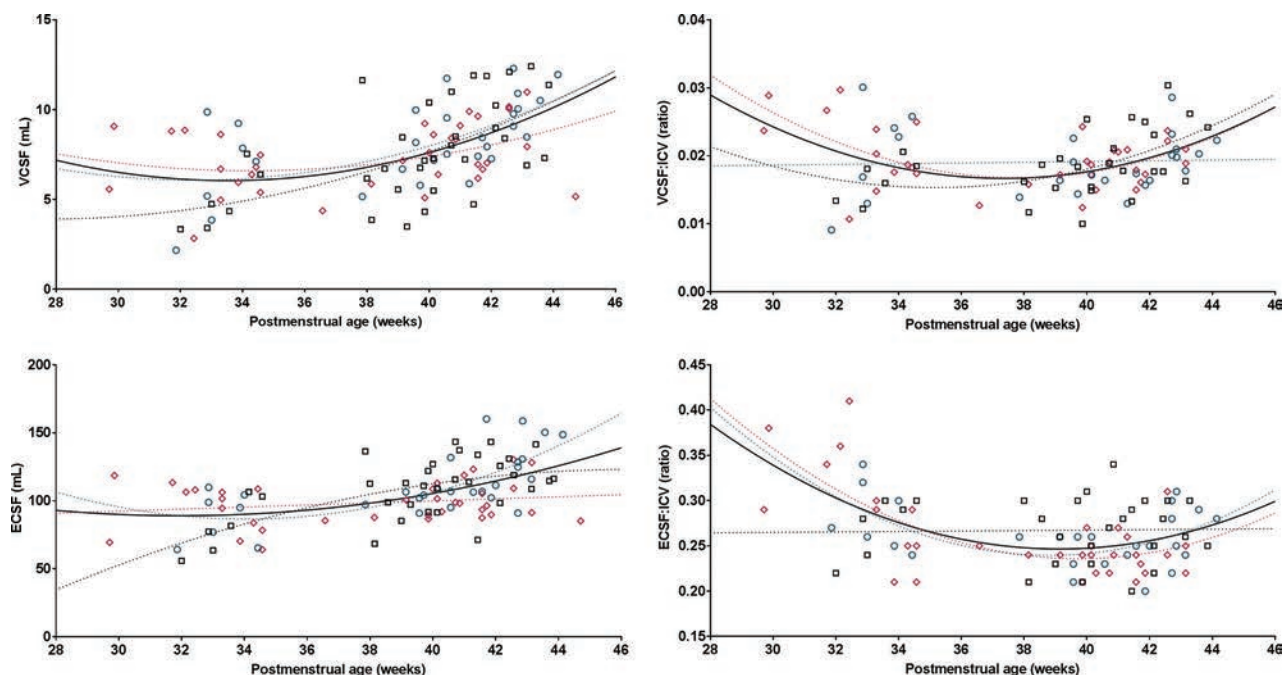


**FIG 3.** Fetal and neonatal CSF volumes in relation to postmenstrual age. Plotted are CSF volumes (y-axis) in relation to postmenstrual age at scanning (x-axis) for transposition of the great arteries (pink diamonds), left ventricle outflow tract obstruction (green circles), and single-ventricle physiology (black squares). Either the regression or quadratic line was fitted separately for each congenital heart defect (dotted lines), also as 1 line for all subjects (solid black line).  $R^2$  values reflecting the goodness of fit: VCSF, 0.27; ECSF, 0.27; VCSF:ICV, 0.14; ECSF:ICV, 0.24.

Revealing the association between fetal brain imaging parameters and neonatal brain abnormalities provides important information for the potential use of fetal brain imaging parameters to estimate neonatal neurologic findings in critical CHD.

In neonates with critical CHD, volumes of the largest brain structures occupying most of the total brain volume, ie, UWM, CGM, and cerebellum, correlated with the volumes measured in the same individuals around 33 weeks of gestation. The findings of this study support the hypothesis that neonatal brain volumes are the result of antenatal brain growth and strengthen the possibility of detecting delayed brain growth at an early stage, even before birth. In our study, the association of fetal UWM and CGM was stronger with preoperative neonatal UWM and CGM than with postoperative UWM and CGM. This finding suggests that growth of UWM and CGM after birth is dependent on other neonatal factors than antenatal brain growth alone.

In our study, the association between fetal and neonatal age was less strong for the cerebellum than it was for UWM and CGM. However, the proportion of fetal TBV occupied by the cerebellum was strongly associated with the proportion of preoperative and postoperative neonatal TBV occupied by the cerebellum. The cerebellum is the brain structure with the highest increase in volume between 30 and 40 weeks PMA in extremely preterm infants.<sup>12</sup> Previous studies have shown that in the third trimester of gestational age, cerebellar volume was comparable between fetuses with and without CHD,<sup>13,14</sup> whereas at term age, a reduction of 20% in the cerebellum has been observed in neonates with critical CHD.<sup>4</sup>

Together with the relative reduction in brain volumes with increasing gestation, a relative increase in CSF spaces has been described in fetuses with critical CHD compared with healthy

fetuses.<sup>6</sup> Larger CSF spaces are seen as an expression of brain underdevelopment.<sup>15</sup> In healthy fetuses, CSF volumes plateau late in the third trimester,<sup>16</sup> and the proportion of ICV occupied by CSF decreases during the third trimester from 0.4 to 0.1.<sup>6</sup> In our study, the proportion of ICV occupied by VCSF and ECSF was higher than 0.1 throughout the antenatal and neonatal period for all neonates with critical CHD. Absolute and proportional CSF volumes did decrease during the third trimester of gestation, to increase again in the neonatal period. In addition, the findings of our study revealed that increased absolute and proportional CSF volumes at fetal age did correlate with increased neonatal CSF volumes. This increase in CSF spaces seems abnormal and might be a sign of further brain underdevelopment or the result of brain tissue loss. Studies in older children with single-ventricle physiology have shown an association between larger CSF spaces and poorer neurodevelopment.<sup>17</sup>

Although it is becoming well-established that WM, CGM, and cerebellar volumes are smaller in fetuses and neonates with various types of critical CHD compared with healthy controls,<sup>4,6,13,14,18,19</sup> the contribution of these findings to neurodevelopment later in childhood remains largely unknown. Smaller neonatal brain volumes are associated with abnormal neonatal neurobehavior<sup>20</sup> and lower 6-year intelligence in children with critical CHD.<sup>3</sup> In adolescents with critical CHD, decreased TBV is strongly correlated with poorer cognitive and executive functioning.<sup>21</sup>

In our study, ischemic and hemorrhagic brain injury was not seen in any of the fetuses. This finding supports the common thought that acquired brain injury has its onset after birth, in the neonatal intensive care and surgical period. The rate of preoperative and new postoperative neonatal ischemic injury in our pop-

ulation is comparable with that in previous reports.<sup>1</sup> All individuals included in this study had antenatal CHD diagnosis, which has been suggested as a protective factor for preoperative neonatal ischemic brain injury.<sup>2</sup> In neonates with critical CHD, WMI and focal infarction are the most common forms of acquired brain injury, and especially WMI has been shown to be associated with poorer motor and cognitive outcomes in the long term.<sup>2,3</sup>

The results of this study revealed a correlation of smaller fetal TBV, UWM, CGM, and cerebellum with acquired neonatal ischemic brain injury (ie, moderate-severe WMI or focal infarction) in neonates with an antenatal diagnosis of critical CHD. Absolute fetal volumes of UWM, CGM, and the cerebellum (corrected for PMA) showed a stronger correlation with acquired neonatal brain injury than the proportion of TBV occupied by any of these brain structures. Previous studies have also suggested a link between neonatal brain underdevelopment and acquired neonatal brain injury.<sup>22,23</sup> However, our study cannot reveal whether there is a causal relationship between smaller brain volumes and acquired brain injury. Brain underdevelopment might be accompanied by an increased vulnerability of the brain to disturbances in cerebral blood flow and cerebral oxygen delivery during intensive care admission and cardiac surgery.

All critical CHD groups have reduced oxygen delivery compared with healthy controls, and this reduction in brain oxygen delivery is directly associated with smaller fetal and neonatal brain volumes.<sup>5,7</sup> Oxygen delivery is dependent on cerebral blood flow and blood oxygen content. As a result of the cardiac defect, cerebral blood flow is most severely altered in single-ventricle physiology and left-ventricle outflow tract obstruction, whereas cerebral blood oxygen content is lowest in transposition of the great arteries.<sup>24</sup> Despite these differences in antenatal cerebral circulatory disturbances, we found no differences in growth trajectories of brain volumes among these CHD groups, reflecting most critical cardiac defects. Smaller fetal TBV<sup>6</sup> and lower neonatal brain growth rate<sup>25</sup> have been described in single-ventricle physiology compared with other cardiac defects; however, most neonatal studies have shown comparable reductions in the volumes of UWM and CGM among transposition of the great arteries and single-ventricle physiology.<sup>4,18</sup> All individuals with critical CHD are at risk of reduced antenatal brain growth; however, other patient-related factors than the cardiac defect itself might determine the degree of brain underdevelopment.

This study is one of the first to explore the correlation between fetal and neonatal brain volumes using quantitative longitudinal MR imaging. This study provides important information for future research investigating whether there is a causal relationship between brain underdevelopment and brain injury, fetal brain underdevelopment as an early biomarker for neurodevelopmental outcomes, and potential strategies to improve antenatal brain growth.

This study has several limitations. First, postnatal CHD diagnosis increases the risk of preoperatively acquired ischemic brain injury, especially when low cardiac output syndrome is present. However, this population cannot be included in fetal MR imaging studies and was therefore not examined in this study. Second, absolute brain and CSF volumes are dependent on the MR imaging protocol and postimaging processing methods and are there-

fore difficult to compare among studies. Third, the subgroup sample size (by heterogeneity of CHD populations) limited the possibility of performing subgroup analysis. The subgroup analysis of fetal-neonatal brain volumes by PMA is at risk of type 2 errors, potentially not showing differences among the groups.

## CONCLUSIONS

Linking longitudinal fetal and neonatal brain and CSF volumes, this study reveals the strong relationship between brain volumes over postmenstrual age in individuals with critical CHD. Additionally, the results show a negative correlation between fetal brain volumes and neonatal ischemic brain injury. Combining these findings, this study suggests that fetal MR imaging can be used as an early biomarker to estimate neonatal neurologic findings in critical CHD.

## ACKNOWLEDGMENTS

The authors would like to thank Gabrielle van Iperen, Raymond Stegeman, and Felix Haas for their contributions to the brain imaging program, and the Congenital Heart Disease Life Span study group of the Wilhelmina Children's Hospital in Utrecht, which includes the Department of Neonatology, Department of Pediatric Intensive Care, Department of Obstetrics, Department of Pediatric Cardiology, Department of Pediatric Cardiothoracic Surgery, Department of Pediatric Anesthesiology, Department of Radiology, Department of Medical Psychology and Child Development, and Exercise Center.

Disclosures: Ivana Isgum—UNRELATED: Grants/Grants Pending: research grant funded by Nutricia Research, University Medical Center Utrecht, Utrecht University\*; Patents (Planned, Pending or Issued): I am an inventor of 1 accepted and 1 pending patent; Stock/Stock Options: I am a scientific founder and shareholder of Quantib-U B.V.; Linda S. de Vries—UNRELATED: Employment: Consultant Neonatologist at UMCU\*; Grants/Grants Pending: ZonMw grant for neonatal stroke\*; Payment for Lectures Including Service on Speakers Bureaus: yearly ultrasound course in London, Imperial College, sometimes honorarium for giving a lecture\*; Royalties: 3 books: Hellström-Westas L, de Vries LS, Rosen I. *An Atlas of Amplitude-Integrated EEGs in The Newborn*. 2nd ed, Informa Health, London, August 2008; Govaert P, de Vries LS. *An Atlas of Neonatal Brain Sonography*, 2nd ed (CDM 182–183), Mac Keith Press, ISBN: 978-1-898683-56-8, July 2010; Volpe's *Textbook Neurology of the Newborn*, Elsevier, 2017.\* \*Money paid to the Institution.

## REFERENCES

1. Claessens NH, Kelly CJ, Counsell SJ, et al. **Neuroimaging, cardiovascular physiology, and functional outcomes in infants with congenital heart disease.** *Dev Med Child Neurol* 2017;59:894–902 CrossRef Medline
2. Peyvandi S, Chau V, Guo T, et al. **Neonatal brain injury and timing of neurodevelopmental assessment in patients with congenital heart disease.** *J Am Coll Cardiol* 2018;71:1986–96 CrossRef Medline
3. Claessens NH, Algra SO, Ouwehand TL, et al; CHD Lifespan Study Group Utrecht. **Perioperative neonatal brain injury is associated with worse school-age neurodevelopment in children with critical congenital heart disease.** *Dev Med Child Neurol* 2018;60:1052–58 CrossRef Medline
4. von Rhein M, Buchmann A, Hagmann C, et al; Heart and Brain Research Group. **Severe congenital heart defects are associated with global reduction of neonatal brain volumes.** *J Pediatr* 2015;167:1259–63 e1 CrossRef Medline
5. Kelly CJ, Makropoulos A, Cordero-Grande L, et al. **Impaired development of the cerebral cortex in infants with congenital heart disease is correlated to reduced cerebral oxygen delivery.** *Sci Rep* 2017; 7:15088 CrossRef Medline
6. Limperopoulos C, Tworetzky W, McElhinney DB, et al. **Brain vol-**

- ume and metabolism in fetuses with congenital heart disease: evaluation with quantitative magnetic resonance imaging and spectroscopy. *Circulation* 2010;121:26–33 CrossRef Medline
7. Sun L, Macgowan CK, Sled JG, et al. **Reduced fetal cerebral oxygen consumption is associated with smaller brain size in fetuses with congenital heart disease.** *Circulation* 2015;131:1313–23 CrossRef Medline
  8. Lim JM, Kingdom T, Saini B, et al. **Cerebral oxygen delivery is reduced in newborns with congenital heart disease.** *J Thorac Cardiovasc Surg* 2016;152:1095–103 CrossRef Medline
  9. Garel C, Alberti C. **Coronal measurement of the fetal lateral ventricles: comparison between ultrasonography and magnetic resonance imaging.** *Ultrasound Obstet Gynecol* 2006;27:23–27 Medline
  10. Papile LA, Burstein J, Burstein R, et al. **Incidence and evolution of subependymal and intraventricular hemorrhage: a study of infants with birth weights less than 1,500 gm.** *J Pediatr* 1978;92:529–34 CrossRef Medline
  11. Moeskops P, Viergever MA, Mendrik AM, et al. **Automatic segmentation of MR brain images with a convolutional neural network.** *IEEE Trans Med Imaging* 2016;35:1252–61 CrossRef Medline
  12. Kersbergen KJ, Makropoulos A, Aljabar P, et al. **Longitudinal regional brain development and clinical risk factors in extremely pre-term infants.** *J Pediatr* 2016;178:93–100.e6 CrossRef Medline
  13. Schellen C, Ernst S, Gruber GM, et al. **Fetal MRI detects early alterations of brain development in tetralogy of Fallot.** *Am J Obstet Gynecol* 2015;213:392 e1–7 CrossRef Medline
  14. Andescavage N, Yarish A, Donofrio M, et al. **3-D volumetric MRI evaluation of the placenta in fetuses with complex congenital heart disease.** *Placenta* 2015;36:1024–30 CrossRef Medline
  15. Brossard-Racine M, du Plessis AJ, Vezina G, et al. **Prevalence and spectrum of in utero structural brain abnormalities in fetuses with complex congenital heart disease.** *AJNR Am J Neuroradiol* 2014;35:1593–99 CrossRef Medline
  16. Andescavage NN, DuPlessis A, McCarter R, et al. **Cerebrospinal fluid and parenchymal brain development and growth in the healthy fetus.** *Dev Neurosci* 2016;38:420–29 CrossRef Medline
  17. Heye KN, Knirsch W, Latal B, et al. **Reduction of brain volumes after neonatal cardiopulmonary bypass surgery in single-ventricle congenital heart disease before fontan completion.** *Pediatr Res* 2018;83:63–70 CrossRef Medline
  18. Claessens NH, Moeskops P, Buchmann A, et al. **Delayed cortical gray matter development in neonates with severe congenital heart disease.** *Pediatr Res* 2016;80:668–74 CrossRef Medline
  19. Clouchoux C, du Plessis AJ, Bouyssi-Kobar M, et al. **Delayed cortical development in fetuses with complex congenital heart disease.** *Cereb Cortex* 2013;23:2932–43 CrossRef Medline
  20. Owen M, Shevell M, Donofrio M, et al. **Brain volume and neurobehavior in newborns with complex congenital heart defects.** *J Pediatr* 2014;164:1121–27 e1 Medline
  21. von Rhein M, Buchmann A, Hagmann C, et al. **Brain volumes predict neurodevelopment in adolescents after surgery for congenital heart disease.** *Brain* 2014;137:268–76 CrossRef Medline
  22. Dimitropoulos A, McQuillen PS, Sethi V, et al. **Brain injury and development in newborns with critical congenital heart disease.** *Neurology* 2013;81:241–48 CrossRef Medline
  23. Andropoulos DB, Hunter JV, Nelson DP, et al. **Brain immaturity is associated with brain injury before and after neonatal cardiac surgery with high-flow bypass and cerebral oxygenation monitoring.** *J Thorac Cardiovasc Surg* 2010;139:543–56 CrossRef Medline
  24. Donofrio MT, Bremer YA, Schieken RM, et al. **Autoregulation of cerebral blood flow in fetuses with congenital heart disease: the brain sparing effect.** *Pediatr Cardiol* 2003;24:436–43 CrossRef Medline
  25. Peyvandi S, Kim H, Lau J, et al. **The association between cardiac physiology, acquired brain injury, and postnatal brain growth in critical congenital heart disease.** *J Thorac Cardiovasc Surg* 2018;155:291–300 e3 CrossRef

# Focal Cortical Dysplasia and Refractory Epilepsy: Role of Multimodality Imaging and Outcome of Surgery

 S. Jayalakshmi,  S.K. Nanda,  S. Vooturi,  R. Vadapalli,  P. Sudhakar,  S. Madigubba, and  M. Panigrahi



## ABSTRACT

**BACKGROUND AND PURPOSE:** Focal cortical dysplasia (FCD) is one of the most common causes of drug resistant epilepsy. Our aim was to evaluate the role of presurgical noninvasive multimodality imaging techniques in selecting patients with refractory epilepsy and focal cortical dysplasia for epilepsy surgery and the influence of the imaging modalities on long-term seizure freedom.

**MATERIALS AND METHODS:** We performed a retrospective analysis of data of 188 consecutive patients with FCD and refractory epilepsy with at least 2 years of postsurgery follow-up. Predictors of seizure freedom and the sensitivity of neuroimaging modalities were analyzed.

**RESULTS:** MR imaging showed clear-cut FCD in 136 (72.3%) patients. Interictal FDG-PET showed focal hypo-/hypermetabolism in 144 (76.6%); in 110 patients in whom ictal SPECT was performed, focal hyperperfusion was noted in 77 (70.3%). Focal resection was the most common surgery performed in 112 (59.6%). Histopathology revealed FCD type I in 102 (54.3%) patients. At last follow-up, 124 (66.0%) were seizure-free. Complete resection of FCD and type II FCD were predictors of seizure freedom. Localization of FCD on either MR imaging or PET or ictal SPECT had the highest sensitivity for seizure freedom at 97.5%. Among individual modalities, FDG-PET had the highest sensitivity (78.2%), followed by MR imaging (75.8%) and ictal SPECT (71.8%). The sensitivity of MR imaging to localize type I FCD (60.8%) was significantly lower than that for type II FCD (84.8%,  $P < .001$ ). Among 37 patients with subtle MR imaging findings and a focal FDG-PET pattern, 30 patients had type I FCD.

**CONCLUSIONS:** During presurgical multimodality evaluation, localization of the extent of the epileptogenic zone in at least 2 imaging modalities helps achieve seizure freedom in about two-thirds of patients with refractory epilepsy due to FCD. FDG-PET is the most sensitive imaging modality for seizure freedom, especially in patients with type I FCD.

**ABBREVIATIONS:** EEG = electroencephalography; FCD = focal cortical dysplasia; ILAE = International League Against Epilepsy

Focal cortical dysplasia (FCD) is the most common malformation of cortical development<sup>1</sup> and an established etiology of drug-resistant epilepsies in children and adolescents.<sup>2</sup> It is the most frequent histopathology in children and the third most common etiology in adult patients undergoing epilepsy surgery.<sup>3</sup> These patients have a high seizure burden: More than 60% have daily seizures.<sup>4</sup> Precise localization of the extent of the epileptogenic zone may influence the surgical outcome. Therefore, in individuals with refractory epilepsy and FCD, the combination of multimodality imaging and electrophysiologic data during pre-

surgical evaluation may help characterize the epileptogenic zone<sup>5</sup> and improve the outcome of the surgery.

Findings from scalp electroencephalography (EEG) in FCDs often have limitations in spatial resolution in recording readings from deeper cortical sites.<sup>5</sup> High-resolution MR imaging helps recognize features typical of FCDs in only two-thirds of patients.<sup>6</sup> Subtle MR imaging changes are often reported in the one-third of patients with FCDs characterized by disturbances in cortical organization that reorganize.<sup>7</sup> Frequent location of FCDs in a central region and poor localization on MR imaging make them a surgeon's challenge,<sup>8</sup> with reported seizure freedom in only one-third of patients postsurgery, significantly lower than the nearly 60% reported in all patients with FCD.<sup>9</sup>

FDG-PET offers a 3D, high-resolution analysis and is highly sensitive in detecting MR imaging negative for FCDs.<sup>10</sup> FDG-PET helps to delineate the cortical abnormalities with a higher sensitivity than MR imaging, especially in patients with mild type I FCD.<sup>11</sup> It has been reported that incorporating FDG-PET/MR

Received December 19, 2018; accepted after revision March 12, 2019.

From the Departments of Neurology (S.J., S.K.N., S.V.), Radiology (R.V.), Nuclear Medicine (P.S.), Pathology (S.M.), and Neurosurgery (M.P.), Krishna Institute of Medical Sciences, Secunderabad, India.

Please address correspondence to Sita Jayalakshmi, DM, Department of Neurology, Krishna Institute of Medical Sciences, Minister Rd, 1-8-31/1, Secunderabad-03, India; e-mail: sita\_js@hotmail.com; sita.js@gmail.com

<http://dx.doi.org/10.3174/ajnr.A6041>

imaging coregistration into the multimodality presurgical evaluation enhances the detection and successful surgical treatment of patients with FCD, especially those with type I FCD.<sup>10</sup> In patients in whom both MR imaging and FDG-PET fail to localize the epileptogenic zone, ictal SPECT has been associated with postsurgical seizure freedom in 86% of patients with FCD in whom the zone of ictal hyperperfusion detected on SPECT was completely resected.<sup>12</sup> Hence multimodality presurgical investigations are often required, with coregistration on FDG-PET or ictal SPECT in complex MR imaging negative cases<sup>13</sup> because each technique has its own limitations.<sup>12</sup>

With increasing use of noninvasive multimodality imaging in the evaluation of refractory epilepsy with suspected FCD, it becomes imminent to determine the number of modalities required to localize the extent of the epileptogenic zone and the sensitivity of each modality for long-term seizure freedom. Moreover, it is also imperative to determine how these modalities complement each other in selecting the patient and planning the extent of resection. In fact, most of the literature compares multimodality evaluation with intracranial EEG both for confirmation of the ictal onset zone and determining the extent of surgical resection.<sup>14</sup> Very few studies have investigated the role of presurgical multimodality evaluation with postoperative seizure freedom. In those studies that reported seizure freedom, the findings were observed in small study populations or with a short follow-up. We evaluated the role of presurgical noninvasive multimodality imaging techniques in selecting a patient with refractory epilepsy and FCD for epilepsy surgery and the imaging techniques influence on long-term seizure freedom in a large cohort.

## MATERIALS AND METHODS

Of the 792 patients who underwent an epilepsy surgery between January 2005 and June 2016, data of 188 consecutive patients operated for drug-resistant epilepsy and a diagnosis of FCD were analyzed. The study was performed at a tertiary referral center with comprehensive epilepsy care and a dedicated epilepsy surgery program running for >14 years. The program comprises a neurologist, neuroradiologist, nuclear medicine specialist, neurosurgeon, and neuropathologist with substantial expertise. The inclusion criteria were the following: 1) type I or type II FCD within the surgical specimen, and 2) at least 2 years of postsurgery follow-up. Exclusion criteria were the following: 1) FCD type III, and 2) hemispheric dysplasia, tuberous sclerosis, and periventricular nodular heterotopias. The presurgical, surgical, and postsurgical data were collected using a structured data-collection form. Seizure classification was performed according to the International League Against Epilepsy (ILAE) Task Force on Classification and Terminology Guidelines.<sup>15</sup> The study was approved by the institutional ethics committee.

### Presurgical Evaluation

Presurgical neurologic evaluation and surgery were performed after the necessary consents were obtained. Preoperative seizure frequency was calculated for the year preceding the surgery, excluding auras. A 3T brain MR imaging, FDG-PET with PET-MR imaging fusion, video-electroencephalography (video-EEG), and a detailed neuropsychological and developmental evaluation were

performed in all patients. Ictal SPECT was performed in cases in which there was a discordance of the EEG data or in those with insufficient information on 3T MRI and/or FDG-PET. Functional MR imaging was performed in selected cases for lateralization of language, memory, and motor functions.

All the patients underwent MR imaging on a 3T scanner (Ingenia 3T; Philips Healthcare, Best, the Netherlands) with a dedicated epilepsy protocol. The protocol included a conventional DWI with b-values of 0 and 1000; 2D-FLAIR; axial 3D-volume T1; 3D-volume FLAIR; 3D-volume double inversion recovery sequences in the sagittal plane; and DTI with 15 directions using a dedicated 16-channel head coil. 3D imaging parameters were as follows—3D T1 fast-field echo: TR = 7.9 ms, TE = 3.6 ms, acquisition matrix = 232 × 224, acquired spatial voxel resolution = 0.99 × 1.00 × 1.00 mm, reconstructed spatial resolution = 0.53 × 0.50 × 0.50 with a data-acquisition time of 4 minutes and 17 seconds; 3D-FLAIR volume sequence: TR = 4800 ms, TE = 289 ms, TI = 1650 ms, acquisition matrix = 224 × 224, acquired spatial voxel resolution = 1.12 × 1.12 × 1.12 mm, reconstructed spatial resolution = 0.98 × 0.98 × 0.56 mm, data acquisition time = 4 minutes and 5 seconds; 3D double inversion recovery sequence: TR = 5000 ms, TE = 288 ms, TI = 2550 ms, acquisition matrix = 208 × 208, acquired spatial voxel resolution = 1.2 × 1.12 × 1.3 mm, reconstructed spatial resolution = 0.98 × 0.98 × 0.65 mm, data acquisition time = 5 minutes and 36 seconds.

The volume sequences were then processed by multiplanar reconstruction and volume-rendering in the axial, coronal, and sagittal planes for delineation of any sulcal, gyral abnormalities such as cortical laminar architectural abnormalities and blurring of gray-white matter interfaces. The MRIs were read by a neuro-radiologist and neurologist with expertise in epilepsy imaging. The MR imaging data were reanalyzed after FDG-PET in cases in which the MR imaging findings were reported as normal or with minor gyral abnormalities. An MR imaging abnormality was classified as clear-cut FCD and subtle FCD (when the MR imaging lesion was indistinct and confirmed on the basis of FDG-PET hypo-/hypermetabolism).

Prolonged video-EEG monitoring was performed and at least 2 seizures were recorded. Interictal spikes were grouped as unilateral (when >75% of spikes were confined to the side of lesion), bilateral, and multifocal. The seizure semiology was grouped as lateralizing, nonlateralizing, and contralateral. The ictal EEG patterns were classified as focal, regional, hemispheric, generalized,<sup>16</sup> and contralateral. Unilateral spikes, lateralization on semiology, and regional ictal EEG onset patterns were compared for analysis with the rest of the parameters in the respective groups.

All patients underwent [<sup>18</sup>F] FDG-PET using Biograph mCT (Siemens, Erlangen, Germany) in a 3D mode. PET-MR imaging fusion was performed using syngo MultiModality Workplace software (Siemens). FDG-PET and PET-MR imaging fusion images were analyzed in all 3 projections. The PET metabolism was classified as focal hypometabolism, hypermetabolism, and normal metabolism. The extent of hypo-/hypermetabolism was classified as focal when confined to the lesion/lobe, lateralized if it was beyond 1 lobe but in the same hemisphere, and not informative if it was normal or uncertain. For analysis, focal hypo-/hypermetabolism and the rest were organized into 2 groups.

Ictal SPECT was performed in 110 patients. Under video-EEG monitoring, 740-MBq of technetium Tc99m ethyl cysteinate dimer (Tc99m-ECD) was injected during the ictal phase. Brain SPECT images were acquired using a Millennium MG (GE Healthcare, Milwaukee, Wisconsin) dual-head gamma camera equipped with low-energy, high-resolution, and parallel hole collimators. The SPECT hyperperfusion was classified as focal when confined to the lesion/lobe, lateralized if it was beyond 1 lobe but in the same hemisphere, and contralateral and noninformative if it was bilateral, normal, or uncertain. Focal hyperperfusion and the rest were separated into 2 groups for analysis.

### **Surgery**

All patients underwent surgery after the review of the multimodality evaluation data in a multidisciplinary case conference. Surgery was performed only if there was a concordance in at least 2 imaging modalities: Namely, the lesion was clear-cut on MR imaging, or a localized FDG-PET pattern or a localized ictal SPECT pattern was present. The types of surgeries performed were focal resection (corticectomy/lesionectomy/lobectomy), multilobar resection, standard anterior temporal lobectomy with amygdalohippocampectomy, and posterior disconnection. During focal resections for a clear-cut lesion, the FCD along with a minimum of a 1-cm circumferential cortex was resected. However, when the extent of FDG-PET hypometabolism (in cases with a localized PET pattern in a noneloquent cortex) was more than that of the MR imaging lesion, the PET abnormality was also resected along with the lesion. All the resections were guided by neuronavigation and intraoperative electrocorticography. The motor cortex was defined by direct intraoperative cortical stimulation in cases in which the lesion was close to or overlapping the motor cortex.

### **Pathology**

Pathologic examination of the resected tissue was performed by a neuropathologist with expertise in epilepsy pathology. The FCDs were classified as FCD type I, FCD type IIa, and FCD type IIb according to the ILAE classification.<sup>17</sup> FCD type I was characterized by isolated lesions, which present as either radial and/or tangential dyslamination of the neocortex. FCD type II was an isolated lesion characterized by cortical dyslamination and dysmorphic neurons without (type IIa) or with balloon cells (type IIb).<sup>17</sup>

### **Postsurgical Evaluation and Outcome**

The postoperative hospital course, complications, and outcome data were analyzed. Acute postoperative seizures were defined as seizures occurring within 7 days after surgery. All the patients underwent routine interictal EEG, at 3 months and 1 year postsurgery. Brain MR imaging was performed at 1 year postsurgery. Outcome at the last follow-up was assessed according to ILAE classification where patients were categorized as ILAE class 1 (seizure-free) and the rest (persistent seizures).<sup>15</sup>

### **Statistical Analysis**

The study population was divided into 2 groups based on seizure freedom or the type of FCD. Comparison between groups for

categorical variables was performed using the Fisher exact test, whereas an independent Student *t* test was used for comparing continuous variables. Logistic regression was performed to evaluate predictors of seizure freedom. Comparison for sensitivities was performed using the McNemar test. Data analysis was performed using SPSS for Windows, Version 17.0 (IBM, New York). A *P* value  $\leq .05$  was considered statistically significant.

## **RESULTS**

### **Clinical Variables**

The average age at onset of epilepsy was  $7.93 \pm 7.56$  years (range, 0–50 years) with a mean duration of epilepsy of  $9.75 \pm 7.17$  years (range, 0–29 years). The average age at the surgery was  $17.31 \pm 11.26$  years (range, 2–64 years) with 92 (48.9%) women. Daily seizures were reported in 106 (56.4%). Febrile convulsions were reported in 23 (12.2%) patients, while there was a family history of epilepsy in 34 (18.1%), and 29 (15.4%) had history of status epilepticus. Developmental delay was reported in 47 (25.0%). Multiple seizure types were reported in 52 (27.7%) patients, and an aura was reported in 43 (22.9%) (Table 1).

### **Presurgical Variables**

The interictal EEG showed regional epileptiform discharges in 93 (49.5%) patients, and 88 (46.8%) had regional ictal EEG onset. Interictal FDG-PET showed hypo- or hypermetabolism in 181 (96.3%) and a focal PET pattern in 144 (76.6%). In the 110 patients in whom ictal SPECT was performed, focal hyperperfusion was noted in 77 (70.3%) patients. MR imaging showed clear-cut FCD in 136 (72.3%) patients. In the remaining 52 (27.7%) patients with subtle MR imaging findings, a regional interictal or ictal EEG onset pattern was noted in 27 patients. Among these 27 patients, a focal FDG-PET pattern was observed in 21 patients (Fig 1). In the remaining 6 patients, ictal SPECT showed focal hyperperfusion in 3. Among the 25 patients with subtle MR imaging findings and in whom ictal or interictal EEG was nonlocalizing, a focal FDG-PET pattern was observed in 16 patients. Among the remaining 9 patients, ictal SPECT showed focal hyperperfusion in 3 patients. Surgery was performed in the remaining 6 patients with subtle MR imaging findings after invasive EEG evaluation.

### **Surgical Variables**

Focal resection was the most common surgery performed in 112 (59.6%), followed by amygdalohippocampectomy in 31 (16.5%) patients. Resections involved the frontal lobe in 101 (53.7%), the temporal lobe in 33 (17.6%), the parietal lobe in 17 (9.0%), and the occipital lobe in 10 (5.3%), and they were multilobar in 27 (14.4%). The FCD was close to an eloquent cortex in 36 (19.1%). There was no mortality. Postsurgery, 17 (9.0%) had complications, which improved by 3 months (motor weakness in 10, language dysfunction in 4, mutism in 2, and hemianopia in 1). Complete resection of the FCD was performed in 133 (70.7%) patients in whom the lesion was clear-cut on MR imaging. Histopathology was suggestive of FCD type I in 102 (54.3%), type II in 79 (42.0%), and mixed types I and II in the remaining 7 (3.7%) patients.

**Table 1: Comparison of study variables for seizure freedom (n = 188)**

Variable	Seizure-Free (n = 124)	Persistent (n = 64)	P Value
Age at surgery (mean) (yr)	18.68 ± 11.43	14.66 ± 10.50	.020
Age of onset (mean) (yr)	8.45 ± 8.18	6.91 ± 6.09	.198
Duration of epilepsy (mean) (%)	10.72 ± 7.31	7.90 ± 6.56	.012
Women (%)	56 (45.2%)	36 (56.3%)	.168
Febrile convulsions (%)	15 (12.1%)	8 (12.7%)	1.000
Multiple types of seizures (%)	21 (16.9%)	31 (48.4%)	<.001
Delayed development (%)	23 (18.5%)	24 (37.5%)	.007
Daily seizures (%)	63 (50.8%)	43 (67.2%)	.043
Presence of aura (%)	35 (28.2%)	8 (12.5%)	.017
Regional spikes on interictal EEG (%)	66 (54.1%)	27 (42.2%)	.168
Regional ictal EEG onset pattern (%)	62 (50.0%)	26 (46.2%)	.280
Clear-cut FCD on MRI (%)	94 (75.8%)	42 (65.6%)	.169
Focal FDG-PET pattern (%)	97 (78.2%)	47 (73.4%)	.472
Focal ictal SPECT pattern (%)	51 (71.8%)	26 (66.7%)	.664
Eloquent cortex location (%)	16 (12.9%)	20 (31.3%)	.003
FCD type I (%)	57 (47.5%)	45 (73.8%)	.001
FCD type II (%)	63 (52.5%)	16 (26.2%)	.001
FCD type I and II (%)	4 (3.2%)	3 (4.6%)	.691
Acute postoperative seizures (%)	32 (25.8%)	32 (50.0%)	.001
Complete resection (%)	105 (96.3%)	28 (54.9%)	<.001

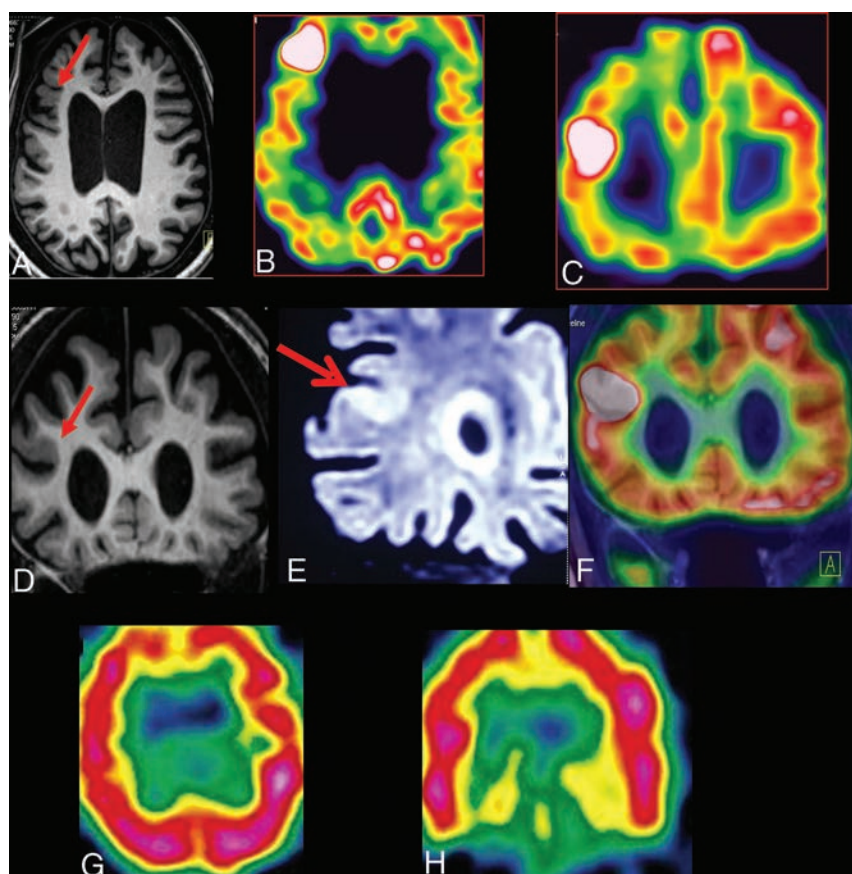


**FIG 1.** A case of refractory epilepsy with daily seizures of 21 years' duration with moderate mental retardation. Brain MR imaging 3D-T1 volume fast-field echo sequences of axial (A), coronal (D), and coronal (E) 3D-FLAIR volume show a right middle frontal gyrus cortical laminar architectural abnormality with cortical thickening (arrow). The MR imaging abnormality was detected retrospectively after the FDG-PET (B and C) and MR imaging/FDG-PET coregistration (F) showed the focal hypermetabolic focus. The ictal SPECT (G and H) findings were inconclusive.

### Outcome

The postsurgery follow-up ranged from 2 to 13 years. At the latest follow-up, 124 (66.0%) patients were seizure-free (ILAE class 1) and an additional 20 (10.6%) had >90% seizure reduction (ILAE

classes 2 and 3), while 20 (10.6%) had >50% seizure reduction (ILAE class 4).

### Predictors of Outcome

On analysis of factors influencing seizure freedom, more patients with persistent seizures had daily seizures (50.8% versus 67.2%,  $P = .043$ ), multiple types of seizures (16.9% versus 48.4%,  $P < .001$ ), acute postoperative seizures (25.8% versus 50.0%,  $P = .001$ ), and FCD close to an eloquent cortex (12.9% versus 31.3%,  $P = .003$ ). Auras (28.2 versus 12.5%,  $P = .017$ ), type II FCD (52.5% versus 26.2%,  $P = .001$ ), and complete resection of the FCD (96.3% versus 54.9%,  $P < .001$ ) were significantly more common in patients with seizure freedom (Table 1). On logistic regression analysis among the variables that were significantly associated with seizure freedom, complete resection of the FCD ( $\beta = 0.043$ ,  $P < .001$ ), type II FCD ( $\beta = 3.07$ ,  $P = .021$ ), and a single type of seizure ( $\beta = 0.339$ ,  $P = .042$ ) were predictors of seizure freedom, whereas acute postoperative seizures showed a trend for predicting persistent seizures ( $\beta = -0.398$ ,  $P = .072$ ).

### Imaging Modalities and Sensitivity

On analysis of sensitivities of various modalities for seizure freedom, localization of FCD on either MR imaging or PET or ictal SPECT had the highest sensitivity at 97.5% followed by localization on either MR imaging or PET at 92.7%. Among individual modalities, localization on PET had a sensitivity of 78.2% followed by MR imaging with 75.8% and ictal SPECT with 71.8% (Fig 2A).

The sensitivity of localization of FCD either on MR imaging or PET or ictal SPECT was highest for both type I FCD (95.9%) and type II FCD (97.6%). This was followed by localization on either MR imaging or PET at 90.1% and 94.1% for type I and type II FCDs, respectively. The sensitivity of MR imaging to localize type I FCD (60.7%) was significantly lower ( $P < .001$ ) than the sensitivity for localizing type II FCD (86.0%) (Fig 2B, -C). On the McNemar test, localization

of FCD on either MR imaging or PET or ictal SPECT had significantly higher sensitivity ( $P < .001$ ) for seizure freedom than any other individual technique.

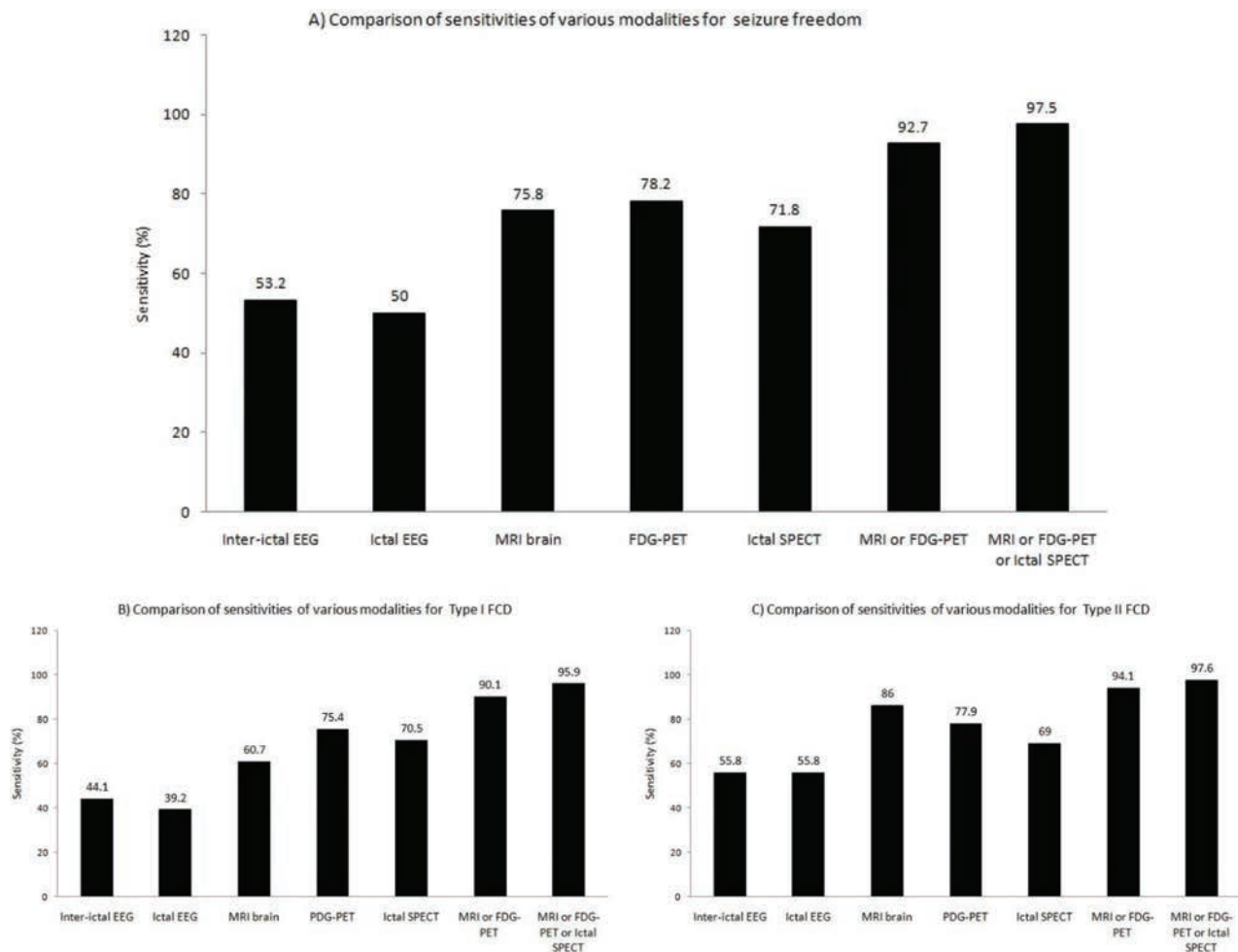


**FIG 2.** Comparison of sensitivities of various modalities for seizure freedom (A), type I FCD (B), and type II FCD (C).

### Comparison of FCD Types I and II

On comparison of factors between type I and type II FCD, there were no differences between the types of FCD for demographic characteristics. More patients with type I FCD were multilobar in location (20.6% versus 3.8%;  $P < .001$ ) and had developmental delay (31.4% versus 16.5%,  $P = .025$ ). Clear-cut FCD on MR imaging (60.8% versus 84.8%,  $P < .001$ ), a regional ictal EEG pattern (39.2% versus 58.4%,  $P = .024$ ), and complete resection of FCD (77.8% versus 90.3%,  $P = .048$ ) were more common in patients with type II FCD (Table 2). In a subset of 37 patients with subtle MR imaging findings and a focal FDG-PET pattern, 30 patients had type I FCD, while 7 had type II FCD. In this subset, there was no difference in seizure freedom based on the type of FCD (56.6% versus 57.1%,  $P = 1.000$ ).

### DISCUSSION

In the current study, we report that in patients with refractory epilepsy due to FCD, multimodality imaging helps achieve seizure freedom in nearly two-thirds of patients. More than one-fourth of the patients with FCD and refractory epilepsy had subtle MR imaging findings in which FDG-PET helped localize the epileptogenic zone in 71%. On correlating with histopathology, most (80%) of these patients in whom FDG-PET helped localize the epileptogenic zone had type I FCD. Predictors of postsurgical sei-

zure freedom are a single type of seizure, complete resection of the FCD, and type II FCD. However, we could not replicate previously reported predictors such as younger age at the operation and shorter duration of epilepsy.<sup>14</sup>

We report seizure freedom in 66.0% of patients with an additional 10.6% of patients reporting a >90% seizure reduction. This result is similar to the 65% favorable outcome reported by Fauser et al<sup>9</sup> and the >56% seizure freedom reported by Kral et al.<sup>18</sup> The most common reason for incomplete resection in the current study was a lesion located in close proximity to the eloquent cortex, observed in 17.3% of our study population. Subtotal resections are common in these patients to avoid the risk of an unacceptable postoperative neurologic deficit.<sup>3</sup> Another commonly attributed reason for incomplete resection is type I FCD. Previously Kim et al<sup>19</sup> reported that patients with FCD of a severe-pathologic group (type II) had more chances of complete resection of FCD and subsequent seizure freedom. In the current study, we found that both completeness of resection and seizure freedom were higher in patients with type II FCD, possibly due to clear-cut focal lesions on MR imaging. In fact, having a dedicated 3T MR imaging protocol itself could have influenced the seizure outcome in the present study, as previously suggested by Ahmed et al.<sup>20</sup>

**Table 2: Comparison of study variables for FCD types I and II (n = 181)**

Variable	FCD Type I (n = 102)	FCD Type II (n = 79)	P Value
Age at surgery (mean) (yr)	16.54 ± 10.76	18.11 ± 11.05	.338
Age of onset (mean) (yr)	8.29 ± 7.88	7.76 ± 7.31	.655
Duration of epilepsy (mean) (%)	9.08 ± 6.91	10.82 ± 7.60	.117
Women (%)	50 (49.0%)	40 (50.6%)	.881
Multilobar distribution of FCD (%)	21 (20.6%)	3 (3.8%)	<.001
Febrile convulsions (%)	12 (11.9%)	9 (11.4%)	1.000
Multiple types of seizures (%)	31 (30.4%)	19 (24.1%)	.403
Delayed development (%)	32 (31.4%)	13 (16.5%)	.025
Daily seizures (%)	57 (55.9%)	48 (60.8%)	.546
Aura (%)	18 (17.6%)	23 (29.1%)	.076
Regional ictal EEG onset pattern (%)	40 (39.2%)	45 (58.4%)	.024
Clear-cut FCD on MRI (%)	62 (60.8%)	67 (84.8%)	<.001
Focal FDG-PET pattern (%)	77 (75.5%)	63 (79.7%)	.592
Focal ictal SPECT pattern (%)	48 (70.6%)	29 (72.5%)	1.000
Eloquent cortex location (%)	21 (20.6%)	15 (19.0%)	.852
Seizure-free (%)	57 (55.8%)	63 (79.7%)	.008
Acute postoperative seizures (%)	38 (37.3%)	24 (30.4%)	.348
Complete resection (%)	63 (77.8%)	65 (90.3%)	.048

We also agree with Ahmed et al “that a dedicated 3T MR imaging protocol may increase the cost of presurgical evaluation, simultaneously considering the risks of administering general anesthetic for the MR imaging, especially in some children. However, additional MR imaging could improve not only the detection of a lesion, but could assist with subsequent management.”<sup>20</sup>

The sensitivity of MR imaging to localize type II FCD was significantly higher than the sensitivity for type I FCD. This finding may be because of our concurrent findings that nearly one-fifth of patients with type I FCD had a multilobar distribution compared with a mere 3.8% of patients with type II FCD. This extensive distribution of type I FCD is perhaps the reason for our observation of higher rates of incomplete resection and persistent seizures in type I FCD. Furthermore, Jin et al<sup>21</sup> reported incomplete resection of FCD and habitual acute postoperative seizures as strong predictors of seizure recurrence after surgery, similar to the present study. As Hauptman and Mathern<sup>3</sup> suggested, given the poor localization with EEG and normal MR imaging findings, we need better and preferably noninvasive tools to not only identify the lesion but also provide ways to detect the borders of the histopathology and whether the lesion involves the functional cerebral cortex. The present study demonstrates that FDG-PET is complementary to MR imaging to detect the extent of epileptogenic zone, especially in type I FCD.

The sensitivity of a clear-cut FCD on MR imaging for seizure freedom in the current study at 75.8% is similar to previously reported sensitivities of 60%–90%.<sup>10,14</sup> Similarly, a sensitivity of 78.2% for localization of FCD on FDG-PET and a sensitivity of approximately 70% for ictal SPECT are similar to those reported by previous studies.<sup>8</sup> We report that evaluation with ≥2 modalities increases the sensitivity for seizure freedom in these patients. Most interesting, in 71% of 52 patients in whom MR imaging was not helpful, FDG-PET helped localize the FCD, and ictal SPECT, in 11.5% more patients in whom MR imaging and FDG-PET both were not helpful. Especially, in patients with type I FCD, in which MR imaging did not localize FCD, we report that FDG-PET helped localize the lesion and improve seizure freedom. These

observations suggest that FDG-PET is a useful adjunct to MR imaging, especially in patients with type I FCD.

### Limitations

The correlation between hypometabolism on FDG-PET and findings on MR imaging may not be precise because both evaluations were not studied within a short period. A retrospective design of the study did not permit us to determine false-negative reports. Furthermore, the retrospective design also did not allow blinding of any of the team members for diagnoses already performed, thus preventing us from observing variability between and within an observer. Ictal SPECT was performed in only a fraction of patients

because coregistration of MR imaging/FDG-PET was sufficient in most patients.

### Implications for Clinical Practice

In developing countries, the cost of epilepsy surgery using an invasive evaluation is 4 times that with noninvasive multimodality evaluation.<sup>22</sup> The findings of the current study that localization of FCD in ≥2 noninvasive imaging modalities is sufficient to achieve satisfactory seizure freedom may have potential cost-effective implications for the feasibility of epilepsy surgery after multimodality evaluation in countries with limited resources.

### CONCLUSIONS

During presurgical multimodality evaluation, localization of the extent of the epileptogenic zone in at least 2 imaging modalities helps achieve seizure freedom in about two-thirds of patients with refractory epilepsy due to FCD. FDG-PET is the most sensitive imaging technique for seizure freedom, especially in patients with type I FCD.

### REFERENCES

1. Barkovich AJ, Guerrini R, Kuzniecky RI, et al. **A developmental and genetic classification for malformations of cortical development: update 2012.** *Brain* 2012;135(Pt 5):1348–69 CrossRef Medline
2. Palmini A, Holthausen H. **Focal malformations of cortical development: a most relevant etiology of epilepsy in children.** *Handb Clin Neurol* 2013;111:549–65 CrossRef Medline
3. Hauptman JS, Mathern GW. **Surgical treatment of epilepsy associated with cortical dysplasia: 2012 update.** *Epilepsia* 2012;53(Suppl 4):98–104 CrossRef Medline
4. Chapman K, Wyllie E, Najm I, et al. **Seizure outcome after epilepsy surgery in patients with normal preoperative MRI.** *J Neurol Neurosurg Psychiatry* 2005;76:710–13 CrossRef Medline
5. Pittau F, Mégevand P, Sheybani L, et al. **Mapping epileptic activity: sources or networks for the clinicians?** *Front Neurol* 2014;5:218 CrossRef Medline
6. Colombo N, Salamon N, Raybaud C, et al. **Imaging of malformations of cortical development.** *Epileptic Disord* 2009;11:194–205 CrossRef Medline
7. Janszky J, Ebner A, Kruse B, et al. **Functional organization of the brain with malformations of cortical development.** *Ann Neurol* 2003;53:759–67 CrossRef Medline

8. Chassoux F, Landré E, Mellerio C, et al. **Type II focal cortical dysplasia: electroclinical phenotype and surgical outcome related to imaging.** *Epilepsia* 2012;53:349–58 CrossRef Medline
9. Fauser S, Essang C, Altenmüller DM, et al. **Long-term seizure outcome in 211 patients with focal cortical dysplasia.** *Epilepsia* 2015;56:66–76 CrossRef Medline
10. Salamon N, Kung J, Shaw SJ, et al. **FDG PET/MRI coregistration improves detection of cortical dysplasia in patients with epilepsy.** *Neurology* 2008;71:1594–601 CrossRef Medline
11. Kim SK, Na DG, Byun HS, et al. **Focal cortical dysplasia: comparison of MRI and FDG-PET.** *J Comput Assist Tomogr* 2000;24:296–302 CrossRef Medline
12. Guerrini R, Duchowny M, Jayakar P, et al. **Diagnostic methods and treatment options for focal cortical dysplasia.** *Epilepsia* 2015;56:1669–86 CrossRef Medline
13. Jayakar P, Gaillard WD, Tripathi M, et al; Task Force for Paediatric Epilepsy Surgery, Commission for Paediatrics, and the Diagnostic Commission of the International League Against Epilepsy. **Diagnostic test utilization in evaluation for resective epilepsy surgery in children.** *Epilepsia* 2014;55:507–18 CrossRef Medline
14. Kim YH, Kang HC, Kim DS, et al. **Neuroimaging in identifying focal cortical dysplasia and prognostic factors in pediatric and adolescent epilepsy surgery.** *Epilepsia* 2011;52:722–27 CrossRef Medline
15. Wieser HG, Blume WT, Fish D, et al; Commission on Neurosurgery of the International League Against Epilepsy (ILAE). **ILAE Commission Report: proposal for a new classification of outcome with respect to epileptic seizures following epilepsy surgery.** *Epilepsia* 2001;42:282–86 Medline
16. Jayalakshmi S, Panigrahi M, Kulkarni DK, et al. **Outcome of epilepsy surgery in children after evaluation with non-invasive protocol.** *Neurol India* 2011;59:30–36 CrossRef Medline
17. Blümcke I, Thom M, Aronica E, et al. **The clinicopathologic spectrum of focal cortical dysplasias: a consensus classification proposed by an ad hoc Task Force of the ILAE Diagnostic Methods Commission.** *Epilepsia* 2011;52:158–74 CrossRef Medline
18. Kral T, von Lehe M, Podlogar M, et al. **Focal cortical dysplasia: long term seizure outcome after surgical treatment.** *J Neurol Neurosurg Psychiatry* 2007;78:853–56 CrossRef Medline
19. Kim DW, Lee SK, Chu K, et al. **Predictors of surgical outcome and pathologic considerations in focal cortical dysplasia.** *Neurology* 2009;72:211–16 CrossRef Medline
20. Ahmed R, Rubinger L, Go C, et al. **Utility of additional dedicated high-resolution 3T MRI in children with medically refractory focal epilepsy.** *Epilepsy Res* 2018;143:113–19 CrossRef Medline
21. Jin B, Wang J, Zhou J, et al. **A longitudinal study of surgical outcome of pharmaco-resistant epilepsy caused by focal cortical dysplasia.** *J Neurol* 2016;263:2403–10 CrossRef Medline
22. Rathore C, Radhakrishnan K. **Epidemiology of epilepsy surgery in India.** *Neurol India* 2017;65(Supplement):S52–59 CrossRef Medline

# Persisting Embryonal Infundibular Recess in Morning Glory Syndrome: Clinical Report of a Novel Association

 A. D'Amico,  L. Ugga,  R. Cuocolo,  M. Cirillo,  A. Grandone, and  R. Conforti

## ABSTRACT

**SUMMARY:** Morning glory syndrome is characterized by a congenital optic disc defect that resembles the eponymous flower. We present the MR imaging findings of 2 pediatric patients with morning glory disc anomaly and persisting embryonal infundibular recess, another rare malformative finding, a previously unreported association. Neuroradiologists should be aware of the possible presence of a persisting embryonal infundibular recess in patients with morning glory syndrome, to aid in the differential diagnosis including other pituitary malformations such as pituitary stalk duplication.

**ABBREVIATIONS:** MGDA = morning glory disc anomaly; MGS = morning glory syndrome; PEIR = persisting embryonal infundibular recess

The morning glory disc anomaly (MGDA) is a rare, congenital ocular defect diagnosed by fundoscopy. It is characterized by a funnel-shaped macropapilla with central neuroglial remnants, surrounded by an elevated, pigmented chorioretinal ring, named after its resemblance to the morning glory flower.<sup>1,2</sup> While it is usually unilateral, bilateral MGDA may occur.<sup>3</sup> Even though it may be an isolated finding, it can present in the context of a morning glory syndrome (MGS) when associated with other congenital abnormalities, including craniofacial, skull base, optic pathway, corpus callosum, vascular, and pituitary ones.<sup>2,4</sup>

The embryonal infundibular recess is a funnel-shaped liquor space of the third ventricle floor extending into the pituitary stalk, normally obliterated during development, whose persistence is defined as persisting embryonal infundibular recess (PEIR). It has been rarely reported<sup>5,6</sup> and appears as an unusual expansion of the third ventricle floor into the sella turcica with loss of the normal recess contours. At MR imaging, it appears as an intrasellar cyst, communicating with the third ventricle. The sella turcica may be expanded, and the pituitary gland is typically thinned (empty sella).

We present 2 patients with fundoscopically confirmed MGDA whose brain MR imaging showed several of the above-mentioned anomalies as well as a PEIR. The association between MGDA and PEIR has not been reported currently, to the best of our knowledge.

## Case Series

**Patient 1.** This 3-year-old boy presented with short stature and migraine. Fundoscopy revealed a MGDA of the right eye. Several stimulus tests confirmed a complete growth hormone isolated deficiency.

MR imaging showed hypophyseal hypoplasia (Fig 1) and a stubby, thickened, and inferiorly dropped optic chiasm with normal signal intensity (Fig 2). Sagittal images also showed a dysmorphic hypothalamic infundibulum and pituitary stalk. Indeed, there was a direct communication between the third ventricle and the sellar cavity, suggesting a PEIR (Fig 1). The acquisition of a constructive interference in steady state sequence confirmed this finding, better depicting a tubular morphology of the pituitary stalk in the absence of sphenoidal meningocele (Fig 1). The sella was mildly enlarged, and there was clival hypoplasia. Additional findings included a corpus callosum body and splenium partial agenesis and a small interhemispheric arachnoid cyst (Fig 1).

Finally, bilateral supraclinoid ICA and M1 MCA segment narrowing was detected on MRA, with thin collateral lenticulostriate vessels, suggestive of Moyamoya syndrome (Fig 3). Due to these findings and the history of headache, a DSC PWI study was performed, indicating a preserved cerebrovascular reserve capacity.

Received October 22, 2018; accepted after revision January 14, 2019.

From the Department of Advanced Biomedical Sciences (A.D., L.U., R. Cuocolo), University of Naples "Federico II," Naples, Italy; and Dipartimento di Scienze Mediche, Chirurgiche, Neurologiche (M.C.), Metaboliche e dell'Invecchiamento, Dipartimento della Donna (A.G.), del Bambino e di Chirurgia Generale e Specialistica, and Dipartimento di Medicina di Precisione (R. Conforti), University of Campania "Luigi Vanvitelli," Naples, Italy.

Please address correspondence to Renato Cuocolo, MD, Department of Advanced Biomedical Sciences, University of Naples "Federico II", Via S. Pansini 5, 80131, Naples, Italy; e-mail: renato.cuocolo@gmail.com; @renatocuocolo

<http://dx.doi.org/10.3174/ajnr.A6005>

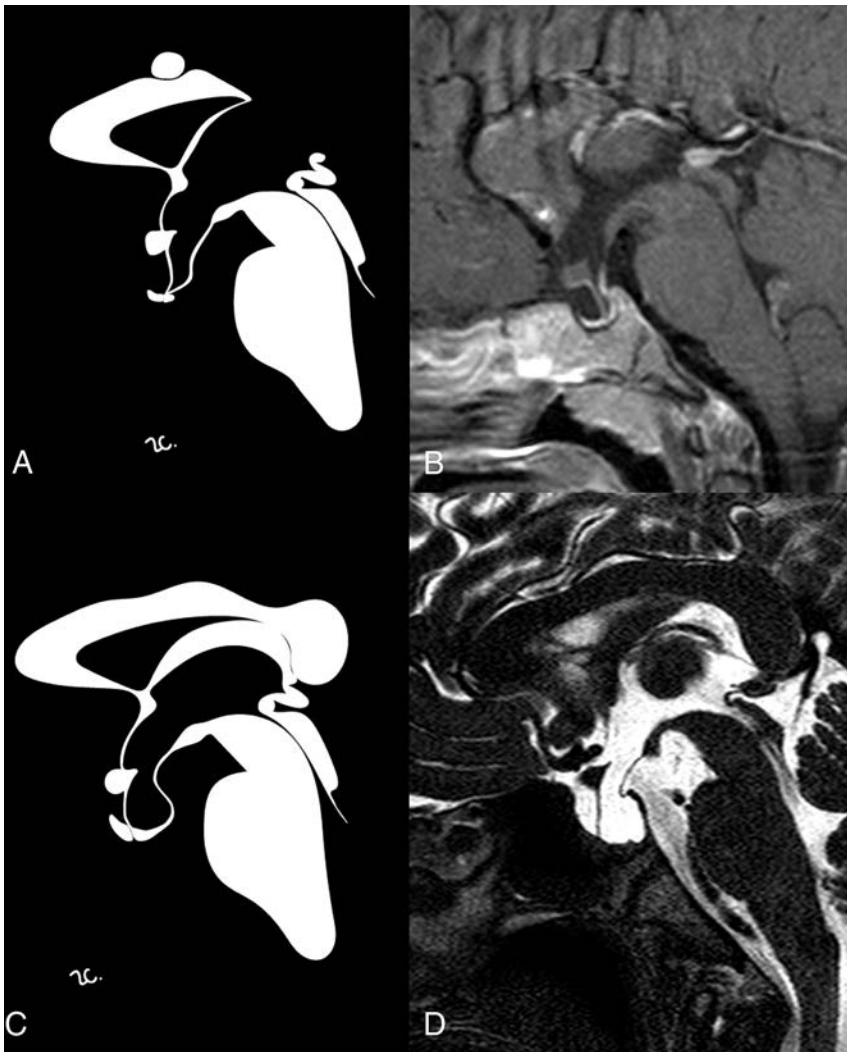


**FIG 1.** Sagittal contrast-enhanced T1-weighted (B) and high-resolution T2-weighted (D) images with corresponding stylized anatomic drawings (A and C) of patient 1 (upper row) and patient 2 (lower row) depicting the main findings reported in the text, including PEIR.

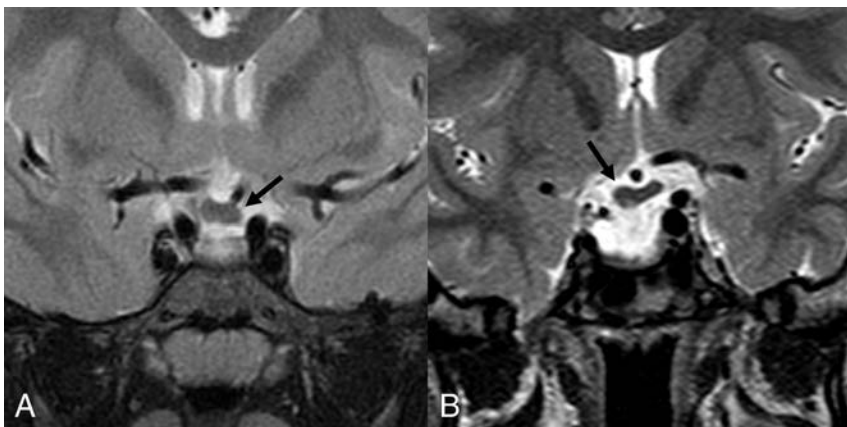


**FIG 2.** Coronal T2-weighted images of patient 1 (A) and patient 2 (B) showing thickening of the optic chiasm (arrows).

Genetic testing did not identify any *PAX6* gene mutations, encoding a transcriptional regulator involved in lens placode formation, previously reported in several ocular anomalies, including MGDA.<sup>7</sup>

pituitary stalk malformative conditions, such as duplication.<sup>2</sup> The anomalous infundibulum perforation, in the absence of meningoencephaloceles, was clearly defined by high-resolution volumetric T2-weighted sequences (CISS and driven equilibrium in

**Patient 2.** This 13-year-old boy came to our attention for short stature and chronic headache. Laboratory tests confirmed growth hormone deficiency.

Brain MR imaging showed sellar enlargement, adenohypophysis hypoplasia, and PEIR (Fig 1). The last finding was better defined on a sagittal driven equilibrium sequence, which demonstrated an evident communication between the third ventricle and sella turcica. The infundibular recess was, in fact, absent, and consequently, the pituitary stalk had a tubular appearance with thin walls.

The right part of the optic chiasm and the ipsilateral prechiasmatic optic nerve were displaced slightly downward. On the same side, partial hypoplasia of the sphenoid body with a small meningoencephalocele was found (Fig 2). A thin posterior defect of the right ocular globe was also noted. The corpus callosum was uniformly slightly thickened (according to Garel et al<sup>8</sup>), but not clearly dysplastic.

MRA detected right ICA hypoplasia with severe supraclinoid narrowing and distal basilar artery stenosis (Fig 3). DSC-PWI showed only mild elongation of right frontal lobe MTT. This, associated with MRA findings, prompted yearly follow-up MR imaging which, during a 3-year period, did not show progression.

On the basis of these findings, MGS was suspected, and the patient underwent an ophthalmologic evaluation, confirming an MGDA.

## DISCUSSION

MGDA is a sporadic condition, but it has been previously described as an isolated finding in a mother and child.<sup>9</sup> Our patients were initially referred for pituitary MR imaging due to growth hormone deficiency, revealing a PEIR. The pituitary stalk was apparently duplicated on coronal images because of its tubular morphology and direct communication with the third ventricle. This finding should be carefully evaluated to avoid a potential misdiagnosis of other

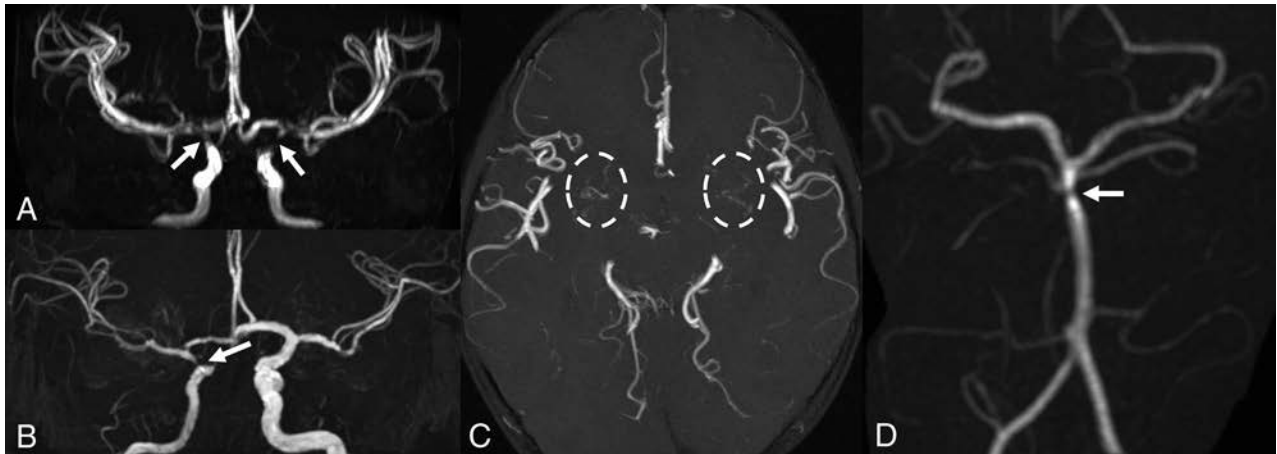


**FIG 3.** MR angiography. Patient 1 (A and C) has bilateral focal stenoses of the internal carotid arteries (arrows) with thin collateral vessels in the lenticulostriate regions (dashed circles). Patient 2 shows unilateral stenosis of the right internal carotid (B) and basilar (D) arteries (arrows).

our cases). To the best of our knowledge, among reported MGDA cases in the literature, none had associated PEIR.

Among the possible midline abnormalities reported in MGS, there is the craniopharyngeal canal, not present in our patients.<sup>10</sup> It represents a rare, well-corticated midline channel of the sphenoid body that develops from the sellar floor to the nasopharynx. Its origin has been hypothesized from incomplete closure of the Rathke pouch, the precursor of the adenohypophysis. This entity can be variably associated with encephalocele and hypopituitarism, most likely due to ectopic adenohypophysis and even tumors (gliomas, dermoids, teratomas, craniopharyngiomas, or adenomas).<sup>11</sup>

Both of our patients had chiasmatic abnormalities with thickening and inferior drooping. On the basis of our experience and the lack of progression on follow-up imaging, we agree with Doneda et al<sup>12</sup> on the dysplastic and not neoplastic nature of the chiasmatic thickening. In our second patient, in the absence of sellar floor defects, chiasmatic prolapse was related to ipsilateral sphenoidal hypoplasia, which could be considered the less severe form of a sphenoid malformative spectrum ending with a meningoencephalocele.

While corpus callosum partial agenesis has already been described in MGS,<sup>2</sup> global thickening, as observed in the second case, though in the absence of dysmorphisms or psychomotor delay, has never been reported.

Intracranial vascular abnormalities in MGS, not necessarily ipsilateral to the optic disc anomaly, could be due to the close relationship of the ICA and optic vesicle development during the fourth week of gestation.<sup>1,4,12</sup> Arterial involvement, most commonly affecting the anterior circulation, ranges from mild hypoplasia to focal stenosis or complete agenesis and progressive Moyamoya syndrome.<sup>3,13</sup> Arterial alterations in our patients were not associated with cerebrovascular reserve impairment. While it is not possible to completely exclude Moyamoya syndrome without more prolonged monitoring, we believe a nonprogressive arterial dysplasia is a more probable diagnosis. We recommend PWI in addition to MRA and follow-up for MGS-associated vasculopathy evaluation.

## CONCLUSIONS

While different craniofacial, pituitary, optic, vascular, and cerebral midline anomalies have been previously reported in association with MGDA, our patients are the first in whom PEIR has also been found. Neuroradiologists should be aware of the possible presence of PEIR in patients with MGS, to aid in the differential diagnosis including other pituitary malformations such as pituitary stalk duplication. We also suggest the use of high-resolution T2-weighted sequences on the sagittal plane to better define the infundibulum in case of abnormalities.

## ACKNOWLEDGMENTS

The authors thank Rosanna Cianniello for the anatomic drawings.

## REFERENCES

1. Thoma D, Nijs I, Demaerel P, et al. Morning glory disc anomaly with an ipsilateral enlargement of the optic nerve pathway. *Eur J Paediatr Neurol* 2017;21:787–791 CrossRef Medline
2. Kalra VB, Gilbert JW, Levin F, et al. Spectrum of MRI findings in morning glory syndrome. *Neurographics* 2014;4:56–60 CrossRef
3. Nezzar H, Mbekeani JN, Dalens H. Morning glory syndrome with carotid and middle cerebral artery vasculopathy. *Optom Vis Sci* 2015;92:e437–41 CrossRef Medline
4. Ellika S, Robson CD, Heidary G, et al. Morning glory disc anomaly: characteristic MR imaging findings. *AJNR Am J Neuroradiol* 2013;34:2010–14 CrossRef Medline
5. Steno A, Popp AJ, Wolfsberger S, et al. Persisting embryonal infundibular recess. *J Neurosurg* 2009;110:359–62 CrossRef Medline
6. Belotti F, Lupi I, Cosottini M, et al. Persisting embryonal infundibular recess (PEIR): two case reports and systematic literature review. *J Clin Endocrinol Metab* 2018;103:2424–29 CrossRef Medline
7. Azuma N, Yamaguchi Y, Handa H, et al. Mutations of the PAX6 gene detected in patients with a variety of optic-nerve malformations. *Am J Hum Genet* 2003;72:1565–70 CrossRef Medline
8. Garel C, Cont I, Alberti C, et al. Biometry of the corpus callosum in children: MR imaging reference data. *AJNR Am J Neuroradiol* 2011;32:1436–43 CrossRef Medline
9. Nagy V, Kettesy B, Toth K, et al. Morning glory syndrome: a clinical study of two cases [in German]. *Klin Monbl Augenheilkd* 2002;219:801–05 CrossRef Medline
10. Kasim N, Choudhri A, Alemzadeh R. Craniopharyngeal canal, morning glory disc anomaly and hypopituitarism: what do they

- have in common?** *Oxf Med Case Reports* 2018;2018:omy018 CrossRef Medline
11. Abele TA, Salzman KL, Harnsberger HR, et al. **Craniopharyngeal canal and its spectrum of pathology.** *AJNR Am J Neuroradiol* 2014; 35:772–77 CrossRef Medline
  12. Doneda C, Pinelli L, Scaramuzzi M, et al. **Morning glory disc anomaly associated with ipsilateral optic nerve and chiasm thickening: three cases and review of the literature.** *Neuropediatrics* 2017;48: 463–66 CrossRef Medline
  13. Lenhart PD, Lambert SR, Newman NJ, et al. **Intracranial vascular anomalies in patients with morning glory disk anomaly.** *Am J Ophthalmol* 2006;142:644–50 CrossRef Medline

# Oculodentodigital Dysplasia: A Hypomyelinating Leukodystrophy with a Characteristic MRI Pattern of Brain Stem Involvement

I. Harting, S. Karch, U. Moog, A. Seitz, P.J.W. Pouwels, and N.I. Wolf



## ABSTRACT

**SUMMARY:** Oculodentodigital dysplasia, a rare genetic disorder caused by mutations in the gene encoding gap junction protein 1, classically presents with typical facial features, dental and ocular anomalies, and syndactyly. Oligosymptomatic patients are common and difficult to recognize, in particular if syndactyly is absent. Neurologic manifestation occurs in approximately 30% of patients, and leukodystrophy or T2 hypointensity of gray matter structures or both have been noted in individual patients. To investigate MR imaging changes in oculodentodigital dysplasia, we retrospectively and systematically reviewed 12 MRIs from 6 genetically confirmed patients. Diffuse supratentorial hypomyelination, T2-hypointense Rolandic and primary visual cortex, and symmetric involvement of middle cerebellar peduncle, pyramidal tract, and medial lemniscus was present in all, T2-hypointense pallidum and dentate nucleus in 2 patients each. This consistent, characteristic pattern of diffuse supratentorial hypomyelination and brain stem involvement differs from other hypomyelinating and nonhypomyelinating leukodystrophies with brain stem involvement, and its recognition should trigger genetic testing for oculodentodigital dysplasia.

**ABBREVIATIONS:** NAWM = normal appearing white matter; ODDD = oculodentodigital dysplasia

Oculodentodigital dysplasia (ODDD) is a rare genetic disorder caused by mutations in the gene encoding gap junction protein 1, also called Connexin 43 (*GJA1*; Online Mendelian Inheritance in Man Nos. 164200 and 257850). Patients show typical facial features including a narrow nose, hypoplastic alae nasi, short palpebral fissures, and epicanthal folds (92% of patients). Ocular, in particular anterior chamber, anomalies, and dental involvement, namely microdontia and enamel hypoplasia (approximately 70%), as well as syndactyly of fourth and fifth finger (in 80%) are common.<sup>1</sup> Neurologic manifestations occur in approximately 30% of patients, including spastic paraparesis, prominent urinary incontinence, ataxia, dysarthria, seizures, and, infrequently, developmental delay or mild intellectual disability.<sup>1,2</sup>

Beighton et al<sup>3</sup> first reported CT with calcification of the basal ganglia in patients with ODDD in 1979. T2 hypointensity of deep gray matter structures and supratentorial cortical regions (eg, the central region) was subsequently reported for individual patients examined with MR imaging. Diffuse T2 hyperintensity of supratentorial white matter has been observed in individual cases, brainstem involvement in three.<sup>4-6</sup> Having noted brain stem involvement in our patients, we retrospectively reviewed cranial MR imaging, including <sup>1</sup>H-MR spectroscopy and DWI, of 6 genetically confirmed patients with MR imaging seen at our institutions to investigate the pattern of MR imaging changes in ODDD.

## MATERIALS AND METHODS

We retrospectively identified 6 patients with ODDD from 4 families with previous MR imaging who were diagnosed and/or followed at University Hospital Heidelberg and VU University Medical Center and Amsterdam Neuroscience. Their 12 cranial MRI scans (age at examination, 5–52 years; mean/median, 25.9/18.7 years) were systematically reviewed in consensus by a neuroradiologist (I.H.) and pediatric neurologist (N.I.W.), each with >15 years of experience in assessing white matter diseases. The study was approved by Heidelberg University (S-760/2018). Axial T2WI and T1WI were available for all 12 MRI scans, and sagittal T1WI/T2WI and DWI with ADC, for at least 1 MRI per patient (11/12 and 9/12 MRIs, respectively). MR imaging was assessed for the extent of T2WI white matter

Received December 7, 2018; accepted after revision March 12, 2019.

From the Department of Neuroradiology (I.H., A.S.) and Centre for Child and Adolescent Medicine (S.K.), Clinic I, Division of Neuropaediatrics and Metabolic Medicine, University Hospital Heidelberg, Heidelberg, Germany; Institute of Human Genetics (U.M.), Heidelberg University, Heidelberg, Germany; and Departments of Radiology and Nuclear Medicine (P.J.W.P.) and Child Neurology (N.I.W.), VU University Medical Center and Amsterdam Neuroscience, Amsterdam, the Netherlands.

Please address correspondence to Inga Harting, MD, Department of Neuroradiology, University of Heidelberg Medical Center, Im Neuenheimer Feld, 400, D-69120 Heidelberg, Germany; e-mail: inga.harting@med.uni-heidelberg.de

 Indicates article with on-line tables.

 Indicates article with supplemental on-line photos.

<http://dx.doi.org/10.3174/ajnr.A6051>

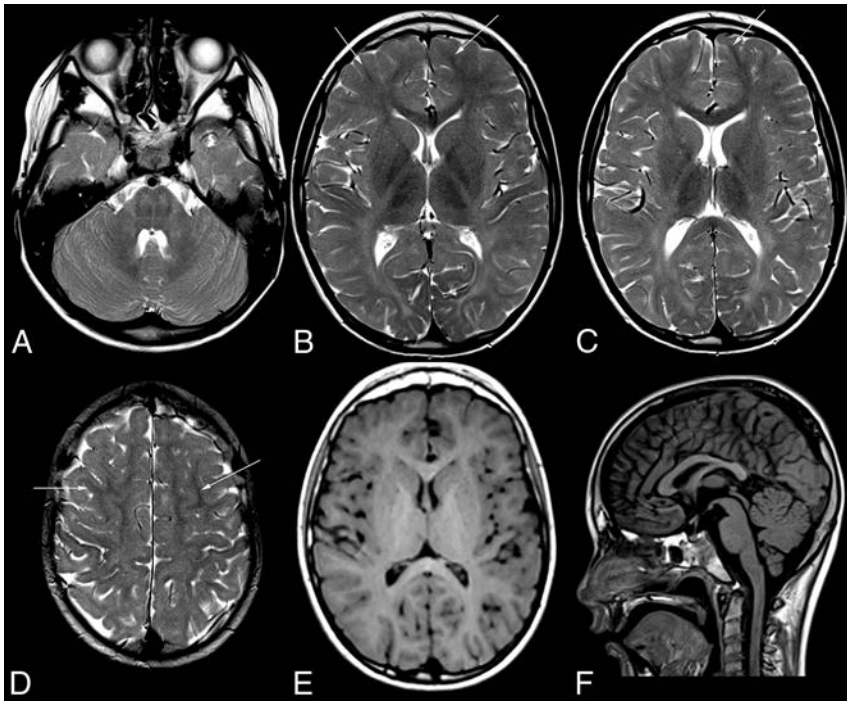


**FIG 1.** MR imaging pattern of ODDD. Mild, diffuse T2 hyperintensity of the supratentorial white matter (B–D) and normal T1 signal (E) characteristic of hypomyelination in patient 1 with involvement of the posterior limb of the internal capsule (B), lateral splenium (C), and typical brain stem tract involvement at the level of the pons (A). Note T2 hypointensity of the Rolandic cortex compared with subcortical NAWM (arrows) of the medial and superior frontal gyri (B–D) and of the primary visual cortex compared with the anterior limb of the internal capsule, genu, and subcortical frontal NAWM (B and C). The craniocervical junction is normal (F). For an overview of MR imaging changes of all patients see On-line Fig 1.

changes (focal/diffuse), corresponding T1WI signal changes, and involvement of specific white matter structures, namely the corpus callosum, anterior and posterior limbs of the internal capsule, pyramidal tract, brain stem tracts, and cerebellar peduncles. The central region and primary visual cortex, pallidum, thalamus, substantia nigra, red nucleus, and dentate nucleus were visually compared with normal-appearing white matter (NAWM) and with contrast in age-matched controls.

Gradient-echo T2\* and SWI, available for 4 patients (6 MRIs: patient 1 [last MRI], patient 2, patient 5, patient 6), were checked for T2\* hypointensities due to calcifications and were compared with contrast in age-matched controls. DWI and ADC maps were inspected for areas of altered diffusion compared with surrounding NAWM or gray matter. Quantitative <sup>1</sup>H-MR spectroscopy of the supratentorial white matter was acquired in all patients (point-resolved spectroscopy sequence or STEAM localization, TE = 20–35 ms). Metabolite values were quantified using LCModel (<http://www.lcmmodel.com/>),<sup>7</sup> compared with control values for each scanner,<sup>8–10</sup> and graded as normal (within the mean ± 1 SD of controls), high/low-to-normal (differing by 1–2 SDs from the mean of controls), and high/low (above/below the mean ± 2 SDs).

### Patients

Diagnosis was confirmed by mutation analysis of *GJA1* in all patients; genetic and MR imaging findings are summarized in On-line Table 1.

Patient 1 had had correction of bilateral syndactyly of D IV and V at 9 months and was evaluated for action and intention tremor at 4 years of age. He also showed myopia, astigmatism, and hypodontia. His father (patient 5), older sister, paternal uncle, and grandmother (no MRIs) also had syndactyly of D IV and V partly in association with ocular and dental findings. Patients 2 and 6, adolescent daughter and mother, had bilateral syndactyly corrected in childhood; spastic paraparesis and urinary incontinence had developed in the mother in her mid-30s.<sup>11,12</sup> Patient 3 had mild motor delay. At 6 years of age, neurogenic bladder was diagnosed with secondary incontinence and frequent bouts of cystitis. Neurologic examination revealed mild spasticity and posterior column signs. Patient 4 had syndactyly of D IV and V of her right hand. She had normal motor milestones but was always clumsy. Motor symptoms became more prominent around 40 years of age with mild spastic paraparesis, ataxia, and posterior column signs on examination. She also developed neurogenic bladder. Optic discs were pale, pursuit movements saccadic.

### MR Imaging

All patients had diffuse, mild T2 hyperintensity of the supratentorial white matter with normal T1 signal, characteristic of hypomyelination (Fig 1 and On-line Fig 1). Three patients had additional, focally more pronounced T2 hyperintensity with corresponding T1 hypointensity. The corpus callosum was involved in all patients, varying from T2 hyperintensity of the lateral splenium in the last MR imaging of patient 1 at 8.9 years of age to an entirely T2 hyperintense corpus callosum (patient 4). On sagittal images, the corpus callosum was thin in patients 2–6. The posterior limb of the internal capsule was T2 hyperintense in all patients and MRIs, while the anterior limb was normal in the youngest 2 and was involved to a varying extent in the older 4 patients. The younger 3 patients imaged within the first 2 decades had some subcortical NAWM, while this was scarce (patient 5) or absent (patients 4 and 6) in the older patients imaged at 41–52 years of age (On-line Fig 1).

Infratentorially, all patients had T2 hyperintensity of the pontine pyramidal tract, medial lemniscus, raphe, and middle cerebellar peduncles, as well as a small, triangular T2 hyperintensity in the lateral pons with its base at the anterolateral pons, located medial to the entry zone, and an intraparenchymal course of the trigeminal nerve, consistent with the anterolateral portion of the middle cerebellar peduncle within the pons. T2 hyperintensity resulted in a typical pattern of signal changes at the level of the pons (Fig 2). In the youngest patient, the pontine pyramidal tract

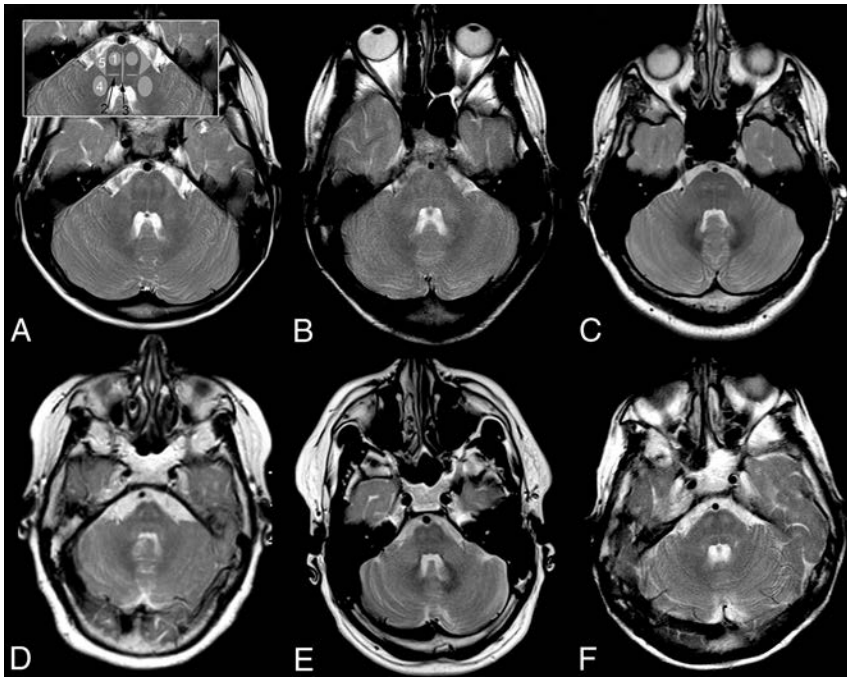


**FIG 2.** Pattern of brain stem tract involvement. T2WI at the level of the pons demonstrates characteristic involvement of the pyramidal tract (1), lemniscus medialis (2, *black arrow*), raphe pontis (3, *black arrow*), middle cerebellar peduncle (4), and the triangular lateral pontine T2 hyperintensity consistent with the anterior course of the pontocerebellar fibers forming the middle cerebellar peduncle (5); schematic representation of tracts is given in inset in A 2, 3 in *black*. A, Patient 1, B, patient 2, C, patient 3, D, patient 4, E, patient 5, F, patient 6. Field strength is 3T in patient 3; otherwise, it is 1.5T. Images are from the last scan from patients with multiple scans.

only became clearly T2 hyperintense at 7.5 years of age; in patients 3 and 4, the T2 hyperintensity extended into the pyramis. Inconsistently involved infratentorial white matter structures were the inferior cerebellar peduncle, superior cerebellar peduncle, and decussation of superior cerebellar peduncles ( $n = 2, 1,$  and  $1,$  respectively; On-line Fig 2).

The Rolandic and primary visual cortices appeared abnormally T2 hypointense, in patient 1 with hypo- instead of hyperintensity to NAWM visible in the same slice (Fig 1B, D) but without corresponding T2\* hypointensity in the 4 patients with T2\*/SWI. Due to white matter hyperintensity, the deep gray matter generally appeared relatively T2 hypointense. Compared with age-matched controls, however, only the pallidum (patients 2 and 6) and dentate nucleus (patients 3 and 5) were more T2 hypointense in 2 patients each, the pallidum with corresponding T2\* hypointensity in both, T1 hyperintensity in patient 2 (On-line Fig 2), and the dentate without corresponding hypointensity in patient 5 with T2\*WI.

DWI did not reveal areas of restricted diffusion. Although in some patients, the ADC was slightly increased in affected white matter areas, this was not very prominent. The craniocervical junction was depicted on sagittal images at least once in all patients, without evidence of stenosis or compression of the medulla.

White matter <sup>1</sup>H-MR spectroscopy findings were normal in patient 3. In the other 5 patients, Cr was high or high-to-normal; mIns was high, high-to-normal, or normal; NAA was normal or low-to-normal; and Cho was normal, low-to-normal, or low. These findings resulted in low or low-to-normal metabolite ratios

of Cho/Cr and NAA/Cr, consistent with hypomyelination (On-line Table 2). Lactate was not detected, and thus was normal.

## DISCUSSION

While syndactyly in combination with typical facial features suggests ODDD, oligosymptomatic patients are common and – in particular if syndactyly is absent – difficult to recognize. Usually only patients with neurologic presentation, occurring in approximately 30%, will be referred for cranial MR imaging. In individual patients with MR imaging previously reported, white matter changes have commonly been observed,<sup>2,4-6,13-25</sup> including brain stem involvement in 3<sup>4-6</sup> and, less commonly, T2 hypointensity of cortical or deep gray matter structures.<sup>2,5,6,14-16,22,23</sup> As yet, there are no histopathologic data.

The pattern of brain structures involved in leukodystrophies has been shown to be highly specific and effective for a differential diagnosis using a practical diagnostic algorithm, with differentiation between hypomyelinating and nonhypomyelinating leukodystrophies as the first discriminator.<sup>26</sup> Hypomyelination is characterized by moderate T2 hyperintensity, less bright than in nonhypomyelinating leukodystrophies, eg, demyelination or vacuolation. T1 signal depends on the amount of myelin deposited and is often normal or otherwise iso- or mildly hypointense.<sup>26,27</sup> On <sup>1</sup>H-MR spectroscopy, elevated Cr and mIns in combination with normal or near-normal NAA, low (-normal) NAA/Cr, and low (-normal) Cho are typical.<sup>8,9</sup>

In all MRIs of our patients, supratentorial white matter changes were characteristic of hypomyelination and accompanied by typical <sup>1</sup>H-MR spectroscopy findings in 5 of 6. Three patients imaged during late adolescence and adulthood had foci of more pronounced white matter changes consistent with small areas of secondary degeneration with loss of myelin and astrogliosis. Scarce or absent subcortical NAWM and involvement of the anterior limb of internal capsule only in the 3 oldest patients suggest progression of white matter changes with time as does extension of pyramidal tract hyperintensity from the mesencephalon to the pons during follow-up in the youngest patient.

Hypomyelinating leukodystrophies can be differentiated on the basis of additional, characteristic MR findings, eg, as in hypomyelination with atrophy of basal ganglia and cerebellum (H-ABC) or by the presence of non-neurological features, eg, congenital cataract in hypomyelination with congenital cataract (HCC), hypodontia and/or delayed puberty in 4H syndrome, or syndactyly in ODDD.<sup>27</sup> However, systemic manifestations are not obligatory and therefore may not be present in all patients, as seen in patient 3 who presented with mild spas-

ticity, sensory deficit, and neurogenic bladder but without syndactyly. Even within families, signs and symptoms may vary.<sup>1</sup> Notably, all our patients, irrespective of the presence or absence of neurologic manifestation or syndactyly, had a characteristic pattern of brain stem tract involvement in addition to supratentorial hypomyelination, which differed from other hypomyelinating leukodystrophies with brain stem involvement. In Pelizaeus-Merzbacher-like disease, there is prominent T2 hyperintensity of the basis pontis, not always restricted to the pyramidal tract<sup>28</sup>; in 4H syndrome the medial lemniscus is relatively spared<sup>29</sup>; in hypomyelination of early myelinating structures<sup>30</sup> the medulla oblongata and caudal pons are more extensively involved than in ODDD; moreover, none of these disorders involve the middle cerebellar peduncles. Whereas hypomyelination with brain stem and spinal cord involvement and leg spasticity<sup>31</sup> involves the medial lemniscus and pyramidal tract similar to ODDD, the inferior and superior but not middle cerebellar peduncles are T2 hyperintense.

When using prominent brain stem involvement as a starting point of an MR imaging–based differential diagnosis, ODDD must also be differentiated from 3 nonhypomyelinating leukodystrophies: Brain stem involvement is similar in autosomal dominant leukodystrophy related to duplication of the *lamin B1* gene,<sup>32</sup> but supratentorial white matter changes are more T2 hyperintense, not consistent with hypomyelination, and tend to spare a periventricular rim. T2 hyperintensity of the middle cerebellar peduncles in fragile X premutation carriers is combined with T2 hyperintensity of the deep cerebellar white matter, while the medial lemniscus and pyramidal tract are not affected.<sup>33</sup> Leukoencephalopathy with brain stem and spinal cord involvement and lactate elevation<sup>34</sup> involves the medial lemniscus and pyramidal tract, inferior and superior, but not the middle cerebellar peduncle and again differs by much more prominent supratentorial T2 hyperintensity not consistent with hypomyelination.

It has previously been noted that patients with ODDD imaged in the first decade may have MR imaging changes despite the absence of neurologic symptoms.<sup>1</sup> Similarly, all 6 patients had extensive pyramidal tract involvement and involvement of the medial lemniscus on MR imaging, irrespective of the presence of spasticity or impaired sensibility. Compression of the medulla at the craniocervical junction, as initially suggested due to a hyperostotic skull base,<sup>3</sup> was not confirmed on MR imaging, either in later reports or in our patients.

Earlier reports also noted calcifications of the basal ganglia, which are a likely correlate of the T2 hypointensity reported in the literature<sup>5,6,14-16,23</sup> and of pallidal T2/T2\* hypointensity in patients 2 and 6, though we cannot exclude abnormal iron accumulation as previously suggested.<sup>6</sup> Consistent with previous reports, the Rolandic and primary visual cortices appeared abnormally T2 hypointense, however without corresponding T2\* hypointensity and, therefore, not suggestive of either calcification or abnormal brain iron accumulation.

## CONCLUSIONS

Brain imaging in 6 patients from 4 families with genetically confirmed ODDD shows a characteristic MR imaging pattern of

brain stem tract involvement, consisting of the middle cerebellar peduncle, pyramidal tract, and medial lemniscus in combination with diffuse, supratentorial hypomyelination. Recognition of this pattern should trigger genetic evaluation of undiagnosed patients and thereby shorten the diagnostic process.

## REFERENCES

1. Paznekas W, Karczeski B, Vermeer S, et al. **GJA1 mutations, variants, and connexin 43 dysfunction as it relates to the oculodentodigital dysplasia phenotype.** *Hum Mutat* 2009;30:724–33 CrossRef Medline
2. Loddenkemper T, Grote K, Evers S, et al. **Neurological manifestations of the oculodentodigital dysplasia syndrome.** *J Neurol* 2002; 249:584–95 CrossRef Medline
3. Beighton P, Hamersma H, Raad M. **Oculodento-osseous dysplasia: heterogeneity or variable expression?** *Clin Genet* 1979;16:169–77 Medline
4. Park KW, Ryu HS, Kim J, et al. **Oculodentodigital dysplasia presenting as spastic paraparesis: the first genetically confirmed Korean case and a literature review.** *J Mov Disord* 2017;10:149–53 CrossRef Medline
5. Furuta N, Ikeda N, Hirayanagi K, et al. **Novel GJA1 mutation in oculodentodigital dysplasia with progressive spastic paraplegia and sensory deficits.** *Intern Med* 2012;51:93–98 CrossRef Medline
6. Gutmann DH, Zackai EH, McDonald-McGinn DM, et al. **Oculodentodigital dysplasia syndrome associated with abnormal cerebral white matter.** *Am J Med Genet* 1991;41:18–20 CrossRef Medline
7. Provencher S. **Estimation of metabolite concentrations from localized in vivo proton NMR spectra.** *Magn Reson Med* 1993;30:672–79 CrossRef Medline
8. van der Voorn JP, Pouwels PJ, Hart AA, et al. **Childhood white matter disorders: quantitative MR imaging and spectroscopy.** *Radiology* 2006; 241:510–17 CrossRef Medline
9. Steenweg ME, Wolf NI, van Wieringen WN, et al. **Quantitative MRI in hypomyelinating disorders: correlation with motor handicap.** *Neurology* 2016;87:752–58 CrossRef Medline
10. Harting I, Boy N, Heringer J, et al. **(1)H-MRS in glutaric aciduria type I: impact of biochemical phenotype and age on the cerebral accumulation of neurotoxic metabolites.** *J Inherit Metab Dis* 2015; 38:829–38 CrossRef Medline
11. Thomsen M, Schneider U, Weber M, et al. **The different appearance of the oculodentodigital dysplasia syndrome.** *J Pediatr Orthop B* 1998;7:23–26 Medline
12. Wiest T, Herrmann O, Stögbauer F, et al. **Clinical and genetic variability of oculodentodigital dysplasia.** *Clin Genet* 2006;70:71–72 CrossRef Medline
13. Alao MJ, Bonneau D, Holder-Espinasse M, et al. **Oculo-dento-digital dysplasia: lack of genotype–phenotype correlation for GJA1 mutations and usefulness of neuro-imaging.** *Eur J Med Genet* 2010;53: 19–22 CrossRef Medline
14. Ganos C, Münchau A, Holst B, et al. **Teaching neuroimages: oculodentodigital dysplasia.** *Neurology* 2012;79:e140 CrossRef Medline
15. Barzegar M, Sayadnasiri M, Tabrizi A. **Epilepsy as a rare neurologic manifestation of oculodentodigital dysplasia.** *Iran J Child Neurol* 2012;6:39–43 Medline
16. Ginsberg LE, Jewett T, Grub R, et al. **Oculodentodigital dysplasia: neuroimaging in a kindred.** *Neuroradiology* 1996;38:84–86 CrossRef Medline
17. Jamsheer A, Badura-Stronka M, Sowińska A, et al. **A severe progressive oculodentodigital dysplasia due to compound heterozygous GJA1 mutation.** *Clin Genet* 2010;78:94–97 CrossRef Medline
18. Norton K, Carey J, Gutmann D. **Oculodentodigital dysplasia with cerebral white matter abnormalities in a two-generation family.** *Am J Med Genet* 1995;57:458–61 CrossRef Medline
19. Shapiro R, Griffin J, Stine O. **Evidence for genetic anticipation in the oculodentodigital syndrome.** *Am J Med Genet* 1997;71:36–41 CrossRef Medline
20. Stanislaw CL, Narvaez C, Rogers RG, et al. **Oculodentodigital dys-**

- plasia with cerebral white matter abnormalities: an additional case.** *Proc Greenwood Genet Center* 1998;17:20–24
21. van Es RJ, Wittebol-Post D, Beemer FA. **Oculodentodigital dysplasia with mandibular retrognathism and absence of syndactyly: a case report with a novel mutation in the connexin 43 gene.** *Int J Oral Maxillofac Surg* 2007;36:858–60 CrossRef Medline
  22. Amador C, Mathews AM, Del Carmen Montoya M, et al. **Expanding the neurologic phenotype of oculodentodigital dysplasia in a 4-generation Hispanic family.** *J Child Neurol* 2008;23:901–05 CrossRef Medline
  23. Schrandner-Stumpel C, Franke C. **Central nervous system abnormalities in oculodentodigital dysplasia.** *Genet Counsel* 1996;7:233–35
  24. Kogame T, Dainichi T, Shimomura Y, et al. **Palmoplantar keratosis in oculodentodigital dysplasia with a GJA1 point mutation out of the C-terminal region of connexin 43.** *J Dermatol* 2014;41:1095–97 CrossRef Medline
  25. Tumminelli G, Di Donato I, Guida V, et al. **Oculodentodigital dysplasia with massive brain calcification and a new mutation of GJA1 gene.** *J Alzheimers Dis* 2016;49:27–30 CrossRef Medline
  26. Schiffmann R, van der Knaap M. **Invited article: an MRI-based approach to the diagnosis of white matter disorders.** *Neurology* 2009;72:750–59 CrossRef Medline
  27. Pouwels PJ, Vanderver A, Bernard G, et al. **Hypomyelinating leukodystrophies: translational research progress and prospects.** *Ann Neurol* 2014;76:5–19 CrossRef Medline
  28. Biancheri R, Rosano C, Denegri L, et al. **Expanded spectrum of Pelizaeus-Merzbacher-like disease: literature revision and description of a novel GJC2 mutation in an unusually severe form.** *Eur J Hum Genet* 2013;21:34–39 CrossRef Medline
  29. Cayami FK, Bugiani M, Pouwels PJ, et al. **4H leukodystrophy: lessons from 3T imaging.** *Neuropediatrics* 2018;49:112–17 CrossRef Medline
  30. Steenweg ME, Wolf NI, Schieving JH, et al. **Novel hypomyelinating leukoencephalopathy affecting early myelinating structures.** *Arch Neurol* 2012;69:125–28 CrossRef Medline
  31. Taft RJ, Vanderver A, Leventer RJ, et al. **Mutations in DARS cause hypomyelination with brain stem and spinal cord involvement and leg spasticity.** *Am J Hum Genet* 2013;92:774–80 CrossRef Medline
  32. Dos Santos MM, Grond-Ginsbach C, Aksay SS, et al. **Adult-onset autosomal dominant leukodystrophy due to LMNB1 gene duplication.** *J Neurol* 2012;259:579–81 CrossRef Medline
  33. Brunberg JA, Jacquemont S, Hagerman RJ, et al. **Fragile X premutation carriers: characteristic MR imaging findings of adult male patients with progressive cerebellar and cognitive dysfunction.** *AJNR Am J Neuroradiol* 2002;23:1757–66 Medline
  34. Scheper GC, van der Kloot T, van Andel RJ, et al. **Mitochondrial aspartyl-tRNA synthetase deficiency causes leukoencephalopathy with brain stem and spinal cord involvement and lactate elevation.** *Nat Genet* 2007;39:534–39 CrossRef Medline

# Lumbar Spinal Stenosis Severity by CT or MRI Does Not Predict Response to Epidural Corticosteroid versus Lidocaine Injections

F.A. Perez, S. Quinet, J.G. Jarvik, Q.T. Nguyen, E. Aghayev, D. Jitjai, W.D. Hwang, E.R. Jarvik, S.S. Nedeljkovic, A.L. Avins, J.M. Schwalb, F.E. Diehn, C.J. Standaert, D.R. Nerenz, T. Annaswamy, Z. Bauer, D. Haynor, P.J. Heagerty, and J.L. Friedly



## ABSTRACT

**BACKGROUND AND PURPOSE:** Epidural steroid injections may offer little-to-no short-term benefit in the overall population of patients with symptomatic spinal stenosis compared with lidocaine alone. We investigated whether imaging could identify subgroups of patients who might benefit most.

**MATERIALS AND METHODS:** A secondary analysis of the Lumbar Epidural Steroid Injections for Spinal Stenosis prospective, double-blind trial was performed, and patients were randomized to receive an epidural injection of lidocaine with or without corticosteroids. Patients ( $n = 350$ ) were evaluated for qualitative and quantitative MR imaging or CT measures of lumbar spinal stenosis. The primary clinical end points were the Roland-Morris Disability Questionnaire and the leg pain numeric rating scale at 3 weeks following injection. ANCOVA was used to assess the significance of interaction terms between imaging measures of spinal stenosis and injectate type on clinical improvement.

**RESULTS:** There was no difference in the improvement of disability or leg pain scores at 3 weeks between patients injected with epidural lidocaine alone compared with corticosteroid and lidocaine when accounting for the primary imaging measures of qualitative spinal stenosis assessment (interaction coefficients for disability score,  $-0.1$ ; 95% CI,  $-1.3$  to  $1.2$ ;  $P = .90$ ; and for the leg pain score,  $0.1$ ; 95% CI,  $-0.6$  to  $0.8$ ;  $P = .81$ ) or the quantitative minimum thecal sac cross-sectional area (interaction coefficients for disability score,  $0.01$ ; 95% CI,  $-0.01$  to  $0.03$ ;  $P = .40$ ; and for the leg pain score,  $0.01$ ; 95% CI,  $-0.01$  to  $0.03$ ;  $P = .33$ ).

**CONCLUSIONS:** Imaging measures of spinal stenosis are not associated with differential clinical responses following epidural corticosteroid injection.

**ABBREVIATIONS:** AP = anteroposterior; ESI = epidural steroid injection; ML = mediolateral; NRS = numeric rating scale; RDQ = Roland-Morris Disability Questionnaire

Lumbar spinal stenosis is a common cause of low back pain, radicular pain, and neurogenic claudication leading to disability.<sup>1,2</sup> Imaging for lumbar stenosis is controversial because there is

no consistent correlation between the severity of stenosis by imaging and the severity of symptoms.<sup>3-5</sup>

Spinal stenosis symptoms may, in part, be due to nerve root inflammation and/or ischemia related to compression.<sup>6</sup> Epidural steroid injections (ESIs) are often used to reduce local inflamma-

Received January 24, 2019; accepted after revision March 19.

From the Department of Radiology (F.A.P., J.G.J., Q.T.N., D.H.), Comparative Effectiveness, Cost and Outcomes Research Center (J.G.J., P.J.H., J.L.F.), Departments of Neurological Surgery (J.G.J.), Health Services (J.G.J.), Orthopedics and Sports Medicine (Q.T.N.), Biostatistics (P.J.H.), and Rehabilitation Medicine (J.L.F.), University of Washington, Seattle, Washington; Department of Radiology (S.Q.), College of Wisconsin, Milwaukee, Wisconsin; Spinal Centre Division (E.A.), Schulthess Klinik, Zurich, Switzerland; Oregon Health Sciences University (D.J.) Portland, Oregon; TRA Medical Imaging (W.D.H.), Tacoma, Washington; University of Washington Medicine (E.R.J.), Seattle, Washington; Department of Anesthesiology, Perioperative and Pain Medicine and Spine Unit (S.S.N.), Harvard Vanguard Medical Associates, Brigham and Women's Hospital, Boston, Massachusetts; Division of Research (A.L.A.), Kaiser Permanente Northern California, Oakland, California; Department of Neurosurgery (J.M.S., D.R.N.), Henry Ford Medical Group, Detroit, Michigan; Department of Radiology (F.E.D.), Mayo Clinic, Rochester, Minnesota; Department of Physical Medicine and Rehabilitation (C.J.S.), University of Pittsburgh School of Medicine, Pittsburgh, Pennsylvania; Department of Physical Medicine and Rehabilitation (T.A.), VA North Texas Healthcare System, Dallas, Texas; and Cancer and

Blood Disorders Center (Z.B.), Seattle Children's Research Institute, Seattle, Washington.

This work was supported by the Agency for Healthcare Research and Quality (grants 1R01HS019222-01 and 1R01HS022972-01) and the Patient-Centered Outcomes Research Institute (contract CE-12-11-4469).

Paper previously presented at: American Society of Neuroradiology Annual Meeting and the Foundation of the ASNR Symposium, April 25–30, 2015; Chicago, Illinois. "Qualitative Assessment of Lumbar Spinal Stenosis by CT and MRI: Stenosis Severity Does Not Predict Response to Epidural Glucocorticoid Injections."

Please address correspondence to Janna L. Friedly, MD, Department of Rehabilitation Medicine, Comparative Effectiveness, Cost and Outcomes Research Center, University of Washington, Box 359859, Seattle, Washington 98104; e-mail: friedlyj@uw.edu

Indicates open access to non-subscribers at [www.ajnr.org](http://www.ajnr.org)

Indicates article with supplemental on-line tables.

<http://dx.doi.org/10.3174/ajnr.A6050>

tion and therefore improve lumbar spinal stenosis symptoms.<sup>7-9</sup> Given the variable results with ESI, there is a need to understand the patient, disease, and procedural factors associated with improved outcomes. Patients with severe nerve root compression due to disc herniation may be less likely to benefit from an ESI, perhaps related to the predominance of mechanical compression rather than inflammation.<sup>10</sup> However, there is a lack of rigorous data to determine whether imaging severity predicts the response to ESI in lumbar central spinal stenosis.<sup>10-15</sup> Prior studies examining the relationship between outcomes of ESI for spinal stenosis and imaging severity have been small and uncontrolled, leading to mixed results.

The Lumbar Epidural Steroid Injections for Spinal Stenosis (LESS) multicenter, double-blind randomized trial found that ESIs offered little-to-no short-term benefit compared with an epidural injection of lidocaine alone.<sup>16</sup> However, the primary analysis of this study did not specifically assess whether imaging spinal stenosis severity predicted a differential response to injections of epidural corticosteroid and lidocaine versus lidocaine alone.<sup>17</sup>

Our objective was to determine whether lumbar spine MR imaging or CT measures of lumbar spinal stenosis severity predicted a response to epidural injection of corticosteroid and lidocaine versus lidocaine alone. We hypothesized that patients with less severe central stenosis, in which inflammation may play a larger role than mechanical compression, would have a more favorable response to corticosteroid injections compared with treatment with lidocaine alone.

## MATERIALS AND METHODS

### Patients

A secondary, retrospective analysis of patient data from the LESS trial was performed (ClinicalTrials.gov identifier: NCT01238536).<sup>16,18</sup> The study was Health Insurance Portability and Accountability Act-compliant, we obtained institutional review board approval at each of the 16 clinical sites in the United States, and patients provided written informed consent. Detailed inclusion and exclusion criteria and patient characteristics have been previously described.<sup>16</sup> Inclusion criteria were patients 50 years of age and older with MR imaging or CT evidence of lumbar central spinal stenosis assessed by an enrolling clinician; moderate-to-severe symptoms consistent with neurogenic claudication with an average pain numeric rating scale (NRS) of  $\geq 5$  (on a scale of 0–10 with 0 indicating no pain and 10 indicating most severe pain) for pain in the lower back, buttock, leg, or a combination of these sites on standing, walking, or spinal extension in the past week; and a score of  $\geq 7$  on the Roland-Morris Disability Questionnaire (RDQ), in which scores range from 0–24, with higher scores indicating greater disability. Patients with a history of prior lumbar surgery, ESI in the previous 6 months, or spondylolisthesis requiring surgery were excluded.

### Interventions

Patients were randomized to receive an epidural injection of either corticosteroid with lidocaine ( $n = 200$ ) or lidocaine alone ( $n = 200$ ). Injections were performed by 26 board-certified anesthesiologists, physiatrists, and radiologists with ESI expertise and

trained to perform the injections using standardized techniques. Study physicians and outcome assessors were blinded to the injectate administered. Physicians chose either an interlaminar or transforaminal injection approach based on clinical judgment and experience because there remains uncertainty about the relative effectiveness. Interlaminar injections were performed 1 spinal level below the maximal canal stenosis as determined by the treating physician or, if not technically feasible, as close to the level of maximal stenosis as possible. Interlaminar injections were not performed at the level of maximum stenosis to avoid the theoretic possibility of worsening thecal sac compression by the epidural injectate, and a prior study has demonstrated consistently  $>1$  spinal level of epidural injectate dispersal following interlaminar injection.<sup>19</sup> Transforaminal injections were performed at the most symptomatic nerve root level and, in many cases, with multilevel and/or bilateral injections to optimize injectate delivery.<sup>20</sup> Under fluoroscopic guidance, an 18- to 25-ga Quincke or Tuohy spinal needle was used to inject 2 mL of 0.25%–1% lidocaine followed by 1–3 mL of corticosteroid or 1–3 mL of 0.25%–1% lidocaine. The volume, dose, and type of corticosteroid were determined by the treating physician (60–120 mg of methylprednisolone; 6–12 mg of betamethasone; 60–120 mg of triamcinolone; or 8–10 mg of dexamethasone). Additional injection procedure details are available.<sup>16,18</sup>

### Clinical Outcomes

Detailed outcome measures for this trial have been previously described.<sup>16</sup> For the current analysis, the 2 predetermined primary outcomes were the RDQ and mean leg pain NRS at 3 weeks following injection because the greatest clinical response to the injection was observed at that time point in the LESS trial. Secondary clinical outcome measures included the following: RDQ and leg pain NRS at 6 weeks postinjection; back pain NRS and mean of leg and back pain NRS at 3 and 6 weeks postinjection; and the Swiss Spinal Stenosis Questionnaire<sup>21</sup> symptom subscale (scores of 1–5, with higher scores indicating worse symptoms) and the physical function subscale (scores of 1–4, with higher scores indicating worse function) at 3 and 6 weeks postinjection.

### Imaging

MR imaging studies included at least sagittal T1, sagittal T2, and axial T2-weighted images; CT studies included at least axial soft-tissue algorithm images. Analysis was limited to patients with lumbar spine CT or MR imaging studies performed within 2 years of study enrollment (350/400 enrolled patients). Imaging studies were anonymized and reviewed on a PACS at the data-coordinating center for qualitative and quantitative measures of lumbar central stenosis.

### Qualitative Imaging Measures of Lumbar Central Stenosis

Qualitative central stenosis was determined for all eligible patients at each lumbar spine level on CT (41 studies) or MR imaging (309 studies) on the basis of the degree of central canal narrowing on axial images relative to its expected normal cross-sectional area as follows: 0 = normal, 1 = mild stenosis, less than or equal to one-third loss of the expected normal area; 2 = moderate stenosis,

one-third to two-thirds loss of the expected normal area; 3 = severe stenosis, more than two-thirds loss of the expected normal area.<sup>22,23</sup> For 308 of 309 patients with MR imaging studies, we qualitatively assessed lumbar spine perineural CSF effacement at each lumbar spine level as a secondary measure on axial T2 MR imaging using the grading system of Lee et al<sup>24</sup>: 0 = normal, 1 = mild, 2 = moderate, and 3 = severe (1 MR imaging study could not be assessed on this measure due to missing axial T2 sequences). For each patient, we assessed up to 5 lumbar spine levels qualitatively and derived several single-summary measures of overall spinal stenosis. The predetermined primary qualitative imaging measure was the maximum qualitative central stenosis grade representing the worst level of stenosis. Other secondary measures included the maximum qualitative CSF effacement score and the mean central stenosis and qualitative CSF effacement scores to represent the overall degree of stenosis, taking into account the degree of stenosis at multiple levels.

Two experienced imaging readers (W.D.H., a fellowship-trained neuroradiologist with 5 years of experience; and Q.T.N., a radiology physician assistant with 17 years of experience interpreting spinal imaging) performed qualitative imaging assessment blinded to patient injectate and symptoms. Imaging studies were randomly divided between the 2 readers for review. Seventy-one studies were reviewed by both readers independently to assess interrater reliability.

### **Quantitative Imaging Measures of Lumbar Central Stenosis**

We excluded patients with CT studies from quantitative analysis because we could not reliably determine these measurements on CT. We performed quantitative analysis at each lumbar spinal level for 304 of 309 patients who underwent MR imaging; due to file-format limitations, cross-referencing of axial and sagittal images could not be performed for 5 patients.

The cross-sectional thecal sac area was measured at each intervertebral level by tracing its outline with an ROI tool on axial T2 images. Because axial images were not always acquired parallel to the intervertebral disc level and perpendicular to the spinal canal, a correction factor was applied to each level by multiplying the measured cross-sectional area by the cosine of the angle between the axial images and a line parallel to the adjacent vertebral body endplate. We measured the maximum anteroposterior (AP) and mediolateral (ML) diameters of the thecal sac on axial T2 images, and the AP thecal sac diameter was also determined for each lumbar intervertebral disc level using midline sagittal T2 images.

For each patient, readers quantitatively assessed up to 5 lumbar spine levels, and several single-summary measures of overall spinal stenosis were derived. The predetermined primary quantitative imaging measure was the minimum, angle-corrected, thecal sac cross-sectional area representing the worst level of stenosis. Other secondary measures included the mean of the angle-corrected, thecal sac cross-sectional area (as a summary measure for multilevel stenosis) as well as minimum and mean summary measures for each remaining measure (Table); non-angle-corrected measures were also evaluated.

Five trained readers performed quantitative assessment

(F.A.P. and S.Q., fellowship-trained neuroradiologists both with 5 years of experience; E.A., an orthopedic surgeon; D.J. and E.R.J., undergraduate research assistants) blinded to patient injectate and symptoms. After training, the readers reviewed a verification set of 20 MR imaging studies or 100 lumbar spinal levels to evaluate reliability before beginning study imaging review.

All imaging studies were then divided among the 5 trained readers for review. Statistical analysis was performed using data from a single reader per patient.

### **Statistical Analysis**

Data analysis was performed using R statistical and computing software, Version 3.1.2 (<http://www.r-project.org/>).<sup>23</sup>

We evaluated the interrater agreement of qualitative assessments of stenosis severity between the 2 experienced readers using unweighted  $\kappa$  analysis. For the quantitative imaging predictors, interrater reliability was assessed among the 5 trained readers using an intraclass correlation coefficient analysis of the verification imaging studies.

ANCOVA for each potential imaging predictor and each clinical outcome was constructed with adjustments for the baseline clinical measure value and patient recruitment site. The dependent variable in each model was the clinical outcome measure. Independent variables were injectate group (lidocaine alone versus corticosteroid and lidocaine) and the imaging measure of spinal stenosis severity. The primary statistical analysis was whether the effect of injectate type on a clinical outcome differed depending on an imaging measure of stenosis severity. This was assessed by including an imaging measure by injectate type interaction term in the model and evaluating the statistical significance with a likelihood ratio test. For post hoc comparison testing, the Tukey Honestly Significant Difference test was performed. For the predefined analysis using primary imaging measures and primary clinical end points, statistical significance was  $P < .05$ . For exploratory analysis of secondary measures, a predetermined statistical significance threshold of  $P < .01$  was used to minimize false discoveries.

## **RESULTS**

### **Patients**

There were no statistically significant differences in baseline clinical or imaging features between patients randomized to epidural corticosteroid and lidocaine versus lidocaine alone injection in the subset of patients included in this analysis ( $n = 350$ , Table). Imaging studies were performed a median of 43 days from study enrollment with an interquartile range of 132 days (Q1 = 20 days and Q3 = 152 days). Seventy-four percent (260/350) of patients had at least 1 lumbar spine level of moderate or severe stenosis, and 50% (175/350) of patients had at least 1 lumbar spine level of severe stenosis.

### **Epidural Injection Approach and Level**

The characteristics of epidural injections were similar between treatment groups.

Sixty-eight percent (239/350) of patients had interlaminar injections, and 32% (111/350) had transforaminal injections. For

### Summary of patient baseline clinical and imaging characteristics<sup>a</sup>

	Lidocaine (n = 175)	Corticosteroid and Lidocaine (n = 175)
Patient demographics		
Female	53% (93/175)	57% (100/175)
Age range; mean (SD)	50–96; 68 (9.9)	50–89; 68 (9.6)
Baseline clinical measures		
RDQ disability score	15.6 (4.3)	16.1 (4.5)
Leg pain NRS	7.2 (1.7)	7.1 (1.9)
Back pain NRS	6.6 (2.6)	6.6 (2.4)
Mean of leg and back pain NRS	6.6 (1.2)	6.5 (1.5)
SSSQ symptom subscale score	3.1 (0.6)	3.2 (0.6)
SSSQ physical function subscale score	2.5 (0.5)	2.5 (0.5)
Injection characteristics		
Interlaminar approach	68% (119/175)	69% (120/175)
Transforaminal approach	32% (56/175)	31% (55/175)
Mean lumbar level distance from injection to level of qualitative worst stenosis	0.6 (0.6)	0.5 (0.7)
Qualitative CT and MRI	n = 175	n = 175
Measures		
Maximum qualitative central stenosis	2.2 (0.8)	2.3 (0.9)
Mean qualitative central stenosis	1.2 (0.4)	1.2 (0.5)
Qualitative MRI measures	n = 150	n = 158
Maximum qualitative CSF effacement	2.0 (1.1)	2.0 (1.1)
Mean qualitative CSF effacement	0.7 (0.6)	0.7 (0.6)
Quantitative MRI measures	n = 148	n = 156
Minimum thecal sac cross-sectional area (mm <sup>2</sup> )	72 (38)	73 (39)
Mean thecal sac cross-sectional (mm <sup>2</sup> )	130 (40)	130 (38)
Minimum thecal sac AP diameter on axial images (mm)	7.2 (2.5)	7.2 (2.4)
Mean thecal sac AP diameter on axial images (mm)	10.6 (2.0)	10.5 (2.0)
Minimum thecal sac AP diameter on sagittal images (mm)	6.2 (2.3)	6.4 (2.4)
Mean thecal sac AP diameter on sagittal images (mm)	9.5 (2.0)	9.6 (2.0)
Minimum thecal sac ML diameter (mm)	11.6 (3.2)	11.6 (3.1)
Mean thecal sac ML diameter (mm)	16.1 (2.7)	16.1 (2.5)

**Note:**—SSSQ indicates Swiss Spinal Stenosis Questionnaire.

<sup>a</sup> Values represent mean and SD unless otherwise specified.

each injection approach, half of patients received epidural corticosteroid and lidocaine and half received lidocaine alone (Table). Epidural injections were performed within 1 lumbar spinal level of the qualitatively worst stenosis in 92% of patients (321/350; for example, in a patient with a maximum stenosis at L5–S1, an interlaminar epidural injection at L4–L5 is 1 lumbar spinal level away and a transforaminal epidural injection at L5 is a one-half lumbar spinal level away). There was no difference in the mean distance of epidural injection from the level of maximum stenosis between treatment groups (Table,  $P = .72$ ).

#### Interrater Agreement for Evaluation of Imaging Studies

For the primary qualitative imaging measure of the worst level of central stenosis (maximum qualitative central stenosis score), there was 74% agreement among the 2 experienced readers on a level-by-level basis (agreement in 261 of 355 lumbar spinal levels) with a  $\kappa$  score of 0.72, consistent with substantial agreement.<sup>25</sup> On a per-patient basis, using the maximum spinal stenosis score for each patient indicating the worst level of stenosis, there was 86% agreement (61/71 patients) between the 2 experienced readers with a  $\kappa$  score of 0.84. For the primary quantitative imaging measure of the angle-corrected thecal sac cross-sectional area, there was excellent agreement among the 5 trained readers with an intraclass correlation coefficient of 0.91.<sup>26</sup>

#### Primary Imaging Measures as Predictors of Improvement in the RDQ Disability Score or Leg Pain NRS following Epidural Injection

Regardless of the type of epidural injectate, study patients had an average 3.4-point improvement in the RDQ disability score (95% CI,  $-4.0$  to  $-2.9$ ;  $P < .0001$ ) and an average 2.5-point improvement in the leg pain NRS at 3 weeks (95% CI,  $-2.8$  to  $-2.2$ ;  $P < .0001$ ). Patients who received corticosteroid with lidocaine injections had a slightly greater improvement in the RDQ disability score and leg pain NRS than patients injected with lidocaine alone at 3 weeks (adjusted mean differences for the RDQ,  $-1.7$  points; 95% CI,  $-2.8$  to  $-0.7$ ;  $P < .01$ ; and for the leg pain NRS,  $-0.6$  points; 95% CI,  $-1.2$  to  $0$ ;  $P < .05$ ) similar to rates previously reported.<sup>16</sup> By means of the predetermined primary imaging measure of the maximum qualitative central stenosis score, patients with moderate central stenosis had slightly greater improvement in the RDQ disability score and leg pain NRS regardless of the type of injectate at 3 weeks (Fig 1) compared with those patients with mild stenosis (adjusted average treatment effect between moderate and mild central stenosis for RDQ,  $-2.1$  points; 95% CI,  $-1.9$  to  $-0.6$ ;  $P < .05$ ; and for leg pain NRS,  $-1.0$  point; 95% CI,  $-1.8$  to  $-0.2$ ;  $P < .05$ ) but not severe stenosis (adjusted average treatment effect between moderate and severe central stenosis for the RDQ,  $-1.3$  points; 95% CI,  $-0.56$  to  $-0.1$ ;  $P = .15$ ; and for the leg pain NRS,  $-0.6$  points; 95% CI,  $-1.4$  to  $-0.1$ ;  $P = .20$ ).

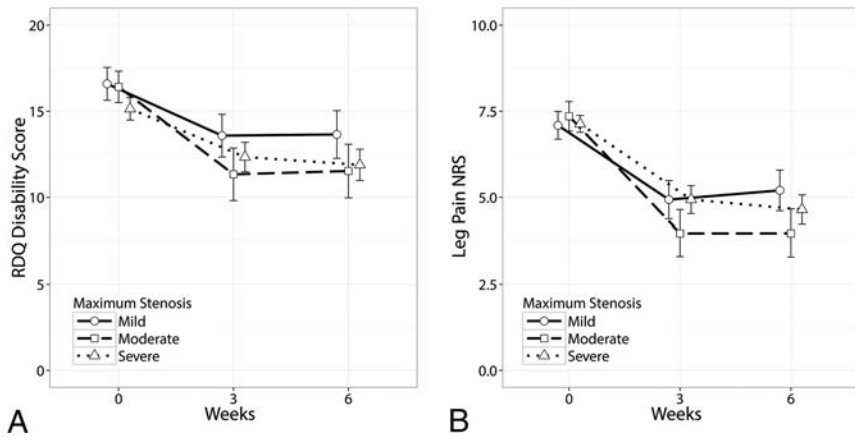


**FIG 1.** Mean and 95% CI for the RDQ disability score (A) and the leg pain NRS (B) are presented at baseline, 3 weeks, and 6 weeks following epidural injection, including all patients regardless of injectate type, and subdivided by the severity of spinal stenosis on imaging (mild = solid line with circle; moderate = dash line with square; severe = dotted line with triangle). Patients with moderate stenosis demonstrated slightly greater improvement in disability scores at 3 weeks and leg pain scores at 3 and 6 weeks compared with patients with mild stenosis.

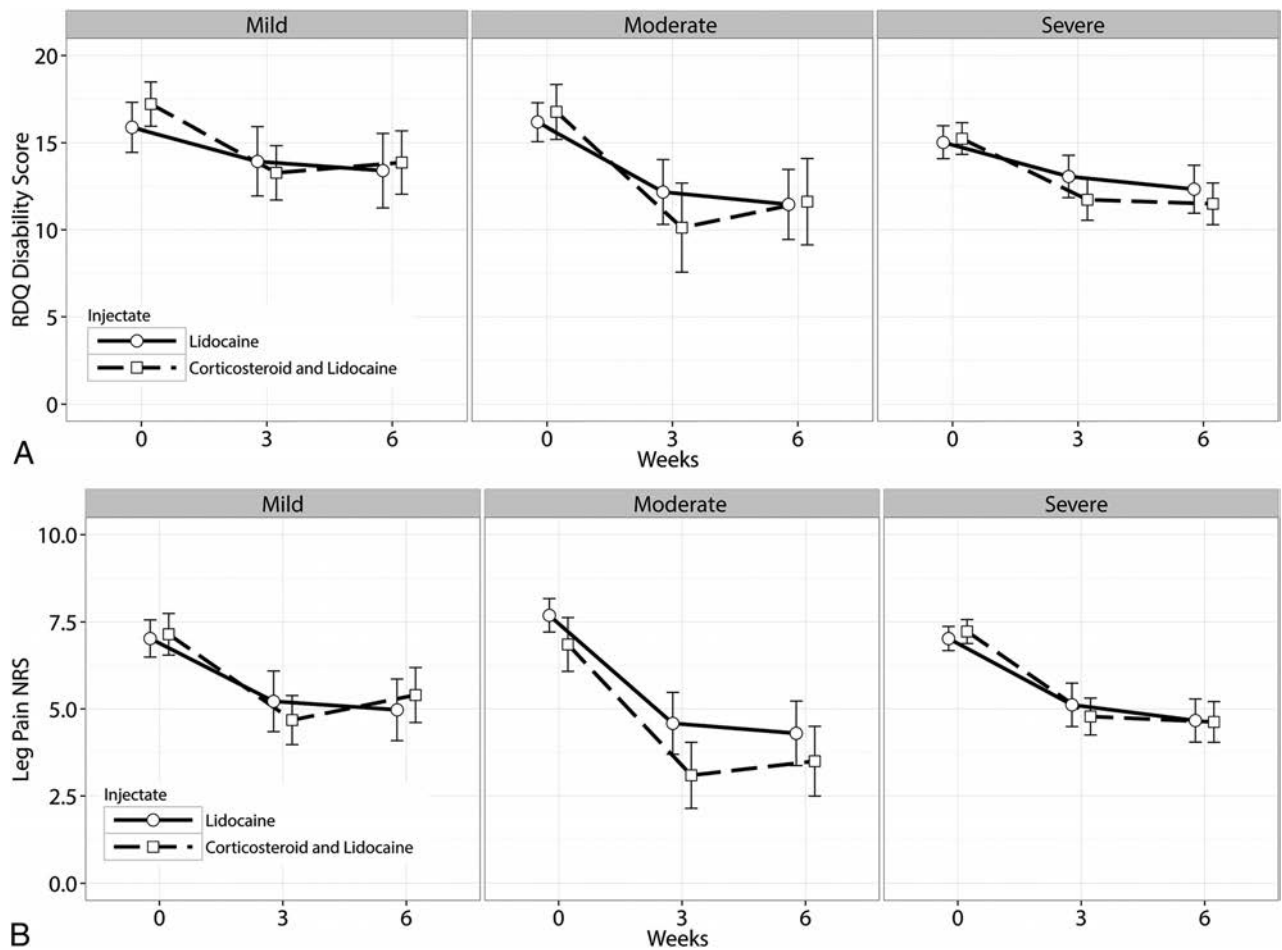


**FIG 2.** Mean and 95% CI RDQ disability score (A) and leg pain NRS (B) at baseline, 3 weeks, and 6 weeks after epidural injection are presented for patients randomized to lidocaine alone (circles and solid line) and corticosteroid and lidocaine (squares and dotted line), subdivided by the severity of qualitative spinal stenosis on imaging (mild, moderate, and severe). There were no differences in responses when taking into account spinal stenosis severity.

Analysis of primary clinical outcomes using ANCOVA models that include interaction terms between primary imaging measures of spinal stenosis severity and epidural injectate revealed no difference in the degree of improvement in the RDQ disability scores or the leg pain NRS at 3 weeks using the imaging measures

of the qualitative maximum central stenosis score (Fig 2; interaction coefficients of maximum central stenosis score and epidural injectate for RDQ,  $-0.1$ ; 95% CI,  $-1.3$  to  $1.2$ ;  $P = .90$ ; and for the leg pain NRS,  $0.1$ ; 95% CI,  $-0.6$  to  $0.8$ ;  $P = .81$ ) or the quantitative minimum thecal sac cross-sectional area (Fig 3; interaction

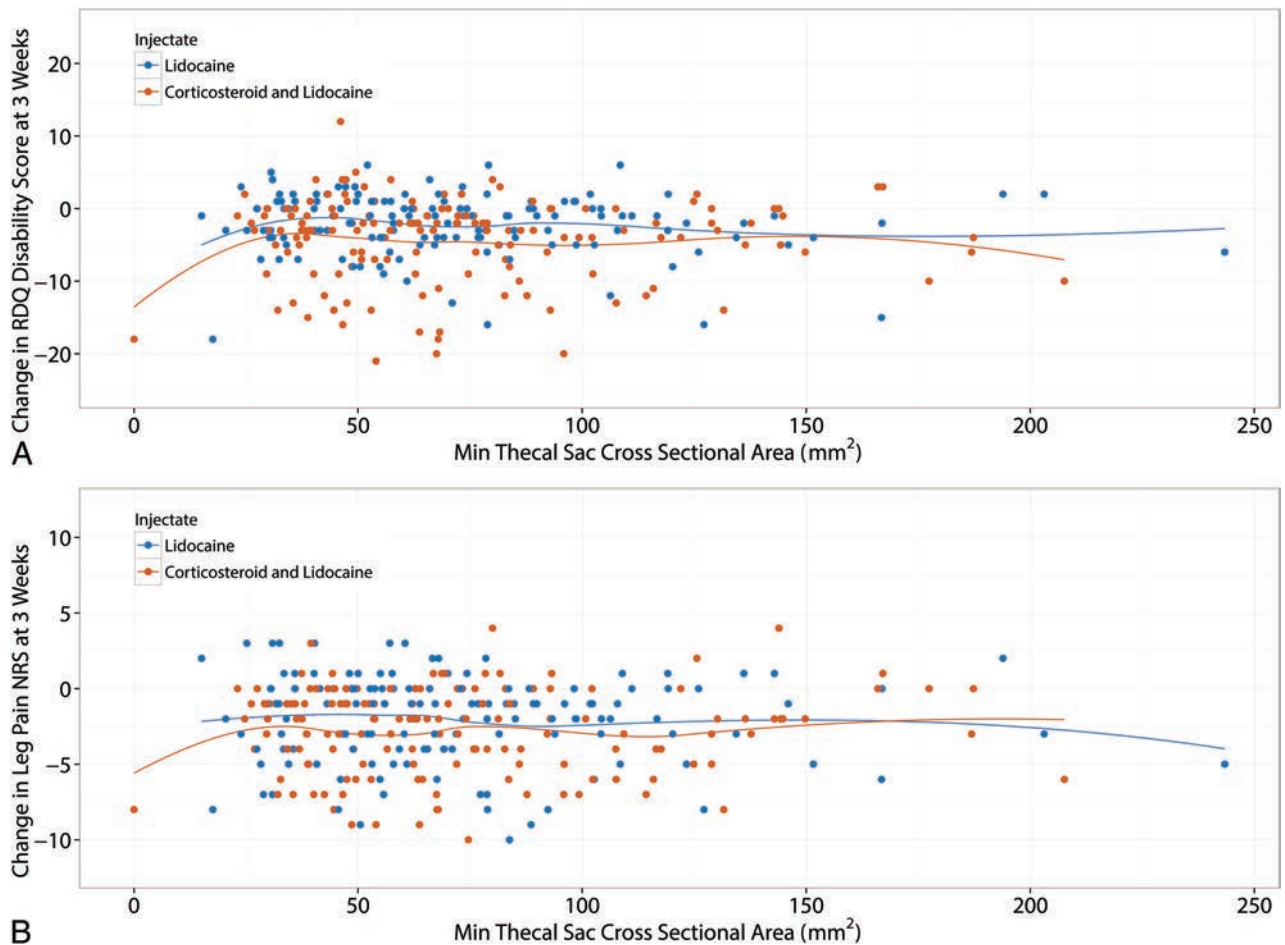


**FIG 3.** Change in the RDQ disability score (A) and leg pain NRS (B) at 3 weeks is presented as a function of minimum thecal sac cross-sectional area subdivided by injectate type with locally weighted scatterplot smoothing lines and 95% CI bands. The degree of spinal stenosis as assessed quantitatively was not associated with differential improvement between patients receiving lidocaine alone and corticosteroid and lidocaine. Min indicates minimum.

coefficients of minimum thecal sac cross-sectional area and epidural injectate for the RDQ, 0.01; 95% CI,  $-0.01$  to  $0.03$ ;  $P = .40$ ; and for the leg pain NRS, 0.01; 95% CI,  $-0.01$  to  $0.03$ ;  $P = .33$ ). Because the chronicity of pain could be a confounding variable, a self-reported duration of pain symptoms at enrollment was included as a covariate in ANCOVA models for the primary clinical end points and imaging measures at 3 weeks with similar results.

#### Subgroup and Exploratory Data Analysis

Subgroup analysis taking into account the injection approach (interlaminar versus transforaminal) and the distance of the injection from the maximum stenosis identified no significant interactions between the epidural injectate and primary imaging measures of spinal stenosis (On-line Tables 1 and 2). Exploratory statistical analyses using ANCOVA models with all combinations of clinical outcome measures (at 3 and 6 weeks) and imaging measures of spinal stenosis demonstrated no significant interactions to indicate a differential clinical response to injectate based on the severity of the spinal stenosis on imaging (On-line Tables 3 and 4). Additional subgroup analyses were performed by categorizing patients on the basis of the degree of improvement, at least 30% or 50%, in the primary clinical outcome measures of the RDQ disability score or the leg pain NRS at 3 or 6 weeks. There

were no differences in the primary imaging measures of maximum qualitative central stenosis or minimum thecal sac cross-sectional area among these subgroups, regardless of responders versus nonresponders or injectate type (On-line Table 5).

#### DISCUSSION

In this secondary analysis of the CT and MR imaging studies of the LESS trial participants, we found no differences in baseline imaging characteristics between those receiving epidural corticosteroid and lidocaine and those receiving lidocaine alone injections. No imaging measures of spinal stenosis were associated with a differential response to corticosteroids, indicating that imaging parameters of spinal stenosis did not predict a response to epidural corticosteroids.

Prior studies evaluating the relationship between spinal stenosis imaging findings and the response to ESI are inconsistent, with most not demonstrating a clear association between the degree of stenosis and outcomes following ESI. Kapural et al<sup>27</sup> found that patients with multilevel stenosis were more likely to improve following a series of ESIs than those with single-level stenosis, but degree of stenosis was not related to pain outcomes after a series of ESIs. The current study is in line with previously reported findings

demonstrating a lack of association of spinal canal dimensions by CT with the outcome of the ESI<sup>11</sup> and prior MR imaging–based studies demonstrating lack of a statistically significant difference between responders and nonresponders to ESI in the presence or absence of spinal stenosis<sup>12</sup> or by stenosis severity.<sup>14,28</sup>

We hypothesized that patients with less severe central stenosis, for which inflammation may play a larger role than mechanical compression, would have a more favorable response to corticosteroid injections compared with treatment with lidocaine alone; however, we found that imaging measures of spinal stenosis were not associated with a differential degree of improvement. There was clinical improvement in both treatment groups, and overall slightly greater improvement was seen in patients with moderate stenosis compared with mild stenosis. Because there was improvement regardless of corticosteroid injection, the anti-inflammatory properties of corticosteroids may not have much of a role in the treatment of spinal stenosis. This clinical improvement could be due to the natural history of spinal stenosis, placebo effect, or lidocaine effect. A sham injection group was not included, and the efficacy of lidocaine alone could not be assessed. Our results do not exclude inflammation as a contributing factor in symptomatic spinal stenosis, though there are likely other factors that contribute to an individual patient's symptoms and possible differential response to therapy. Moreover, if inflammation is a contributing factor, spinal stenosis severity may not correlate with the degree of inflammation. Nevertheless, the severity of spinal stenosis on imaging was not a reliable biomarker to predict treatment response following epidural corticosteroid injection versus lidocaine alone, which adds to the many other patient characteristics, including demographics and chronicity of pain, that were previously also not found to reliably predict a differential response in the LESS trial.<sup>29</sup>

The current study has several limitations. First, the causes of spinal canal compromise (such as type of disc herniation, epidural lipomatosis, congenital stenosis, and facet or ligamentum flavum hypertrophy) and possible associated foraminal or lateral recess stenosis were not specifically assessed. Previous studies in other conditions, such as radiculopathy, have found that focal disc herniations and imaging severity of nerve root compression can predict short-term pain relief after ESI.<sup>10,13,30</sup> Similarly, in a study that excluded patients with spinal stenosis, herniated discs in the foraminal and extraforaminal zones predicted a better response to ESI compared with discs in the central and subarticular zones.<sup>31</sup> Moreover, Choi et al<sup>12</sup> found no relationship between the response to ESI and spinal stenosis on MR imaging; however, they reported that the disc location and nerve root compression grades were associated with outcomes. Second, we did not localize a likely spinal level to account for each patient's symptoms in all cases, which would have enabled us to correlate potential imaging findings at a symptomatic level; nevertheless, epidural injections were performed within 1 lumbar spinal level of the worst stenosis in >90% of patients, and transforaminal injections were targeted to the most symptomatic level. Third, the statistical power to detect interaction effects may be low, despite large sample sizes, due to multiple potential sources of heterogeneity, including pain and disability levels, treatment approaches, and type and dose of corticosteroids. However, small interaction effects are unlikely to

have clinical utility to prospectively identify patients most likely to benefit from epidural corticosteroid injection compared with lidocaine alone for the treatment of symptomatic spinal stenosis.

## CONCLUSIONS

The severity of lumbar spinal stenosis on CT or MR imaging in patients with a clinical diagnosis of lumbar spinal stenosis does not predict differential improvement in pain or disability following epidural corticosteroid with lidocaine injection compared with lidocaine injection alone.

## ACKNOWLEDGMENTS

We thank the research staff for data collection and their overall dedication to this study. In addition, we would like to thank the LESS Scientific Advisory Board for their support.

Disclosures: Jeffrey G. Jarvik—*RELATED: Grant:* Agency for Healthcare Research and Quality, *Comments:* federal grant\*; *Support For Travel to Meetings for the Study or Other Purposes:* Agency for Healthcare Research and Quality\*; *Fees for Participation in Review Activities Such as Data Monitoring Boards, Statistical Analysis, Endpoint Committees, and the Like:* Agency for Healthcare Research and Quality\*; *Payment for Writing or Reviewing the Manuscript:* Agency for Healthcare Research and Quality\*; *UNRELATED: Consultancy:* UpToDate, *Comments:* section editor/consultant; *Grants/Grants Pending:* National Institutes of Health, Patient-Centered Outcomes Research Institute\*; *Payment for Lectures Including Service on Speakers Bureaus:* Radiological Society of North America, *Comments:* Clinical Trials Methodology Workshop faculty member; *Royalties:* UpToDate, Springer Publishing; *Travel/Accommodations/Meeting Expenses Unrelated to Activities Listed:* Association of University Radiologists (AUR) and General Electric (GE), *Comments:* GE-AUR Radiology Research Academic Fellowship annual retreat. Emin Aghayev—*UNRELATED: Employment:* Schulthess Clinic Zurich, Swiss Federal Government, University of Bern. Ella R. Jarvik—*RELATED: Grant:* Agency for Healthcare Research and Quality, *Comments:* 1R01HS01922201.\* Andrew L. Avins—*RELATED: Grant:* Agency for Healthcare Research and Quality, *Comments:* as part of the Agency for Healthcare Research and Quality–funded multicenter clinical trial.\* Jason M. Schwalb—*RELATED: Grant:* Agency for Healthcare Research and Quality, *Comments:* 1R01HS0192222\*. *UNRELATED: Other:* Blue Cross Blue Shield of Michigan, *Comments:* salary support for my role as Co-Director of the Michigan Spine Surgery Improvement Collaborative.\* Christopher J. Standaert—*RELATED: Grant:* Agency for Healthcare Research and Quality, Patient-Centered Outcomes Research Institute.\* David R. Nerenz—*RELATED: Grant:* Agency for Healthcare Research and Quality, *Comments:* standard research grant with funds used to cover the cost of conducting the study at our institution\*; *UNRELATED: Board Membership:* Medicare Payment Advisory Commission, *Comments:* The Commission work involves the full range of Medicare payment issues. I served as a Medicare Payment Advisory Commission commissioner from 2012 to 2018; *Employment:* Henry Ford Health System, *Comments:* I was a full-time employee of the Henry Ford Health System during the entire time covered by this disclosure. Thiru Annaswamy—*RELATED: Grant:* Agency for Healthcare Research and Quality, *Comments:* The LESS study was funded by the Agency for Healthcare Research and Quality\*; *UNRELATED: Employment:* federal government, *Comments:* I am a full-time employed physician at the VA. Zoya Bauer—*RELATED: Grant:* Agency for Healthcare Research and Quality.\* Srdjan S. Nedeljkovic—*RELATED: Grant:* Brigham and Women's Hospital.\* Janna L. Friedly—*RELATED: Grant:* Agency for Healthcare Research and Quality, Patient-Centered Outcomes Research Institute.\* Patrick J. Heagerty—*RELATED: Grant:* National Institutes of Health.\* \*Money paid to the institution.

## REFERENCES

1. Deyo RA, Gray DT, Kreuter W, et al. **United States trends in lumbar fusion surgery for degenerative conditions.** *Spine* 2005;30:1441–45; discussion 1446–47 CrossRef Medline
2. Taylor VM, Deyo RA, Cherkin DC, et al. **Low back pain hospitalization: recent United States trends and regional variations.** *Spine* 1994;19:1207–12; discussion 13 CrossRef Medline
3. Steurer J, Roner S, Gnannt R, et al. **Quantitative radiologic criteria for the diagnosis of lumbar spinal stenosis: a systematic literature review.** *BMC Musculoskelet Disord* 2011;12:175 CrossRef Medline
4. Kovacs FM, Urrutia G, Alarcón JD. **Surgery versus conservative treatment for symptomatic lumbar spinal stenosis: a systematic re-**

- view of randomized controlled trials. *Spine* 2011;36:E1335–51 CrossRef Medline
5. Moojen WA, Schenck CD, Lycklama À Nijeholt GJ, et al; Leiden-The Hague Spine Intervention Prognostic Study Group (SIPS). **Preoperative MRI in patients with intermittent neurogenic claudication: relevance for diagnosis and prognosis.** *Spine* 2018;43:348–55 CrossRef Medline
  6. Harrast MA. **Epidural steroid injections for lumbar spinal stenosis.** *Curr Rev Musculoskelet Med* 2008;1:32–38 CrossRef Medline
  7. Friedly J, Chan L, Deyo R. **Increases in lumbosacral injections in the Medicare population: 1994 to 2001.** *Spine* 2007;32:1754–60 CrossRef Medline
  8. Friedly J, Nishio I, Bishop MJ, et al. **The relationship between repeated epidural steroid injections and subsequent opioid use and lumbar surgery.** *Arch Phys Med Rehabil* 2008;89:1011–15 CrossRef Medline
  9. Abdi S, Datta S, Trescot AM, et al. **Epidural steroids in the management of chronic spinal pain: a systematic review.** *Pain Physician* 2007;10:185–212 Medline
  10. Ghahreman A, Bogduk N. **Predictors of a favorable response to transforaminal injection of steroids in patients with lumbar radicular pain due to disc herniation.** *Pain Med* 2011;12:871–79 CrossRef Medline
  11. Campbell MJ, Carreon LY, Glassman SD, et al. **Correlation of spinal canal dimensions to efficacy of epidural steroid injection in spinal stenosis.** *J Spinal Disord Tech* 2007;20:168–71 CrossRef Medline
  12. Choi SJ, Song JS, Kim C, et al. **The use of magnetic resonance imaging to predict the clinical outcome of non-surgical treatment for lumbar intervertebral disc herniation.** *Korean J Radiol* 2007;8:156–63 CrossRef Medline
  13. Paidin M, Hansen P, McFadden M, et al. **Contrast dispersal patterns as a predictor of clinical outcome with transforaminal epidural steroid injection for lumbar radiculopathy.** *PM R* 2011;3:1022–27 CrossRef Medline
  14. Park CH, Lee SH. **Correlation between severity of lumbar spinal stenosis and lumbar epidural steroid injection.** *Pain Med* 2014;15:556–61 CrossRef Medline
  15. Benny BV, Patel MY. **Predicting epidural steroid injections with laboratory markers and imaging techniques.** *Spine J* 2014;14:2500–08 CrossRef Medline
  16. Friedly JL, Comstock BA, Turner JA, et al. **A randomized trial of epidural glucocorticoid injections for spinal stenosis.** *N Engl J Med* 2014;371:11–21 CrossRef Medline
  17. Andersson GB. **Epidural glucocorticoid injections in patients with lumbar spinal stenosis.** *N Engl J Med* 2014;371:75–76 CrossRef Medline
  18. Friedly JL, Bresnahan BW, Comstock B, et al. **Study protocol: Lumbar Epidural steroid injections for Spinal Stenosis (LESS)—a double-blind randomized controlled trial of epidural steroid injections for lumbar spinal stenosis among older adults.** *BMC Musculoskelet Disord* 2012;13:48 CrossRef Medline
  19. Paisley K, Jeffries J, Monroe M, et al. **Dispersal pattern of injectate after lumbar interlaminar epidural spinal injection evaluated with computerized tomography.** *Global Spine J* 2012;2:27–32 CrossRef Medline
  20. Lee JH, An JH, Lee SH. **Comparison of the effectiveness of interlaminar and bilateral transforaminal epidural steroid injections in treatment of patients with lumbosacral disc herniation and spinal stenosis.** *Clin J Pain* 2009;25:206–10 CrossRef Medline
  21. Stucki G, Daltroy L, Liang MH, et al. **Measurement properties of a self-administered outcome measure in lumbar spinal stenosis.** *Spine* 1996;21:796–803 CrossRef Medline
  22. Lurie JD, Tosteson AN, Tosteson TD, et al. **Reliability of readings of magnetic resonance imaging features of lumbar spinal stenosis.** *Spine* 2008;33:1605–10 CrossRef Medline
  23. Andreisek G, Deyo RA, Jarvik JG, et al; LSOS working group. **Consensus conference on core radiological parameters to describe lumbar stenosis: an initiative for structured reporting.** *Eur Radiol* 2014;24:3224–32 CrossRef Medline
  24. Lee GY, Guen YL, Lee JW, et al. **A new grading system of lumbar central canal stenosis on MRI: an easy and reliable method.** *Skeletal Radiol* 2011;40:1033–39 CrossRef Medline
  25. Landis JR, Koch GG. **The measurement of observer agreement for categorical data.** *Biometrics* 1977;33:159–74 CrossRef Medline
  26. Fleiss JL. *The Design and Analysis of Clinical Experiments.* Hoboken: John Wiley & Sons, Inc; 1986:1–32
  27. Kapural L, Mekhail N, Bena J, et al. **Value of the magnetic resonance imaging in patients with painful lumbar spinal stenosis (LSS) undergoing lumbar epidural steroid injections.** *Clin J Pain* 2007;23:571–75 CrossRef Medline
  28. Cosgrove JL, Bertolet M, Chase SL, et al. **Epidural steroid injections in the treatment of lumbar spinal stenosis efficacy and predictability of successful response.** *Am J Phys Med Rehabil* 2011;90:1050–55 CrossRef Medline
  29. Turner JA, Comstock BA, Standaert CJ, et al. **Can patient characteristics predict benefit from epidural corticosteroid injections for lumbar spinal stenosis symptoms?** *Spine J* 2015;15:2319–31 CrossRef Medline
  30. Maus TP, El-Yahouchi CA, Geske JR, et al. **Imaging determinants of clinical effectiveness of lumbar transforaminal epidural steroid injections.** *Pain Med* 2016;17:2176–84 CrossRef Medline
  31. Lee JW, Choi SW, Park SH, et al. **MR-based outcome predictors of lumbar transforaminal epidural steroid injection for lumbar radiculopathy caused by herniated intervertebral disc.** *Eur Radiol* 2013;23:205–11 CrossRef Medline

# It Is Not Necessary to Discontinue Seizure Threshold–Lowering Medications Prior to Myelography

M. Krupa, H. Salts, and F. Mihlon

## ABSTRACT

**BACKGROUND AND PURPOSE:** There is no consensus on whether patients undergoing myelography should discontinue medications that could lower their seizure threshold. The purpose of this study was to document the most commonly prescribed seizure threshold–lowering medications in patients undergoing myelography and determine whether withholding such medications decreases the incidence of seizures.

**MATERIALS AND METHODS:** We performed a retrospective observational study of all the myelograms obtained in 2016 at 2 affiliated hospitals. At hospital A, seizure threshold–lowering medications are discontinued before myelography, and prophylactic diazepam is given for all cervical myelograms. At hospital B, seizure threshold–lowering medications are not withheld before the procedure, and medical seizure prophylaxis is not implemented. The seizure threshold–lowering medications the patients were taking at the time of the procedure and postmyelographic seizure incidence were documented.

**RESULTS:** A total of 311 patients underwent myelography during 2016. One hundred eleven patients (36%) were on at least 1 seizure threshold–lowering medication, and 30 (10%) were on at least 2. The most common medications were duloxetine, sertraline, venlafaxine, bupropion, and trazodone. The most common tricyclic antidepressant was amitriptyline. Three patients across both sites had a controlled seizure disorder and were on antiepileptics. None of the patients at either hospital had seizures during or within 3 hours following any of the myelograms during the study period.

**CONCLUSIONS:** Continuing seizure threshold–lowering medications during myelography does not increase the risk of seizures. Screening for and withholding seizure threshold–lowering medications are not indicated for routine myelography.

**ABBREVIATIONS:** STLM = seizure threshold–lowering medication; TCA = tricyclic antidepressant

Myelography remains a useful diagnostic procedure to evaluate spinal disease, especially in patients with contraindications to MR imaging.<sup>1</sup> The risks of myelography are related to the lumbar puncture itself and the intrathecal administration of contrast.<sup>2</sup> Iodinated contrast agents used for myelography have been in use for >90 years. The earliest agents such as iodophendylate were oil-based and not readily resorbed from the CSF, and the oil residue caused arachnoid adhesions in 3 of 4 patients who received the agent.<sup>3</sup> The first water-soluble myelographic contrast

agents were introduced in the early 1970s, and of these, metrizamide gained mainstream adaptation. Metrizamide compared favorably with iodophendylate because it resorbed with the CSF, but it was well-known to carry a non-negligible risk of neurologic symptoms, including seizure, with intrathecal administration.<sup>4</sup> Since the advent of second-generation, nonionic water-soluble contrast agents such as iohexol, myelography-related seizure activity has become a very rare event. There have been only scattered individual case reports of seizures occurring in patients undergoing myelography with these agents, and most of these case reports had extenuating circumstances such as a history of epilepsy or an overdosage of the intrathecal contrast agent.<sup>5–8</sup> Nonetheless, the published guidelines for clinical practice surrounding myelography have changed little since the transition from metrizamide to second-generation, nonionic water-soluble contrast agents.

The American College of Radiology–American Society of Neuroradiology–Society of Pediatric Radiology clinical practice guidelines recommend screening patients' medications and dis-

Received January 30, 2019; accepted after revision March 10.

From the Department of Radiology, Eastern Virginia Medical School, Norfolk, Virginia.

Paper previously presented, in part, at: Annual Meeting of the American Society of Neuroradiology and the Foundation of the ASNR Symposium, June 4–7, 2018; Vancouver, British Columbia, Canada.

Please address correspondence to Frank Mihlon, MD, Eastern Virginia Medical School, Department of Radiology, 600 Gresham Dr, Norfolk, Virginia 23507; e-mail: frank@mihlon.com; @frankmihlon

<http://dx.doi.org/10.3174/ajnr.A6027>

continuing those that may lower the seizure threshold.<sup>1</sup> The guidelines advise withholding seizure threshold-lowering medications (STLMs) for 48 hours pre- and 24 hours postmyelography. However, institutional and individual practices vary widely in their adherence to these recommendations. In 2005, 63% of practitioners screened for STLMs.<sup>9</sup> In 2018, only 43% of practitioners screened for such medications.<sup>10</sup> Decreased adherence to these recommendations is likely attributable to increased familiarity with the newer contrast agents. Furthermore, >100 medications fall into the category of STLMs. Identifying and withholding such medications before myelography and then resuming them after the procedure are laborious clinical tasks and are anxiety-provoking for the patient. In addition, referring clinicians and patients can become frustrated by such requirements, particularly when they result in delaying or rescheduling of procedures. In a study on the emotional implications of cancelled pediatric outpatient operations, 45% of parents were “disappointed” and 16% were “frustrated” by the cancellation.<sup>11</sup>

This investigation is a retrospective observational study comparing the policies surrounding STLM continuation during myelography at 2 large hospitals (Sentara Norfolk General Hospital and Sentara Virginia Beach General Hospital) within the same institutional network and the associated myelography-induced seizure rates. The 2 hospitals have different radiology groups and different policies surrounding the continuation of outpatient STLM regimens during myelography, but the contrast agent used and other circumstances such as postmyelography care are otherwise the same. The purpose of this study was to determine whether there is a difference in the incidence of seizures between these 2 sites and, as a consequence, whether allowing patients to continue to take their outpatient STLM regimens during myelography affects the rate of myelography-induced seizures.

## MATERIALS AND METHODS

Following institutional review board approval at Eastern Virginia Medical School, a retrospective chart review was conducted on all the patients who underwent myelography in 2016 at 2 hospitals in a single institutional network. At hospital A (Sentara Virginia Beach General Hospital), patients are screened for STLMs, and they are discontinued 48 hours before the myelography and resumed 48 hours after the procedure. Prophylactic diazepam is given for all cervical myelograms. At hospital B (Sentara Norfolk General Hospital), patients are not screened for STLMs, no changes are made to patients’ medication regimens, and no diazepam is given for seizure prophylaxis. All myelograms were obtained with Omnipaque (iohexol; GE Healthcare, Piscataway, New Jersey) intrathecal contrast. Administered doses varied with procedure level, with cervical and total spine myelograms using, on average, 10 mL of iohexol, 300 mg I/mL, and lumbar myelograms using, on average, 16 mL of iohexol, 180 mg I/mL. Administered doses for thoracic myelograms varied with regard to contrast concentration and volume. Anticoagulants were managed in the same manner at both sites and discontinued before the procedure.

Demographic information (age at the procedure, sex), type of myelogram (total spine, cervical, thoracic, or lumbar), contrast agent and volume used, list of medications at the time of the

**Table 1: Demographic information of all patients undergoing myelography in 2016 at the 2 sites**

	Screened/Held	Not Screened/Held
Sex		
Male	81	78
Female	87	65
Age (yr)		
Median	58.5	57
Mean	57.4 ± 14	56.9 ± 12
Minimum	24	24
Maximum	87	85
Myelogram		
Cervical	34	40
Thoracic	1	3
Lumbar	121	61
Multilevel (>1 level)	12	39
Seizures	0	0

myelography, and the presence or absence of seizures during or within 3 hours after the procedure were recorded. STLMs were defined according to the Omnipaque package insert: “Phenothiazine derivatives . . . MAO inhibitors, tricyclic antidepressants, CNS stimulants, and psychoactive drugs described as analeptics, major tranquilizers, or antipsychotic drugs.”<sup>12</sup>

## RESULTS

Between hospitals A and B, a total of 311 patients underwent myelography during 2016 (Table 1). One hundred sixty-eight myelograms were obtained at hospital A, which screens and holds STLMs for myelography, and 143 myelograms were obtained at hospital B, which does not screen and hold STLMs for myelography. At hospital A, 43 (26%) patients undergoing myelography were on an outpatient regimen that included at least 1 STLM, and these were withheld for 48 hours before and following myelography. At hospital B, 68 (48%) patients were on an outpatient regimen that included at least 1 STLM, and these patients underwent myelography without having the medications withheld.

There were no significant differences in age ( $P = .094$ ) or sex ( $P = .266$ ) between the 2 patient populations. The distribution of the types of myelograms performed at the 2 hospitals varied, with hospital A performing more lumbar myelograms and hospital B performing more total spine myelograms. There were no reported seizures during or within 3 hours of any of the myelograms at either of the 2 hospitals.

The neurologic medication most frequently used by patients was duloxetine (26 patients, 8%), followed by sertraline and venlafaxine (Table 2). The most frequently used tricyclic antidepressant (TCA) was amitriptyline. Other infrequently encountered TCAs were nortriptyline, amoxapine, and imipramine. In total, 13 (4%) patients were on a TCA. Additionally, 13 (4%) patients were on bupropion at the time of myelography. Six patients were taking 1 antiepileptic medication (4 at the screened site, 2 at the nonscreened site). Medications included carbamazepine, levetiracetam, and lamotrigine. Three of these patients had a documented seizure disorder (2 at the screened site, 1 at the nonscreened site). One of these patients, who was part of the nonscreened group, was taking amitriptyline concurrently. The remaining 3 patients were taking lamotrigine for bipolar disorder and chronic pain.

**Table 2: Frequency of neurologic medications reported in patients undergoing myelography at the 2 sites**

Medication	Class	Total	Screened/ Held	Not Screened/ Held
Duloxetine	SNRI	26	11	15
Sertraline	SSRI	18	4	14
Venlafaxine	SNRI	16	7	9
Bupropion	Mixed	13	5	8
Trazodone	Mixed	11	7	4
Amitriptyline	TCA	10	2	8
Fluoxetine	SSRI	10	3	7
Paroxetine	SSRI	10	5	5
Citalopram	SSRI	7	4	3
Escitalopram	SSRI	6	3	3
Quetiapine	Antipsychotic	4	2	2
Desvenlafaxine	SNRI	3	0	3
Lurasidone	Antipsychotic	2	1	1
Mirtazapine	Mixed	1	0	1
Nortriptyline	TCA	1	0	1
Amoxapine	TCA	1	0	1
Imipramine	TCA	1	1	0
Fluvoxamine	SSRI	1	1	0
Risperidone	Antipsychotic	1	1	0

**Note:**—SSRI indicates selective serotonin reuptake inhibitors; SNRI, serotonin and norepinephrine reuptake inhibitors.

## DISCUSSION

In the earlier days of medical imaging, myelography was the only way to image spinal neural impingement. The advent of MR imaging brought with it the ability to image the spinal neural structures without the need for an invasive procedure, and subsequently, it largely replaced myelography as the diagnostic test of choice for spinal neural impingement. Today, many patients undergo myelography because they are precluded from MR imaging, either due to safety reasons, such as having a pacemaker or claustrophobia, or due to artifacts from surgical hardware.<sup>1</sup> Myelography is also commonly used in instances in which the myelographic data are superior to data portrayed by MR imaging. These specific situations include localization of the site of a CSF leak in cases of intracranial hypotension; some instances of surgical planning, particularly in the case of a failing fusion construct; and in cases of dynamic/positional neural impingement, which can be diagnosed during the fluoroscopic portion of the examination.

The first generation of water-soluble nonionic contrast agents, primarily metrizamide with regard to contrast use in myelography, exhibited evidence of neurotoxicity and include many described episodes of encephalopathy, seizures, and other neurologic manifestations.<sup>8</sup> Iohexol is a second-generation water-soluble nonionic contrast agent approved by the Food and Drug Administration for myelography in the mid-1980s and was the contrast agent used in this retrospective observational study. Studies comparing iohexol with metrizamide have shown that iohexol causes significantly less frequent and less severe adverse reactions than metrizamide.<sup>13</sup> In a parallel, double-blind, randomized study comparing iohexol and metrizamide in 60 consecutive patients undergoing lumbar myelography, iohexol did not produce any epileptiform activity, but epileptiform activity was detected in 5 patients receiving metrizamide.<sup>14</sup> In another double-blind comparative study of 30 patients undergoing cervical myelography, pyramidal signs and seizures occurred only after

metrizamide myelography.<sup>15</sup> It is unclear why iohexol has a lower risk of seizures compared with metrizamide. This may be due to the lower penetration of iohexol into the central nervous system structures. Unlike metrizamide, which has a glucose side chain, iohexol presumably does not interfere with glucose metabolism in the brain.<sup>8</sup>

There are only a few case reports describing seizures in patients undergoing myelography with iohexol.<sup>16-19</sup> Alimohammadi et al<sup>16</sup> reported generalized tonic-clonic seizure in a 48-year-old man who underwent outpatient lumbar myelography using 18 mL of iohexol, 240  $\mu\text{g/mL}$ , which ultimately resulted in death. Kertmen et al<sup>18</sup> reported postprocedural generalized tonic-clonic seizure after 3 mL of iohexol was inadvertently injected intrathecally during an outpatient transforaminal percutaneous endoscopic lumbar discectomy for a lumbar disc herniation in a 20-year-old woman. Rosenberg and Grant<sup>19</sup> reported a 52-year-old man who developed a generalized tonic-clonic seizure 30 minutes after lumbar myelography with iohexol (dose not specified) and who subsequently developed a malignant hyperthermia-like syndrome. In all these cases, patients were not taking any prescription medications; therefore, screening for STLMs before the procedure would not have changed the clinical outcome.

Despite the tenuous evidence of a significant risk of seizures with intrathecal administration of second-generation water-soluble nonionic contrast agents, the current guidelines provided both by the relevant medical societies<sup>1</sup> and in the iohexol package insert<sup>12</sup> recommend screening and withholding STLMs for myelography. These seizure-conscious guidelines could be in response to the cited case reports but also may simply reflect a hold-over from the days of metrizamide. When neuroradiologists decide whether to implement the guidelines in their own medical practice, they must weigh the effect on their patients. Discontinuing STLMs temporarily may cause antidepressant discontinuation syndrome and increase the risk of relapse of depression or anxiety,<sup>20</sup> among other conditions. In addition, hospital systems, referring clinicians, and radiologists alike can get frustrated with screening and holding the ever-growing list of STLMs because miscommunications and other potential breakdowns of that process can result in otherwise needlessly rescheduling or cancelling appropriate myelographic procedures.

Interestingly, the data suggest that more than half of practicing neuroradiologists have decided that the societally recommended screen-and-hold approach is indeed not best for their clinical practice. In a 2018 survey of 700 American Society of Neuroradiology members, only 43% of respondents reported screening for STLMs.<sup>10</sup> A mere 3% reported having had a patient experience a postprocedural seizure during their entire personal history of clinical myelography practice. There was no statistically significant difference in postmyelographic seizures between practices that discontinued STLMs and those that did not. A similar survey-based study performed in 2005 found that 63% of practitioners screened for STLMs at that time,<sup>9</sup> indicating that across time, the screen-and-hold practice is falling out of favor among neuroradiologists.

Our investigation, a retrospective observational study comparing the policies surrounding STLM continuation during myelography at 2 large hospitals within the same institutional net-

work, showed that no seizures occurred in either the 168 patients who had their STLMs screened and held for myelography or the 143 patients who were allowed to continue their STLM outpatient regimen. Perhaps the most interesting number produced by our study is the 68 patients at hospital B who were on at least 1 STLM as an outpatient and were allowed to continue their medical regimen during myelography; there were no postmyelography seizures in this supposedly higher risk group. This finding supports the notion that the current second-generation, nonionic contrast agents do not present a significant risk of seizure when used for myelography, even when allowing patients to continue their outpatient STLM regimens in the time surrounding the procedure. This finding is in line with the survey data that show that the currently recommended screen-and-hold approach to STLMs for myelography is increasingly not being used by neuroradiologists who perform myelography as they become more familiar with the current generation of contrast agents.

Our study has several limitations, mainly the low sample size and the retrospective nature of the investigation. Given the rare occurrence of myelography-related seizures using the current generation of contrast agents, the sample number that would be needed to find a seizure, even retrospectively, would have to be prohibitively large and would likely not achieve statistical significance in terms of establishing causation. The sample size that would be required to achieve statistical significance even to answer the question of noninferiority would similarly be prohibitively large. Thus, retrospective-type reviews like ours and surveys will, in all likelihood, remain the type of data on which the relevant societies will have to rely to make recommendations surrounding the issue of STLMs and myelography. With regard to limitations peculiar to our study, it is odd that there was such a discrepancy in the percentage of patients who were on STLMs at one hospital versus the other (26% versus 48%). One could speculate as to the innumerable potential reasons for this finding, from patient population to the accuracy of patient reporting, but it is, nonetheless, fortuitous in terms of the meaningfulness of our study that the larger group of individuals on STLMs was at hospital B, which does not screen and hold STLMs for myelography and is functionally the experimental group in this investigation.

## CONCLUSIONS

We found no evidence that continuing STLMs such as TCAs and selective serotonin reuptake inhibitors during myelography presents an increased risk of seizures. The reported benefits of screening for such medications are anecdotal and based on studies using older neurotoxic contrast agents, mainly metrizamide. In line with the reports of the changing practice patterns and in lieu of high-level prospective studies, our single-institution retrospective observational study supports the growing body of literature that suggests that screening for and holding STLMs is not indicated for routine myelography.

## REFERENCES

1. ACR-ASNR-SPR Practice Parameter for the Performance Myelography and Cisternography. <https://www.acr.org/-/media/ACR/Files/Practice-Parameters/Myelog-Cisternog.pdf>. Accessed December 21, 2018
2. Eames FA, Cloft HJ. **Discontinuing patient medications prior to myelography.** *AJR Am J Roentgenol* 2005;184:695 CrossRef Medline
3. Johnson AJ, Burrows EH. **Thecal deformity after lumbar myelography with iophendylate (Myodil) and meglumine iothalamate (Conray 280).** *Br J Radiol* 1978;51:196–202 CrossRef Medline
4. Killebrew K, Whaley RA, Hayward JN, et al. **Complications of metrizamide myelography.** *Arch Neurol* 1983;40:78–80 CrossRef Medline
5. Lipman JC, Wang AM, Brooks ML, et al. **Seizure after intrathecal administration of iopamidol.** *AJNR Am J Neuroradiol* 1988;9:787–88 Medline
6. Klein KM, Shiratori K, Knake S, et al. **Status epilepticus and seizures induced by iopamidol myelography.** *Seizure* 2004;13:196–99 CrossRef Medline
7. Simon JH, Ekholm SE, Kido DK, et al. **High-dose iohexol myelography.** *Radiology* 1987;163:455–58 CrossRef Medline
8. Fedutes BA, Ansani NT. **Seizure potential of concomitant medications and radiographic contrast media agents.** *Ann Pharmacother* 2003;37:1506–10 CrossRef Medline
9. Sandow BA, Donnal JF. **Myelography complications and current practice patterns.** *AJR Am J Roentgenol* 2005;185:768–71 CrossRef Medline
10. Shah LM, Kranz PG, Anzai Y, et al. **Critical assessment of myelography practices: a call for rational guideline revision.** *AJNR Am J Neuroradiol* 2018;39:2378–84 CrossRef Medline
11. Tait AR, Voepel-Lewis T, Munro HM, et al. **Cancellation of pediatric outpatient surgery: economic and emotional implications for patients and their families.** *J Clin Anesth* 1997;9:213–19 CrossRef Medline
12. Omnipaque (iohexol) injection [package insert]. Piscataway: GE Healthcare; 2010
13. Hindmarsh T, Ekholm SE, Kido DK, et al. **Lumbar myelography with iohexol and metrizamide: a double-blind clinical trial.** *Acta Radiol Diagn (Stockh)* 1984;25:365–68 CrossRef Medline
14. Maly P, Bach-Gansmo T, Elmqvist D. **Risk of seizures after myelography: comparison of iohexol and metrizamide.** *AJNR Am J Neuroradiol* 1988;9:879–83 Medline
15. Reisin R, Ethier R, de la Sayette V, et al. **Metrizamide compared with iohexol for cervical myelography: a double-blind study.** *Can Assoc Radiol J* 1988;39:107–10 Medline
16. Alimohammadi H, Abdalvand A, Safari S, et al. **Status epilepticus after myelography with iohexol (Omnipaque).** *Am J Emerg Med* 2012;30:2092.e1–3 CrossRef Medline
17. Park KS, Moon JY, Oh CS, et al. **Acetabular central fracture dislocation after generalized seizure during lumbar myelography with iohexol.** *Case Rep Orthop* 2013;2013:190917 CrossRef Medline
18. Kertmen H, Güreş B, Yılmaz ER, et al. **Postoperative seizure following transforaminal percutaneous endoscopic lumbar discectomy.** *Asian J Neurosurg* 2016;11:450 CrossRef Medline
19. Rosenberg H, Grant M. **Ascending tonic-clonic syndrome secondary to intrathecal Omnipaque.** *J Clin Anesth* 2004;16:299–300 CrossRef Medline
20. Gabriel M, Sharma V. **Antidepressant discontinuation syndrome.** *CMAJ* 2017;189:E747 CrossRef Medline

# Assessing Vascularity of Osseous Spinal Metastases with Dual-Energy CT-DSA: A Pilot Study Compared with Catheter Angiography

Y.-C. Huang, F.-Y. Tsuang, C.-W. Lee, C.-Y. Wu, and Y.-H. Lin

## ABSTRACT

**BACKGROUND AND PURPOSE:** Spine debulking surgery in patients with hypervascular spinal metastasis is associated with massive intraoperative blood loss, but currently, the vascularity of tumor is determined by invasive conventional angiography or dynamic contrast MR imaging. We aimed to investigate the usefulness of noninvasive dual-energy CT-DSA, comparing it with conventional angiography in evaluating the vascularity of spinal metastasis.

**MATERIALS AND METHODS:** We conducted a retrospective study from January to December 2018. A total of 15 patients with spinal metastasis undergoing dual-energy CT, conventional DSA, and subsequent debulking surgery were included. CT-DSA images were produced after rigid-body registration and subtraction between CT phases. Qualitative and quantitative assessments of tumor vascularity were conducted. Correlations between CT-DSA and conventional DSA results were evaluated using the Spearman coefficient. The mean enhancement in the estimated tumor volume and surgical blood loss was compared between hypervascular and nonhypervascular groups using the Wilcoxon rank sum test.

**RESULTS:** The CT-DSA and DSA results were strongly correlated, with  $\rho = 0.87$  ( $P < .001$ ). The DSA and the quantitative enhancement index also showed a strong correlation with  $\rho = 0.83$  ( $P < .001$ ). Wilcoxon rank sum testing between hypervascular and nonhypervascular CT-DSA groups showed a difference in enhancement indices ( $P = .0003$ ). The blood loss between the hypervascular and nonhypervascular groups was nonsignificant ( $P = .09$ ).

**CONCLUSIONS:** Dual-energy CT-DSA correlates well with conventional DSA in assessing the vascularity of spinal metastasis. It may serve as a noninvasive preoperative evaluation option before debulking surgery.

**ABBREVIATION:** DECT = dual-energy CT

Bony metastases of the spine can be very detrimental to a patient's quality of life because they can cause severe pain, instability, and neurologic deficits secondary to spinal cord and root compression.<sup>1,2</sup> In selected cases, debulking surgery improves local control and quality of life to a greater degree than conventional methods.<sup>3</sup> However, aggressive spinal surgery could be complicated by massive intraoperative hemorrhage in hypervascular osseous metastases. Related studies have demonstrated that preoperative transarterial embolization might reduce intraoperative blood loss,<sup>4-9</sup> especially for pathologies prone to hypervascular

metastases such as thyroid carcinoma, renal cell carcinoma, and hepatocellular carcinoma. However, not all metastases from such tumors are hypervascular,<sup>5,10</sup> and metastases from other tumor pathologies could be hypervascular as well. Therefore, it is recommended that tumor vascularity be assessed before spinal surgery.<sup>4</sup> DSA is considered a reference standard for vascularity assessment of bone tumors. However, DSA is an invasive imaging tool, and quantitative measurements using DSA have not been comprehensively explored, to our knowledge.

CT is one of the most commonly available imaging tools in modern medicine. It is excellent at demonstrating osseous integrity and fracture margins at rapid scanning speeds.<sup>11</sup> In cases of osseous metastases, the degree of enhancement is often hindered by the inherent high density of mineral components. Additionally, in small osseous metastases without substantial bone morphologic changes, conventional CT has poor detection abilities compared with MR imaging and PET.<sup>12,13</sup> Therefore, CT plays a supplementary role in diagnosing spinal metastases. Recent ad-

Received November 13, 2018; accepted after revision March 6, 2019.

From the Department of Medical Imaging (Y.-C.H., C.-W.L., Y.-H.L.), Division of Neurosurgery (F.-Y.T.), Department of Surgery, and Department of Anesthesiology (C.-Y.W.), National Taiwan University Hospital, Taipei, Taiwan.

Please address correspondence to Yen-Heng Lin, MD, MS, Department of Medical Imaging, National Taiwan University Hospital, No. 7, Chung-Shan South Rd, Taipei 100, Taiwan, ROC; e-mail: cryhungry@gmail.com

<http://dx.doi.org/10.3174/ajnr.A6023>

vancements in CT registration and subtraction have enabled demonstration of hypervascular bone tumors, marrow edema, and spinal arteries.<sup>14-16</sup> The contrast-to-noise ratio can be optimized when the images are reconstructed at selected monoenergetic levels by performing dual-energy CT (DECT).<sup>17</sup>

In this pilot study, we evaluated the potential of dual-energy CT-DSA, compared with DSA, for assessing the vascularity of osseous spinal metastasis before debulking surgery.

## MATERIALS AND METHODS

### Patients

This study was approved by the institutional review board of our hospital. All patients who underwent dual-energy spinal CT angiography for osseous metastases from January to December 2018 at a single tertiary referral center were retrospectively reviewed. Patients were included if they underwent spinal surgery and DSA at the target levels with histopathology-proved metastatic malignancy. Patients were excluded from the analysis if they had prior spinal surgery at the target levels or if the image quality of DSA and CT was poor for post-image processing.

### CTA Acquisition and Image Postprocessing

All CT scans were performed on a 256-detector row fast-kV-switching DECT system (Revolution CT; GE Healthcare, Milwaukee, Wisconsin). The scan range contained at least 5 vertebral body levels centered at the target level. The scan range was extended in sacral and cervical lesions to include possible distal collateral blood supplies. The scans were obtained in dual-energy mode on a fast-kV-switching DECT system that switched tube potentials between 140 and 80 kV. Radiation doses were adjusted according to the diagnostic reference levels<sup>18,19</sup> and previously reported doses that could identify the anterior spinal artery.<sup>20-22</sup> Narrow collimation (between 4 and 8 cm) and a low scan pitch factor (lower than 1) were used to reduce the conebeam artifacts and enhance the z-axis resolution while maintaining a scan time of <8 seconds. We obtained 4 CT phases: noncontrast, early arterial, late arterial, and venous. Intravenous nonionic contrast medium was injected into the antecubital vein at a flow rate of 4 mL/s; the total contrast amount was between 60 and 80 mL, which had been tailored to the scan time. Autoscan triggering was used with the ROI situated at the aorta at the starting position of the scan range. The scan started 2.6 seconds after the ROI had reached 100 HU to acquire the early arterial phase; the late arterial phase started 4 seconds after the early arterial phase had been completed. The venous phase was then performed after a 60-second delay. The patients were instructed to maintain shallow, slow breathing during the scans. The images were reconstructed on 0.625-mm-thick contiguous slices with a 16- to 20-cm FOV.

A stand-alone workstation (Advantage Workstation, Version 4.7; GE Healthcare) was used for postprocessing images. First, a 40-keV monochromatic CT image was reconstructed from the DECT data file to enhance the contrast conspicuity. Late arterial phase images were then registered to a noncontrast scan through rigid-body registrations. Subtraction images between the late arterial phase and noncontrast phase images were then obtained to produce pure enhanced images, namely CT-DSA images. Figure 1 depicts CT-DSA before and after registration.

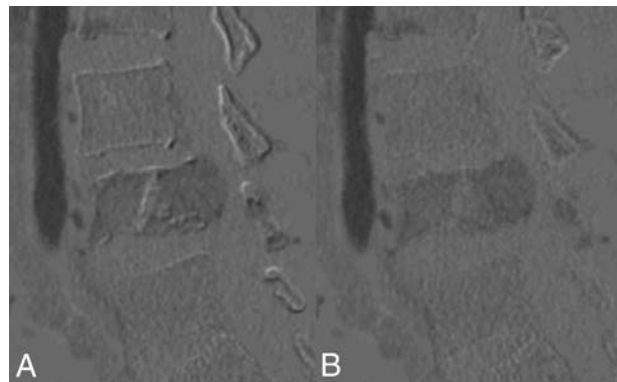


**FIG 1.** Sagittal subtraction CT before and after rigid-body registration. If we set the subtracted image to a proper window, the quality of registration can be assessed using a DSA-like visual inspection method. *A*, Unregistered image shows an overt misalignment artifact over bony edges. *B*, After solid-body registration, the number of artifacts is greatly reduced.

### Quantitative Measurement and Qualitative Evaluation of CT-DSA

After the production of subtracted images, quantitative measurements were performed on a stand-alone workstation by one of the authors (with 4 years' experience in neuroradiology) blinded to the clinical information. The tumor mass was segmented along the axial plane, slice by slice, to form a 3D ROI. Vessels and misregistered artifacts were excluded from the selection. Tumor volume and mean enhancement were obtained from the resultant ROI. The following enhancement index was formulated to represent the percentage of tumor enhancement compared with that of the artery:

Enhancement Index =

$$\frac{\text{Mean Enhancement of the Estimated Tumor Volume}}{\text{Enhancement of Aorta or Great Artery}}$$

For qualitative evaluation, the subtracted images were reformatted to standard 3-mm axial, coronal, and sagittal images with color-coded displays. The color scale was set between the part of the scan range that showed the best enhancement (typically the aorta) and zero Hounsfield units. The color map image was read on a standard PACS for clinical diagnostic purposes. Two neuro-radiologists (with 9 and 4 years' experience, respectively) read the studies independently; they were blinded to the clinical information and catheter spinal angiography results. Tumor vascularity was classified into 5 grades: 0 = enhancement lower than that of the nondiseased adjacent vertebral bodies, 1 = peak enhancement area similar to that of the nondiseased adjacent vertebral bodies but lower than that of one-third of the aortic enhancement, 2 = peak enhancement area higher than that of one-third of the aortic enhancement, 3 = peak enhancement area higher than that of one-third of the aortic enhancement with the presence of early venous enhancement. Figure 2 shows the color map of CT-DSA alongside the corresponding catheter spinal angiography images.

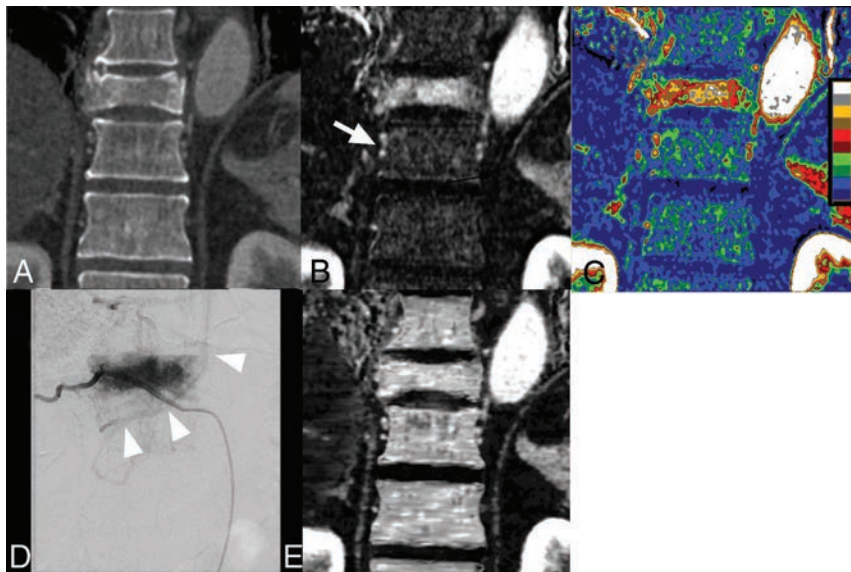


**FIG 2.** A 68-year-old male patient with hepatocellular carcinoma with a hypervascular bony metastasis in the T10 vertebral body. *A*, Coronal 40-keV monoenergetic image of the late arterial phase shows a T10 vertebral body osteolytic lesion with a pathologic compression fracture. *B*, Coronal 40-keV subtracted CTA after registration shows that the T10 vertebral body had been replaced by a metastatic tumor with avid enhancement stronger than that of the marrow in the adjacent vertebral body. An earlier segmental draining vein (*white arrow*) parallel to the segmental artery is shown for comparison with a single enhancing segmental artery at the adjacent normal level. *C*, Color-coded display of the subtracted images demonstrates the degree of enhancement more clearly. The color map is set to a 10-stepped scale with 10% increments for each step to assist in visual grading. *D*, Frontal view of DSA at the same level shows a typical hypervascular bony metastasis. Early venous drainage to a hemizygous vein is noted (*arrowheads*), indicating arteriovenous shunting within the metastatic lesion. A smaller part of the vertebral body supplied by the left segmental artery is not opacified in this DSA image. *E*, Iodine map derived from the material decomposition algorithm shows falsely high iodine content in normal bone marrow. The map failed to demonstrate the expected enhancement difference between the tumor and normal bone marrow because of limitations of the dual-energy CT iodine-based material decomposition in bony tissue.

### Spinal Angiography

Catheter spinal angiography was performed and read by a neurointerventionalist (with 4 years' experience in neurointervention and 9 years' experience in neuroradiology) with the patient under local anesthesia. If a target metastasis was in the cervical spine, the cervical spinal angiography included bilateral vertebral angiography. For thoracolumbar disease, segmental artery angiography was performed at both the target and adjacent levels. For a target level lower than L3, iliac artery angiography was also performed. Tumor vascularity was classified into 5 categories according to the literature<sup>23</sup>: 0 = decreased enhancement compared with that in a normal nondiseased vertebral body, 1 = same degree of enhancement compared with that in a normal nondiseased vertebral body, 2 = mild tumor blush, 3 = moderate tumor blush with an opacity similar to that of the segmental artery proper, and 4 = marked tumor blush with early arteriovenous shunting. The angiography study was also used to identify the Adamkiewicz and anterior spinal arteries.

### Preoperative Embolization

Preoperative embolization was performed after the complete angiography study if no anterior spinal arteries had been identified at the target levels. For tumors in the thoracic-to-sacral regions, embolization was performed with particles (Contour and Embozene particles; Boston Scientific, Natick, Massachu-

setts) at the target level and adjacent segmental arteries when tumor stain was present. The embolization was assisted by a coil for flow redistribution and proximal occlusion when necessary.<sup>24,25</sup> For tumors at the cervical level and when the vertebral artery was encased by a tumor, coil embolization of the affected vertebral artery at both the distal and proximal tumor edges was performed when the collateral supply from the contralateral vertebral artery was adequate according to CTA and selective angiography.

### Surgical Procedure

A surgical plan was developed by a multidisciplinary spine oncology board, and the treatment options were determined according to the Tomita survival scores,<sup>26</sup> revised Tokuhashi Scores,<sup>27</sup> and an algorithm proposed by Cappuccio and Boriana.<sup>28</sup> All patients underwent intralesional debulking surgery or total en bloc spondylectomy, in which surgeons removed the vertebrae with the tumor in piecemeal fashion or as a whole. Vertebral reconstructions were performed 2 levels above and below the resected vertebra with prefabricated metallic implants or polymethyl methacrylate and posterior fixation.

### Statistical Analysis

Individual patient data were provided in detail. Spearman rank correlation of DSA to the enhancement index and CT-DSA grade was conducted. The interrater reliability of qualitative data was evaluated by weighted  $\kappa$  values. We further dichotomized the patients into hypervascular and nonhypervascular groups according to their CT-DSA enhancement grades. Mean enhancement in the estimated tumor volume and surgical blood loss was compared between the 2 groups using the Wilcoxon rank sum test. The significance level was set at .05. All statistical analyses were performed using SAS software, Version 9.4 (SAS Institute, Cary, North Carolina).

### RESULTS

A total of 47 patients evaluated for preoperative spinal CTA were analyzed during the study period. Seven patients did not undergo surgery after the multidisciplinary board judged that surgery was unnecessary, 17 patients had no preoperative DSA, 2 patients had pathologies other than metastases, and 6 patients were excluded from this study because of prior palliative surgery. Finally, 15 patients were included for analysis. Among them, 3 patients had 2 target levels, and the remaining 12 patients had 1 target level. The tumor types varied, comprising 1 melanoma, 1 colonic carcinoma, 1 renal cell carcinoma, 1 thyroid cancer, 1 parotid epithelial-myoepithelial carcinoma, 3 breast cancers, 1 cervical cancer, 2

## Patient characteristics

Patient	Sex	Age (yr)	Tumor Type	Tumor Location	DSA Grade, Reader 1/2	CT-DSA Grade, Reader 1/2	Estimated Tumor Volume (cm <sup>3</sup> )	Enhancement Index	Surgical Approach/Procedure	Preoperative Embolization	Blood Loss (cm <sup>3</sup> )
1	M	67	Melanoma	L3	1/1	1/1	78.83	0.1574	Posterior/debulking	Yes	2300
2	M	55	Colon cancer	L4	3/3	3/3	49.59	0.1659	Posterior/debulking	Yes	3950
3	F	44	Renal cell carcinoma	C4	4/4	3/4	16.28	0.6254	Anterior/debulking	Yes	600
4	M	72	Thyroid cancer	C7	2/1	2/3	11.93	0.1522	Anterior/debulking	Yes	800
5	M	54	Breast cancer	L4	3/3	4/4	36.74	0.2586	Posterior/debulking	Yes	10,000
6	M	69	Hepatocellular carcinoma	T10	4/4	3/4	18.14	0.2917	Posterior/debulking	Yes	4600
7	F	69	Lung cancer	T4	1/0	1/1	10.86	0.1653	Posterior/debulking	Yes	3000
8	M	74	Hepatocellular carcinoma	T10	2/3	1/1	22.25	0.0673	Posterior/debulking	No	1000
9	F	58	Cervical cancer	L4–5	2/4	2/2	91.14	0.0734	Posterior/debulking	Yes	1400
10	F	51	Lung cancer	L4–5	4/3	3/3	11.61	0.2183	Posterior/debulking	Yes	3400
11	M	60	Hepatocellular carcinoma	T4	4/4	4/4	14.19	0.3325	Posterior/debulking	Yes	1400
12	M	64	Hepatocellular carcinoma	T3	4/4	4/3	26.47	0.1888	Posterior/debulking	Yes	2000
13	F	64	Breast cancer	T3–4	2/2	3/2	29.06	0.1107	Posterior/debulking	Yes	600
14	F	44	Breast cancer	L5	0/1	2/2	42.86	0.0450	Posterior/debulking	Yes	200
15	F	58	Parotid epithelial-myoepithelial carcinoma	T4	1/2	2/2	4.05	0.0339	Posterior/en bloc	No	2700

lung cancers, and 4 hepatocellular carcinomas. The target vertebrae included 2 cervical, 7 thoracic, and 6 lumbar vertebrae. Thirteen patients underwent preoperative embolization before surgery. All patients underwent debulking surgery for spinal metastases; among them, 2 patients had anterior approaches for cervical metastasis debulking, and 13 with thoracolumbar metastases underwent debulking surgery through a single posterior approach. Individual patient data are listed in the Table.

The volume CT dose index of the present study was 9.33–20.93 mGy (median, 12.64 mGy) for a single late CTA phase and 5.98–20.93 mGy (median, 12.25 mGy) for other single phases.

Spearman coefficients demonstrated a strong correlation between the DSA and CT-DSA grades, with  $\rho = 0.87$  ( $P < .001$ ). The DSA grade and CT-DSA enhancement index were also strongly correlated, with  $\rho = 0.83$  ( $P < .001$ ). For the interrater reliability of DSA and CT-DSA, the weighted  $\kappa$  values were 0.64 (range, 0.43–0.84) and 0.74 (95% CI, 0.51–0.96), respectively. The patients with CT-DSA grades 3 and 4 were assigned to the hypervascular group, and those with grades 0, 1, and 2 were assigned to the nonhypervascular group. The Wilcoxon rank sum test revealed a difference in the enhancement indices of the 2 groups ( $P = .0003$ ). The hypervascular group had higher mean surgical blood loss than the nonhypervascular group ( $3707 \pm 3121$  versus  $1500 \pm 1041$  mL); however, this difference was not significant ( $P = .09$ ).

## DISCUSSION

Spine bony metastases often result in severe pain, instability, and neurologic deficits<sup>1,2</sup> in patients with late-stage malignancies. Debulking surgeries in selected cases provide improved local control rates and neurologic outcomes but can be complicated by massive intraoperative blood loss.<sup>3</sup> Currently, DSA is used as a reference standard for evaluating tumor vascularity before surgery.<sup>10,23,29</sup> However, DSA is an invasive procedure that has only moderate interrater and intrarater reliability for classifying the vascularity of spinal metastases.<sup>30</sup> In our study, the CT-DSA grading system and quantification measurements were strongly correlated with the DSA grading system.

DSA grading can be suboptimal because of variations in angiography techniques, anatomy, and tumor burden. In case 5 of our series, DSA exhibited lower vascularity than CT-DSA (grade 3 versus 4) because the planned injection rate was insufficient for

the hypertrophied artery. Conversely, the degree of perfused arterial enhancement was uniform in the CTA image, which was unaffected by technique or anatomy variation during catheterization. Comparisons between adjacent levels may be more reliable.

Currently, there is no consensus on the CT classification of tumor vascularity. The proposed CT-DSA classification criteria were designed to be clinically useful and similar to the DSA classification criteria. On the basis of discussions with spinal surgeons of the multidisciplinary spine oncology board, we stratified grades 3 and 4 and 0, 1, and 2 as the closest matches for clinical experience. The development of an appropriate and clinically relevant classification scheme requires well-designed studies on a large scale with a sufficient follow-up duration. For a pilot study with a low case number, a solid suggestion regarding classification criteria is difficult to postulate. However, we believe that our current study demonstrates that CT-DSA is practical and potentially useful as a robust noninvasive tool for the preoperative evaluation of tumor vascularity.

In related studies, specialized MR imaging protocols applying dynamic contrast enhancement and high-resolution MRA have been described as a means of obtaining information regarding perfusion and arterial anatomy; these protocols are complex and require specialized MR imaging sequences that are not routinely performed.<sup>23,29,31</sup> Meanwhile, conventional MR imaging sequences might not provide sufficient information regarding the anatomy or degree of vascularity.<sup>31</sup> The CTA protocol described in our study requires only minimal modification from standard CTA protocols for other body parts; thus, this protocol might be easier to incorporate into clinical practice. The correlation between CT-DSA vascularity grading and intraoperative blood loss was nonsignificant in this study. However, there is a trend suggesting that high-grade tumors have high intraoperative blood loss. Because only 15 patients were included in this study, the primary reason for the nonsignificant result ( $P = .09$ ) was insufficient statistical power and other uncontrolled parameters, including tumor location, tumor size, surgical method, and degree of embolization. Thus, in this study, conclusions were difficult to draw, and further large-scale studies are needed to clarify the correlation between CT-DSA and intraoperative blood loss.

DECT scans are mainly used to optimize the contrast-to-noise

ratios and improve the conspicuity of the anterior spinal and Adamkiewicz arteries.<sup>32</sup> In this study, the unique abilities of DECT to perform material decomposition and virtual noncontrast studies were not comprehensively explored for a reason. We initially attempted to use a material decomposition algorithm to produce iodine mapping; however, material decomposition algorithms operate poorly in vertebral body scans. Iodine maps produced by commercial standard material decomposition algorithms (with 2 base material pairs: iodine-hydroxyapatite and iodine-water) and custom-made software that implements multiple material decomposition algorithms, as described elsewhere,<sup>33</sup> show falsely high iodine content in normal bone marrow (Fig 2E). In the present study, 11 of the 15 cases (73%) exhibited higher iodine content in normal vertebral marrow than did tumors on iodine maps derived from multiple material decomposition algorithms. We believe that this finding was a result of the implemented algorithm being unable to decompose 4 materials simultaneously.<sup>34-37</sup> In addition to the 3-material model used in the literature for demonstrating bone marrow content distributions,<sup>38,39</sup> iodine is added as a fourth material in enhanced spine studies. The introduction of a fourth material violates the assumption of the 3-material decomposition algorithm and renders the algorithm unsuitable for use in contrast spine CT. Virtual unenhanced CT images have the same limitations because they are based on the algorithm that performs multiple material decompositions. Nevertheless, the role of DECT in vertebral metastases is yet to be determined, and we still consider DECT an appealing imaging tool for vertebral body analysis worthy of further investigation.

In the present study, CT-DSA images were produced with pre-contrast and late CTA scans only. The early arterial phases are not used in CT-DSA, but it depicted segmental arteries well, because the late arterial phase might have fading enhancements in arteries that preclude small artery anatomic assessment. The venous phase provides an enhanced series to make differential diagnoses and can depict adjacent large venous structures (eg, the azygos vein and the epidural venous plexus). These structures may not be identified during an operation because of the limited surgical FOV.

Although CT-DSA was performed with DECT scans in our study, registration and subtraction can be performed without the dual-energy scan mode. We believe that DECT scans are not mandatory for subtracting CT to evaluate vascularity, and CT-DSA can be used at most CT sites.

Our study had several limitations. The first limitation was the small size of the pilot study group, which prevented further control and analysis of variables. A study with a larger sample size is warranted to confirm the correlations with general patient conditions. The second limitation concerns the retrospective nature of this study. The subjects analyzed in this study were patients who had undergone surgical interventions, which only represent a subgroup of all patients. This feature rendered the analysis vulnerable to selection bias. The third limitation was the use of registration and subtraction, which may not be available at every CT site. However, solid body registration and subtraction are fast and relatively easy postprocessing steps that are commercially available from most CT vendors and in open-source image-processing

packages.<sup>40</sup> For CT sites where registration is not available, subtraction of unregistered phases might be helpful.

The final limitation was the high radiation dose in the proposed protocol. Although we adjusted our radiation exposure levels in accordance with reported diagnostic reference levels in the literature and implemented standard dose-reduction techniques, radiation exposure remained high because of multiple phase acquisitions and a high single-phase radiation dose for spine CTs. Careful patient selection is warranted when using this protocol in clinics. Patients with malignant osseous spinal metastases are more likely to benefit from preoperative vascular imaging when the potential detriment of radiation exposure is considered. When CT-DSA is used in patients for whom radiation exposure is a concern, physicians could consider skipping the early arterial or venous phases to reduce exposure.

## CONCLUSIONS

Dual-energy CT-DSA correlates well with conventional DSA in assessing the vascularity of spinal metastasis. It may serve as a potentially useful noninvasive tool for evaluating the vascularity of spinal metastasis.

## REFERENCES

- Mut M, Schiff D, Shaffrey ME. **Metastasis to nervous system: spinal epidural and intramedullary metastases.** *J Neurooncol* 2005;75:43–56 CrossRef Medline
- Gilbert RW, Kim JH, Posner JB. **Epidural spinal cord compression from metastatic tumor: diagnosis and treatment.** *Ann Neurol* 1978;3:40–51 CrossRef Medline
- de Ruyter GC, Nogaredo CO, Wolfs JF, et al. **Quality of life after different surgical procedures for the treatment of spinal metastases: results of a single-center prospective case series.** *Neurosurg Focus* 2017;42:E17 CrossRef Medline
- Robial N, Charles YP, Bogorin I, et al. **Is preoperative embolization a prerequisite for spinal metastases surgical management?** *Orthop Traumatol Surg Res* 2012;98:536–42 CrossRef Medline
- Pazonis TJ, Papanastassiou ID, Maybody M, et al. **Embolization of hypervascular bone metastases reduces intraoperative blood loss: a case-control study.** *Clin Orthop Relat Res* 2014;472:3179–87 CrossRef Medline
- Kickuth R, Waldherr C, Hoppe H, et al. **Interventional management of hypervascular osseous metastasis: role of embolotherapy before orthopedic tumor resection and bone stabilization.** *AJR Am J Roentgenol* 2008;191:W240–47 CrossRef Medline
- McDonald K, Murphy LE, Eames N. **Is it necessary to embolise all spinal metastases from primary renal tumours?** *J Orthop* 2016;13:472–74 CrossRef Medline
- Qiao Z, Jia N, He Q. **Does preoperative transarterial embolization decrease blood loss during spine tumor surgery?** *Interv Neuroradiol* 2015;21:129–35 CrossRef Medline
- Mendel E, Bourekas E, Gerszten P, et al. **Percutaneous techniques in the treatment of spine tumors: what are the diagnostic and therapeutic indications and outcomes?** *Spine* 2009;34:S93–100 CrossRef Medline
- Schmidt R, Rupp-Heim G, Dammann F, et al. **Surgical therapy of vertebral metastases: are there predictive parameters for intraoperative excessive blood loss despite preoperative embolization?** *Tumori* 2011;97:66–73 CrossRef Medline
- Mauch JT, Carr CM, Cloft H, et al. **Review of the imaging features of benign osteoporotic and malignant vertebral compression fractures.** *AJNR Am J Neuroradiol* 2018;39:1584–92 CrossRef Medline
- Jeong D, Bui M, Peterson D, et al. **FDG avid breast cancer bone metastases silent on CT and scintigraphy: a case report with radiologic**

- pathologic correlation.** *Acta Radiol Open* 2017;6:2058460117734243 CrossRef Medline
13. Al-Muqbel KM. **Bone marrow metastasis is an early stage of bone metastasis in breast cancer detected clinically by F18-FDG-PET/CT imaging.** *Biomed Res Int* 2017;2017:9852632 CrossRef Medline
  14. Gondim Teixeira PA, Hossu G, Lecocq S, et al. **Bone marrow edema pattern identification in patients with lytic bone lesions using digital subtraction angiography-like bone subtraction on large-area detector computed tomography.** *Invest Radiol* 2014;49:156–64 CrossRef Medline
  15. Gondim Teixeira PA, Gervaise A, Louis M, et al. **Musculoskeletal wide detector CT: principles, techniques and applications in clinical practice and research.** *Eur J Radiol* 2015;84:892–900 CrossRef Medline
  16. Nishii T, Kono AK, Nishio M, et al. **Bone-subtracted spinal CT angiography using nonrigid registration for better visualization of arterial feeders in spinal arteriovenous fistulas.** *AJNR Am J Neuroradiol* 2015;36:2400–06 CrossRef Medline
  17. Yu L, Christner JA, Leng S, et al. **Virtual monochromatic imaging in dual-source dual-energy CT: radiation dose and image quality.** *Med Phys* 2011;38:6371–79 CrossRef Medline
  18. Hayton A, Wallace A, Marks P, et al. **Australian diagnostic reference levels for multi detector computed tomography.** *Australas Phys Eng Sci Med* 2013;36:19–26 CrossRef Medline
  19. Directorate-General for Energy, Directorate D, Nuclear Safety and Fuel Cycle, Unit D3, Radiation Protection. *RADIATION PROTECTION No. 180 Diagnostic Reference Levels in Thirty-six European Countries (Part 2)*. European Commission; 2014. <https://ec.europa.eu/energy/sites/ener/files/documents/RP180%20part2.pdf>. Accessed January 15, 2018
  20. Takase K, Sawamura Y, Igarashi K, et al. **Demonstration of the artery of Adamkiewicz at multi-detector row helical CT.** *Radiology* 2002;223:39–45 CrossRef Medline
  21. Kudo K, Terae S, Asano T, et al. **Anterior spinal artery and artery of Adamkiewicz detected by using multi-detector row CT.** *AJNR Am J Neuroradiol* 2003;24:13–17 Medline
  22. Yoshioka K, Tanaka R, Takagi H, et al. **Ultra-high-resolution CT angiography of the artery of Adamkiewicz: a feasibility study.** *Neuroradiology* 2018;60:109–15 CrossRef Medline
  23. Mazura JC, Karimi S, Pauliah M, et al. **Dynamic contrast-enhanced magnetic resonance perfusion compared with digital subtraction angiography for the evaluation of extradural spinal metastases: a pilot study.** *Spine* 2014;39:E950–54 CrossRef Medline
  24. Shi HB, Suh DC, Lee HK, et al. **Preoperative transarterial embolization of spinal tumor: embolization techniques and results.** *AJNR Am J Neuroradiol* 1999;20:2009–15 Medline
  25. Suzuki H, Kondo T, Kuwatsuru R, et al. **Decompressive surgery in combination with preoperative transcatheter arterial embolization: successful improvement of ambulatory function in renal cell carcinoma patients with metastatic extradural spinal cord compression.** *Int J Urol* 2011;18:718–22 CrossRef Medline
  26. Tomita K, Kawahara N, Kobayashi T, et al. **Surgical strategy for spinal metastases.** *Spine* 2001;26:298–306 CrossRef Medline
  27. Tokuhashi Y, Matsuzaki H, Oda H, et al. **A revised scoring system for preoperative evaluation of metastatic spine tumor prognosis.** *Spine* 2005;30:2186–91 CrossRef Medline
  28. Cappuccio M, Gasbarrini A, Van Urk P, et al. **Spinal metastasis: a retrospective study validating the treatment algorithm.** *Eur Rev Med Pharmacol Sci* 2008;12:155–60 Medline
  29. Saha A, Peck KK, Lis E, et al. **Magnetic resonance perfusion characteristics of hypervascular renal and hypovascular prostate spinal metastases: clinical utilities and implications.** *Spine* 2014;39:E1433–40 CrossRef Medline
  30. Clausen C, Dahl B, Christiansen Frevert S, et al. **Inter- and intra-rater agreement in the assessment of the vascularity of spinal metastases using digital subtraction angiography tumor blush.** *Acta Radiol* 2017;58:734–39 CrossRef Medline
  31. Khadem NR, Karimi S, Peck KK, et al. **Characterizing hypervascular and hypovascular metastases and normal bone marrow of the spine using dynamic contrast-enhanced MR imaging.** *AJNR Am J Neuroradiol* 2012;33:2178–85 CrossRef Medline
  32. Shimoyama S, Nishii T, Watanabe Y, et al. **Advantages of 70-kV CT angiography for the visualization of the Adamkiewicz artery: comparison with 120-kV imaging.** *AJNR Am J Neuroradiol* 2017;38:2399–405 CrossRef Medline
  33. Mendonca PR, Lamb P, Sahani DV. **A flexible method for multi-material decomposition of dual-energy CT images.** *IEEE Trans Med Imaging* 2014;33:99–116 CrossRef Medline
  34. Dinkel J, Khalilzadeh O, Phan CM, et al. **Technical limitations of dual-energy CT in neuroradiology: 30-month institutional experience and review of literature.** *J Neurointerv Surg* 2015;7:596–602 CrossRef Medline
  35. Gupta R, Phan CM, Leidecker C, et al. **Evaluation of dual-energy CT for differentiating intracerebral hemorrhage from iodinated contrast material staining.** *Radiology* 2010;257:205–11 CrossRef Medline
  36. Kuno H, Onaya H, Iwata R, et al. **Evaluation of cartilage invasion by laryngeal and hypopharyngeal squamous cell carcinoma with dual-energy CT.** *Radiology* 2012;265:488–96 CrossRef Medline
  37. Hiyama T, Kuno H, Sekiya K, et al. **Bone subtraction iodine imaging using area detector CT for evaluation of skull base invasion by nasopharyngeal carcinoma.** *AJNR Am J Neuroradiol* 2019;40:135–41 CrossRef Medline
  38. Ali IT, Wong WD, Liang T, et al. **Clinical utility of dual-energy CT analysis of bone marrow edema in acute wrist fractures.** *AJR Am J Roentgenol* 2018;210:842–47 CrossRef Medline
  39. Mallinson PI, Coupal TM, McLaughlin PD, et al. **Dual-energy CT for the musculoskeletal system.** *Radiology* 2016;281:690–707 CrossRef Medline
  40. Yushkevich PA, Piven J, Hazlett HC, et al. **User-guided 3D active contour segmentation of anatomical structures: significantly improved efficiency and reliability.** *Neuroimage* 2006;31:1116–28 CrossRef Medline

# Celebrating 35 Years of the AJNR

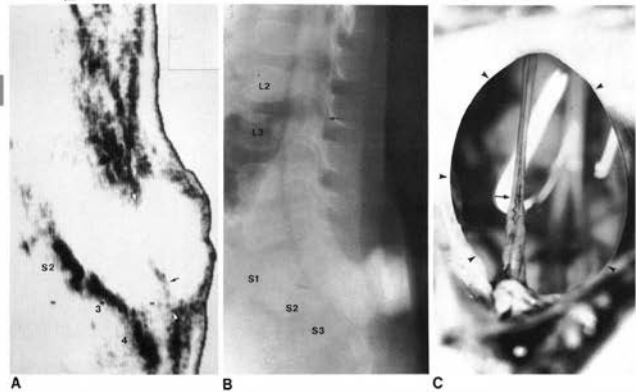
May 1984 edition

## John Caffey Award Sonography of the Caudal Spine and Back: Congenital Anomalies in Children

Thomas P. Naidich  
Sandra K. Fernbach  
David G. McLone<sup>1</sup>  
Arnold Shkolnik<sup>2</sup>

Articulated-arm, B-mode 3.5-5.0 MHz sonograms from 27 children with congenital anomalies of the caudal spine were analyzed retrospectively and correlated directly with patient appearance, preoperative myelograms, intraoperative photographs, and pathologic specimens to determine how effectively sonography could display the major pathologic features known to be present. Anterior spina bifida, posterior spina bifida, and (partial) sacral agenesis were displayed as focal absence of normal spinal echoes and distortions of the paraspinous/gluteal muscles. Subcutaneous anechoic spaces continuous with the spinal canal through a spina bifida identified the presence, site, and configuration of each meningocele present. Highly echogenic masses were easily discerned at the sites of 14 of 16 lipomas and at the solid fibroadipose portions of both sacroccoccygeal teratomas. Echoes from the surface of the spinal cord and occasionally from the central canal identified abnormally low cord position in 16 of 17 cases and identified herniation of the cord (or filum) into a concurrent meningocele in seven of 10 cases. Sonographic display of an anechoic meningocele bordered by a lobular, highly echogenic, subcutaneous lipoma that inserted onto a low-lying or herniated spinal cord reliably identified lipomyelomeningocele. Despite limitations discussed in the text, initial experience suggests that sonography will be a useful method for screening patients for possible tethered spinal cord, lipomyelomeningocele, sacroccoccygeal teratoma, and other anomalies of the caudal spinal axis.

In patients with myelodysplasia and other anomalies of the caudal spine, cranial sonography has been widely accepted for assessing concurrent intracranial pathology and for intraoperative placement of ventricular shunt catheters [1-3]. Renal sonography has proved equally valuable for detecting associated renal agenesis, renal ectopia, and hydronephrosis [4, 5]. Spinal sonography, however, has received relatively little attention, even though sonographic windows are provided by the incomplete ossification of the posterior elements in children under 1 year of age and by spina bifida [6-19].



This article appears in the May/June 1984 issue of AJNR and the June 1984 issue of AJR. Received September 28, 1983; accepted after revision January 23, 1984.

Presented in part at the Symposium Neuro-radiology, Washington, DC, October 1982, and the annual meeting of the Society for Pediatric Radiology, Atlanta, April 1983.

<sup>1</sup>Department of Radiology, Children's Memorial Hospital and Northwestern University Medical School, 3300 Children's Plaza, Chicago, IL 60614. Address reprint requests to T. P. Naidich.

<sup>2</sup>Division of Neurosurgery, Children's Memorial Hospital and Northwestern University Medical School, Chicago, IL 60614.

AJNR 5:221-234, May/June 1984  
0195-6108/84/050221-00\$0.00  
© American Roentgen Ray Society

## Sonography of Brain Tumors in Infants

Bokyung K. Han<sup>1</sup>  
Diane S. Babcock  
Alan E. Oestreich

Cranial sonograms of six children with brain tumors (one newborn, four infants, a one 4-year-old child) are presented. In four, sonography showed a large tumor mass and displacement of adjacent structures. In two, the tumors were demonstrated as areas of abnormal brain parenchymal echogenicity without obvious mass effect. Two of the tumors were diffusely echogenic, one was primarily cystic, and three were of mixed echogenicity. Areas of cystic degeneration and calcification within the tumors were demonstrated. Correlation was made with cranial computed tomography (CT) in patients; in each case sonography accurately demonstrated the location and extent of the tumor. Since sonography is used as a screening procedure in infants with a large head or an abnormal neurologic examination, sonography may be the first examination to demonstrate the tumor mass. However, since the sonographic features are nonspecific for neoplasms, further clarification of the process by CT should be recommended.

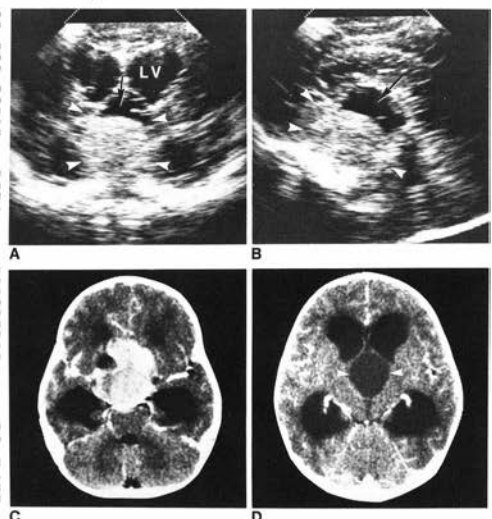
Sonography has become an important imaging method for the evaluation of infant head. Its value in the recognition and follow-up of patients with hydrocephalus and intracranial hemorrhage has been well established [1-6]. However, little information is available about the sonographic appearance of brain tumors [1, 2, 7]. We present our experience with brain tumors in six patients.

### Materials and Methods

Of 1528 children who had cranial sonograms at Children's Hospital Medical Center, from May 1978 to November 1982, six patients with histologically proven brain tumors were identified. Five patients were under 1 year of age and one patient was 4 years old when the diagnosis was made. Cranial sonograms were obtained with a static or in-time scanner in both axial, coronal, and sagittal planes. A 3.5- or 5.0 MHz transducer was used. In the five infants under 1 year old, the sonogram was obtained through the open fontanelles. In the 4-year-old child, sonography was possible because of the skull sutures due to increased intracranial pressure. Sonographic findings were compared with computed tomographic (CT) findings in all six patients. Five patients had plain films of the skull and three patients had brain angiography. The patients' charts were reviewed clinically.

### Results

Most patients presented with nonspecific symptoms of increased intracranial pressure. Sonographic and radiographic findings are summarized in table 1. There were four astrocytomas, one teratoma, and one ependymoma. In five of the children, the tumor was supratentorial. In four (cases 1, 3, 4, and 5), sonography showed a large tumor mass and displacement of adjacent structures (figs. 1, 2, and 4). In two (case 2 and 6), there were no mass effects, and sonography demonstrated changes in brain parenchymal echoes and architecture (figs. 2 &



This article appears in the May/June 1984 issue of AJNR and the July 1984 issue of AJR. Received May 31, 1983; accepted after revision October 26, 1983.

<sup>1</sup>All authors: Division of Radiology, Children's Hospital Medical Center, and Departments of Radiology and Pediatrics, University of Cincinnati College of Medicine, Cincinnati, OH 45229. Address reprint requests to B. K. Han, Children's Hospital Medical Center, Eland & Bethesda Ave., Cincinnati, OH 45229.

AJNR 5:253-259, May/June 1984  
0195-6108/84/050253-00\$0.00  
© American Roentgen Ray Society

## Use of Balanced Steady-State Free Precession Sequences in Evaluation of Drop Metastases

Recently, an overseas colleague had reached out to us, having trouble implementing the sequences suggested by Buch et al<sup>1</sup> for their patients in pediatric oncology. We believe that the issue was rooted in some inaccuracies relating to the sequences described in the article. We are writing this letter to clarify the terminology and sequence families for those who wish to use these classes of sequences. This letter by no means reduces the value of the article. We are quite happy to see that Buch et al have done a formal evaluation of the potential advantages of these sequences in further evaluation of drop metastases over previous anecdotal evidence.

3D driven equilibrium pulses typically are not relevant to or applied in balanced steady-state free precession (bSSFP), which is a gradient recalled-echo sequence. These pulses use a  $-90^\circ$  flip of the spins to enhance the T1 recovery of CSF, for example, in short-TR 3D fast spin-echo sequences.<sup>2</sup> This results in a bright CSF signal in relatively short time, though it does not have true T2-weighting.

In addition, regular bSSFP sequences (also known as true fast imaging with steady-state precession [TruFISP], FIESTA, and balanced fast-field echo [bFFE] by various manufacturers) will not work well for the reported intended purposes of Buch et al<sup>1</sup> due to phase shift errors and banding, particularly considering the long TR of 3D sequences.<sup>3</sup> However, a further modification of bSSFP needs to be made using 2 back-to-back sequence pairs with and without phase alterations and using maximum intensity projection at the end to cancel the phase errors, hence the longer acquisition times. This additional modification has been implemented as FIESTA-C (not FIESTA) and CISS and is the one to which the authors would have been referring.<sup>4</sup>

On another note, one must consider that the presumed benefits of using these balanced SSFP sequences compared with T1-weighted images is highly dependent on how the baseline T1-weighted images are acquired and if other sequences, such as high-quality T2-weighted sequences, are used in the protocol as well. Having more than one plane postcontrast T1-weighted image, using newer thin-section T1-weighted images, and combining them with relatively higher resolution T2-weighted images will likely dampen the advantages of bSSFP because they will no longer be compared with a limited single-plane spin-echo T1-weighted sequence. Nevertheless, using high-resolution bSSFP-derived sequences can certainly be useful.

### REFERENCES

1. Buch K, Caruso P, Ebb D, et al. **Balanced steady-state free precession sequence (CISS/FIESTA/3D driven equilibrium radiofrequency reset pulse) increases the diagnostic yield for spinal drop metastases in children with brain tumors.** *AJNR Am J Neuroradiol* 2018;39:1355–61 [CrossRef Medline](#)
2. Melhem ER, Itoh R, Folkers PJ. **Cervical spine: three-dimensional fast spin-echo MR imaging—improved recovery of longitudinal magnetization with driven equilibrium pulse.** *Radiology.* 2001;218:283–88 [CrossRef Medline](#)
3. Bieri O, Scheffler K. **Fundamentals of balanced steady state free precession MRI.** *J Magn Reson Imaging.* 2013;38:2–11 [CrossRef Medline](#)
4. Casselman JW, Kuhweide R, Deimling M, et al. **Constructive interference in steady state-3DFT MR imaging of the inner ear and cerebellopontine angle.** *AJNR Am J Neuroradiol* 1993;14:47–57 [Medline](#)

✉ A. Vossough

Children's Hospital of Philadelphia  
University of Pennsylvania  
Philadelphia, Pennsylvania

✉ E.R. Melhem

Department of Radiology  
University of Maryland Medical Center  
Baltimore, Maryland

<http://dx.doi.org/10.3174/ajnr.A5964>

**REPLY:**

**W**e appreciate the comments made by Drs Vossough and Melhem and wish to clarify the techniques described in our article.

We acknowledge your comment that 3D driven equilibrium pulses are not typically relevant to or applied in balanced steady-state free precession (bSSFP), which is a gradient recalled-echo sequence. By the use of this term in the title, we did not mean to imply a technical equivalency but simply included the 3D driven equilibrium radiofrequency reset pulse in this setting because of its use in similar indications, such as the evaluation of drop metastases or vestibular schwannomas on a Philips platform.

While your comments about bSSFP, off-resonance banding artifacts, long TRs, and the 2-pass phase alternation strategy for mitigating phase-shift errors and banding are well taken, FIESTA sequences do work well, in our experience, for the evaluation of drop metastases. We found that these artifacts are less troublesome when using a TR of 5.288–5.948 ms on our 1.5T Signa scanner (GE Healthcare, Milwaukee, Wisconsin). In fact, our study includes cases with FIESTA and does not include cases with

the longer 2-pass FIESTA-C version. On the 3T Tim Trio (Siemens, Erlangen, Germany) scanner platform, however, the TR of 11.69 ms is quite long for a bSSFP scan, especially at 3T in which the phase cycling of the different signal pathways will be increased, and this was the very reason why the 2-pass CISS approach was used.

Our article provides accurate parameters and sequence designations for both the CISS and FIESTA sequences used on all patients included in our study.

In our article, we highlighted the utility of the bSSFP sequence as an adjunct to the postcontrast T1-weighted images of the spine for the detection of drop metastases in pediatric patients with primary brain tumors. While newer thin-section imaging techniques may potentially improve the diagnostic yield of postgadolinium T1 imaging for the evaluation of drop metastases, we believe the bSSFP sequence will remain very useful, particularly in the setting of nonenhancing and small drop metastases.

● **K. Buch**

● **S. Rincon**

● **P. Caruso**

Department of Neuroradiology

● **J.E. Kirsch**

MR Division, Department of Radiology

Massachusetts General Hospital

Boston, Massachusetts

<http://dx.doi.org/10.3174/ajnr.A6049>

## Across the Pons and to the Milky Way: Where Are the Neuroradiology Publications?

Five years ago, we published an article in the *American Journal of Neuroradiology* that demonstrated that publications describing imaging features of various uncommon CNS diseases predominate in the clinical, rather than radiology, literature.<sup>1</sup> Short, simple, and purely an enumeration of journal articles, Impact Factors, and radiologist authorship, our article was a practical wake-up call to authors, reviewers, and publishers of radiologic content that remains relevant today. Specifically, there continue to be frequent reports of novel neuroradiology findings of important conditions, even in instances in which such imaging findings are the primary purpose, embedded within the nonradiology literature. While a clinician target audience is understandable in many cases in which the impact of such findings on clinical care is paramount, even in these instances, acknowledged neuroradiology interpretation of the images and neuroradiology authorship can be lacking.<sup>1</sup>

For example, consider just 1 disease process: progressive multifocal leukoencephalopathy. A few months ago, an interesting case report described the “punctate MR imaging pattern” in the setting of systemic lupus erythematosus-associated progressive multifocal leukoencephalopathy.<sup>2</sup> This case report is found in a clinical journal with authors affiliated with neurology, pathology, and virology departments. Various other recently reported imaging patterns or “signs” of progressive multifocal leukoencephalopathy discussed within this article or related articles include the “across the pons sign,” “inverse trident sign,” “barbell sign,” “laminar cortical hypointensity” and other findings on susceptibility-weighted imaging, and the “Milky Way” appearance.<sup>2-8</sup> Although some of these other articles on this topic did include representation of radiologists in the authorship list, only the “barbell sign” was found to be primarily described in a radiology journal. To research further, I performed a PubMed search from January 1, 2017, to January 1, 2019, with the following criteria: (MR imaging OR MR imaging) AND (PML or progressive multifocal leukoencephalopathy). This search resulted in 96 publications, 6 (6%) of which were published in radiology journals.

Clinicians may be exposed to (and, indeed, may independently author) articles describing neuroradiology features and

signs that could evade members of the neuroradiology community. Although the reasons for this phenomenon of radiology descriptions appearing in clinical journals are multifactorial, 1 factor is that a high percentage of these signs are found in case reports, which are still published in some clinical journals but not as frequently in radiology journals. Other factors may include the larger number of clinical, compared with radiology, journals or perhaps articles by highly subspecialized clinicians who have a preference for publishing in a clinical journal.

One could submit that in the era of electronic article searches, the precise journal classification is less relevant than it was in the past. However, it is not always easy to find these described findings embedded in clinical journals during a busy shift, and neuroradiologists may not be prompted to search for them if they are unaware of their existence. In addition, due to blinding of the peer-review process, it is not known how frequently radiologists are invited to participate in the adjudication of such articles before publication in clinical journals, potentially contributing to variability in the utility and accuracy of reported findings. Five years after our study demonstrated a preponderance of neuroradiology-focused literature published in clinical journals, it appears as though this practice persists. It is incumbent on the neuroradiologist to be cognizant of alternate sources of information and to challenge and/or validate findings in the peer-reviewed radiology literature. Finally, wherever possible, it is important that neuroradiologists be visible within multidisciplinary care teams and engaged in clinical research. Such participation may help raise the quality of reporting of radiologic findings and ensure that they are represented in the appropriate specialty literature sources.

### REFERENCES

1. Lehman VT, Doolittle DA, Hunt CH, et al. **Intracranial imaging of uncommon diseases is more frequently reported in clinical publications than in radiology publications.** *AJNR Am J Neuroradiol* 2014;35:45–48 CrossRef Medline
2. Ishii J, Shishido-Hara Y, Kawamota M, et al. **A punctate magnetic resonance imaging pattern in a patient with systemic lupus erythematosus is an early sign of progressive multifocal leukoencephalopathy: a clinicopathologic study.** *Intern Med* 2018;57:2727–34 CrossRef Medline
3. Hodel J, Darchis C, Outteryck O, et al. **Punctate pattern: a promising**

- imaging biomarker for the diagnosis of natalizumab-associated PML. *Neurology* 2016;86:1516–23 CrossRef Medline
4. Jain RS, Nagpal S, Tejwani S. ‘Hot-cross bun’ and ‘inverse trident sign’ in progressive multifocal leukoencephalopathy with HIV seropositivity. *Neurol India* 2014;62:341–42 CrossRef Medline
  5. Sinnecker T, Othman J, Kühl M, et al. 7T MRI in natalizumab-associated PML and ongoing MS activity: a case study. *Neurol Neuroimmunol Neuroinflamm* 2015;2:e171 CrossRef Medline
  6. Bezuidenhout AF, Andronikou S, Ackermann C, et al. “Barbell Sign”: a diagnostic imaging finding in progressive multifocal leukoencephalopathy. *J Comput Assist Tomogr* 2018;42:527–30 CrossRef Medline
  7. Pontillo G, Cocozza S, Lanzillo R, et al. Brain susceptibility changes in a patient with natalizumab-related progressive multifocal leukoencephalopathy: a longitudinal quantitative susceptibility mapping and relaxometry study. *Front Neurol* 2017;8:294 CrossRef Medline
  8. Papadimitropoulos GN, Lachanis S, Zompola C, et al. Laminar cortical hypointensities in susceptibility-weighted imaging in a case of progressive multifocal leukoencephalopathy. *J Clin Neurol* 2017;13:201–02 CrossRef Medline

© V.T. Lehman

Department of Radiology  
Mayo Clinic College of Graduate Medical Education  
Rochester, Minnesota

## Radiogenomics in Medulloblastoma: Can the Human Brain Compete with Artificial Intelligence and Machine Learning?

We read with keen interest “MR Imaging-Based Radiomic Signatures of Distinct Molecular Subgroups of Medulloblastoma” published recently in your prestigious journal.<sup>1</sup> We would like to congratulate the authors for their multi-institutional collaborative study wherein radiomic features extracted from MR imaging coupled with machine learning led to the prediction of molecular subgroups in medulloblastoma. Recently, it has become increasingly possible to extract meaningful information beyond staging from diagnostic imaging (radiophenotypes) for correlation with genomic data and molecular markers (molecular phenotypes), leading to the exciting and emerging field of radiogenomics.<sup>2,3</sup> The introduction of computer-based algorithms (including artificial intelligence and machine learning approaches) has not only refined the assessment of semantic features but also allows simultaneous extraction of agnostic features (histograms, textures, wavelets, and fractal dimensions), which generally go beyond the limited capabilities of the human brain. Such automated high-throughput processing of big data significantly reduces time and virtually eliminates interobserver variability.

In the referenced study, Iv et al,<sup>1</sup> extracted 590 radiomic features such as intensity-based histograms, tumor-edge sharpness, Gabor features, and local area integral invariant features from T1- and T2-weighted MR imaging in a multi-institutional cohort of 109 children with medulloblastoma and used support vector machine algorithms to identify the 4 molecular subgroups: wingless (WNT), sonic hedgehog (SHH), group 3, and group 4, respectively. Receiver operating characteristic (ROC) analysis revealed better performance of the double 10-fold cross-validation model for predicting SHH, group 3, and group 4 medulloblastoma using a combination of T1- and T2-weighted images as demonstrated by high area under the curve (AUC) values. The independent 3-dataset cross-validation strategy demonstrated acceptably high predictive accuracy of select radiomic features for SHH and group 4 medulloblastoma.

Most interesting, we had also reported similar results<sup>4</sup> in a single-institution cohort of 111 patients with medulloblastoma, which, surprisingly, was not even cited by the authors. In our study, preoperative multiparametric MR imaging (primarily T1-

and T2-weighted sequences including postcontrast images) was rigorously evaluated visually by a multidisciplinary team of radiologists and clinicians (blinded to molecular subgrouping) to document and categorize a set of 13 predefined semantic imaging features and assign a probable molecular subgroup. Two-thirds of patients were chosen randomly from individual subgroups to form the training cohort, while the remaining one-third constituted the validation cohort. Multinomial logistic regression analysis was performed in the training cohort to identify imaging features with the highest discrimination of 1 subgroup from the other 3 subgroups to construct subgroup-specific binary nomograms, which were subsequently tested in the validation cohort. Predictive accuracy of subgroup-specific nomograms was defined by AUC on ROC analysis, which was highest for the SHH subgroup followed by group 4 medulloblastoma. Group 3 and WNT subgroup nomograms had suboptimal and unacceptable accuracy.

A comparison of the predictive accuracy of MR imaging features (radiomic versus semantic) for molecular subgrouping of medulloblastoma is presented in the Table. A somewhat similar (if not better) performance of the human brain compared with computer-based algorithms via artificial intelligence and machine learning approaches, though somewhat intriguing, is quite reassuring and encouraging. Neither radiomic nor semantic MR imaging features identified the WNT pathway (best survival) and group 3 medulloblastoma (worst survival) robustly and accurately, posing considerable challenges in adopting imaging biomarkers in contemporary neuro-oncologic practice. However, we do believe that the inclusion of advanced and additional MR imaging sequences like diffusion-weighted imaging, gradient-echo,

**Comparison of predictive accuracy defined as AUC on ROC analyses reported in the 2 studies<sup>1,4</sup>**

Molecular Subgrouping of Medulloblastoma	AUC Using Radiomic MRI Signatures		AUC Using Semantic MRI Features	
	Double 10-Fold Cross-Validation Model	3-Dataset Cross-Validation Model	Training Cohort (n = 76)	Validation Cohort (n = 35)
WNT	0.45	0.45	0.75	0.69
SHH	0.79	0.70	0.94	0.99
Group 3	0.70	0.39	0.73	0.60
Group 4	0.83	0.80	0.85	0.79

and spectroscopy, coupled with further technologic refinement of advanced machine-classifier tools could potentially further improve the predictive accuracy of such radiogenomic correlation.

## REFERENCES

1. Iv M, Zhou M, Shpanskaya K, et al. **MR imaging-based radiomic signatures of distinct molecular subgroups of medulloblastoma.** *AJNR Am J Neuroradiol* 2019;40:154–61 CrossRef Medline
2. Kuo MD, Jamshidi N. **Behind the numbers: decoding molecular phenotypes with radiogenomics: guiding principles and technical considerations.** *Radiology* 2014;270:320–25 CrossRef Medline
3. Zhou M, Scott J, Chaudhury B, et al. **Radiomics in brain tumor: image assessment, quantitative feature descriptors, and machine-learning approaches.** *AJNR Am J Neuroradiol* 2018;39:208–16 CrossRef Medline
4. Dasgupta A, Gupta T, Pungavkar S, et al. **Nomograms based on pre-operative multiparametric magnetic resonance imaging for prediction of molecular subgrouping in medulloblastoma: results from a radiogenomics study of 111 patients.** *Neuro Oncol* 2019;21:115–24 CrossRef Medline

● A. Dasgupta

● T. Gupta

Department of Radiation Oncology  
Tata Memorial Centre  
Mumbai, India